

Search for Compressed Supersymmetry in Electroweak Vector Boson Fusion Topologies with 0-, 1-
and 2- Low Energy Lepton Final States in Proton-Proton Collisions at $\sqrt{s} = 13$ TeV

By

Brenda Fabela Enriquez

Dissertation

Submitted to the Faculty of the
Graduate School of Vanderbilt University
in partial fulfillment of the requirements
for the degree of

DOCTOR OF PHILOSOPHY

in

Physics

May 31, 2022

Nashville, Tennessee

Approved:

Alfredo Gurrola, Ph.D.

Paul Sheldon, Ph.D.

Will Johns, Ph.D.

David Ernst, Ph.D.

Julia Velkovska, Ph.D.

Copyright © 2022 Brenda Fabela Enriquez
All Rights Reserved

To my Mom and sisters Nathalie and Cristina: you are my home, the most divine and precious gift in my life. There is nothing I could ever do without you, and your unconditional love and support. God gave me the best family to walk this journey, and navigate this wonderful life together. I love you with my whole heart.

To my aunt María del Carmen, my aunt María del Rosario, my cousin Ana Karen, my uncle Rubén, and his wife María Elena: the time we shared in this world was not enough, and though I miss you every day, I can feel your loving presence every moment,

and,

to my grandfather Juan: every time I see my eyes in the mirror, I know you are with me. You had to leave before I concluded this chapter of my life, but I have faith in that you are proud of who I am and of how far I have come.

Para mi Mamá y hermanitas Nathalie y Cristina: ustedes son mi hogar, el más divino y preciado regalo en mi vida. No hay nada que yo pueda lograr sin ustedes, sin su amor y apoyo incondicionales. Dios me dio la mejor familia para acompañarme en este viaje, y para navegar juntas esta maravillosa vida. Las amo con todo mi ser.

Para mi tía María del Carmen, mi tía María del Rosario, mi prima Ana Karen, mi tío Rubén, y su esposa María Elena: nuestro tiempo en este mundo no fue suficiente, y aunque los extraño cada día, puedo sentir su presencia amorosa en cada momento,

y,

para mi abuelito Juan: cada vez que veo mis ojos en el espejo, sé que usted está conmigo. Sé que tuvo que partir antes de que yo cerrara este capítulo de mi vida, pero tengo fe en que está orgulloso de quien soy y de lo lejos que he llegado.

ACKNOWLEDGMENTS

Writing the acknowledgments is an excellent appreciation exercise about the journey these years have meant. I have learned and grown a lot in the professional aspect, in that way, fulfilling one of the goals of my Ph.D. program. Personally, I dare to say that the life lessons I have gained in this period of time are way greater and more valuable. There are many of them, which I commit to share in my day-to-day, through my ideas, thoughts, words, and actions. It is important to mention that I have never walked throughout this journey alone. I have been surrounded by people who love me, who care about me, and support me in the best way they can.

First of all, I thank God for allowing me to arrive to this point of my life, healthy, complete, and alongside my family, despite of the big challenges that have come our way, including a long pandemic. I thank and acknowledge my mom, for always supporting me and loving me beyond measure; for raising me to be a persevering and upstanding woman, and also a woman of faith. Thank you mom for being my light and my safe place; you are the best mom in the world without a doubt. I thank my sisters Nathalie and Cristina, for being the best sisters in the world, for filling my life with joy and wisdom, and for always being with me. To my grandparents, my uncles, aunts, and cousins, thank you for your love and praying for me every day. I thank my friends who have stayed with me throughout the years and the distance, from high school and college to graduate school; for being with me in the good times, and staying in the challenging ones. Thank you for sharing with me your love and showing me that good friendships exist. I always carry you in my thoughts and heart.

I am deeply grateful to the members of my Ph.D. committee. I thank my thesis advisor, Dr. Alfredo Gurrola, for contributing to my professional growth and his guidance in the world of high energy physics. Thanks to Dr. Paul Sheldon and his wife Sue Sheldon, for their sincere support and genuine friendship. I thank Dr. Will Johns for being a great listener and offering me sensible words. I thank Dr. David Ernst and Dr. Julia Velkovska, for trusting me before knowing me, and for giving me the opportunity to grow in the Physics department at Vanderbilt University. I specially acknowledge Dr. Alejandro Puga Candelas, for his continued support as a mentor, even after graduating from college, and for being a great and true friend. Also, I thank all my teachers, mentors, professors, and advisors, who have been part of my education since day one, for sharing their knowledge with me. Most importantly, I thank you because, with your words and actions, you have motivated me to keep moving forward in my career, and you have provided me with the opportunities I needed. I thank my fellow graduate students, for trusting me and allowing me to guide them, while learning together. Thanks to the students who I have had the pleasure to work with, for giving me the gift of learning through teaching. Thanks to my friend Savanna for all the shared adventures, and for the amount of growth we have achieved together during these years.

Last, but not least, I thank six-year-old Brenda who, one day, with the help of her mom, counted the number of years left to finish her education. Thank you, little Brenda, for all your effort, and your determination to learn and keep going. Back then it seemed too far away in time, and we have finally reached the end of that count. Thank you for all the dedication and love you have put to bring me to this point of space and time. You have always been enough and deserving of everything you have dreamed of. I promise you I will continue your legacy, and together we will keep growing and materializing that that we have yet to live. I love you with all my being.

AGRADECIMIENTOS

Escribir estos agradecimientos es un excelente ejercicio de apreciación por todo el camino recorrido durante estos años. Es cierto que he aprendido mucho en el aspecto profesional, cumpliendo así con uno de los objetivos de mi formación de doctorado. En lo personal, me atrevo a decir que las lecciones de vida que he ganado son muchísimo mayores y más valiosas. Hay tantas de ellas, y me comprometo a compartirlas en mi día a día, a través de mis ideas, pensamientos, palabras, y acciones. Es muy importante mencionar que este caminar jamás ha sido solitario. Siempre he estado rodeada de personas que me aman, me estiman, y me apoyan siempre de la mejor manera que está a su alcance.

Primero, le doy gracias a Dios por permitirme llegar a este punto de mi vida, sana, completa, y junto con mi familia, a pesar de los retos tan grandes que hemos enfrentado, incluyendo una larga pandemia. Gracias a mi mamá, por siempre apoyarme y amarme sin medida, por educarme para ser una mujer perseverante, de bien y de fe. Gracias por ser mi luz y mi lugar seguro; tú eres sin duda alguna la mejor mamá del mundo. Gracias a mis hermanitas Nathalie y Cristina, por ser también las mejores hermanas del mundo, por llenar mi vida de alegría y sabiduría, y por acompañarme siempre. A mis abuelitos, mis tíos, tías, y primos, gracias por su amor y tenerme en sus oraciones. Gracias a mis amigas y amigos, quienes han permanecido conmigo a través de los años y de la distancia, desde la preparatoria y licenciatura hasta el doctorado; por acompañarme en los buenos momentos, y no dejarme sola en los difíciles. Gracias por compartir conmigo su cariño, y demostrarme que las amistades buenas existen. A ustedes los llevo siempre en mi pensamiento y mi corazón.

Expreso mi profunda gratitud para los miembros de mi comité doctoral: mi asesor, el Dr. Alfredo Gurrola, gracias por ser partícipe de mi crecimiento profesional, y guiarme en el mundo de la física de altas energías; al Dr. Paul Sheldon y su esposa Sue Sheldon por su apoyo y amistad sinceros; al Dr. Will Johns por escuchar atento y ofrecerme palabras sensatas. Gracias al Dr. David Ernst y la Dra. Julia Velkosvka, por confiar en mí aún sin conocerme, y darme la oportunidad de crecer en el departamento de Física de Vanderbilt University. Un agradecimiento especial a mi tutor, el Dr. Alejandro Puga Candelas, por continuar siendo mi mentor aún después de terminar mi licenciatura, y por ser un gran y verdadero amigo. También agradezco a todos los maestros, mentores, profesores, y asesores que han formado parte de mi formación académica desde el primer día, no sólo por compartir su conocimiento conmigo... Les agradezco aún más, porque, con sus palabras y acciones, me han motivado a seguir adelante en mi carrera, y me han dado las oportunidades que he necesitado. Agradezco a mis compañeros de doctorado, por confiar en mí y permitirme guiarlos mientras aprendíamos juntos. A los estudiantes con quienes he tenido el placer de trabajar, gracias por darme el regalo de aprender enseñando. Muchas gracias también a mi amiga Savanna, por todas las aventuras compartidas y lo mucho que hemos crecido juntas durante estos años.

Por último, pero no menos importante, le doy gracias a Brenda de seis años, que un día, con la ayuda de su mamá, hizo la cuenta de los años que le faltaban para terminar su educación. Gracias, pequeña Brenda, por todo tu empeño, tus ganas de aprender y de salir adelante. En ese entonces parecía muy lejano, y ahora hemos llegado al final de esa cuenta. Gracias por la dedicación y amor que has puesto para traerme hasta aquí. Siempre has sido suficiente y mercedora de todo lo que has soñado. Te prometo que continuaré tu legado, y juntas seguiremos creciendo y cristalizando todo aquello que nos falta por vivir. Te amo con todo mi ser.

TABLE OF CONTENTS

	Page
LIST OF TABLES	ix
LIST OF FIGURES	xiii
1 Introduction	1
2 Theoretical motivation	4
2.1 The standard model of particle physics	4
2.2 Open questions in the SM	20
2.3 Supersymmetry as a solution to the SM issues	23
2.4 Dark matter: bridge between particle physics and cosmology	28
3 Experimental motivation	43
3.1 Dark matter detection techniques	43
3.2 Compressed SUSY searches at hadron colliders	44
3.3 Electroweak vector boson fusion	45
4 Objective of the study	51
4.1 Description of the research project	51
4.2 Physics models for interpretation of results	52
5 The LHC and the CMS detector	56
5.1 The Large Hadron Collider (LHC)	56
5.2 The Compact Muon Solenoid detector (CMS)	59
6 Event reconstruction and particle identification with the Particle Flow (PF) algorithm	69
6.1 Basic elements of the PF algorithm	69
6.2 Particle reconstruction and identification	80
7 Event reconstruction and physics objects for data analysis at CMS	86
7.1 Pileup interactions	86
7.2 Muons	88
7.3 Electrons	91
7.4 Jets	96
7.5 Missing transverse momentum	112
7.6 Hadronic tau leptons	115
7.7 b-quark jets	127
8 Data and simulation samples	131
8.1 Signal simulation samples	131
8.2 Background simulation samples	136
8.3 Data samples	137

9	Analysis strategy	140
9.1	Description of analysis strategy	140
9.2	Signal region event selections	144
9.3	Event selection optimization in the 2-lepton signal regions	146
10	Background estimation	163
10.1	Description of the methodology	163
10.2	Calibration of central and VBF efficiencies	164
10.2.1	Z+jets	164
10.2.2	$t\bar{t}$ +jets	176
10.2.3	Diboson	186
10.3	QCD multijet background estimation	196
10.4	Final remarks on background estimation	207
11	Uncertainties	208
11.1	Statistical uncertainties	208
11.2	Systematic uncertainties	209
12	Results with $\mathcal{L}_{int} = 35.9 \text{ fb}^{-1}$ and interpretation	213
12.1	Results	213
12.2	Interpretation	213
13	Projection of interpretations with $\mathcal{L}_{int} = 137 \text{ fb}^{-1}$	218
13.1	Prediction in the signal region	218
14	Conclusions and future work	224
A	Jets	226
A.1	Introduction	226
A.2	Hard scattering processes	227
A.3	Parton showering	232
A.4	Matching and merging	238
A.5	Underlying event	240
A.6	Hadronization models	245
A.7	Jet fragmentation functions	252
A.8	Summary and conclusions	254
	References	256

LIST OF TABLES

Table	Page	
2.1	Chiral and gauge supermultiplets in the MSSM [7].	27
2.2	Particle content of the MSSM, considering the sfermion mixing of the first two generations to be negligible [7].	28
2.3	Cosmological parameters measured by the Planck collaboration [59, 62], where $h = H_0/(100 \text{ km/s/Mpc})$ is the reduced Hubble parameter.	31
4.1	Event composition ratio for different electroweakino pair combinations included in the signal processes. In both interpretations, the fractions correspond to a benchmark scenario $m(\tilde{\chi}_2^0) = 100 \text{ GeV}$; in the higgsino case a $\Delta m(\tilde{\chi}_2^0, \tilde{\chi}_1^0) = 5 \text{ GeV}$ was considered.	52
4.2	Description of the branching ratios for SUSY particles in various SUSY physics interpretations used in this analysis.	53
5.1	Values of LHC key parameters for pp collisions in Run II [96].	58
5.2	Properties of lead tungstate PbWO_4 crystals.	63
6.1	Seeding configuration and targeted tracks of the ten tracking iterations. R is the targeted distance between the track production position and the beam axis [111].	71
6.2	Clustering parameters for the ECAL, HCAL and preshower. All values result from optimizations based on the simulation of single photons, π^0 , K_L^0 , and jets [111]. .	76
7.1	Selection criteria for the loose and tight muon ID definitions.	89
7.2	Selection criteria for the customized soft muon SUSY ID [128].	91
7.3	Selection criteria for the veto and loose electron ID working points and their corresponding efficiencies. Electron candidates are classified according to the η position of the corresponding SC as barrel ($ \eta \leq 1.479$) or endcap ($ \eta > 1.479$) electrons. .	95
7.4	Selection criteria for the medium and tight electron ID working points and their corresponding efficiencies. Electron candidates are classified according to the η position of the corresponding SC as barrel ($ \eta \leq 1.479$) or endcap ($ \eta > 1.479$) electrons.	95
7.5	Selection criteria for the customized soft electron SUSY ID [128].	96
7.6	Jet identification criteria for the loose PF jet ID working point (2016).	109
7.7	Jet identification criteria for the tight PF jet ID working point (2017).	110
7.8	Jet identification criteria for the tight PF jet ID working point (2018).	111
7.9	Summary of the decay modes and branching ratios of the τ lepton. The generic symbol h^- represents a charged hadron, pion or kaon.	116
7.10	Summary of the π^0 properties.	117
7.11	Description of the HPS decay modes based on the particle multiplicity of the τ_h decay, and the mass constraints applied during reconstruction.	119
7.12	Sources of misidentified τ_h leptons and their causes in descending order of importance.	120
7.13	Target τ_h identification efficiencies for the different working points defined for the three different DEEPTAU discriminators (Adapted from [141]).	123
7.14	Input variables used for the Run I version of the CSV algorithm and for the CSVv2 algorithm. The definition of the variables can be found in Ref. [142].	129
7.15	Taggers, working points and identification efficiency for b-jets with $p_T > 20 \text{ GeV}$ in simulated $t\bar{t}$ events (Adapted from [142]).	129
7.16	Discriminator cuts for the various working points and taggers. CSVv2 was not available for use in 2018 data.	130
8.1	Description of the signal data sets, including details on branching ratios for the SUSY signal interpretations.	132

8.2	Mixing parameters and values of the $(m(\tilde{\chi}_2^0), \Delta m)$ scan for the SUSY signal interpretations.	132
8.3	Mixing parameters, values of the $(\Lambda, m(\chi))$ scan for the ADM interpretation.	133
9.1	Selection criteria for the loose and tight muon ID definitions.	144
9.2	Definition of physics objects in the signal regions.	144
9.3	p_T requirements for the lepton vetoes applied in the signal regions.	144
9.4	Event selections in the signal regions for the VBF SUSY analysis.	145
9.5	Lepton multiplicity selections for the different signal regions considered in the VBF SUSY analysis.	145
9.6	Final event yields for signal and background in the $\mu\tau_h$ signal regions (OS and LS) for 2016-2018. Only statistical uncertainties have been included. Note: the QCD μ -enriched MC samples were used in these studies.	147
9.7	Expected ULs on the signal cross section for the signal point $m(\tilde{\chi}_2^0) = 300$ GeV and two Δm benchmark values in the OS $\mu\tau_h$ final state.	148
9.8	Expected ULs on the signal cross section for the signal point $m(\tilde{\chi}_2^0) = 300$ GeV and two Δm benchmark values in the LS $\mu\tau_h$ final state.	149
9.9	Expected ULs on the signal cross section for the signal points $m(\tilde{\chi}_2^0) = 300$ GeV and $\Delta m = 50$ and 75 GeV, combining OS+LS and the full Run II luminosity in the $\mu\tau_h$ +jj SRs.	149
9.10	Expected ULs on the signal cross section with the original and smooth background shapes for the signal point $m(\tilde{\chi}_2^0) = 300$ GeV and $\Delta m = 50$ GeV in the $\mu\tau_h$ SRs with the 2016 simulation data set.	153
9.11	Expected ULs on the signal cross section with the original and smooth background shapes for the signal point $m(\tilde{\chi}_2^0) = 300$ GeV and $\Delta m = 75$ GeV in the $\mu\tau_h$ SRs with the 2016 simulation data set.	154
9.12	Expected σ_{UL} for the signal points with $m(\tilde{\chi}_2^0) = 200$ GeV and $\Delta m = 30$ and 50 GeV in the OS $\mu\tau_h$ +jj SR with the 2016 simulation data set, comparing VBF1 and VBF2 selections.	160
9.13	Expected σ_{UL} for the signal points with $m(\tilde{\chi}_2^0) = 200$ GeV and $\Delta m = 30$ and 50 GeV in the LS $\mu\tau_h$ +jj SR with the 2016 simulation data set, comparing VBF1 and VBF2 selections.	161
9.14	Updated definition of physics objects after optimization of selections in the signal regions.	161
10.1	$Z(\rightarrow \tau_h\tau_h)$ +jets CR selection cuts.	165
10.2	Summary of SFs for the $Z(\rightarrow \tau_h\tau_h)$ +jets CR for all years, including central selections.	166
10.3	$Z(\rightarrow \tau^+\tau^- \rightarrow \mu\tau_h)$ +jets CR selection cuts.	168
10.4	Summary of event yields in the ABCD regions for the QCD estimation in the $Z(\rightarrow \tau_\mu\tau_h)$ +jets CR for 2016 after applying central and VBF2 selections. Uncertainties included in this table are only statistical.	170
10.5	Summary of event yields in the ABCD regions for the QCD estimation in the $Z(\rightarrow \tau_\mu\tau_h)$ +jets CR for 2017 after applying central and VBF2 selections. Uncertainties included in this table are only statistical.	170
10.6	Summary of event yields in the ABCD regions for the QCD estimation in the $Z(\rightarrow \tau_\mu\tau_h)$ +jets CR for 2018 after applying central and VBF2 selections. Uncertainties included in this table are only statistical.	170
10.7	Summary of results from the fits to a pol-0 and pol-1 polynomials of the leading $m(\text{jj})$ ratios in CRC and CRD ($\text{TF}_{\text{OS}\rightarrow\text{LS}}$) for VBF2 selections. The $\text{TF}_{\text{OS}\rightarrow\text{LS}}$ measured after applying central and VBF2 selections from the event yields in this region is also included.	171

10.8	Summary of results from the fits to a pol-0 and pol-1 polynomials of the leading $m(\text{jj})$ ratios in CRB and CRD ($\text{TF}_{\text{nom.} \rightarrow \text{inv. iso}}$) for VBF2 selections. The $\text{TF}_{\text{nom.} \rightarrow \text{inv. iso}}$ measured after applying central and VBF2 selections from the event yields in this region is also included.	172
10.9	Summary of SFs for the $Z(\rightarrow \tau_\mu \tau_h)$ +jets CR for Run II including central and VBF2 selections, including the QCD data-driven estimation. Only statistical uncertainties are included.	173
10.10	$t\bar{t} \rightarrow \mu \tau_h$ CR selection cuts.	176
10.11	Summary of SFs for the $t\bar{t}(\rightarrow \mu \tau_h)$ +jets CR for all years, including central, VBF1 and VBF2 selections. Only statistical uncertainties are included.	177
10.12	Summary of χ^2/N values in the largest $m(\text{jj})$ distributions in the $t\bar{t}(\rightarrow \mu \tau_h)$ +jets CR for 2016-2018, including VBF1 and VBF2 selections, after correcting with the central and VBF efficiency SFs.	185
10.13	Diboson $\rightarrow 3\mu$ CR selection cuts.	186
10.14	Summary of SFs for the diboson($\rightarrow 3\mu$) CR for all years, including central, VBF1 and VBF2 selections. Only statistical uncertainties are included.	187
10.15	Summary of χ^2/N values in the largest $m(\text{jj})$ distributions in the diboson($\rightarrow 3\mu$)+jets CR for 2016-2018, including VBF1 and VBF2 selections, after correcting with the central and VBF efficiency SFs. N/A means that there were not enough data points to perform a fit.	195
10.16	Summary of event yields in CRB, CRC, their combination (before applying the $ \Delta\phi(j, p_T^{\text{miss}}) _{\text{min}}$ cut), and, CRA for the QCD estimation in the $\tau_h \tau_h$ SRs for 2016 after applying central and VBF2 selections. The prediction for non-QCD backgrounds in the OS and LS $\tau_h \tau_h$ SR are shown as well.	198
10.17	Summary of results from the fits to a pol-0 and pol-1 polynomials of the $\text{TF}_{ \Delta\phi(j, p_T^{\text{miss}}) _{\text{min}}}$ vs. leading $m(\text{jj})$ for VBF2 selections. The $\text{TF}_{ \Delta\phi(j, p_T^{\text{miss}}) _{\text{min}}}$ measured from the event yields in this region is also included. The TF measured from the fit and event yields are consistent within statistical uncertainties.	198
10.18	Summary of results from the fits to a pol-0 and pol-1 polynomials of the $R_{\text{OS(LS)}}$ ratios vs. leading $m(\text{jj})$ in the $Z(\rightarrow \tau_\mu \tau_h)$ +jets CR. The $R_{\text{OS(LS)}}$ measured from the event yields in this region are also included. The ratios measured from the fit and event yields are consistent within statistical uncertainties.	200
10.19	Summary of event yields in CRB, CRC, and CRA for the QCD estimation in the $\tau_h \tau_h$ +jj SRs for 2017 after applying central and VBF2 selections.	201
10.20	Summary of event yields in CRB, CRC, and CRA for the QCD estimation in the $\tau_h \tau_h$ +jj SRs for 2018 after applying central and VBF2 selections.	201
10.21	Summary of event yields in CRB, CRC, and CRA for the QCD estimation in the $\mu \tau_h$ +jj SRs for 2016 after applying central and VBF2 selections.	202
10.22	Summary of event yields in CRB, CRC, and CRA for the QCD estimation in the $\mu \tau_h$ +jj SRs for 2017 after applying central and VBF2 selections.	203
10.23	Summary of event yields in CRB, CRC, and CRA for the QCD estimation in the $\mu \tau_h$ +jj SRs for 2018 after applying central and VBF2 selections.	203
10.24	Summary of event yields in CRA for the QCD estimation in the $e \tau_h$ +jj SRs for 2016-2018 after applying central and VBF2 selections.	205
10.25	Summary of R_{OS} and R_{LS} ratios obtained in the QCD background estimation for the $\ell \tau_h$ SRs.	206
10.26	Summary of $\text{TF}_{ \Delta\phi(j, p_T^{\text{miss}}) _{\text{min}}}$ obtained in the QCD background estimation for the $\ell \tau_h$ SRs.	206
10.27	Predicted event yields for the QCD multijet background in the various $\ell \tau_h$ +jj SRs.	206
11.1	Summary of event yield variations and absolute % differences $\left(\left \frac{N_{\text{nom}} - N_{\text{shift}}}{N_{\text{nom}}} \right \times 100 \right)$ in the OS $\tau_h \tau_h$ channel for JES uncertainties, including a benchmark signal point and a dominant background in this SR.	211

11.2	Summary of event yield variations and absolute % differences $\left(\left \frac{N_{\text{nom}}-N_{\text{shift}}}{N_{\text{nom}}}\right \times 100\right)$ in the 0-lepton channel for JES uncertainties, including a benchmark signal point and a dominant background in this SR.	211
12.1	Number of observed events and corresponding pre-fit background predictions, where “pre-fit” refers to the predictions determined as described in the text, before constraints from the fitting procedure have been applied. The uncertainties include the statistical and systematic components [171].	213

LIST OF FIGURES

Figure	Page
2.1	Summary of the SM particles, their charge, mass and spin [39]. 5
2.2	Pictorial representation of the QED Lagrangian with elements of Feynman diagrams. 9
2.3	Pictorial representation of the Higgs potential $V(\Phi)$ for different values of ρ and λ (Adapted from [42]). 13
2.4	Representative Feynman diagrams for the different one-loop corrections to the Higgs mass. 21
2.5	Galaxy rotation curve of a spiral galaxy [50]. 23
2.6	The SM particles and their supersymmetric counterparts when exact SUSY is assumed [58]. 25
2.7	Comparison of a thermal and a non thermal evolution of the early Universe (Adapted by [65]). 41
3.1	Diagram showing possible DM detection methods [71]. 43
3.2	Representative Feynman diagrams of SUSY production and decays which motivate searches for $\tilde{\chi}_1^0$ DM (Adapted from [72]). 44
3.3	Feynman diagrams for $\tilde{\chi}_2^0\tilde{\chi}_1^\pm$ production in pp collisions via DY and VBF processes. 45
3.4	Typical Feynman diagrams for $pp \rightarrow e^+\nu_e\mu^+\nu_\mu jj$ and $pp \rightarrow e^+\nu_e\mu^+\nu_\mu jj$ via VBF production [73]. 46
3.5	Representative Feynman diagrams for VBF Higgs production (Adapted from [73]). 47
3.6	Normalized LO differential distributions for VBF Higgs and W^+W^+ production at the LHC with $\sqrt{s} = 13$ TeV. The top row includes distributions for the leading (j_1) and sub-leading (j_2) jets. In the middle row, the rapidity of the leading jet (y_{j_1}) and the difference in rapidity for the VBF jets (Δy_{jj}) is shown. The bottom panel depicts the correlation between the dijet invariant mass $m(jj)$ and Δy_{jj} , as well as the histogram for $m(jj)$ [73]. 49
3.7	Initial comparison of (a) the angular jet η separation ($\Delta\eta(jj)$) and (b) the dijet invariant mass distributions for SM diboson background processes (solid) and signal (line), considering different $m_{\tilde{\chi}_1^\pm}$ hypothesis at parton level. The distributions are normalized to unity. 50
4.1	Representative Feynman diagrams for the wino-bino models with democratic light slepton decays (left), $\tilde{\tau}$ -dominated decays (middle), W^*/Z^* decays (right). 53
4.2	Representative Feynman diagram for the wino-bino model (left) and higgsino model (middle and right) with W^*/Z^* decays. 54
4.3	Representative Feynman diagrams for VBF ADM production. 55
5.1	The four main LHC detectors and its geographical location: ALICE, ATLAS, CMS, and LHCb [94]. 57
5.2	CERN accelerator complex [97]. 58
5.3	Transverse view of the CMS detector [99]. 60
5.4	Transverse cross section of a CMS detector slice [100]. 60
5.5	Left: Representative diagram of a CMS pixel module [101]. Right: Layout of the present (bottom) and upgraded (top) pixel detector in the $r - z$ plane [102]. 61
5.6	Left: Layout of a CMS silicon sensor [103]. Right: View of one quarter of the silicon strip tracker [103]. 62
5.7	Schematics of a quadrant of the tracking and calorimeters at CMS [104]. 64
5.8	Schematic view of the CMS HCAL geometry during the 2016 LHC operation [106]. 65
5.9	Single cells for each of the detector technologies used in the muon system of the CMS experiment [109]. 66

5.10	$r - z$ cross section of a quadrant of the CMS detector showing the geometry of the muon system. The DT stations are labeled as MB (Muon Barrel), the CSC stations as ME (Muon Endcap), and the RPC stations located in the barrel and the endcap are labeled RB and RE, respectively [107].	67
6.1	Efficiency and mis-reconstruction rate of the global combinatorial track finder (black squares) and the iterative tracking method (green triangles: prompt iterations based on seeds with at least one hit in the pixel detector; red circles: all iterations including those with displaced seeds), as a function of the track p_T , for charged hadrons in multijet events without pileup interactions. Efficiency and mis-reconstruction rate are determined only with tracks with $ \eta < 2.5$. The efficiency is displayed for tracks originating within 3.5 cm of the beam axis and ± 30 cm of the nominal interaction point along the beam axis (Adapted from [111]).	72
6.2	Event display of an illustrative jet made of five particles only on the (x, y) plane (top) and (η, ϕ) plane of the ECAL (lower left) and HCAL (lower right) surfaces. (Adapted from [111]).	75
6.3	Photon pair invariant mass distribution in the barrel ($ \eta < 1.0$) for simulation (left) and data (right). The π^0 signal is modeled by a Gaussian (red curve) and the background by an exponential function (blue curve). The Gaussian mean value (vertical dashed line) and its standard deviation are denoted as m^{fit} and σ_m , respectively. (Adapted from [111]).	78
6.4	Left: Calibration coefficients b and c obtained from single hadrons in the barrel as a function of E for different energy deposit configurations in the calorimeter clusters. Right: Relative raw and calibrated energy response and resolution for single hadrons in the barrel as a function of E . (Adapted from [111]).	79
7.1	Tag-and-probe efficiency for muon reconstruction and identification in 2015 data and simulation for tight muons with $p_T \geq 20$ GeV [127].	90
7.2	Efficiency for muon reconstruction and identification in 2017 data and simulation for tight muons with $2 < p_T < 40$ GeV as a function of p_T and η	90
7.3	Tag-and-probe efficiency for the tight PF isolation working point on top of the tight ID as a function of p_T for muons within the acceptance of the muon spectrometer (right) and pseudorapidity for muons with $p_T > 20$ GeV [127].	91
7.4	$\sigma_{\eta\eta}$ distribution for barrel electrons and jets [130].	93
7.5	Electron identification efficiency measured in data (top panels) and data-to-simulation efficiency ratios (bottom panels) as a function of the electron p_T for the medium cut-based working point for 2016-2018 data sets.	95
7.6	Electron identification efficiency measured in data (top panels) and data-to-simulation efficiency ratios (bottom panels) as a function of the SC η for the medium cut-based working point 2016-2018 data sets.	96
7.7	Jet reconstruction in a simulated dijet event. The particles clustered in the two PF jets are displayed with a thicker line. The PF jet \vec{p}_T , indicated with a radial line, is compared to the \vec{p}_T of the corresponding generated Ref and Calo jets. The 4-momentum of the jet is obtained by adding the 4-momenta of its constituents and no jet energy correction is applied (Adapted from [111]).	97
7.8	Jet angular resolution in the barrel (left) and endcap (right) regions, as a function of the p_T of the reference jet. The ϕ resolution is expressed in radians. (Adapted from [111]).	98
7.9	Jet angular resolution in the barrel (left) and endcap (right) regions, as a function of the p_T of the reference jet. The ϕ resolution is expressed in radians. (Adapted from [111]).	99
7.10	Jet angular resolution in the barrel (left) and endcap (right) regions, as a function of the p_T of the reference jet. The ϕ resolution is expressed in radians. (Adapted from [111]).	100

7.11	Jet angular resolution in the barrel (left) and endcap (right) regions, as a function of the p_T of the reference jet. The ϕ resolution is expressed in radians. (Adapted from [111]).	100
7.12	Jet angular resolution in the barrel (left) and endcap (right) regions, as a function of the p_T of the reference jet. The ϕ resolution is expressed in radians. (Adapted from [111]).	101
7.13	Consecutive stages of JEC for data and MC simulation. All corrections marked with MC are derived from simulation studies. RC stands for random cone, and MJB refers to the analysis of multijet events. (Adapted from [121]).	101
7.14	Data to simulation comparison for average offset per pileup interaction as a function of jet η , calculated for each type of PF candidates (Adapted from [133]).	103
7.15	Evolution of data to simulation scale factors in Run II for representative $\langle\mu\rangle$ for a given data period (Adapted from [133]).	103
7.16	Jet response correction based on simulation for the different data sets in Run II. (Adapted from [133]).	105
7.17	Relative η -dependent residual jet response corrections for the different data sets in Run II. (Adapted from [133]).	106
7.18	Comparison of the data-to-simulation ratio of the jet response measurements after applying the corrections for JES as well as the nuisance parameter values found by the global fit (L3 residual corrections). (Adapted from [133]).	106
7.19	Data-to-simulation η dependent scale factors for jet energy resolution for the different data sets in Run II. (Adapted from [133]).	107
7.20	Data-to-simulation η dependent scale factors for jet energy resolution for the 2018 data set. (Adapted from [133]).	108
7.21	Data-to-simulation η dependent scale factors for jet energy resolution for the 2018 dataset. (Adapted from [133]).	109
7.22	Distributions of PF jet variables for central jets $ \eta < 0.5$ as measured in signal enriched back-to-back dijet events and for noise enriched events from a minimum bias selection before applying the PF jet ID [135].	110
7.23	Data-to-simulation comparison for two input variables to the PU jet ID calculation for CHS jets with $30 < p_T < 50$ GeV [136].	111
7.24	Data-to-simulation comparison of the PU jet ID BDT output for AK4 CHS jets with $30 < p_T < 50$ GeV for the detector region within the tracker volume (left) and $3 < \eta < 5$ (right).	112
7.25	Feynman diagrams of the leptonic and hadronic τ lepton decay modes.	116
7.26	Schematics of the experimental signatures of the hadronic τ decays in the CMS detector [139].	117
7.27	Representative schematics for strip reconstruction in the CMS ECAL [139].	117
7.28	Pictorial representation of a τ_h candidate reconstructed with the HPS algorithm.	118
7.29	HPS efficiency for different τ_h decay topologies, estimated in $Z/\gamma^*(\rightarrow \tau\tau)$ simulated events [141].	119
7.30	Distributions, normalized to unity, in observables related to the isolation sums, used as input variables to the MVA-based isolation discriminant, for τ_h decays in simulated $Z/\gamma^* \rightarrow \tau\tau$ (blue) and jets in simulated W+jets (red) events [140].	121
7.31	Distributions, normalized to unity, in observables used as input variables to the MVA-based isolation anti-jet discriminant, for τ_h decays in simulated $Z/\gamma^* \rightarrow \tau\tau$ (blue) and jets in simulated W+jets (red) events [140].	122
7.32	Left: MVA output distribution for the anti-jet τ_h identification discriminant that includes lifetime information for τ_h decays in simulated $Z/\gamma^* \rightarrow \tau\tau$ (blue), and jets in simulated W+jets (red) events (Adapted from [138]). Right: Mis-identification probability as a function of τ_h identification efficiency evaluated using $H \rightarrow \tau\tau$ and QCD MC samples (Adapted from [140]).	123

7.33	τ_h identification efficiency for Z+jets events (inclusive leptonic decays) in 2016, 2017 and 2018, as a function of p_T^{reco} , using the various working points of the MVATAU anti-jet discriminator.	124
7.34	τ_h identification efficiency for $t\bar{t}$ events (2016: inclusive decays, 2017-2018: fully leptonic + semi leptonic decays), as a function of p_T^{reco} , using the various working points of the MVATAU anti-jet discriminator.	124
7.35	τ_h identification efficiency for $H \rightarrow \tau\tau$ events with 2018 simulation samples, as a function of p_T^{reco} , using the various working points of the MVATAU anti-jet discriminator.	125
7.36	τ_h identification efficiency for Z+jets events (inclusive leptonic decays) in 2016, 2017 and 2018, as a function of p_T^{reco} , using the various working points of the DEEPTAU anti-jet discriminator.	125
7.37	τ_h identification efficiency for $t\bar{t}$ events (2016: inclusive decays, 2017-2018: fully leptonic + semi leptonic decays), as a function of p_T^{reco} , using the various working points of the DEEPTAU anti-jet discriminator.	125
7.38	τ_h identification efficiency for $H \rightarrow \tau\tau$ events with 2018 simulation samples, as a function of p_T^{reco} , using the various working points of the MVATAU anti-jet discriminator.	125
7.39	τ_h mis-identification probability estimated in QCD multijet events, as a function of p_T^{reco} , using the various working points of the MVATAU anti-jet discriminator.	126
7.40	τ_h mis-identification probability estimated in QCD multijet events, as a function of p_T^{reco} , using the various working points of the DEEPTAU anti-jet discriminator.	126
7.41	Illustration of a heavy-flavor jet topology with a SV from the decay of a b or c hadron. (Adapted from [142]).	128
7.42	Distributions of the CSVv2 (left) and DeepCSV (right) discriminator values for jets of different flavors in $t\bar{t}$ events simulated with 2016 experimental conditions, normalized to unit area. (Adapted from [142]).	129
7.43	Efficiencies and mis-identification probabilities for the DeepCSV tagger as a function of jet p_T , jet η and PU multiplicity for b, c, and light flavor jets in $t\bar{t}$ for the various working points. (Adapted from [142]).	130
8.1	Transverse momentum distributions for the (left) leading and (right) sub-leading $\tilde{\chi}_i$	133
8.2	Angular (left) $\eta(\tilde{\chi}_{i,\text{lead}})$ (middle) $\Delta\phi(\tilde{\chi}_{i,\text{lead}}\tilde{\chi}_{j,\text{sublead}})$ and (right) $\Delta\phi(\tilde{\chi}_{j,\text{lead}},\tilde{j}_{i,\text{lead}})$ distributions.	133
8.3	Example diagram of relative \vec{p} between $\tilde{\chi}'_i$ s and VBF jets.	134
8.4	Kinematic distributions for the (right) jet transverse momentum, (middle) jet pseudorapidity and (left) invariant dijet mass.	134
8.5	(Transverse momentum distributions for the (left) leading and (right) sub-leading $\tilde{\chi}_i$	135
8.6	Angular (left) $\eta(\tilde{\chi}_{i,\text{lead}})$ (middle) $\Delta\phi(\tilde{\chi}_{i,\text{lead}}\tilde{\chi}_{j,\text{lead}})$ and (right) $\Delta\phi(\tilde{\chi}_{i,\text{sublead}}\tilde{\chi}_{j,\text{sublead}})$ distributions.	135
8.7	Kinematic distributions for the (right) jet transverse momentum, (middle) jet pseudorapidity and (left) invariant dijet mass.	135
8.8	Dilepton invariant mass distribution for two example combinations of $\{m(\tilde{\chi}_2^0), m(\tilde{\chi}_1^0)\}$. in the wino-bino and higgsino scenarios.	135
8.9	Kinematic distributions for jet transverse momentum, jet pseudorapidity, invariant dijet mass, and missing transverse momentum for the ADM interpretation.	136
8.10	Efficiency of the HLT_PFMETNoMu120_PFMHTNoMu120_IDTight trigger as a function of the offline p_T^{miss}	139
9.1	Initial kinematic comparison for the lepton p_T distribution between signal and the sum of all expected backgrounds with two different $\Delta m(\tilde{\chi}_2^0, \tilde{\chi}_1^0)$ scenarios.	141
9.2	Initial kinematic comparison for the $m_T(\mu, p_T^{\text{miss}})$ distribution between signal and the sum of all expected backgrounds with three different $\Delta m(\tilde{\chi}_2^0, \tilde{\chi}_1^0)$ scenarios.	141

9.3	Initial kinematic comparison for the jet p_T , jet η , leading $m(\text{jj})$, and p_T^{miss} distributions between signal and the sum of all expected backgrounds.	143
9.4	Representative Feynman diagrams for the $t\bar{t}$ and QCD multijet production. We assume $W \rightarrow \ell\nu_\ell$	143
9.5	Representative Feynman diagrams for W +jets, Z +jets and diboson production. We assume $W \rightarrow \ell\nu_\ell$ and $Z \rightarrow \ell^+\ell^-$	143
9.6	Leading $m(\text{jj})$ distributions for the OS $\mu\tau_h$ signal region in the 2016-2018 data sets.	148
9.7	Leading $m(\text{jj})$ distributions for the LS $\mu\tau_h$ signal region in the 2016-2018 data sets.	148
9.8	Cumulative efficiency in the baseline OS $\mu\tau_h$ signal region for signal $m(\tilde{\chi}_2^0) = 300$ GeV and $\Delta m = 50$ GeV, $\Delta m = 75$ GeV, and total background in the 2016-2018 data sets.	150
9.9	Cumulative efficiency in the baseline LS $\mu\tau_h$ signal region for signal $m(\tilde{\chi}_2^0) = 300$ GeV and $\Delta m = 50$ GeV, $\Delta m = 75$ GeV, and total background in the 2016-2018 data sets.	150
9.10	Shape comparison of the leading $m(\text{jj})$ distributions for signal $m(\tilde{\chi}_2^0) = 300$ GeV and $\Delta m = 50$ GeV (left), $\Delta m = 75$ GeV (middle) and total background (right) in the OS $\mu\tau_h$ signal region in the 2016-2018 data sets.	151
9.11	Shape comparison of the leading $m(\text{jj})$ distributions for signal $m(\tilde{\chi}_2^0) = 300$ GeV and $\Delta m = 50$ GeV (left), $\Delta m = 75$ GeV (middle) and total background (right) in the LS $\mu\tau_h$ signal region in the 2016-2018 data sets.	151
9.12	Smooth background shapes obtained after relaxing some of the central selections in the baseline $\mu\tau_h$ SR for 2016.	152
9.13	Comparison of the total background shapes in the OS $\mu\tau_h$ SR vs. the smooth background shapes obtained after relaxing some of the central selections in the baseline $\mu\tau_h$ SR for 2016.	152
9.14	Comparison of the total background shapes in the LS $\mu\tau_h$ SR vs. the smooth background shapes obtained after relaxing some of the central selections in the baseline $\mu\tau_h$ SR for 2016. Both sets of bins derived for the leading $m(\text{jj})$ in the in the LS (top) and OS (bottom) SR were tested.	153
9.15	Ratio of the σ_{UL} 's for each τ_h isolation working point tested and the minimum UL obtained among all cuts tested.	155
9.16	Ratio of the σ_{UL} 's for each selection of number of τ_h prongs tested and the minimum UL obtained among all cuts tested, considering the Loose (left) and Tight (right) τ_h ID WPs.	156
9.17	Ratio of the σ_{UL} 's for each selection of $p_T^{\text{max}}(\tau_h)$ tested and the minimum UL obtained among all cuts tested, considering the Loose (left) and Tight (right) τ_h ID WPs.	156
9.18	Ratio of the σ_{UL} 's for each selection of p_T^{miss} tested and the minimum UL obtained among all cuts tested, considering the Loose (left) and Tight (right) τ_h ID WPs.	157
9.19	Ratio of the σ_{UL} 's for each selection of μ ID + $p_T^{\text{min}}(\mu)$ combinations tested and the minimum UL obtained among all cuts tested, considering different signal points for the $\tilde{\tau}$ -dominated decay scenario (left) and the virtual W/Z decay scenario (right).	158
9.20	Ratio of the σ_{UL} 's for each selection of $p_T^{\text{max}}(\mu)$ tested and the minimum UL obtained among all cuts tested.	159
9.21	Ratio of the σ_{UL} 's for each selection of τ_h anti-electron discriminator tested and the minimum UL obtained among all cuts tested.	159
9.22	Leading $m(\text{jj})$ distribution for predicted backgrounds and three benchmark signal points in the OS $\mu\tau_h$ +jj SR, after applying VBF1 (left) and VBF2 (right) selections.	160
9.23	Leading $m(\text{jj})$ distribution for predicted backgrounds and three benchmark signal points in the LS $\mu\tau_h$ +jj SR, after applying VBF1 (left) and VBF2 (right) selections.	160
9.24	Signal acceptance in the wino-bino model with $\tilde{\tau}$ -dominated decays for the various decay channels considered in this analysis.	162
9.25	Signal acceptance in the wino-bino model with virtual W/Z decays for the various decay channels considered in this analysis.	162

10.1	Kinematic distributions for the τ_h candidates, p_T^{miss} , $m_T(\tau_h, \cancel{E}_T)$ and $m(\tau_h\tau_h)$ after applying central selections for 2016 data.	166
10.2	Kinematic distributions for the τ_h candidates, p_T^{miss} , $m_T(\tau_h, \cancel{E}_T)$ and $m(\tau_h\tau_h)$ after applying central selections for 2017 data.	167
10.3	Kinematic distributions for the τ_h candidates, p_T^{miss} , $m_T(\tau_h, \cancel{E}_T)$ and $m(\tau_h\tau_h)$ after applying central selections for 2018 data.	167
10.4	ABCD diagram for the QCD estimation in the $Z(\rightarrow \tau^+\tau^- \rightarrow \mu\tau_h)\text{+jets}$ CR, which corresponds to CRA. The OS/LS transfer factor is obtained from CRC and CRD, and the QCD shape is taken from CRB.	169
10.5	Kinematic distributions for the leading $m(\text{jj})$ in CRB for 2016 (left), 2017 (middle) and 2018 (right) after applying central and VBF2 selections.	169
10.6	Kinematic distributions for the leading $m(\text{jj})$ in CRC for 2016 (left), 2017 (middle) and 2018 (right) after applying central and VBF2 selections.	169
10.7	Kinematic distributions for the leading $m(\text{jj})$ in CRD for 2016 (left), 2017 (middle) and 2018 (right) after applying central and VBF2 selections.	170
10.8	OS/LS transfer factor after VBF2 selections for 2016 (left), 2017 (middle), and 2018 (right) data and corresponding fits to a 0th degree (top) and 1st degree (bottom) polynomial.	171
10.9	Nominal/inverted isolation transfer factor after VBF2 selections for 2016 (left), 2017 (middle), and 2018 (right) data and corresponding fits to a 0th degree (top) and 1st degree (bottom) polynomial.	172
10.10	Distributions for jet multiplicity, $p_T(j)$, $\eta(j)$, leading jet p_T , η and p_T^{miss} after applying central and VBF2 selections for 2016 data in CRA. Distribution for QCD is obtained from the data-driven estimation.	173
10.11	Distributions for leading $m(\text{jj})$ and $\Delta\eta(\text{jj})$ for this dijet pair after applying central and VBF2 selections for 2016 data in CRA. Distribution for QCD is obtained from the data-driven estimation.	174
10.12	Distributions for jet multiplicity, $p_T(j)$, $\eta(j)$, leading jet p_T , η and p_T^{miss} after applying central and VBF2 selections for 2017 data in CRA. Distribution for QCD is obtained from the data-driven estimation.	174
10.13	Distributions for leading $m(\text{jj})$ and $\Delta\eta(\text{jj})$ for this dijet pair after applying central and VBF2 selections for 2017 data in CRA. Distribution for QCD is obtained from the data-driven estimation.	174
10.14	Distributions for jet multiplicity, $p_T(j)$, $\eta(j)$, leading jet p_T , η and p_T^{miss} after applying central and VBF2 selections for 2018 data in CRA. Distribution for QCD is obtained from the data-driven estimation.	175
10.15	Distributions for leading $m(\text{jj})$ and $\Delta\eta(\text{jj})$ for this dijet pair after applying central and VBF2 selections for 2018 data in CRA. Distribution for QCD is obtained from the data-driven estimation.	175
10.16	p_T (left), η (middle) and m_T (right) distributions for μ (top) and τ_h (bottom) after applying central selections for 2016 data.	177
10.17	Multiplicity (left), p_T (middle) and η (right) distributions for jets (top) and b-jets (bottom) after applying central selections for 2016 data.	178
10.18	Distributions for the leading (left) and subleading jet p_T (middle), and p_T^{miss} (right) after applying central selections for 2016 data.	178
10.19	Jet multiplicity (left), p_T (middle) and η (right) distributions after applying central + VBF1 selections for 2016 data.	178
10.20	Distributions for the leading (left) and subleading jet p_T (middle), and p_T^{miss} (right) after applying central + VBF1 selections for 2016 data.	178
10.21	Distributions for the leading dijet mass $m(\text{jj})$ and $\Delta\eta(\text{jj})$ for this dijet pair after applying central + VBF1 selections for 2016 data.	179
10.22	Jet multiplicity (left), p_T (middle) and η (right) distributions after applying central + VBF2 selections for 2016 data.	179

10.23	Distributions for the leading (left) and subleading jet p_T (middle), and p_T^{miss} (right) after applying central + VBF2 selections for 2016 data.	179
10.24	Distributions for the leading dijet mass $m(\text{jj})$ and $\Delta\eta(\text{jj})$ for this dijet pair after applying central + VBF2 selections for 2016 data.	179
10.25	p_T (left), η (middle) and m_T (right) distributions for μ (top) and τ_h (bottom) after applying central selections for 2017 data.	180
10.26	Multiplicity (left), p_T (middle) and η (right) distributions for jets (top) and b-jets (bottom) after applying central selections for 2017 data.	180
10.27	Distributions for the leading (left) and subleading jet p_T (middle), and p_T^{miss} (right) after applying central selections for 2017 data.	180
10.28	Multiplicity (left), p_T (middle) and η (right) distributions for jets after applying central + VBF1 selections for 2017 data.	181
10.29	Distributions for the leading (left) and subleading jet p_T (middle), and p_T^{miss} (right) after applying central + VBF1 selections for 2017 data.	181
10.30	Distributions for the leading dijet mass $m(\text{jj})$ and $\Delta\eta(\text{jj})$ for this dijet pair after applying central + VBF1 selections for 2017 data.	181
10.31	Multiplicity (left), p_T (middle) and η (right) distributions for jets after applying central + VBF2 selections for 2017 data.	181
10.32	Distributions for the leading (left) and subleading jet p_T (middle), and p_T^{miss} (right) after applying central + VBF2 selections for 2017 data.	182
10.33	Distributions for the leading dijet mass $m(\text{jj})$ and $\Delta\eta(\text{jj})$ for this dijet pair after applying central + VBF2 selections for 2017 data.	182
10.34	p_T (left), η (middle) and m_T (right) distributions for μ (top) and τ_h (bottom) after applying central selections for 2018 data.	182
10.35	Multiplicity (left), p_T (middle) and η (right) distributions for jets (top) and b-jets (bottom) after applying central selections for 2018 data.	183
10.36	Distributions for the leading (left) and subleading jet p_T (middle), and p_T^{miss} (right) after applying central selections for 2018 data.	183
10.37	Multiplicity (left), p_T (middle) and η (right) distributions for jets after applying central + VBF1 selections for 2018 data.	183
10.38	Distributions for the leading (left) and subleading jet p_T (middle), and p_T^{miss} (right) after applying central + VBF1 selections for 2018 data.	183
10.39	Distributions for the leading dijet mass $m(\text{jj})$ and $\Delta\eta(\text{jj})$ for this dijet pair after applying central + VBF1 selections for 2018 data.	184
10.40	Multiplicity (left), p_T (middle) and η (right) distributions for jets after applying central + VBF2 selections for 2018 data.	184
10.41	Distributions for the leading (left) and subleading jet p_T (middle), and p_T^{miss} (right) after applying central + VBF2 selections for 2018 data.	184
10.42	Distributions for the leading dijet mass $m(\text{jj})$ and $\Delta\eta(\text{jj})$ for this dijet pair after applying central + VBF2 selections for 2018 data.	184
10.43	$p_T(\mu)$, $\eta(\mu)$, and $m(\mu\mu)$ distributions after applying central selections for 2016 data.	186
10.44	Jet multiplicity, $p_T(j)$, and $\eta(j)$ distributions after applying central selections for 2016 data.	187
10.45	p_T distributions for leading jet, subleading jet, and p_T^{miss} after applying central selections for 2016 data.	187
10.46	$p_T(\mu)$, $\eta(\mu)$, and $m(\mu\mu)$ distributions after applying VBF1 selections for 2016 data.	187
10.47	Jet multiplicity, $p_T(j)$, and $\eta(j)$ distributions after applying VBF1 selections for 2016 data.	188
10.48	p_T distributions for leading jet, subleading jet, and p_T^{miss} after applying VBF1 selections for 2016 data.	188
10.49	Kinematic distributions for the leading $m(\text{jj})$ and $\Delta\eta(\text{jj})$ for this dijet pair after applying VBF1 selections for 2016 data.	188
10.50	$p_T(\mu)$, $\eta(\mu)$, and $m(\mu\mu)$ distributions after applying VBF2 selections for 2016 data.	188

10.51	Jet multiplicity, $p_T(j)$, and $\eta(j)$ distributions after applying VBF2 selections for 2016 data.	189
10.52	p_T distributions for leading jet, subleading jet, and p_T^{miss} after applying VBF2 selections for 2016 data.	189
10.53	Kinematic distributions for the leading $m(\text{jj})$ and $\Delta\eta(\text{jj})$ for this dijet pair after applying VBF2 selections for 2016 data.	189
10.54	$p_T(\mu)$, $\eta(\mu)$, and $m(\mu\mu)$ distributions after applying central selections for 2017 data.	189
10.55	Jet multiplicity, $p_T(j)$, and $\eta(j)$ distributions after applying central selections for 2017 data.	190
10.56	p_T distributions for leading jet, subleading jet, and p_T^{miss} after applying central selections for 2017 data.	190
10.57	$p_T(\mu)$, $\eta(\mu)$, and $m(\mu\mu)$ distributions after applying VBF1 selections for 2017 data.	190
10.58	Jet multiplicity, $p_T(j)$, and $\eta(j)$ distributions after applying VBF1 selections for 2017 data.	190
10.59	p_T distributions for leading jet, subleading jet, and p_T^{miss} after applying VBF1 selections for 2017 data.	191
10.60	Kinematic distributions for the leading $m(\text{jj})$ and $\Delta\eta(\text{jj})$ for this dijet pair after applying VBF1 selections for 2017 data.	191
10.61	$p_T(\mu)$, $\eta(\mu)$, and $m(\mu\mu)$ distributions after applying VBF2 selections for 2017 data.	191
10.62	Jet multiplicity, $p_T(j)$, and $\eta(j)$ distributions after applying VBF2 selections for 2017 data.	191
10.63	p_T distributions for leading jet, subleading jet, and p_T^{miss} after applying VBF2 selections for 2017 data.	192
10.64	Kinematic distributions for the leading $m(\text{jj})$ and $\Delta\eta(\text{jj})$ for this dijet pair after applying VBF2 selections for 2017 data.	192
10.65	$p_T(\mu)$, $\eta(\mu)$, and $m(\mu\mu)$ distributions after applying central selections for 2018 data.	192
10.66	Jet multiplicity, $p_T(j)$, and $\eta(j)$ distributions after applying central selections for 2018 data.	192
10.67	p_T distributions for leading jet, subleading jet, and p_T^{miss} after applying central selections for 2018 data.	193
10.68	$p_T(\mu)$, $\eta(\mu)$, and $m(\mu\mu)$ distributions after applying VBF1 selections for 2018 data.	193
10.69	Jet multiplicity, $p_T(j)$, and $\eta(j)$ distributions after applying VBF1 selections for 2018 data.	193
10.70	p_T distributions for leading jet, subleading jet, and p_T^{miss} after applying VBF1 selections for 2018 data.	193
10.71	Kinematic distributions for the leading $m(\text{jj})$ and $\Delta\eta(\text{jj})$ for this dijet pair after applying VBF1 selections for 2018 data.	194
10.72	$p_T(\mu)$, $\eta(\mu)$, and $m(\mu\mu)$ distributions after applying VBF2 selections for 2018 data.	194
10.73	Jet multiplicity, $p_T(j)$, and $\eta(j)$ distributions after applying VBF2 selections for 2018 data.	194
10.74	p_T distributions for leading jet, subleading jet, and p_T^{miss} after applying VBF2 selections for 2018 data.	194
10.75	Kinematic distributions for the leading $m(\text{jj})$ and $\Delta\eta(\text{jj})$ for this dijet pair after applying VBF2 selections for 2018 data.	195
10.76	ABCD diagram for the QCD estimation in the $\ell\tau_h$ SRs ($\ell = e, \mu, \tau_h$).	196
10.77	Kinematic distribution for the $ \Delta\phi(j, p_T^{\text{miss}}) _{\text{min}}$ in CRB after applying central and VBF2 selections and before applying the $ \Delta\phi(j, p_T^{\text{miss}}) _{\text{min}}$ cut for 2016.	197
10.78	Kinematic distributions for the leading $m(\text{jj})$ in CRB (left) and CRC (right) after applying central, VBF2 and the corresponding $ \Delta\phi(j, p_T^{\text{miss}}) _{\text{min}}$ selections.	198
10.79	Top: $\text{TF}_{ \Delta\phi(j, p_T^{\text{miss}}) _{\text{min}}}$ vs. leading $m(\text{jj})$ for QCD events in CRB and CRC (Figure 10.76). Middle and bottom: $R_{\text{OS(LS)}}$ vs. leading $m(\text{jj})$ for QCD events in the $Z(\rightarrow \tau_\mu\tau_h)+\text{jets}$ CR measured from CRC, CRD and their combination (Figure 10.4).	199

10.80	TF $_{ \Delta\phi(j,p_T^{\text{miss}}) _{\text{min}}}$ vs. leading $m(\text{jj})$ for QCD events in CRB and CRC (Figure 10.76) for the $\tau_h\tau_h+\text{jj}$ SRs in 2017.	201
10.81	TF $_{ \Delta\phi(j,p_T^{\text{miss}}) _{\text{min}}}$ vs. leading $m(\text{jj})$ for QCD events in CRB and CRC (Figure 10.76) for the $\tau_h\tau_h+\text{jj}$ SRs in 2018.	202
10.82	TF $_{ \Delta\phi(j,p_T^{\text{miss}}) _{\text{min}}}$ vs. leading $m(\text{jj})$ for QCD events in CRB and CRC (Figure 10.76) for the $\mu\tau_h+\text{jj}$ SRs in 2016.	203
10.83	TF $_{ \Delta\phi(j,p_T^{\text{miss}}) _{\text{min}}}$ vs. leading $m(\text{jj})$ for QCD events in CRB and CRC (Figure 10.76) for the $\mu\tau_h+\text{jj}$ SRs in 2017.	204
10.84	TF $_{ \Delta\phi(j,p_T^{\text{miss}}) _{\text{min}}}$ vs. leading $m(\text{jj})$ for QCD events in CRB and CRC (Figure 10.76) for the $\mu\tau_h+\text{jj}$ SRs in 2018.	204
11.1	Leading $m(\text{jj})$ distributions for the nominal and $\pm 1\sigma$ systematic variations on jet energy scale (top pad) and the corresponding ratios (bottom pad) for a signal benchmark scenario (a-c) and Z+jets (d-f) in the 0-lepton channel.	211
11.2	Leading $m(\text{jj})$ distributions for the nominal and $\pm 1\sigma$ systematic variations on jet energy scale (top pad) and the corresponding ratios (bottom pad) for a signal benchmark scenario (a-c) and Z+jets (d-f) in the OS $\tau_h\tau_h$ channel.	212
12.1	The observed m_T and $m(\text{jj})$ distributions in the $e+\text{jj}$ (upper left), $\mu+\text{jj}$ (upper right), $\tau_h+\text{jj}$ (lower left), and $0\ell+\text{jj}$ (lower right) signal regions compared with the post-fit SM background yields from the fit described in the text. The pre-fit background yields and shapes are determined using data-driven methods for the major backgrounds, and based on simulation for the smaller backgrounds. Expected signal distributions are overlaid. The last bin in the m_T distributions of the $\ell+\text{jj}$ channels all events with $m_T > 210$ GeV. The last bin of the $m(\text{jj})$ distributions of the $0\ell+\text{jj}$ channel include all events with $m(\text{jj}) > 3800$ GeV [171].	214
12.2	Expected 95% CL UL on the cross section as a function of $m(\tilde{\chi}_1^\pm)$. The results correspond to $\Delta m = 1$ GeV (left) and $\Delta m = 50$ GeV (right) for the wino-bino model with democratic light slepton decays.	215
12.3	Observed 95% CL UL on the cross section as a function of $m(\tilde{\chi}_1^\pm)$. The results correspond to $\Delta m = 1$ GeV (left) and $\Delta m = 50$ GeV (right) for the wino-bino model with democratic light slepton decays [171].	216
12.4	Expected and observed 95% CL UL on the cross section as a function of $m(\tilde{\chi}_1^\pm) = m(\tilde{\chi}_2^0)$, for the $\Delta m = 1$ GeV and 30 GeV hypotheses. The wino-bino model with democratic light slepton decays (left) and virtual W/Z decays (right) were considered [171].	216
12.5	Expected and observed 95% CL UL on the cross section as a function of $m(\tilde{\chi}_1^\pm) = m(\tilde{\chi}_2^0)$ and Δm . The wino-bino model with democratic light slepton decays (left) and virtual W/Z decays (right) were considered [171].	217
12.6	Exclusion limits for $\tilde{\chi}_i\tilde{\chi}_j$ searches at the LHC as a function of $m(\tilde{\chi}_2^0)$ and Δm . Results obtained with $(L)_{\text{int}} = 35.9 \text{ fb}^{-1}$ in the VBF SUSY analysis by CMS correspond to the green contour.	217
13.1	Leading $m(\text{jj})$ distributions in the $e\tau_h+\text{jj}$ signal regions for the different subsets of the Run II data.	219
13.2	Leading $m(\text{jj})$ distributions in the $\mu\tau_h+\text{jj}$ signal regions for the different subsets of the Run II.	220
13.3	Leading $m(\text{jj})$ distributions in the $\tau_h\tau_h+\text{jj}$ signal regions for the different subsets of the Run II data.	221
13.4	Expected 95% CL upper limits on the cross section as a function of $m(\tilde{\chi}_2^0) = m(\tilde{\chi}_1^\pm)$, for the $\tilde{\tau}$ -dominated decays hypothesis with $\Delta m = 50$ GeV. The expected ULs for the OS+LS combination of the $e\tau_h+\text{jj}$, $\mu\tau_h+\text{jj}$ and $\tau_h\tau_h+\text{jj}$ channels is shown separately, as well as the full combination of the $\ell\tau_h+\text{jj}$ channels.	222

13.5	Expected 95% CL upper limits on the cross section for the combination of all decay channels considered in the analysis, displayed as a function of $m(\tilde{\chi}_2^0) = m(\tilde{\chi}_1^\pm)$, for the $\tilde{\tau}$ -dominated decays hypothesis with $\Delta m = 50$ GeV.	222
13.6	Expected 95% CL upper limits on the cross section for the combination of all decay channels considered in the analysis. They are displayed as a function of $m(\tilde{\chi}_2^0) = m(\tilde{\chi}_1^\pm)$, for the W^*/Z^* decays hypotheses with (left) $\Delta m = 5$ GeV, and (right) $\Delta m = 30$ GeV.	223
A.1	Electron-proton inelastic scattering [181].	228
A.2	The proton structure function F_2^p measured by different experiments [28].	231
A.3	Parton branching of an incoming parton, which corresponds to a space-like branching.	232
A.4	Parton branching of an outgoing parton, which corresponds to a time-like branching.	232
A.5	Spin-averaged Altarelli-Parisi splitting functions for (a) quark-gluon, (b) gluon-gluon and (c) quark-quark splittings. [182, 28].	234
A.6	Representation of a parton branching by paths in (t, x) -space. Each branching corresponds to a step downwards from a higher to a lower value of the momentum fraction x , at a value of t equal to the negative virtual mass-squared q^2 after the branching ($q^2 = -Q^2$) [180].	236
A.7	Parton shower in e^+e^- annihilation [180].	238
A.8	Illustration of MC simulation of a proton-(anti)proton collision, where a hard scattering (orange) has occurred and the event contains particles from initial- (green) and final-state (blue) radiation. The remaining particles come from the beam remnants and their interaction, contributing to what is known as “underlying event”. Figure taken from [205].	240
A.9	Particle multiplicity per unit rapidity for elastic scattering (green) and some of the diffraction classes in inelastic scattering: single diffractive (blue), double diffractive (magenta) and non-diffractive (red). Figure taken from [206].	242
A.10	Particle multiplicity per unit rapidity in the events with jet pedestals. Adapted from [206].	242
A.11	Comparison of models that include (or not) MPI and parton showers and the charged particle multiplicity measured by the ATLAS experiment for particles with $p_T > 100$ MeV, $ \eta < 2.5$ and $c\tau > 10$ mm, in events where at least to particles satisfy these conditions. Figure taken from [179].	243
A.12	Simple picture of the behavior of the jet production cross section and the total pp interaction cross section at $\sqrt{s} = 14$ TeV above a minimum value of p_T . Figure taken from [206].	244
A.13	Elementary hadronization vertex in the independent fragmentation model. Figure adapted from [216].	246
A.14	Hadronization chain in the independent fragmentation model proposed by Field and Feynman. Figure adapted from [216].	246
A.15	(a) Color “flux tube” in a chromodynamic dipole. (b) Qualitative picture of the QCD potential between a colorless $q\bar{q}$ pair. Figures adapted from [216, 218].	247
A.16	Simplified color-field topology in a $q\bar{q}$ system and its further simplified string representation. Figure taken from [217].	247
A.17	Illustration of string breaking by $q\bar{q}$ creation in the string field. Figure taken from [28].	248
A.18	Motion and breakup of a string system. The diagonal lines represent (anti)quarks and the horizontal ones are snapshots of the string field. Figure taken from [219].	248
A.19	Schematic illustration of the $q\bar{q}g$ configuration, showing the gluon as a kink in the string that connects the $q\bar{q}$ pair [179].	248
A.20	Conditions on nearby string breaks. Figure taken from [179].	249
A.21	Invariant mass distribution of color-singlet clusters in HERWIG. Figure taken from [179].	250
A.22	Color structure of a parton shower to leading order in N_c . Figure taken from [179].	251

A.23	General picture of the cluster hadronization algorithm. The pre-confinement is shown with local color flows. Figure taken from [205].	251
A.24	K/π ratio as measured by ALICE at 7 TeV. Comparison between the default version of HERWIG, two new approaches including dynamical strangeness production and PYTHIA. One can appreciate that the default method used in HERWIG does not describe the experimental data properly, but after implementing improvements to the algorithm, in this case, related to strangeness production, it can have a similar prediction power as the string model. Figure taken from [222].	252
A.25	Fragmentation functions $D_i^{\pi^+}$ at their respective input scales [223].	254

CHAPTER 1

Introduction

One of the most outstanding successes of physics in the twentieth century, has been the establishment of a framework that sums up the various experimental results and theoretical developments related to most fundamental components of matter and their interactions, known as the standard model (SM) of particle physics. The SM has proved to explain and predict many experimental phenomena involving the electromagnetic, weak and strong interactions with high precision. There are two main groups of particles in the SM: *fermions*, which are the building blocks of matter, and *gauge bosons* (also known as *force carriers*), which are in charge of communicating the interactions between fermions. In order to explain how fermions and the weak bosons acquire mass, the Brout-Englert-Higgs (BEH) mechanism was proposed [1, 2, 3]. A consequence of such mechanism is the prediction of the existence of a new scalar neutral massive boson, known as the Higgs boson. In 2012, two of the CERN Large Hadron Collider (LHC) experimental collaborations, A Toroidal LHC ApparatuS (ATLAS) and Compact Muon Solenoid (CMS), confirmed the detection of a particle with the properties of the SM Higgs boson [4, 5, 6].

Regardless of its remarkable success, the SM is incomplete since it does not answer several questions. Some examples are the origin of the BEH mechanism, neutrino oscillations, the matter-antimatter asymmetry, the particle nature of dark matter (DM), etc. One of the questions that the SM is unable to answer is the *electroweak hierarchy problem* [7], which can be defined as the quadratic sensitivity of the Higgs boson mass m_H corrections introduced by virtual effects coming from particles that couple directly or indirectly to the Higgs field, whether they are within the SM or belong to new physics activating at some mass scale Λ_α ($\delta m_{H,\alpha}^2 \sim \Lambda_\alpha^2$) [8, 9]. Experimental evidence for this problem comes from the relatively small measured Higgs boson mass.

One way to solve the electroweak hierarchy problem is by introducing a symmetry that relates fermions and bosons. This symmetry is known as *supersymmetry* (SUSY) and it assigns a scalar boson counterpart to each SM fermion field and vice versa. As a result, new supersymmetric particles called *superpartners* are hypothesized for all the SM particles. Each superpartner carries the same quantum numbers as its SM partner except for the spin, which differs by half a unit [7, 10, 11]. In the simplest SUSY extension of the SM, after the electroweak symmetry breaking, the SUSY partners of the SM electroweak gauge fields, which are the bino, wino and higgsino fields, mixed together to form four neutral mass eigenstates called *neutralinos* $\tilde{\chi}_i^0$ ($i = 1, 2, 3, 4$) and two with charge ± 1 known as *charginos* $\tilde{\chi}_j^\pm$ ($j = 1, 2$)¹ In R-parity conserving models, the lightest neutralino ($\tilde{\chi}_1^0$) is assumed to be the lightest supersymmetric particle (LSP) [7, 12] and also a stable particle.

One of the most exemplary connections between particle physics and cosmology is the link between SUSY and DM. Many astronomical observations and measurements provide evidence that around 84% of the matter in the Universe corresponds to DM [13]. None of the SM particles have the right characteristics (mass, couplings, etc.) to explain these results. Therefore, the DM particle

¹The labels i, j are assigned in ascending mass order.

candidate has been hypothesized to be a non-SM particle, weakly interacting and massive, which is consistent with the characteristics of the $\tilde{\chi}_1^0$ [7, 12, 14].

In most thermal Big Bang models, the SM and DM particles were in thermal equilibrium in the early universe, and their abundances could increase or decrease primarily through DM+DM \leftrightarrow SM+SM (DM annihilation) reactions. As the Universe expanded, the temperature dropped down to a *freeze-out* point ($T < m_{\text{DM}}$), when the kinetic energy of SM particles was insufficient for the SM+SM \rightarrow DM+DM process to take place. As a result, the DM abundance began to decrease to its current steady value, known as *DM relic density* ($\Omega_{\text{DM}}h^2$). In theory, the DM relic density is inversely proportional to the thermally averaged DM annihilation cross section (σ_{A}):

$$\Omega_{\text{DM}}h^2 \propto [\langle\sigma v\rangle]^{-1}, \quad \sigma \rightarrow \sigma_{\text{A}}.$$

The DM relic density will change depending on the super-field composition of the LSP. For example, if $\tilde{\chi}_1^0$ is bino-like², only considering DM annihilation as the only DM reduction mechanism, will predict a DM relic density larger than that measured experimentally by the Wilkinson Microwave Anisotropy Probe (WMAP) and Planck collaborations [13, 15, 16, 17]. However, a more complete picture requires us to contemplate other processes by which the $\tilde{\chi}_1^0$ could also interact and produce SM particles. One example can be reactions where the DM interacts with another particle X, producing SM particles: DM+X \rightarrow SM+SM [14, 18]. In the context of DM reduction mechanisms, these processes are known generally as *coannihilation* (CA) processes.

The CA cross section depends on the mass difference $\Delta m = m_{\text{X}} - m_{\text{DM}}$ as $\sigma_{\text{CA}} \propto \exp[-\Delta m/T]$. The σ_{CA} is enhanced for small values of Δm , resulting in an effective annihilation cross section $\sigma_{\text{eff}} = \sigma_{\text{A}} + \sigma_{\text{CA}}$ large enough to predict a $\Omega_{\tilde{\chi}_1^0}h^2$ consistent with $\Omega_{\text{DM}}h^2(\text{obs.})$ [19, 20, 21]. The most natural CA candidate in SUSY is the tau scalar lepton, or tau *slepton* ($\tilde{\tau}$) [22, 23, 24]. The regions of parameter space where $m(\tilde{\tau}) \sim m(\tilde{\chi}_1^0)$ are known as *SUSY compressed mass spectrum scenarios*. Therefore, searches that probe these sectors are essential, since they could lead to the discovery of $\tilde{\chi}_1^0$ DM and the connection to cosmology. However, these scenarios are experimentally challenging, because of the weakly interacting nature of $\tilde{\chi}_1^0$ and its likely large mass, which reduces its production rate. Thus, new techniques must be developed in order to detect $\tilde{\chi}_1^0$ DM in compressed SUSY models at the LHC, which is the main purpose of this dissertation [15, 25, 26].

The conventional methodology to search for $\tilde{\chi}_1^0$ DM at the LHC is via associated Drell-Yan (DY) chargino-neutralino ($\tilde{\chi}_1^\pm \tilde{\chi}_2^0$) production ($q\bar{q} \rightarrow W^* \rightarrow \tilde{\chi}_1^\pm \tilde{\chi}_2^0$), followed by their decays ending in $\tilde{\chi}_1^0$ s: $\tilde{\chi}_1^\pm \rightarrow \ell^\pm \nu_\ell \tilde{\chi}_1^0$ and $\tilde{\chi}_2^0 \rightarrow \ell^\pm \ell^\mp \tilde{\chi}_1^0$. The final state involves multiple leptons and missing transverse momentum (p_T^{miss}) from the undetected $\tilde{\chi}_1^0$ particles. At present, the existence of $\tilde{\chi}_1^\pm$ with $m(\tilde{\chi}_1^\pm) < 650$ GeV has been excluded, assuming $m(\tilde{\chi}_1^0) = 0$. These mass exclusion limits weaken to $m(\tilde{\chi}_1^\pm) < 112$ (175) GeV for $m(\tilde{\chi}_1^\pm) - m(\tilde{\chi}_1^0) < 1$ (30) GeV, depending on the assumed decay scenarios [27, 28]. Therefore, large portions of the electroweak SUSY parameter space remain inaccessible and loosely constrained, in particular, those corresponding to compressed mass spectra. The limited sensitivity in these regions can be attributed to the low-momentum $\tilde{\chi}_1^\pm \tilde{\chi}_2^0$ decay products, which are lost during reconstruction or among the large hadronic activity in the collisions.

Thus, it is crucial to develop dedicated strategies targeting distinctive experimental signatures, so that the soft particles in these final states can be distinguished against the more abundantly pro-

²A simple way to interpret this, is that $\tilde{\chi}_1^0$ interacts mainly through the Z boson with other particles.

duced SM background processes. Searches that focus on a rare production mode called *electroweak vector boson fusion* (VBF) are among the most promising of such methods, regardless of their low production rates [27, 29]. VBF processes are characterized by energetic quarks, scattered off weak bosons radiated by the interacting constituents of the incoming protons (*partons*). These quarks will travel close to the beam line in opposite directions, which result into two energetic jets whose combined reconstructed momenta correspond to TeV scale invariant masses (Fig. 3.7). A kinematic boost is created on the particles produced in the hard scattering and those in the subsequent decays. Hence, the probability of reconstructing and identifying soft particles increases, expanding the range of compressed mass spectra DM scenarios that could be explored.

The work presented in this document consists of a search for the production of supersymmetric DM at the LHC via electroweak VBF processes, in proton-proton collision data collected by the CMS experiment. This data analysis is the only search at the LHC that results in a series of observables which allow the relevant parameters for a measurement of the DM relic density to be deduced. For the first time at a collider experiment, the DM relic density can be measured to an accuracy that complements the results from astronomical observations.

It will be possible to test if the $\tilde{\chi}_1^0$ is the DM particle through the calculation of its relic density $\Omega_{\tilde{\chi}_1^0} h^2$ from the experimental observables obtained in the analysis. The theoretical VBF $\tilde{\chi}_1^\pm \tilde{\chi}_2^0$ production cross section is predicted to be about 10^2 fb [30, 31], which is large enough to be probed with the 137.1 fb^{-1} of integrated luminosity recorded by CMS during the 2016-2018 data-taking period (Run II). Preliminary studies suggest a 5σ sensitivity for a scenario with $m(\tilde{\chi}_1^\pm) = m(\tilde{\chi}_2^0) < 350$ GeV and $\Delta m = m(\tilde{\tau}) - m(\tilde{\chi}_1^0) = 25$ GeV, surpassing the discovery reach from any other experiments to date.

The document is organized as follows: in Chapters 2 and 3 the theoretical and experimental motivations are presented for the current data analysis. Chapter 4 states the general objective of the research project and describes the physics models that were used for the interpretation of the results. The description of the LHC, the CMS detector and how the data collected is processed to obtain high-level physics objects used in data analysis at CMS are included in Chapters 5, 6, and 7. Details on the data and simulation samples are listed in Chapter 8. The specific analysis strategy is outlined in Chapter 9, which introduces and motivates the event selections reported in the same chapter. The background estimation methodology and the results for the different studies on this task is included in Chapter 10. A brief description of the uncertainties present in the data analysis is done in Chapter 11. The results of this analysis with an integrated luminosity of $\mathcal{L}_{\text{int}} = 35.9 \text{ fb}^{-1}$, corresponding to the data set collected in the first year of the LHC Run II period (2016), as well as their interpretation are presented in Chapter 12. The predicted results and expected signal sensitivity for the total Run II integrated luminosity $\mathcal{L}_{\text{int}} = 137.1 \text{ fb}^{-1}$ are described in Chapter 13. Finally, the conclusions and future work are presented in Chapter 14.

CHAPTER 2

Theoretical motivation

The SM is the theoretical framework based on a quantum field theory that summarizes our current knowledge of the fundamental components of matter and their interactions. It has explained and predicted many experimental phenomena involving the electromagnetic, weak, and strong interactions with high precision. However, like with any other model in physics, it is not possible that the SM could provide the answers to all the questions in particle physics. There are problems that we can classify as conceptual issues, related to the basic assumptions in the model but which are not in conflict with the experimental data. Another category involves observations which deviate from the SM theoretical predictions, which we denote as observational issues. A great diversity of ideas have been proposed to provide a solution to these problems. Some of them target one or two specific issues, but some others can naturally explain many conceptual and observational problems in the SM.

In this chapter, a description of the SM using the symmetry formalism is presented. This is used as a motivation for introducing the idea of supersymmetry as a solution to the electroweak hierarchy problem, which is a conceptual problem. Extensions of the SM based on SUSY can actually solve many observational problems, including the particle nature of dark matter [14], the B -meson decay anomalies [32, 33], and the muon $g - 2$ anomaly [34, 35, 36, 37]. In this document, we focus only on the dark matter particle nature. A brief description of how particle physics and cosmology are connected through the DM is included. This includes a summary of the possible scenarios for the evolution of the early Universe and how SUSY DM arises in both of these contexts. This chapter serves as the foundation for the work presented in this dissertation.

2.1 The standard model of particle physics

In the SM, the particles that compose matter are known as fermions, which have spin¹ $s = \frac{1}{2}$. They are classified into two groups: *leptons* and *quarks*. Leptons are involved in electromagnetic and weak interactions, while quarks are additionally involved in strong interactions. For every fermion, there is a corresponding particle with the same mass but opposite electric charge, called an *anti fermion*. So far, the properties of *antimatter* have been observed to be similar to those of their matter counterparts.

There are three charged lepton *flavors* — electron, muon and tau ($\ell = e, \mu, \tau$) — and three neutral ones, which are called neutrinos (ν_e, ν_μ, ν_τ). Similarly, there are six quarks, each of a different flavor ($u, d, s, c, b, \text{ and } t$) that can be divided according to their electric charge into “up-type” and “down-type” quarks. Quarks have an additional charge called *color* q_c (r, g or b), which characterizes their involvement in strong interactions. Only particles with zero total color charge

¹In natural units: $\hbar = c = 1$.

have been observed experimentally. Thus, quarks are always *confined* or grouped together to make composite particles, named *hadrons*.

Quarks and leptons are further classified according to their mass, in what is known as *mass generation*. There are three mass generations in the SM, composed of an up-type quark, a down-type quark, a charged lepton, and a neutrino. The first generation groups the lightest particles for each quark and charged lepton categories², and the third generation contains the heaviest of these particles.

The SM is based on a quantum field theory (QFT) in which the relevant fundamental interactions are derived from the requirement of *local gauge invariance* [38]. In simple terms, the local gauge invariance refers to the invariance of the Lagrangian of a system under space-time dependent unitary (gauge) transformations. New fields need to be introduced for this purpose, and they are interpreted as the force carrier fields (this is where the gauge boson term comes from). As a consequence, a set of particles called gauge bosons arise for each interaction. These bosons are responsible for “communicating” the interactions between fermions. Therefore, they are known as force carriers or *mediators*. The photon mediates the electromagnetic interaction, the gluons carry the strong force, and the mediators of the weak interaction are the W^\pm and Z bosons.

The last piece of the SM corresponds to the BEH mechanism, which was proposed to explain how the weak bosons and fermions acquire their mass. This mechanism predicts the existence of a new scalar neutral massive boson, known as the Higgs boson, detected by the ATLAS and CMS collaborations in 2012, with a measured mass of $m_H^{exp} \simeq 125.8$ GeV [4, 5, 6].

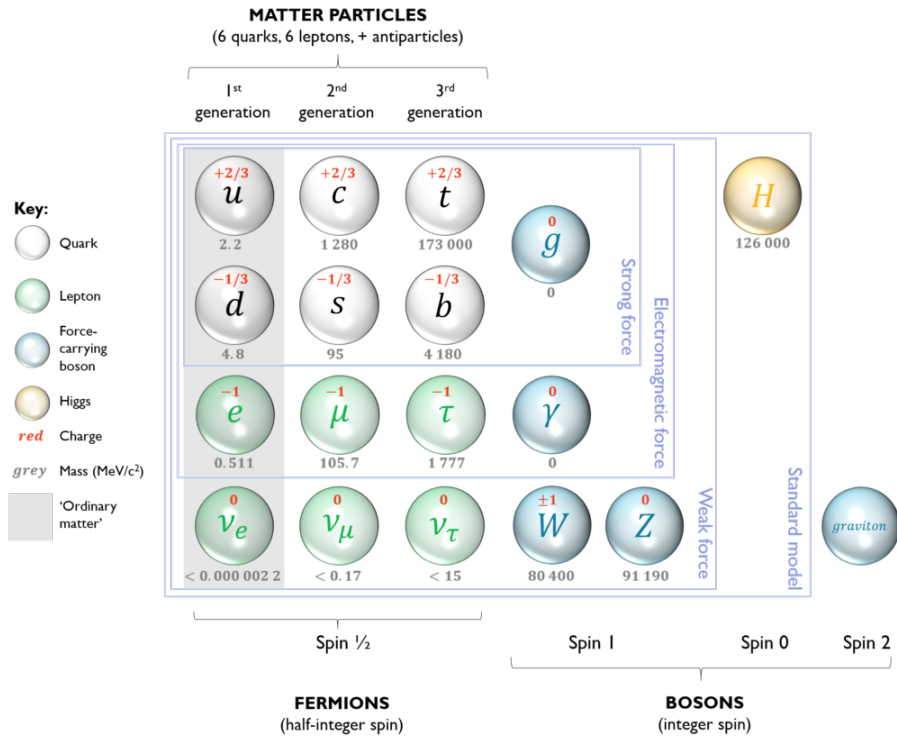


Figure 2.1: Summary of the SM particles, their charge, mass and spin [39].

²At the moment, it is not possible to know if the electron neutrino is the lightest of the SM neutrinos, since there is not a precise measurement of all neutrinos mass yet.

In the subsections to follow, the mathematical description of the SM symmetry group is presented.

Symmetries in physics

Symmetries are an essential concept to our current understanding of physics, and specially, particle physics. Mathematically, a symmetry exists in a physical system if its Hamiltonian (a mathematical operator related to the energy of the system) is invariant under a given transformation represented by S :

$$SHS^\dagger = H. \tag{2.1}$$

If the set of independent symmetries of a system generate the algebraic structure of a group, then it is said that there exists a symmetry group. Symmetries can be classified in two main categories:

- *Discrete symmetries*: the defining parameters of this type of symmetries are discrete. Some examples include the parity (P), charge-conjugation (C), and time-reversal (T) symmetries.
- *Continuous symmetries*: in this case, the defining parameters can take values in a continuum. Typical examples of continuous symmetries are rotations $R(\theta)$. Continuous symmetries can be divided into two main groups:
 - *Space-time symmetries*: they act on the space-time and are described by the Poincaré group, and they include time translations, space translations, rotations and Lorentz boosts, and,
 - *Internal or “gauge” symmetries*: acting on the internal quantum numbers of a system. These symmetries are usually described by Lie groups. These symmetries are related to phases of wave functions and gauged potentials.

Moreover, internal symmetries can be categorized into:

- *Global symmetries*: the transformation parameters **do not depend** on the spacetime coordinates, and,
- *Local symmetries*: the transformation parameters **depend** on the spacetime coordinates.

Conceptually, the existence of a symmetry is equivalent to say there is a conserved quantity. A central theorem to the development of the SM of particle physics is *Noether’s theorem*, which states that if the Lagrangian of a system has a global symmetry, then there exists a conserved current and the associated charge is conserved. The Lagrangian is an operator similar to the Hamiltonian, which contains information about the energy of the system. The interactions in the SM can be understood mathematically as the result of local gauge invariance of a combination of $U(1)$, $SU(2)$ and $SU(3)$ symmetries, where:

- the electromagnetic interaction is described by the *quantum electrodynamics (QED)* theory, based on a $U(1)$ local gauge symmetry,
- the weak interaction is associated with an $SU(2)$ local gauge symmetry, invariant under rotations in *weak isospin space*, and,

- the strong interaction is described by the *quantum chromodynamics (QCD)* theory, corresponding to a non-Abelian SU(3) local gauge symmetry.

Symmetries in particle physics are important not only because the SM relies on them, but also because one of the core motivations for this research project is based on the concept of supersymmetry, which is also a symmetry. Therefore, the intention of presenting the mathematical details of the SM symmetries is to introduce the reader to how they give rise to each interaction and how the idea can be expanded to more general symmetries and its physical consequences. The description of these interactions presented in this document follow the approach presented in Ref. [40].

Electromagnetic interaction: U(1) symmetries

The Lagrangian of a free spin- $\frac{1}{2}$ Dirac field ψ with mass m is given by

$$\mathcal{L}_{\text{Dirac}} = \bar{\psi}(x) (i\gamma^\mu \partial_\mu - m) \psi(x), \quad (2.2)$$

which is derived by requiring Lorentz invariance. It can be shown that $\mathcal{L}_{\text{Dirac}}$ is also invariant under a transformation of the U(1) group:

$$\psi(x) \rightarrow \psi'(x) = e^{-i\alpha} \psi(x), \quad (2.3)$$

$$\partial_\mu \psi(x) \rightarrow \partial_\mu \psi'(x) = e^{-i\alpha} \partial_\mu \psi(x), \quad (2.4)$$

where α is an arbitrary real number. Applying this transformation, we find

$$\mathcal{L}'_{\text{Dirac}} = \bar{\psi}'(x) (i\gamma^\mu \partial_\mu - m) \psi'(x) = \mathcal{L}_{\text{Dirac}}. \quad (2.5)$$

The transformation in Eq. 2.4 is called a global transformation, because it does not depend on space-time coordinates and therefore, the field $\psi(x)$ is multiplied at every point x by the same constant factor $e^{i\alpha}$. This invariance can also be expressed in terms of the infinitesimal global U(1) transformation [41] and we can derive the conserved current

$$j^\mu = (\rho, \vec{J}) \bar{\psi}(x) \gamma^\mu \psi(x), \quad (2.6)$$

which represents the conservation of the electric charge (ρ) and electromagnetic current (\vec{J}). In a more realistic case, the $e^{i\alpha}$ factor at one point in spacetime should be correlated to the factor at another point in spacetime, because spacial relativity establishes that no information can travel faster than light. For a global symmetry, the choice will be fixed immediately for any point in the whole universe [40]. Thus, promoting the U(1) transformation from global to a local,

$$e^{-i\alpha} \rightarrow e^{-ig\alpha(x)}, \quad g = \text{constant} \quad (2.7)$$

$$\psi(x) \rightarrow \psi'(x) = e^{-ig\alpha(x)} \psi(x), \quad (2.8)$$

$$\partial_\mu \psi(x) \rightarrow \partial_\mu \psi'(x) = \partial_\mu [e^{-ig\alpha(x)} \psi(x)] = e^{-ig\alpha(x)} [\partial_\mu \psi(x) - ig (\partial_\mu \alpha(x)) \psi(x)] \quad (2.9)$$

we transform the Lagrangian and obtain

$$\mathcal{L}'_{\text{Dirac}} = \mathcal{L}_{\text{Dirac}} - g(\partial_\mu \alpha(x)) \bar{\psi} \gamma^\mu \psi(x) \neq \mathcal{L}_{\text{Dirac}}, \quad (2.10)$$

which means that $\mathcal{L}_{\text{Dirac}}$ is invariant under the global $U(1)$ symmetry but not invariant under the local $U(1)$ symmetry.

On the other hand, the Lagrangian for a free spin-1 field of mass m is given by

$$\mathcal{L}_{\text{Proca}} = \frac{1}{2} [\partial^\mu A^\nu (\partial_\mu A_\nu - \partial_\nu A_\mu) + m^2 A^\mu A_\mu]. \quad (2.11)$$

$\mathcal{L}_{\text{Proca}}$ is also invariant under a global $U(1)$ transformation of the form

$$A_\mu \rightarrow A'_\mu = A_\mu + \alpha_\mu, \quad (2.12)$$

$$\partial_\nu A_\mu \rightarrow \partial_\nu A'_\mu = \partial_\nu A_\mu + \partial_\nu \alpha_\mu = \partial_\nu A_\mu, \quad (2.13)$$

where α_μ is a constant 4-vector, if $m = 0$ ($\mathcal{L}_{\text{Proca}} \rightarrow \mathcal{L}_{\text{Maxwell}}$).

If we now consider a local $U(1)$ transformation,

$$A_\mu \rightarrow A'_\mu = A_\mu + \partial_\mu \alpha(x), \quad (2.14)$$

the transformed $\mathcal{L}_{\text{Maxwell}}$ will remain invariant,

$$\mathcal{L}'_{\text{Maxwell}} = \mathcal{L}_{\text{Maxwell}}. \quad (2.15)$$

Going back to $\mathcal{L}_{\text{Dirac}}$, it is worth noticing that considering a new term $A_\mu \bar{\psi}(x) \gamma^\mu \psi(x)$ for which we transform $\psi(x)$, $\bar{\psi}(x)$, and A_μ simultaneously, then we obtain:

$$A_\mu \bar{\psi}(x) \gamma^\mu \psi(x) \rightarrow A'_\mu \bar{\psi}'(x) \gamma^\mu \psi'(x) = A_\mu \bar{\psi}(x) \gamma^\mu \psi(x) + (\partial_\mu(\alpha(x))) A_\mu \bar{\psi}(x) \gamma^\mu \psi(x). \quad (2.16)$$

The second term is has the same form as the extra term obtained after transforming $\mathcal{L}_{\text{Dirac}}$ under a local $U(1)$ symmetry, which prevented its invariance, except with the opposite sign. Then, adding the term $g A_\mu \bar{\psi}(x) \gamma^\mu \psi(x)$ to $\mathcal{L}_{\text{Dirac}}$,

$$\mathcal{L}_{\text{Dirac+extra term}} = i \bar{\psi}(x) \gamma^\mu \partial_\mu \psi(x) - m \bar{\psi}(x) \psi(x) + g A_\mu \bar{\psi}(x) \gamma^\mu \psi(x), \quad (2.17)$$

which is invariant under the simultaneous local $U(1)$ transformation of the $\psi(x)$, $\bar{\psi}(x)$, and A_μ fields. This extra term can be interpreted physically as the interaction of the spin- $\frac{1}{2}$ field with a mass-less spin-1 field with a strength given by the value of the “coupling constant” g . In order to obtain the full description of the system, we need to add $\mathcal{L}_{\text{Maxwell}}$ as well, which will describe the kinematics of the free massless spin-1 field A_μ , which has been shown to be invariant under the local $U(1)$ transformation:

$$\mathcal{L}_{\text{Dirac+extra term+Maxwell}} = i \bar{\psi}(x) \gamma^\mu \partial_\mu \psi(x) - m \bar{\psi}(x) \psi(x) + g A_\mu \bar{\psi}(x) \gamma^\mu \psi(x) + \frac{1}{2} [\partial^\mu A^\nu (\partial_\mu A_\nu - \partial_\nu A_\mu)]. \quad (2.18)$$

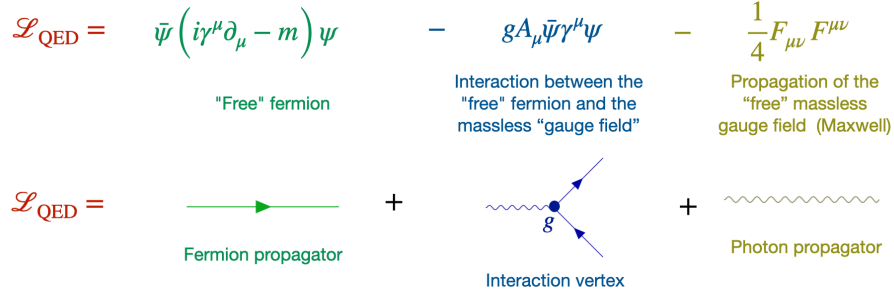


Figure 2.2: Pictorial representation of the QED Lagrangian with elements of Feynman diagrams.

Usually, this notation is shortened by introducing a new symbol D_μ , called the *covariant derivative*, defined as

$$D_\mu\psi(x) \equiv [i\partial_\mu - igA_\mu]\psi(x). \quad (2.19)$$

In addition, using the notation for the electromagnetic tensor $F_{\mu\nu}$,

$$F_{\mu\nu} = \partial_\mu A_\nu - \partial_\nu A_\mu, \quad (2.20)$$

we arrive to the expression of the Lagrangian for the QFT of electrodynamics, called *quantum electrodynamics (QED)*:

$$\mathcal{L}_{\text{QED}} = \bar{\psi}(i\gamma^\mu D_\mu - m)\psi(x) - \frac{1}{4}F_{\mu\nu}F^{\mu\nu}. \quad (2.21)$$

Going back to the full \mathcal{L}_{QED} (Eq. 2.18), we can represent each term pictorially with the help of Feynman diagrams, as it is shown in Fig. 2.2.

SU(2) symmetries

In this subsection, we will perform a similar treatment of the U(1) symmetries to the SU(2) symmetries, which will later be useful to understand the QFT description of the weak interactions. In this section, we now study a system of two massless spin- $\frac{1}{2}$ fields. The Lagrangian takes the form:

$$\mathcal{L}_{1+2} = i\psi_1\gamma^\mu\partial_\mu\psi_1 + i\bar{\psi}_2\gamma^\mu\partial_\mu\psi_2 \quad (2.22)$$

Defining a two component object, called *doublet*,

$$\Psi = \begin{pmatrix} \psi_1 \\ \psi_2 \end{pmatrix}, \quad \bar{\Psi} = (\bar{\psi}_1 \bar{\psi}_2) \quad (2.23)$$

we can rewrite the Lagrangian as

$$\mathcal{L}_{1+2} = i\bar{\Psi}\gamma^\mu\partial_\mu\Psi. \quad (2.24)$$

Applying a global SU(2) transformation to \mathcal{L}_{1+2} ,

$$\Psi \rightarrow \Psi' = e^{-i\frac{\vec{\tau}}{2}\cdot\vec{\theta}}\Psi, \quad (2.25)$$

$$\bar{\Psi} \rightarrow \bar{\Psi}' = \bar{\Psi}e^{i\frac{\vec{\tau}}{2}\cdot\vec{\theta}} \quad (2.26)$$

where $\vec{\theta}$ represents a three dimensional constant vector, and $\frac{\vec{\tau}}{2}$ are the generators of the SU(2) group with the Pauli matrices $\vec{\tau} = (\sigma_1, \sigma_2, \sigma_3)$. The transformed Lagrangian becomes

$$\begin{aligned} \mathcal{L}'_{1+2} &= i\bar{\Psi}'\gamma^\mu\partial_\mu\Psi' \\ &= i\bar{\Psi}e^{i\frac{\vec{\tau}}{2}\cdot\vec{\theta}}\gamma^\mu\partial_\mu e^{-i\frac{\vec{\tau}}{2}\cdot\vec{\theta}}\Psi \\ &= i\bar{\Psi}\gamma^\mu\partial_\mu\Psi = \mathcal{L}_{1+2}. \end{aligned} \quad (2.27)$$

However, when we look at how \mathcal{L}_{1+2} changes when applying a local SU(2) transformation,

$$\Psi \rightarrow \Psi' = \mathcal{U}(x)\Psi = e^{-i\frac{\vec{\tau}}{2}\cdot\vec{\theta}(x)}\Psi, \quad (2.28)$$

we obtain

$$\mathcal{L}'_{1+2} = \mathcal{L}_{1+2} + i\bar{\Psi}\gamma^\mu\mathcal{U}^\dagger(x)[\partial_\mu\mathcal{U}(x)]\Psi \neq \mathcal{L}_{1+2}. \quad (2.29)$$

From our experience with local U(1) symmetries, we can ensure invariance under local SU(2) transformations by introducing a covariant derivative³

$$D_\mu\Psi = \left(\partial_\mu - ig\frac{\vec{\tau}}{2}\cdot\vec{W}_\mu\right)\Psi, \quad (2.30)$$

where W_μ are spin-1 fields. The transformation law for the \vec{W}_μ fields should be such that it satisfies

$$D_\mu\Psi \rightarrow (D_\mu\Psi)' = D'_\mu\Psi' = \mathcal{U}(x)D_\mu\Psi, \quad \Rightarrow \quad D'_\mu = \mathcal{U}(x)D_\mu\mathcal{U}^{-1}(x) \quad (2.31)$$

and is given by

$$\frac{\vec{\tau}}{2}\cdot\vec{W}'_\mu = \mathcal{U}(x)\left(\frac{\vec{\tau}}{2}\cdot\vec{W}_\mu\right)\mathcal{U}^{-1}(x) - \frac{i}{g}[\partial_\mu\mathcal{U}(x)]\mathcal{U}^{-1}(x). \quad (2.32)$$

In analogy with QED, introducing the covariant derivative for SU(2) transformations is equivalent to introduce an interaction term between the free massless spin- $\frac{1}{2}$ fields and three new spin-1 fields. In order to fully describe this system, we need to add the Lagrangian that describes the kinematics of the free \vec{W}_μ fields. Since these fields have a specific local SU(2) symmetry, the Maxwell Lagrangian

$$\mathcal{L}_{\vec{W}_\mu \text{ Maxwell}} = \frac{1}{4}(W_{\mu\nu})_1(W^{\mu\nu})_1 + \frac{1}{4}(W_{\mu\nu})_2(W^{\mu\nu})_2 + \frac{1}{4}(W_{\mu\nu})_3(W^{\mu\nu})_3 = \frac{1}{4}\vec{W}_{\mu\nu}\cdot\vec{W}^{\mu\nu}, \quad (2.33)$$

with

$$(W_{\mu\nu})_i = \partial_\mu(W_\nu)_i - \partial_\nu(W_\mu)_i \quad (2.34)$$

³The 4-vector W_μ can be written as $W_\mu = (W_0, \vec{W})$, and we denote $\vec{W}_\mu = \vec{W}$.

is not invariant under the transformation described in Eq. 2.32. Defining a new object \mathcal{W}_μ to account for the matrix nature of the transformations,

$$\mathcal{W}_\mu \equiv \vec{W}_\mu \cdot \vec{\tau}, \quad (2.35)$$

we can construct a field strength tensor that has the same transformation behavior as in Eq. 2.31. The field strength tensor $\mathcal{W}_{\mu\nu}$ given by

$$\mathcal{W}_{\mu\nu} \equiv \frac{i}{g} [D^\mu, D^\nu] = \frac{i}{g} (D^\mu D^\nu - D^\nu D^\mu), \quad (2.36)$$

satisfies

$$\mathcal{W}_{\mu\nu} \rightarrow (\mathcal{W}_{\mu\nu})' = \mathcal{U}(x)\mathcal{W}_{\mu\nu}\mathcal{U}^{-1}(x). \quad (2.37)$$

Rewriting D_μ and $\mathcal{W}_{\mu\nu}$ in terms of \mathcal{W}_ν (Eq. 2.35),

$$D_\mu = \partial_\mu - ig\mathcal{W}_\mu, \quad (2.38)$$

$$\mathcal{W}_{\mu\nu} = \partial_\mu\mathcal{W}_\nu - \partial_\nu\mathcal{W}_\mu - ig[\mathcal{W}_\mu, \mathcal{W}_\nu], \quad (2.39)$$

we arrive to the Lagrangian that is invariant under local SU(2) transformations:

$$\mathcal{L}_{\text{locally SU(2) invariant}} = i\bar{\Psi}\gamma^\mu(\partial_\mu - ig\mathcal{W}_\mu)\Psi - \frac{1}{4}\text{Tr}(\mathcal{W}_{\mu\nu}, \mathcal{W}^{\mu\nu}) = i\bar{\Psi}\gamma^\mu D_\mu\Psi - \frac{1}{4}\text{Tr}(\mathcal{W}_{\mu\nu}, \mathcal{W}^{\mu\nu}), \quad (2.40)$$

where $\text{Tr}(\mathcal{W}_{\mu\nu}\mathcal{W}^{\mu\nu})$ is the trace of the $\mathcal{W}_{\mu\nu}\mathcal{W}^{\mu\nu}$ matrix.

SU(2)×U(1) symmetries for massive fields: the Higgs sector

From the treatment of the locally SU(2) invariant Lagrangian, it is important to note that the $\mathcal{L}_{\text{locally SU(2) invariant}}$ was obtained by assuming that the fermions in the doublets are massless, and the spin-1 fields are massless as well. Although we have observed massless spin-1 fields in nature (the photon), we know from experimental observations that the known spin- $\frac{1}{2}$ fields (fermions) are not massless. Therefore, in order to use $\mathcal{L}_{\text{locally SU(2) invariant}}$ to describe systems in nature, we need to find a way to incorporate mass terms.

We can combine the locally SU(2) invariant Lagrangian (Eq. 2.40) with a locally U(1) invariant Lagrangian of the form:

$$\mathcal{L}_{\text{locally U(1) invariant}}(\Psi) = i\bar{\psi}\gamma^\mu(\partial_\mu - igB_\mu)\psi - m\bar{\psi}\psi - \frac{1}{4}B_{\mu\nu}B^{\mu\nu}, \quad (2.41)$$

with $B_{\mu\nu} = \partial_\mu B_\nu - \partial_\nu B_\mu$. The combination will be then done, still assuming that the spin- $\frac{1}{2}$ fields are massless,

$$\mathcal{L}_{\text{SU(2) and U(1) invariant}} = i\bar{\Psi}\gamma^\mu(\partial_\mu - igB_\mu - ig'\mathcal{W}_\mu)\Psi - \frac{1}{4}\text{Tr}(\mathcal{W}_{\mu\nu}, \mathcal{W}^{\mu\nu}) - \frac{1}{4}B_{\mu\nu}B^{\mu\nu}. \quad (2.42)$$

Before looking into how to add mass terms to this Lagrangian, we can study the symmetry of a complex spin-0 field. The Lagrangian of a complex spin-0 field is given by

$$\mathcal{L}_{\text{spin-0}} = \frac{1}{2} (\partial_\mu \Phi^\dagger \partial^\mu \Phi - m^2 \Phi^\dagger \Phi), \quad (2.43)$$

which is invariant under global U(1) transformations. A locally invariant version of $\mathcal{L}_{\text{spin-0}}$ can be derived following a procedure analogous to the one for spin- $\frac{1}{2}$ fields, obtaining

$$\mathcal{L}_{\text{spin-0 locally U(1) invariant}} = \frac{1}{2} (D_\mu \Phi^\dagger D^\mu \Phi - m^2 \Phi^\dagger \Phi), \quad D_\mu = \partial_\mu - igB_\mu. \quad (2.44)$$

We can rename $m \rightarrow \rho$ and add one more **arbitrary term** to Eq. 2.44:

$$\mathcal{L}_{\text{spin-0 locally U(1) invariant+extra term}} = \frac{1}{2} (D_\mu \Phi^\dagger D^\mu \Phi) - \rho^2 \Phi^\dagger \Phi + \lambda(\Phi^\dagger \Phi)^2, \quad (2.45)$$

which is symmetric under the transformations:

$$B_\mu \rightarrow B'_\mu = B_\mu + \partial_\mu \alpha(x), \quad (2.46)$$

$$\Phi(x) \rightarrow \Phi'(x) = e^{-i\alpha(x)} \Phi(x). \quad (2.47)$$

Similar to the locally SU(2) and U(1) invariant Lagrangian for spin- $\frac{1}{2}$ fields, we can write a locally SU(2) and U(1) invariant Lagrangian for doublets of spin-0 fields as

$$\mathcal{L}_{\text{SU(2) and U(1) invariant}}(\Phi) = ((\partial_\mu + ig'\mathcal{W}_\mu + igB_\mu)\Phi^\dagger) ((\partial^\mu - ig'\mathcal{W}^\mu - igB^\mu)\Phi) - \rho^2 \Phi^\dagger \Phi + \lambda(\Phi^\dagger \Phi)^2, \quad (2.48)$$

with

$$\Phi = \begin{pmatrix} \phi_1 \\ \phi_2 \end{pmatrix}, \quad (2.49)$$

and the symmetries

$$\mathcal{W}^\mu \rightarrow \mathcal{W}'^\mu = \mathcal{U}(x)\mathcal{W}^\mu\mathcal{U}^{-1}(x) + \frac{i}{g} (\partial^\mu \mathcal{U}(x))\mathcal{U}^{-1}(x), \quad (2.50)$$

$$\Phi \rightarrow \Phi' = \mathcal{U}(x)\Phi, \quad (2.51)$$

$$\bar{\Phi} \rightarrow \bar{\Phi}' = \bar{\Phi}\mathcal{U}^\dagger(x). \quad (2.52)$$

The last two terms in Eq. 2.48 can be interpreted as a potential $V(\Phi)$,

$$V(\Phi) = \lambda(\Phi^\dagger \Phi)^2 - \rho^2 \Phi^\dagger \Phi, \quad (2.53)$$

$$V(\Phi) = \lambda(\phi_1^\dagger \phi_1)^2 - \rho^2 \phi_1^\dagger \phi_1 + \lambda(\phi_2^\dagger \phi_2)^2 - \rho^2 \phi_2^\dagger \phi_2,$$

$$V(\Phi) = V_1(\phi_1) + V_2(\phi_2), \quad (2.54)$$

which is often called the *Higgs potential* (Fig. 2.3). This potential is thought to have changed its shape as the Universe evolved, and it can be characterized by its minimum, also known as the *vacuum expectation value* (VEV).

It is assumed that in the early stages of the evolution, $V(\Phi)$ only had one minimum at $\phi = 0$. As the temperature decreased with the Universe's expansion, the shape of $V(\Phi)$ changed in such a way that there are many possible minima, given by

$$\phi_{\min} = \sqrt{\frac{\rho^2}{2\lambda}} e^{i\varphi}. \quad (2.55)$$

Equation 2.55 tells us that any ϕ lying on a circle of radius $\sqrt{\frac{\rho^2}{2\lambda}}$ is a minimum of $V(\phi)$.

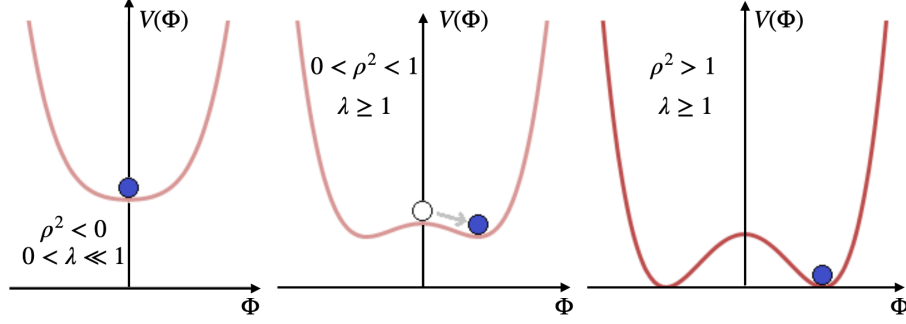


Figure 2.3: Pictorial representation of the Higgs potential $V(\Phi)$ for different values of ρ and λ (Adapted from [42]).

Since we are studying a scalar doublet, we can choose for convenience

$$\Phi_{\min} = \begin{pmatrix} \phi_{1,\min} \\ \phi_{2,\min} \end{pmatrix} = \begin{pmatrix} 0 \\ \frac{v}{\sqrt{2}} \end{pmatrix}, \quad (2.56)$$

where $v \equiv \sqrt{\frac{\rho^2}{\lambda}}$. Shifting the Φ field to this minimum, we can express it as

$$\Phi = \begin{pmatrix} \phi_{1re} + i\phi_{1im} \\ \frac{v}{\sqrt{2}} + \phi_{1re} + i\phi_{1im} \end{pmatrix}, \quad (2.57)$$

and rewrite as

$$\Phi = e^{\vec{\theta} \cdot \frac{\vec{\tau}}{2}} \begin{pmatrix} 0 \\ \frac{v+h}{\sqrt{2}} \end{pmatrix}. \quad (2.58)$$

A general local $SU(2)$ transformation for Φ that allows to eliminate the exponential factor in Eq. 2.58 is

$$\Phi \rightarrow \Phi' = e^{i\vec{b}(x) \cdot \frac{\vec{\tau}}{2}} \Phi, \quad (2.59)$$

where $\vec{b}(x)$ is chosen accordingly. Thus, the complex scalar doublet in this *unitary gauge* is:

$$\Phi_{\text{un}} = \begin{pmatrix} 0 \\ \frac{v+h}{\sqrt{2}} \end{pmatrix}. \quad (2.60)$$

From the four components in the complex scalar doublet (Eq. 2.57), three of them are equivalent to the $SU(2)$ gauge freedom, only remaining a *physical gauge field* h , called the *Higgs field*. Going back to the Lagrangian for the spin-0 field, we rewrite it as

$$\mathcal{L}_{\text{spin-0 SU(2) and U(1) invariant}}(\Phi) = \left((\partial_\mu + ig' \vec{W}_\mu \cdot \vec{\tau} + i\frac{g}{2} B_\mu) \Phi^\dagger \right) \left((\partial^\mu - ig' \vec{W}^\mu \cdot \vec{\tau} - ig\frac{g}{2} B^\mu) \Phi \right) - V(\Phi). \quad (2.61)$$

Evaluating Eq. 2.61 at $\Phi_{min} = \begin{pmatrix} 0 \\ \frac{v}{\sqrt{2}} \end{pmatrix}$ ⁴, we obtain

$$\mathcal{L}_{\text{spin-0 SU(2) and U(1) invariant}} \left[\begin{pmatrix} 0 \\ \frac{v}{\sqrt{2}} \end{pmatrix} \right] = \frac{v^2}{8} \left| \left((g' \vec{\tau} \cdot \vec{W}^\mu + g B^\mu) \begin{pmatrix} 0 \\ 1 \end{pmatrix} \right) \right|^2. \quad (2.62)$$

Expanding $\vec{\tau} \cdot \vec{W}_\mu$,

$$\vec{\tau} \cdot \vec{W}_\mu = \begin{pmatrix} W_3 & W_1 - iW_2 \\ W_1 + iW_2 & -W_3 \end{pmatrix}, \quad (2.63)$$

we arrive to the expression

$$\mathcal{L}_{\text{spin-0 SU(2) and U(1) invariant}} \left[\begin{pmatrix} 0 \\ \frac{v}{\sqrt{2}} \end{pmatrix} \right] = \frac{v^2}{8} \left((g')^2 ((W_1^\mu)^2 + (W_2^\mu)^2) + (g'W_3^\mu - gB^\mu)^2 \right). \quad (2.64)$$

Defining two new vector fields,

$$(W^+)_\mu \equiv \frac{1}{\sqrt{2}}(W_\mu^1 - iW_\mu^2), \quad (2.65)$$

$$(W^-)_\mu \equiv \frac{1}{\sqrt{2}}(W_\mu^1 + iW_\mu^2), \quad (2.66)$$

we can see that the first term in Eq. 2.64 is equivalent to

$$\frac{(g'v)^2}{8} (W_1^\mu)^2 + (W_2^\mu)^2 = \left(\frac{g'v}{2} \right)^2 (W^+)_\mu (W^-)^\mu, \quad (2.67)$$

where we interpret $\left(\frac{g'v}{2} \right)^2$ as a mass term, m_W^2 . By writing the second term in Eq. 2.64 in matrix form

$$(g'W_3^\mu - gB^\mu)^2 = \begin{pmatrix} W_3^\mu & B_\mu \end{pmatrix} \begin{pmatrix} (g')^2 & -g'g \\ -g'g & g^2 \end{pmatrix} \begin{pmatrix} W_3^\mu \\ B_\mu \end{pmatrix}, \quad (2.68)$$

we can also interpret the 2×2 matrix as a mass term. In order to do that, this matrix denoted by G needs to be diagonalized,

$$G_{\text{diag}} = M^{-1}GM, \quad (2.69)$$

where⁵

$$M = \frac{1}{\sqrt{g^2 + (g')^2}} \begin{pmatrix} g & g' \\ g' & -g \end{pmatrix}. \quad (2.70)$$

⁴When we evaluate the Lagrangian at Φ_{un} , all the terms containing h will represent the interactions of the self-interactions of the Higgs field.

⁵A useful definition can be made at this point: the Weinberg angle θ_W , which is defined as $\tan(\theta_W) = \frac{g'}{g}$. g' is also found in the literature as g_W .

Using this matrix, we can obtain the *physical states* A^μ and Z_μ :

$$\begin{pmatrix} A^\mu \\ Z_\mu \end{pmatrix} \equiv M^{-1} \begin{pmatrix} W_3^\mu \\ B_\mu \end{pmatrix} = \frac{1}{\sqrt{g^2 + (g')^2}} \begin{pmatrix} gW_3^\mu + g'B^\mu \\ g'W_3^\mu - gB^\mu \end{pmatrix}. \quad (2.71)$$

In the literature, g' is often referred as g_W . Using this convention, we find that

$$(g_W W_3^\mu - g B^\mu)^2 = \begin{pmatrix} W_3^\mu & B_\mu \end{pmatrix} G \begin{pmatrix} W_3^\mu \\ B_\mu \end{pmatrix} \quad (2.72)$$

$$= \begin{pmatrix} A^\mu & Z_\mu \end{pmatrix} G_{\text{diag}} \begin{pmatrix} A^\mu \\ Z_\mu \end{pmatrix} \quad (2.73)$$

$$= (g^2 + (g_W)^2)(Z^\mu)^2 + 0 \cdot (A^\mu)^2. \quad (2.74)$$

This section is concluded by recalling the original intention of introducing mass terms to the locally SU(2) and U(1) invariant Lagrangian for fermion fields. As we can see, it is possible to introduce mass terms which will correspond to the masses of the vector fields incorporated to ensure local SU(2) invariance. This is done by introducing the interaction of these fields with a complex scalar field Φ . After the process of spontaneous symmetry breaking (when we shifted the scalar potential to one value of the multiple possible minima), we get three mass terms:

- $m_W^2 = \frac{1}{4}v^2(g_W)^2$, which is physically interpreted as the mass of the charged W^\pm bosons, which carry the weak interaction,
- $m_Z^2 = \frac{v^2}{8}(g^2 + (g_W)^2)$, interpreted as the mass of the neutral Z boson, also a weak force carrier, and,
- $m_\gamma^2 = 0$, corresponding to the mass of the electromagnetic interaction boson, the photon.

Typically, this theoretical treatment is known as the “*electroweak unification*” model⁶ However, it is important to note this does not necessarily mean that in nature the electromagnetic and weak interactions are the same type of interaction. Rather, this theoretical treatment provides a more concise mathematical framework to describe both interactions in nature.

Weak interaction and parity violation

One of the most important characteristics of the weak interaction is that it maximally violates the *parity symmetry*. In other words, the weak bosons (W^+ , W^- and Z) only interact with *left-handed chiral particles*. This feature was discovered experimentally by the physicist Chien-Shiung Wu [43]. In order to incorporate this fact into the description of the weak interactions, we make use of the projection operators P_L and P_R :

$$P_L = \frac{1 - \gamma_5}{2} \begin{pmatrix} 1 & 0 \\ 0 & 0 \end{pmatrix} \quad \text{and} \quad P_R = \frac{1 + \gamma_5}{2} \begin{pmatrix} 0 & 0 \\ 0 & 1 \end{pmatrix}, \quad (2.75)$$

where

$$\gamma^5 = i\gamma^0\gamma^1\gamma^2\gamma^3 \quad (2.76)$$

⁶Also known as the Glashow-Salam-Weinberg (GSW) model of electroweak interactions.

is the *chirality operator*. In Equation 2.40, we need to change the term that refers to the interaction of the weak fields with the fermion is $g\bar{\Psi}\gamma_\mu\mathcal{W}^\mu\Psi$ to $g\bar{\Psi}\gamma_\mu\mathcal{W}^\mu P_L\Psi$, such that

$$\bar{\Psi}\gamma_\mu\mathcal{W}^\mu P_L\Psi = \bar{\Psi}_L\gamma_\mu\mathcal{W}^\mu\Psi_L \quad (2.77)$$

and,

$$\mathcal{L}_{\text{weak}} = i\bar{\Psi}\gamma^\mu(\partial_\mu - ig\mathcal{W}_\mu P_L)\Psi - \frac{1}{4}\text{Tr}(\mathcal{W}_{\mu\nu}, \mathcal{W}^{\mu\nu}). \quad (2.78)$$

Equation 2.77 can be physically interpreted as the rotation of the components of the left-chiral doublets through the weak interaction. In other words, the field $(\psi_1)_L$ in the SU(2) doublet will transform into $(\psi_2)_L$ when interacting weakly. The right-chiral fields do not interact via the weak force, therefore $(\psi_1)_R$ and $(\psi_2)_R$ do not transform into each other. In summary, the weak interactions group the left-handed SM fermions into SU(2) doublets:

$$\Psi_L = \begin{pmatrix} (\psi_1)_L \\ (\psi_2)_L \end{pmatrix}, \quad (2.79)$$

which transform under the two-dimensional representation of SU(2):

$$\Psi_L \rightarrow \Psi'_L = e^{i\vec{\theta}\cdot\frac{\vec{\tau}}{2}}\Psi_L. \quad (2.80)$$

The right-handed SM fermions are grouped into SU(2) *singlets* (objects with a single component), $(\psi_i)_R$, $i = 1, 2$, and transform under the one dimensional representation of SU(2):

$$(\psi_i)_R \rightarrow (\psi_i)'_R = e^0(\psi_i)_R = (\psi_i)_R. \quad (2.81)$$

Lepton and quark mass terms

Mass terms for the spin- $\frac{1}{2}$ fields can be introduced without spoiling the SU(2) symmetry in our Lagrangian, by making use of the Higgs scalar field. New terms of the form

$$\bar{\Psi}\Phi\psi_R, \quad (2.82)$$

known as *Yukawa terms*. Such terms are invariant under local SU(2) and U(1) transformations, as well as *Lorentz transformations*. Yukawa terms are added to the Lagrangian following

$$\mathcal{L}_{\text{Yukawa},2} = -\lambda_2 (\bar{\Psi}_L\Phi(\psi_2)_R + (\bar{\psi}_2)_R\bar{\Phi}\Psi_L). \quad (2.83)$$

λ_2 is known as the *Yukawa coupling*, and indicates the interaction strength between the fermions and the Higgs field, leading the mass terms for the spin- $\frac{1}{2}$ fields after symmetry breaking. After evaluating $\mathcal{L}_{\text{Yukawa}}$ at the VEV (Eq. 2.61), we obtain

$$\mathcal{L}_{\text{Yukawa},2}(\Phi_{\text{un}}) = -\frac{\lambda_2(v+h)}{\sqrt{2}} ((\bar{\Psi}_2)_L(\psi_2)_R + (\bar{\psi}_2)_R(\Psi_2)_L) = -\frac{\lambda_2 v}{\sqrt{2}}(\bar{\psi}_2\psi_2) - \frac{\lambda_f h}{\sqrt{2}}(\bar{\psi}_2\psi_2). \quad (2.84)$$

The first term in Eq. 2.84 represent the *fermion mass term* for the ψ_2 component of the doublet, and the second is the *fermion-Higgs interaction*. The mass can be generated for ψ_1 in a similar way, but considering instead the charge conjugated Higgs field,

$$\tilde{\Phi} = \epsilon\Phi^* = \begin{pmatrix} 0 & 1 \\ -1 & 0 \end{pmatrix} \begin{pmatrix} 0 \\ \frac{v+h}{\sqrt{2}} \end{pmatrix} = \begin{pmatrix} \frac{v+h}{\sqrt{2}} \\ 0 \end{pmatrix}. \quad (2.85)$$

The resulting mass terms for ψ_1 are then

$$\mathcal{L}_{\text{Yukawa},1} = -\lambda_f \left(\bar{\Psi}_L \tilde{\Phi} (\psi_1)_R + (\bar{\psi}_1)_R \tilde{\Phi} \Psi_L \right). \quad (2.86)$$

Generalizing to all the fermions in the SM, the weak interaction groups the left-handed particles into SU(2) doublets,

$$\begin{array}{cc} \textit{Quarks} & \textit{Leptons} \\ \left(\begin{array}{c} u \\ d \end{array} \right)_L, & \left(\begin{array}{c} c \\ s \end{array} \right)_L, & \left(\begin{array}{c} t \\ b \end{array} \right)_L, & \left(\begin{array}{c} \nu_e \\ e \end{array} \right)_L, & \left(\begin{array}{c} \nu_\mu \\ \mu \end{array} \right)_L, & \left(\begin{array}{c} \nu_\tau \\ \tau \end{array} \right)_L. \end{array}$$

The mass of each fermion in the SM can be generated through their interaction with the Higgs field, and takes the form:

$$m_f = \frac{\lambda_f v}{\sqrt{2}}. \quad (2.87)$$

The coupling strength of the fermion with the Higgs is given by,

$$c_f = \frac{\lambda_f h}{\sqrt{2}} = \frac{m_f h}{v}. \quad (2.88)$$

This last expression indicates that the coupling strength of the fermions with the Higgs field is proportional to the mass of the fermion, which can be tested experimentally.

As a final note, we will mention a few words on the conserved quantity following from the SU(2) symmetry. In the case of the U(1) symmetry, we identified the conserved quantities to be the electric charge density and the electric current. From Noether's theorem, the analogous quantity to the electric charge in the SU(2) symmetry is known as *isospin*.

Strong interaction: SU(3) symmetries

It is possible to write a locally SU(3) invariant Lagrangian for *three* fermion fields, in the same way it was done for two fermion fields and the SU(2) transformations. The corresponding covariant derivative takes the form

$$D_\mu Q \equiv \left[\partial_\mu - ig_s (T_\alpha) G_\mu^\alpha \right] Q, \quad \alpha = 1, 2, 3, \dots, 8. \quad (2.89)$$

Q represents a SU(3) triplet of fermion fields

$$Q = \begin{pmatrix} q_1 \\ q_2 \\ q_3 \end{pmatrix}, \quad (2.90)$$

where g_s is the coupling for the strong interaction. T_α are the generators of the SU(3), which are related to the *Gell-Mann matrices*⁷ λ_α of dimensions 3×3 :

$$T_\alpha = \frac{\lambda_\alpha}{2}, \quad (2.91)$$

which satisfy the Lie algebra:

$$[T_\alpha, T_\beta] = i f^{\alpha\beta\gamma} T^\gamma. \quad (2.92)$$

$f^{\alpha\beta\gamma}$ are called the structure constants of SU(3)⁸, analogous to the Levi-Civita symbol in SU(2). G_μ^α are fields analogous to the fields introduced in the SU(2) case. We define,

$$\mathcal{G}_\mu \equiv T_\alpha G_\mu^\alpha \quad (2.93)$$

as the *spin-1 massless gluon fields*, and the field strength tensor $\mathcal{G}_{\alpha\beta}$ is defined as

$$\mathcal{G}_{\alpha\beta} = \partial_\alpha \mathcal{G}_\beta - \partial_\beta \mathcal{G}_\alpha - g_s [\mathcal{G}_\alpha, \mathcal{G}_\beta]. \quad (2.94)$$

The Lagrangian that is invariant under the local SU(3) transformations:

$$Q(x) \rightarrow Q'(x) = \exp\left(i \frac{\theta_\alpha(x) \lambda^\alpha}{2}\right) Q(x),$$

$$D_\mu Q(x) \rightarrow D'_\mu Q'(x) = \exp\left(i \frac{\theta_\alpha(x) \lambda^\alpha}{2}\right) D_\mu Q(x), \quad (2.95)$$

$$\mathcal{G}_\mu(x) \rightarrow \mathcal{G}'_\mu(x) = \mathcal{G}_\mu(x) + f^{\alpha\beta\gamma} T^\gamma \theta_\beta(x) G_{\mu\gamma}(x) - \frac{1}{g_s} \partial_\mu (\theta^\alpha(x)), \quad (2.96)$$

can be written as

$$\mathcal{L}_{\text{locally SU(3) invariant}} = \bar{Q}(i D_\mu \gamma^\mu - m) Q - \frac{1}{4} \mathcal{G}_{\alpha\beta} \mathcal{G}^{\alpha\beta} = \mathcal{L}_{\text{QCD}}, \quad (2.97)$$

which corresponds to the Lagrangian of quantum chromodynamics (QCD), the QFT for the strong interactions, only experienced by quarks.

Using Noether's theorem, the quantity conserved is *color*. There are three color charges, since there are only three diagonal generators in SU(3), which are labeled as *red*, *blue* and *green*⁹. There-

⁷In analogy to the relation between the SU(2) generators and the Pauli matrices.

⁸ $f^{123} = 1$, $f^{147} = -f^{156} = f^{246} = f^{257} = f^{345} = -f^{367} = \frac{1}{2}$, and $f^{458} = f^{678} = \frac{\sqrt{3}}{2}$.

⁹Hence, the name *chromodynamics*.

fore, each quark is a SU(3) triplet (Eq. 2.90) of quark fields in three different colors :

$$q_c = Q = \begin{pmatrix} q_r \\ q_b \\ q_g \end{pmatrix}, \quad \text{where } c = r, b, g. \quad (2.98)$$

One final note about \mathcal{L}_{QCD} is that the symmetry is conserved even when adding mass terms for the fermions in the triplet $\bar{Q}mQ$, as long as the particles have the same mass, which is the case.

Concluding remarks

The weak coupling G_F ¹⁰, in principle, can be different for each fermion in the SM. The study of the decays of the muon ($\mu^- \rightarrow e^- \bar{\nu}_e \nu_\mu$) and tau leptons ($\tau^- \rightarrow e^- \bar{\nu}_e \nu_\tau$ and $\tau^- \rightarrow \mu^- \bar{\nu}_\mu \nu_\tau$) experimentally, it has been observed that the weak couplings of the electron, muon and tau leptons are consistent:

$$G_F^{(e)} = G_F^{(\mu)} = G_F^{(\tau)}, \quad (2.99)$$

providing strong experimental evidence for the *lepton universality of the weak charged current* [41]. In other words, there is a *universal* coupling strength at the $W e \nu_e$, $W \mu \nu_\mu$ and $W \tau \nu_\tau$ vertices.

On the other hand, the weak coupling can also be measured for quarks, for example, in nuclear β -decays. The cross section will be proportional to $G_F^{(e)}$ and $G_F^{(\beta)}$, where $G_F^{(\beta)}$ is the coupling at the weak interaction vertex of the quarks. In this example, it has been found that the coupling at the ud quark weak interaction vertex is 5% smaller than the $\mu^- \nu_\mu$ vertex. Other measurements comparing the decays of $K^- (u\bar{s}) \rightarrow \mu^- \bar{\nu}_\mu$ and $\pi^- (u\bar{d}) \rightarrow \mu^- \bar{\nu}_\mu$ shows that the $G_F^{(u\bar{s})}$ is about 20 times smaller than $G_F^{(u\bar{d})}$, therefore, indicating there are no universal weak couplings to the quarks. This difference was originally explained by the Cabibbo hypothesis, which states that the weak couplings to quarks have the same strength as the weak couplings to leptons, except that the *weak eigenstates* of quarks (q') are not the same as the mass eigenstates (q). The Cabibbo mechanism is extended to the three generations of the SM, and the relation between the weak and mass quark eigenstates is given by the Cabibbo-Kobayashi-Maskawa (CKM) matrix:

$$\begin{pmatrix} d' \\ s' \\ b' \end{pmatrix} = \begin{pmatrix} V_{ud} & V_{us} & V_{ub} \\ V_{cd} & V_{cs} & V_{cb} \\ V_{td} & V_{ts} & V_{tb} \end{pmatrix} \begin{pmatrix} d \\ s \\ b \end{pmatrix}. \quad (2.100)$$

Conceptually, a similar phenomenon is observed for neutrinos. Experimental results on neutrino experiments have shown that ν_e , ν_μ , and ν_τ are not fundamental particle states. Instead, they are linear combinations of the mass eigenstates ν_1 , ν_2 and ν_3 . The relationship between the weak and mass neutrino eigenstates is given by the 3×3 Pontecorvo-Maki-Nakagawa-Sakata (PMNS) matrix [41]:

¹⁰ G_F is the Fermi constant and is related to the weak coupling g_W by $\frac{G_F}{\sqrt{2}} = \frac{g_W^2}{8m_W^2}$

$$\begin{pmatrix} \nu_e \\ \nu_\mu \\ \nu_\tau \end{pmatrix} = \begin{pmatrix} U_{e1} & U_{e2} & U_{e3} \\ U_{\mu1} & U_{\mu2} & U_{\mu3} \\ U_{\tau1} & U_{\tau2} & U_{\tau3} \end{pmatrix} \begin{pmatrix} \nu_1 \\ \nu_2 \\ \nu_3 \end{pmatrix}. \quad (2.101)$$

2.2 Open questions in the SM

The SM is one of the greatest triumphs of modern physics, being able to reproduce the experimental data for a wide variety of natural phenomena at the small scales. However, the SM cannot provide an explanation for all physical phenomena. Assuming neutrinos are Dirac fermions, there are 26 free parameters in the SM that need to be put by hand, which is a testament to the fact that the SM is a model where the parameters are chosen to match the observations, rather than coming from a higher theoretical principle [41]. Among the aspects that the SM cannot answer are:

- the origin of the electroweak spontaneous symmetry breaking,
- the relatively small Higgs boson mass,
- the different coupling strengths for each interaction,
- the nature of dark matter and dark energy,
- the origin of neutrino oscillations, which implies non-zero neutrino masses,
- the origin of the matter-antimatter asymmetry in the universe,
- the description of gravity at quantum scales,
- the experimental deviations from the SM prediction for the muon anomalous magnetic moment ($a_\mu = g_\mu - 2$) and B-meson decay rates, etc.

We can categorize these problems into two main classes: conceptual problems and observational problems. Conceptual problems are issues in the model that do not go against any experimental results, but are bothersome from the theoretical point of view. Observational problems are issues related to deviations from the SM predictions observed in experimental data. **The work presented in this document was inspired by one conceptual problem and one observational problem: the electroweak hierarchy problem and the nature of dark matter**, respectively. In this section, I briefly state some highlight points for four of the SM problems.

Conceptual problem: the electroweak hierarchy problem

The *hierarchy problem* in physics can be thought of as the difference in the coupling strengths for each interaction. One example of this is indicated by the large difference between the scales for the weak and gravitational interactions:

$$\frac{G_F}{G_N} \sim 10^{33}, \quad (2.102)$$

where G_F is the Fermi constant, and G_N is the Newtonian constant of gravitation, which indicates the gravitational force strength. In the SM, the *electroweak hierarchy problem* [7] can be defined as the quadratic sensitivity of the Higgs boson mass m_H corrections introduced by virtual effects coming from particles that couple directly or indirectly to the Higgs field [8, 9]:

$$m_H^2 = \underbrace{m_{H,0}^2}_{\text{“bare” Higgs mass}} + \delta m_H^2, \quad \text{where } \delta m_H^2 \sim \Lambda_X. \quad (2.103)$$

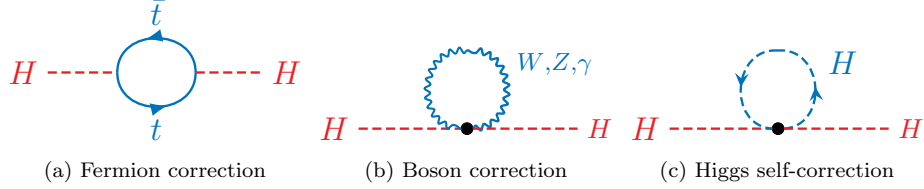


Figure 2.4: Representative Feynman diagrams for the different one-loop corrections to the Higgs mass.

In the previous section, most of the discussion on the spontaneous electroweak symmetry breaking was based on considering tree-level diagrams. However, we know that there are contributions from higher order processes (loops), which will introduce corrections to the Higgs boson mass. Some representative Feynman diagrams for various one-loop corrections to the Higgs mass are shown in Fig. 2.4. The corresponding corrections are:

- (a) Dirac fermion loops: $\delta m_{H,f}^2 = -\frac{|\lambda_f|^2}{8\pi^2} \Lambda_X^2$, where c_f is the Higgs-fermion coupling,
- (b) boson loops: $\delta m_{H,b}^2 = +\frac{1}{16\pi^2} g_W^2 \Lambda_X^2$, where g is the electroweak coupling,
- (c) Higgs self-interaction: $\delta m_{H,H}^2 = +\frac{1}{16\pi^2} \lambda^2 \Lambda_X^2$, where λ refers to the second term of the Higgs potential (Eq. 2.54).

The SM is renormalizable, which means that no divergences will be obtained for all the loop corrections, regardless of how large are the virtual momenta in the loop integrals. Nevertheless, it is natural to assume that the SM is part of a larger theory that includes *new physics* at some high energy scale Λ_X . Experimental evidence for this problem comes from the relatively small measured Higgs boson mass ($m_H^{\text{obs.}} = 125.8$ GeV). The Higgs boson mass is not the only one affected by these corrections. Since the SM fermions and weak bosons get their mass from their interaction with the Higgs field, then the entire mass spectrum of the SM is directly or indirectly sensitive to the cutoff scale Λ_X .

If yet undiscovered heavy particles exist, then more corrections need to be taken into account which could blow up the physical mass value of the Higgs. For example, if we consider that new physics is present at the scale when quantum gravity becomes important, which is thought to be indicated by the Planck mass, $\Lambda_X = m_{\text{Planck}} \propto G_N^{-1/2} \simeq 2.4 \times 10^{18}$ GeV, then, the order of the expected corrections to the Higgs mass would be $\delta m_{H,\text{Planck}}^2 \sim 10^{36}$ GeV. Even when these new particles didn't interact directly with the Higgs field, as long as they interact with other particles which do couple to the Higgs field, they will give large contributions to δm_H^2 from diagrams with three or more loops.

There are many ways in which this behavior can be explained and has given room for several hypothesis. For example, one possibility is that the Higgs boson field is not fundamental (composite Higgs); however, the experimental evidence indicates otherwise [44]. Another option is that the ultimate ultraviolet cutoff scale is much lower than the Planck scale. This would imply that there is no new physics above the electroweak scale, which is a challenging assumption to make. So, if the Higgs boson is a fundamental particle and there is new physics above the electroweak scale, then the only remaining options are (i) *none* of the high-mass particles or condensates couple to the Higgs scalar field at all, or, (ii) some mysterious cancellation happens between the various contributions to δm_{H}^2 .

One way this cancellation can happen is if there exists another *hidden symmetry*. It is important to note that higher order corrections to the scalar Higgs mass from fermion loops carry a relative negative sign with respect to the boson loops. Then, a logical assumption would be to think that there exists a symmetry that relates fermions and bosons, which would neatly cancel the Λ_{X}^2 contributions to δm_{H}^2 . Such symmetry, known as *supersymmetry* (SUSY), essentially assigns a scalar boson counterpart to each SM fermion field and vice versa. As a result, new supersymmetric particles called *superpartners* are hypothesized for all the SM particles. Each superpartner carries the same quantum numbers as its SM partner except for the spin, which differs by half a unit [7, 10, 11]. This idea will be explored in more detail in the next section.

Observational problem 1: Dark matter

The Swiss astronomer Fritz Zwicky proposed the term *dark matter* (DM) in 1933, after observing evidence of the potential presence of a non-luminous matter that would account for the radial velocity dispersion of galaxies in the Coma cluster [45]. These observations were later observed in the Virgo cluster and later in the local group [46, 47]. Another set of observations which are regarded as the classic evidence for the existence of DM are related to the rotational velocity curves of spiral galaxies. More specifically, in 1939, it was found that the outer regions of the Andromeda galaxy were rotating at larger velocities than the ones expected based on the *luminous* matter distribution [48, 49] (Fig. 2.5).

The DM hypothesis started to gain more relevance in the 1970s, when Ostriker and Peebles showed that introducing a *halo*, a massive spherical component in models of galaxy disks could solve the instabilities of flattened galaxies that would have been otherwise predicted [51, 52]. More observational data accumulated in the years that followed, including the detection of X-rays from hot gas in elliptical galaxies, gravitational lensing, and the cosmic microwave background (CMB) [53, 54, 55]. Measurements based on the CMB provide evidence that around 84% of the matter in the Universe corresponds to DM [13]. It turns out that none of the SM particles have the right characteristics (mass, couplings, etc.) to explain these results. Therefore, the need to extend the SM to incorporate new types of particles is important, in order to provide a particle description of DM.

Combining the information from different astronomical probes, these are the main known characteristics of DM [56]:

- it is electrically neutral,

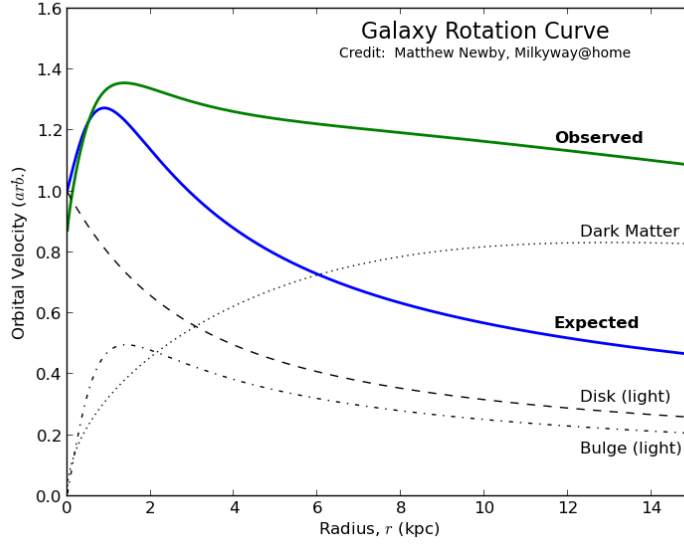


Figure 2.5: Galaxy rotation curve of a spiral galaxy [50].

- it is not made up of SM particles, but it is stable on Hubble time scales,
- it is “cold”, meaning, it is non relativistic, and,
- it is effectively non-interacting and not self-interacting due the stability of the halo.

2.3 Supersymmetry as a solution to the SM issues

Many resources introduce the concept of supersymmetry by looking at a simple supersymmetric field theory [7, 9, 57]. In this document, we will follow the same approach to introduce the basic concepts of a supersymmetric theory which can then be extended to the minimal supersymmetric standard model (MSSM), the simplest SUSY extension of the SM, which is used as the benchmark scenario for the work presented. The description to follow is based on the notes presented in Ref. [57].

Consider a free theory with a massive fermion $\psi(x)$ with mass m , and two complex scalar bosons of mass m (same mass) which will be denoted by $\phi_+(x)$ and $\phi_-(x)$. The Lagrangian for this system is:

$$\mathcal{L} = (\partial^\mu \phi_+^*)(\partial_\mu \phi_+) - m^2 |\phi_+|^2 + (\partial^\mu \phi_-^*)(\partial_\mu \phi_-) - m^2 |\phi_-|^2 + \bar{\psi}(i\gamma^\mu \partial_\mu - m)\psi. \quad (2.104)$$

This Lagrangian has spacetime symmetries, including translations¹¹, rotations, and boosts¹². The spinor in this theory will have its left- and right-handed components, ψ_L and ψ_R transforming

¹¹Translation transformations: $x^\mu \rightarrow x^\mu + a^\mu$, so $\phi(x) \rightarrow \phi(x - a) = \phi(x) - a^\mu \partial_\mu \phi(x)$, $\Rightarrow \delta_a \phi(x) = a^\mu \partial_\mu \phi(x)$

¹²Given by the Lorentz transformations: $x^\mu \rightarrow x^\mu + w^{\mu\nu} x_\nu$, so $\phi(x^\mu) \rightarrow \phi(x^\mu - w^{\mu\nu} x_\nu) \Rightarrow \delta_w \phi(x) = w^{\mu\nu} x_\nu \partial_\nu \phi(x) = \frac{1}{2} w^{\mu\nu} (x_\mu \partial_\nu - x_\nu \partial_\mu) \phi(x)$

differently under Lorentz transformations:

$$\psi_L \rightarrow \psi'_L = \left(1 - i\theta^i \frac{\sigma^i}{2} - \beta^i \frac{\sigma^i}{2}\right), \quad (2.105)$$

$$\psi_R \rightarrow \psi'_R = \left(1 - i\theta^i \frac{\sigma^i}{2} + \beta^i \frac{\sigma^i}{2}\right). \quad (2.106)$$

Any R-handed spinor can be written in terms of a L-handed one, by using

$$\psi_R = -\epsilon \chi_L^*, \quad \epsilon \equiv -i\sigma^2 = \begin{pmatrix} 0 & -1 \\ 1 & 0 \end{pmatrix}. \quad (2.107)$$

Writing the Lagrangian in terms of two left-handed spinors ψ_+ and ψ_- , where $\psi_L = \psi_+$ and $\psi_R = -\epsilon\psi_-^*$, we obtain:

$$\begin{aligned} \mathcal{L} = & (\partial^\mu \phi_+^*)(\partial_\mu \phi_+) + \psi_+^\dagger i\bar{\sigma}^\mu \partial_\mu \psi_+ + (\partial^\mu \phi_-^*)(\partial_\mu \phi_-) + \psi_-^\dagger i\bar{\sigma}^\mu \partial_\mu \psi_- \\ & - m^2(|\phi_+|^2 + |\phi_-|^2) - m(\psi_+^T \epsilon \psi_- + h.c.). \end{aligned} \quad (2.108)$$

\mathcal{L} possesses one more symmetry, which is given by the transformation:

$$\delta_\xi \phi_\pm = \sqrt{2}\xi^T \epsilon \psi_\pm, \quad (2.109)$$

$$\delta_\xi \psi_\pm = \sqrt{2}i\sigma^\mu \epsilon \xi^* \partial_\mu \phi_\pm, \quad (2.110)$$

where ξ is a constant anti-commuting 2-component L-spinor. Basically, this is a transformation that takes a fermion into a boson and vice versa. The invariance under this type of transformation is the so-called "supersymmetry". SUSY is a spacetime symmetry, since the transformation parameters carry spinor indices. Note that one of the main assumptions in this "toy" theory is that the fermion and boson states have the same mass. Also, there are equal numbers of fermionic and bosonic degrees of freedom. As an additional note, the algebra of the SUSY transformations is consistent with that of a translation:

$$[\delta_\xi, \delta_\eta] \phi_L = a^\mu \partial_\mu \chi_L, \quad \text{with} \quad a^\mu = 2i(\xi^\dagger \bar{\sigma}^\mu \eta - \eta^\dagger \bar{\sigma}^\mu \xi). \quad (2.111)$$

Solution to the electroweak hierarchy problem

From Noether's theorem, the conserved charge for translations in time is the Hamiltonian H . Therefore, the anti commutator of two SUSY transformations gives the Hamiltonian, and the VEV will be

$$\langle 0 | \{T_{\text{SUSY}}, T'_{\text{SUSY}}\} | 0 \rangle \propto \langle 0 | H | 0 \rangle. \quad (2.112)$$

If SUSY is unbroken, the ground state is supersymmetric and $T_{\text{SUSY}}|0\rangle = 0$ and the ground energy state, $\langle 0|H|0\rangle = 0$. This means that in a SUSY theory, the ground state energy does not have any quartic divergences. As it was discussed in the previous section, the higher order corrections to the mass of a scalar field are usually proportional to the square of the energy scale. This is not the case

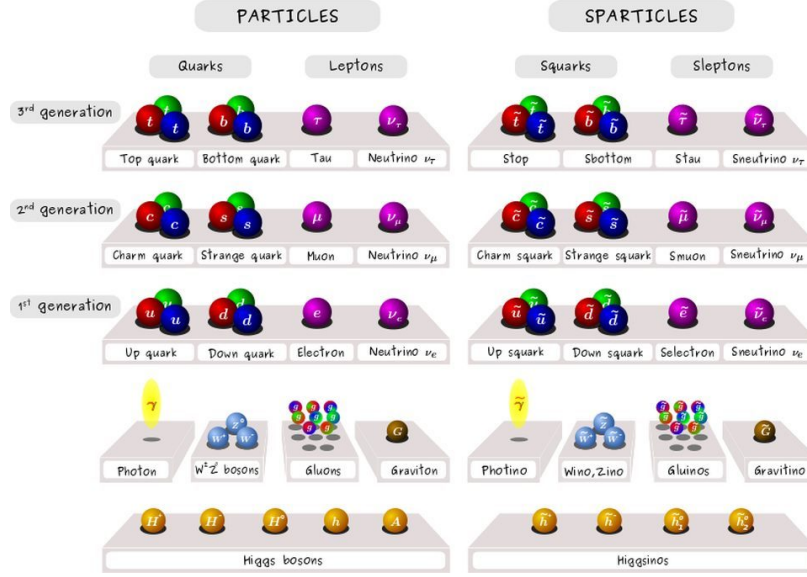


Figure 2.6: The SM particles and their supersymmetric counterparts when exact SUSY is assumed [58].

for fermions, which at worst can show logarithmic divergences

$$\delta m_f \propto m_{0,f} \log \left(\frac{m_{0,f}}{\Lambda} \right) \quad (2.113)$$

Combining the fact about fermion mass corrections and the fact that in SUSY the fermion and boson masses are equal, leads to the statement that **in a SUSY theory, there is no quadratic divergence in the boson mass**, which is the core of the electroweak hierarchy problem in the SM.

The basic SUSY *modules* are a complex scalar and a left-handed 2-component spinor of the same mass,

$$(\phi_+, \psi_+), \quad (\phi_-, \psi_-), \quad (2.114)$$

forming a representation called *chiral supermultiplet*. The ψ_+ and ψ_- components are the analogs to the left- and right-handed components of the SM fermions. After applying SUSY, two scalars need to be added, one for each SM chiral component (ϕ_+ , ϕ_-). Though scalar fields do not have chirality, each SUSY field is commonly referred by the chirality of their fermionic partners. For example, for the tau lepton, we have the τ_L and τ_R spinors and the corresponding superfields are the left- and right-handed staus $\tilde{\tau}_L$ and $\tilde{\tau}_R$. In the SM there are also spin-1 gauge bosons, A_μ^a , with a denoting the gauge group index. In SUSY theories, we also have vector supermultiplets

$$(A_\mu^a, \lambda^a), \quad (2.115)$$

where λ^a corresponds to a *gaugino*. Each on-shell gauge field has two degrees of freedom (two physical transverse polarization states), so λ^a is a 2-component spinor. Given that A_μ^a is real, then

λ^a can be written as a 4-component spinor if it is a Majorana spinor:

$$\begin{pmatrix} \lambda \\ -\epsilon\lambda^* \end{pmatrix} \quad (2.116)$$

We know that in order for SUSY to exist and be consistent with the experimental data, it must be broken. The best indication for this is that we have not detected any scalar particles with the masses of the SM particles. Even with this constraint, SUSY is relevant to solve the hierarchy problem because although it may be broken by mass terms, there is no reintroduction of quadratic divergences. This can be seen using only a dimensional analysis. Adding an extra constant term \tilde{m}^2 to the scalar mass term in the Lagrangian:

$$m_{0,s}^2 = m_{0,f}^2 + \tilde{m}^2, \quad (2.117)$$

we can see that if $\tilde{m}^2 = 0$, there should not be a quadratic divergence. Therefore, for $\tilde{m}^2 \neq 0$,

$$\delta m_s^2 \sim \Lambda^2 + m_{0,s}^2 \log\left(\frac{m_{0,f}}{\Lambda}\right) \rightarrow \tilde{m}^2 + m_{0,s}^2 \log\left(\frac{m_{0,f}}{\Lambda}\right). \quad (2.118)$$

but there is nothing in perturbation theory that can provide this type of correction. Hence, even though the fermion and scalar masses are different, the cancellation of the quadratic divergences remains, which is known as *soft supersymmetry breaking*. A more complete picture on soft supersymmetry breaking is based on spontaneous SUSY breaking. If SUSY is spontaneously broken, then the ground state,

$$T_{\text{SUSY}}|0\rangle \neq 0, \quad (2.119)$$

and it has a non-zero positive energy. Similar to the spontaneous electroweak symmetry breaking mechanism, a potential will be present for each scalar field in SUSY, taking the form

$$V(\phi_+, \phi_-, h) = |y|^2 [|\phi_+|^2 |\phi_-|^2 + |h|^2 |\phi_-|^2 + |h|^2 |\phi_+|^2] \quad (2.120)$$

Minimal Supersymmetric Standard Model

In the minimal supersymmetric extension of the SM, each SM particle has one or two superpartners, and a second Higgs doublet is added to the Higgs sector. The chiral and gauge supermultiplets are described in Tab. 2.1. After electroweak symmetry breaking, the W^0 and B^0 fields mix together to give the physical (mass) eigenstates corresponding to the photon γ and Z bosons. The corresponding mixtures of the \tilde{W}^0 and \tilde{B}^0 bosons are called the zino \tilde{Z}^0 and photino $\tilde{\gamma}$ (Fig. 2.6).

The effective Lagrangian of the MSSM can be written as

$$\mathcal{L}_{\text{MSSM}} = \mathcal{L}_{\text{SUSY}} + \mathcal{L}_{\text{soft}}, \quad (2.121)$$

with $\mathcal{L}_{\text{SUSY}}$ as the Lagrangian containing all the gauge and Yukawa interactions and symmetric under SUSY transformations, and $\mathcal{L}_{\text{soft}}$ as the Lagrangian which violates SUSY but only contains mass terms and coupling parameters with positive dimension [7].

	Names		spin-0	spin- $\frac{1}{2}$	SU _C (3), SU _L (2), U _Y (1)
Chiral	squarks, quarks (3 families)	Q	$(\tilde{u}_L, \tilde{d}_L)$	(u_L, d_L)	$(\mathbf{3}, \mathbf{2}, \frac{1}{6})$
		\bar{u}	\tilde{u}_R^*	u_R^\dagger	$(\bar{\mathbf{3}}, \mathbf{1}, -\frac{2}{3})$
		\bar{d}	\tilde{d}_R^*	d_R^\dagger	$(\bar{\mathbf{3}}, \mathbf{1}, \frac{1}{3})$
	sleptons, leptons 3 families	L	$(\tilde{\nu}, \tilde{e}_L)$	(ν, e_L)	$(\mathbf{1}, \mathbf{2}, -\frac{1}{2})$
		\bar{e}	\tilde{e}_R^*	e_R^\dagger	$(\mathbf{1}, \mathbf{1}, 1)$
	Higgs, higgsinos	H_u	(H_u^+, H_u^0)	$(\tilde{H}_u^+, \tilde{H}_u^0)$	$(\mathbf{1}, \mathbf{2}, +\frac{1}{2})$
H_d		(H_d^0, H_d^-)	$(\tilde{H}_d^0, \tilde{H}_d^-)$	$(\mathbf{1}, \mathbf{2}, -\frac{1}{2})$	
	Names		spin- $\frac{1}{2}$	spin-1	SU _C (3), SU _L (2), U _Y (1)
Gauge	gluino, gluon		\tilde{g}	g	$(\mathbf{8}, \mathbf{1}, 0)$
	winos, W bosons		$\tilde{W}^\pm, \tilde{W}^0$	W^\pm, W^0	$(\mathbf{1}, \mathbf{3}, 0)$
	bino, B boson		\tilde{B}^0	B^0	$(\mathbf{1}, \mathbf{1}, 0)$

Table 2.1: Chiral and gauge supermultiplets in the MSSM [7].

An important symmetry in the MSSM is called *R-parity*. In the SM, the baryon number B and lepton number L conservation is assumed since there is no experimental evidence that indicates otherwise. In the MSSM, some of the terms included in the super potential can violate B and L . A new symmetry, referred to as *matter symmetry*, is introduced to avoid the presence of these terms, and it is defined as

$$P_M = (-1)^{3(B-L)}, \quad (2.122)$$

which is a multiplicatively conserved quantum number. All members of a supermultiplet have the same matter parity, which makes matter parity and SUSY commute. R-parity is expressed as a modified version of the matter parity that includes information of the spin s of a given particle:

$$P_R = (-1)^{3(B-L)+2s}. \quad (2.123)$$

Phenomenologically, P_R is equivalent to a charge that indicates if a particle is supersymmetric or not. The SM particles and Higgs bosons have even R-parity ($P_R = +1$), whereas the squark, sleptons, gauginos and higgsinos have odd R-parity ($P_R = -1$). If R-parity is conserved,

- there is no mixing between particles with opposite R-parities (no mixing between SM and SUSY particles),
- every interaction vertex in the theory contains an even number of SUSY particles \rightarrow conservation of number of SUSY particles,
- as a consequence, the lightest supersymmetric particle (LSP) in the theory must be stable,
- all SUSY particles but the LSP will decay into a state with an odd number of LSPs, and,
- SUSY particles can only be produced in even numbers in particle collisions.

Once the electroweak symmetry breaking and SUSY breaking effects are included, the electroweak gauginos and the higgsinos can mix, as well as the various sets of squarks, sleptons and Higgs scalars

that have the same electric charge. Gluinos are the exception to the mixing, since they do not have the appropriate quantum numbers to mix with any other particles. Thus, the physical SUSY states will be a combination of the different SUSY fields.

Names	Spin	P_R	Gauge eigenstates	Mass eigenstates
Higgs bosons	0	+1	$H_u^0, H_d^0, H_u^+, H_d^-$	h^0, H^0, A^0, H^\pm
squarks	0	-1	$\tilde{u}_L, \tilde{u}_R, \tilde{d}_L, \tilde{d}_R$ $\tilde{s}_L, \tilde{s}_R, \tilde{c}_L, \tilde{c}_R$ $\tilde{t}_L, \tilde{t}_R, \tilde{b}_L, \tilde{b}_R$	(same) (same) $\tilde{t}_1, \tilde{t}_2, \tilde{b}_1, \tilde{b}_2$
sleptons	0	-1	$\tilde{e}_L, \tilde{e}_R, \tilde{\nu}_e$ $\tilde{\mu}_L, \tilde{\mu}_R, \tilde{\nu}_\mu$ $\tilde{\tau}_L, \tilde{\tau}_R, \tilde{\nu}_\tau$	(same) (same) $\tilde{\tau}_1, \tilde{\tau}_2, \tilde{\nu}_\tau$
neutralinos	$\frac{1}{2}$	-1	$\tilde{B}^0, \tilde{W}^0, \tilde{H}_u^0, \tilde{H}_d^0$	$\tilde{\chi}_1^0, \tilde{\chi}_2^0, \tilde{\chi}_3^0, \tilde{\chi}_4^0$
charginos	$\frac{1}{2}$	-1	$\tilde{W}^\pm, \tilde{H}_u^\pm, \tilde{H}_d^\pm$	$\tilde{\chi}_1^\pm, \tilde{\chi}_2^\pm$
gluino	$\frac{1}{2}$	-1	\tilde{g}	(same)
Goldstino (gravitino)	$\frac{1}{2}$ ($\frac{3}{2}$)	-1	\tilde{G}	(same)

Table 2.2: Particle content of the MSSM, considering the sfermion mixing of the first two generations to be negligible [7].

The electroweak gauginos and higgsinos mix with each other due to the effects from the electroweak symmetry breaking. The neutral Higgsinos and neutral gauginos combine to form four mass eigenstates known as *neutralinos*, denoted by $\tilde{\chi}_i^0$, with $i = 1, 2, 3, 4$. The charged higgsinos and winos mix together to form two mass eigenstates with charge ± 1 , called *charginos*, represented by $\tilde{\chi}_j^\pm$, with $j = 1, 2$. The labels i and j are assigned in such a way that they are in mass ascending order ($m_1 < m_2 < m_3 < m_4$), both for charginos and neutralinos. Throughout this text, we refer to charginos and neutralinos generally as *electroweakinos*.

In the case of the squarks and sleptons, the mixing is more pronounced for the third-generation mass superpartners (\tilde{t}, \tilde{b} and $\tilde{\tau}$), because of the larger Yukawa and soft couplings. This is not the case for the first- and second-generation mass superpartners, which in turn have negligible Yukawa couplings. Table 2.2 summarizes the particle content of the MSSM in its R-parity conserving and most general version.

2.4 Dark matter: bridge between particle physics and cosmology

When R-parity is conserved, the lightest neutralino ($\tilde{\chi}_1^0$) is assumed to be the lightest supersymmetric particle (LSP) [7, 12]. The DM particle candidate has been hypothesized to be a non-SM particle, weakly interacting and massive, which is consistent with the characteristics of the $\tilde{\chi}_1^0$ [7, 12, 14]. Therefore, the $\tilde{\chi}_1^0$ is a canonical DM candidate. However, regardless of having a DM candidate with the characteristics inferred from astronomical observations, another important test is the correct prediction of the measured DM relic density [13, 15, 16, 17]. In this section, I briefly introduce the relevant elements of the standard model of cosmology. Although the standard cosmological model offers a framework to study the evolution of the Universe, it does not describe the phenomena which

may have occurred in the early Universe [59]. These periods are not observable directly, because the photons emitted during these early phases interacted so strongly with the plasma of different particle species to be able to carry information. Only after the period known as "recombination" [59, 60], when neutral atoms were formed, photons *decoupled*¹³ from the other particles and could travel freely, carrying information¹⁴. Therefore, specific models are required to describe the early evolution of the Universe. Since it is challenging to experimentally verify these models, a wide variety of them have been proposed. In particular, there are two main categories for the early evolution, known as *thermal* and *non-thermal evolution*. In both cases, the $\tilde{\chi}_1^0$ DM hypothesis is relevant. I will discuss the differences between thermal and non-thermal scenarios, as well as the characteristics of the $\tilde{\chi}_1^0$ DM hypothesis in each one of them. At the end of the section, I summarize the main ideas to take away as the theoretical motivation for this research project and create a connection with the experimental motivation, presented in the next chapter.

Friedmann-Lemaître-Robertson-Walker cosmology

In this subsection, I review the cosmological standard model following a similar approach found in Refs. [59, 61]. Modern cosmology is based on the *cosmological principle*, which states that the Universe is homogeneous and isotropic at large scales¹⁵. It is evident that the length scale at which this principle holds true is larger than the size of our Solar system and the size of our galaxy, and it is actually difficult to determine [61].

When looking at the geometry of the Universe, only small deviations have been found, indicating the validity of the cosmological principle. In the cosmological standard model, the geometry of the universe is described by the Friedmann-Lemaître-Robertson-Walker (FLRW) metric, which is defined in terms of the proper time t in a spherical coordinate system $x^\mu = (t, r, \theta, \phi)$ as

$$ds^2 = g_{\mu\nu} dx^\mu dx^\nu = dt^2 - a^2(t) \left\{ \frac{dr^2}{1 - kr^2} + r^2 (d\theta^2 + \sin^2(\theta)d\phi^2) \right\}, \quad (2.124)$$

where $a(t)$ is known as the *scale* factor that quantifies the expansion of the Universe as a function of the cosmological time, and k is a constant that characterizes the global curvature of the Universe¹⁶. The cosmological principle tells us that these quantities only have a time (not space) dependence. It also allows us to treat the different types of energy and matter as ideal fluids. The total density ρ and pressure P of the energy-matter content of the Universe leads to the energy-momentum tensor

$$T^{\mu\nu} = (P + \rho)U^\mu U^\nu - P g^{\mu\nu}, \quad (2.125)$$

¹³That is, photons did not interacted strongly with other particles.

¹⁴These photons can be observed today in the cosmic microwave background (CMB), and constitute the basis of the measurements done by the WMAP and Planck collaborations.

¹⁵The cosmological principle is an extension of the Copernican principle that applies to the position of the Milky Way in the Universe as not being statistically different from the position of any other galaxies.

¹⁶ $k = 0$ indicates a Euclidean (flat) topology, $k > 0$ a spherical topology (closed) and $k < 0$ a hyperbolic (open) topology.

where U^μ is the 4-velocity. In the rest frame of each fluid, the non-zero components are $T^{00} = \rho$ and $T^{ij} = -Pg^{ij}$. The condition of energy conservation for each fluid,

$$D_\mu T_{\text{fluid}}^{\mu\nu} = 0, \quad (2.126)$$

where D_μ is the covariant derivative, and results into the expression

$$\dot{\rho}_{\text{fluid}} = -3\frac{\dot{a}(t)}{a(t)}(\rho_{\text{fluid}} + P_{\text{fluid}}), \quad \dot{a}(t) = \frac{da(t)}{dt}, \quad (2.127)$$

where the Hubble parameter H is defined as

$$H \equiv \frac{\dot{a}}{a}. \quad (2.128)$$

The Einstein equation,

$$G_{\mu\nu} = 8\pi G_{\text{N}} T_{\mu\nu} - g_{\mu\nu} \Lambda, \quad \Lambda = \text{cosmological constant} \quad (2.129)$$

relates the Einstein tensor to the energy-momentum content of the Universe. These equations can be expressed in the FLRW metric as:

$$H^2 = \frac{8\pi G_{\text{N}}}{3}\rho - \frac{k}{a^2} + \frac{\Lambda}{3}, \quad (2.130)$$

$$\frac{\ddot{a}}{a} = -\frac{4\pi G_{\text{N}}}{3}(\rho + 3P) + \frac{\Lambda}{3}, \quad (2.131)$$

Equation 2.130 implies that the rate of expansion $H = \frac{\dot{a}}{a}$ increases with the density of matter ρ , and Eq. 2.131 shows that the expansion of the universe is decelerated by ρ and P . Combining both of these equations, we can arrive to the covariant conservation equation of the energy-momentum tensor [60]:

$$\dot{\rho} + 3H(\rho + P) = 0. \quad (2.132)$$

The expansion rate of the Universe as a function of time can be determined by specifying the matter or energy content through an *equation of state* that relates ρ and P . Assuming that they are linearly related, $w \equiv P/\rho$, the conservation of energy momentum would be

$$\dot{\rho} + 3H\rho(1 + w) = 0, \quad (2.133)$$

and the scale factor $a(t)$,

$$a(t) \propto \left(\frac{t}{t_0}\right)^{\frac{2}{3(1+w)}}. \quad (2.134)$$

Another relevant equation is the expression for conservation of entropy per *comoving volume*¹⁷:

$$\frac{d}{dt}(sa^3) = 0, \quad (2.135)$$

¹⁷Comoving volume is the volume where the Universe expansion effects are removed. A non-evolving system would stay at a constant density in comoving coordinates even though the density is in fact decreasing due to the expansion of the Universe.

where s is the entropy density of the Universe. In cosmology, one usually refers to the scale factor a of the Universe at a certain point in time using the *redshift* z , such as

$$z = \frac{a_0}{a} - 1, \quad (2.136)$$

so that the redshift of the present time is $z = 0$ and the very beginning of the Universe corresponds to a $z \rightarrow \infty$ redshift. At the present time, the values of the parameters are denoted with a 0 index, the H_0 is the *Hubble constant* and ρ_0^c is called the *critical density*:

$$H_0^2 = \frac{8\pi G_N}{3}\rho_0 - \frac{k}{a_0^2} = \frac{8\pi G_N}{3}\rho_0^c. \quad (2.137)$$

In general, the densities of each energy-mass type (fluid) in the universe are normalized to the critical density,

$$\Omega_{\text{fluid}} = \frac{\rho_0^{\text{fluid}}}{\rho_0^c}, \quad (2.138)$$

and the Ω_{fluid} densities are called *cosmological parameters*. In addition, the curvature term can be thought of as a curvature energy density:

$$\rho_k = -\frac{3k}{8\pi G_N a^2}, \quad (2.139)$$

and has a pressure $P_k = -\rho_k/3$. There are three main types of energy fluids in the Universe:

- matter ($w = 0$): dark matter and baryonic matter (described by the SM),
- radiation ($w = 1/3$): composed of relativistic particle species (photons and neutrinos), and,
- dark energy: an unidentified component of negative pressure.

In the standard cosmological model, dark matter is considered not relativistic (cold), and dark energy is considered to be a *cosmological constant* Λ , with a constant density and pressure ($\rho_\Lambda = -P_\Lambda$). The most recent measurements of the cosmological parameters and the Hubble constant were done by the Planck collaboration and are summarized in Tab. 2.3.

Parameter	Symbol	Value
Hubble constant	H_0	67.66 ± 0.42 km/s/Mpc
Cosmological parameters		
Total matter	Ω_m	0.3111 ± 0.0056
Cold dark matter	$\Omega_c h^2$	0.11933 ± 0.00091
Baryonic matter	$\Omega_b h^2$	0.02242 ± 0.00014
Cosmological constant	Ω_Λ	0.6889 ± 0.0056
Curvature energy	Ω_k	0.0007 ± 0.0037

Table 2.3: Cosmological parameters measured by the Planck collaboration [59, 62], where $h = H_0/(100 \text{ km/s/Mpc})$ is the reduced Hubble parameter.

The age of the universe can be determined with the Hubble parameter written as a function of the cosmological parameters and the a scale factor as

$$H(a) = H_0 a (\Omega_k a^{-2} + \Omega_m^0 a^{-3} + \Omega_r^0 a^{-4} + \Omega_\Lambda)^{1/2}, \quad (2.140)$$

by integrating $[H(a)]^{-1}$ from $a = 0$ to $a = 1$.

Standard thermal evolution of the early Universe

The standard cosmological model is based on the Big Bang model. The beginning of the history of the Universe is set at $t = 0$, with $a(0) = 0$. In general, it is often considered that our current physical description of Nature is not valid before $t_{\text{Planck}} = 5.39 \times 10^{-44}$ s, where a quantum gravity description would be necessary. There are different models that describe the potential evolution of the early Universe before the energy and time scale we are able to probe with experiments like particle colliders. The present day laboratory energy constraints are of the order of $\mathcal{O}(E) \approx 10$ TeV, which is equivalent to a mean temperature¹⁸ of the Universe of $T = 10^{16}$ K, and a scale of $a \approx 10^{-16}$. The standard cosmological model is based on thermal history of the Universe, which is described in the next section. A brief description of the non-thermal evolution is also included in a later section of this chapter. The research project described in this document is relevant for both scenarios, being a testament of the great impact this data analysis on both particle physics and cosmology.

The first instants after the Big Bang, the Universe is said to be in a *radiation dominated era*, when its state was of extreme heat and pressure, occupying a tiny volume ($z \in (\infty, 3400)$). Times earlier than $t(a = 10^{-16})$ are thought to be times when physics beyond the Standard Model was present, such as SUSY. As the Universe cooled down, the primordial plasma condensed to quarks, gluons, vector bosons, leptons, baryons and unstable mesons. This is known as the *matter dominated era* ($z = (3400, 0.3)$). Particle behavior in the statistical ensemble is determined by the number of spin states for each particle species. All particles were relativistic and constantly colliding and exchanging energy and momentum with each other and with the radiation photons. *Thermal equilibrium* could be reached after a few collisions. In this stage, the available energy was distributed evenly among all particles in a stable energy spectrum (*blackbody spectrum*).

The particles that were involved in thermal equilibrium at a given energy depends on the reaction rate of the particle, and the expansion rate of the Universe. If the reaction rate is slower than the expansion rate, then the distance between particles grows so fast that they cannot find each other. Therefore, those particles drop out of thermal equilibrium [60]. For most of this era, the reaction rates of particles in the Universe have been much greater than the Hubble expansion rate, so thermal equilibrium should have been maintained in any local comoving volume element. Since there is no net flow of energy, the expansion is defined as *adiabatic*.

When the temperature fell to $T = 10^{11}$ K ($E \approx 300$ MeV), the energy of all electrons and photons was below the threshold for $p\bar{p}$ production. Baryon density no longer increased due to thermal collisions; instead, it decreased exponentially because baryons became non-relativistic. At this point, they annihilated into lepton pairs, pion pairs or photons. At this time, a matter-antimatter

¹⁸The conversion is done using $E = kT$, with k as the Boltzmann constant.

asymmetry should have been already present in the Universe, since after this stage, we ended up living in a matter-dominated Universe.

As the Universe continued its expansion and the temperature reached energy-equivalent of 70 and 50 MeV, it was below the energy thresholds for pion and muon pair production, respectively. Given the mean lifetime of such particles, they all decayed, leaving most of the matter density being dominated by relativistic electrons and neutrinos and non-relativistic nucleons. At $kT \sim 2.3$ MeV, the lightest neutrinos decoupled from all interactions, and began a free expansion.

The primordial photons were thermalized by the elastic scattering against free electrons, coupling these two particle species. Electrons decoupled when they formed neutral atoms with protons during the *recombination era*. Photons with $E(\gamma) < m(e)$ were not able to produce e^+e^- , but the energy exchange between photons and electrons still continued by elastic scattering. The $e^+e^- \rightarrow \gamma\gamma$ annihilation reaction became important at this stage and photons were created with energy above the ambient photon temperature at that time, which resulted in the photon particle species being reheated by a factor of 1.40. The photons emitted at the recombination time can still be observed today in the CMB.

From the time when $kT \approx 1$ eV, when the temperatures of matter and radiation were equal, cold matter and hot radiation decoupled, matter cooling faster than radiation, dropping out of thermal equilibrium. After recombination, density perturbations in matter were no longer damped by interaction with radiation, so they could grow into structures through gravitational instability. In addition, photons were able to travel freely through the Universe, which is often referred to the time when the Universe became *transparent*. Free photons continued as microwaves and infrared light from their last point of contact with matter on a spherical shell called the *last scattering surface* (LSS) [60].

In this part of the evolution, nuclear fusion reactions started to build light elements. As the Universe cooled the neutron-producing reaction stopped, a fraction of these neutrons decayed into protons until the neutron/proton ratio had been reduced from 1 to 1/7. The remaining neutrons fused into deuterons and subsequently via a chain of reactions into ^4He . The end result of this process called *Big Bang nucleosynthesis*, which took place 100-700 s after the Big Bang is a Universe composed almost entirely of hydrogen and helium.

Based on the characteristics that DM is expected to have from the astronomical measurements, one of the particles predicted in extensions of the SM based on SUSY is a benchmark DM particle candidate: the lightest neutralino ($\tilde{\chi}_1^0$). In models where R-parity is conserved, $\tilde{\chi}_1^0$ is the lightest supersymmetric particle (LSP) and a stable particle. SUSY models became popular, not only because of the ability to provide a solution to the electroweak hierarchy problem, but also for the prediction of a particle with the characteristics of dark matter, so-called *WIMP miracle*. The relic abundance of a thermally produced DM particle species left after the universe cools down and freezes out of thermal equilibrium is obtained by the Boltzmann equation, which will be described in the next section. Assuming that the DM couplings are of the order of the weak interaction (G_F), then the Boltzmann equation predicts that the DM mass should be on the order of 100 GeV to 1 TeV, independently of the particle physics model considered. This is exactly the mass range where we expect to find new physics that could explain the hierarchy problem and shed light on the mechanism of electroweak symmetry breaking.

Dark matter relic density

In this section, I include a summary of the calculation of the DM relic density using the Boltzmann equation in the standard cosmological model based on Refs. [56, 63]. The basis of this derivation lies on the assumption that particles were in thermal equilibrium in the early Universe. A quantity that characterizes this stage of the evolution is the reaction rate per particle, given by

$$\Gamma = n\sigma v, \quad (2.141)$$

where n is the number density of particles, σ is the interaction cross section of a specific particle species, and v is the relative velocity. When $\Gamma \gg H(t)$, then equilibrium thermodynamics can be applied and the system can be characterized by state variables like volume, temperature, energy, internal energy, entropy, etc., with temperature being the most relevant in the early Universe. Since $T \propto 1/a$, the Hubble constant and reaction rates can be written in terms of T . The temperature will also indicate how much thermal energy is available to create particles with a particular mass. The relations for number density, energy density and entropy density of particles can be derived using statistical thermodynamics. The distributions for fermions and bosons will be given by the Fermi-Dirac and Bose-Einstein statistics, respectively. The relative number of particles with a momentum p for a particle species i is given by the distribution factor

$$f_i(p) = \frac{1}{\exp\left[\frac{E_i - \mu_i}{T}\right] \pm 1}, \quad E_i = \sqrt{m_i^2 + p^2}, \quad (2.142)$$

where μ_i is the chemical potential¹⁹ of the species i and the last term in the denominator has a negative sign for fermions (-1) and positive for bosons (+1). With this distribution factor, the number and energy densities for the species i are

$$n_i = \frac{g_i}{(2\pi)^3} \int f_i(p) d^3p = \frac{g_i}{(2\pi)^3} \int p^2 f_i(p) dp, \quad (2.143)$$

$$\rho_i = \frac{g_i}{(2\pi)^3} \int E_i f_i(p) d^3p = \frac{g_i}{2\pi^2} \int p^2 E_i f_i(p) dp, \quad (2.144)$$

where $d^3p = 4\pi p^2 dp$. The term g_i represents the number of *internal degrees of freedom*, which refer to the number of possible combinations of states of a particle. For example, for quarks:

$$g_q = \underbrace{2}_{\text{spin states}} \times \underbrace{3}_{\text{color states}} \times \underbrace{2}_{\text{n}_{\text{quarks}} \text{ per generation}}. \quad (2.145)$$

The integrals for the number and energy densities in the non-relativistic regime ($m_i \gg T$) are

$$n_{i,\text{NR}} = g_i \left(\frac{m_i T}{2\pi}\right)^{3/2} \exp\left(-\frac{m_i}{T}\right), \quad (2.146)$$

$$\rho_{i,\text{NR}} = m_i n_{i,\text{NR}}, \quad (2.147)$$

¹⁹Energy associated with change in particle number.

where Eq. 2.146 is a Maxwell-Boltzmann distribution. These expressions apply both for fermions and bosons, since they are not distinguishable in this regime. In the relativistic regime, where $m_i \ll T$, these quantities are given separately for fermions and bosons by

$$n_{i,R} = \begin{cases} \frac{1}{\pi^2} \zeta(3) g_i T^3 & \text{for bosons,} \\ \frac{3}{4\pi^2} \zeta(3) g_i T^3 & \text{for fermions,} \end{cases} \quad (2.148)$$

and,

$$\rho_{i,R} = \begin{cases} \frac{\pi^2}{30} \zeta(3) g_i T^4 & \text{for bosons,} \\ \frac{7}{8} \frac{\pi^2}{30} \zeta(3) g_i T^4 & \text{for fermions,} \end{cases} \quad (2.149)$$

with ζ the Riemann Zeta function. From these results, one can see that the the total number and energy density are driven by the relativistic particles at any given temperature of the universe.

As a consequence of the thermal equilibrium, the processes which converted heavy particles into lighter ones occurred at the same time:

$$\text{Rate}(\text{DM} + \text{DM} \rightarrow \text{SM} + \text{SM}) = \text{Rate}(\text{SM} + \text{SM} \rightarrow \text{DM} + \text{DM}), \quad m(\text{DM}) \sim m(\text{SM}) + T \quad (2.150)$$

As the Universe expanded and cooled down, lighter particles no longer had sufficient thermal kinetic energy to produce heavier particles through interactions. Additionally, the Universe's expansion diluted the number of particles such that interactions did not occur as frequently, or at all,

$$\text{Rate}(\text{DM} + \text{DM} \rightarrow \text{SM} + \text{SM}) \gg \text{Rate}(\text{SM} + \text{SM} \rightarrow \text{DM} + \text{DM}), \quad m(\text{DM}) \gg m(\text{SM}) + T. \quad (2.151)$$

At the *freeze-out* point, the density of a particular particle species became too low to support frequent interactions and conditions for thermal equilibrium were violated, causing the number density of that species to remain constant. The exact time or temperature of freeze-out can be calculated by equating

$$\Gamma = H(t) \Rightarrow n\sigma v = \frac{\dot{a}(t)}{a(t)}. \quad (2.152)$$

The density of the species at the freeze-out point is also known as the *relic density*. The Boltzmann equation gives an expression for the changing number density of a certain particle over time:

$$\frac{1}{a^3} \frac{d(na^3)}{dt} = \langle \sigma v \rangle [(n_{\text{eq}})^2 - n^2]. \quad (2.153)$$

This expression can be simplified by taking advantage of the fact that aT is independent of time, rewriting $na^3 = na^3 T^3 / T^3$. Equation 2.153 becomes:

$$\frac{dn}{dt} = -3Hn + \langle \sigma v \rangle [(n_{\text{eq}})^2 - n^2]. \quad (2.154)$$

The Boltzmann equation can be rewritten in terms of two dimensionless quantities:

$$x = \frac{m}{T}, \quad (2.155)$$

which will essentially represent a time coordinate relative to the freeze-out point ($x = 1$), and,

$$Y \equiv \frac{n}{s} \propto \frac{n}{T^3}, \quad (2.156)$$

and Y is proportional to the relic density. The relevant conversion between s and T is

$$s = \frac{2\pi^2}{45} g_* T^3, \quad (2.157)$$

and g_* is the number of relativistic degrees of freedom of the particle species. Using the change of variables involving Y and T first, the Boltzmann equation becomes

$$\frac{dY}{dt} = T^3 \langle \sigma v \rangle (Y_{\text{eq}}^2 - Y^2). \quad (2.158)$$

The equilibrium number density is given by

$$Y_{\text{eq}} = \frac{n_{\text{eq,NR}}}{s}. \quad (2.159)$$

Now changing variables from t to x , we make use of the Hubble's law, $\frac{dx}{dt} = Hx$. Since DM production typically occurs in the radiation era, where energy density scales like T^4 (Stefan-Boltzmann law), then the Hubble parameter is $H = H(m)/x^2$. We also define a parameter λ that relates the annihilation rate to the expansion rate of the Universe:

$$\lambda = \frac{m^3 \langle \sigma v \rangle}{H(m)}, \quad (2.160)$$

leading to the equation

$$\frac{dY}{dx} = -\frac{\lambda}{x^2} (Y^2 - Y_{\text{eq}}^2). \quad (2.161)$$

Assuming that in a velocity expansion, the leading order term of $\langle \sigma v \rangle$ goes like the p -th power of v , $\langle \sigma v \rangle \propto v^p$. From the Boltzmann velocity distribution, $\langle v \rangle \propto T^{1/2}$, so we can write:

$$\langle \sigma v \rangle \propto x^{-l}, \quad l = p/2. \quad (2.162)$$

Then, we can express $\langle \sigma v \rangle = \langle \sigma v \rangle_0 x^{-l}$ and

$$\lambda_0 = \frac{m^3 \langle \sigma v \rangle_0}{H(m)} = \lambda x^l, \quad (2.163)$$

and the Eq. 2.161 becomes

$$\frac{dY}{dx} = -\frac{\lambda_0}{x^{l+2}} (Y^2 - Y_{\text{eq}}^2) \quad (2.164)$$

We can now solve this equation for Y , changing to another variable $\Delta = Y - Y_{\text{eq}}$ and using the fact that when the particle species was at equilibrium, the temperature was much higher than at times after freeze-out, therefore $Y_{\text{eq}} \ll Y$. We arrive to the differential equation

$$\frac{dY}{dx} \approx -\frac{\lambda_0}{x^{l+2}} Y^2 \rightarrow \frac{dY}{Y^2} = -\lambda_0 \frac{dx}{x^{l+2}}. \quad (2.165)$$

Denoting the freeze-out point as x_f , we can integrate the approximation above from x_f to $x \rightarrow \infty$, where $x \rightarrow \infty$ represents the present day. The resulting expression is

$$Y_\infty = \frac{l+1}{\lambda_0} x_f^{l+1}. \quad (2.166)$$

x_f is obtained with the condition $\Delta(x_f) = cY_{\text{eq}}(x_f)$, with c a constant determined empirically. The relic density of a non-relativistic particle species will be then given by Eq. 2.147. Once a particle has frozen out, its number density will fall off with the scale factor a^{-3} . Hence, the mass density today will be given by $m \left(\frac{a_1}{a_0}\right) n$, where a_1 is assumed to be the scale at which $Y \approx Y_\infty$. Combining this information, we get

$$\rho = mY_\infty T_0^3 \left(\frac{a_1 T_1}{a_0 T_0}\right)^3 \approx \frac{mY_\infty T_0^3}{30}, \quad (2.167)$$

and the cosmological parameter for the DM relic density will be given by

$$\Omega_{\text{DM}} = \frac{\rho_{\text{DM}}}{\rho_0^c} = \frac{x_f}{\lambda} \frac{m_{\text{DM}} T_0^3}{30 \rho_0^c} = \frac{H(m_{\text{DM}}) x_f T_0^3}{30 m_{\text{DM}}^2 \langle \sigma v \rangle \rho_0^c}. \quad (2.168)$$

The explicit dependence on the DM particle mass in the expression for Ω_{DM} can be removed by considering the Hubble rate at $T = m_{\text{DM}}$ ²⁰:

$$H(T) = T^2 \sqrt{\frac{4\pi^3 G_{\text{N}} g_*(T)}{45}} = H(m_{\text{DM}}), \quad (2.169)$$

Substituting Eq. 2.169 in Eq. 2.168, the DM relic abundance can be expressed as:

$$\Omega_{\text{DM}} = \sqrt{\frac{4\pi^3 G_{\text{N}} g_*(m)}{45}} \frac{x_f T_0^3}{30 \langle \sigma v \rangle \rho_0^c} \propto \frac{1}{\langle \sigma v \rangle}. \quad (2.170)$$

Although Ω_{DM} depends implicitly on m_{DM} through g_* , it is mainly driven by the thermally averaged cross section $\langle \sigma v \rangle$.

Neutralino DM relic density, coannihilation, and compressed SUSY

Recall from Sec. 2.3 that neutralinos (physical mass eigenstates) in the MSSM are the result of a superposition of the neutral Higgsinos and neutral gauginos:

$$|\tilde{\chi}_j^0\rangle = c_{1,j} |\tilde{B}^0\rangle + c_{2,j} |\tilde{W}^0\rangle + c_{3,j} |\tilde{H}_u^0\rangle + c_{4,j} |\tilde{H}_d^0\rangle, \quad j = 1, 2, 3, 4. \quad (2.171)$$

The $c_{i,j}$ coefficients can also be thought of as an indication of the "gaugino composition" of the mass eigenstates²¹. In our benchmark scenario where the particle species composing DM is only the $\tilde{\chi}_1^0$, the electroweakino mixing composition of this particle will determine the interaction cross section and therefore affect the relic density.

²⁰In the cosmological standard model, the Universe reached $T = m_{\text{DM}}$ during the radiation dominated era.

²¹A useful exercise is to use the Stern-Gerlach experiment [64] as an analogy to give an interpretation to these coefficients.

The primary mechanism for the reduction of the DM content in the Universe after dropping out of thermal equilibrium is considered to be annihilation reactions of the type DM+DM \rightarrow SM+SM in standard cosmology ($\langle\sigma v\rangle = \langle\sigma_A v\rangle$). When the $\tilde{\chi}_1^0$ is considered to be bino-like ($|c_{1,1}|^2 \gg |c_{i,1}|^2$, for $i = 2, 3, 4$), it interacts with other particles primarily through the Z boson. The resulting cross section for $\tilde{\chi}_1^0\tilde{\chi}_1^0$ annihilation will predict $\Omega_{\tilde{\chi}_1^0} > \Omega_{\text{DM}}^{\text{obs}}$, that is, an overabundance of DM in the Universe, compared to the experimental observations by the WMAP and Planck collaborations [13, 16, 17].

However, a more complete picture of the early evolution of the Universe includes other interactions that the DM particle(s) had with other particles, either within or outside the scope of the SM, which could produce SM particles. These additional processes could contribute to the reduction of DM density after DM dropped out of thermal equilibrium. Reactions of this nature become relevant as additional reduction mechanisms besides DM annihilation under certain conditions, as explained in Ref. [18].

An example of such conditions corresponds to the scenario where the DM particle is the lightest of a set of similar particles whose masses are nearly degenerate. The relic abundance of the DM particle will be then determined not only by its annihilation cross section, but also by the annihilation of heavier particles, which will later decay to the lightest of them. This case is better known as *coannihilation* (CA).

Using the SUSY hypothesis, the $\tilde{\chi}_1^0$ could also interact with other SUSY particles, in processes of the type $X + \tilde{\chi}_1^0 \rightarrow \text{SM} + \text{SM}$, where X is referred to as the CA partner of $\tilde{\chi}_1^0$, X_{CA} . Since the $\tilde{\chi}_1^0$ is the LSP, and there are heavier neutralinos and charginos which will decay to the $\tilde{\chi}_1^0$, the conditions for the scenario described above are satisfied when the mass difference between the LSP and other charginos and neutralinos is small. In this case, X_{CA} corresponds to the next-to-lightest electroweakinos. There are other SUSY particles that could also be CA partners, for example, the tau slepton $\tilde{\tau}$.

In order to understand how the effective cross section in scenarios where CA is relevant, we consider the evolution of a class of non-SM particles χ_i with $i = 1, 2, \dots, N$, labeled in increasing mass order. We assume that χ_i particles differ from SM particles by a multiplicatively conserved quantum number. There are three main types of reactions that determine their abundances in the early universe:

$$\chi_i + \chi_j \leftrightarrow X_{\text{SM}} + X'_{\text{SM}} \quad (2.172)$$

$$\chi_i + X_{\text{SM}} \leftrightarrow \chi_j + X'_{\text{SM}} \quad (2.173)$$

$$\chi_j \leftrightarrow \chi_i + X_{\text{SM}} + X'_{\text{SM}} \quad (2.174)$$

The abundances of each particle species will be given by a set of N Boltzmann equations:

$$\begin{aligned} \frac{dn_i}{dt} = & -3Hn_i - \sum_{j, X_{\text{SM}}} [\langle\sigma_{ij}v\rangle(n_i n_j - n_{i,\text{eq}} n_{j,\text{eq}}) \\ & - \langle\sigma'_{ij}v\rangle n_i n_{X_{\text{SM}}} - \langle\sigma'_{ji}v\rangle n_j n_{X_{\text{SM}}} - \Gamma_{ij}(n_i - n_{i,\text{eq}})], \end{aligned} \quad (2.175)$$

where $\sigma_{ij} = \sigma(\chi_i \chi_j \rightarrow X_{\text{SM}} + X'_{\text{SM}})$, $\sigma'_{ij} = \sigma(\chi_i X_{\text{SM}} \rightarrow \chi_j + X'_{\text{SM}})$ and $\Gamma_{ij} = \Gamma(\chi_i \rightarrow \chi_j + X_{\text{SM}} + X'_{\text{SM}})$.

Eventually, all the χ_i particles which survive annihilation will decay into χ_1 . Therefore, the quantity of interest will be the total number density of χ_i particles, $n = \sum_{i=1}^N n_i$. The Boltzmann equation then becomes,

$$\frac{dn}{dt} = -3Hn - \sum_{i,j=1}^N \langle \sigma_{ij} v \rangle (n_i n_j - n_{i,\text{eq}} n_{j,\text{eq}}) \quad (2.176)$$

Since the $\chi_i + \chi_j \leftrightarrow X_{\text{SM}} + X'_{\text{SM}}$ reactions will determine the freeze-out, we can use the approximation in which the ratio of the total χ_i density to total χ density, n_i/n maintains its value at equilibrium, $n_{i,\text{eq}}/n_{\text{eq}}$ before, during and after freeze-out.

The effective annihilation cross section σ_{eff} for a system of N (co)annihilating particles i of mass m_i featuring a relative mass splitting with respect to the stable particle species χ_1 of mass m_{χ_1} ,

$$\delta_i \equiv \frac{m_i - m_{\chi_1}}{m_{\chi_1}}, \quad (2.177)$$

is given by the expression

$$\sigma_{\text{eff}} = \sum_{i,j=1}^N \sigma_{ij} \frac{g_i g_j}{g_{\text{eff}}} (1 + \delta_i)^{3/2} (1 + \delta_j)^{3/2} \exp[-x(\delta_i + \delta_j)], \quad (2.178)$$

where $x = \frac{m_{\chi_1}}{T}$, g_i is the number of internal degrees of freedom associated with the particle i , and

$$g_{\text{eff}} = \sum_{i=1}^N g_i (1 + \delta_i)^{3/2} \exp[-x\delta_i]. \quad (2.179)$$

Expanding Eq. 2.178,

$$\begin{aligned} \sigma_{\text{eff}} = & \sum_{j=1}^N \sigma_{1j} \frac{g_1 g_j}{g_{\text{eff}}} (1 + \delta_1)^{3/2} (1 + \delta_j)^{3/2} \exp[-x(\delta_1 + \delta_j)] \\ & + \sum_{j=1}^N \sigma_{2j} \frac{g_2 g_j}{g_{\text{eff}}} (1 + \delta_2)^{3/2} (1 + \delta_j)^{3/2} \exp[-x(\delta_2 + \delta_j)] \\ & + \sum_{i=3}^N \sum_{j=1}^N \sigma_{ij} \frac{g_i g_j}{g_{\text{eff}}} (1 + \delta_i)^{3/2} (1 + \delta_j)^{3/2} \exp[-x(\delta_i + \delta_j)], \end{aligned} \quad (2.180)$$

where the contribution of each term in the sum is driven by the exponential factor. If we assume that for $i, j \geq 3$, $m_{i,j} \gg m_{\chi_2}$, $\delta_{i,j}$ will be large, and so will $\exp[-x(\delta_i + \delta_j)] \rightarrow 0$. Therefore, we can simplify the equation above,

$$\begin{aligned} \sigma_{\text{eff}} \approx & \sum_{j=1}^N \sigma_{1j} \frac{g_1 g_j}{g_{\text{eff}}} (1 + \delta_1)^{3/2} (1 + \delta_j)^{3/2} \exp[-x(\delta_1 + \delta_j)] \\ & + \sum_{j=1}^N \sigma_{2j} \frac{g_2 g_j}{g_{\text{eff}}} (1 + \delta_2)^{3/2} (1 + \delta_j)^{3/2} \exp[-x(\delta_2 + \delta_j)]. \end{aligned} \quad (2.181)$$

Using the same argument, a further simplified version of the expression for σ_{eff} is

$$\begin{aligned}\sigma_{\text{eff}} \approx & \sigma_{11} \frac{g_1^2}{g_{\text{eff}}} (1 + \delta_1)^3 \exp[-2x\delta_1] + \sigma_{22} \frac{g_2^2}{g_{\text{eff}}} (1 + \delta_2)^3 \exp[-2x\delta_2] \\ & + \sigma_{12} \frac{g_1 g_2}{g_{\text{eff}}} (1 + \delta_1)^{3/2} (1 + \delta_2)^{3/2} \exp[-x(\delta_1 + \delta_2)] \\ & + \sigma_{21} \frac{g_2 g_1}{g_{\text{eff}}} (1 + \delta_2)^{3/2} (1 + \delta_1)^{3/2} \exp[-x(\delta_2 + \delta_1)].\end{aligned}\quad (2.182)$$

For $i = 1$, $\delta_1 = 0$, therefore,

$$\sigma_{\text{eff}} = \sigma_{11} \frac{g_1^2}{g_{\text{eff}}} + 2\sigma_{12} \frac{g_1 g_2}{g_{\text{eff}}} (1 + \delta_2)^{3/2} \exp[-x\delta_2] + \sigma_{22} \frac{g_2^2}{g_{\text{eff}}} (1 + \delta_2)^3 \exp[-2x\delta_2].\quad (2.183)$$

We can identify $\sigma_{11} = \sigma(\text{DM} + \text{DM} \rightarrow X_{\text{SM}} + X'_{\text{SM}})$, $\sigma_{12} = \sigma_{21} = \sigma(X_{\text{CA}} + \text{DM} \leftrightarrow X_{\text{SM}} + X'_{\text{SM}})$, and $\sigma_{22} = \sigma(X_{\text{CA}} + X_{\text{CA}} \rightarrow X_{\text{SM}} + X'_{\text{SM}})$. Assuming that $\sigma_{12} \gg \sigma_{22}$, we can approximate the σ_{eff} as

$$\sigma_{\text{eff}} \approx \sigma_{11} \frac{g_1^2}{g_{\text{eff}}} + 2\sigma_{12} \frac{g_1 g_2}{g_{\text{eff}}} (1 + \delta_2)^{3/2} \exp[-x\delta_2],\quad (2.184)$$

we can already interpret each term as the annihilation and CA cross sections:

$$\sigma_{\text{A}} = \frac{g_1^2}{g_{\text{eff}}} \sigma_{11},\quad (2.185)$$

$$\sigma_{\text{CA}} = \frac{2g_1 g_2}{g_{\text{eff}}} (1 + \delta_2)^{3/2} \sigma_{12} \exp[-x\delta_2].\quad (2.186)$$

Rewriting in terms of m_{DM} , $\Delta m = m_{\text{CA}} - m_{\text{DM}}$ and T , we get that the CA cross section is

$$\sigma_{\text{CA}} = \frac{2g_1 g_2}{g_{\text{eff}}} \left(1 + \frac{\Delta m}{m_{\text{DM}}}\right)^{3/2} \sigma_{12} \exp\left[-\frac{\Delta m}{T}\right].\quad (2.187)$$

One of the most natural CA candidates in the MSSM is the stau ($\tilde{\tau}$), since we expect $m_{\text{SUSY}} \propto [m_{\text{SM}}]^{-1}$, for the corresponding particles in the SUSY-SM supermultiplet²² [22, 23, 24]. The regions of parameter space where $m(\tilde{\tau}) \sim m(\tilde{\chi}_1^0)$ are known as *SUSY compressed mass spectrum scenarios*.

Relevance of compressed SUSY in a non-thermal evolution of the Universe

Up to this point, we have considered a thermal evolution of the early Universe, the existence of SUSY and a bino-like $\tilde{\chi}_1^0$ as the DM particle. We have found that in order for this hypothesis to be consistent with the measured DM relic density, the SUSY parameter space of interest corresponds to the compressed mass spectrum scenarios, where the mass gap between the $\tilde{\chi}_1^0$ and other SUSY particles is small. However, the SUSY DM hypothesis is also relevant when a non-thermal evolution of the Universe is considered.

The thermal history for the early Universe can be used to try to understand the primordial origin of dark matter particles, baryons, and the matter-antimatter asymmetry. However, the primordial density perturbations cannot be causally generated in a strictly thermal universe. Inflation provides

²²The τ lepton is the heaviest of the charged leptons in the SM.

the most compelling model for their origin, and during this epoch the universe was not in thermal equilibrium. After inflation, the universe transitions to a *reheating* phase which then leads to the establishment of the thermal bath of elementary particles [65].

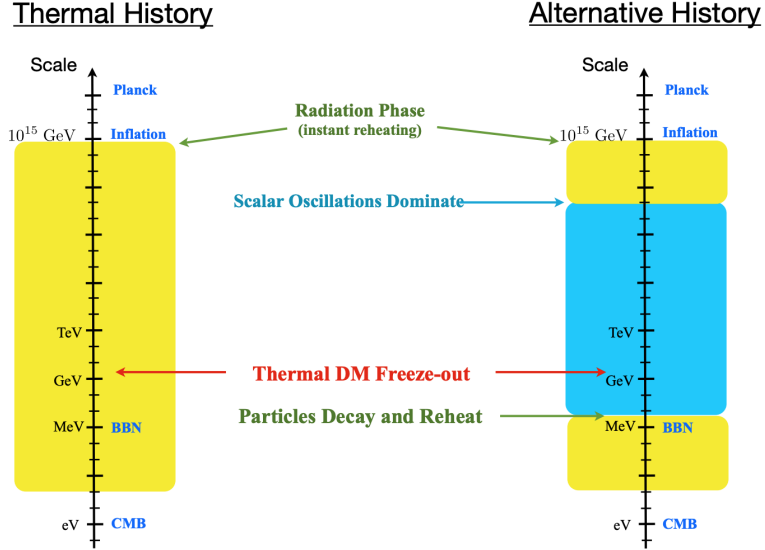


Figure 2.7: Comparison of a thermal and a non thermal evolution of the early Universe (Adapted by [65]).

Although the the thermal evolution of the universe is simple, elegant and predictive, there is no direct evidence for it. The agreement between the theoretical predictions from Big Bang Nucleosynthesis (BBN) and the astronomical observations show that the Universe was in a radiation dominated era when it was one second old. As mentioned at the beginning of this chapter, these observations do not provide more information about the state of the Universe at earlier times.

Hence, there is no reason to assume that a standard cosmological evolution took place before the BBN. This has motivated the proposal of models for a non-standard thermal history of the Universe [65, 66]. In these models, an *early matter-dominated phase* (EMD) is typically predicted before the onset of BBN [65] (Fig. 2.7). The EMD is usually driven by the energy density of a single particle species with zero pressure, which is typically consistent with coherent oscillations of a scalar field that arises in the extensions of the SM, for example, SUSY.

The generic presence of gravitationally coupled particles, like gravitinos, in UV complete theories can change the cosmological evolution of the Universe. Another type of scalar fields that could have the same effect are known as *moduli*. Moduli get displaced from their late-time minimum during inflation due to the inflationary energy density [67]. After the end of inflation, their VEV decreases with the Hubble parameter, until $H \sim m$ and the moduli start oscillating to dominate the energy density of the universe, introducing an EMD. When H becomes of the order of the moduli decay rate, Γ_ϕ , the moduli decay, heating the thermal bath and producing an entropy that dilutes everything that has been produced before. Furthermore, the decay of the moduli leads to the non-thermal production of the LSP [67].

In the non-thermal evolution of the universe, the DM relic density depends on two parameters: the LSP annihilation rate and the reheating temperature, or equivalently, the moduli mass. References [67, 68] has a great derivation of the DM relic density in the non-thermal scenario. A higgsino-like neutralino hypothesis is favored (Eq. 2.171), where $\tilde{\chi}_1^0$, $\tilde{\chi}_2^0$, and $\tilde{\chi}_1^\pm$ are the lightest SUSY particles and their masses are very close [67, 69]. The level of mass degeneracy for these particles depends mainly on the mass of the bino M_1 and wino M_2 gaugino fields in the MSSM. The heavier M_1 and M_2 are, the more degenerate $\tilde{\chi}_1^0$, $\tilde{\chi}_2^0$, and $\tilde{\chi}_1^\pm$ will be, leading to a SUSY compressed mass spectrum. Experimentally, pure Higgsino LSP scenarios are constrained by the results from direct and indirect DM detection experiments [67, 70], briefly described in the next section. However, it is possible to have a small mixing with the wino and bino fields, which will lead to larger mass gaps between the $\tilde{\chi}_1^0$, $\tilde{\chi}_2^0$, and $\tilde{\chi}_1^\pm$, which have not been ruled out by experimental observations and could still predict the right DM relic density.

I transition now to the next chapter, where I present the motivation for the experimental detection of SUSY DM via novel techniques which provide sensitivity to the compressed mass SUSY spectrum in collider experiments.

CHAPTER 3

Experimental motivation

3.1 Dark matter detection techniques

In the quest to experimentally determine the nature of DM, multiple methods have been developed to detect DM particles, which are complementary between each other and divided in three major categories (Fig. 3.1):

- *Scattering (direct detection)*: DM is detected via the signals produced by DM scattering with SM particles. The detectors and technologies used for this type of detection are similar to those used in neutrino detection experiments.
- *Annihilation (indirect detection)*: the goal is to detect SM particles with the characteristics from a DM-DM annihilation reaction. An example of a detector for indirect detection is the Fermi telescope, which searches for anomalous gamma ray signals, expected to come from DM annihilation.
- *Production (collider experiments)*: following the different hypotheses for the evolution of the early Universe, it is possible to use accelerator experiments which collide particles at large enough energies to recreate the energy and temperature conditions in which DM particles interacted with SM particles. Nowadays, the most powerful particle collider is the Large Hadron Collider (LHC), with which numerous searches for DM production in proton-proton collisions have been performed since the beginning of its operation.

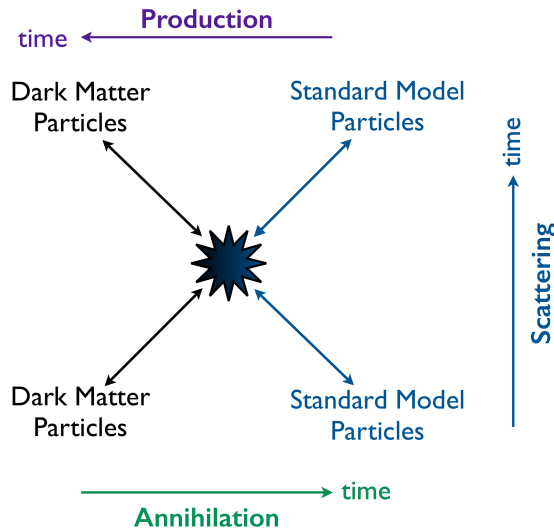


Figure 3.1: Diagram showing possible DM detection methods [71].

Some sets of DM models or hypotheses can be more easily tested with a specific detection category. In particular, for the SUSY DM hypothesis, the most typical technique is DM production

at particle colliders. The main reason is that SUSY particles are expected to be discovered at the electroweak energy scale, which is exactly the energy range that the high energy accelerators, like the LHC can probe. In the next section, a brief overview of the types of DM searches motivated by SUSY performed at the LHC is described.

3.2 Compressed SUSY searches at hadron colliders

Continuing with the compressed SUSY benchmark scenario, there are different ways to produce $\tilde{\chi}_1^0$ DM in proton-proton collisions. The colliding particles are composed of quarks and gluons, generally referred as *partons*. In these particles collisions, each constituent will carry a very small fraction of the total proton-proton collision energy, and being more than one, will produce multiple types of interactions or “mini-collisions”. Most of the time, these interactions will correspond to processes which happen via the well-known SM interactions.

Since the colliding particles are made of quarks and gluons, these processes are most of the time initiated via the strong interaction, which in fact becomes stronger at higher energy scales. Assuming that SUSY exists, then it is more likely that the superpartners of the SM quarks and gluons¹, are produced in these reactions than, for example, the physical gaugino states obtained after the electroweak and SUSY breaking. This includes the $\tilde{\chi}_1^0$, which by default would not be possible to detect if it is directly produced, because of its neutral and weakly interacting nature.

Thus, the focus of $\tilde{\chi}_1^0$ searches at the LHC is centered in detecting the production of heavier SUSY particles, that later decay into $\tilde{\chi}_1^0$. Figure 3.2 shows the typical SUSY processes used in these searches, including colored and electroweak sector decays. In general, more SM particles like leptons and quarks will be present in the final state of such decays, allowing experimentalists to tag these processes and discriminate against other more commonly produced known processes.

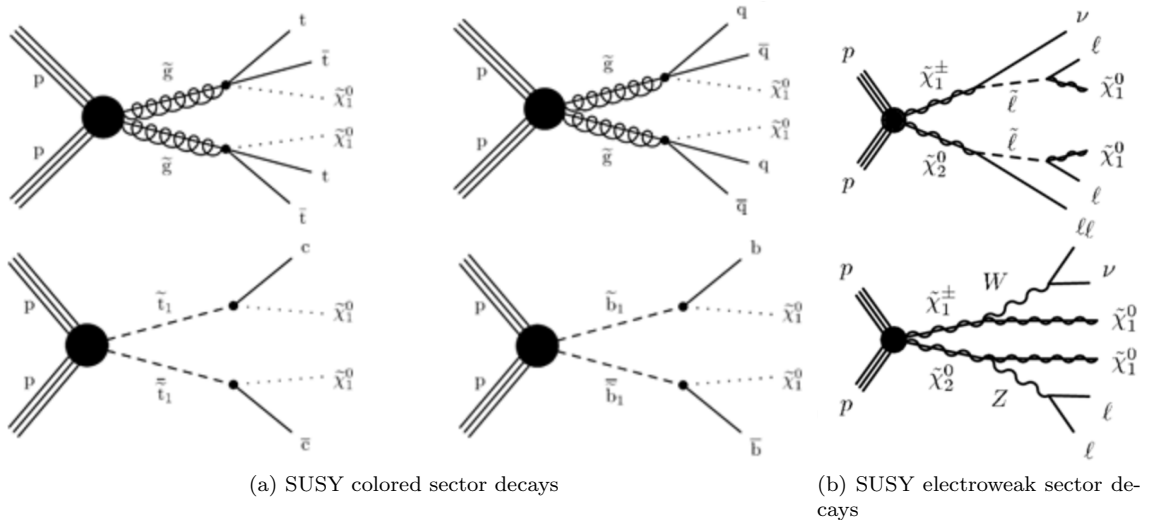


Figure 3.2: Representative Feynman diagrams of SUSY production and decays which motivate searches for $\tilde{\chi}_1^0$ DM (Adapted from [72]).

¹referred to as the SUSY colored sector

The conventional methodology to search for $\tilde{\chi}_1^0$ DM at the LHC is via associated Drell-Yan² (DY) chargino-neutralino ($\tilde{\chi}_1^\pm \tilde{\chi}_2^0$) production (Fig. 3.3a), followed by their decays ending in $\tilde{\chi}_1^0$ s: $\tilde{\chi}_1^\pm \rightarrow \ell^\pm \nu_\ell \tilde{\chi}_1^0$ and $\tilde{\chi}_2^0 \rightarrow \ell^\pm \ell^\mp \tilde{\chi}_1^0$ (Fig. 3.3).

One of the most important challenges that searches for $\tilde{\chi}_1^0$ DM production at the LHC face is related to the SUSY phase space relevant for these searches, which corresponds to the compressed mass spectra. Historically, these regions of parameter space have been inaccessible and loosely constrained by searches at the LHC. The limited sensitivity in these regions is attributed to the low-momentum (*soft*) that is available to transfer to the SM particles in the resulting decays. The smaller is the mass gap between $\tilde{\chi}_1^0$ and the other electroweakinos, the softer will the decay products be. Experimentally, these decay particles are then lost during reconstruction or among the large hadronic activity in the collisions.

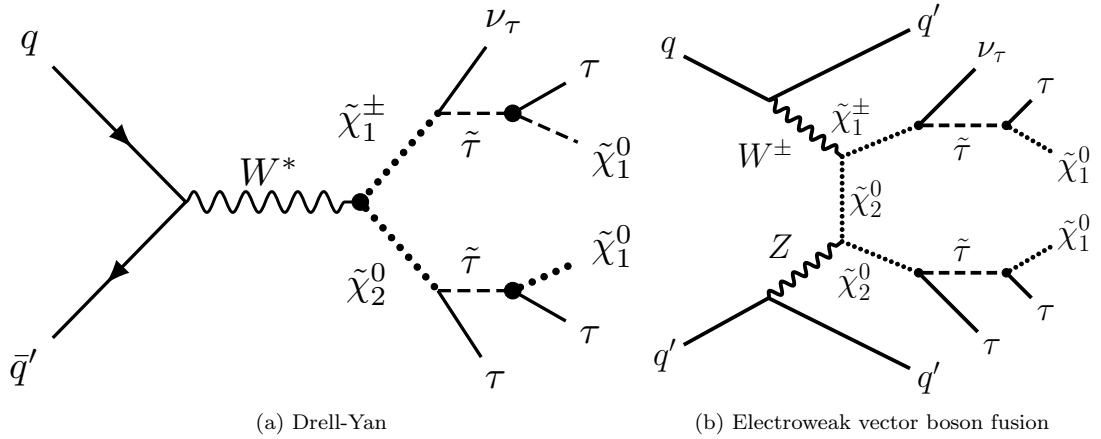


Figure 3.3: Feynman diagrams for $\tilde{\chi}_2^0 \tilde{\chi}_1^\pm$ production in pp collisions via DY and VBF processes.

Thus, it is crucial to develop dedicated strategies targeting distinctive experimental signatures, so that the soft particles in these final states can be distinguished against the more abundantly produced SM background processes. Searches that focus on a rare production mode called *electroweak vector boson fusion* (VBF) are among the most promising of such methods, regardless of their low production rates (Fig. 3.3b) [27, 29]. A general overview on these types of processes is summarized in the next section.

3.3 Electroweak vector boson fusion

VBF processes are characterized by energetic quarks, scattered off weak bosons radiated by the interacting quarks in each proton. In this section, we will start by describing some of the characteristics of these processes, focusing only on SM electroweak processes, based on the work presented in Ref. [73]. The most dominant diagrams in VBF production correspond to the diagrams in the top row of Fig. 3.4, using as example to process $pp \rightarrow e^+ \nu_e \mu^+ \nu_\mu jj$ ($pp \rightarrow e^+ \nu_e \mu^+ \nu_\mu jj$). The virtual W bosons emitted off each initial (anti)quark and the final state W bosons describe a 2→2 scattering [73].

²quark-(anti)quark annihilation

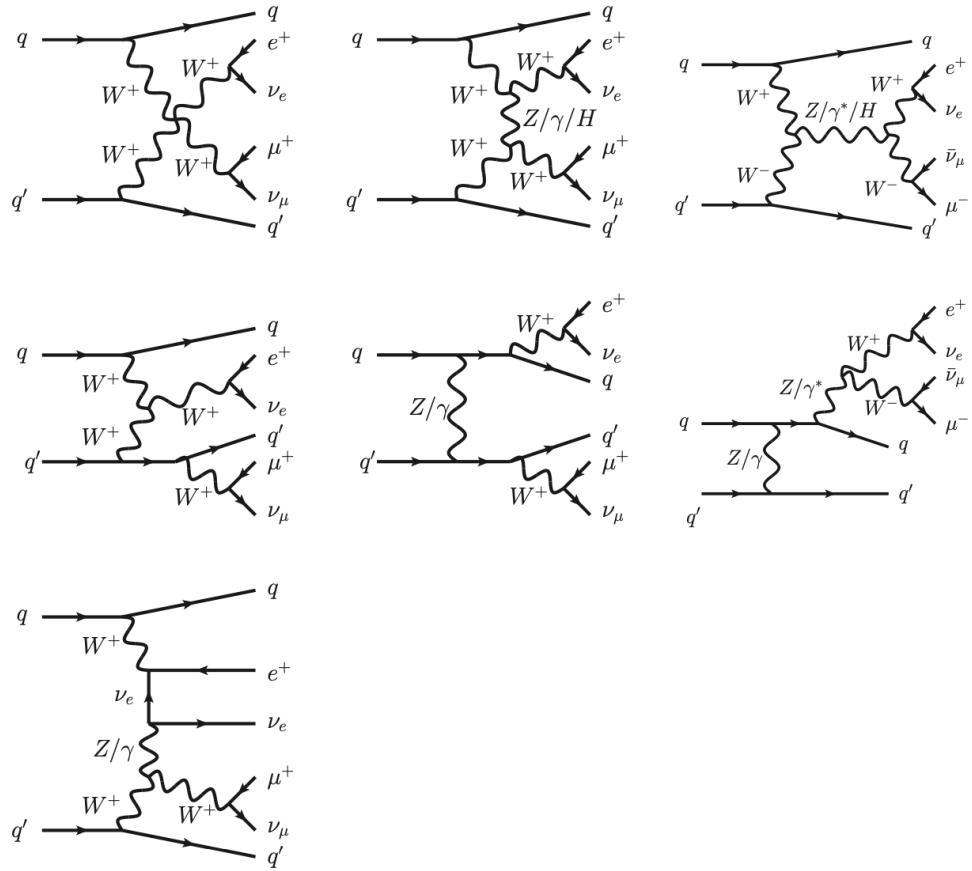


Figure 3.4: Typical Feynman diagrams for $pp \rightarrow e^+ \nu_e \mu^+ \nu_\mu jj$ and $pp \rightarrow e^+ \nu_e \mu^+ \nu_\mu jj$ via VBF production [73].

The main difference with a real scattering process is that the incoming bosons are space-like ($q^2 < 0$)³ and not on-shell. The interaction can happen via a quartic gauge coupling (upper left, Fig. 3.4), via the exchange of a space-like boson (t -channel, upper center, Fig. 3.4), which can either be a γ , a Z or a Higgs boson in this particular example. For other final states, s -channel interactions also contribute to the cross section of this process.

A gauge-invariant set of Feynman diagrams will, in addition, include the rest of Feynman diagrams in Fig. 3.4. These include W emission directly from one or both quark lines, or the emission of W bosons from quarks after having interacted through the exchange of a Z or γ bosons, or via a triple gauge coupling.

After the scattering, these quarks or *jets*⁴ will travel close to the beam line in opposite directions, which is equivalent to say that they have a large separation in rapidity⁵.

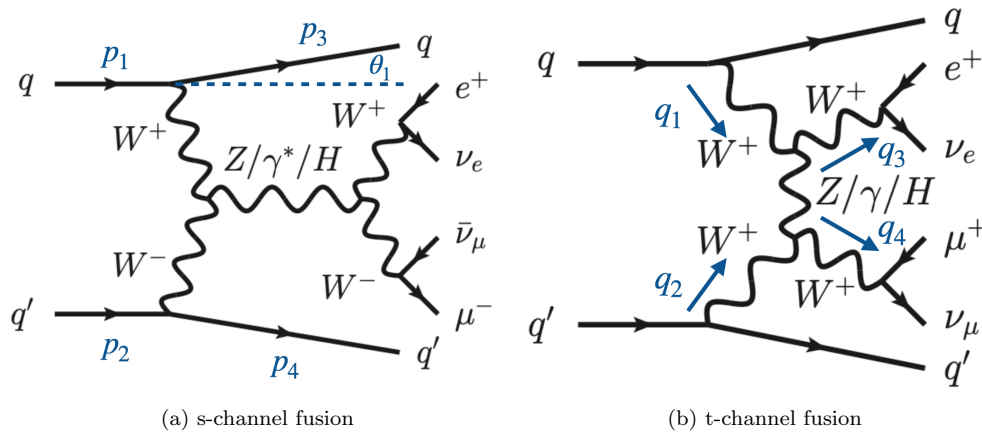


Figure 3.5: Representative Feynman diagrams for VBF Higgs production (Adapted from [73]).

As an illustrative example, we can consider Higgs production via VBF (Fig. 3.4, upper right), focusing on the exchange via s -channel fusion. For simplicity, we consider the case in which only W boson exchange is possible. Labeling the 4-momenta of the incoming and outgoing quarks as $\{p_1, p_2\}$ and $\{p_3, p_4\}$, respectively (Fig. 3.5a), we can arrive to an expression of squared matrix element:

$$|\mathcal{M}_{fi}|^2 \propto \frac{(p_1 \cdot p_2)(p_3 \cdot p_4)}{(q_1^2 - m_W^2)^2(q_2^2 - m_W^2)^2}, \quad (3.1)$$

where $q_1 = p_1 - p_3$ and $q_2 = p_2 - p_4$ denote the momenta of the virtual W bosons. There are two ways to maximize Eq. 3.1: we can increase the numerator and decrease the denominator. At a fixed partonic center-of-mass energy ($\sqrt{\hat{s}} = \sqrt{2p_1 \cdot p_2}$), then the numerator can be increased by making $p_3 \cdot p_4$ larger. This means that the invariant mass of the outgoing jets, $m(jj) = \sqrt{2p_3 \cdot p_4}$ should be high.

³ $q^2 = (p_1 + p_2)^2$, where p_1 and p_2 are the 4-momenta of the two particles in the initial state.

⁴Jets are the experimental signature of quarks produced in high energy scattering processes. Appendix A expands extensively on this topic.

⁵In particle colliders, the rapidity is measured relative to a beam axis and it is given by $y = \frac{1}{2} \ln \left[\frac{E+p_z}{E-p_z} \right]$. Another typical quantity used is the *pseudorapidity*, defined in Eq. 5.5, where $p \gg m$.

Now, in the denominator, since we assume all quarks to be massless ($p \gg m$ limit), we can arrive for an expression for q_1 :

$$\begin{aligned} q_1^2 &= (p_1 - p_3)^2 \approx -2p_1 \cdot p_3 = -2E_1 E_3 (1 - \cos \theta_1) \\ &= -\frac{2}{1 + \cos \theta_1} \frac{E_1}{E_3} p_{T,3}^2, \end{aligned} \quad (3.2)$$

where θ_1 is the scattering angle between \vec{p}_1 and \vec{p}_3 . and the absolute value of the transverse component of \vec{p}_3 is

$$p_{T,3} = E_3 \sin \theta_1. \quad (3.3)$$

From the expression for q_1 (Eq. 3.2), its maximum value is $q_1 = 0$. Therefore, the inverse W-boson propagator $q_1^2 - m_W^2$ reaches its minimum value for $q_1 = 0$. This is accomplished when the scattering angle θ_1 becomes small. In that case, $\cos \theta_1 \approx 1$, and the propagator can be rewritten as

$$(q_1^2 - m_W^2) \simeq -\left(\frac{E_1}{E_3} p_{T,3}^2 + m_W^2\right). \quad (3.4)$$

We can analyze Eq. 3.4 to understand the kinematics of this process. First, the p_T of the W boson, which is equal to the p_T of the outgoing quark ($p_{T,W} = p_{T,3}$) should not significantly exceed m_W , in order to maintain the whole expression small. Consequently, θ_1 should be small. The outgoing quarks then, will have a large p_z component. Each of the W bosons will typically carry a small fraction of the momentum of the corresponding incoming partons that radiated them, but the energy carried should be large enough to produce the final-state Higgs boson, which on average should be $\frac{m_H}{2}$. This is because we expect $q_H = q_1 + q_2$, due to the s -channel fusion.

Putting all together, the final state of VBF processes will have two outgoing jets with large energies, or equivalently, large p_z component and moderate p_T , and a large $m(\text{jj})$. The correlation between $m(\text{jj})$ and the rapidity separation between the jets Δy_{jj} is given by [73],

$$m(\text{jj}) = \sqrt{2p_{T,j_1} p_{T,j_2} [\cosh(\Delta y_{\text{jj}}) - \cos(\Delta \phi_{\text{jj}})]}, \quad (3.5)$$

where $\Delta \phi_{\text{jj}}$ is the separation in the azimuthal direction between the two jets⁶.

This will be true in general for any of the three top diagrams in Fig. 3.4. However, there are slight differences for the kinematics of processes occurring via s -channel versus t -channel fusion, where we assume W^+W^+ fusion (Fig. 3.5b). For the t -channel fusion, the squared matrix element would be similar to Eq. 3.1, except that it would need to be multiplied by extra factors that account for the momentum exchange between the fusing W bosons, of the type $q^2 - m_{W,H}^2$.

In contrast to the s -channel fusion, where all the momentum of the virtual W bosons from VBF was going into the production of the Higgs boson, in the t -channel fusion, these bosons need to carry enough energy in order to (1) exchange with each other and produce the intermediate weak boson (γ , Z , or Higgs) and (2) scatter off. Kinetically, the energy of the fusing W bosons needs to be larger, and as a consequence, a larger transverse momentum is required. This translates into outgoing VBF quarks with larger p_T , and, in order to maximize $|\mathcal{M}_{fi}|^2$ the scattering angle range is more constrained, such that the production of central jets is more suppressed compared to what

⁶This equation is correct for the case in the limit of massless jets (quarks).

is found in the s -channel fusion. A comparison of the kinematics for VBF Higgs production via s -channel and W^+W^+ t -channel fusion is shown in Fig. 3.6.

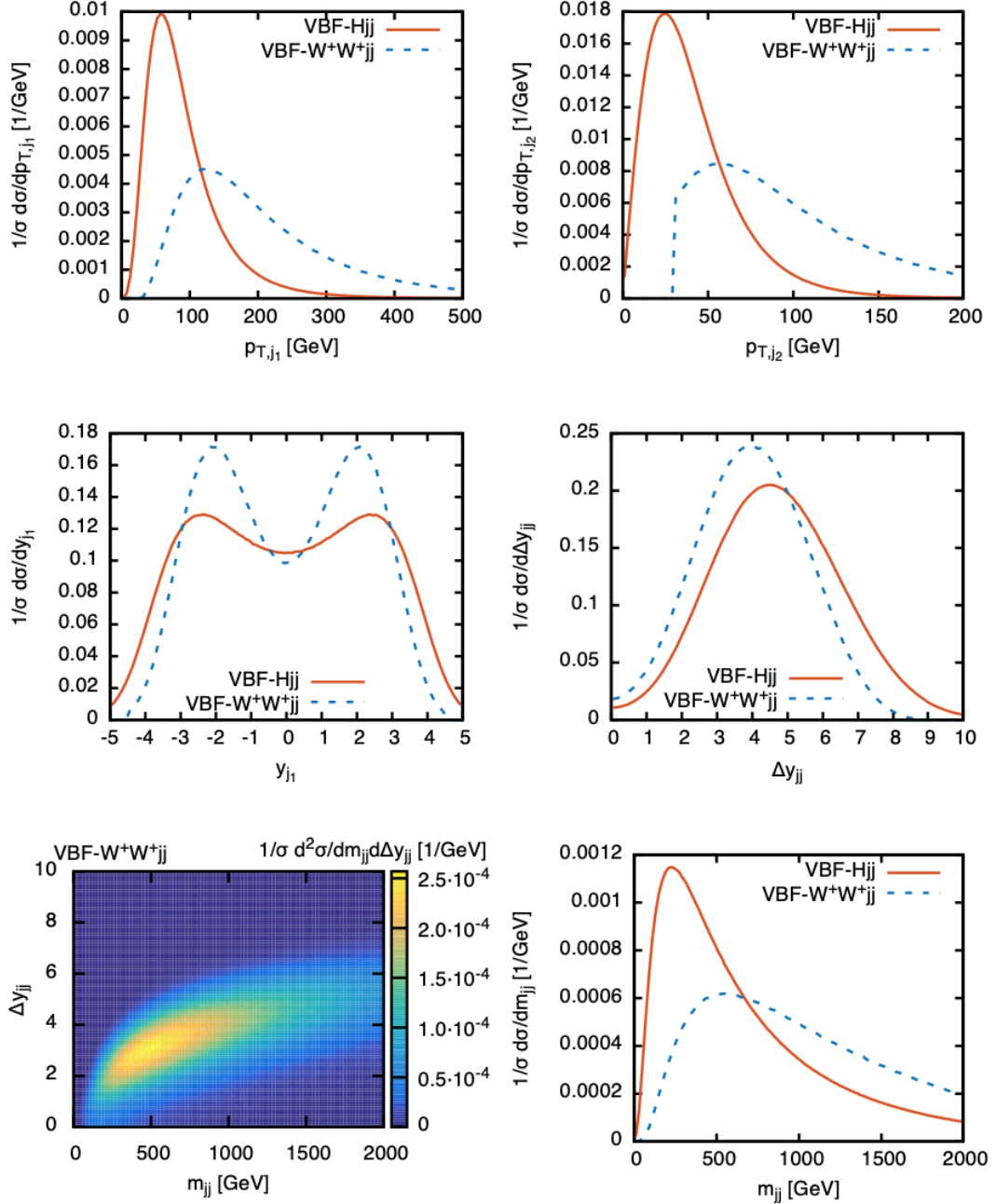


Figure 3.6: Normalized LO differential distributions for VBF Higgs and W^+W^+ production at the LHC with $\sqrt{s} = 13$ TeV. The top row includes distributions for the leading (j_1) and sub-leading (j_2) jets. In the middle row, the rapidity of the leading jet (y_{j_1}) and the difference in rapidity for the VBF jets (Δy_{jj}) is shown. The bottom panel depicts the correlation between the dijet invariant mass $m(jj)$ and Δy_{jj} , as well as the histogram for $m(jj)$ [73].

Naturally, for the case of VBF Higgs production, the s -channel fusion is favored because it is energetically more “efficient”. That is, the energy needed for the fusing weak bosons is less

compared with the t -channel fusion. In addition, the Higgs boson is relatively light ($m_H \sim 125$ GeV). However, if we now look at electroweakino production via electroweak VBF (Fig. 3.3b), we expect the electroweakinos to be much heavier than the Higgs and the weak bosons. Thus, the weak bosons involved in the VBF process should carry more energy in order to produce the electroweakinos. In VBF SUSY production, the most dominant type of Feynman diagrams will be the t -channel production of electroweakinos, leading to the presence of VBF jets with larger p_T in the final state, as well as $m(jj)$ values in the TeV scale (Fig. 3.7).

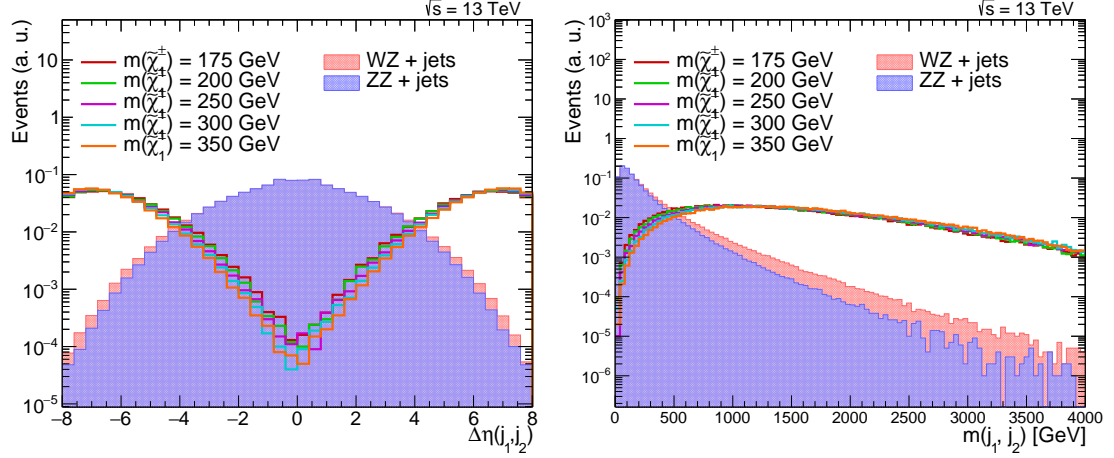


Figure 3.7: Initial comparison of (a) the angular jet η separation ($\Delta\eta(jj)$) and (b) the dijet invariant mass distributions for SM diboson background processes (solid) and signal (line), considering different $m_{\tilde{\chi}_{1\pm}}$ hypothesis at parton level. The distributions are normalized to unity.

Another important consequence of VBF processes is that a kinematic boost is created on the particles produced in the hard scattering, which will be propagated to the particles in the subsequent decays, including leptons and the $\tilde{\chi}_1^0$ particles. Hence, in our scenario of interest, the probability of reconstructing and identifying soft leptons increases. A final note on the experimental signature of VBF processes is that, due to the presence of the VBF jets and the kinematic boost, a larger p_T^{miss} will be present in these events as well. Therefore, another important kinematic quantity that could be useful to distinguish between VBF and non-VBF processes is the transverse mass m_T between the p_T^{miss} and any of the leptons produced in the decays:

$$m_T(\ell, p_T^{\text{miss}}) = \sqrt{2p_{T,\ell}p_T^{\text{miss}} [1 - \cos [\Delta\phi(\vec{p}_{T,\ell}, \vec{p}_T^{\text{miss}})]]}. \quad (3.6)$$

It is important to note that, in general, VBF processes have an extremely unique signature which can help to discriminate against all the other processes produced in particle collisions, regardless of its lower production rates due to the presence of more electroweak vertices. All of the characteristics of VBF production combined, make up for a powerful and novel technique to probe the range of compressed mass spectra $\tilde{\chi}_1^0$ DM scenarios with the experimental machines in our days. In the next chapter, I state the aim of the present research project and talk about the specific physics models for interpretation based on the discussion of the present and previous chapters.

CHAPTER 4

Objective of the study

4.1 Description of the research project

As outlined in Chapter 1, the scope of the research project presented in this dissertation consists of a data analysis to search for electroweakino pair production ($\tilde{\chi}_i\tilde{\chi}_j$) via pure electroweak VBF in pp collisions at $\sqrt{s}=13$ TeV. The analysis will use data collected by the CMS detector at the LHC during the Run II data-taking period (2016-2018). The data sample corresponds to an integrated luminosity of $\mathcal{L}_{\text{int}} = 137 \text{ fb}^{-1}$. Events satisfying the VBF topologies will be selected, that is, events containing two energetic jets largely separated in pseudorapidity η and large missing transverse momentum $p_{\text{T}}^{\text{miss}}$. In addition, various lepton multiplicities will be considered, with either one, two or no leptons in the final state. My focus will be in the final states containing two *soft*¹ τ leptons, resulting from the decay chains of the electroweakinos. One of the τ leptons will be identified in its hadronic decay (τ_h), and the second τ lepton will be identified in its leptonic (e, μ) or hadronic decays.

The search strategy consists of finding a set of selections based on the topology and kinematics of the process of interest, denominated *signal region (SR)*. By applying the SR selections, the detection of the signal process will be favored with maximal discovery potential. Since the experimental characteristics of VBF processes are not well modeled in current simulations, different *control regions (CRs)* or *control samples* will be defined by modifying a subset of the SR criteria. For a particular CR, most of the events passing the selections of such CR will correspond to a specific SM process identified as *background*, and the contamination from signal events is minimal.

In each control sample, the efficiencies of the event selections applied in the SR will be measured, being of particular importance the efficiency of VBF selections, which are typically not well modeled in current MC simulations. This approach will be used to obtain an accurate estimate of the background yields in the SR using MC simulation. SM processes which cannot be accurately determined with simulation will be estimated in the SR using a fully data-driven method.

The region of the SUSY phase space of interest corresponds to the compressed mass spectrum scenarios, which have a critical link to cosmology through the $\tilde{\chi}_1^0$ DM hypothesis. In addition, the experimental observables obtained in this analysis can be used to test the $\tilde{\chi}_1^0$ DM hypothesis from the cosmology standpoint, by calculating its relic density $\Omega_{\tilde{\chi}_1^0} h^2$ [15].

There are different physics interpretations in the compressed mass spectrum regions of the SUSY phase space which are relevant to cosmology. In the present analysis, the results will be interpreted in the context of the simplified R-parity conserving MSSM with different parameters for the electroweakino mixing and decays (these are related to the hypotheses for co-annihilating partners), as well as a non SUSY interpretation based on a DM effective field theory (EFT), and are presented in detail in the following section.

¹Soft: low momentum or low energy.

4.2 Physics models for interpretation of results

The number of physics interpretations will expand those that have been included in the existing VBF SUSY searches at CMS [74, 75]. Such interpretations are divided into two main categories: (i) simplified R-parity conserving MSSM interpretations and (ii) a DM EFT interpretation based on anapole DM. Interpretation (ii) provides a less model-dependent approach by using a EFT framework, where the only free parameters varied are the mass of the DM particle (m_{DM}) and the cutoff scale Λ .

Simplified R-parity conserving MSSM interpretations

In this category, the goal of using a simplified approach is to reduce the number of free parameters in the original R-parity conserving MSSM and look at specific scenarios of interest. The simplifications done in this analysis refer to the composition or mixing of the first and second mass generation electroweakinos ($\tilde{\chi}_1^0$ and $\tilde{\chi}_2^0$, $\tilde{\chi}_1^\pm$, respectively) and the masses of the SUSY particles. It is assumed that each of these particles contain only one component of the electroweak superfields. In addition, $\tilde{\chi}_2^0$ and $\tilde{\chi}_1^\pm$ are set to be mass degenerate, $m(\tilde{\chi}_2^0) = m(\tilde{\chi}_1^\pm)$.

Process	$\tilde{\chi}_1^\pm \tilde{\chi}_2^0$	$\tilde{\chi}_1^\pm \tilde{\chi}_1^0$	$\tilde{\chi}_1^\pm \tilde{\chi}_1^\pm$	$\tilde{\chi}_2^0 \tilde{\chi}_2^0$	$\tilde{\chi}_2^0 \tilde{\chi}_1^0$	$\tilde{\chi}_1^0 \tilde{\chi}_1^0$
Composition ratio [%]						
bino- $\tilde{\chi}_1^0$ & wino- $\tilde{\chi}_1^\pm, \tilde{\chi}_2^0$	30.5	$\ll 0.1$	54.7	14.8	$\ll 0.1$	$\ll 0.1$
higgsino- $\tilde{\chi}_1^0, \tilde{\chi}_2^0$ & $\tilde{\chi}_1^\pm$	26.5	36.6	19.4	1.7	13.4	2.5

Table 4.1: Event composition ratio for different electroweakino pair combinations included in the signal processes. In both interpretations, the fractions correspond to a benchmark scenario $m(\tilde{\chi}_2^0) = 100$ GeV; in the higgsino case a $\Delta m(\tilde{\chi}_2^0, \tilde{\chi}_1^0) = 5$ GeV was considered.

There are two main subcategories based on the electroweakino mixing: (a) the *wino-bino model*, where $\tilde{\chi}_2^0$ and $\tilde{\chi}_1^\pm$ are assumed to be 100% wino and $\tilde{\chi}_1^0$ to be 100% bino, and (b) the *higgsino model*, where $\tilde{\chi}_1^0, \tilde{\chi}_2^0$ and $\tilde{\chi}_1^\pm$ are considered to be purely higgsino. In this analysis, we consider the production of the various electroweakino pair combinations obtained with the first and second mass generation electroweakinos: $\tilde{\chi}_1^0 \tilde{\chi}_1^0 + \text{jj}$, $\tilde{\chi}_1^0 \tilde{\chi}_1^\pm + \text{jj}$, $\tilde{\chi}_1^0 \tilde{\chi}_2^0 + \text{jj}$, $\tilde{\chi}_1^\pm \tilde{\chi}_1^\pm + \text{jj}$, $\tilde{\chi}_1^\pm \tilde{\chi}_2^0 + \text{jj}$ and $\tilde{\chi}_2^0 \tilde{\chi}_2^0 + \text{jj}$. The process composition ratio in each scenario changes with the gaugino mixing as it is described on Tab. 4.1.

Besides the electroweakino composition, there are several decay chains these particles can undergo. In this project, three were considered under the wino-bino model and one for the higgsino model and are described in detail in the following subsections. The branching ratios for decays in this scenario are summarized in Tab. 4.2 for each relevant SUSY particle. From now on, we will refer to Δm defined as the mass difference between $\tilde{\chi}_2^0$ and $\tilde{\chi}_1^0$:

$$\Delta m \equiv \Delta m(\tilde{\chi}_2^0, \tilde{\chi}_1^0) = m(\tilde{\chi}_2^0) - m(\tilde{\chi}_1^0). \quad (4.1)$$

Wino-bino model with “democratic” light slepton decays

The three charged first generation sleptons (\tilde{e} , $\tilde{\mu}$, and $\tilde{\tau}$) are mass degenerate, left-handed ($\ell_1 = \ell_L$), and the next-to-lightest supersymmetric particle (NLSP). The slepton masses are parameterized in terms of $m(\tilde{\chi}_1^0)$, $m(\tilde{\chi}_2^0)$, and a $x_{\tilde{\ell}}$ variable,

$$m(\tilde{\ell}) = x_{\tilde{\ell}} [m(\tilde{\chi}_2^0) + m(\tilde{\chi}_1^0)], \quad (4.2)$$

where $0 < x_{\tilde{\ell}} < 1$. In the current simplified approach, we take $x_{\tilde{\ell}} = 0.5$, so that $m(\tilde{\ell})$ is the average of $m(\tilde{\chi}_1^0)$ and $m(\tilde{\chi}_2^0)$. Since $m(\tilde{\ell}) = m(\tilde{e}) = m(\tilde{\mu}) = m(\tilde{\tau})$, $\tilde{\chi}_2^0$ and $\tilde{\chi}_1^\pm$ are assumed to have similar branching fractions for each light slepton flavor (hence the term *democratic*). Figure 4.1 (left) shows a representative Feynman diagram for this model.

SUSY particle	wino-bino, democratic light $\tilde{\ell}$		wino-bino $\tilde{\tau}$ -dominated		wino-bino W^*/Z^*		higgsino	
	Decay chain	\mathcal{B} [%]	Decay chain	\mathcal{B} [%]	Decay chain	\mathcal{B} [%]	Decay chain	\mathcal{B} [%]
$\tilde{\chi}_1^\pm$	$\tilde{\chi}_1^\pm \rightarrow \tilde{e}\nu_e$	33.3	$\tilde{\chi}_1^\pm \rightarrow \tilde{\tau}\nu_\tau$	100	$\tilde{\chi}_1^\pm \rightarrow W^*\tilde{\chi}_1^0$	100	$\tilde{\chi}_1^\pm \rightarrow W^*\tilde{\chi}_1^0$	100
	$\tilde{\chi}_1^\pm \rightarrow \tilde{\mu}\nu_\mu$	33.3						
	$\tilde{\chi}_1^\pm \rightarrow \tilde{\tau}\nu_\tau$	33.3						
$\tilde{\chi}_2^0$	$\tilde{\chi}_2^0 \rightarrow \tilde{e}^\pm e^\mp$	33.3	$\tilde{\chi}_2^0 \rightarrow \tilde{\tau}^\pm \tau^\mp$	100	$\tilde{\chi}_2^0 \rightarrow Z^*\tilde{\chi}_1^0$	100	$\tilde{\chi}_2^0 \rightarrow Z^*\tilde{\chi}_1^0$	100
	$\tilde{\chi}_2^0 \rightarrow \tilde{\mu}^\pm \mu^\mp$	33.3						
	$\tilde{\chi}_2^0 \rightarrow \tilde{\tau}^\pm \tau^\mp$	33.3						
$\tilde{\ell}$	$\tilde{e} \rightarrow e\tilde{\chi}_1^0$	100	$\tilde{\tau} \rightarrow \tau\tilde{\chi}_1^0$	100	-	-	-	-
	$\tilde{\mu} \rightarrow \mu\tilde{\chi}_1^0$	100						
	$\tilde{\tau} \rightarrow \tau\tilde{\chi}_1^0$	100						

Table 4.2: Description of the branching ratios for SUSY particles in various SUSY physics interpretations used in this analysis.

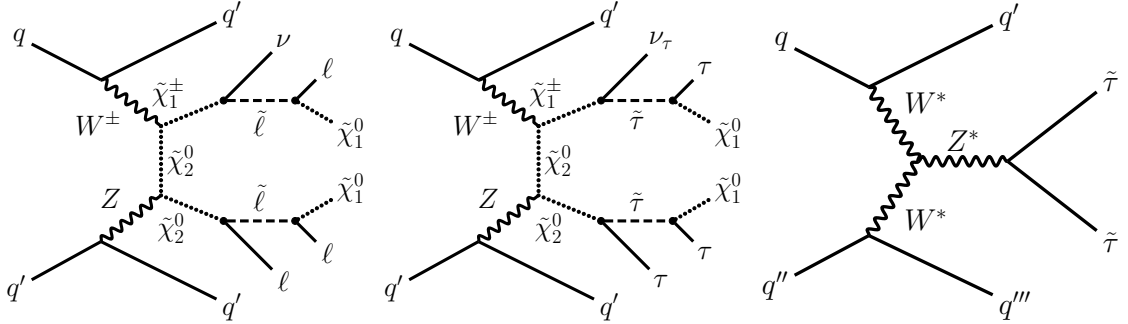


Figure 4.1: Representative Feynman diagrams for the wino-bino models with democratic light slepton decays (left), $\tilde{\tau}$ -dominated decays (middle), W^*/Z^* decays (right).

Wino-bino model with $\tilde{\tau}$ -dominated decays

In this scenario, the $\tilde{\tau}$ is the NLSP and the other sleptons ($\tilde{e}, \tilde{\mu}$) are decoupled, that is, $m(\tilde{e}), m(\tilde{\mu}) \gg m(\tilde{\chi}_2^0) > m(\tilde{\chi}_1^0)$. Therefore, the branching ratios are: $\mathcal{B}(\tilde{\chi}_1^\pm \rightarrow \tilde{\tau}\nu_\tau) = 1$, $\mathcal{B}(\tilde{\tau} \rightarrow \tilde{\chi}_1^0\tau) = 1$, $\mathcal{B}(\tilde{\chi}_2^0 \rightarrow \tilde{\tau}^\pm\tau^\mp) = 1$. The $\tilde{\tau}$ mass is calculated according to:

$$m(\tilde{\tau}) = \frac{1}{2} [m(\tilde{\chi}_2^0) + m(\tilde{\chi}_1^0)]. \quad (4.3)$$

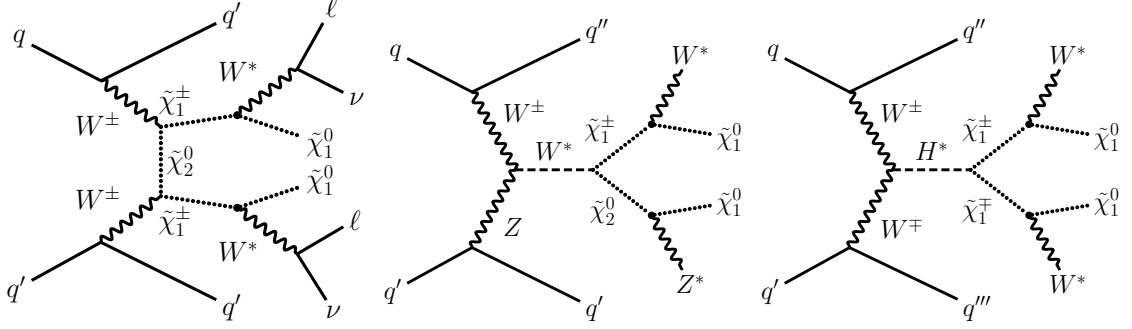


Figure 4.2: Representative Feynman diagram for the wino-bino model (left) and higgsino model (middle and right) with W^*/Z^* decays.

Another relevant process that can be included is direct $\tilde{\tau}$ pair production via VBF. Representative Feynman diagrams are shown on Fig. 4.1.

Wino-bino model with virtual W/Z decays

In this case, the sleptons are heavier than the $\tilde{\chi}_1^\pm$ and $\tilde{\chi}_2^0$, and therefore, the only way in which these electroweakinos can decay are via virtual W and Z bosons. Therefore, the corresponding branching ratios are: $\mathcal{B}(\tilde{\chi}_1^\pm \rightarrow \tilde{\chi}_1^0 W^*) = 1$ and $\mathcal{B}(\tilde{\chi}_2^0 \rightarrow \tilde{\chi}_1^0 Z^*) = 1$. A representative Feynman diagram is shown on Fig. 4.2 (left).

Higgsino model with virtual W/Z decays

In the full MSSM formalism, when the gaugino states of the $\tilde{\chi}_1^0$, $\tilde{\chi}_2^0$ and $\tilde{\chi}_1^\pm$ are purely higgsino, the mass splittings among them are $\mathcal{O}(\Delta m) \sim \text{MeV}$. By introducing additional mixing with wino or bino states, these mass differences increase to values of $\mathcal{O}(\Delta m) \sim \text{GeV}$. Therefore, the production cross section in the higgsino scenario increases with the mass differences. Another important difference between the wino-bino and higgsino models is the final state kinematics. In the wino-bino model, the mass eigenvalue product $m(\tilde{\chi}_2^0) \times m(\tilde{\chi}_1^0)$ can be either positive or negative. However, in the higgsino case, this product can only take negative values.

In our simplified approach, the neutralino and chargino mixing matrices are fixed such that $\tilde{\chi}_1^0$, $\tilde{\chi}_2^0$ and $\tilde{\chi}_1^\pm$ are all pure higgsino states, regardless of the Δm value. $\tilde{\chi}_1^0$ is the LSP and $\tilde{\chi}_1^\pm$ is the NLSP. Because of that, the cross sections to be used for this interpretation will be different from those obtained in the simplified SUSY signal samples, in order to be consistent with theoretical constraints. The $\tilde{\chi}_1^\pm$ mass is parameterized as

$$m(\tilde{\chi}_1^\pm) = \frac{1}{2} [m(\tilde{\chi}_2^0) + m(\tilde{\chi}_1^0)]. \quad (4.4)$$

Similar to the wino-bino model counterpart, the $\tilde{\chi}_2^0$ and $\tilde{\chi}_1^\pm$ only couple to weak bosons. Thus, the $\tilde{\chi}_2^0$ and $\tilde{\chi}_1^\pm$ decays occur only through W^*/Z^* bosons. The dominant diagrams for higgsino electroweakino production are s-channel (Fig. 4.2), in contrast to the wino-bino model (t-channel).

Anapole DM

The nature of DM is a problem that can be solved naturally by SUSY extensions of the SM. Considering a thermal evolution of the Universe, this hypothesis is relevant when taking into consideration DM reduction mechanisms like coannihilation. As explained in previous chapters, this is because of the experimental constraints placed by the measurement of the DM relic density $\Omega_{\text{DM}}h^2$ with astronomical probes.

However, there is a wide variety of non-supersymmetric models which provide an explanation for the DM particle nature, without considering coannihilation. One class of such models is based on the assumption that DM is electrically neutral and couples to the electromagnetic current through higher-dimensional operators. In other words, DM particles can interact electromagnetically with ordinary matter through higher order multipoles ([76, 77, 78, 79, 80, 81, 82, 83, 84, 85, 86], [87] and references therein). For example, DM with a non-zero electric and (or) magnetic dipole moment have been proposed, but are tightly constrained by results coming from direct DM detection experiments. Another option, which remains less constrained is a DM particle with an anapole moment (ADM), which couples to the SM photon [87]. In an EFT framework and remaining agnostic about the UV completion, the ADM operator is:

$$\mathcal{L}_{\text{eff,anapole}} = \frac{g}{\Lambda^2} \chi \gamma^\mu \gamma^5 \chi \partial^\nu F_{\mu\nu}, \quad (4.5)$$

where Λ denotes the cutoff scale and $\tilde{\chi}$ represents the DM particle, which is assumed to be a spin- $\frac{1}{2}$ Majorana fermion. One of the possible UV completion scenarios could be a bino-DM coupling to sleptons in SUSY. Previous phenomenological work [88] has shown that VBF ADM production cross sections dominate over mono-Z and mono-jet processes for all relevant values of Λ and m_χ . In this analysis, we expand the list of physics interpretations by focusing on the ADM model, only interpreting the results from the 0-lepton channel.

The dominant Feynman diagrams in VBF ADM production are s-channel WW fusion, in contrast to the VBF SUSY case, where the t-channel WW/WZ/ZZ are more important (Fig. 4.3). A distinguishing feature of VBF ADM production is the presence of significantly more forward jets and a larger $|\Delta\eta(\text{jj})|$ gap. In this analysis, we consider a fixed coupling constant $g = 1$ (Eq. 4.5) and several combinations of Λ and m_χ values.

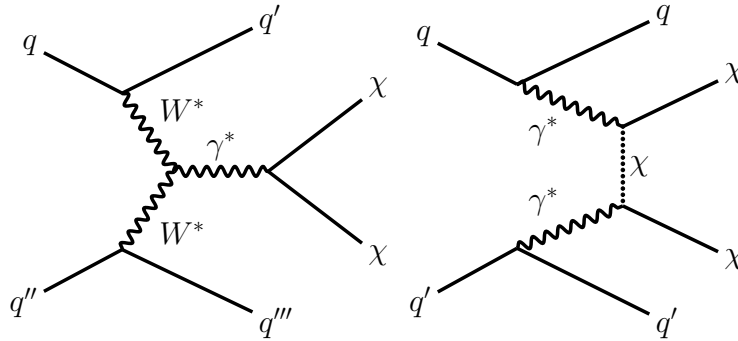


Figure 4.3: Representative Feynman diagrams for VBF ADM production.

CHAPTER 5

The LHC and the CMS detector

In this chapter, I present a general overview of the characteristics of the LHC and the detectors that form part of the experimental complex. I focus on the CMS experiment (*Compact Muon Solenoid*), one of the two general purpose detectors of the LHC which is known by their great capabilities and was fundamental in the discovery of the SM Higgs boson.

5.1 The Large Hadron Collider (LHC)

The LHC [89] is an accelerator and hadron collider that consists of two superconducting rings, installed in the tunnel built between 1984 and 1898 for the Large Electron-Positron Collider (LEP), located approximately 100 m underground the French-Swiss border, at the European Organization for Nuclear Research (CERN). These rings have a circumference of approximately 26.7 km. The main goal of the LHC is to elucidate the nature of the spontaneous electroweak symmetry breaking caused by the Higgs mechanism. The results from experimental studies of this mechanism at energies of the order of TeV are used to confirm the mathematical consistency of the SM at higher energy scales. In addition, experiments at the LHC aim to search for and possibly discover physics beyond the SM, based on the various conceptual and observational issues discussed in previous chapters.

There are four main detectors located in the beam interaction points of the LHC ring: ALICE (*A Large Ion Collider Experiment*) [90], ATLAS [91], CMS [92], and LHCb (*Large Hadron Collider beauty*) [93]. ALICE is a heavy ion detector whose main purpose is to study the characteristics of the quark-gluon plasma generated in the Pb-Pb ion collisions. LHCb is designed to study the b-quark physics, CP symmetry violation and quark mixing. ATLAS and CMS are the two largest general-purpose detectors for high-luminosity¹ searches whose goal is to explore a broad physics program at the TeV energy scale, which includes SM physics, and searches for extra dimensions, DM, etc.

The performance of a particle collider is mainly dictated by the luminosity. The collision rate can be defined in terms of the luminosity and the interaction cross section σ_p of the beams as follows,

$$\frac{dN_p}{dt} = \sigma_p \mathcal{L}. \quad (5.1)$$

The collision rate is also inversely proportional to the transverse beam size of the interaction point. The machine parameters define the luminosity, which at first approximation is given by

$$\mathcal{L} = \frac{f_{rev} n_b}{4\pi} \cdot \frac{N_1 N_2}{\sigma_1 \sigma_2}, \quad (5.2)$$

where f_{rev} is the revolution frequency, n_b is the number of bunches per beam, and N_1 (N_2) is the number of protons per bunch for beam 1 (beam 2) with transverse beam size σ_1 (σ_2) at the

¹*Luminosity*: Number of collisions per time unit and beam cross sectional area.

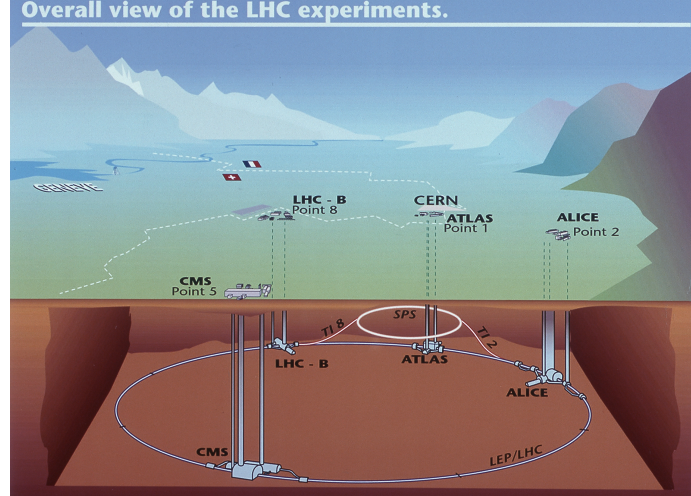


Figure 5.1: The four main LHC detectors and its geographical location: ALICE, ATLAS, CMS, and LHCb [94].

interaction point. ϵ is known as the *emittance* parameter and it is related to σ_i [95]. Emittance can be defined as the smallest distance that the beam can be squeezed through. Particles in a low emittance beam are confined to a small distance and have nearly the same momentum. Besides ϵ , the amplitude function β is useful to describe the transverse beam size. The amplitude function is determined by the accelerator magnet configuration and powering. It can be written as a function of the transverse beam size and the emittance:

$$\beta = \frac{\pi\sigma^2}{\epsilon}. \quad (5.3)$$

A narrow beam will have a small value of β ; if β is large, the beam is wide and straight. The value of the amplitude function at the interaction point is denoted as β^* . With these two values, the luminosity can be expressed as:

$$\mathcal{L} \propto f_{rev} n_b \frac{N_1 N_2}{\epsilon \beta^*}, \quad (5.4)$$

The LHC was designed to collide proton beams in opposite directions with a center of mass energy of 14 TeV and an instantaneous luminosity of $\mathcal{L} = 10^{34} \text{ cm}^{-2}\text{s}^{-1}$. Besides protons, the LHC can collide heavy ion beams ($^{208}\text{Pb}^{82+}$) with energies of 2.76 TeV/nucleon, adding up to a total center-of-mass energy of 1.148 PeV and a nominal luminosity of $\mathcal{L} = 10^{27} \text{ cm}^{-2}\text{s}^{-1}$.

The process to produce a high energy proton beam is done in stages, using the CERN accelerator complex (Fig. 5.2). Protons are produced at 92 keV; they are introduced and collected in the LINAC2 (*Linear Accelerator 2*), which increases its energy up to 50 MeV. Then, the *Booster* or *Proton Synchrotron Booster* (PSB) raises the beam energy up to 1.4 GeV. Then, protons are accelerated up to 25 GeV in the *Proton Synchrotron* (PS), which in addition separates the proton bunches, which contain around 10^{11} particles, with a time separation of ~ 25 ns. Finally, the *Super Proton Synchrotron* (SPS) elevates the beam energy to 450 GeV and injects the beams to the LHC ring (Fig. 5.2).

Quantity	Design	2016	2017	2018
Circumference [km]	26.659		26.659	
Center of mass energy [TeV]	14		13	
Bunch intensity ($N_{\text{particles}}$ per bunch)	1.15×10^{11}	1.10×10^{11}	1.25×10^{11}	1.15×10^{11}
Number of bunches per beam	2808	2200	1900	2500
Bunch spacing [ns]	25		25	
Emittance ϵ [μm]	3.5	2.5	2.0	2.2
β^* [cm]	55	40	30	25-30
Number of turns per second	–		11245	
Peak luminosity [$\text{cm}^{-2}\text{s}^{-1}$]	1.0×10^{34}	1.5×10^{34}	1.5×10^{34}	2.0×10^{34}
Peak pileup	25	45	65	60

Table 5.1: Values of LHC key parameters for pp collisions in Run II [96].

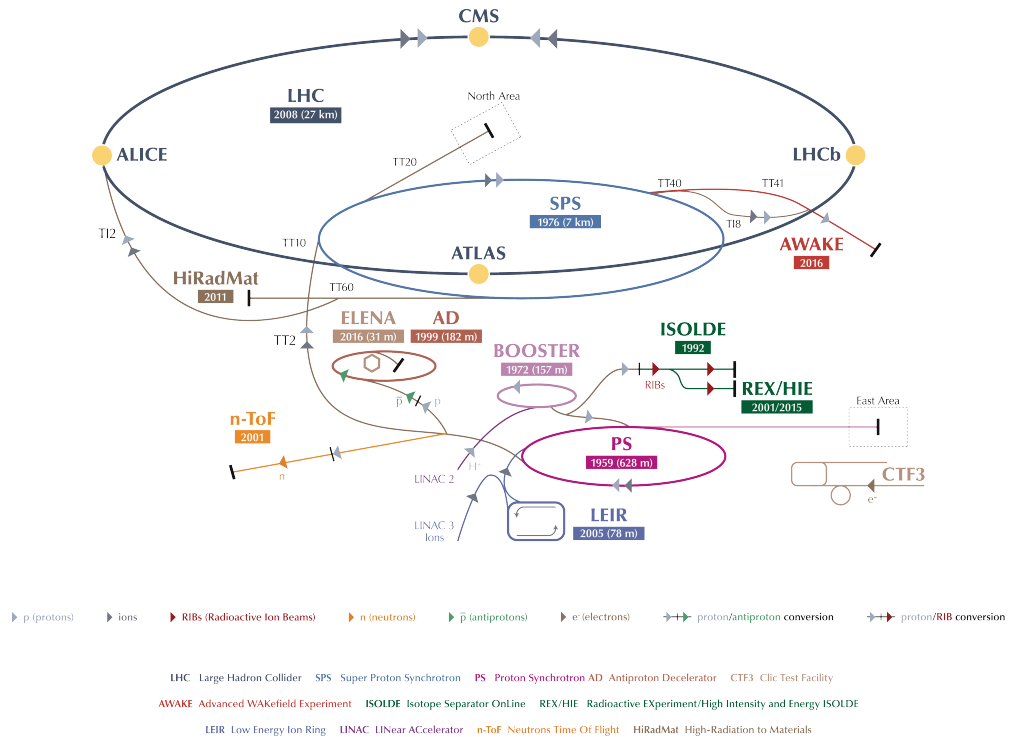


Figure 5.2: CERN accelerator complex [97].

The LHC accelerator is made of 1232 superconducting dipoles and more than 2500 magnets that collimate the beams down to a diameter of approximately $16\ \mu\text{m}$. On the other hand, heavy ions are obtained from a lead steam source which enters the LINAC3 before being collected and accelerated in the *Low Energy Ion Ring* (LEIR). After this, they follow the same acceleration chain as the protons.

By design, the expected luminosity peak for the LHC is $10^{34}\ \text{cm}^{-2}\text{s}^{-1} = 10\ \text{nb}^{-1}\text{s}^{-1}$. In Run II, this value was surpassed as described in Tab. 5.1. The general-purpose detectors will record an event rate of approximately 10^9 inelastic collisions per second. The nominal luminosity, an average of about 50 simultaneous inelastic interactions per bunch crossing, which is known as *pileup* (PU). This effect can be resolved by utilizing of high granularity detectors with good time resolution, which is equivalent to having a large number of electronic channels that need to well synchronized, besides an optimal design of the data acquisition system at the moment of data taking that would decrease the rate of events to approximately 100 events per second for its storage and later analysis.

5.2 The Compact Muon Solenoid detector (CMS)

CMS is a general-purpose detector at the LHC. It has a broad physics program that studies from SM physics to searches for extra dimensions and dark matter particles. The CMS experiment is one of the largest international scientific collaborations, involving around 4300 people including physicists, engineers, technicians, students and staff personnel from 182 institutions across 42 countries.

The experimental challenges that the CMS detector faces in order to record and collect collision data, and the characteristics that the CMS detector needs to accomplish the LHC physics program goals include [98]:

- good muon identification and momentum resolution over a broad range of momenta and angular acceptance,
- good momentum resolution for charged particles and reconstruction efficiency in charged particle trajectories in the tracking system,
- good efficiency in the event selection and identification of τ leptons and b-jets,
- good electromagnetic energy resolution and isolation efficiency for photons and leptons at high luminosities,
- a hadronic calorimeter with large geometrical acceptance and a fine lateral segmentation in order to get a good resolution for missing transverse energy.

The main features of the CMS detector are its high intensity solenoidal magnetic field for muon momentum measurement, produced by a superconducting solenoid, an entirely silicon-based tracking system and an electromagnetic calorimeter based on homogeneous scintillating crystals.

The CMS detector has a length of 28.7 m, a diameter of 15.0 m and a total weight of 14 000 tons. A superconducting solenoid is present in the center of the detector with a length 13 m and internal diameter of 6 m, producing a magnetic field of 3.8 T and a curvature power of 12 T·m, which allows CMS to measure the curvature angle of muons by the muon system.

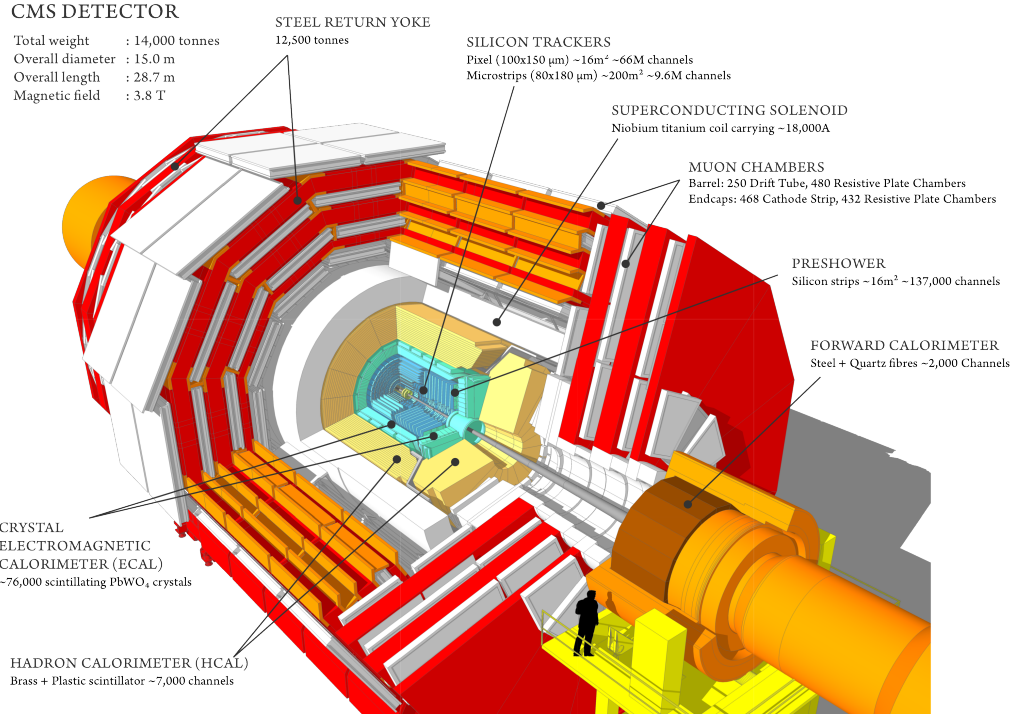


Figure 5.3: Transverse view of the CMS detector [99].

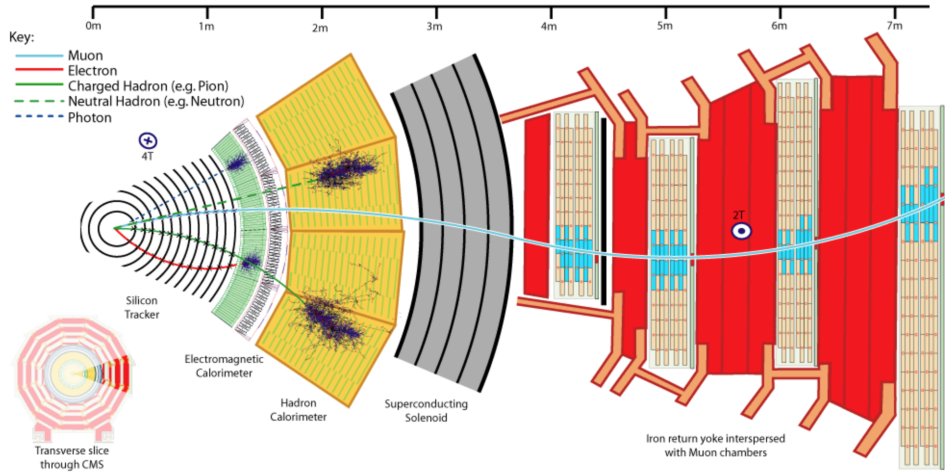


Figure 5.4: Transverse cross section of a CMS detector slice [100].

The coordinate system used at CMS has its origin centered at the nominal collision point inside the detector: the y axis points vertically upwards (towards the Earth surface), the x axis points radially towards the center of the LHC ring, and the z axis points in the direction of the beam that circulates towards the Jura mountains from the detector's location.

The azimuthal angle ϕ is measured from the x axis on the xy plane (transverse plane) and the radial coordinate is denoted by r . The polar angle θ is measured starting from the z axis. The pseudorapidity is defined as,

$$\eta = -\ln \left[\tan \left(\frac{\theta}{2} \right) \right]. \quad (5.5)$$

The transverse momentum p_T and energy E_T to the beam's direction are calculated from the momentum components in x and y . The imbalance of the measured energy in the transverse plane is known as *missing transverse energy* denoted by E_T^{miss} .

Tracking system

The internal tracking system or *tracker* is designed to provide an efficient and accurate measurement of the charged particle trajectories produced in the LHC collisions, as well as a precise reconstruction of secondary vertices. The tracker is divided in two main sub-detectors: the pixel detector and the silicon strip detector.

The CMS pixel detector is the closest detector to the beam line and has the ability to withstand millions of particles per square-centimeter per second traveling through the detector. When a charged particle passes through the pixel detector, it leaves behind electron-hole pairs in the silicon material. The ejected charges are collected for amplification and readout via readout chips (ROCs). The total coverage of the pixel detector extends out to approximately $|\eta| < 2.5$ [101]. The layout of a basic element of pixel detector is shown in Fig. 5.5a. The cell size is of $100 \mu\text{m}$ in the $r - \phi$ plane and $150 \mu\text{m}$ along the beam direction.

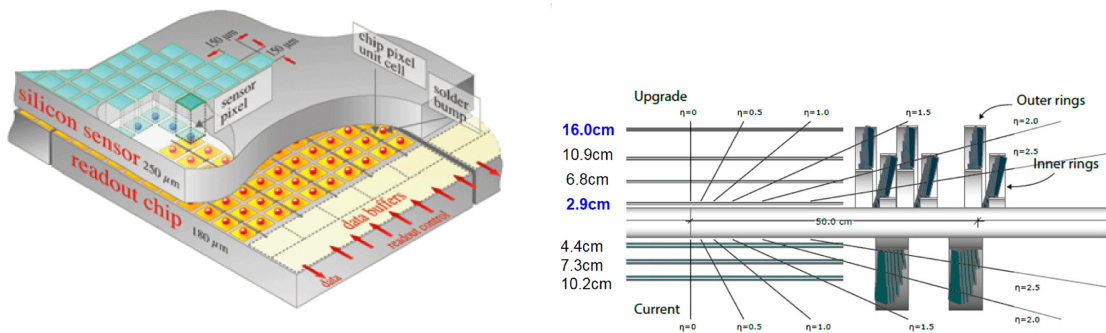


Figure 5.5: Left: Representative diagram of a CMS pixel module [101]. Right: Layout of the present (bottom) and upgraded (top) pixel detector in the $r - z$ plane [102].

During the Run II data taking period, the CMS detector upgraded the pixel detector between 2016 and 2017, with a entirely new detector (Fig. 5.5b). The geometry in 2016 is known as the Phase-0 pixel detector, which was comprised by three layers of pixel modules in the barrel region (BPIX) and two disks on each side on the forward regions (each side of the interaction point, known

as the FPIX). The high pileup and hit rates caused by the proton beams having a bunch spacing of 25 ns, degraded the hit efficiency by 16% in the innermost barrel layer of the Phase-0 pixel detector. The Phase-1 upgrade was designed to recover the hit and tracking efficiency and reduce the amount of material present in the pixel detector, more substantially in the forward regions ($1.2 < |\eta| < 2.5$). The main upgrades to the detector are [102]:

- new and improved readout chip that will recover the hit efficiency,
- an additional fourth barrel layer and third disk that allows for a 4-hit coverage over the full detector acceptance,
- reduced radial distance of the innermost barrel layer (from 4.4 cm to 2.9 cm),
- reduced amount of material by using an evaporative CO₂ cooling system, relocating electronic boards to more forward pseudorapidities and using a lighter mechanical support structure.

The next layer of detection technology the silicon strip detector. The silicon strip detector covers a radial range between 20 and 120 cm [103] and it is comprised of a total of ten layers in the barrel region ($|z| < 120$ cm). The barrel is divided in the tracker inner barrel (TIB) with four cylindrical layers and the tracker outer barrel (TOB) made of six cylindrical layers. The TIB system is closed by three inner disks, and it is known as the *tracker inner disk* (TID). Outside this $r - z$ range, the endcaps of the strips detector (TEC+ and TEC-) cover the spatial regions of $124 < |z| < 282$ cm and $22.5 < |r| < 113.5$ cm [103].

The silicon modules used in each layer in the strips tracker have a dedicated design depending on their position in the detector. The general design contains three elements: a set of silicon sensors, a mechanical support structure and readout electronics (Fig. 5.6b). Similar to the pixel modules, a charged particle crossing this detector material will eject electrons from the atoms, causing a small pulse of current. This current which only lasts a few nanoseconds, is amplified and readout by Analogue Pipeline Voltage (APV25) chips [103]. A strong cooling system (-10° C) is needed for this detector in order to minimize noise in the electronics caused by radiation damage.

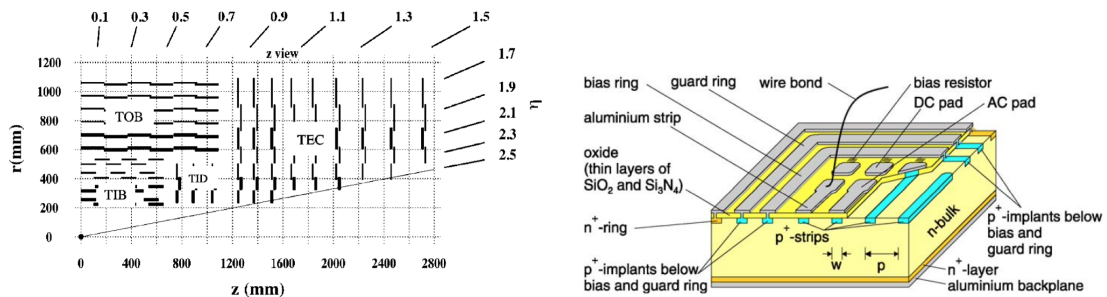


Figure 5.6: Left: Layout of a CMS silicon sensor [103]. Right: View of one quarter of the silicon strip tracker [103].

Electromagnetic calorimeter (ECAL)

The main functions of the electromagnetic calorimeter or ECAL [104] are to:

- 1) identify and measure the energy of photons and electrons,
- 2) measure the energy of particles produced and (or) decaying electromagnetically within jets, and
- 3) provide a hermetic coverage that helps the precise determination of missing transverse energy.

The ECAL will play a major role in the electron/photon identification and rejection against hadrons and jets. Likewise, this calorimeter is fundamental to the proper reconstruction and identification of hadronic τ decays and their separation from jets produced in purely QCD driven interactions.

The ECAL is a hermetical calorimeter comprised of homogeneous crystals of lead tungstate PbWO_4 (Tab. 5.2). This material will allow for a fast response, fine granularity, radiation hardness, as well as good energy resolution. The geometrical acceptance of the ECAL crystals extends up to $|\eta| = 3$ (Fig. 5.7). These crystals are highly transparent and scintillate when electrons and photons pass through them, and the amount of light produced is proportional to the energy of the particle(s).

Property	PbWO_4
Density [g/cm ³]	8.28
Radiation length [cm]	0.89
Interaction length [cm]	22.4
Moliere radius [cm]	2.19
Light decay time [ns]	5 (39%)
	15 (60%)
	100 (1%)
Refractive index n	2.30
Maximum of emission [nm]	440
Temperature coefficient [%/°C]	-2
Relative light output	1.3

Table 5.2: Properties of lead tungstate PbWO_4 crystals.

There are 36 supermodules of crystals containing 1700 trapezoidal crystals per super-module. In total, there are 61,200 crystals in the barrel region (EB), covering a range in $|\eta|$ up to 1.479. The crystals have a volume of 8.14 m³ and weighs about 67.4 tons. The endcap regions (EE) have a total of 4 Dees, with 5382 crystals per Dee, resulting in a total of 21528 crystals. The EEs cover the $|\eta|$ interval between 1.48 and 3.0. The scintillating light is detected by Avalanche Photodiodes (APD) in the barrel and Vacuum Phototriodes (VPT) in the endcaps.

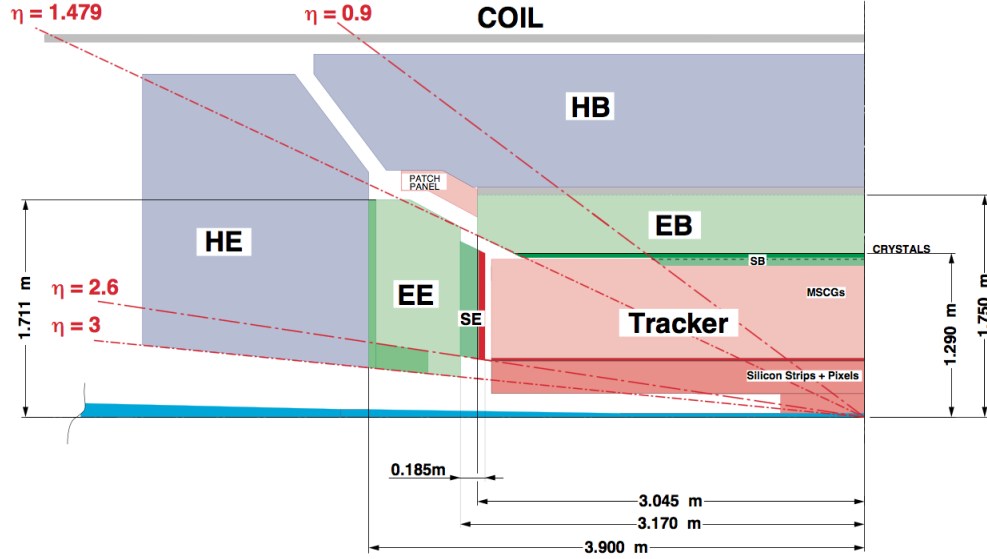


Figure 5.7: Schematics of a quadrant of the tracking and calorimeters at CMS [104].

The ECAL also includes preshower detectors to include extra spatial precision and covers a range of $1.65 < |\eta| < 2.61$, in each endcap. The main functions of this detector are to provide $\pi^0 - \gamma$ separation in the forward region. Neutral pions falling in the rapidity interval covered by the endcaps can be misidentified as photons. After an energetic π^0 decays to a pair of photons, these particles will be so closely spaced that it will be challenging to distinguish this signature from a single photon shower in the crystal ECAL. This subsystem is comprised of two lead layers followed by silicon sensors, similar to those used in the tracker, which measure the deposited energy and the transverse cascade profiles.

Hadronic calorimeter (HCAL)

The hadronic calorimeter or HCAL [105] plays a crucial role in the detection of hadrons, particles made of quarks and gluons. Additionally, it provides indirect measurement of the presence of non-interacting, uncharged particles such as neutrinos. Specifically, the HCAL is designed to measure the energy and direction of the *jets*, as well as the direction of the *missing transverse energy*, objects described in Chapter 7. The HCAL is also used to perform the correct identification of electrons, photons and muons, combined with the information from the ECAL and the muon system.

The HCAL is divided in four major sub-detectors: the hadron barrel (HB), the hadron endcap (HE), the hadron forward (HF), and the hadron outer (HO) calorimeters. The HB and HE are sampling detectors, composed of alternating layers of fluorescent plastic scintillator and absorber materials that produce a fast light pulse when a particle passes through, which leads to the determination of the position, energy and arrival time of the particle. The HB is divided in two half-barrels along the beam axis and it is assembled from 18 wedges. Each wedge contains absorber plates made of brass (70% copper and 30% zinc) that are bolted together, and the inner and outer plates are made out of stainless steel. It is located between 177.5 and 287.6 cm along the radial direction and

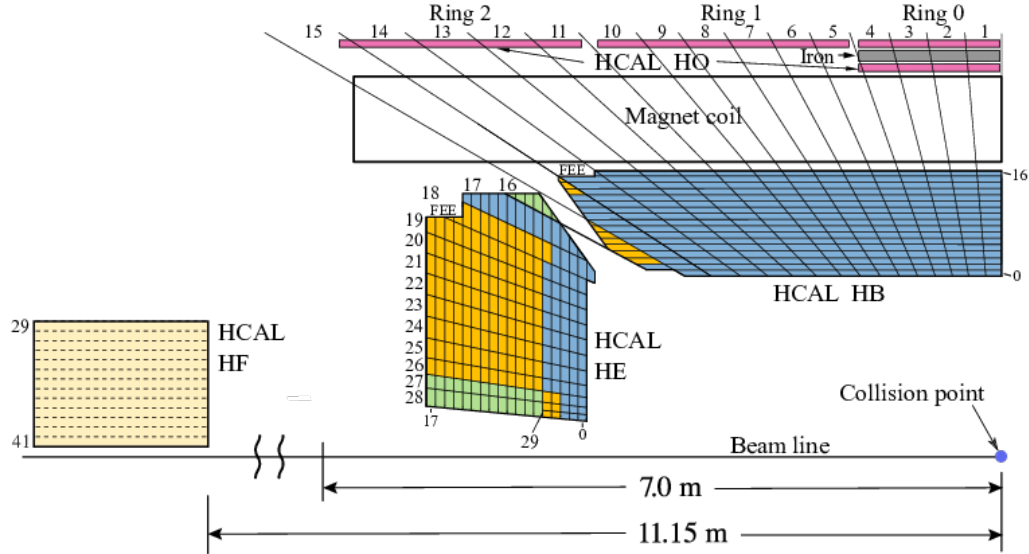


Figure 5.8: Schematic view of the CMS HCAL geometry during the 2016 LHC operation [106].

has an acceptance of $|\eta| < 1.39$. The HE covers a $|\eta|$ range between 1.30 and 3.00, has an 18-fold symmetry in ϕ and is divided into 14 sectors along η . The top edge of the front part of the endcap module has a slope of 53° corresponding to the gap angle between the HB and HE calorimeters [106].

The HO is located outside the magnetic coil. It is divided into 5 rings, with 12 ϕ -sectors each. The central ring is comprised of two layers of scintillator on either side of a stainless steel block, whereas the rest of the rings only have one layer of scintillators. The segmentation of the HO matches closely the one in the HB and has a geometrical acceptance of $|\eta| < 1.26$.

The light produced by the scintillators in the HB and HE calorimeters is carried through clear fibers to hybrid photodiodes (HPDs), and each signal is digitized in time intervals of 25 ns by a charge integrator and encoder (QIE). In the HO, the light is collected by silicon photomultipliers (SiPMs) and also digitized by QIEs.

The HF calorimeters are located on either side of the CMS detector. The front faces of these calorimeters are 11.2 m away from the interaction point, cover a pseudorapidity range of $2.85 < |\eta| < 5.19$, and a radial distance of $0.125 < r < 1.570$ m. In particular, these detectors are crucial for the type of experimental signatures explored in the work presented in this document, since forward jets are a distinctive characteristic of VBF processes. The detection technology used for these calorimeters is based on Cerenkov light emission by secondary charged particles going through the quartz fibers. Fibers with two different lengths (long: 1.649 m, and short: 1.426 m) are alternated with a separation of 5 mm. The long fibers reach the front face of the calorimeter and the short ones are placed at 12.5 radiation lengths into the calorimeter. A photodetector is placed at the back of these fibers and by measuring the difference in energy deposits in the long and short fibers, the electromagnetic and hadronic showers can be separated. The light collected from each fiber is converted to charge by a photomultiplier tube and digitized by the QIE.

Muon system

The detection of muons is one important tool to identify interesting process over the high background rates expected for the LHC operating at nominal luminosity [107, 108], and plays a central role in the physics studied by the CMS detector. Thus, the CMS design includes a robust muon detection system with the purpose of muon identification, momentum measurement, and as a part of the trigger system.

The CMS muon system is made up of three types of gas ionization chambers: drift tube (DT) chambers, cathode strip chambers (CSC) and resistive plate chambers (RPC). Due to the placement of the solenoid in the detector, the muon system is divided in a cylindrical section (barrel), where DTs are located, and CSCs are used in both endcap regions. RPCs are located in both the barrel and endcap regions.

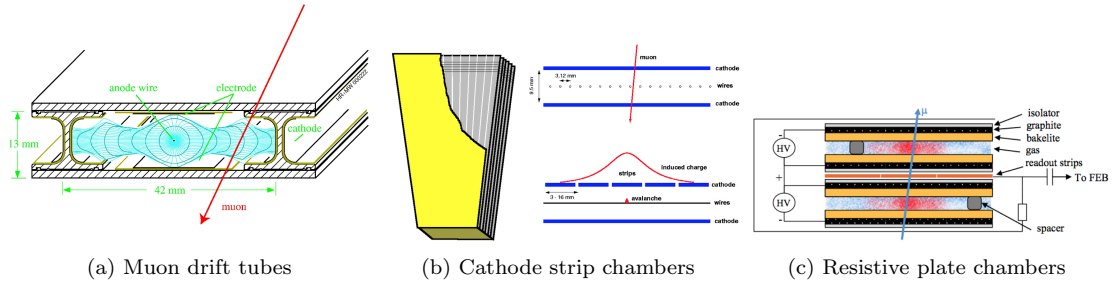


Figure 5.9: Single cells for each of the detector technologies used in the muon system of the CMS experiment [109].

The DTs are segmented into drift cells, and the muon position is determined by the measurement of the drift time to an anode wire of a cell with a shaped electric field [107]. These detectors cover a region of $|\eta| < 1.2$, a region where the noise produced by neutrons and the muon rate are low, as well as having a homogeneous magnetic field.

On the other hand, the muon rate production and background levels are larger in the endcap regions. Furthermore, the magnetic field in these regions is not uniform. CSCs are located in these regions, covering an acceptance of $0.9 < |\eta| < 2.4$, since they have fast time response, fine segmentation and are resistant to the non-homogeneity of the magnetic field. The CSCs function as standard multi-wire proportional counters, with the addition of a finely segmented cathode strip readout. These elements together allow for an accurate measurement of the coordinate of the bending plane ($r - \phi$) position at which the muon crosses the gas volume.

The DT and CSC regions together cover a range of $|\eta| < 2.4$, ensuring good muon identification in the $10^\circ < \theta < 170^\circ$ range. The typical muon reconstruction efficiency is between 95% and 99%. The most important properties of the combination of both technologies are the identification of the bunch which produced the muon and the activation of the trigger system based on the measured muon p_T , with the ability of rejecting backgrounds via timing discrimination.

The third type of muon detectors, the RPC chambers, are complementary to the DTs and CSCs and dedicated to the trigger system, given their excellent timing resolution. The RPCs are double-gap chambers operated in avalanche mode. The timing information obtained from the RPCs allow

the measurement of the bunch crossing time. They also provide a quick and independent selection of muons based on a looser p_T requirement in the $|\eta| < 1.9$ region.

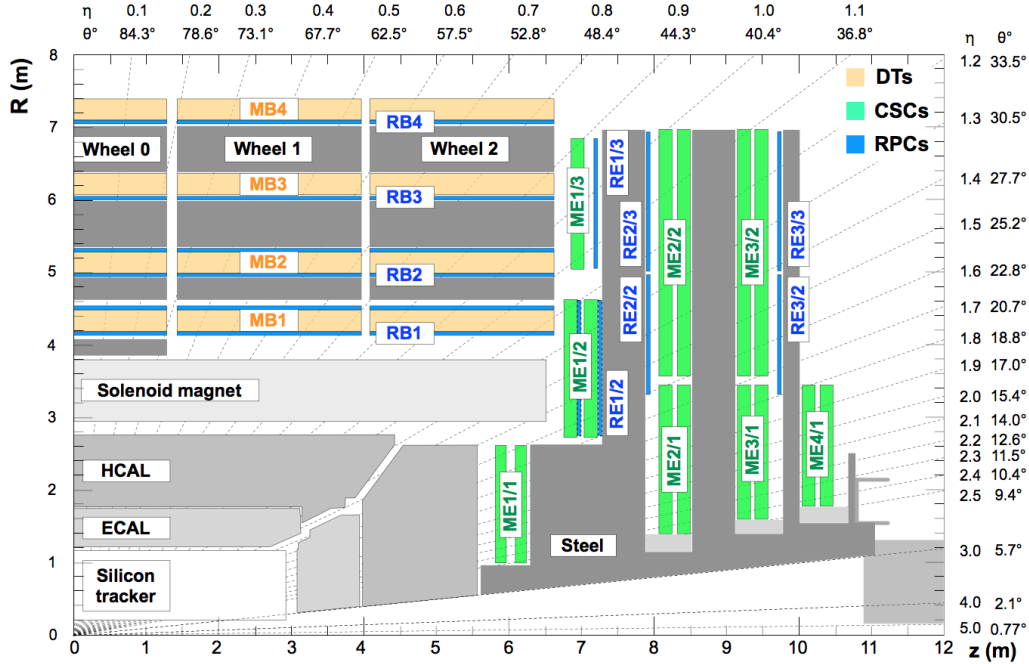


Figure 5.10: $r-z$ cross section of a quadrant of the CMS detector showing the geometry of the muon system. The DT stations are labeled as MB (Muon Barrel), the CSC stations as ME (Muon Endcap), and the RPC stations located in the barrel and the endcap are labeled RB and RE, respectively [107].

Trigger system

An *event* is the result of a measurement in the detector electronics and, in general, the signals produced by particles, tracks, energy deposits, etc., present in a specific proton bunch crossing.

The Trigger and Data Acquisition System (TriDAS) [110] has the main function of selecting from the millions of interactions per second recorded in the detector approximately 100 events per second, and storing them for future analysis. An event is required to satisfy two independent sets of selections, known as trigger levels. The first trigger level, called Level 1 (L1) trigger is designed to reduce the event rate recorded by the detector to 100 kHz in less than $4 \mu\text{s}$, by applying a set of tests entirely based on electronic signals. The algorithms used in the L1 trigger search for high momentum tracks in the muon system, a large energy deposition in the ECAL or HCAL or a combination of both.

The next trigger level, which consists of more sophisticated tests, is known as the High Level Trigger (HLT), at which the number of events is further reduced in two steps: Level 2 (L2) and Level 3 (L3) triggers. At L2, the decisions made at L1 are confirmed using algorithms that are more

complex, which use the finest granularity of the detector. Finally, at L3, the output events from L2 undergo a more complete reconstruction, where higher-level objects are created during processing. These trigger objects are subsequently used for particle reconstruction and identification as described in the following chapter, which will in the end, result in the physics objects used for data analysis.

CHAPTER 6

Event reconstruction and particle identification with the Particle Flow (PF) algorithm

As described in Chapter 5, the CMS detector is a general-purpose detector based on the concept of cylindrical detection layers, concentric to the beam axis. The five major systems in the CMS detector include a tracker, an electromagnetic calorimeter (ECAL), a hadronic calorimeter (HCAL), a muon detection system and a superconducting solenoid. When particles are produced in the beam crossing point, they interact first with the tracker. The trajectories of charged particles are detected and reconstructed from signals or *hits* left in the tracker layers, and consist of their origins and their actual trajectories, also known as *vertices* and *tracks*, respectively. The magnetic field produced by the solenoid bends the trajectories of such particles and from the produced curvature, the momenta and charge can be measured.

Further particle identification can be performed by studying the interactions of the produced particles with the other systems. Electrons and photons will be absorbed in the ECAL, producing electromagnetic showers, which are detected as *clusters*. Similarly, charged and neutral hadrons will produce showers which may be initiated in the ECAL and will consequently be fully absorbed in the HCAL. Finally, besides the interactions with the tracker, muons will barely interact with the material present in the calorimeters and produce hits in the muon detectors. Neutrinos and weakly interacting neutral particles, like neutralinos, will escape the detector undetected.

The description of events in the CMS detector is done by the *particle-flow (PF) reconstruction*, in which the basic elements from all detector layers are correlated to perform particle identification and the information from the measurements done by each system combined to reconstruct the properties of each particle after identification [111]. The PF algorithm requires fine segmentation in each of the sub-detectors, such that individual particles can be identified with good separation, which results in a robust global description of each event.

In the following two sections, I present a description of the basic elements of the PF algorithm and how they are combined together to perform particle reconstruction and identification. These particles are the basis of more complex objects used in physics analyses.

6.1 Basic elements of the PF algorithm

The basic elements of the PF reconstruction are charged particle tracks and vertices and calorimeter clusters. An overview of these elements is presented in the following two sections.

Charged particle tracks and vertices

The original goals of charged particle track reconstruction was the measurement of energetic and isolated muons and the identification of isolated hadronic τ decays and tagging of b-quark jets, since

the latter two present a secondary vertex structure. The reconstruction of these tracks is done using a combinatorial track finder based on Kalman Filtering (KF) [112]:

1. initial seed generation with a few hits compatible with a charged-particle trajectory,
2. pattern recognition to gather hits from all tracker layers along such trajectory,
3. final fitting to determine the charged particle properties: origin, transverse momentum and direction.

Originally, all tracks reconstructed this way had to originate from within a cylinder of a few mm radius centered around the beam axis and to have p_T larger than 0.9 GeV. Tracks used for analysis were required to be seeded with two consecutive layers in the pixel detector and reconstructed with at least eight hits in total (each contributing to less than 30% of the overall track goodness-of-fit χ^2) and only missing at most one hit along the way. For a charged particle to accumulate this number of hits along its trajectory, it needs to traverse the beam pipe, the pixel detector, the inner tracker and the first layers of the outer tracker before undergoing the first significant nuclear interaction. The performance of the combinatorial track finder algorithm is measured in terms of the reconstruction efficiency and mis-reconstruction. The reconstruction efficiency is defined as the fraction of simulated tracks reconstructed with at least 50% of the associated simulated hits, and with less than 50% of unassociated simulation hits. The mis-reconstruction rate is the fraction of reconstructed tracks that cannot be associated with a simulated track.

Some of the caveats in the original approach include:

- reduced efficiency for charged pions with $p_T > 1$ GeV (~ 70 -80%), compared to 99% for isolated muons;
- the possibility for pions to experience a nuclear interaction within the tracker material is practically the only mechanism that could allow to differentiate them from muons, when these particles have a $p_T \lesssim \mathcal{O}(10\text{GeV})$;
- the probability for a hadron to interact within the tracker material is about 10-30%, which will cause the track to be missed because of not fulfilling the hit number requirement;
- track reconstruction efficiency for particles with $p_T > 10$ GeV, mostly found in energetic jets, is limited by the ability to disentangle hits from overlapping particles (silicon detector pitch) and results in a reduction of this efficiency.

Charged hadrons missed by the tracking algorithm would be detected by the calorimeters as neutral hadrons with reduced efficiency, largely degraded resolution, and biased direction due to the bending of its trajectory in the magnetic field. On average, charged hadrons carry about two thirds of the jet energy, a 20% tracking inefficiency would double the energy fraction of identified neutral hadrons in a jet from 10% to 20% and therefore, would degrade the jet energy and angular resolutions by about 50%.

Thus, increasing the track reconstruction efficiency while keeping the mis-reconstructed rate unchanged is essential for PF event reconstruction. In order to achieve that, the combinatorial track finder is applied in several successive iterations, each with moderate efficiency but as high a purity as possible. The mis-reconstruction rate is reduced with quality criteria on the track seeds, the

track fit χ^2 and on the track compatibility with originating from one of the reconstructed primary vertices, adapted to the track p_T , $|\eta|$ and number of hits n_{hits} , applied at each iteration.

The quality criteria is not applied to tracks reconstructed with $n_{\text{hits}} \geq 8$, since the mis-reconstruction rate is already low for these tracks. The hits associated with the selected tracks are masked in order to reduce the probability of random hit-to-seed association in the next iteration. The remaining hits may be used in the next iteration to form new seeds and tracks with relaxed quality criteria, increasing the total tracking efficiency without degrading the purity. The same operation is repeated several times with progressively more complex and time consuming seeding, filtering, and tracking algorithms.

The seeding configuration and targeted tracks of each of the ten iterations are summarized in Table 6.1. In the first three iterations, tracks are seeded with triplets of pixel hits with additional criteria on their distance of closest approach to the beam axis. The resulting high purity permits loosening the original n_{hits} and p_T requirements to $n_{\text{hits}} \geq 3$ and $p_T > 200$ MeV. The tracks in these iterations have an efficiency of $\sim 80\%$ and account for 40% (20%) of the hits in the pixel (strip) detector in a given event, which will be masked for the next iterations. The main goal of iterations 4 and 5 is to recover tracks with one or two missing hits in the pixel detector, addressing mostly detector inefficiencies and particle interactions and decays within the pixel detector volume.

Iteration	Name	Seeding	Targeted tracks
1	InitialStep	pixel triplets	prompt, high p_T
2	Detached triplet	pixel triplets	from b hadron decays, $R \lesssim 5$ cm
3	LowPtTriplet	pixel triplets	prompt, low p_T
4	PixelPair	pixel pairs	recover high p_T
5	MixedTriplet	pixel+strip triplets	displaced, $R \lesssim 7$ cm
6	PixelLess	strip triplets / pairs	very displaced, $R \lesssim 25$ cm
7	TobTec	strip triplets / pairs	very displaced, $R \lesssim 60$ cm
8	JetCoreRegional	pixel+strip pairs	inside high p_T jets
9	MuonSeededInOut	muon-tagged tracks	muons
10	MuonSeededOutIn	muon detectors	muons

Table 6.1: Seeding configuration and targeted tracks of the ten tracking iterations. R is the targeted distance between the track production position and the beam axis [111].

Very displaced tracks are reconstructed in the next two iterations. These do not have seeds based on pixel hits, and thanks to the reduction of available hits from the masking in the first five iterations, they can be reconstructed more efficiently. The eighth iteration is aimed to reconstructing tracks in the dense core of high p_T jets. Merged pixel hit clusters, found in narrow regions compatible with the direction of high-energy deposits in the calorimeters, are split into several hits. Each of these hits is paired with one of the remaining hits in the strip detector to form a seed for this iteration. The last two iterations are specifically designed to increase the muon-tracking reconstruction efficiency with the use of the muon detector information in the seeding step.

Besides addressing some of the issues of using the combinatorial track finder, the use of the iterative approach extends the acceptance to the of particles with p_T as small as 200 MeV, typically below the calorimeter thresholds, and increases the reconstruction speed by a factor of two compared to doing track reconstruction in a single step. Although tracking efficiency remains limited at high

p_T and the mis-reconstructed track rate increases, the information obtained from the calorimeters and the muon system helps to address this problem (Fig. 6.1).

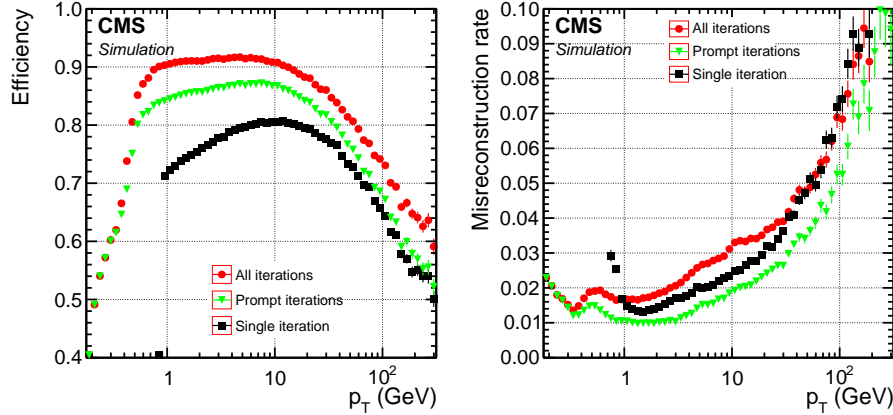


Figure 6.1: Efficiency and mis-reconstruction rate of the global combinatorial track finder (black squares) and the iterative tracking method (green triangles: prompt iterations based on seeds with at least one hit in the pixel detector; red circles: all iterations including those with displaced seeds), as a function of the track p_T , for charged hadrons in multijet events without pileup interactions. Efficiency and mis-reconstruction rate are determined only with tracks with $|\eta| < 2.5$. The efficiency is displayed for tracks originating within 3.5 cm of the beam axis and ± 30 cm of the nominal interaction point along the beam axis (Adapted from [111]).

When particles undergo nuclear interactions in the tracker material, they may cause a kink in the original hadron trajectory or the production of a number of secondary particles. On average, two thirds of the secondary particles are charged and their reconstruction is enhanced by iterations 6 and 7 of the iterative tracking. Displaced-track iterations usually add 5% to the tracking efficiency but also increase the total mis-reconstruction rate by 1% for tracks with $1 < p_T < 20$ GeV, which represents $\sim 20\%$ of the total mis-reconstruction rate in this p_T range. A separate algorithm is used to identify tracks linked to a common secondary displaced vertex in the tracker volume [113, 114].

Tracking for electrons and muons

Reconstruction of isolated **electrons** was naturally based on the measurement of energetic ECAL clusters ($E_T > 4$ GeV), also known as the *ECAL-based approach*. The cluster energy and positions are used to infer the position of the hits expected in the innermost tracker layer under the assumptions that the cluster is produced by either an electron or a positron. Because of the significant tracker thickness, most electrons emit a considerable fraction of their energy as bremsstrahlung photons before reaching the ECAL. Hence, the performance of this method depends on the capacity to collect all the radiated energy corresponding exclusively to a single electron. The energy of the electron and possible bremsstrahlung photons is gathered by grouping the ECAL clusters reconstructed in a small (extended) window in η (ϕ) around the electron direction into a *supercluster* (SC).

However, for electrons in jets, inefficiencies and mis-reconstruction rates increase because of:

- bias of the associated SC energy and position due the overlapping contributions from other particle deposits,

- higher compatibility of the super cluster with many hits from other charged particles in the innermost tracker layers when doing the backward propagation from the SC to the interaction region. This can be solved by applying strict isolation requirements, however these values become not optimal for electrons in jets when aiming for a global event description.

Furthermore, the trajectories of low- p_T electrons will be significantly bent by the magnetic field, making unfeasible the inclusion of all deposits from their radiated energy in the SC, given the extended region over which the energy is spread. As a consequence, the position of the SC is biased and does not allow the matching with the proper hits in the innermost tracker layers.

A *tracker-based* electron seeding method was developed to reconstruct electrons missed by the ECAL approach. The reconstruction efficiency for the tracks of these electrons is high with the iterative tracking method. Tracks from non-radiating electrons can be reconstructed with an efficiency similar to muons. Radiating electrons, whose tracks will be shorter or have lower p_T , will be largely recovered by the loose n_{hits} and p_T requirements in the latter iterations of the tracking algorithm. Consequently, all tracks obtained with the iterative tracking and with $p_T > 2$ GeV can be used as seeds for electrons.

In the tracker-based approach, electrons and charged hadrons are differentiated by taking advantage of the large probability for electrons to radiate in the tracker material. In general, there are three reconstruction scenarios based on the amount of energy radiated by the electron:

- i) *the electron radiates a small fraction of its energy*: the corresponding track can be reconstructed with a well-behaved χ^2 and safely propagated to the ECAL inner surface, where it can be matched with the closest ECAL cluster. In order to form an electron seed, the ratio between the track momentum and cluster energy is required to be consistent with unity;
- ii) *the electron emits soft photons*: pattern recognition may succeed in tracing most hits along the electron trajectory, most likely with a large χ^2 value.
- iii) *the electron radiates energetic photons*: most likely, trajectory building will be unable to keep up with the change in electron momentum, producing tracks with small number of hits.

To properly account for scenarios ii) and iii), a pre-selection based on the number of hits and χ^2 is applied to all electron tracks and the ones selected are fit again with a Gaussian-sum filter (GSF) [115], which allows for sudden and substantial energy losses along the trajectory. Following the GSF fitting, the number of hits, the χ^2 of the GSF track fit and its ratio to that of the KF track fit, the energy lost along the GSF track, and the distance between the extrapolation of the track to the ECAL inner surface and that of the closest ECAL cluster are used as inputs for a boosted-decision-tree (BDT) classifier and a final requirement is applied in the score obtained from it for the creation of tracker-based electron seeds.

Electron seeds obtained with the tracker and ECAL-based approaches are merged into a unique collection and are submitted to the full electron tracking with twelve GSF components. The efficiency increase obtained by adding the tracker-based seeding is close to a factor of two and the electron reconstruction can be done down to a p_T of about 2 GeV. Although these improvements come with a cost of larger mis-identification rate, this is handled at later stages of the PF reconstruction, when more information is available.

The tracker-based seeding is also effective at selecting electrons and positrons from conversions in the tracker material, for both prompt and bremsstrahlung photons. In order to minimize energy double counting from converted photons, these are associated to their parent electrons in the course of the PF reconstruction.

On the other hand, given that the CMS detector includes a muon spectrometer, **muons** can be identified with high efficiency over the full detector acceptance. Large muon purity is obtained since the calorimeters absorb all the other particles produced in a given event (except for neutrinos). The inner tracker produces a precise measurement of the muon momentum. The final collection of high-level muon physics objects is composed of three muon types:

- i) *standalone muon*: the seeds for a standalone muon are based on track segments formed by clustering hits within each DT or CSC detector. Pattern recognition is used in the muon spectrometer to gather all DT, CSC and RPC hits along the muon trajectory, resulting in a *standalone-muon track*.
- ii) *tracker muon*: tracks in the inner tracker (*inner track*) with $p_T > 0.5$ GeV and a total momentum p in excess of 2.5 GeV are extrapolated to the muon system. If at least one muon segment matches the extrapolated track, the inner track qualifies as a *tracker muon track*. The matching is performed in a local (x, y) coordinated system defined in a plane transverse to the beam axis¹. The muon segment and extrapolated track are matched if one of the two conditions are satisfied:
 - the absolute value of the difference between their x -coordinates is smaller than 3 cm, or,
 - the ratio of this distance to its uncertainty (*pull*) is smaller than 4.

This method is particularly efficient to reconstruct muons with $p_T \lesssim 10$ GeV.

- iii) *global muon*: each standalone-muon track is matched to a inner track if the parameters of the two tracks propagated onto a common surface are compatible. The hits from each of these tracks are combined and fit to form a *global-muon track*. At large transverse momenta ($p_T \gtrsim 200$ GeV), the global-muon fit improves the momentum resolution with respect to the tracker-only fit. Muons which leave a trace in more than one detector plane are efficiently reconstructed with this method.

About 99% of the muons produced within the geometrical acceptance of the muon system are reconstructed either as a global muon or a tracker muon and frequently as both. When a global muon and a tracker muon share the same inner track, it is merged into a single candidate. Muons reconstructed only as standalone muons usually have lower momentum resolution and a significant fraction of them correspond to muons coming from cosmic rays.

In some cases where hadron shower remnants (produced by charged hadrons) reach the muon system, charged hadrons may be reconstructed as muons (*punch-through*). Identification criteria based on the association of energy deposits in the the ECAL and HCAL systems with muon tracks are applied to improve the performance of muon identification (Sec. 6.2).

¹ x is the better measured coordinate.

Calorimeter clusters

The main goals of the calorimeter clustering algorithm are [111]:

- detection of stable neutral particles (photons and neutral hadrons) and measurement of their corresponding energy and direction,
- separation of neutral particle energy deposits from charged hadron energy deposits,
- reconstruction and identification of electrons and associated bremsstrahlung photons, and,
- provide redundancy for the energy measurement of charge hadrons whose track parameters were not determined accurately (low-quality and high- p_T tracks).

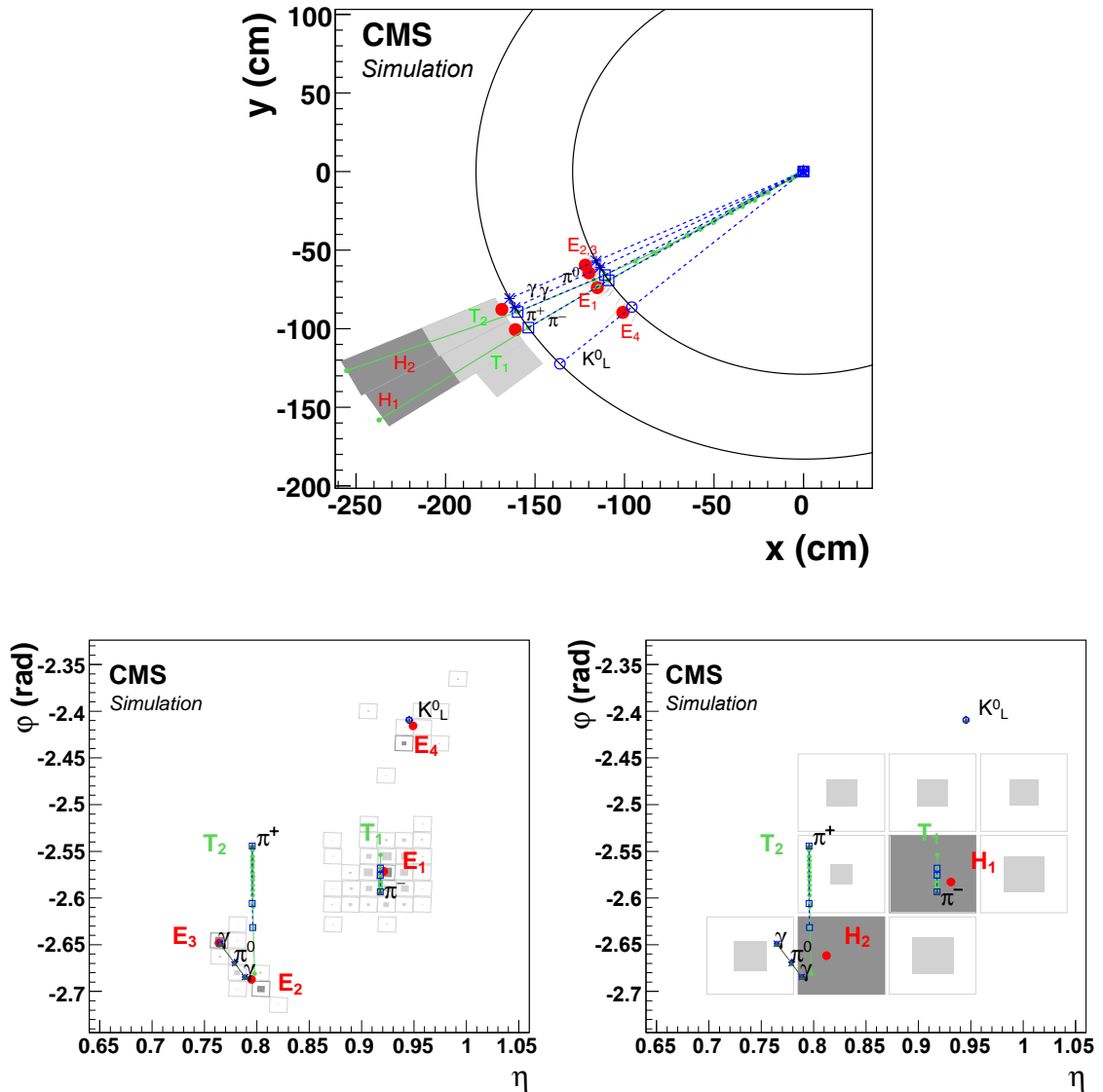


Figure 6.2: Event display of an illustrative jet made of five particles only on the (x, y) plane (top) and (η, ϕ) plane of the ECAL (lower left) and HCAL (lower right) surfaces. (Adapted from [111]).

For the PF event reconstruction, a dedicated clustering algorithm was developed, designed for high detection efficiency of low-energy particles and good separation of close energy deposits. The clustering is carried out separately for each calorimeter² with the exception of the HF. In the HF, the electromagnetic or hadronic components of each cell are directly measured as an *HF EM* cluster and an *HF HAD* cluster.

Figure 6.2 shows the event display of an illustrative jet made of five particles. In the lower left, the surface of the ECAL is represented in the (η, ϕ) plane. The K_L^0 , the π^- and photons from the π^0 decays are detected as four well-separated ECAL clusters. The π^+ does not generate a cluster in the ECAL. Both charged pions are reconstructed as charged particle tracks shown as vertical solid lines in the (η, ϕ) views and circular arcs in the (x, y) plane. These tracks point towards the two reconstructed HCAL clusters. Cells with an energy larger than those in the neighboring cells are shown in dark gray. Cluster positions are represented by dots, the simulated particles by dashed lines, and the positions of their impacts on the calorimeter surfaces by various open markers.

Similar to the reconstruction of tracks, *cluster seeds* are identified as calorimeter cells with an energy above a specific seed threshold, and larger than the energy of the surrounding or *neighboring cells*³. Then, *topological clusters* are constructed by adding cells with at least one corner in common with any of the neighboring cluster seed cells and an energy above a cell threshold set to twice the noise level. In the ECAL endcaps, an additional E_T threshold requirement is required, since the noise level increases as a function of θ .

	ECAL		HCAL		Preshower
	Barrel	Endcaps	Barrel	endcaps	
Cell E threshold [MeV]	80	300	800	800	0.06
Number of closest cells to seed	8	8	4	4	8
Seed E threshold [MeV]	230	600	800	1100	0.12
Seed E_T	–	150	–	–	–
Gaussian width [cm]	1.5	1.5	10.0	10.0	0.2

Table 6.2: Clustering parameters for the ECAL, HCAL and preshower. All values result from optimizations based on the simulation of single photons, π^0 , K_L^0 , and jets [111].

The reconstruction of clusters within a topological cluster is performed by using an expectation-maximization algorithm [116] based on a Gaussian-mixture model⁴. The input parameters for such model are the amplitude A_i and the coordinates of the mean $\vec{\mu}_i$ of each Gaussian in the (η, ϕ) plane. The width of the Gaussian σ has a set value for each specific calorimeter. The energy and position of the seeds are used as initial values for the parameters of the corresponding Gaussian functions and the expectation-maximization cycle is repeated until convergence. After this, the positions and energies of the Gaussian functions are taken as cluster parameters. The numerical values of the clustering algorithm parameters are summarized in Table 6.2.

²ECAL barrel and endcaps, HCAL barrel and endcaps, and the two preshower layers.

³A neighboring cell is defined as a cell which shares a side (four closest cells) or a corner (eight closest cells) with the seed candidate.

⁴The Gaussian-mixture model postulates that the energy deposits in the M individual cells of the topological cluster are the result of N Gaussian energy deposits, where N is the number of seeds [111].

Neutral particles (photons and neutral hadrons) are more challenging to reconstruct with the PF algorithm, since the only information available for them are the calorimeter clusters. Thus, it is important to accurately calibrate the calorimeter response to photons and hadrons (both charged and neutral), in order to maximize the identification probability, minimize the mis-identification rate of neutral particles as mis-reconstructed energy excesses⁵ and obtain the right energy scale for them.

Calibration of electromagnetic energy deposits from photons.

The absolute calibration of the ECAL response to electrons and photons was initially estimated with several techniques prior to the start of collision data taking and was refined with collision data at $\sqrt{s} = 7$ and 8 TeV. More details can be found in [117]. An additional residual energy calibration is determined from simulated single photons to account for the effects of the several thresholds applied to ECAL cell energies in the clustering algorithm. Such calibration is applied before the hadron cluster calibration and particle identification.

The photons considered for the residual energy calibration are simulated to have energies between 0.25 to 100 GeV and are processed through a GEANT4 [118] simulation of the CMS detector. After this, only photons which do not undergo a e^+e^- conversion before their first interaction with the ECAL are kept for the analysis, with the intention of focusing on single cluster calibration.

The calibration is done separately for the barrel and endcap regions of the ECAL. In the barrel, the residual correction to be applied to the measured cluster energy is obtained by fitting an analytical function of the type $f(E, \eta) = g(E)h(\eta)$ to the two-dimensional distribution of the average ratio $\langle E^{\text{true}}/E \rangle$ in the (E, η) plane, where E and η are the energy and pseudorapidity of the cluster, respectively, and E^{true} is the true photon energy.

In the endcaps, the ECAL crystals are partly shadowed by the preshower. Hence, the calibrated cluster energy is expressed as

$$E^{\text{calib}} = \alpha (E^{\text{true}}, \eta^{\text{true}}) E_{\text{ECAL}} + \beta (E^{\text{true}}, \eta^{\text{true}}) [E_{\text{PS1}} + \gamma (E^{\text{true}}, \eta^{\text{true}}) E_{\text{PS2}}], \quad (6.1)$$

where E_{ECAL} is the energy measured in the ECAL, and $E_{\text{PS1(PS2)}}$ are the energies measured in the two preshower layers.

The calibration parameters α , β and γ are chosen in each $(E^{\text{true}}, \eta^{\text{true}})$ bin to minimize the χ^2 defined as

$$\chi^2 = \sum_{i=1}^{\text{Nevents}} \frac{(E_i^{\text{calib}} - E_i^{\text{true}})^2}{\sigma_i^2}, \quad (6.2)$$

where σ_i is an estimate of the energy measurement uncertainty for the i th photon. α , β and γ are fit with analytical functions of the type $g'(E^{\text{true}})h'(\eta^{\text{true}})$. The calibration for photons that leave energy in one of the two preshower layers is done similarly, except that the χ^2 minimization only includes two parameters. If no energy is measured in the preshower, the calibration of the ECAL energy in the endcap (outside the preshower acceptance) is done with the same method used for the ECAL barrel.

⁵When energy deposits from neutral particles overlap with clusters from charged particles, these deposits are detected as energy excesses with respect to the sum of associated particle momenta.

The evaluation of calibration parameters for clusters in the actual preshower region, η^{true} is estimated from the ECAL cluster pseudorapidity, and E^{true} is approximated by a linear combination of E_{ECAL} , E_{PS1} , and E_{PS2} with fixed coefficients. From these calibrations, it is found that energetic photons lose about 5% of their energy in the preshower material and softer photons can lose up to 40%.

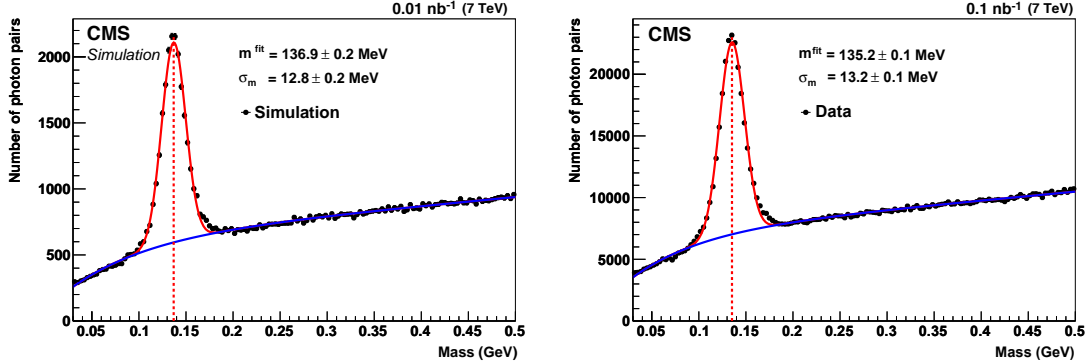


Figure 6.3: Photon pair invariant mass distribution in the barrel ($|\eta| < 1.0$) for simulation (left) and data (right). The π^0 signal is modeled by a Gaussian (red curve) and the background by an exponential function (blue curve). The Gaussian mean value (vertical dashed line) and its standard deviation are denoted as m^{fit} and σ_m , respectively. (Adapted from [111]).

The calibrations for residual energy in the electromagnetic clusters are validated in data with photons coming from the abundant production of π^0 's in pp collisions. Neutral pions are reconstructed by pairing two photons reconstructed as explained in this section, considering all ECAL clusters with a calibrated energy above 400 MeV. The diphoton pair is required to have a total energy larger than 1.5 GeV. The resulting photon pair invariant mass distribution is shown in Fig. 7 for simulated events and data recorded in 2010 at $\sqrt{s} = 7$ TeV. The effectiveness of the simulation-based ECAL cluster calibration for low energy photons is shown by the agreement of the fitted mass resolutions in data and simulation, and that of the fitted mass values with the nominal π^0 mass.

Calibration of energy deposits from neutral hadrons.

In general, hadrons will leave energy in both the ECAL, for which the response to neutral hadrons is different than that to photons, and the HCAL. The calorimeter response to neutral hadrons is not linear and depends on the fraction of the shower energy deposited in the ECAL. The calibrated calorimetric energy associated with a hadron is given by

$$E_{\text{calib}} = a + b(E) f(\eta) E_{\text{ECAL}} + c(E) g(\eta) E_{\text{HCAL}}, \quad (6.3)$$

where the E_{ECAL} is the calibrated energy measured in the ECAL and E_{HCAL} is the energy measured in the HCAL, where E and η are the true energy and pseudorapidity of the hadron. In Equation 6.3, a accounts for the energy lost due to the energy thresholds of the clustering algorithm and is assumed to be independent of E . The determination of the calibration coefficients a , b and c is done using a method similar to the ECAL cluster energy calibration, but instead of using single photons,

samples of single K_L^0 's are simulated. Hadrons that interact with the tracker material are rejected. Initially, $f(\eta)$ and $g(\eta)$ are fixed to unity and for a given value of a in each bin of E , the χ^2 defined as

$$\chi^2 = \sum_{i=1}^N \frac{(E_i^{\text{calib}} - E_i)^2}{\sigma_i^2}, \quad (6.4)$$

is minimized with respect to the coefficients b and c . E_i and σ_i represent the true energy and the expected calorimetric energy resolution of the i th single hadron in Eq. 6.4. A Gaussian is fit to the distribution of $E_{\text{ECAL}} + E_{\text{HCAL}} - E$ in each bin of true energy. Then, b and c are fit to the evolution of the Gaussian standard deviation as a function of E in order to minimize χ^2 . Both of these operations are repeated in the following iterations, for which the calibrated energy E_{calib} is substituted by the raw energy ($E_{\text{ECAL}} + E_{\text{HCAL}}$). This procedure converges at the second iteration.

Also, the barrel and endcap regions are treated separately. The determination of b and c is performed separately for hadrons depositing energy only in the HCAL (only c is determined) and those depositing energy in both the ECAL and HCAL. The small residual dependence of the calibrated energy on the particle pseudorapidity is corrected for in a third iteration of the χ^2 minimization with second-order polynomials for $f(\eta)$ and $g(\eta)$, and with $b(E)$ and $c(E)$ taken from the result of the second iteration.

Given that the true hadron energy E might not be available in data, a is chosen to minimize the dependence on E of the coefficients b and c for $E > 10\text{GeV}$. This results in estimated values of 3.5 GeV (2.5 GeV) for hadrons showering in both the ECAL and HCAL (only the HCAL). Fig. 6.4 (left) shows b and c as a function of E . The residual dependence of these coefficients with E is fitted to appropriate continuous functional forms $b(E)$ and $c(E)$ for later use in the PF reconstruction. The dependence of b and c with E up to large values is a consequence of the nonlinear calorimeter response to hadrons.

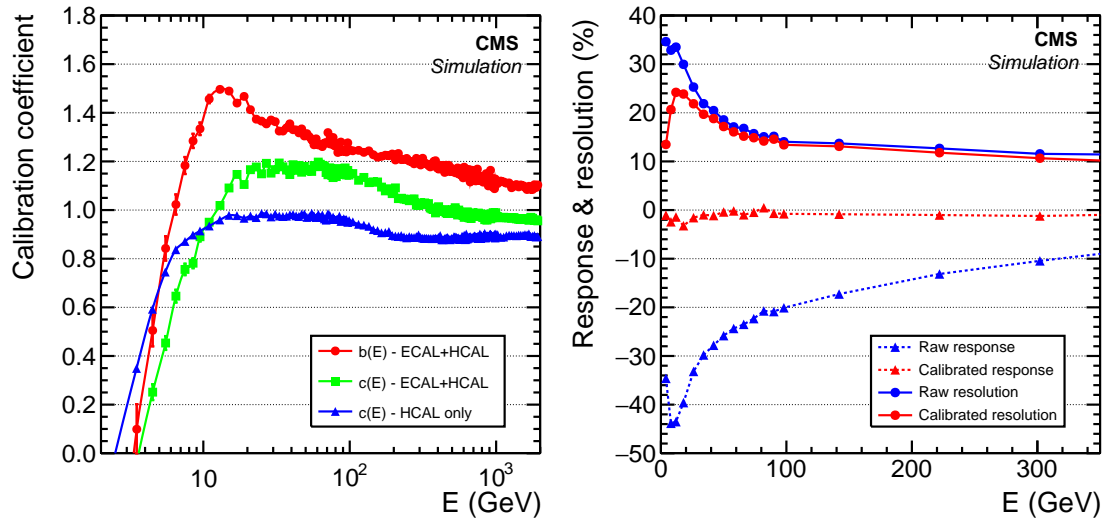


Figure 6.4: Left: Calibration coefficients b and c obtained from single hadrons in the barrel as a function of E for different energy deposit configurations in the calorimeter clusters. Right: Relative raw and calibrated energy response and resolution for single hadrons in the barrel as a function of E . (Adapted from [111]).

Fig. 6.4 (right) also shows a comparison of the *calibrated* and *raw* response⁶ and resolution for single hadrons. Both the response and resolution are obtained by a Gaussian fit to the distribution of the relative difference between the calibrated (raw) calorimetric energy and the true hadron energy. We observe that the calibrated response is much closer to zero, whereas the raw response can underestimate the hadron energies up to 40%. Therefore, the calibration procedure restores the linearity of the calorimeter response. Likewise, a considerable improvement is observed on the relative calibrated energy resolution, specially for $E < 40$ GeV. Finally, isolated charged hadrons from data collected at $\sqrt{s} = 0.9, 2.2$ and 7 TeV were used to validate these calibration coefficients.

6.2 Particle reconstruction and identification

In this section, particle reconstruction and identification using the basic elements of the PF algorithm is described for the physics objects that will subsequently be used to create higher-level physics objects which are used in the data analysis presented in this document. The PF elements are combined using a link algorithm that will later give place to the identification and reconstruction of muons, electrons, isolated photons as well as hadrons and non isolated photons, typically produced in the hadronization process resulting from the production of an energetic parton in the collisions.

Link algorithm

The first step in the particle reconstruction process is done via a *link algorithm* which connects the PF elements from the different detector layers/systems. The limitations present for this algorithm's probability to:

- *link elements from a single particle* is determined by the granularity of the various sub-detectors and by the number of particles to resolve per unit of solid angle, and,
- *link all elements of a given particle* is given by the amount of material found upstream of the calorimeters and the muon detector, which can lead to trajectory kinks or the production of secondary particles.

Only PF elements considered nearest neighbors in the (η, ϕ) plane as obtained with a k -dimensional tree are considered by the link algorithm to be combined in pairs. If two elements can be linked, the quality of the link is evaluated by the algorithm based on the distance between such elements in the (η, ϕ) plane or the (x, y) plane, according to the nature of the elements to be linked. Then *PF blocks* are produced, which consist of elements associated either by a direct link or by an indirect link through common elements.

There are five main types of links between two given pairs of PF elements:

⁶Response is defined as the mean relative difference between the calibrated (raw) energy and the true energy.

Track-to-cluster link:

The track is extrapolated from its last measured hit in the tracker to (a) the preshower layers, (b) the ECAL at a depth corresponding to the expected maximum typical longitudinal electron shower profile, and (c) the HCAL at a depth corresponding to one interaction length, within the corresponding angular acceptance. If the extrapolated position of the track is within the *cluster area*⁷, which is enlarged up to the size of a cell in each direction to account for (i) any gaps between calorimeter cells or cracks between calorimeter modules, (ii) the uncertainty in the position of the shower maximum, and (iii) the effect of multiple scattering on low-momentum charged particles. In the presence of multiple clusters linked to a single track, only the link with the smallest distance is kept.

For photons emitted by electron bremsstrahlung, their energy is collected by extrapolating tangents to the GSF tracks to the ECAL from the intersection points between the track and each of the tracker layers. When the extrapolated tangent position is within the boundaries of a given cluster and the distance between the GSF track extrapolation in η is smaller than 0.05, then the cluster is linked to the GSF track.

Likewise, prompt and bremsstrahlung photons have a large probability to convert into a e^+e^- pair in the tracker material. In the case of bremsstrahlung photons, if the converted photon direction, obtained from the sum of the two track momenta, is found to be compatible with one of the track tangents, a link is created between each of these two tracks and the original case. More details about the dedicated method to create links between two tracks compatible with photon conversion was developed and is described in [119].

Cluster-to-cluster link:

These links aim to connect HCAL and ECAL clusters, as well as ECAL clusters and preshower clusters in the preshower acceptance. When the cluster position in the more granular calorimeter (preshower or ECAL) is within the cluster envelope in the less granular calorimeter (ECAL or HCAL), then a link is established. If multiple HCAL (ECAL) clusters are linked to the same ECAL (preshower) cluster(s), only the link with the smallest distance is kept. If an ECAL cluster and an ECAL SC share at least one ECAL cell, a trivial link is established.

Track-to-track link:

For nuclear interaction reconstruction, charged particle tracks may be linked through a common secondary vertex. The condition for a displaced vertex to be kept is to have at least three tracks. Only one of these tracks can be an incoming track, reconstructed with tracker hits between the primary vertex and the displaced vertex. The invariant mass of the remaining two (outgoing) tracks must be larger than 0.2 GeV.

⁷Defined by the area covered by all the cluster cells in the (η, ϕ) plane for the ECAL and HCAL barrel or the (x, y) plane for the ECAL endcaps and the preshower.

Track-to-muon segment link:

These links are done to create global and tracker muons as described in Sec. 6.1.

Once all PF blocks are created, the identification and reconstruction of particle candidates is done sequential steps. At each step, tracks and clusters from the identified particles are removed from the PF block. The order in which particles are identified goes as:

- i. muons,
- ii. electrons and energetic isolated photons (converted and unconverted); at this point, tracks with a p_T uncertainty above the calorimetric energy resolution expected for charged hadrons are masked (Fig. 6.4), which allows for a reduction of the mis-reconstruction rate at high p_T (Fig. 6.1),
- iii. hadrons and photons coming from parton fragmentation, hadronization and decays in jets⁸,
- iv. hadrons which interact with the tracker material (secondary particles).

After this process is completed, a revision of the global description of the event is performed, in order to identify potential particle mis-identification and mis-reconstruction which produces an artificially large missing transverse momentum p_T^{miss} . Each one of these steps are described in further detail in the sections to follow. The particles reconstructed and identified after event post-processing are used to create more complex physics objects which can be used in data analysis.

Muons

Muons are identified by applying selections based on the properties of global and tracker muons. There are two main scenario in muon identification:

- i. *isolated global muons*: an isolation criterion is applied to the global muon candidate, for which the p_T sum of the tracks and the E_T of the calorimeter energy deposits, both within a distance $\Delta R \leq 0.3$ is below 10% of the muon p_T . Most hadrons that could be mis-identified as muons are rejected only with this requirement;
- ii. *non-isolated global muons*: these are muons produced inside jets, from the leptonic decays of hadrons produced in the hadronization process. These muons are required to satisfy the “tight-muon” selection (described in [120]) and to either have at least three matching track segments in the muon detectors or that the calorimeter deposits associated with the track are compatible with the muon hypothesis. Muons can fail the tight-muon selection because of a poorly reconstructed inner track or a poor global fit. In the first case, muons can be recovered if the standalone muon track fit is of high quality and is associated with a large number of hits in the muon detectors; in the second case, they can be recovered if a high quality fit is obtained with at least 13 hits in the tracker and the associated calorimeter clusters are consistent with the muon hypothesis.

⁸Jets are defined in Sec. 7.4.

The muon momentum is selected to be the momentum of the inner track if $p_T < 200$ GeV; otherwise, the momentum is chosen to be that of the track that gives the smallest χ^2 probability from the track fits considering (a) tracker only, (b) tracker and first muon pane, (c) global, and, (c) global without the muon detector panes presenting a large occupancy.

Electrons and isolated photons

Since electrons and photons have similar probabilities of interacting with the tracker material, the basic properties and challenges for their corresponding reconstruction are alike. Electron candidates are seeded from a GSF track for which the corresponding ECAL cluster is not linked to three or more additional tracks. Photon candidates are seeded from an ECAL SC with $E_T > 10$ GeV and no link to a GSF track.

For ECAL-based electron candidates (Sec. 6.1) and photon candidates, the sum of the energies measured in the HCAL cells with a distance $\Delta R < 0.15$ to the SC position must be less than 10% of the SC energy. The following sets of tracks and clusters elements are associated to the candidate:

- all ECAL clusters in the PF block linked either to the SC or to one of the GSF track tangents,
- tracks linked to the above ECAL clusters if their individual momenta and the energy of the HCAL cluster linked to each track is consistent with the electron hypothesis, and,
- tracks and ECAL clusters identified as a product of photon conversions linked to the GSF track tangents.

Additional identification criteria is applied to electron candidates, based on the output from BDTs trained separately in the ECAL barrel and endcaps acceptance. Up to 14 variables related to the GSF track and cluster properties for isolated and non-isolated electrons are used as an input for these BDTs. Photon candidates obtained in this stage must be isolated from other tracks and clusters in the event and their corresponding ECAL cell energy distribution and HCAL to ECAL energy ratio must be consistent with those expected from a photon shower.

Before continuing with hadron and non isolated photon reconstruction and identification, besides the tracks and cluster associated to the electron and photon candidates, any tracks identified to come from a photon conversion which have not been associated are masked as well.

Hadrons and non isolated photons

Particles identified in this process include charged hadrons (π^\pm , K^\pm , or protons), neutral hadrons (K_L^0 , neutrons, etc.), non isolated photons coming from π^0 decays, and, with extremely few exceptions, muons from early decays of charged hadrons. First, within the tracking coverage ($|\eta| < 2.5$), ECAL clusters not linked to any track are identified as photons and HCAL clusters satisfying this condition as neutral hadrons. "Track-less" ECAL clusters are turned into photons before neutral hadrons, since, on average, the energy fraction carried by photons in a jet is 25%, whereas only 10% is carried by neutral hadrons: 3% left in the ECAL and the remaining 7% is deposited in the HCAL.

For $|\eta| \geq 2.5$, where tracking is not available due to its acceptance, it is not possible to distinguish between charged and neutral hadrons and they both leave 25% of the total jet energy in the ECAL. Therefore, ECAL and HCAL clusters linked together are assumed to be the result from the same hadron shower, while not-linked ECAL clusters are identified as photons. The HF EM and HF HAD clusters are added to the particle list as *HF photons* and *HF hadrons*, without further calibration (calibrations described in Sec. 6.1).

Next, charged hadrons are identified: each of the unmasked HCAL clusters in a given PF block is linked to one or several tracks, which are not linked to any other HCAL cluster. Then, such tracks can be individually linked to one of the remaining ECAL clusters. The calibrated calorimetric energy is determined as described in Sec. 6.1. The true energy is estimated to be the largest of either the sum of the momenta of the tracks or the sum of the raw ECAL and HCAL energies. Then, the sum of the track momenta is compared to the calibrated calorimetric energy (E^{calib}) to determine the particle content. Defining $\Delta E \equiv E^{\text{calib}} - \sum_{i=1}^{n_{\text{tracks}}} p_i$ as the difference between the calibrated energy and the sum of the track momenta, two main scenarios are possible: $\Delta E > 0$ or $\Delta E \sim 0$. For $\Delta E > 0$, particle identification goes as follows:

- a) if $500 \text{ MeV} < \Delta E < E_{\text{ECAL}}$, this is interpreted as a photon with an energy corresponding to ΔE after recalibration under the photon hypothesis;
- b) if $\Delta E \geq E_{\text{ECAL}}$, ΔE is recalibrated under the photon hypothesis, turning into a photon. Any remaining energy excess above 1 GeV after recalibration is classified as a neutral hadron.

Then, each track is identified as a charged hadron whose momentum and energy is determined from the track momentum, assuming the charged-pion mass hypothesis.

When $\Delta E \sim 0$, the track-to-cluster link(s) is identified as a charged hadron. The measurement of its momentum is improved by performing a χ^2 fit of the measurements in the tracker and the calorimeters. If only one track is linked to the HCAL cluster, this results in a weighted average. Particles with large energies or detected at large pseudorapidities are particularly benefited from such refinement in the momentum measurement. In general, for all energy regimes, the energy resolution from the combination of the tracking and calorimeter systems is always better than the energy measured only in the calorimeter.

The scenario in which $\Delta E < 0$ is also possible and rarely found in event reconstruction. Usually, this is a result of muons produced in hadron in-flight decays. If $|\Delta E|$ is larger than three standard deviations, a search for muons with loosened identification criteria and depositing little energy in the calorimeters is performed.

Nuclear interactions in the tracker material

After the identification of nuclear interaction vertices, the secondary charged particle particles associated with the charged particle tracks are replaced in the reconstructed particle list by a single primary charged hadron. Its direction will be given by the vectorial sum of the momenta of the secondary particles, its energy (E_{sec}) by the sum of their energies and its mass is set to the charged pion mass. If an incoming track is included in the vertex, then the direction is taken to be that of the incoming track. When the momentum of the incoming track is well measured (p_{prim}), it is used

to estimate the energy of undetected secondary particles which were not reconstructed as secondary charged or neutral particles. The energy of the primary charged hadron in this case is estimated as

$$E = E_{\text{sec}} + f(\eta, p_{\text{prim}})p_{\text{prim}}, \quad (6.5)$$

where $f(\eta, p_{\text{prim}})p_{\text{prim}}$ is obtained from the simulation of single charged-hadron events.

Event post-processing

The purpose of processing events after all particles have been identified is to find and correct for any artificially large missing transverse momentum ($p_{\text{T}}^{\text{miss}}$) reconstructed in the event. The most common source of such $p_{\text{T}}^{\text{miss}}$ is the mis-identification or mis-reconstruction of a high- p_{T} muon. There are three steps to the post-processing algorithm:

1. particles whose large p_{T} may lead to a large artificial $p_{\text{T}}^{\text{miss}}$ are selected,
2. the correlation between the particle \vec{p}_{T} and $\vec{p}_{\text{T}}^{\text{miss}}$ is quantified (magnitude and direction),
3. the identification and reconstruction of these particles are modified, if this change reduces $p_{\text{T}}^{\text{miss}}$ by at least one half.

The three main causes of muon-related artificial $p_{\text{T}}^{\text{miss}}$ are (1) the presence of genuine muons from cosmic rays traversing CMS in coincidence with an LHC beam crossing, (2) severe mis-reconstruction of the muon momentum and (3) particle mis-identification (e.g., punch-through charged hadrons). The steps taken to identify the source of the artificial $p_{\text{T}}^{\text{miss}}$ and correct it are described in [111].

CHAPTER 7

Event reconstruction and physics objects for data analysis at CMS

After a collision event is reconstructed and the particles in it have been identified by the PF algorithm, they can be used for physics analysis, either as they are after reconstruction with further quality selection criteria applied (electrons, photons and muons) or to build more complex physics objects (jets, hadronically decaying taus and missing transverse momentum). The physics objects used in the data analysis presented in this document are described in this chapter.

7.1 Pileup interactions

Given the high instantaneous luminosity at the LHC, multiple proton-proton collisions take place within a single beam crossing [121]. These interactions occur along the beam axis around the origin of the CMS coordinate system, following a normal distribution. Interactions happening at the same time as the primary hard interaction and leaving energy deposits in the calorimeter as well as additional tracks, are generically known as *in-time pileup* (IT PU). Pileup interactions occurring in the previous or subsequent beam crossing for a particular beam crossing can also contribute to pileup, since the calorimeters have a finite signal decay time and these interactions can be recorded in the same time window. This contribution from pileup is known as *out-of-time pileup* (OOT PU).

Pileup interactions will produce additional particles, in particular charged hadrons, photons and neutral hadrons. On average, these will add approximately 1 GeV per pileup interaction per unit area in the (η, ϕ) plane to the p_T measurements. There are several ways to estimate the amount of pileup present in each collision event, and are listed below.

Number of primary vertices (N_{PV}).

The primary vertices are ordered by the quadratic sum of the p_T of their tracks ($\sum p_T^2$). The primary vertex with the largest $\sum p_T^2$ is identified as the hard-scatter (HS) vertex, whereas the other vertices are considered pileup vertices [111, 122]. A general pileup reduction approach is based on the *pileup charged-hadron subtraction algorithm* (CHS). In this technique, charged hadrons can be identified to be coming from pileup interactions if their tracks are associated with a pileup vertex. These charged hadrons are removed from the particle list used to form physics objects.

Pileup (diffuse) offset energy density.

Neutral particles and all particles reconstructed outside the tracker acceptance, cannot be identified as being originated from pileup interactions with the CHS algorithm, because there is no track associated to them. Therefore, a different approach based on estimating the pileup offset energy density is used. Neutral particles and all particles reconstructed outside the tracker acceptance, cannot be

identified as pileup particles with this algorithm, therefore a different approach based on estimating the pileup offset energy density is used. The p_T density of pileup interactions is expected to be uniform across the (η, ϕ) plane. Therefore, the average p_T contributions from pileup can be subtracted in the form of a diffuse offset energy density ρ measured per event. It can be calculated with jet clustering techniques using the list of all reconstructed particles as input [111, 123, 124].

Another way to estimate pileup consists of combining the measurement of the inelastic proton-proton cross section [125, 126] and the determination of the instantaneous luminosity of the given bunch crossing with dedicated detectors.

Lepton isolation.

Pileup can be quantified in a specific region of the (η, ϕ) plane through the calculation of *isolation* variables, and it is typically done for leptons. In absence of pileup, the particle-based (relative) isolation relative to the lepton p_T is given by

$$I_{PF} = \frac{1}{p_T} \left(\sum_{h^\pm} p_T^{h^\pm} + \sum_{\gamma} p_T^{\gamma} + \sum_{h^0} p_T^{h^0} \right). \quad (7.1)$$

The sums run over the charged hadrons (h^\pm), photons (γ) and neutral hadrons (h^0) with a distance ΔR to the lepton smaller than either 0.3 or 0.5 [111], with

$$\Delta R = \sqrt{(\Delta\phi)^2 - (\Delta\eta)^2}. \quad (7.2)$$

In the presence of pileup, the *pileup-mitigated absolute lepton isolation* is defined as

$$I_{PF}^{\text{abs}} = \sum_{h^\pm, \text{HS}} p_T^{h^\pm} + \max \left(0, \sum_{\gamma} p_T^{\gamma} + \sum_{h^0} p_T^{h^0} - \Delta\beta \sum_{h^\pm, \text{pileup}} p_T^{h^\pm} \right). \quad (7.3)$$

In the first term of Equation 7.3, only charged hadrons associated with the HS vertex are considered. The expected contribution from charged hadrons produced in pileup interactions is subtracted from the p_T sums of neutral hadrons and photons. Such contribution is estimated from the scalar sum of the p_T of charged hadrons in the cone identified as coming from pileup vertices $\left(\sum_{h^\pm, \text{pileup}} p_T^{h^\pm} \right)$. This sum is multiplied by a $\Delta\beta = 0.5$ factor, corresponding to the approximate ratio of the neutral particle to charged hadron production in inelastic proton-proton collisions, obtained from simulation [111] The relative lepton isolation accounting for pileup is given by $I_{PF} = I_{PF}^{\text{abs}}/p_T$.

Simulation samples are generated with the best approximation of the pileup conditions expected to be measured in data. However, due to unexpected changes in the experimental conditions not foreseen during the production of simulation samples, simulated events need to be reweighted to fit the PU distribution observed in data. These weights are derived by calculating the ratio of the probabilities for obtaining n interactions in data ($P_{\text{data}}(n_{\text{PU}})$) and simulation ($P_{\text{sim}}(n_{\text{PU}})$):

$$w(n_{\text{PU}}) = \frac{P_{\text{data}}(n_{\text{PU}})}{P_{\text{sim}}(n_{\text{sim}})}. \quad (7.4)$$

7.2 Muons

In the current analysis, muon leptons are expected in the final state as a result of the decays from W and Z bosons, τ leptons, and/or from slepton ($\tilde{\ell}$) decays. These muons fall into the category of *prompt muons* [111]. Additional quality criteria need to be applied to the muons identified with the PF algorithm, related to tighter identification criteria (ID) and isolation (Sec. 7.1).

Besides the PF muon properties, other relevant variables and algorithms used to define muon identification types include [127]:

- *Muon segment compatibility*: estimated by propagating the muon tracker track to the muon system and evaluating both the number of matched segments in all stations and the closeness of the matching in position and direction. This process results in values ranging from 0 to 1, with 1 representing the highest degree of compatibility,
- *Kink-finding algorithm*: the muon tracker track is split into two separate tracks at several places along the particle trajectory. For each split, the algorithm, makes a comparison between the two separate tracks. A large value of χ^2 is interpreted as the two tracks being incompatible to be a single track, and,
- *Compatibility with the primary vertex*: this algorithm is similar to the muon segment compatibility, except that the reconstructed vertex with the largest value of summed physics-object p_T^2 is used to perform the matching.

There are five main muon IDs for CMS physics analyses: *loose*, *medium*, *tight*, *soft* and *high momentum*¹ ID, defined in [127] (Tab. 7.1).

Muons identified with *loose ID* are PF muons, classified as either a tracker or a global muon. The loose ID is aimed to identify prompt muons originated at the primary vertex and from light and heavy hadron decays.

The *medium muon ID* expands the selections of the loose ID, by requiring loose muons to have a tracker track with hits from more than 80% of the inner tracker layers it traverses. For tracker-only muons, the muon segment compatibility is required to be larger than 0.451. For muons reconstructed both as global and tracker muons, the muon segment compatibility requirement is relaxed to be greater than 0.303, with an additional selection on the global muon fit goodness-of-fit per degree of freedom of $\chi^2/n_{\text{dof}} < 3$. The position match between the tracker muon and standalone-muon must have $\chi^2 < 12$, and the maximum χ^2 computed by the kink-finding algorithm must satisfy $\chi^2 < 20$.

A muon passing *tight ID* is a loose muon, whose tracker track uses hits from at least six layers of the inner tracker, including at least one pixel hit. A tight muon must be reconstructed both as a tracker muon and a global muon. The global muon fit must have $\chi^2/n_{\text{dof}} < 10$ and include at least one hit from the muon system. In addition, the tight muon tracker track must be compatible with the primary vertex, with a transverse impact parameter $|d_{xy}| < 0.2$ cm, and a longitudinal impact parameter $|d_z| < 0.5$ cm.

Tracker-only muons can be identified with a *soft muon ID*². The tracker track is required to pass a high purity flag selection [127, 122], and have hits in at least six layers in the inner tracker

¹The description of this ID is not included as it is not relevant to the data analysis presented in the present document.

²Not to be confused with the term *soft* to denote a low momentum particle.

including at least one pixel hit. The tracker muon reconstruction must have tight segment matching, having pulls less than 3 both in local x and local y . Also, selections on the impact parameters with respect to the primary vertex are applied: $|d_{xy}| < 0.3$ cm and $|d_z| < 20$ cm.

Variable	Loose μ ID	Tight μ ID
PF muon	True	True
Global muon	True	True
Global or tracker muon	True	False
Strip tracker layers with hits	–	> 5
Pixel layers with hits	–	≥ 1
$ d_{xy} $ [cm]	–	< 0.2
$ d_z <$ [cm]	–	< 0.5
Global muon track fit χ^2/n_{dof}	–	< 10
n_{hits} in muon chambers	–	≥ 1
Matching muon stations	–	≥ 2

Table 7.1: Selection criteria for the loose and tight muon ID definitions.

Muon momentum is determined with the *Tune-P* algorithm, which selects the p_T measurement from one of the following refits based on goodness-of-fit information and $\sigma(p_T)/p_T$ criteria to reduce tails in the momentum resolution due to poor quality fits: *Inner-Track fit*, *Tracker-Plus-First-Muon-Station fit*, *Picky fit*, or *Dynamic-Truncation fit*. These fits are described in Ref. [120]. The information obtained with the Tune-P algorithm is further refined by the PF algorithm, utilizing the information from the full event.

An isolation requirement is applied to muons, with the purpose of discriminating muons from weak decays within jets and prompt muons. There are two strategies to estimate the muon isolation: the *track-based isolation* (using reconstructed tracks) and the *PF isolation* (using information from three PF charged hadrons, neutral hadrons and photons, as described in Sec. 7.1). Tight and loose isolation working points are defined for each one of these strategies, with corresponding efficiencies of 95% and 98%. For PF isolation, the cone radius for the computation of isolation is $\Delta R = 0.4$ and the value for tight (loose) isolation is 0.15 (0.25).

The efficiency of muon reconstruction and identification with the tight working point in data and simulation as a function of η for muons with $p_T \geq 20$ GeV is shown in Fig. 7.1. The efficiency for this set of muons is found to be independent of p_T . The dips in efficiency observed around $|\eta| = 0.3$ are caused by the reduced instrumentation between the central muon wheel and the two neighboring wheels. In the low- p_T regime, the efficiency is nonlinear and can fluctuate between 81-99% (Fig. 7.2). For this case, simulation is observed to model data to a level of 4-5%. The isolation efficiency is measured for muons passing the tight ID and the tight PF isolation and is shown in Fig. 7.3.

Besides the official muon identification working points established at CMS, analyses can propose customized identification algorithms that can further improve the signal sensitivity. Another search performed within the collaboration [128], with a focus on the compressed mass SUSY phase space and using a different technique, proposed a customized *soft muon SUSY ID*, aiming to optimize the identification efficiency for *low-momentum prompt muons*, within the $5 < p_T \leq 30$ GeV range. The selection criteria and cuts are summarized in Tab. 7.2. The b-jet veto is based on the DeepCSV algorithm described on Sec. 7.7. The b-tag discriminator cuts for the loose working point listed in Tab. 7.43 for the 2017 and 2018 data sets. In 2016, the b-tag discriminator cut was set to 0.4, to

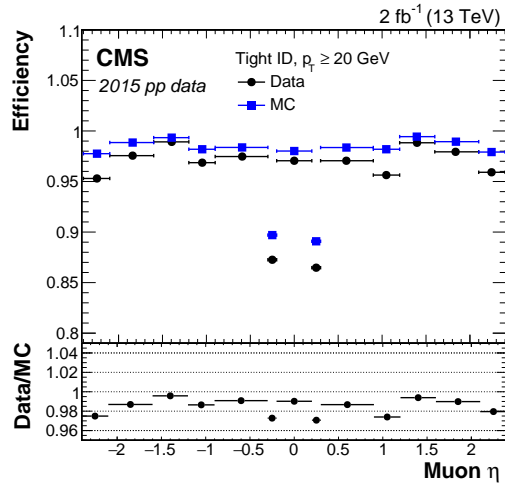


Figure 7.1: Tag-and-probe efficiency for muon reconstruction and identification in 2015 data and simulation for tight muons with $p_T \geq 20$ GeV [127].

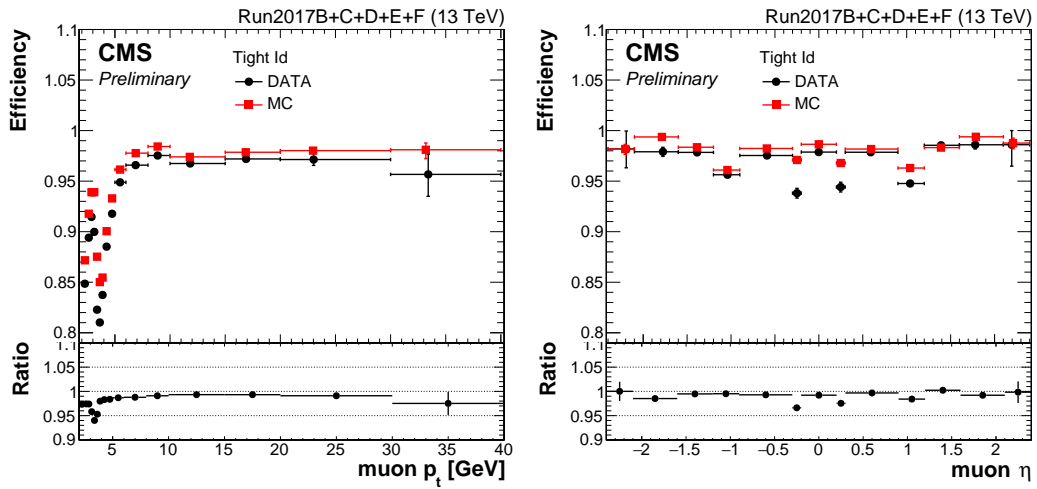


Figure 7.2: Efficiency for muon reconstruction and identification in 2017 data and simulation for tight muons with $2 < p_T < 40$ GeV as a function of p_T and η .

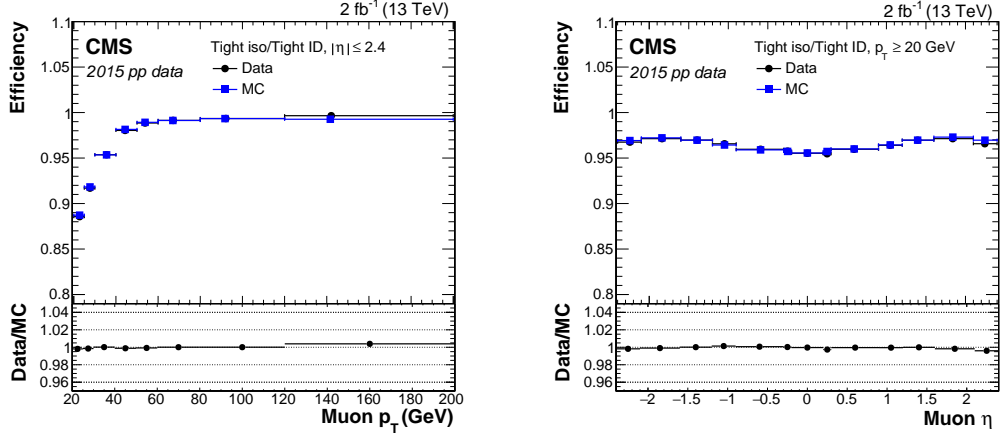


Figure 7.3: Tag-and-probe efficiency for the tight PF isolation working point on top of the tight ID as a function of p_T for muons within the acceptance of the muon spectrometer (right) and pseudorapidity for muons with $p_T > 20$ GeV [127].

approximately match the b-tag efficiency obtained for this working point in 2017 and 2018 datasets. A soft electron SUSY ID was also developed and it is described in the next section.

Variable	Selection cut (Tight WP)
p_T	≥ 3.5 GeV
$ \eta $	≤ 2.4
$IP_{3D} = \sqrt{d_{xy}^2 + d_z^2}$	< 0.01 cm
$\sigma_{IP_{3D}} = IP_{3D}/\Delta(IP_{3D})$	< 2.0
d_{xy}	< 0.05 cm
d_z	< 0.1 cm
$I_{abs} (\Delta R \leq 0.3)$	< 5 GeV
I_{rel}	< 0.5
b-jet veto	custom loose WP (DeepCSV)
Muon ID WP	soft and loose

Table 7.2: Selection criteria for the customized soft muon SUSY ID [128].

7.3 Electrons

Electron candidate reconstruction with the PF algorithm ensures high identification efficiency for genuine electrons by applying loose identification criteria. However, there is still a large probability for charged hadron mis-identification as electrons. Therefore, additional selections are applied to electron candidates to improve the identification efficiency and lower the mis-identification rate. The variables used for the definition of electron identification types are *isolation variables* and *shower shape properties* [129].

Isolation variables.

Isolation variables are obtained from the sum of reconstructed energy in a cone around electrons in different sub-detectors (Sec. 7.1). The energy of the electron is excluded from the sum by defining a veto region inside the isolation cone. The isolation variables are defined as the sum of the transverse momenta of charged hadrons (I_{ch}), photons (I_{γ}) and neutral hadrons (I_{n}), inside an isolation cone with $\Delta R = 0.3$ centered along the electron direction.

The contribution from pileup interactions to the isolation variables is removed by subtracting the average transverse energy density in the isolation region, estimated as the product of the median of the transverse energy density per unit area in the event (ρ), and the area of the isolation region. This area is weighted by factor accounting for the object's η -dependence of the pileup transverse energy density A_{eff} .

Shower shape properties.

The shape of the electromagnetic shower produced in the ECAL has specific characteristics depending on the particle producing the shower. On average, electrons (or photons) resulting from the electromagnetic decays of hadrons will produce a wider shower profile compared with that of a single incident electron. The presence of detector material and the effect of the magnetic field can elongate the electromagnetic cluster in the ϕ direction (transverse plane) for both converted photons, as well as photon pairs from neutral hadron decays, where at least one of the photons has converted. Hence, the ϕ profile of the electromagnetic shower from these particles will be similar for single electrons and photons. However, the η profile of the shower remains mostly unchanged, providing good discriminating power.

The most relevant variables based on the geometrical shape of energy deposits from *prompt electrons (photons)* are:

- *Ratio of hadronic energy over electromagnetic energy (H/E)*, defined as the ratio between the energy deposited in the HCAL in a cone of radius $\Delta R = 0.15$ around the SC direction (H) and the energy of the electron candidate (E). In some cases, the measured hadronic energy for prompt electrons will be non-negligible. For low-energy electrons, HCAL noise and pileup can result in sizeable H . For high-energy electrons, a significant H can be measured due to the leakage of electrons through the inter-module gaps. To account for these effects, the H/E selection requirement takes the form

$$\frac{H}{E} < \frac{X}{E} + \frac{Y\rho}{E} + J, \quad (7.5)$$

where X and Y represent the noise and pileup terms, respectively, and J is a scaling factor for high-energy electrons.

- *$\sigma_{i\eta i\eta}$ variable*, defined as the second moment of the log-weighted distribution of crystal energies in η , calculated in the 5×5 matrix around the most energetic crystal in the SC and re-scaled

to units of crystal size [129],

$$\sigma_{i\eta i\eta} = \sqrt{\frac{\sum_i^{5 \times 5} w_i (\eta_i - \bar{\eta}_{5 \times 5}^2)}{\sum_i^{5 \times 5} w_i}}. \quad (7.6)$$

η_i is the pseudorapidity of the i th crystal, $\bar{\eta}_{5 \times 5}$ denotes the pseudorapidity mean position, and w_i is defined as:

$$w_i = \max(0, 4.7 + \ln(E_i/E_{5 \times 5})). \quad (7.7)$$

w_i is nonzero if $\ln(E_i/E_{5 \times 5}) > -4.7$, i.e., $E_i > 0.009E_{5 \times 5}$, where $E_{5 \times 5}$ is the energy deposited in a 5×5 crystal matrix around the most energetic crystal³. The shower of an electron (photon) spreads into more than one crystal, because of the presence of upstream material and the magnetic field⁴. Given the crystal sizes, the spread of $\sigma_{i\eta i\eta}$ in the endcaps will be double the spread in the barrel, since $\sigma_{i\eta i\eta}$ depends on the distance between two crystals in η . The distribution of $\sigma_{i\eta i\eta}$ is expected to be narrow for single electron (photon) showers and broad for two-photon showers produced in neutral meson decays (Fig. 7.4).

- *Energy weighted η -width and ϕ -width of the SC*, providing further information on the lateral spread of the shower,
- *R_9 variable*, defined as the energy sum of the 3×3 crystal array centered around the most energetic crystal in the SC divided by the energy of the SC [129].
- *σ_{RR} variable*, defined as:

$$\sigma_{RR} = \sqrt{\sigma_{xx}^2 + \sigma_{yy}^2}, \quad (7.8)$$

where σ_{xx} and σ_{yy} represent the lateral spread measured in the two orthogonal directions of the sensor planes of the preshower detector.

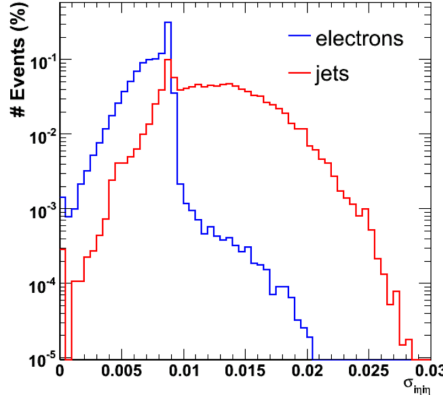


Figure 7.4: $\sigma_{i\eta i\eta}$ distribution for barrel electrons and jets [130].

For electron identification, additional variables mostly concerning information obtained with the tracker detector are considered:

³This requirement is intended to reject ECAL noise, by ensuring that crystals with energy deposits satisfying $E_i > 0.009E_{5 \times 5}$ contribute to the definition of $\sigma_{i\eta i\eta}$.

⁴The crystal size in η varies in the different parts of the ECAL: 0.0175 in the barrel and 0.0175 to 0.05 in the endcaps.

- $|1/E - 1/p|$, where E is the SC energy and p is the track momentum at the point of closest approach to the vertex,
- $|\Delta\eta_{\text{in}}^{\text{seed}}| \equiv |\eta_{\text{seed}} - \eta_{\text{track}}|$, where η_{seed} and η_{track} are the positions in η of the seed cluster and the innermost track position, respectively, and,
- $|\Delta\phi_{\text{in}}| \equiv |\phi_{\text{SC}} - \phi_{\text{track}}|$, which compares the SC energy-weighted position in ϕ and the track ϕ extrapolated from the innermost track position.

Secondary electrons produced in photon conversions in the tracker material are rejected by exploiting the pattern of hits associated with the electron track. In a photon conversion inside the tracker, the first hit of the produced electron tracks will most likely be away from the innermost tracker layer, which means missing hits are expected in the first tracker layers. Therefore, no missing hits are expected in the innermost tracker layers for prompt electrons whose trajectories start from the beam line.

In CMS, there are three strategies to perform electron identification: *cut-based identification*, identification using *multivariate techniques*, and a dedicated identification technique for high energy electrons. Electrons used in the analysis described in this document were identified using the cut-based strategy, which includes the requirements for seven identification variables. The combined PF isolation is given by

$$I_{\text{combined}} = I_{\text{ch}} + \max(0, I_{\text{n}} + I_{\gamma} - I_{\text{PU}}), \quad (7.9)$$

where $I_{\text{PU}} = \rho A_{\text{eff}}$ is the contribution from pileup in the event. I_{combined} is divided by the electron E_{T} and it is called the *relative combined PF isolation*. Four working points or *electron IDs* are defined, based on the relative signal identification efficiency (measured in simulation by comparing with the MC truth) [129]:

- “*veto*” *electron ID*, used in analyses to reject events with more reconstructed electrons than expected from the signal topology,
- *loose electron ID*, used in analyses where backgrounds to electrons are low,
- *medium electron ID*, used for generic measurements involving W or Z bosons, and
- *tight electron ID*, used when backgrounds are larger.

Tables 7.3 and 7.4 show the specific selection criteria for each one of these working points. Once an electron ID working point is selected, there is no need to apply a separate relative isolation requirement, since isolation criteria are included in the definition of the cut-based electron ID.

The efficiency of the electron identification working points in data is measured using a tag-and-probe technique using $Z \rightarrow ee$ events. One electron of the resonance decay (tag) is required to pass the tight cut-based ID WP and the other electron (probe) is used to probe the identification efficiency. Tag electrons are required to satisfy $E_{\text{T}} > 30$ (35) GeV for data collected in 2016 (2017-2018). The probe is required to pass the specific identification criteria under study. The charges of the tag and probe electron pair are required to have opposite signs. The invariant mass of the electron pair must lie between 60 and 120 GeV. If there are two or more probe candidates satisfying these conditions for a given tag, only the probe with the highest E_{T} is kept. The identification efficiency is measured

Variable	Veto WP		Loose WP	
	barrel	endcap	barrel	endcap
$\sigma_{i\eta i\eta}$	<0.0126	<0.0457	<0.0112	<0.0425
$ \Delta\eta_{in}^{seed} $	<0.00463	<0.00814	<0.00377	<0.00674
$ \Delta\phi_{in} $ [rad]	<0.148	<0.190	<0.0884	<0.169
H/E	$< 0.05 + 1.16 \text{ GeV}/E_{SC}$ $+0.0324\rho/E_{SC}$	$< 0.05 + 2.54 \text{ GeV}/E_{SC}$ $+0.183\rho/E_{SC}$	$< 0.05 + 1.16 \text{ GeV}/E_{SC}$ $+0.0324\rho/E_{SC}$	$< 0.0441 + 2.54 \text{ GeV}/E_{SC}$ $+0.183\rho/E_{SC}$
$I_{combined}/E_T$	$< 0.198 + 0.506 \text{ GeV}/p_T$	$0.203 + 0.963 \text{ GeV}/p_T$	$0.112 + 0.506 \text{ GeV}/p_T$	$0.108 + 0.963 \text{ GeV}/p_T$
$ 1/E - 1/p $ [GeV ⁻¹]	<0.209	<0.132	<0.193	<0.111
Number of missing hits	≥ 2	≥ 3	≥ 1	≥ 1
Pass conversion veto	True	True	True	True
Relative identification efficiency	95%		90%	

Table 7.3: Selection criteria for the veto and loose electron ID working points and their corresponding efficiencies. Electron candidates are classified according to the η position of the corresponding SC as barrel ($|\eta| \leq 1.479$) or endcap ($|\eta| > 1.479$) electrons.

Variable	Medium WP		Tight WP	
	barrel	endcap	barrel	endcap
$\sigma_{i\eta i\eta}$	<0.0106	<0.0387	<0.0104	<0.0353
$ \Delta\eta_{in}^{seed} $	<0.0032	<0.00632	<0.00255	<0.00501
$ \Delta\phi_{in} $	<0.0547	<0.0394	<0.0220	<0.0236
H/E	$< 0.046 + 1.16 \text{ GeV}/E_{SC}$ $+0.0324\rho/E_{SC}$	$< 0.0275 + 2.52 \text{ GeV}/E_{SC}$ $+0.183\rho/E_{SC}$	$< 0.026 + 1.15 \text{ GeV}/E_{SC}$ $+0.0324\rho/E_{SC}$	$< 0.0188 + 2.06 \text{ GeV}/E_{SC}$ $+0.0183\rho/E_{SC}$
$I_{combined}/E_T$	$0.0478 + 0.506 \text{ GeV}/p_T$	$0.0658 + 0.963 \text{ GeV}/p_T$	$0.0287 + 0.506 \text{ GeV}/p_T$	$0.0445 + 0.963 \text{ GeV}/p_T$
$ 1/E - 1/p $ [GeV ⁻¹]	<0.184	<0.0721	<0.159	<0.0197
Number of missing hits	≥ 1	≥ 1	≥ 1	≥ 1
Pass conversion veto	True	True	True	True
Relative identification efficiency	80%		70%	

Table 7.4: Selection criteria for the medium and tight electron ID working points and their corresponding efficiencies. Electron candidates are classified according to the η position of the corresponding SC as barrel ($|\eta| \leq 1.479$) or endcap ($|\eta| > 1.479$) electrons.

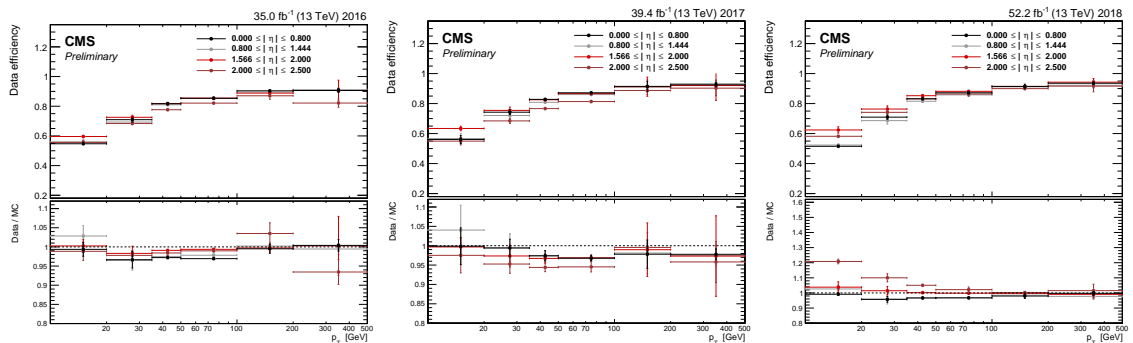


Figure 7.5: Electron identification efficiency measured in data (top panels) and data-to-simulation efficiency ratios (bottom panels) as a function of the electron p_T for the medium cut-based working point for 2016-2018 data sets.

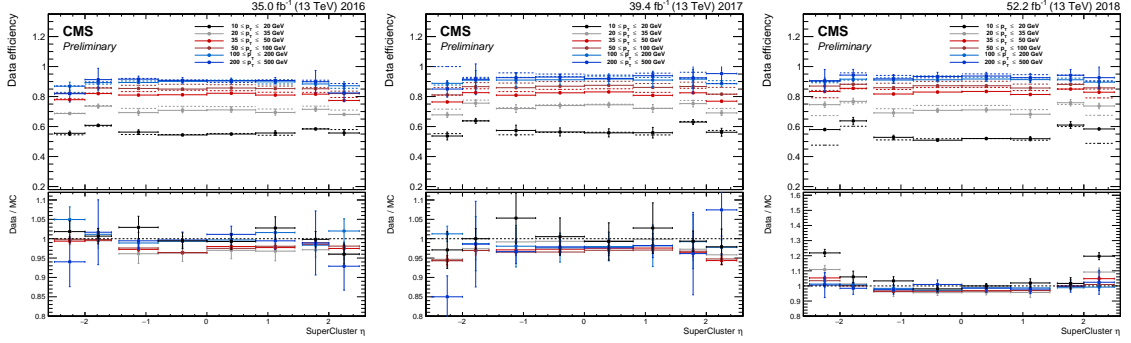


Figure 7.6: Electron identification efficiency measured in data (top panels) and data-to-simulation efficiency ratios (bottom panels) as a function of the SC η for the medium cut-based working point 2016-2018 data sets.

for (probe) electrons with $E_T > 10$ GeV. As an example, the identification efficiency results for the medium working point is shown in Figs. 7.5 and 7.6.

A customized electron ID for low-momentum prompt electrons was developed, using the same motivation as the soft muon SUSY ID, described in the previous section. The selection criteria and cuts are summarized in Tab. 7.5. The electron MVA identification is described in Ref. [129]; the tight working point is selected to provide an identification efficiency of 80%. The b-jet veto is the same used for the soft muon SUSY ID. Both the soft electron and muon SUSY IDs were used for the optimization of the SR selections, presented in Chapter 9.

Variable	Selection cut (Tight WP)
p_T	≥ 5 GeV
$ \eta $	≤ 2.5
$IP_{3D} = \sqrt{d_{xy}^2 + d_z^2}$	< 0.01 cm
$\sigma_{IP_{3D}} = IP_{3D} / \Delta(IP_{3D})$	< 2.0
d_{xy}	< 0.05 cm
d_z	< 0.1 cm
$I_{abs} (\Delta R \leq 0.3)$	< 5 GeV
I_{rel}	< 0.5
b-jet veto	custom loose WP (DeepCSV)
Electron MVA ID	tight WP
Missing pixel hits	= 0
Conversion vertex	False

Table 7.5: Selection criteria for the customized soft electron SUSY ID [128].

7.4 Jets

In high energy collisions, jets are the experimental signatures of quarks and gluons. An extensive literature review about the main physics arguments involved in the modeling of jets in hadron-hadron

collision evolution is presented in Appendix A. In this section, a summary of the reconstruction and calibration of the energy and resolution of jets, as it is done with the CMS experiment is presented.

Jet reconstruction

In CMS, jets are reconstructed with the anti- k_T algorithm as implemented in the FASTJET version 3.0.1, with a radius parameter of $R = 0.4$ [111, 131, 132]. These jets are typically referred to as AK_4 jets. At the jet reconstruction stage, there are three types of jets that can be obtained with the anti- k_T algorithm:

- *PF jets*, resulting after clustering all particles reconstructed by the PF algorithm, their minimum p_T is 15 GeV,
- *Calorimeter or “Calo” jets*, built by the sum of the ECAL and HCAL energies deposited in the calorimeter towers⁵, with their minimum p_T being 20 GeV, and,
- *Generated, simulated particle-level⁶, or “Ref” jets* which are clusters of all stable particles in a generator sample, excluding neutrinos.

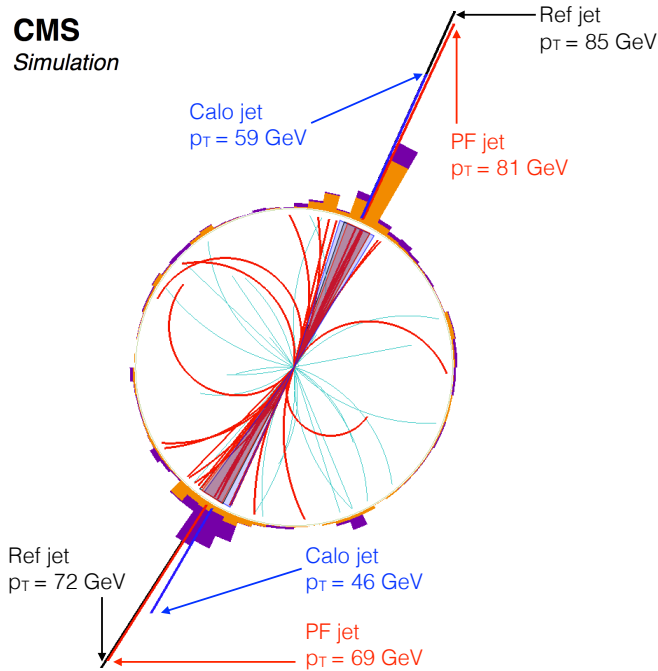


Figure 7.7: Jet reconstruction in a simulated dijet event. The particles clustered in the two PF jets are displayed with a thicker line. The PF jet \vec{p}_T , indicated with a radial line, is compared to the \vec{p}_T of the corresponding generated Ref and Calo jets. The 4-momentum of the jet is obtained by adding the 4-momenta of its constituents and no jet energy correction is applied (Adapted from [111]).

⁵A calorimeter tower is composed of an HCAL tower and the 25 underlying ECAL crystals [111].

⁶In this section, particle-level may also be denoted as "ptcl".

Ignoring the effect from pileup interactions, each PF jet is matched to the closest Ref jet with $\Delta R < 0.1$. For Calo jets, the matching distance in the (η, ϕ) plane is changed to $\Delta R < 0.2$, given that the jet direction resolution is not (about half) as good as it is for PF jets (Fig. 7.7). As seen in Fig. 7.8, the angular resolution for PF jets is better than that for Calo jets and it is explained by the improved precision in the charged hadron directions and momenta obtained with the PF algorithm.

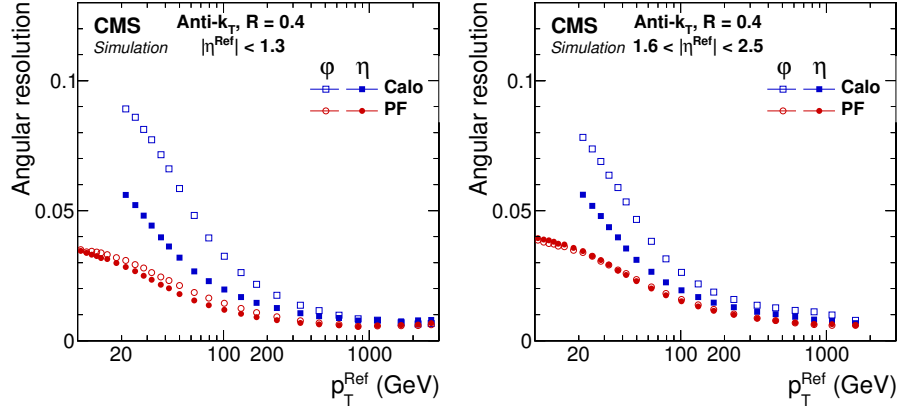


Figure 7.8: Jet angular resolution in the barrel (left) and endcap (right) regions, as a function of the p_T of the reference jet. The ϕ resolution is expressed in radians. (Adapted from [111]).

On average, the energy fractions carried by charged hadrons, photons, and neutral hadrons in a jet are 65%, 25 and 10%, respectively. By comparing the jet energy fractions measured in PF jets and Ref jets, we can assess the ability of the PF algorithm to correctly identify these particles within a jet. An example for jets produced and detected in the barrel (within tracker coverage) is shown in Fig. 7.9. A sizeable fraction of the p_T carried by neutral hadrons is incorrectly identified as coming from photons, for the reasons described in Chapter 6. Nevertheless, about 80% of the neutral hadron energy is recovered when adding the energy of all neutral particles, and comparing it to the sum of the energy from neutral hadrons in the Ref jets (bottom right panel). The remaining energy fraction (20%) is still reconstructed as photon energy, and undergoes the corresponding electromagnetic energy calibration, resulting in an underestimation of about 20-40%.

The *jet energy response*, defined as the mean ratio of the reconstructed jet energy to the Ref jet energy, is depicted in Fig. 7.10. The jet energy response is almost independent of jet p_T and close to unity across the detector acceptance (barrel and endcap). Jet energy corrections are applied to bring the response to unity, removing any dependence on p_T and η . After this correction procedure, the *jet energy resolution*, defined as the Gaussian width of the ratio between the corrected and reference jet energies, is measured and shown in Fig. 7.11.

At this point, it is evident that the performance of PF jets exceeds that of Calo jets, and therefore, PF jets are used for most of the data analyses done at CMS. Another advantage of the PF jets is that it allows to obtain a better jet response for *gluon jets*. Typically, gluon jets contain more low-energy particles than *quark jets*, leading to a lower jet energy response. Since it is difficult to disentangle the originating parton flavor in a jet, the same jet energy corrections are applied to all jets. The difference between gluon and quark jet energy response in PF jets is smaller than in Calo jets, as seen in Fig. 7.12.

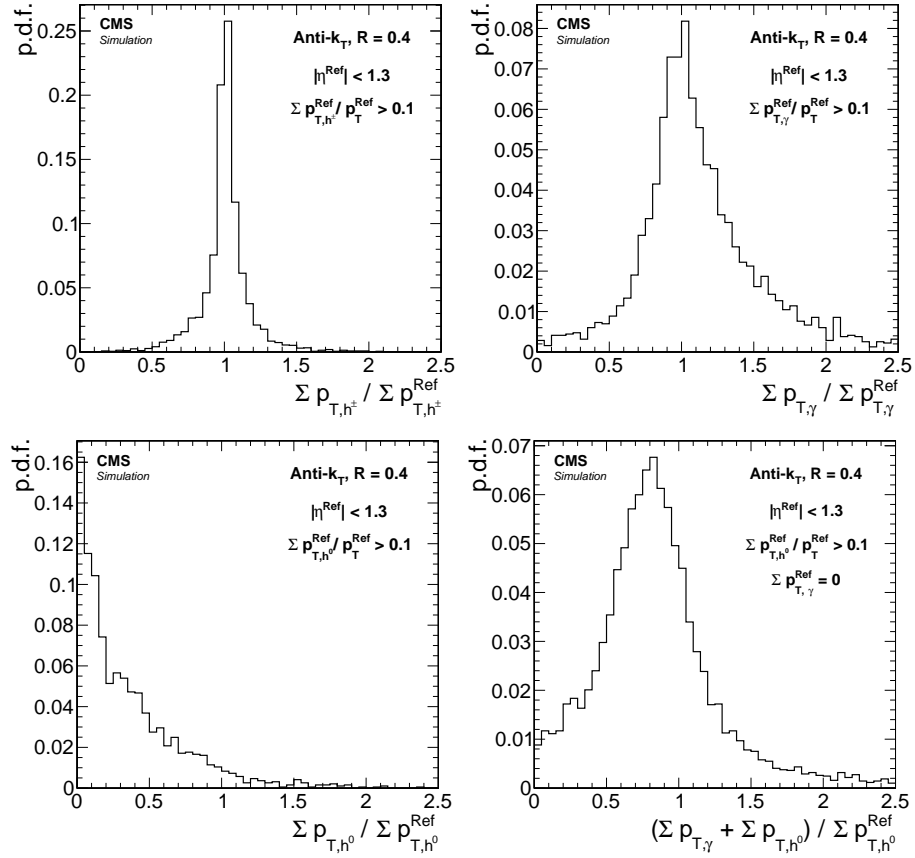


Figure 7.9: Jet angular resolution in the barrel (left) and endcap (right) regions, as a function of the p_T of the reference jet. The ϕ resolution is expressed in radians. (Adapted from [111]).

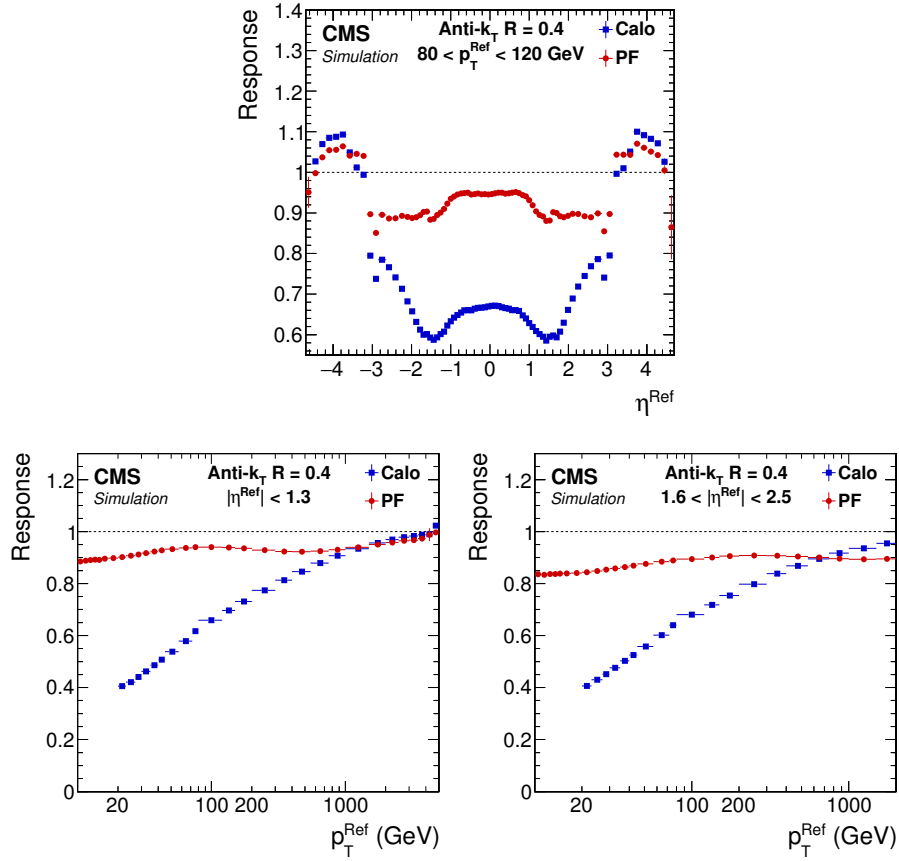


Figure 7.10: Jet angular resolution in the barrel (left) and endcap (right) regions, as a function of the p_T of the reference jet. The ϕ resolution is expressed in radians. (Adapted from [111]).

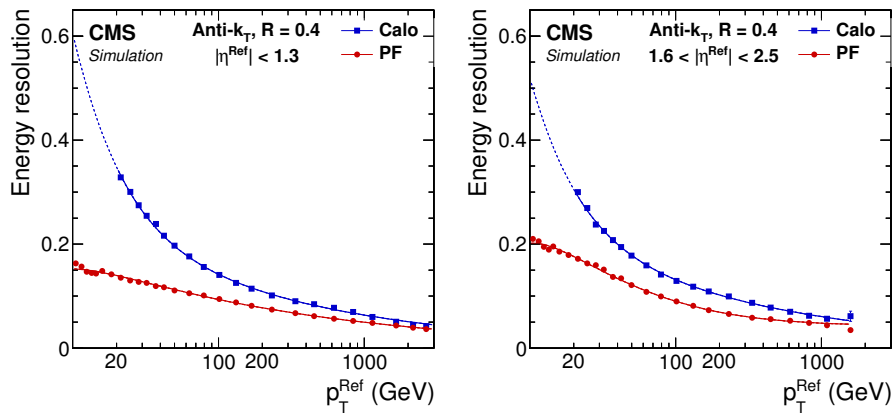


Figure 7.11: Jet energy resolution in the barrel (left) and endcap (right) regions, as a function of the p_T of the reference jet. The ϕ resolution is expressed in radians. (Adapted from [111]).

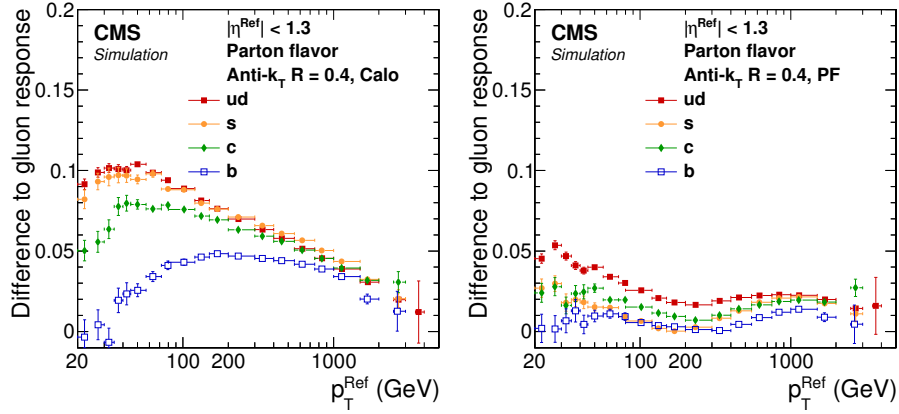


Figure 7.12: Jet angular resolution in the barrel (left) and endcap (right) regions, as a function of the p_T of the reference jet. The ϕ resolution is expressed in radians. (Adapted from [111]).

Calibration of jet energy scale and resolution

In order to account for pileup, jets used in data analyses are reconstructed after the *charged hadron subtraction* has been performed (*PF+CHS jets*). Jets also need to be calibrated to have the correct *jet energy scale (JES)*. Thus, *jet energy corrections (JEC)* are derived. Jet energy corrections are calculated using a detailed Monte Carlo (MC) simulation of the detector and then adjusted for data using a combination of several channels and data-driven methods [121]. JECs correct for: the offset energy coming from pileup interactions, the detector response to hadrons, and residual differences between data and simulation as a function of the jet η and p_T . JECs are applied using factorized and sequential approach (Fig. 7.13). The jet p_T is corrected for the **particle level jets**, clustered from stable⁷ and visible final state particles.

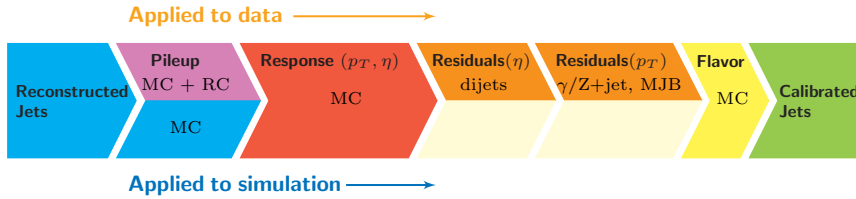


Figure 7.13: Consecutive stages of JEC for data and MC simulation. All corrections marked with MC are derived from simulation studies. RC stands for random cone, and MJB refers to the analysis of multijet events. (Adapted from [121]).

The experimental techniques used for the derivation of all JECs include [133, 121]:

- Dijet and multijet p_T balance: exploiting momentum conservation in the transverse plane,
- $Z/\gamma + p_T$ balance: a γ or Z boson is used as a reference object, whose p_T is accurately measured from the ECAL or muon system,
- Missing transverse energy projection fraction (MPF): used to facilitate a better understanding of systematic uncertainties and perform cross checks,

⁷Stable: decay length $c\tau > 1$ cm; visible: excluding neutrinos.

- Dijet, Z+jet and γ +jet events are used to determine JER,
- Additional jet activity quantified by α variable.

Jet energy scale

Given that the detector response to particles is not linear, it is not straightforward to translate the measured jet energy to the true particle or parton energy. Therefore, jets require energy corrections, in order to allow the proper mapping of the measured jet energy deposition to the particle-level jet energy. Thus, jet energy corrections affect the JES. A summary of the JEC corrections applied, their derivations, and results is presented below.

Pileup offset energy corrections (L1).

These corrections remove the energy coming from pileup events, resulting in the removal of any data set dependence on luminosity, such that higher level JECs are applied upon a luminosity independent sample. L1 corrections are applied to both data and simulation and its derivation and implementation proceeds in steps:

- i. OOT PU is mitigated by calorimeter signal processing and the IT PU is mitigated by running the CHS algorithm,
- ii. pileup jets are tagged with pileup jet identification (see Sec. 7.4),
- iii. the remaining diffuse energy from neutral particles and OOT PU is estimated per event, and subtracted per jet, using a calculation of the effective jet area with the extended hybrid jet area method [121].

In step iii., the pileup offset in simulation is calculated by taking the average difference in p_T between matched jets in simulated samples of QCD dijet events with and without pileup overlay. The average difference in p_T is parameterized as a function of offset energy density (ρ), jet area (A), jet η , and jet p_T . After that, the difference is subtracted from both data and simulation. Any residual differences between data and simulation on the η direction are determined using zero-bias⁸ events and a neutrino gun simulation, with the RC method⁹ [134, 121].

The average offset per pileup interaction μ is monitored for each type of PF candidates (Fig. 7.14):

- photons, neutral hadrons, electromagnetic deposits in HF, hadronic deposits in HF,
- PF charged hadrons: associated with reconstructed PU vertices and therefore removed from the list of particles by the CHS algorithm,
- PF+CHS algorithms: charged hadrons associated with the primary vertex.

⁸The zero-bias sample is collected using a random trigger in the presence of a beam crossing with filled bunches, active during the whole data-taking period with stable collisions conditions and a fully functioning detector. The main sources of energy deposits in zero-bias events are detector noise and pileup [121].

⁹Described in Sec. 6.2.2 of [134].

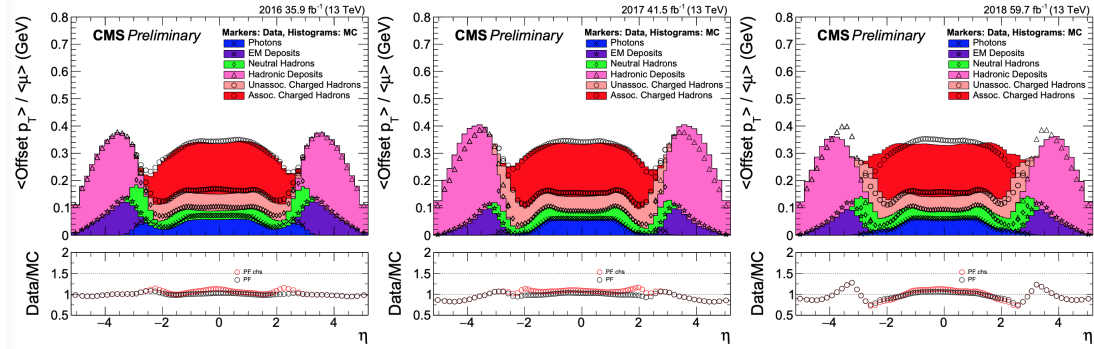


Figure 7.14: Data to simulation comparison for average offset per pileup interaction as a function of jet η , calculated for each type of PF candidates (Adapted from [133]).

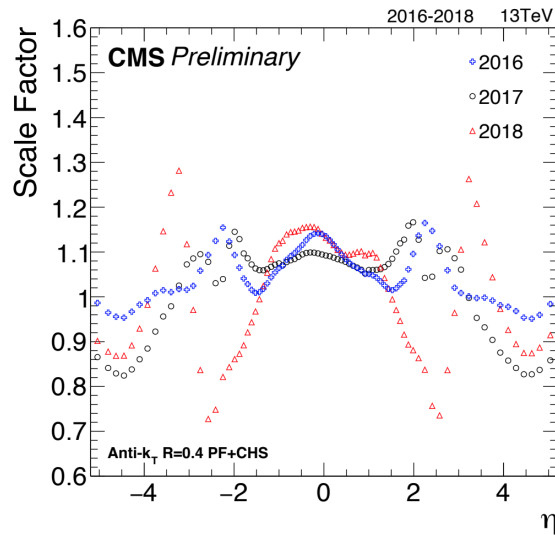


Figure 7.15: Evolution of data to simulation scale factors in Run II for representative $\langle \mu \rangle$ for a given data period (Adapted from [133]).

Simulated response corrections or MC-truth corrections (L2L3).

The L2L3 corrections are based on simulation and correct the energy of reconstructed jets, such that it equals on average the energy of the jets at particle level. These corrections are derived from and applied to jets that have been corrected with L1 corrections and are applied to both data and simulated events.

The simulated jet response corrections are determined on a QCD dijet sample, by comparing the reconstructed jet p_T to the particle-level jet¹⁰ p_T . The generated dijet sample uses a detailed model of the CMS detector geometry, data-based alignment and calibration of the detector elements, and an emulation of the readout electronics. The CMS detector simulation is based upon the GEANT4 package [118], which simulates the evolution of the electromagnetic and hadronic showers and their interactions with the material.

L2L3 corrections are derived using information from simulated events for several reasons:

- the ability to cover regions of phase space not accessible with data, more specifically very low and very high p_T jets (<30 GeV and >1 TeV, respectively) low and high pileup scenarios ($\mu < 5$ and $\mu > 40$, respectively),
- access to accurate information from heavy-flavor jets, and,
- there is not sensitivity to many of the biases inherent in the data-based methods; moreover, the studies exclusively based on simulation will provide a better understanding of the data-based techniques.

The *simulated particle response*¹¹ R_{ptcl} is defined as the ratio of the arithmetic means of matched reconstructed and particle-level jets transverse momenta:

$$R_{\text{ptcl}}(\langle p_T \rangle, \eta) = \frac{\langle p_T \rangle}{\langle p_{T,\text{ptcl}} \rangle} [p_{T,\text{ptcl}}, \eta]. \quad (7.10)$$

A particle-level jet is matched to the closest reconstructed jet if it is within half of the jet cone radius ($\Delta R < 0.2$ for AK4 jets). These corrections are derived in bins of jet $|\eta|$ and $p_{T,\text{ptcl}}$ ¹². The goal of the L2L3 corrections is then to make the simulation response uniform over these two variables. A summary of the jet response estimated for simulation used in the Run II data-taking period is depicted in Fig. 7.16.

Residual corrections for data (L2L3 residual).

The L2 and L3 residual corrections are intended to solve any remaining small differences within jet response in data and simulation. The L2L3 residual corrections are only applied to data. The jet energy response is studied using the p_T balance and MPF methods [134]. In the p_T balance method, the jet response is evaluated by directly comparing the reconstructed jet momentum ($p_{T,\text{jet}}$) to the momentum of the reference object ($p_{T,\text{ref}}$). In the MPF method, the evaluation of the response

¹⁰An important note is that in CMS, particle-level jets do not include energy from neutrino contributions.

¹¹The average response $\langle R \rangle$ is called the jet energy scale (JES).

¹²In Equation 7.10, the square brackets denote the binning variables and the angle brackets indicate the averages within those bins for the variables used to parameterize the response.

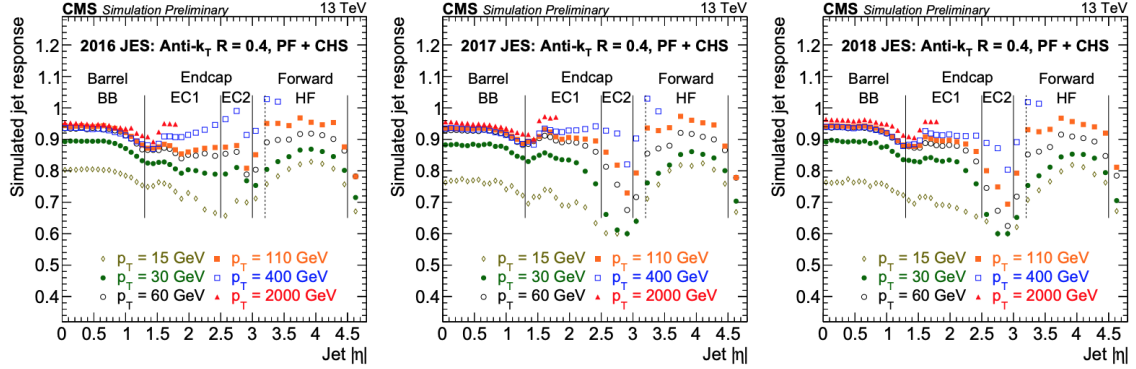


Figure 7.16: Jet response correction based on simulation for the different data sets in Run II. (Adapted from [133]).

considers the whole hadronic activity in the event, recoiling against the reference- k_T object. The response for each method is defined as:

$$R_{\text{jet},p_T} = \frac{p_{T,\text{jet}}}{p_{T,\text{ref}}}, \quad (7.11)$$

$$R_{\text{jet},\text{MPF}} = 1 + \frac{\vec{p}_T^{\text{miss}} \cdot \vec{p}_{T,\text{ref}}}{(p_{T,\text{ref}})^2}. \quad (7.12)$$

A fraction of the transverse momentum imbalance can come from the presence of additional jets in the event. However, this effect is not correlated with the jet response. Thus, all the corrections are studied as a function of the additional jet activity in the event, quantified by the variable α . α is defined as the ratio of the most energetic jet that does not originate from the event topology under study, divided by the typical momentum scale of the event:

$$\alpha = p_T^{\text{add. jet}} / p_T^{\text{ref}}, \quad (7.13)$$

with $p_T^{\text{ref}} = (p_T^{\text{jet1}} + p_T^{\text{jet2}})/2$ for the dijet and multijet analyses, and $p_T^{\text{ref}} = p_T^{Z/\gamma}$ otherwise.

The relative η -dependent (L2-residual) corrections to the jet response are obtained using dijet events with the MPF method (Fig. 7.17). Time-dependent corrections (for each data set) address the evolution of detector ageing.

The absolute JES residual corrections are derived comparing the jet response dependence on p_T in simulation and data. They are determined for barrel jets, using $Z(\rightarrow \mu\mu)+\text{jet}$ and $Z(\rightarrow ee)+\text{jet}$ (combined into $Z+\text{jet}$ events), $\gamma+\text{jet}$ and multijet events, using the MPF and p_T balance methods. A global fit is performed combining all of these results.

Jet energy resolution

The jet p_T resolution is relatively poor compared to the resolution of other physics objects, and biases can cause important effects for steeply falling spectra or resonance decays. Therefore, *jet energy resolution* (JER) corrections are derived based on MC simulation and data-driven methods. The particle level JER is defined as the width (obtained from a Gaussian fit) of the distribution of

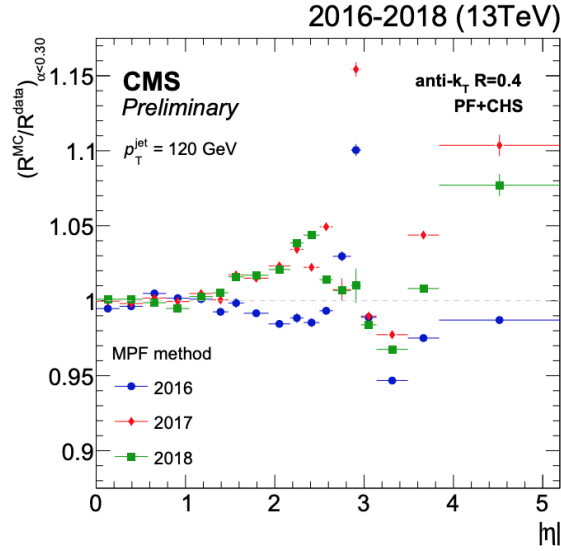


Figure 7.17: Relative η -dependent residual jet response corrections for the different data sets in Run II. (Adapted from [133]).

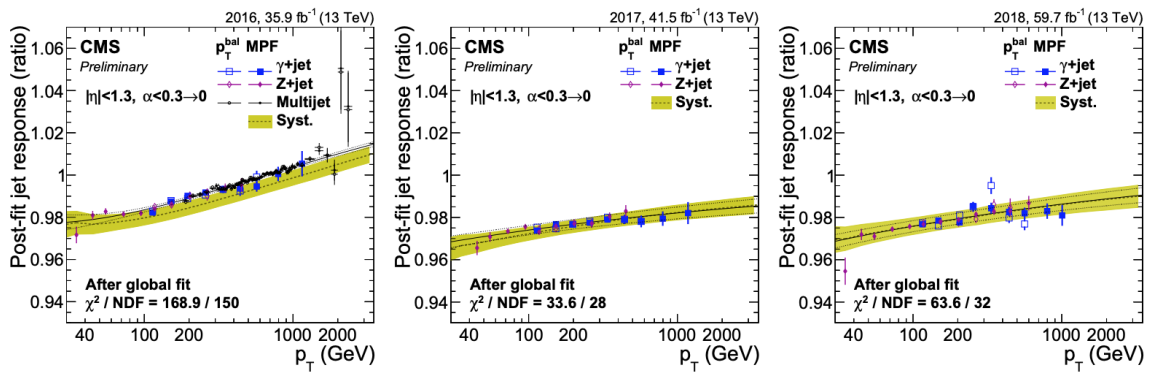


Figure 7.18: Comparison of the data-to-simulation ratio of the jet response measurements after applying the corrections for JES as well as the nuisance parameter values found by the global fit (L3 residual corrections). (Adapted from [133]).

$p_{T,\text{reco}}/p_{T,\text{ptcl}}$, where $p_{T,\text{reco}}$ and $p_{T,\text{ptcl}}$ correspond to the transverse momenta of the reconstructed and particle level jets. The corrections are derived after the JEC are applied.

The measurement of JER is performed using the methods for measuring JES, focusing on the width of the mean response distribution. Additional corrections need to be applied to account for effects that can widen the JES distribution [121]. The particle level JER in simulation (σ_{JER}) is defined as the spread of a Gaussian fit to the $p_{T,\text{reco}}/p_{T,\text{ptcl}}$ distribution in the range $[m-2\sigma, m+2\sigma]$, where m and σ are the mean and width of the Gaussian fit, determined with an iterative procedure. The reconstructed jets are required to be matched to a generated jet with a maximum distance of $\Delta R = 0.2$ for AK4 jets. σ_{JER} is measured in γ +jet and Z+jet events.

The jet p_T resolution in data is measured with the dijet asymmetry method versus $p_{T,\text{ave}} = \frac{1}{2}[p_{T,1\text{st jet}} + p_{T,2\text{nd jet}}]$, as described in Ref. [121]. Constant η -dependent data-to-simulation scale factors, s_{JER} , are derived for jets with $p_T \geq 100$ GeV (Fig. 7.19). s_{JER} corrections are consistent with unity across all η regions, except for the endcap-HF transition region ($2.5 \leq |\eta| \leq 3.0$), where they are larger. For 2018, the dependence of s_{JER} with p_T was additionally studied (Fig. 7.20). A dependence on p_T was found for the endcap-HF transition region as well. These two methods are complementary and aim for full coverage in p_T and η .

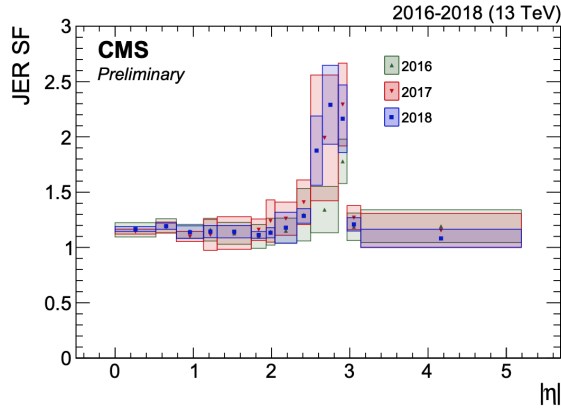


Figure 7.19: Data-to-simulation η dependent scale factors for jet energy resolution for the different data sets in Run II. (Adapted from [133]).

In CMS, there are two main methods utilized to smear reconstructed jets in simulation:

- (1) *Scaling method.* This method is used for *genuine jets*, which are reconstructed jets in simulation matched to a particle-level jet. The 4-momentum of a reconstructed jet is re-scaled with a factor

$$c_{\text{JER}} = 1 + (s_{\text{JER}} - 1) \frac{p_T - p_T^{\text{ptcl}}}{p_T}, \quad (7.14)$$

where p_T is the transverse momentum of the jet, and p_T^{ptcl} is the transverse momentum of the corresponding jet clustered from generator-level particles. The factor c_{JER} is truncated at zero (i.e., if it is negative, it is set to zero). This method only works if a well-matched particle-level jet is present, and can result in a large shift of the response otherwise. The requirements imposed for the matching are

$$\Delta R < R_{\text{cone}}/2, \quad |p_T - p_T^{\text{ptcl}}| < 3\sigma_{\text{JER}}p_T, \quad (7.15)$$

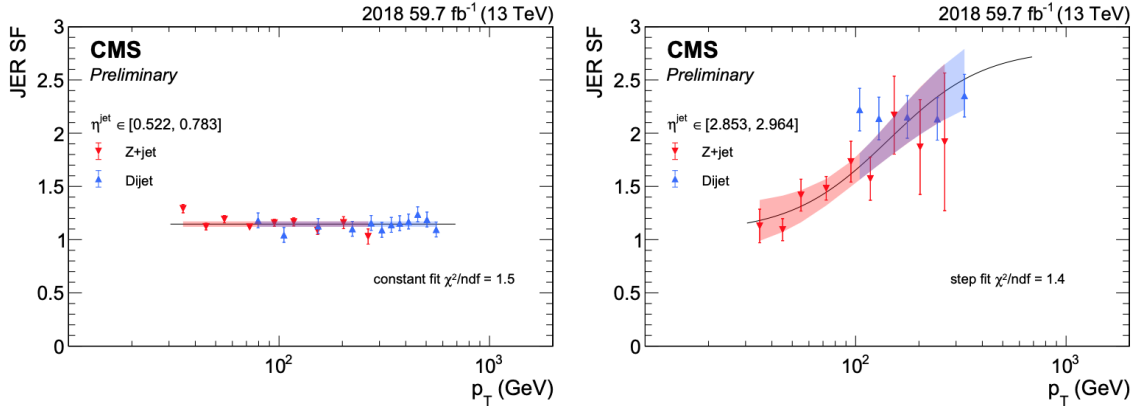


Figure 7.20: Data-to-simulation η dependent scale factors for jet energy resolution for the 2018 data set. (Adapted from [133]).

where R_{cone} is the jet cone size parameter ($R_{\text{cone}} = 0.4$ for AK4 jets), and σ_{JER} is the relative p_{T} resolution, as measured in simulation.

- (2) *Stochastic smearing*. This approach does not require the presence of a matching particle-level jet, therefore, it is applied to *pileup jets*. The 4-momentum of the reconstructed jet is re-scaled with a factor

$$c_{\text{JER}} = 1 + \mathcal{N}(0, \sigma_{\text{JER}}) \sqrt{\max(s_{\text{JER}}^2 - 1, 0)}. \quad (7.16)$$

$\mathcal{N}(0, \sigma_{\text{JER}})$ denotes a random number sampled from a normal distribution with a zero mean and variance σ_{JER}^2 , with a truncation at zero similar to that in the scaling method. The stochastic smearing method only allows to degrade the resolution.

In our analysis, we follow a “hybrid” method, in which the scaling method is used when a matching particle-level jet is found; otherwise, the stochastic method is applied.

Jet composition

Finally, the jet energy contributions from the different types of particles can be studied as way to confirm the stability of JEC [121]. The jet PF composition is studied from dijet events using fully corrected jets. The summary of these results, considering barrel jets ($|\eta| < 1.3$), is shown in Fig. 7.21.

Jet identification

In order to distinguish between noise jets and physical jets, further criteria are applied based upon the jet energy carried by certain types of PF candidates clustered into a jet, as well as the number of PF candidates clustered into a jet. This set of criteria and selections is known as *particle flow jet identification (PF jet ID)* criteria. Three working points are defined: *loose*, *tight* and *tight lepton*

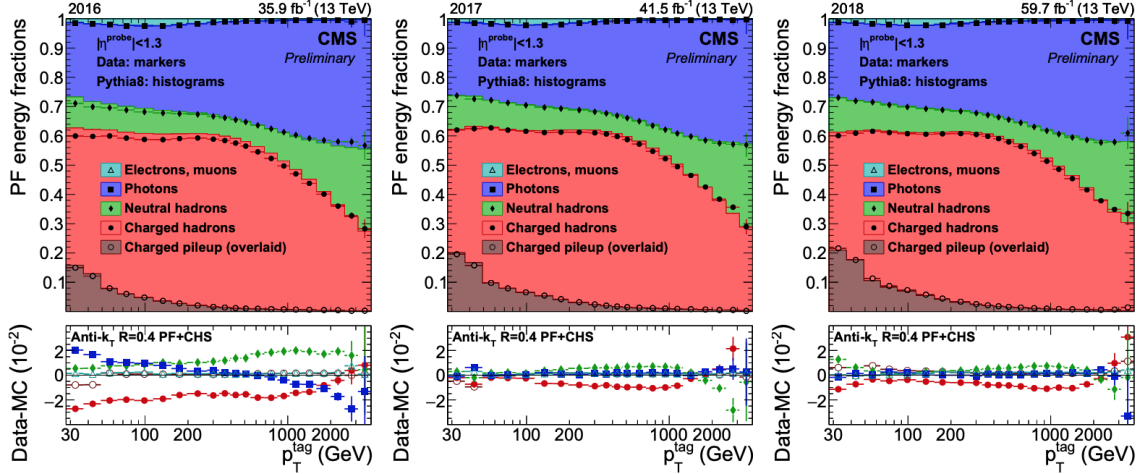


Figure 7.21: Data-to-simulation η dependent scale factors for jet energy resolution for the 2018 dataset. (Adapted from [133]).

veto [135]. In this section, I focus only on the first two working points, as they are the ones used in the data analysis presented. The loose working point of PF jet ID is used for jets in the 2016 data set, and the tight working point is used for the 2017 and 2018 data sets.

An illustration of the differences in the various selection criteria for genuine and noise jets is shown in Fig. 7.22, justifying the selection cuts summarized on Tables 7.6, 7.7, and 7.8. In 2016, the jet reconstruction and ID efficiency in simulation is $>99\%$ for the entire η and p_T range; in 2017 and 2018, an efficiency of more than 98-99% is achieved in all η regions, whereas the background rejection is more than 98% for $|\eta| < 3.0$. In the $3 < |\eta| < 5$ region, only 35% of noise jets are rejected for PF+CHS jets that pass the tight PF jet ID working point as defined for 2017, which yields a genuine jet efficiency of 99% in different regions of η [136].

Criterion	$ \eta(j) \leq 2.4$	$ \eta(j) \leq 2.7$	$2.7 < \eta(j) \leq 3.0$	$ \eta(j) > 3.0$
Neutral hadron energy fraction	<0.99	<0.99	<0.98	–
Neutral EM energy fraction	<0.99	<0.99	>0.01	<0.90
Number of constituents	>1	>1	–	–
Charged hadron energy fraction	>0	–	–	–
Charged multiplicity	>0	–	–	–
Charged EM energy fraction	<0.99	–	–	–
Number of neutral particles	–	–	>2	>10

Table 7.6: Jet identification criteria for the loose PF jet ID working point (2016).

Pileup jet identification

PU jets can be classified in two categories: *QCD-like PU jets*, originating from PU particles from a single PU vertex, and *stochastic PU jets*, originating from PU particles produced in multiple PU vertices [136]. After CHS, the main type of PU jets present in an event are stochastic PU jets. In

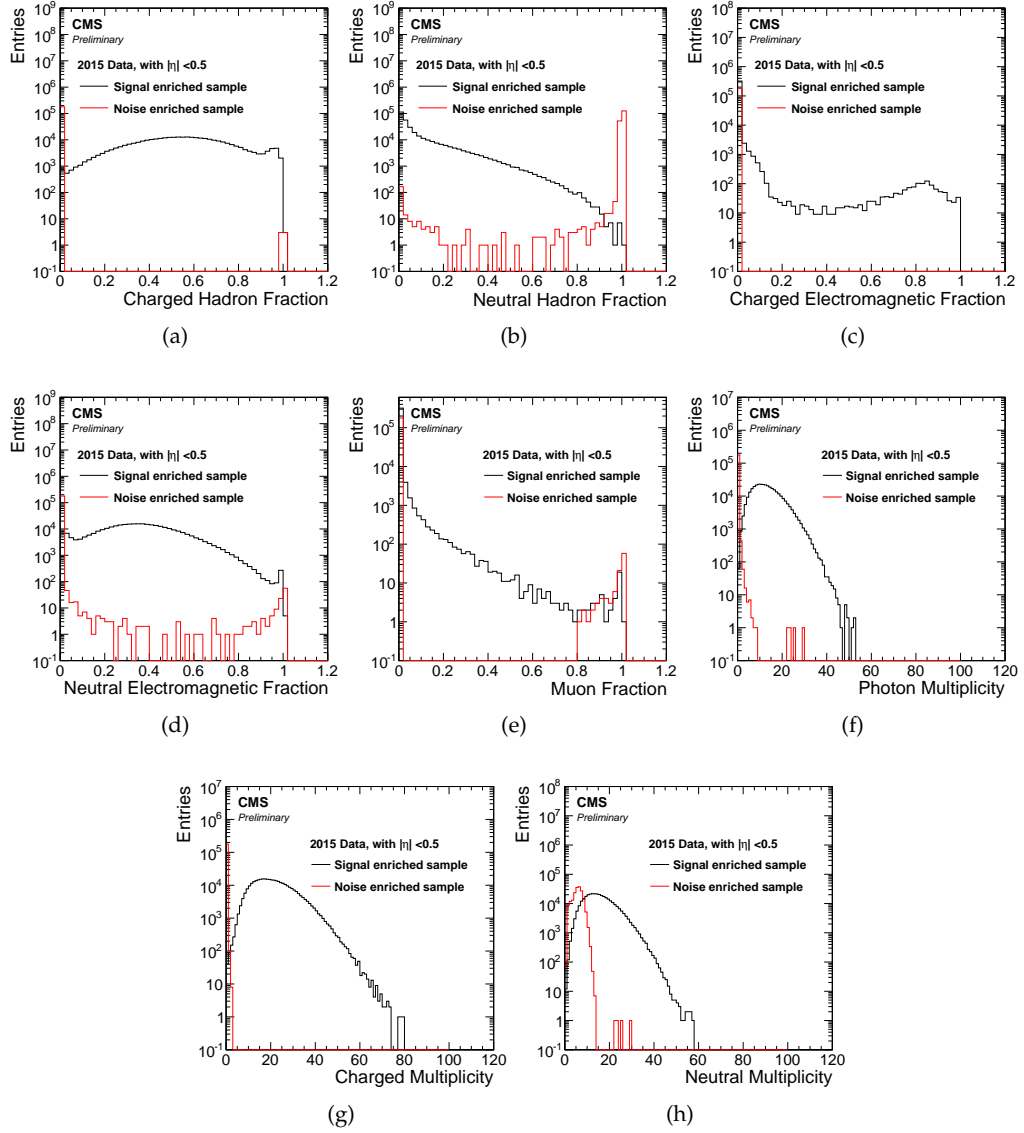


Figure 7.22: Distributions of PF jet variables for central jets $|\eta| < 0.5$ as measured in signal enriched back-to-back dijet events and for noise enriched events from a minimum bias selection before applying the PF jet ID [135].

Criterion	$ \eta(j) \leq 2.4$	$ \eta(j) \leq 2.7$	$2.7 < \eta(j) \leq 3.0$	$ \eta(j) > 3.0$
Neutral hadron energy fraction	< 0.90	< 0.90	–	> 0.02
Neutral EM energy fraction	< 0.90	< 0.90	> 0.02 and < 0.98	< 0.90
Number of constituents	> 1	> 1	–	–
Charged hadron energy fraction	> 0	–	–	–
Charged multiplicity	> 0	–	–	–
Number of neutral particles	–	–	> 2	> 10

Table 7.7: Jet identification criteria for the tight PF jet ID working point (2017).

Criterion	$ \eta(j) \leq 2.6$	$2.6 < \eta(j) \leq 2.7$	$2.7 < \eta(j) \leq 3.0$	$3.0 < \eta(j) \leq 5.0$
Neutral hadron energy fraction	<0.90	<0.90	-	>0.2
Neutral EM energy fraction	<0.90	<0.99	>0.02 and <0.98	<0.90
Number of constituents	>1	-	-	-
Charged multiplicity	>0	>0	-	-
Number of neutral particles	-	-	>2	>10

Table 7.8: Jet identification criteria for the tight PF jet ID working point (2018).

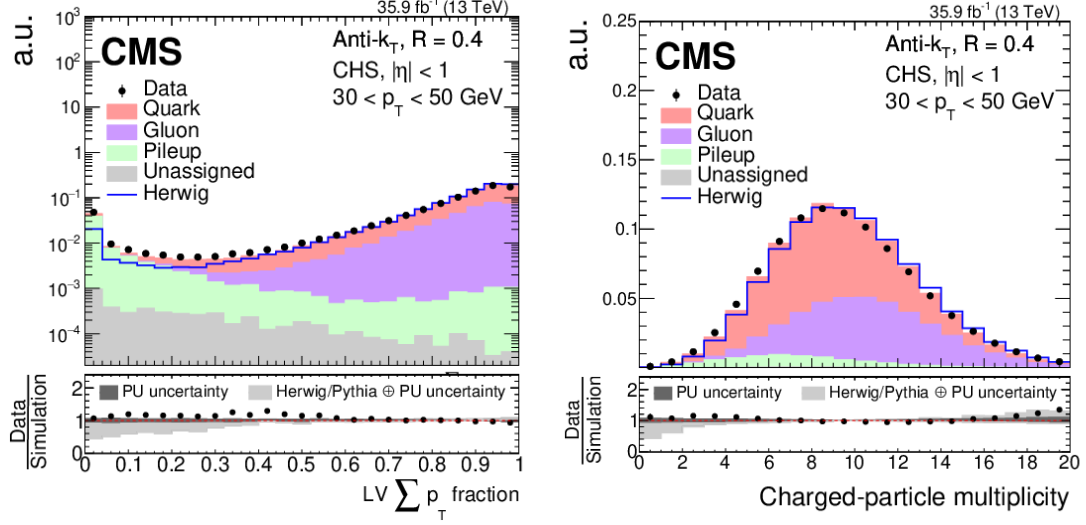


Figure 7.23: Data-to-simulation comparison for two input variables to the PU jet ID calculation for CHS jets with $30 < p_T < 50$ GeV [136].

CMS, a dedicated MVA technique was developed for PF+CHS jets to identify and reject stochastic PU jets, and it is known as *pileup jet ID*. In general, most of the tracks of a PU jet will not be associated with the leading primary vertex (LV) and, for stochastic jets, their structure tends to be more broad and diffuse than jets originated from a quark or a gluon.

The MVA analysis uses 15 variables from the leading primary vertex, number of vertices, and jet shape variables, as the input given to a boosted decision tree (BDT) algorithm [136]. In Figure 7.23, the data-to-simulation comparison for two of the input variables used for PU jet ID: the fraction of p_T of charged particles associated with the LV, defined as $\sum_{i \in LV} p_{T,i} / \sum_i p_{T,i}$, where i iterates over all charged PF particles in the jet, and the number of charged PF candidates. The simulation sample is divided into the different jet types included: quark jets, gluon jets, pileup jets and jets that could not be assigned to any of these categories. As seen in these distributions, these variables provide good separation between genuine and pileup jets.

When a jet passes the PU jet ID, it satisfies a requirement on a specific threshold on the output of the BDT discriminator (Fig. 7.24), which is *correlated with its probability of not being a PU jet*. The tighter the working point a jet passes, the larger the likelihood of being a genuine jet is. Three working points are established, based on their efficiencies and mis-identification rates:

- *tight*, which 80% efficient for quark jets (lowest mis-identification rate),

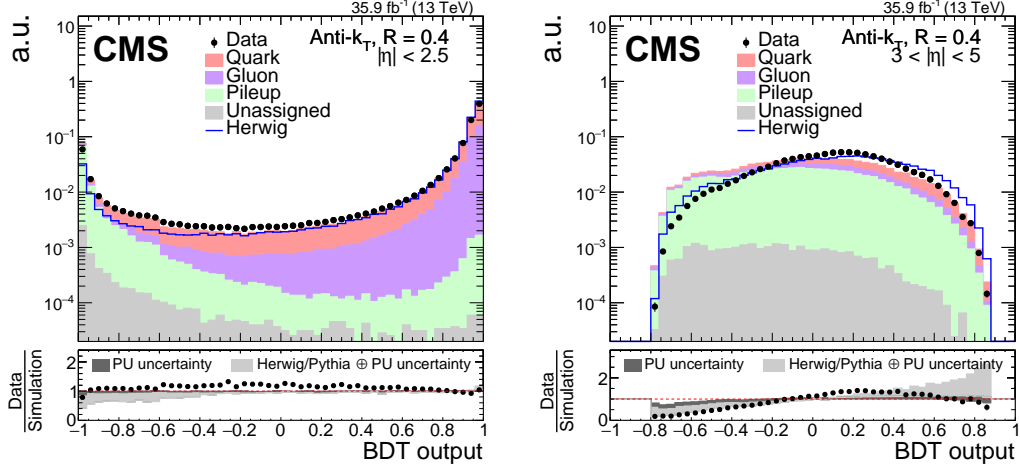


Figure 7.24: Data-to-simulation comparison of the PU jet ID BDT output for AK4 CHS jets with $30 < p_T < 50$ GeV for the detector region within the tracker volume (left) and $3 < |\eta| < 5$ (right).

- *medium*, 90% efficient for quark jets, and,
- *loose*, 99% efficient for quark jets in $|\eta| < 2.5$ and 95% efficient for quark jets in $|\eta| > 2.5$ (highest mis-identification rate).

Since 92% of the PU jets will likely be found in the $p_T < 50$ GeV regime, this identification criteria is intended to be applied to jets with pt below this threshold.

7.5 Missing transverse momentum

CMS is a hermetic detector, making possible to infer the amount of energy or momentum carried out by particles that do not leave traces of interaction in the detector subsystems, such as neutrinos or, in SUSY searches, neutralinos. From momentum conservation, the momentum in the plane perpendicular to the beam direction is, in principle, equal to zero before the collision. Thus, after the collision, the same statement should hold true.

In events where particles like neutrinos or other weakly interacting neutral particles are produced, a non-zero visible momentum imbalance vector will be measured, which is known as *missing transverse momentum* ($\vec{p}_{T}^{\text{miss}}$) and its magnitude is denoted by p_T^{miss} . $\vec{p}_{T}^{\text{miss}}$ is defined as the negative vectorial sum of momenta of all visible particle candidates reconstructed with the PF algorithm:

$$\vec{p}_{T}^{\text{miss}} = - \sum_{i \in \text{vis. part.}} \vec{p}_{T}^i. \quad (7.17)$$

Both in SM precision measurements and searches for new physics, where the final states contain weakly interacting neutral particles, the precise measurement of p_T^{miss} is fundamental, since this quantity is part of the key kinematic observables in these analyses. The p_T^{miss} reconstruction is sensitive to the efficiency of scale and resolution of the visible reconstructed candidates, as well as

other effects introduced by detector artifacts and pileup [137]. To account for these effects, it is necessary to apply a dedicated set of corrections to p_T^{miss} , which will be described below.

Missing transverse momentum calibration

Non-linear response of calorimeters to hadronic particles, minimum energy thresholds in the calorimeters, p_T thresholds, and inefficiencies in the tracker system can lead to an inaccurate estimation of p_T^{miss} . The propagation of the corrections applied to the jet momenta at particle level, as described in Sec. 7.4, improves the estimation of p_T^{miss} .

Uncorrected (raw) p_T^{miss}

Equation 7.17 is known as *raw* p_T^{miss} , where no corrections have been applied to the jets in the event. In the description below, jets will be denoted as *clustered energy*, and the rest of the PF candidates as *unclustered energy*. The expression for the raw p_T^{miss} , dividing the visible particles into two disjoint sets of clustered and unclustered particles, is:

$$\vec{p}_T^{\text{miss, raw}} = - \sum_{i \in \text{vis. part.}} \vec{p}_{T,i}^{\text{raw}} = - \sum_{i \in \text{unclustered}} \vec{p}_{T,i} - \sum_{j \in \text{jets}} \vec{p}_{T,j}^{\text{raw}}, \quad (7.18)$$

Jets are further classified into two subsets: those jets whose L1L2L3 corrected p_T is above the unclustered energy threshold¹³, and those jets which fail this condition. Only jets above the unclustered energy threshold will be corrected with the L1, L2 and L3 jet energy scale corrections. Therefore, $\vec{p}_{T,\text{raw}}^{\text{miss}}$ can be written as:

$$\vec{p}_T^{\text{miss, raw}} = - \sum_{i \in \text{unclustered}} \vec{p}_{T,i} - \sum_{\substack{j \in \text{jets} \\ p_T^{\text{L123}} < 15 \text{ GeV}}} \vec{p}_{T,j}^{\text{raw}} - \sum_{\substack{k \in \text{jets} \\ p_T^{\text{L123}} > 15 \text{ GeV}}} \vec{p}_{T,k}^{\text{raw}}. \quad (7.19)$$

Recalling that the L1 jet energy corrections account for the offset energy coming from pileup events, the offset energy is expressed as:

$$\Delta \vec{p}_{T,\text{jet}}^{\text{L1}} = \vec{p}_{T,\text{jet}}^{\text{raw}} - \vec{p}_{T,\text{jet}}^{\text{L1}}. \quad (7.20)$$

From this expression, one can see that the offset energy $\Delta \vec{p}_{T,\text{jet}}^{\text{L1}}$ and the corrected L1 jet momentum $\vec{p}_{T,\text{jet}}^{\text{L1}}$ are included in Eq. 7.19, since

$$\vec{p}_{T,\text{jet}}^{\text{raw}} = \vec{p}_{T,\text{jet}}^{\text{L1}} + \Delta \vec{p}_{T,\text{jet}}^{\text{L1}}. \quad (7.21)$$

¹³During the Run II data taking period, the unclustered energy threshold was 15 GeV.

Hence, $\vec{p}_T^{\text{miss, raw}}$ can be written as

$$\begin{aligned} \vec{p}_T^{\text{miss, raw}} = & - \sum_{i \in \text{uncl.}} \vec{p}_{T,i} - \sum_{\substack{l \in \text{jets} \\ p_T^{\text{L123}} < 15 \text{ GeV}}} \vec{p}_{T,l}^{\text{raw}} \\ & - \sum_{\substack{m \in \text{jets} \\ p_T^{\text{L123}} > 15 \text{ GeV}}} \vec{p}_{T,m}^{\text{L1}} - \sum_{\substack{n \in \text{jets} \\ p_T^{\text{L123}} > 15 \text{ GeV}}} \Delta \vec{p}_{T,n}^{\text{L1}}. \end{aligned} \quad (7.22)$$

Type-I p_T^{miss} corrections

The p_T^{miss} corrections have the general form:

$$\vec{p}_T^{\text{miss, corr}} = \vec{p}_T^{\text{miss, raw}} + \vec{C}_T^{\text{corr}}. \quad (7.23)$$

When L2 and L3 jet energy corrections are applied to jets, in order to propagate them to the raw p_T^{miss} , the term in Eq.7.22 with $\vec{p}_{T,m}^{\text{L1}}$ is replaced by $\vec{p}_{T,m}^{\text{L123}}$,

$$\vec{C}_T^{\text{Type-I}} = \sum_{\substack{m \in \text{jets} \\ p_T^{\text{L123}} > 15 \text{ GeV}}} \vec{p}_{T,m}^{\text{L1}} - \sum_{\substack{m \in \text{jets} \\ p_T^{\text{L123}} > 15 \text{ GeV}}} \vec{p}_{T,m}^{\text{L123}}. \quad (7.24)$$

Jets in the second term of Eq. 7.24 are also required to have an electromagnetic energy fraction smaller than 0.9, and to not overlap with any PF muon candidate. The term $\vec{C}_T^{\text{Type-I}}$ corresponds to what is known as *type-I* p_T^{miss} corrections. Combining Equations 7.22 and 7.24, the type-I corrected p_T^{miss} is then:

$$\begin{aligned} \vec{p}_T^{\text{miss, Type-I}} = & - \sum_{i \in \text{uncl.}} \vec{p}_{T,i} - \sum_{\substack{l \in \text{jets} \\ p_T^{\text{L123}} < 15 \text{ GeV}}} \vec{p}_{T,l}^{\text{raw}} - \sum_{\substack{m \in \text{jets} \\ p_T^{\text{L123}} > 15 \text{ GeV}}} \vec{p}_{T,m}^{\text{L1}} \\ & - \sum_{\substack{n \in \text{jets} \\ p_T^{\text{L123}} > 15 \text{ GeV}}} \Delta \vec{p}_{T,n}^{\text{L1}} + \sum_{\substack{m \in \text{jets} \\ p_T^{\text{L123}} > 15 \text{ GeV}}} \vec{p}_{T,m}^{\text{L1}} - \sum_{\substack{m \in \text{jets} \\ p_T^{\text{L123}} > 15 \text{ GeV}}} \vec{p}_{T,m}^{\text{L123}} \end{aligned} \quad (7.25)$$

$$\vec{p}_T^{\text{miss, Type-I}} = - \sum_{i \in \text{uncl.}} \vec{p}_{T,i} - \sum_{\substack{j \in \text{jets} \\ p_T^{\text{L123}} < 15 \text{ GeV}}} \vec{p}_{T,j}^{\text{raw}} - \sum_{\substack{k \in \text{jets} \\ p_T^{\text{L123}} > 15 \text{ GeV}}} (\vec{p}_{T,k}^{\text{L123}} + \Delta \vec{p}_{T,k}^{\text{L1}}) \quad (7.26)$$

Type-I p_T^{miss} is widely utilized in CMS analyses, including the present search. Since jets are also corrected for JER in simulation, then the Type-I p_T^{miss} expressions for data and simulation read as

$$\vec{p}_{T,\text{data}}^{\text{miss}} = - \sum_{i \in \text{uncl.}} \vec{p}_{T,i} - \sum_{\substack{j \in \text{jets} \\ p_T^{\text{L123}} < 15 \text{ GeV}}} \vec{p}_{T,j}^{\text{raw}} - \sum_{\substack{k \in \text{jets} \\ p_T^{\text{L123}} > 15 \text{ GeV}}} (\vec{p}_{T,k}^{\text{L123}} + \Delta \vec{p}_{T,k}^{\text{L1}}), \quad (7.27)$$

$$\vec{p}_{T,\text{sim}}^{\text{miss}} = - \sum_{i \in \text{uncl.}} \vec{p}_{T,i} - \sum_{\substack{j \in \text{jets} \\ p_T^{\text{L123}} < 15 \text{ GeV}}} \vec{p}_{T,j}^{\text{raw}} - \sum_{\substack{k \in \text{jets} \\ p_T^{\text{L123}} > 15 \text{ GeV}}} \left(\vec{p}_{T,k}^{\text{L123, JER}} + \Delta \vec{p}_{T,k}^{\text{L1}} \right). \quad (7.28)$$

$\phi(p_T^{\text{miss}})$ modulation corrections

A powerful method to reduce QCD multijet background involves an event selection based on the minimum absolute azimuthal separation between any jet in the event and the direction of \vec{p}_T^{miss} , denoted as $|\Delta\phi(j, p_T^{\text{miss}})|_{\text{min}}$. Therefore, it is crucial to correctly measure and model the ϕ direction of \vec{p}_T^{miss} .

Particles in any collision are produced uniformly in the ϕ direction, causing the distribution of p_T^{miss} to be independent of ϕ , because of the rotational symmetry of the collisions around the beam axis. However, a ϕ -asymmetry has been observed in the \vec{p}_T sums of calorimeter energy deposits, tracks, and particles reconstructed by the PF algorithm, leading to a ϕ -asymmetry in \vec{p}_T^{miss} .

The $\phi(p_T^{\text{miss}})$ distribution has roughly a sinusoidal curve with a 2π period, and it is present both in data and simulation. The cause of this asymmetry could be attributed to anisotropic detector responses in the ϕ direction, misalignment of different detector sub-systems, displacement of the beam spot (~ 4 mm shift between the center of the detector and the beam line), or inactive calorimeter cells and tracking regions.

The ϕ -asymmetry can be represented as a shift in the x and y projection of $p_{T,x}^{\text{miss}}$ and $p_{T,y}^{\text{miss}}$ components, and it increases approximately linearly as a function of PF candidate multiplicity. Equivalently, the amplitude of the modulation increases roughly linearly with the number of pileup interactions. Based on this correlation, a correction is derived in order to reduce the ϕ modulation, by shifting the origin of the coordinate in the transverse momentum plane. This correction, denoted as \vec{C}_T^{xy} , is obtained as a function of the number of primary vertices (n_{PV}) in each event:

$$\vec{C}_T^{xy} = \vec{c}_A + n_{\text{PV}} \vec{c}_B, \quad (7.29)$$

where \vec{c}_A and \vec{c}_B are constant vectors, obtained from linear fits to the correlation of $p_{T,x}^{\text{miss}}$ and $p_{T,y}^{\text{miss}}$ as a function of the number of PF candidates in various η bins. The ϕ -asymmetry corrections are determined separately for data and simulated events, and also serve as a way to mitigate effects from pileup.

7.6 Hadronic tau leptons

The τ lepton is special among the other charged leptons, because of its large mass ($m(\tau) = 1.777$ GeV), which make possible its decay to lighter leptons (e , μ and two neutrinos, one of them being ν_τ), and its decay to hadrons and a neutrino (Tab. 7.9 and Fig. 7.25). In addition, it has a relatively large mean lifetime, of 2.90×10^{-13} s (at rest), and a decay length of $\simeq 90 \mu\text{m}$.

Although electrons and muons originating from τ decays are difficult to distinguish from prompt electrons and muons, it is possible to tag the hadronic decays of τ leptons. Thus, physics objects

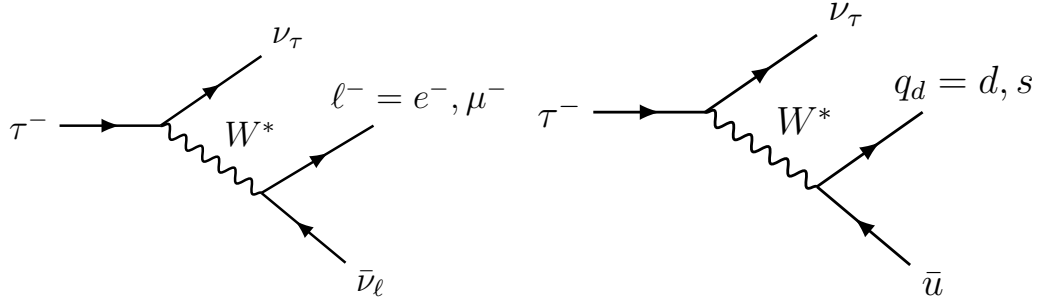


Figure 7.25: Feynman diagrams of the leptonic and hadronic τ lepton decay modes.

known as *hadronic taus* (τ_h), or simply referred as *taus*, can be reconstructed. Experimentally, τ_h 's will be first reconstructed as jets (Sec. 7.4). Jets from hadronic tau decays have unique characteristics that allows them to be distinguished from jets produced by quarks or gluons. Among these properties are: the particle multiplicity, composition, collimation, and the isolation of the decay products.

	Decay mode	Meson resonance	Branching ratio $\mathcal{B}[\%]$
Leptons	$\tau^- \rightarrow e^- \bar{\nu}_e \nu_\tau$	—	17.8
	$\tau^- \rightarrow \mu^- \bar{\nu}_\mu \nu_\tau$	—	17.4
Hadrons	$\tau^- \rightarrow h^- \nu_\tau \gamma$	—	11.5
	$\tau^- \rightarrow h^- \pi^0 \nu_\tau$	$\rho(770)$	26.0
	$\tau^- \rightarrow h^- \pi^0 \pi^0 \nu_\tau$	$a_1(1260)$	9.5
	$\tau^- \rightarrow h^- h^+ h^- \nu_\tau$	$a_1(1260)$	9.8
	$\tau^- \rightarrow h^- h^+ h^- \pi^0 \nu_\tau$	—	4.8
	other modes containing hadrons	—	3.2
	All modes containing hadrons		64.8

Table 7.9: Summary of the decay modes and branching ratios of the τ lepton. The generic symbol h^- represents a charged hadron, pion or kaon.

Hadronic tau reconstruction

Thanks to the information obtained with the PF algorithm, hadronic taus can be reconstructed based on their particle composition. PF particles are used as an input to the *hadron-plus-strips algorithm* (HPS) [138]. The HPS algorithm is seeded by AK4 jets with $p_T > 14$ GeV and $|\eta| < 2.5$. The main goal of the HPS algorithm is to reconstruct the different hadronic decays of the τ lepton. The final states include charge hadrons (“H” in HPS) and neutral pions. π^0 mesons. Neutral pions are special because they decay almost exclusively into pairs of photons $\gamma\gamma$, which most of the time convert into e^+e^- pairs while traversing the tracker material.

Due to the presence of the CMS magnetic field, these e^+e^- pairs are spatially separated in the (ϕ, η) plane. The reconstruction of the full energy of the neutral pions is done by clustering electron and photon candidates that fall within a certain region of $\Delta\phi \times \Delta\eta$, giving as a result a *strip* (“S” in HPS). A pictorial representation of a strip is shown in Fig. 7.27.

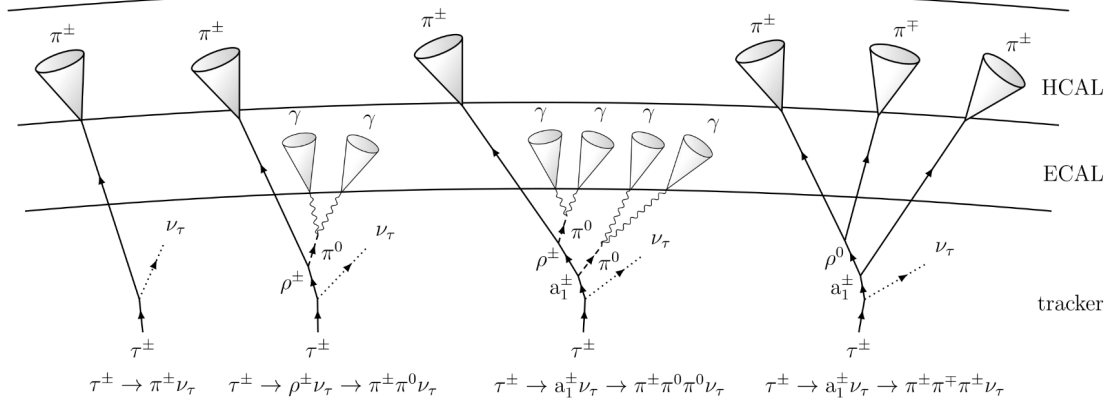


Figure 7.26: Schematics of the experimental signatures of the hadronic τ decays in the CMS detector [139].

Property	Value
Mass [MeV]	135.0
Mean lifetime [s]	8.52×10^{-17} s
Decay length [m]	25.5×10^{-9}
$\mathcal{B}(\pi^0 \rightarrow \gamma\gamma)$ [%]	98.8

Table 7.10: Summary of the π^0 properties.

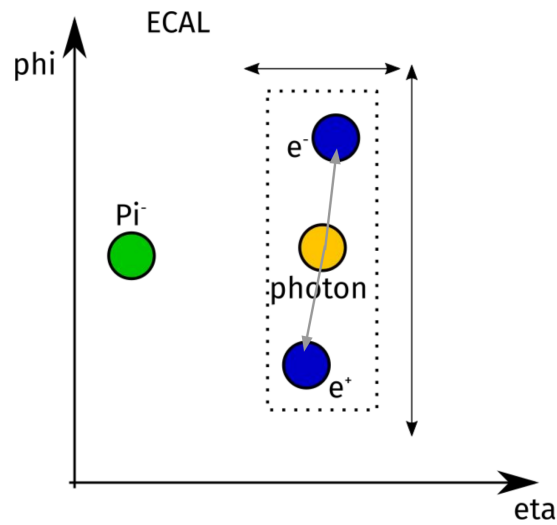


Figure 7.27: Representative schematics for strip reconstruction in the CMS ECAL [139].

Based on the set of charged particles and strips contained in a jet, the HPS algorithm generates all possible combinations of hadrons for the decay modes h^\pm , $h^\pm\pi^0$, $h^\pm\pi^0\pi^0$ and $h^\pm h^\mp h^\pm$. The reconstructed mass of the “visible” hadronic constituents of the τ_h candidate is required to be compatible with either the $\rho(770)$ resonance in the $h^\pm\pi^0$ decay mode, or the $a_1(1260)$ resonance in the $h^\pm\pi^0\pi^0$ and $h^\pm h^\mp h^\pm$ decay modes. The τ_h candidates of charge other than ± 1 are rejected, as well as those candidates with strips outside the *signal cone*, defined by

$$R_{\text{sig}} = \frac{3.0 \text{ GeV}}{p_T}, \quad (7.30)$$

where p_T is that of the hadronic system. The cone size is limited to the range 0.05-0.10. If more than one fitting candidate is found, the algorithm selects only the τ_h candidate with largest charge multiplicity (based on the number of charged hadrons), largest p_T , or largest strip multiplicity, resulting in a single τ_h per jet (Fig. 7.28).

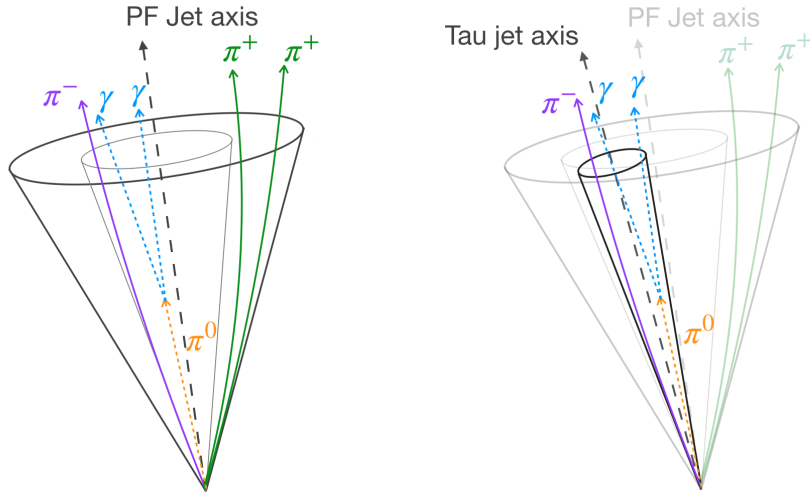


Figure 7.28: Pictorial representation of a τ_h candidate reconstructed with the HPS algorithm.

Strips are reconstructed with variable $(\Delta\eta, \Delta\phi)$ size, known as *dynamic strip reconstruction*. The motivation for a dynamic strip reconstruction comes from the fact that the regional spread of electrons and photons in the strip is p_T -dependent [140]. The strip momentum is calculated by the momentum vectors of all of its constituents. Only the p_T -weighted center (η, ϕ) is required to be within the signal cone (Eq. 7.30).

Table 7.11 details the reconstructed τ_h decay modes obtained with the HPS algorithm. A useful way to classify the various decays is by assigning a code number based on the number of charged hadrons, N_c , and neutral pions, N_p , in the decay. The code is obtained with the expression:

$$\text{decay mode code} = 5(N_c - 1) + N_p. \quad (7.31)$$

The reconstructed mass requirements imposed by the HPS algorithm are also summarized in Tab. 7.11. m_{τ_h} refers to the *reconstructed mass of the visible hadronic constituents* of the τ_h candidate, and Δm_{τ_h} is the change in the mass of the τ_h candidate, brought about by the addition of the e/γ candidates to its strip [140]. For $h^\pm\pi^0$, the mass window is enlarged for high- p_T τ_h candidates to

account for resolution, and the upper limit on the mass window must lie within 1.3 and 4.2 GeV. For $h^\pm\pi^0\pi^0$, the upper limit on the mass window is set to be within the [1.2,4.0] GeV range[140].

The $h^\pm\pi^0$ and $h^\pm\pi^0\pi^0$ modes are consolidated into the $h^\pm\pi^0$ mode, and analyzed together. The number of charged hadrons in the decay mode is also known as the number of *prongs*. The reconstruction of a τ_h candidate ends with the association of it to a decay mode and it has been commissioned for $p_T > 20$ GeV.

HPS decay mode	Code number	Hadronic τ decay(s)	Mass constraints
1 prong + 0 strips	0	$h^\pm\nu_\tau, h^\pm\pi^0\nu_\tau$ (low energy π^0)	–
1 prong + 1 strip	1	$h^\pm\pi^0\nu_\tau, h^\pm\pi^0\pi^0\nu_\tau$	0.3 GeV $-\Delta m_{\tau_h} < m_{\tau_h} < 1.3$ GeV
1 prong + 2 strips	2		$\sqrt{p_T^{\tau_h}/100 \text{ GeV}} + \Delta m_{\tau_h}$
3 prongs	10	$h^\pm h^\mp h^\pm\nu_\tau$	$0.8 < m_{\tau_h} < 1.5$ GeV
3 prongs + 1 strip	11	$h^\pm h^\mp h^\pm\pi^0\nu_\tau$	

Table 7.11: Description of the HPS decay modes based on the particle multiplicity of the τ_h decay, and the mass constraints applied during reconstruction.

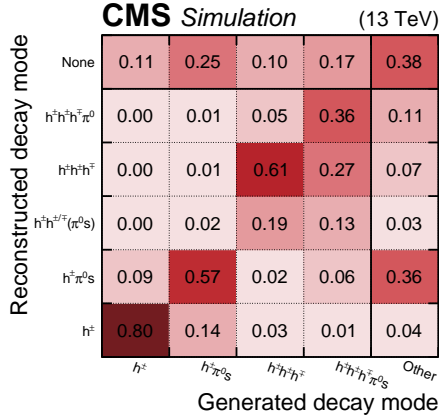


Figure 7.29: HPS efficiency for different τ_h decay topologies, estimated in $Z/\gamma^*(\rightarrow\tau\tau)$ simulated events [141].

Hadronic tau identification

Despite the great reconstruction efficiency obtained from the HPS algorithm (Fig. 7.29), many non- τ_h are reconstructed as τ_h . Jets produced in QCD multijet events, electrons, and muons can have experimental signatures similar to those of a hadronic tau decay (Tab. 7.12). Thus, separate τ_h *identification algorithms* are needed to discriminate genuine τ_h 's from other objects.

In CMS, there are three different discrimination techniques: isolation sums, MVA-based discriminators, and discriminators based on deep neural networks (DNN). A summary of each type of identification algorithms is included below.

Importance	Source	Decay modes affected	Cause(s) of mis-identification
1	$j \mapsto \tau_h$	all	high cross section of the QCD multijet production of quark and gluon jets
2	$e \mapsto \tau_h$	1-prong, 1-prong + π^0	e 's and π^\pm 's leave a track and energy deposit in the ECAL; e 's emit abundant bremsstrahlung, which can be mis-identified as π^0 's.
3	$\mu \mapsto \tau_h$	1-prong	mis-reconstructed muons with no matching segments in the muon system, punch-through muons

Table 7.12: Sources of misidentified τ_h leptons and their causes in descending order of importance.

Isolation sum discriminators

The isolation of the τ_h candidate is computed by summing the transverse momenta of the charged particles with $p_T^{\text{ch}} > 0.5$ GeV, and photons $p_T^\gamma > 0.5$ GeV reconstructed with the PF algorithm within an isolation cone of size $R = 0.3$:

$$I_{\tau_h} = \sum p_T^{\text{ch}}(|d_z| < 0.2 \text{ cm}) + \max\left(0, \sum p_T^\gamma - \Delta\beta \sum p_T^{\text{ch}}(|d_z| > 0.2 \text{ cm})\right). \quad (7.32)$$

The contribution from PU is suppressed by only computing the p_T sum of all charged particles not associated to the τ_h candidate, but originating from the same PV within a distance $|d_z| < 0.2$ cm. The second term corresponds to the contribution of neutral particles minus contributions of charged particles not originating from the PV ($|d_z| > 0.2$ cm), but appearing within a cone of $\Delta R = 0.8$ around the τ_h direction, multiplied by a $\Delta\beta$ factor. $\Delta\beta$ corresponds to the ratio of neutral to charged hadron production in the hadronization process of inelastic proton-proton collisions and the different cone sizes used to estimate the PU contributions. At $\sqrt{s} = 13$ TeV, a $\Delta\beta = 0.2$ factor was used [140].

In this technique, three working points are defined based on different values of identification efficiency: *loose* ($I_{\tau_h} < 2.5$ GeV), *medium* ($I_{\tau_h} < 1.5$ GeV) and *tight* ($I_{\tau_h} < 0.8$ GeV).

MVA-based discriminators (MVATau).

In order to further reduce the $\text{jet} \mapsto \tau_h$ mis-identification probability an MVA-based technique was developed. A classifier based on BDTs is trained, using as inputs isolation and shape variables sensitive to the τ lepton lifetime: $p_{T\tau_h}$, η_{τ_h} , p_T -sum of charged (neutral) hadrons in a cone around τ_h axis, τ_h flight length, number of photons, τ_h decay mode, impact parameters of the leading track, etc. [138, 140]. Examples of these variables are shown in Fig. 7.31, comparing the characteristics of genuine τ_h candidates and jets from W +jets events.

The BDT will classify τ_h candidates and assign a score from -1 to 1. Several identification working points are defined according to their efficiency, ranging from 40% (very loose, or VLoose) to 90% (very very tight, or VVTight) in steps of 10% (Fig. 7.32).

MVA anti-electron and anti-muon discriminators were also developed to reduce the $e \mapsto \tau_h$ and $\mu \mapsto \tau_h$ mis-identification probability, respectively. The variables used for the anti-electron discriminator include observables that quantify the distribution in energy depositions in the ECAL,

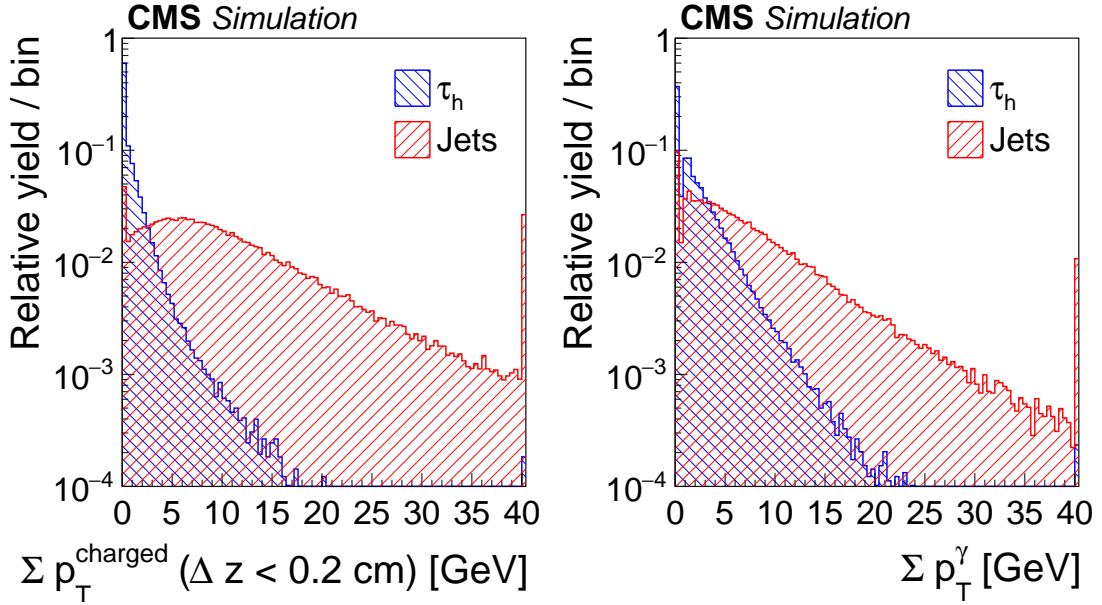


Figure 7.30: Distributions, normalized to unity, in observables related to the isolation sums, used as input variables to the MVA-based isolation discriminant, for τ_h decays in simulated $Z/\gamma^* \rightarrow \tau\tau$ (blue) and jets in simulated W +jets (red) events [140].

observables sensitive to the amount of bremsstrahlung emitted along the leading track, observables related to the overall particle multiplicity, as well as photon related variables [138, 140]. Similar to the anti-jet discriminant, working points are defined for the anti-electron discriminant (from VLoose to VTight), based on their efficiencies.

Additionally, a cut-based anti-muon discriminant was developed to be used in combination with the MVA-based anti-jet and anti-electron discriminators and it is described in [140]. Two working points are defined:

- *loose*: τ_h candidates fail this discriminant when track segments are found in at least two muon stations within a $\Delta R \geq 0.3$ distance, with respect to the direction of the τ_h , or when the sum of the energies in the ECAL and HCAL corresponds to less than 20% the momentum of the leading track of the τ_h candidate.
- *tight*: τ_h candidates pass the loose anti-muon discriminant requirement and no hits are present within a cone of $\Delta R = 0.3$ in the muon system.

DNN-based discriminators (DeepTau).

In Run II, a new identification algorithm based on a multi-classifier using deep neural networks, called DEEPTAU was developed [141]. This algorithm takes 46 high-level variables as inputs, including variables used during τ_h reconstruction, variables that have proven to provide discriminating power in other tau discriminators (MVA TAU), and one global event variable – the average energy deposition density (ρ).

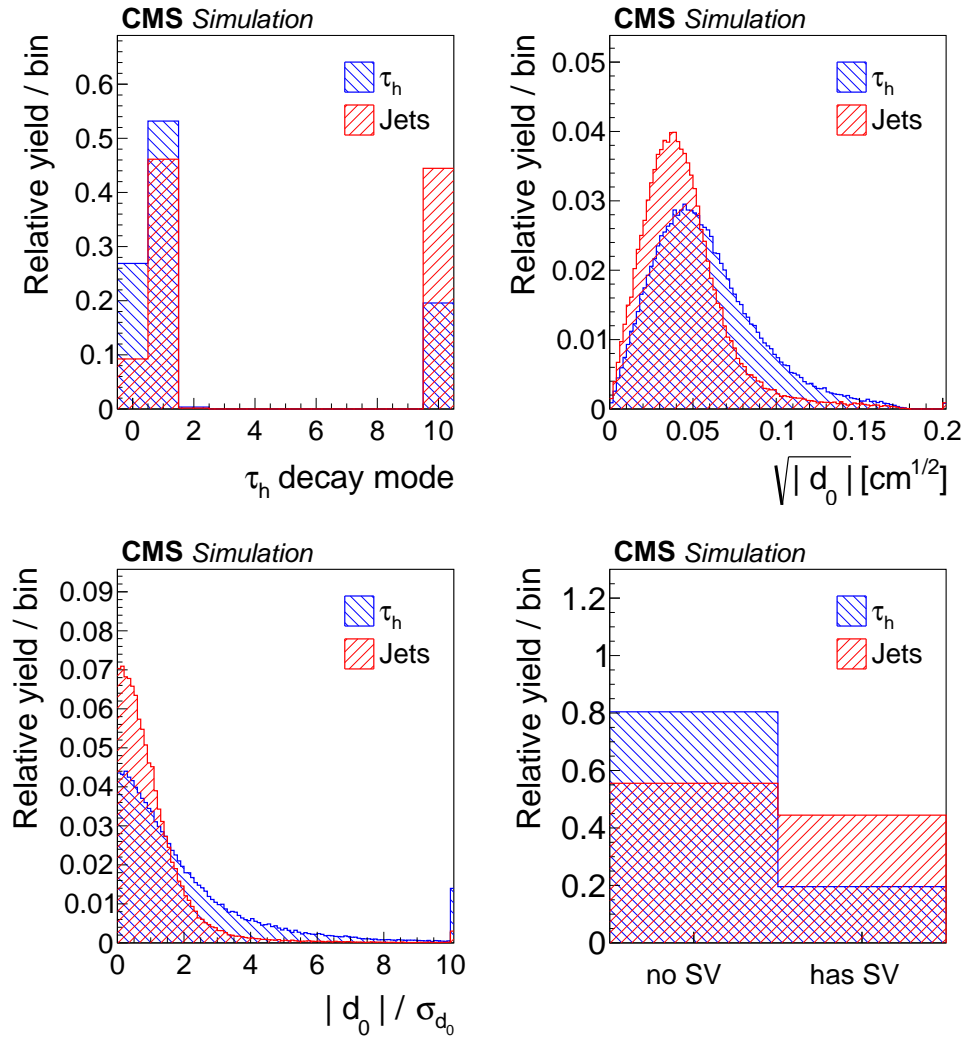


Figure 7.31: Distributions, normalized to unity, in observables used as input variables to the MVA-based isolation anti-jet discriminant, for τ_h decays in simulated $Z/\gamma^* \rightarrow \tau\tau$ (blue) and jets in simulated W +jets (red) events [140].

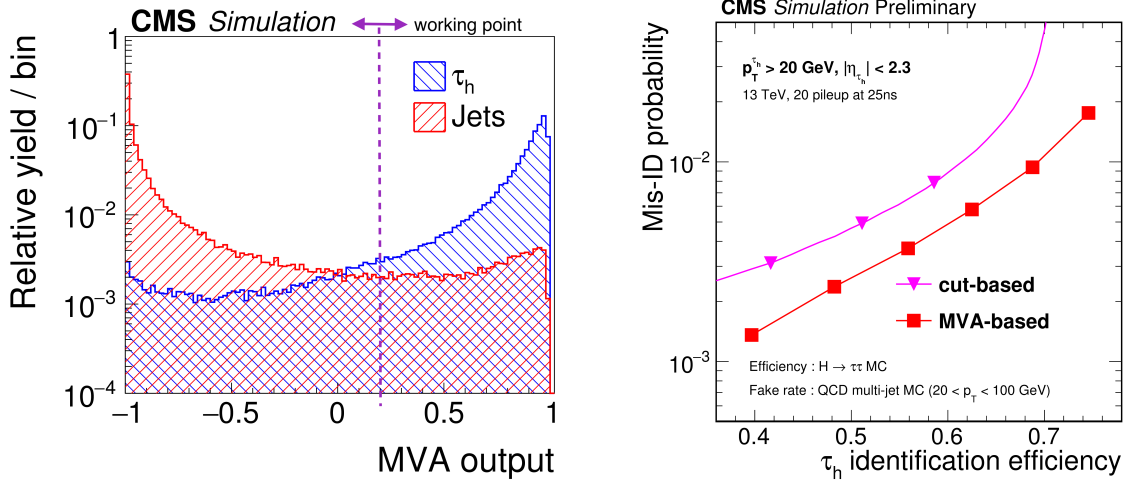


Figure 7.32: Left: MVA output distribution for the anti-jet τ_h identification discriminant that includes lifetime information for τ_h decays in simulated $Z/\gamma^* \rightarrow \tau\tau$ (blue), and jets in simulated W +jets (red) events (Adapted from [138]). Right: Mis-identification probability as a function of τ_h identification efficiency evaluated using $H \rightarrow \tau\tau$ and QCD MC samples (Adapted from [140]).

For each candidate reconstructed within the τ_h signal or isolation cones, information of 4-momentum, track quality, relation with the primary vertex, calorimeter clusters, and muon stations is used, if available. DEEPTAU has shown to outperform BDT discriminators (MVATAU). An anti-jet (D_j), anti-electron (D_e), and anti-muon (D_μ) discriminators are obtained with this technique. Various working points are defined based on the identification efficiency (Tab. 7.13)

Discriminator	Working point							
	VVTight	VTight	Tight	Medium	Loose	VLoose	VVLoose	VVVLoose
D_j	40%	50%	60%	70%	80%	90%	95%	98%
D_e	60%	70%	80%	90%	95%	98%	99%	95%
D_μ	–	–	99.5%	99.8%	99.9%	99.95%	–	–

Table 7.13: Target τ_h identification efficiencies for the different working points defined for the three different DEEPTAU discriminators (Adapted from [141]).

Comparison of the performance of the MVATau and DeepTau algorithms

The performance of the different τ_h *anti-jet discriminators* (MVATAU vs. DEEPTAU) in simulation can be quantified with a short study, where the identification efficiency and the mis-identification probability are measured, based on the *generator- (gen-) level* information, also known as *MC-truth* information.

The goal of the study is to select reconstructed τ_h candidates, τ_h^{reco} , to perform a *matching* to a gen-level τ_h object, (τ_h^{gen}). A reconstructed τ_h is said to be matched to a gen-level τ_h if the distance between them in the (η, ϕ) plane satisfied $\Delta R < (\tau_h^{\text{reco}}, \tau_h^{\text{gen}}) < 0.2$.

The τ_h identification efficiency is obtained both for reconstructed and generated τ_h candidates as a function of p_T , given by:

$$\epsilon_{\tau_h \text{ ID}} = \frac{p_T^x(\text{genuine } \tau_h + \text{pass ID})}{p_T^x(\text{genuine } \tau_h)}, \quad (7.33)$$

where x can be "reco" or "gen".

The set of reconstructed τ_h candidates considered were required to have $p_T > 15$ GeV, $|\eta| < 2.1$, no anti- e/μ discriminator requirements were applied and all τ_h decay modes were considered. Gen-level τ_h are selected with $p_T > 20$ GeV and $|\eta| < 2.1$. All the available anti-jet discriminator working points in each algorithm were tested.

In this study, simulation samples of processes containing genuine τ_h 's were used to measure the τ_h anti-jet discriminator efficiency. The processes considered include: Z +jets events (inclusive leptonic decays, $m_{\ell\ell} > 50$ GeV), $t\bar{t}$ events (inclusive decays in 2016, and fully leptonic and semi-leptonic decays, separately, for 2017-2018), as well as $H \rightarrow \tau\tau$ events.

For the study of mis-identification probability, simulated QCD multijet events were used. The selections utilized for this study are the same than those for the identification efficiency, except that these events do not contain τ_h^{gen} particles. Thus, all τ_h^{reco} candidates are *fake* τ_h 's, and the reco-gen matching requirement is dropped. The mis-identification probability is then given by

$$P_{\tau_h \text{ mis-id.}} = \frac{p_T^{\text{reco}}(\text{pass ID})}{p_T^{\text{reco}}}. \quad (7.34)$$

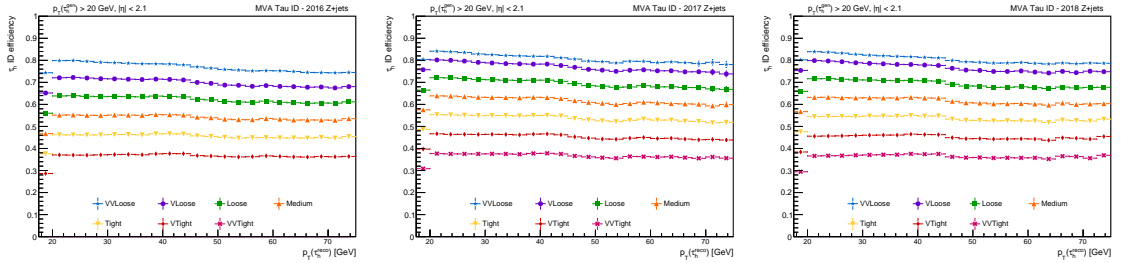


Figure 7.33: τ_h identification efficiency for Z +jets events (inclusive leptonic decays) in 2016, 2017 and 2018, as a function of p_T^{reco} , using the various working points of the MVATAU anti-jet discriminator.

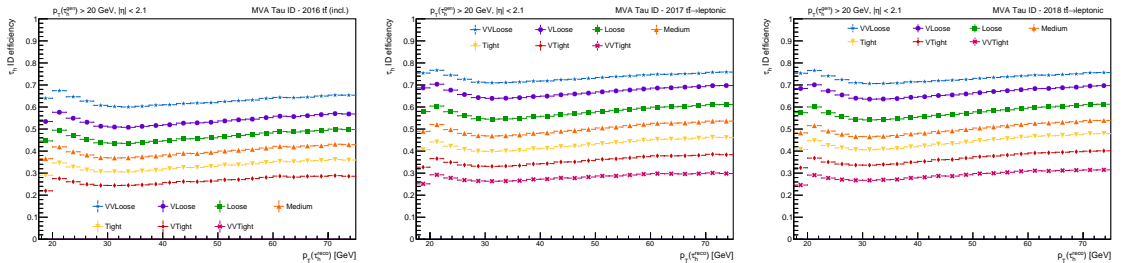


Figure 7.34: τ_h identification efficiency for $t\bar{t}$ events (2016: inclusive decays, 2017-2018: fully leptonic + semi leptonic decays), as a function of p_T^{reco} , using the various working points of the MVATAU anti-jet discriminator.

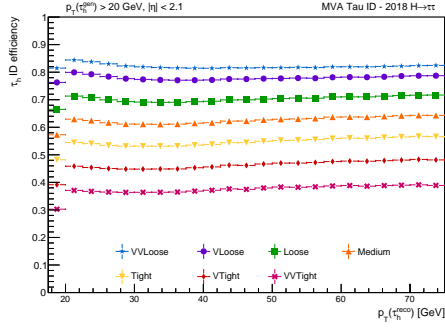


Figure 7.35: τ_h identification efficiency for $H \rightarrow \tau\tau$ events with 2018 simulation samples, as a function of p_T^{reco} , using the various working points of the MVATAU anti-jet discriminator.

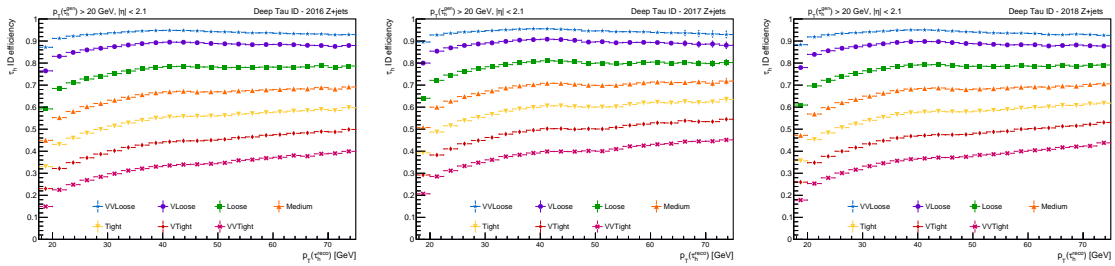


Figure 7.36: τ_h identification efficiency for Z +jets events (inclusive leptonic decays) in 2016, 2017 and 2018, as a function of p_T^{reco} , using the various working points of the DEEPTAU anti-jet discriminator.

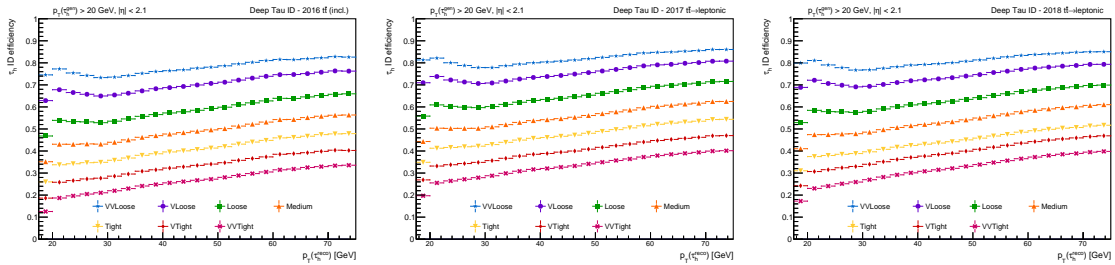


Figure 7.37: τ_h identification efficiency for $t\bar{t}$ events (2016: inclusive decays, 2017-2018: fully leptonic + semi leptonic decays), as a function of p_T^{reco} , using the various working points of the DEEPTAU anti-jet discriminator.

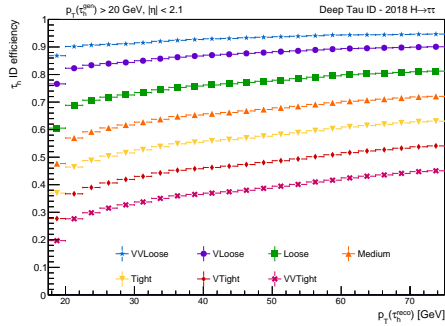


Figure 7.38: τ_h identification efficiency for $H \rightarrow \tau\tau$ events with 2018 simulation samples, as a function of p_T^{reco} , using the various working points of the MVATAU anti-jet discriminator.

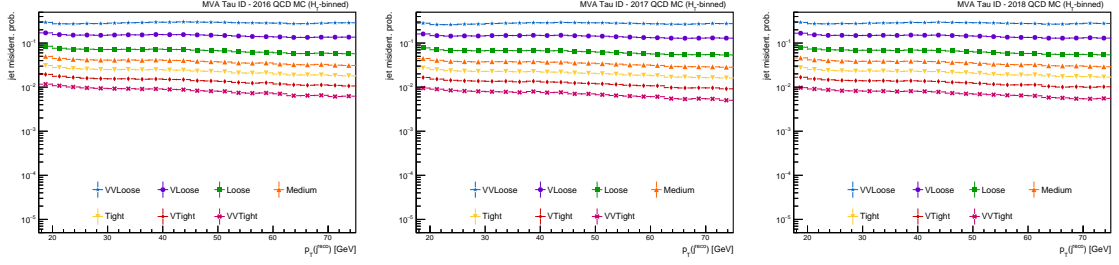


Figure 7.39: τ_h mis-identification probability estimated in QCD multijet events, as a function of p_T^{reco} , using the various working points of the MVATAU anti-jet discriminator.

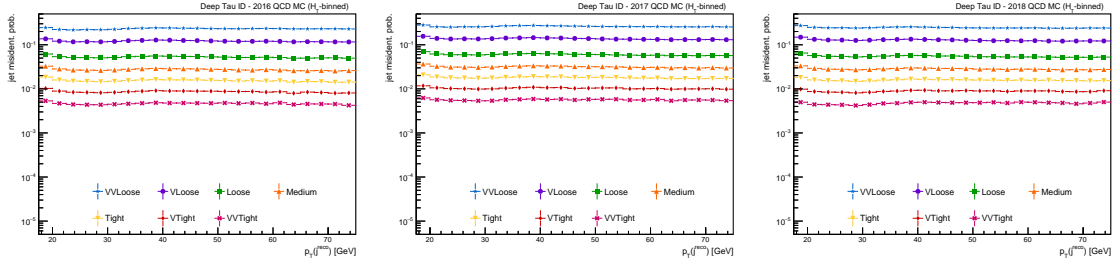


Figure 7.40: τ_h mis-identification probability estimated in QCD multijet events, as a function of p_T^{reco} , using the various working points of the DEEPTAU anti-jet discriminator.

The τ_h identification efficiency is shown in Figs. 7.33, 7.34 and 7.35 (Figs. 7.36, 7.37 and 7.38), for Z +jets, $t\bar{t}$, and $H \rightarrow \tau\tau$ events, respectively, using the MVATAU (DEEPTAU) anti-jet discriminator. The mis-identification probability for the MVATAU (DEEPTAU) anti-jet discriminator is shown in Fig. 7.39 (Fig. 7.40).

Comparing working points with the same nominal identification efficiency in each one of the discriminators (for example, tight in MVATAU vs. tight in DEEPTAU), the observed identification probability is larger, and the mis-identification probability is lower for DEEPTAU, compared to the MVATAU algorithm.

Corrections to eliminate the p_T -dependence of the τ_h identification efficiency are derived for both the MVATAU and DEEPTAU discriminators. These corrections are applied to genuine¹⁴ τ_h candidates in simulation.

In the case of DEEPTAU, there are two sets of corrections for τ_h identification for the DEEPTAU anti-jet discriminators: p_T -dependent and decay mode dependent scale factors. Both sets of corrections are derived using a tag-and-probe method, using $Z \rightarrow \tau\tau$ events, in the $\mu\tau_h$ final state. The decay mode dependent correction factors are recommended for cases in which the trigger selection may influence the decay mode composition. For example, these corrections are used in cases where τ_h and di- τ_h triggers requirements are applied.

Along the same lines, η -dependent corrections for the anti-electron and anti-muon discriminators are derived. These scale factors are divided into barrel and endcap regions. The choice of the η -binning is determined by the CMS ECAL sub-detector geometry, in the case of electrons, and the CMS muon sub-detector and tracker geometries, in the case of muons.

¹⁴Reconstructed τ_h 's matched to a gen-level τ lepton.

Hadronic tau energy scale corrections

The resolution and scale of the τ_h mass reconstruction depends on the τ_h reconstruction, and corrections for the τ_h response and resolution are derived. The τ_h energy scale (TES) is defined as the average reconstructed τ_h energy relative to the gen-level energy of the visible τ decay products.

The corresponding data-to-simulation TES correction is determined by fitting the distributions of the observable sensitive to the energy scale, using a sample of $Z/\gamma^* \rightarrow \tau_\mu \tau_h$ events, with the tag-and-probe technique. The TES is measured for τ_h 's passing the medium working point of DEEPTAU. A $m_T < 50$ GeV selection is imposed to reduce W+jets and $t\bar{t}$ backgrounds.

The observables used to extract the TES are the reconstructed mass of the τ_h candidate, m_{τ_h} , and the reconstructed mass of the muon and τ_h candidate, m_{vis} . m_{τ_h} and m_{vis} response templates for Z+jets events with τ_h objects matched to gen-level τ leptons are varied in TES. The variation is done by scaling the reconstructed τ_h 4-momentum by the TES, which is then propagated to the m_{τ_h} and m_{vis} variables.

In addition, shape templates are produced for Z+jets samples, where the τ_h is matched to a generated τ decay, such that the TES is varied discretely between -3% and +3% in steps of 0.2%. This range is sufficient to contain the measured TES value, as well as the $\pm 1\sigma$ uncertainty interval in each case.

The TES for each τ_h decay mode¹⁵ is extracted, by confronting the data with a likelihood ratio method. The TES recommendation combined two measurements, the low ($p_T < 170$ GeV) and high- p_T ($p_T \geq 170$ GeV) measurements in $Z \rightarrow \tau\tau$ and $W^* \rightarrow \tau\nu$ events, respectively.

Additional corrections for the $e \rightarrow \tau_h$ energy scale are applied to τ_h objects matched to an gen-level electron. The $e \rightarrow \tau_h$ ES is measured in a control region of $Z \rightarrow \tau\tau \rightarrow e\tau_h$ events, where the $Z \rightarrow ee$ process arises as one of the components of irreducible background. The observable visible mass of the $e\tau_h$ invariant system is used to extract these corrections, and are derived for each decay mode.

7.7 b-quark jets

Jets resulting from the hadronization of b-quarks, often referred as *b-jets*, possess unique characteristics, which combined with the capabilities of the CMS detector, can be exploited to perform a dedicated identification of b-jets (b-jet tagging). The b-hadrons produced in the fragmentation and hadronization processes of b-quarks have relatively large masses, long lifetimes and energetic decay products (Figs. 7.41). In particular, the long lifetime will be observed in data as the presence of a secondary vertex (SV).

Several b-tagging algorithms have been developed at CMS, initially aimed to the development of likelihood ratios based on different sets of variables, and seeding from reconstructed and calibrated jets. These variables include the information from track impact parameters, information from the kinematic variables associated with the secondary vertex (flight distance and direction), as well as the properties of the system of secondary tracks. A more complex approach, called the *Combined Secondary Vertex* (CSV) algorithm was employed during the LHC Run I. The CSV algorithm uses

¹⁵1-prong, 1-prong+1-strip, 3-prongs and 3-prongs+1 strip.

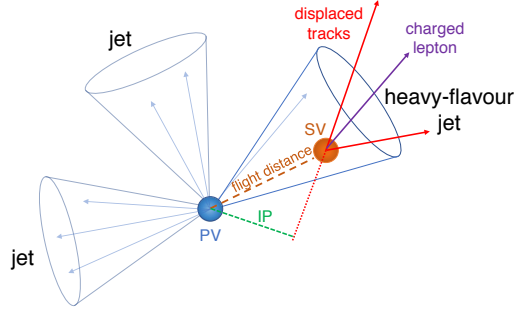


Figure 7.41: Illustration of a heavy-flavor jet topology with a SV from the decay of a b or c hadron. (Adapted from [142]).

the information from variables related to the second vertex combined with track-based lifetime information [143]. An advantage of using the CSV algorithm is related to the ability to tag b-jets in cases where no secondary vertices are found.

For Run II analyses, the CSV algorithm was optimized, and resulted in a new version of this algorithm, referred to as *CSVv2*. Another version that made use of deep machine learning was developed, and it is known as *DeepCSV* [144]. These algorithms are described in detail in Ref. [142], and here a summary will be presented.

CSVv2 tagger

The CSVv2 algorithm is an updated version of the Run I algorithm. Variables from secondary vertex and track-based lifetime (Tab. 7.14) were combined with a MVA technique based on neural networks, instead of using a likelihood ratio. The secondary vertex information is obtained with the Inclusive Vertex Algorithm, described in Ref. [142].

DeepCSV tagger

DeepCSV is an improved version of the CSVv2 algorithm, which makes use of a deep neural network with additional hidden layers and nodes per layer. The set of variables utilized in the CSVv2 algorithm was extended to include more charged particle tracks for training. The DeepCSV tagger outperforms the CSVv2 algorithm, with an absolute b-tagging efficiency improvement of about 4% for a mis-identification probability for light flavor jets of 1% [145].

Both for the CSVv2 and DeepCSV algorithms, three working points (Tab. 7.16) are defined as the values of the discriminator cut for which the rate for mis-identifying a light jet as a b jet is 10% (*loose*), 1% (*medium*) and 0.1% (*tight*). Fig. 7.43 shows the b-tagging efficiency in simulation for the DeepCSV algorithm as an example, as a function of jet p_T , jet η and number of pileup interactions. The b-jet identification efficiency measured in simulated $t\bar{t}$ events, and integrated over the p_T and η phase space of jets, is listed in Tab. 7.15. Similar to the procedure used for τ_h tagging, scale factors are derived to correct the b-jet identification efficiency in simulation, with the purpose of matching the b-tagging efficiency observed in data, and using the methods described in Ref. [142].

Input variable	Run I CSV	CSVv2
SV 2D flight distance significance	✓	✓
Number of SV	–	✓
Track η_{rel}	✓	✓
Corrected SV mass	✓	✓
Number of tracks from SV	✓	✓
SV energy ratio	✓	✓
$\Delta R(SV, \text{jet})$	–	✓
3D IP significance of the first four tracks	✓	✓
Track $p_{T,rel}$	–	✓
$\Delta R(\text{track}, \text{jet})$	–	✓
Track $p_{T,rel}$ ratio	–	✓
Track distance	–	✓
Track decay length	–	✓
Summed tracks E_T ratio	–	✓
$\Delta R(\text{summed tracks}, \text{jet})$	–	✓
First track 2D IP significance above c threshold	–	✓
Number of selected tracks	–	✓
Jet p_T	–	✓
Jet η	–	✓

Table 7.14: Input variables used for the Run I version of the CSV algorithm and for the CSVv2 algorithm. The definition of the variables can be found in Ref. [142].

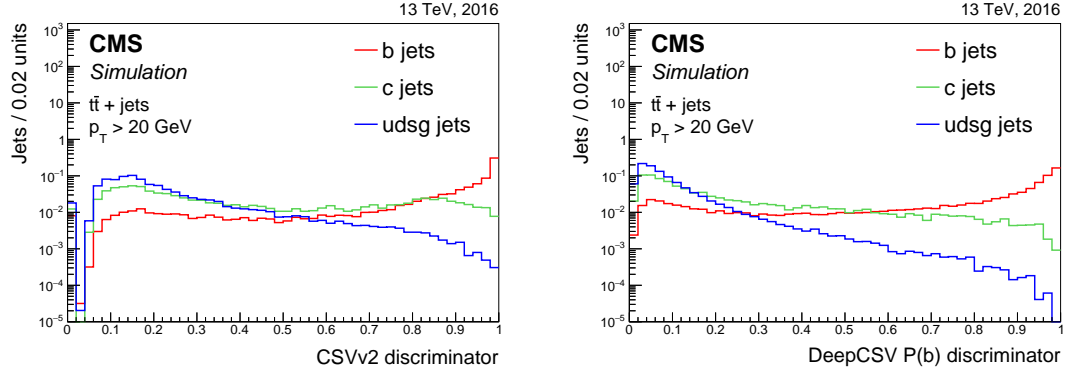


Figure 7.42: Distributions of the CSVv2 (left) and DeepCSV (right) discriminator values for jets of different flavors in $t\bar{t}$ events simulated with 2016 experimental conditions, normalized to unit area. (Adapted from [142]).

Algorithm	Working point	ϵ_b [%]	ϵ_c [%]	ϵ_{udsg} [%]
CSVv2	Loose (CSVv2 L)	81	37	8.9
	Medium (CSVv2 M)	63	12	0.9
	Tight (CSVv2 T)	41	2.2	0.1
DeepCSV	Loose (DeepCSV L)	84	41	11
	Medium (DeepCSV M)	68	12	1.1
	Tight (DeepCSV T)	50	2.4	0.1

Table 7.15: Taggers, working points and identification efficiency for b-jets with $p_T > 20$ GeV in simulated $t\bar{t}$ events (Adapted from [142]).

Algorithm	Working point	Discriminator cut		
		2016	2017	2018
CSVv2	Loose (CSVv2 L)	0.543	0.580	–
	Medium (CSVv2 M)	0.848	0.884	–
	Tight (CSVv2 T)	0.954	0.969	–
DeepCSV	Loose (DeepCSV L)	0.222	0.152	0.124
	Medium (DeepCSV M)	0.632	0.494	0.418
	Tight (DeepCSV T)	0.895	0.800	0.753

Table 7.16: Discriminator cuts for the various working points and taggers. CSVv2 was not available for use in 2018 data.

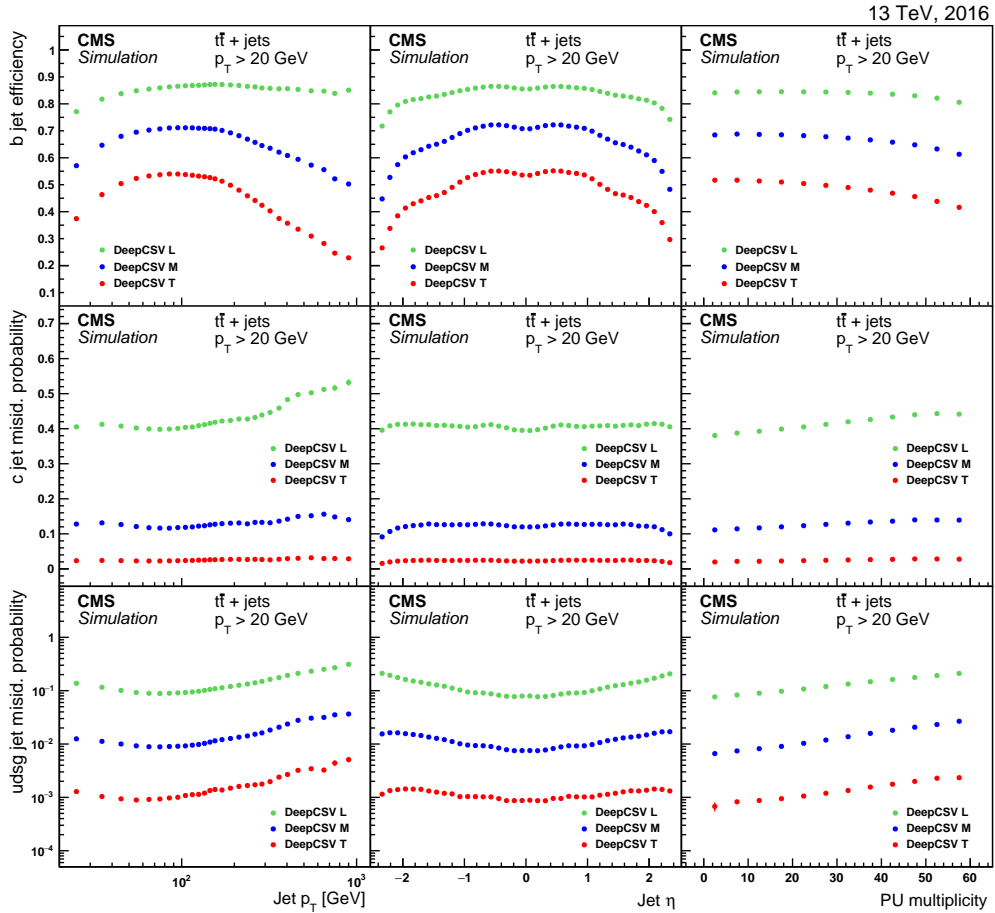


Figure 7.43: Efficiencies and mis-identification probabilities for the DeepCSV tagger as a function of jet p_T , jet η and PU multiplicity for b, c, and light flavor jets in $t\bar{t}$ for the various working points. (Adapted from [142]).

CHAPTER 8

Data and simulation samples

In this chapter, a brief description of the data and simulation samples used in the VBF SUSY analysis is presented. A particular emphasis is placed on signal simulation samples, by including validation studies of the kinematic distributions of signal events, which can be seen as a first introduction to the motivation of the analysis strategy presented in the next chapter. The process of simulation samples can be divided in three main steps.

All the samples of simulated signal background events are generated using MC event generators. The description of the parton shower, hadronization, and fragmentation processes for the particles generated in the events is done with the PYTHIA v8.212 [146] program.

The hard scattering component of a simulated hadron-hadron collision consists of particles from the hadronization of partons, whose kinematics are predicted with perturbative matrix elements, together with partons from initial state radiation (ISR) and final state radiation (FSR), simulated with a showering algorithm. The beam-beam remnants (BBR) and particles resulting from multiple-parton interactions (MPI) compose what is known as the *underlying event* (UE). The accurate description of the observables sensitive to the UE requires a good description of BBR, MPIs, a good modeling of hadronization, ISR, and FSR. PYTHIA have adjustable parameters to control the behavior of their event modeling. A set of these parameters, adjusted to fit some aspects of the data is known as a *tune*. The tunes used for the simulation sample generation are described in Refs. [147] and [148].

Additional pileup interactions are generated with PYTHIA as well, and superimposed on the primary collision process. After the generated events are processed through PYTHIA, the particles are processed through a detailed simulation of the CMS apparatus using the GEANT4 package [149].

8.1 Signal simulation samples

This section is a continuation of the discussion in Section 4.2. Signal samples are produced with the MADGRAPH5_AMC@NLO (MG5) [150] v2.3.3 and v2.4.2 generator, at leading order (LO) precision. The CP2 PYTHIA tune was used, which relies on the NNPDF3.1 parton distribution function (PDF) set at LO [151].

An R-parity conserving simplified MSSM model is used for the generation of these samples. To ensure the consideration of events where electroweakinos were produced purely via electroweak vector boson fusion, Feynman diagrams are required to not have α_{QCD} vertices and the SUSY colored sector is decoupled.

Depending on the decay scenario, this is achieved by setting all the masses of the particles that belong to this sector to large values (10^5 GeV), compared to the mass ranges for the electroweakinos and sleptons of interest. Additionally, these particles are excluded in the MG5 generation com-

mands to further reduce the number of Feynman diagrams included in the event generation, and, consequently, reducing the amount of computing time for sample production.

Different Δm values are considered in the range between 0.5 and 75 GeV. The motivation for the minimum Δm is that it is the upper bound at which $\tilde{\chi}_1^\pm$ and $\tilde{\chi}_2^0$ become long-lived particles; the maximum value was chosen such that we remain below the boundary for which we obtain on-mass shell W^*/Z^* decays. A generator level cut has been imposed on the angular η separation between the jets of $|\Delta\eta(jj)| > 3.5$, to further suppress any contributions from non VBF diagrams. The specific details for each SUSY scenario considered are described in the remainder of this subsection. For the non-SUSY interpretation, which corresponds to the anapole dark matter, a dedicated MG5 model based on a EFT was used.

Five sets of the MC signal simulation samples were centrally produced by the CMS collaboration. The relevant parameters for the event generation with MG5, and the scan over the $(m(\tilde{\chi}_2^0), \Delta m)$ phase space is summarized in Tables 8.1, 8.2 and 8.3.

For the $\tilde{\tau}$ -dominated decays interpretation, the scan in Δm starts at 5 GeV, which is the first smallest value possible to have at least one τ lepton in the final state ($m(\tau) = 1.78$ GeV). In addition, $\tilde{\tau}$ leptons are considered to be fully left-handed ($\tilde{\tau} = \tilde{\tau}_1 = \tilde{\tau}_L$).

Sample set	Scenario	Branching ratios
I	democratic light slepton	$\mathcal{B}(\tilde{\chi}_1^+ \rightarrow \tilde{\ell}\nu_\ell) = \frac{1}{3}$, $\mathcal{B}(\tilde{\ell} \rightarrow \tilde{\chi}_1^0 \ell) = 1$, $\mathcal{B}(\tilde{\chi}_2^0 \rightarrow \ell^\pm \ell^\mp) = \frac{1}{3}$
II	$\tilde{\tau}$ -dominated	$\mathcal{B}(\tilde{\chi}_1^+ \rightarrow \tilde{\tau}\nu_\tau) = 1$, $\mathcal{B}(\tilde{\chi}_2^0 \rightarrow \tilde{\tau}\tau) = 1$, $\mathcal{B}(\tilde{\tau} \rightarrow \tilde{\chi}_1^0 \tau) = 1$
III	virtual WZ decays	$\mathcal{B}(\tilde{\chi}_1^+ \rightarrow \tilde{\chi}_1^0 W^*) = 1$, $\mathcal{B}(\tilde{\chi}_2^0 \rightarrow \tilde{\chi}_1^0 Z^*) = 1$
IV	higgsino	$\mathcal{B}(\tilde{\chi}_1^+ \rightarrow \tilde{\chi}_1^0 W^*) = 1$, $\mathcal{B}(\tilde{\chi}_2^0 \rightarrow \tilde{\chi}_1^0 Z^*) = 1$

Table 8.1: Description of the signal data sets, including details on branching ratios for the SUSY signal interpretations.

Sample set(s)	Fixed parameters		Variable parameters	
	Mixing matrices		$m(\tilde{\chi}_2^0)$ points [GeV]	Δm points [GeV]
I, II, III	NMIX ($\tilde{\chi}_i^0$)	$N_{11} = 1, N_{22} = 1, N_{33} = N_{34} = N_{43} = -N_{44} = \frac{1}{\sqrt{2}}$	100, 125, 150, 175, 200, 225, 250, 275, 300, 325, 350, 375, 400	0.5, 1, 5, 10, 15, 20, 30, 40, 50, 60, 75
	UMIX, VMIX ($\tilde{\chi}_j^\pm$)	$U_{11} = V_{11} = U_{22} = V_{22} = 1$		
	TAUMIX ($\tilde{\tau}$)	$O_{11} = O_{22} = 1$		
IV	NMIX ($\tilde{\chi}_i^0$)	$N_{13} = N_{14} = N_{23} = -N_{24} = \frac{1}{\sqrt{2}}, N_{31} = 1, N_{42} = 1$	50, 75, 100, 125, 150, 175, 200	0.5, 1, 5, 10, 15, 20, 30, 40, 50, 60, 75
	UMIX, VMIX ($\tilde{\chi}_j^\pm$)	$U_{12} = V_{12} = -1, U_{21} = V_{21} = 1$		

Table 8.2: Mixing parameters and values of the $(m(\tilde{\chi}_2^0), \Delta m)$ scan for the SUSY signal interpretations.

Set	Fixed parameters	Variable parameters		Number of events
		Λ [GeV]	$m(\tilde{\chi})$ [GeV]	
V	$g = 1$	500, 750, 1000, 1250, 1500, 1750, 2000	0.1, 1, 10, 50, 100, 200, 300, 400, 500, 750, 1000	Per sample: 100,000; Total: 7,700,000

Table 8.3: Mixing parameters, values of the $(\Lambda, m(\chi))$ scan for the ADM interpretation.

Validation of the signal MC samples

As a form of validation, the relevant kinematic distributions for simulated signal events are presented, produced samples with the parameters described in the previous section for some of the physics interpretations considered.

Wino-bino model with virtual W/Z decays.

Some of the kinematic distributions obtained at parton level for the electroweinos produced in a VBF process are included in Figs. 8.1 and 8.2. We can observe that for larger masses, the $\tilde{\chi}_i$'s are more boosted.

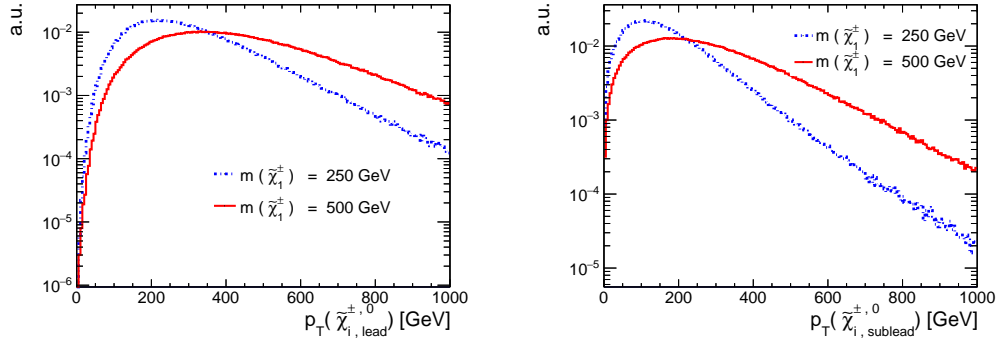


Figure 8.1: Transverse momentum distributions for the (left) leading and (right) sub-leading $\tilde{\chi}_i$.

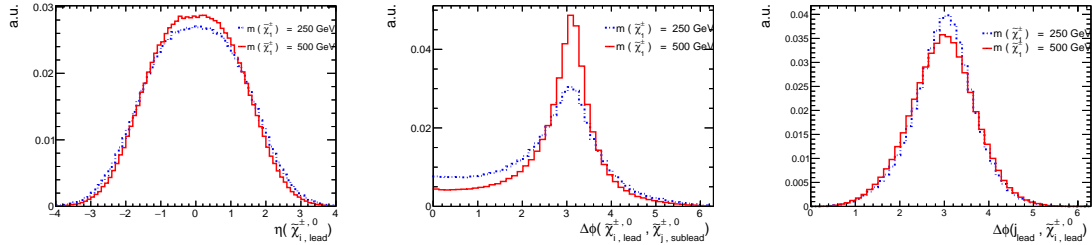


Figure 8.2: Angular (left) $\eta(\tilde{\chi}_{i,lead})$ (middle) $\Delta\phi(\tilde{\chi}_{i,lead}, \tilde{\chi}_{j,sublead})$ and (right) $\Delta\phi(\tilde{\chi}_{j,lead}, j_{i,lead})$ distributions.

From these distributions, we can infer that electroweinos are produced in the central η -direction of the detector and back-to-back on the ϕ -plane with respect to each other. Additionally, $\tilde{\chi}_i$'s travel

in the opposite direction of the leading jet in the ϕ -plane. A diagram of the particle directions is shown in Fig. 8.3.

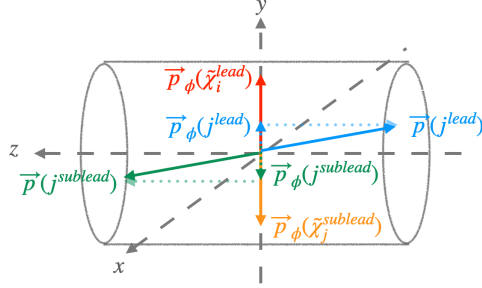


Figure 8.3: Example diagram of relative \vec{p} between $\tilde{\chi}'_i$ s and VBF jets.

In Figure 8.4, distributions for the VBF jets are presented. It can be seen that jets are more energetic with larger $\tilde{\chi}_i$ masses, since a higher boost is required to radiate energetic enough weak bosons which will later produce the electroweakinos. These jets are mainly produced in the forward η regions as expected in VBF processes. This effect is also seen in the invariant dijet mass, which scales with $m(\tilde{\chi}_i)$ as expected.

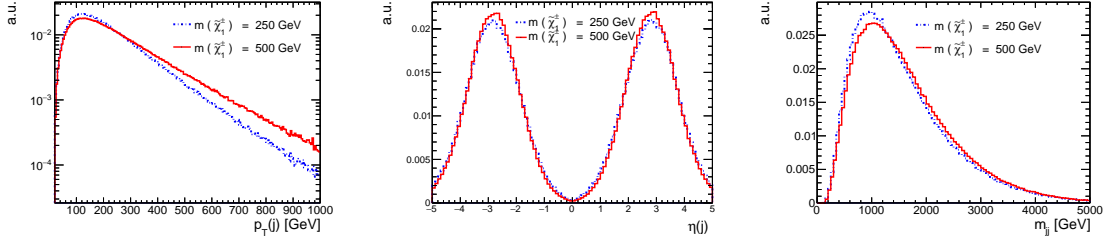


Figure 8.4: Kinematic distributions for the (right) jet transverse momentum, (middle) jet pseudorapidity and (left) invariant dijet mass.

Higgsino model with virtual W/Z decays

For this scenario, the same distributions as in the physics interpretation considered previously were obtained, and are included in Figs. 8.5, 8.6, and 8.7). In this case, a dependence between $p_T(\tilde{\chi}_i)$ and $m(\tilde{\chi}_i)$ is observed as well. However, the fraction of events with a smaller angular separation between $\tilde{\chi}_i$'s is larger than in the wino-bino case, showing the difference in dominant VBF mechanisms (t-channel vs. s-channel). Jet kinematic distributions are also consistent with the VBF topology.

The invariant mass distribution for the two lepton pair is plotted, comparing the wino-bino and higgsino scenarios for two benchmark $m(\tilde{\chi}_2^0)$ and $m(\tilde{\chi}_1^0)$ (Fig. 8.8). These distributions are compatible with the theoretical constraints in a pure higgsino model ($m(\tilde{\chi}_2^0) \times m(\tilde{\chi}_1^0) < 0$), further validating the use of the correct set of generator parameters.

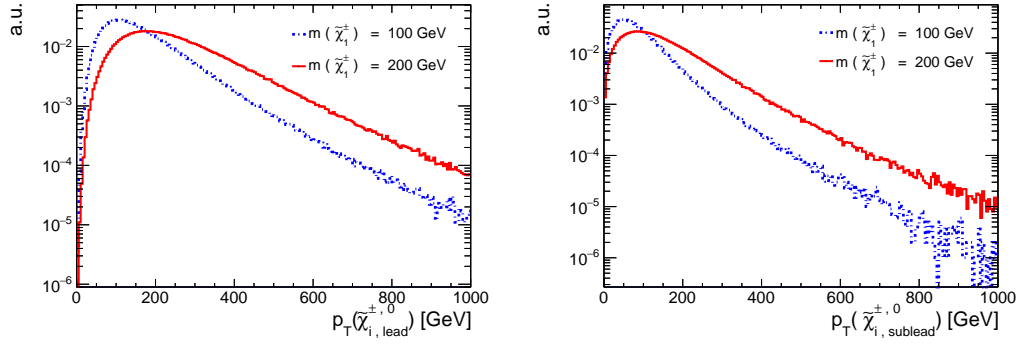


Figure 8.5: (Transverse momentum distributions for the (left) leading and (right) sub-leading $\tilde{\chi}_i$.

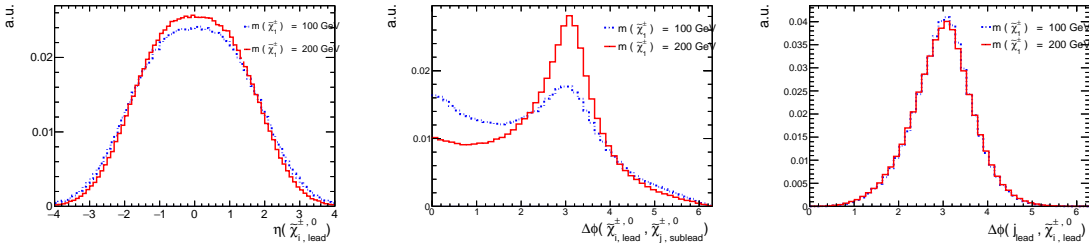


Figure 8.6: Angular (left) $\eta(\tilde{\chi}_{i,lead})$ (middle) $\Delta\phi(\tilde{\chi}_{i,lead}\tilde{\chi}_{j,lead})$ and (right) $\Delta\phi(\tilde{\chi}_{i,sublead}\tilde{\chi}_{j,sublead})$ distributions.

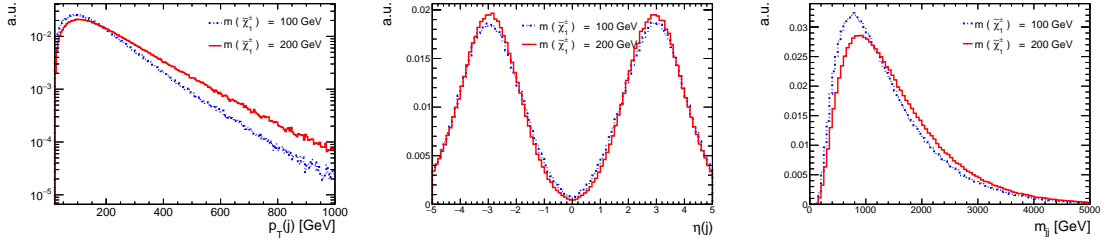


Figure 8.7: Kinematic distributions for the (right) jet transverse momentum, (middle) jet pseudo-rapidity and (left) invariant dijet mass.

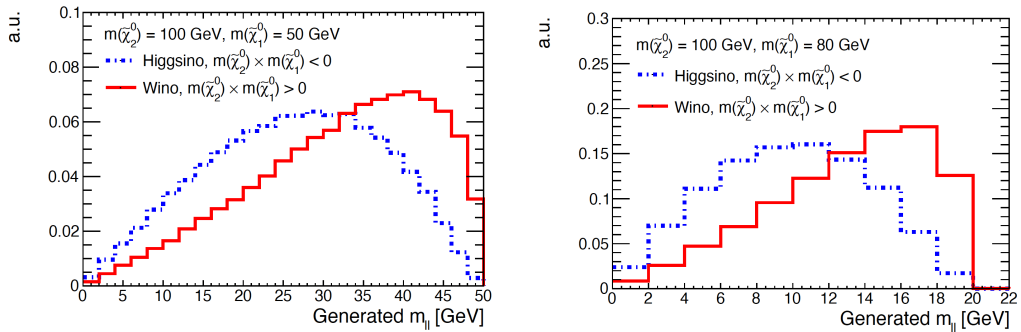


Figure 8.8: Dilepton invariant mass distribution for two example combinations of $\{m(\tilde{\chi}_2^0), m(\tilde{\chi}_1^0)\}$. in the wino-bino and higgsino scenarios.

Anapole DM

For this scenario, distributions for jet kinematics as well as missing transverse momentum were obtained at parton level (Fig. 8.9). Compared to the distributions obtained in the SUSY physics interpretations, the jet transverse momentum spectrum is softer, because the $\chi\chi$ production occurs predominantly through s-channel interactions. The same argument applies for the observed jet η distribution, showing more forward jets, which in turn results in larger $m(jj)$ values.

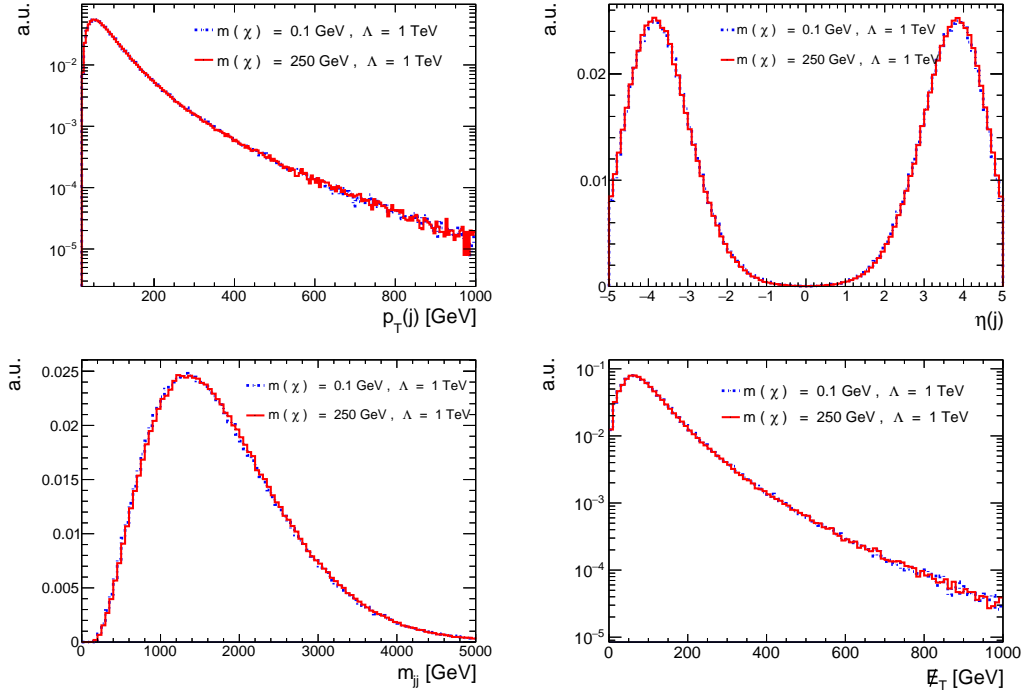


Figure 8.9: Kinematic distributions for jet transverse momentum, jet pseudorapidity, invariant dijet mass, and missing transverse momentum for the ADM interpretation.

8.2 Background simulation samples

The composition of the SM background processes in the signal regions will vary, depending on the final state of each channel, particularly the lepton multiplicity. In the next chapter, a detailed description of the relevant processes and the signal regions is included. Generally speaking, the SM processes typically produced in pp collisions are top-antitop ($t\bar{t}$) quark pairs, single top quark production, W+jets, Z+jets, double weak boson production (*diboson*), and QCD multijet events.

The $Z/\gamma^*(\rightarrow \ell^+\ell^-)+\text{jets}$, $Z(\rightarrow \nu_\ell\bar{\nu}_\ell)+\text{jets}$ and $W(\rightarrow \ell\nu_\ell)+\text{jets}$ backgrounds are simulated at LO precision with the MG5 event generator. Up to four partons in the final state are included in the matrix element calculation. The background processes involving the production of a single weak boson in association with two jets, exclusively through pure electroweak interactions (denoted as EWK V+jets) is simulated at LO with MG5. The QCD multijet background is simulated at LO with MG5 as well, and these samples are used to estimate the contribution from these events in

control regions where QCD events are not a dominant background. Single top and $t\bar{t}$ events are simulated with the POWHEG (PH) [152, 153, 154, 155, 156] v2.0 generator at next-to-leading (NLO) order. For the various diboson processes, the MG5 and PH event generators were used, as well as the LO PYTHIA v8.212 generator. Separate samples containing processes where two weak bosons are produced via electroweak interactions are included and studied under the diboson category.

As mentioned at the beginning of this chapter, the events generated by MG5 and PH are interfaced with PYTHIA, to describe the parton shower, the hadronization, and fragmentation processes. The tunes considered for these samples are CUETP8M1 and CP5. The NNPDF3.0 [157] and NNPDF3.1 LO and NLO PDFs are used in the event generation. The MLM matching scheme [158] is used to remove the double counting of the partons generated with MG5 and PH interfaced with PYTHIA. The NLO cross sections are used to normalize simulated backgrounds.

8.3 Data samples

The data sample used for this analysis corresponds to pp collision event data collected by the CMS detector at $\sqrt{s} = 13$ TeV during the LHC Run II. The full data sample corresponds to an integrated luminosity of $\mathcal{L}_{int} = 137.1 \text{ fb}^{-1}$, divided in three subsets, one per year of the LHC Run II. The integrated luminosities are 35.92 fb^{-1} , 41.53 fb^{-1} , and 59.74 fb^{-1} for the data sets collected in 2016, 2017, and 2018, respectively. These data sets are passed through a data quality certification, and only those run ranges and luminosity sections validated as “good” are selected for analysis.

As briefly described in Sec. 5.2, the pp interaction rate at design luminosity ($1 \times 10^{34} \text{ cm}^{-2}\text{s}^{-1}$) exceeds 1 GHz. From all these collision events, only a small fraction contains hard-scattering pp interactions of interest to the CMS physics program. Furthermore, only a smaller fraction can be stored for later analysis. The trigger system is designed to select such interesting events for offline storage and analysis [159, 160].

There are two levels in the CMS trigger system. The first level (L1) is implemented in custom hardware, and selects events containing candidate objects based on ionization deposits, energy clusters, or tracks with specific characteristics. The second level (HLT) is implemented in software and refines the event selection based on a programmable menu, that focuses on specific candidate objects. For each event, objects like electrons, muons, jets, hadronic taus, etc., are reconstructed and identification criteria are applied in order to select only those events of potential interest for data analysis [159]. This results in several *primary data sets*, whose main difference relies in the HLT menu used to select and store collision events. Another important concept in the HLT system is the *HLT path*, a set of algorithmic processing steps run in a predefined order that both reconstructs physics objects and makes selections on such objects [159]. In Chapters 9–10, the trigger requirements used both in the SRs and CRs will be listed as a requirement on the trigger path.

The primary sets considered in the SRs of this data analysis are collected with p_T^{miss} -based triggers. The primary data sets used in some of the CRs, utilize muon-, electron-, or hadronic tau-based triggers, in order to understand the modeling of selection efficiencies for specific backgrounds, which contain one of these objects in the final state. For example, in a control sample with $Z(\rightarrow \tau_h \tau_h) + \text{jets}$ events, the primary data sets used were obtained using a single- τ_h trigger.

Given that the reconstruction of the physics objects is done in a short window of time at L1, once the collision events are processed through HLT, and further refinement occurs when running the PF algorithm and the algorithms described in Chapter 7, the efficiency of the event selections used at trigger level and at analysis level, most likely, will not be exactly the same.

Therefore, dedicated studies need to be performed to measure the trigger efficiency as a function of the variable(s) used for the trigger decision. The results from these studies help the analyzers to either select the most optimal cut value for a given selection based on where the trigger efficiency plateau is found, or, derive correction factors to match the efficiency to unity, in case the cut value for the given selection is chose outside the plateau. To end this chapter, I present a summary of a trigger efficiency study for the p_T^{miss} -based trigger used in this data analysis, and will serve as an illustration of the discussion in the last paragraph.

Efficiency of a missing transverse momentum trigger

The collision events selected for the search regions in this analysis are required to fire the trigger path named `HLT_PFMETNoMu120_PFMHTNoMu120_IDTight`, which will be referred to as the MET¹ trigger throughout this section. The efficiency of this trigger is measured in a standard $W(\rightarrow \mu\nu_\mu)+\text{jets}$ control sample. The data samples used to create this control region correspond to the single muon data sets, where events are selected with a single muon trigger.

Events are required to pass the `HLT_IsoMu24_eta2p1` trigger. To ensure good purity of $W(\rightarrow \mu\nu_\mu)+\text{jets}$ events, only events with exactly one muon, with $p_T > 30$ GeV, $|\eta| < 2.1$, and passing tight muon ID are considered. The muon p_T selection is selected in such a way that the trigger efficiency is close to unity and on the plateau².

In addition, the VBF selections used in the SR (VBF1, Tab. 9.4), with the purpose of studying events that have signal-like topology. A relatively low p_T^{miss} selection of $p_T^{\text{miss}} > 50$ GeV is applied to these events as well, in order to study the trigger efficiency curve as a function of the offline³ p_T^{miss} . The set of selections described until now, will be referred as the nominal $W+\text{jets}$ CR.

The efficiency of this trigger is then defined as

$$\epsilon_{\text{trigger}} = \frac{N[\text{W} + \text{jets AND pass MET trigger}]}{N[\text{W} + \text{jets}]} \quad (8.1)$$

The trigger efficiency as a function of p_T^{miss} for data and MC backgrounds is shown in Fig. 8.10. The simulated backgrounds are dominated by $W+\text{jets}$ events, where the jets come from ISR (referred to as “all bkg”). A separate simulation sample for VBF W production events, where the jets will correspond to VBF jets is included in this study.

The events in this control regions where further classified into events with both jets lying in the *central* region ($|\eta| < 3$), and events with one central jet and one *forward* jet ($3 < |\eta| < 5$). As seen from the trigger efficiency curves, data and the two sets of simulation samples reach nearly 100%

¹MET: missing transverse energy.

²For reference purposes, see Figure 25 in Ref. [159].

³“Offline p_T^{miss} ” refers to the reconstructed and calibrated p_T^{miss} obtained after the data processing as described in Chapter 7.

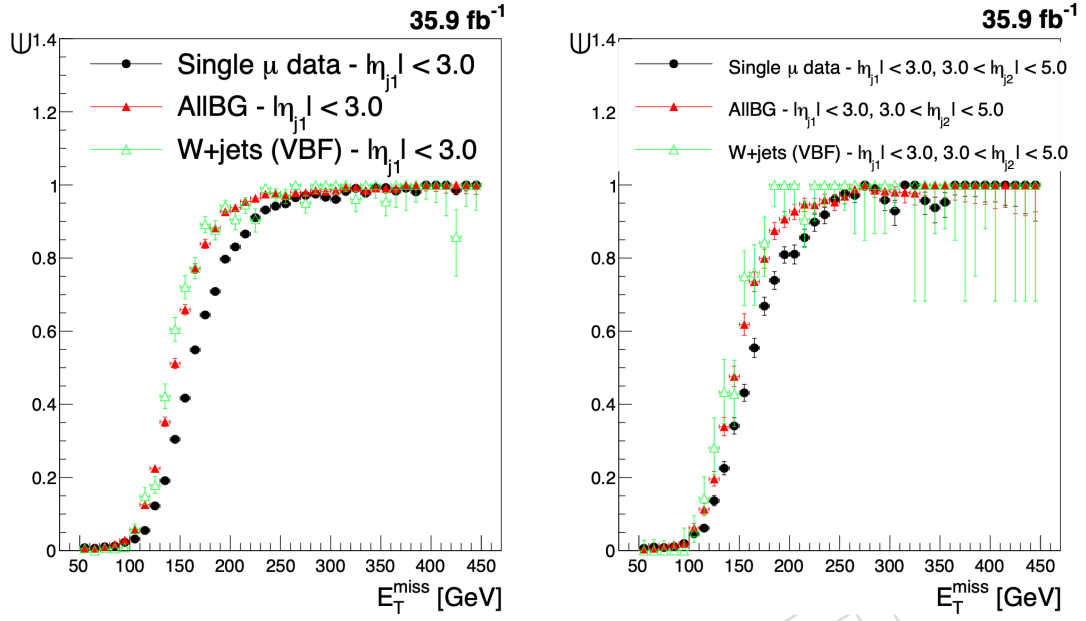


Figure 8.10: Efficiency of the HLT_PFMETNoMu120_PFMHTNoMu120_IDTight trigger as a function of the offline p_T^{miss} .

efficiency for $p_T^{\text{miss}} > 250$ GeV. Therefore, to remain in this regime, we make use of such selection in all the SRs of this analysis, as described in Chapter 9.

CHAPTER 9

Analysis strategy

9.1 Description of analysis strategy

The signal processes in the different physics interpretations are characterized by final states with multiple leptons, two energetic jets produced in opposite hemispheres of the detector with a large separation in $\Delta\eta$, large dijet invariant mass $m(\text{jj})$, and large $p_{\text{T}}^{\text{miss}}$ (Figs. 9.1-9.3). More details about the characteristics of these objects in the signal events can be found below.

Leptons.

Given that we are interested in the compressed mass spectrum regions of the SUSY phase space, the leptons resulting from the decays of SUSY particles will be soft (low momentum). The experimental reconstruction and identification of the leptons is challenging, despite the great capabilities of the CMS detector. Therefore, this analysis includes final states with zero (invisible), one, and two soft leptons, with the purpose of accounting for soft leptons that are lost in the reconstruction and identification stages. This results in three main decay channels, divided in 16 exclusive final states, defined by the lepton flavor(s), multiplicity, and charge combinations (2-lepton channels):

- *0-lepton*: no leptons in the final state ($0\ell+\text{jj}$),
- *1-lepton*: $e+\text{jj}$, $\mu+\text{jj}$, and $\tau_{\text{h}}+\text{jj}$,
- *2-lepton*: $ee+\text{jj}$, $e\mu+\text{jj}$, $\mu\mu+\text{jj}$, $e\tau_{\text{h}}+\text{jj}$, $\mu\tau_{\text{h}}+\text{jj}$, and $\tau_{\text{h}}\tau_{\text{h}}+\text{jj}$ with opposite-sign (OS) and like-sign (LS) charge combinations analyzed separately.

Each main decay channel is targeted to cover a specific region of the compressed mass spectra SUSY parameter space. The invisible channel will provide the best sensitivity for scenarios where $\Delta m(\tilde{\chi}_2^0, \tilde{\chi}_1^0) < 25$ GeV; the 1-lepton channels will have the largest sensitivity to the $25 < \Delta m(\tilde{\chi}_2^0, \tilde{\chi}_1^0) < 50$ GeV range, and the 2-lepton channels to the $\Delta m(\tilde{\chi}_2^0, \tilde{\chi}_1^0) \geq 50$ GeV range.

VBF jets and $p_{\text{T}}^{\text{miss}}$.

The jets produced as a result of the VBF interaction are expected to fall in at least one of the forward regions of the detector. The main experimental challenge that forward jets pose is the degradation of the quality of the JES and JER calibrations. Since the acceptance of the tracking system does not cover the most forward regions (pixel detector coverage up to $|\eta| = 2.1$ and strips detector up to $|\eta| = 2.5$), the performance of the pileup mitigation techniques is limited both for the charged and neutral components. This is specially true for jets with p_{T} between 30 and 60 GeV.

Although this can be solved by only considering jets with $p_{\text{T}} > 60$ GeV, the signal acceptance can be affected if jets with a p_{T} below this threshold are rejected. This would particularly affect

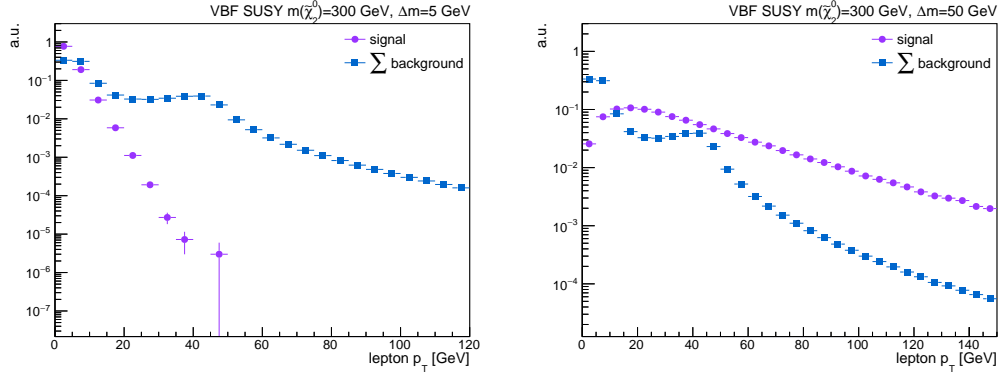


Figure 9.1: Initial kinematic comparison for the lepton p_T distribution between signal and the sum of all expected backgrounds with two different $\Delta m(\tilde{\chi}_2^0, \tilde{\chi}_1^0)$ scenarios.

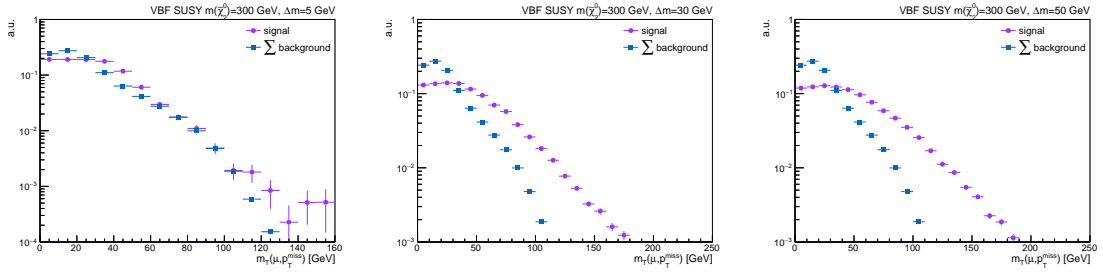


Figure 9.2: Initial kinematic comparison for the $m_T(\mu, p_T^{\text{miss}})$ distribution between signal and the sum of all expected backgrounds with three different $\Delta m(\tilde{\chi}_2^0, \tilde{\chi}_1^0)$ scenarios.

compressed mass spectrum scenarios with $\Delta m(\tilde{\chi}_2^0, \tilde{\chi}_1^0) \geq 50$ GeV. To accommodate the differences in VBF topologies for the various $\Delta m(\tilde{\chi}_2^0, \tilde{\chi}_1^0)$ considered, two different sets of “VBF selections” are considered, referred to as VBF1 and VBF2, and described on Tab. 9.4.

A high p_T^{miss} is expected in the signal region, mainly produced by the presence of the VBF jets¹. Events firing a p_T^{miss} -based trigger are selected for analysis in the signal region, as described in Sec. 8.3. The use of such trigger is motivated by the ability to select leptons free from trigger bias², making possible to consider leptons with very low p_T ($p_T < 70$ GeV). A potential limitation of this approach is that a relatively large p_T^{miss} requirement is needed, driven by the p_T range at which the trigger efficiency is consistent with unity.

The event selections in the signal region are divided in two general categories:

- *Central selections*: these are related to physics objects reconstructed within the acceptance of the pixel tracker system ($|\eta| < 2.1$), and include selections on: lepton kinematics, topological requirements on the leptons (for example, the transverse mass between a lepton and p_T^{miss} , $m_T(\ell, p_T^{\text{miss}})$), as well as the missing transverse momentum p_T^{miss} ;
- *VBF selections*: these are related to the kinematic requirements imposed on the jets present in the event. To be consistent with the VBF hypothesis, the following topological selections are considered: each event must contain at least two jets with large η separation, in opposite hemispheres ($\eta(j_1) \times \eta(j_2)$), and with a large dijet invariant mass $m(jj)$.

The strategy used to assess the presence of signal in data will be to perform a fit of the observed data to the predicted leading dijet invariant mass ($m_{\text{lead}}(jj)$) spectrum. The use of this technique qualifies this analysis as a *shape-based analysis* [161].

Several known SM processes can mimic the final state expected for signal processes, and they are referred to as **SM background processes**. Based on the particles in the final state, the potential main backgrounds for this analysis are: events with (1) W or Z production associated with jets (V+jets, with V=W, Z), (2) top-anti-top ($t\bar{t}$) quark pairs, (3) double weak boson production (VV) and events only containing SM jets produced via the strong interaction, referred to as QCD multijet events (Figs. 9.4-9.5).

The contribution from each background process to the signal region will vary depending on the final state considered. For example, in final states containing at least one τ_h , the QCD multijet events will be the dominant background, whereas in the 2-light lepton final states, the greatest contribution will come from Z+jets or $t\bar{t}$ events.

A summary of the dominant backgrounds in each channel is presented in Tab. 9.1. In the next chapter, the event selections used in the signal region as well as their optimization are outlined. The complete description of the background estimation methodology as well as the results are presented in Chapter 10.

¹Recall that p_T^{miss} is defined as the negative sum of the vectorial p_T of the visible objects.

²The trigger efficiency will be close to unity regardless of the lepton p_T selections, as long as the p_T^{miss} selection is on the efficiency plateau. This would not be possible if lepton-based triggers were used, unless dedicated trigger efficiency corrections are derived and applied. For illustration purposes, see Figure 25 in Ref. [159].

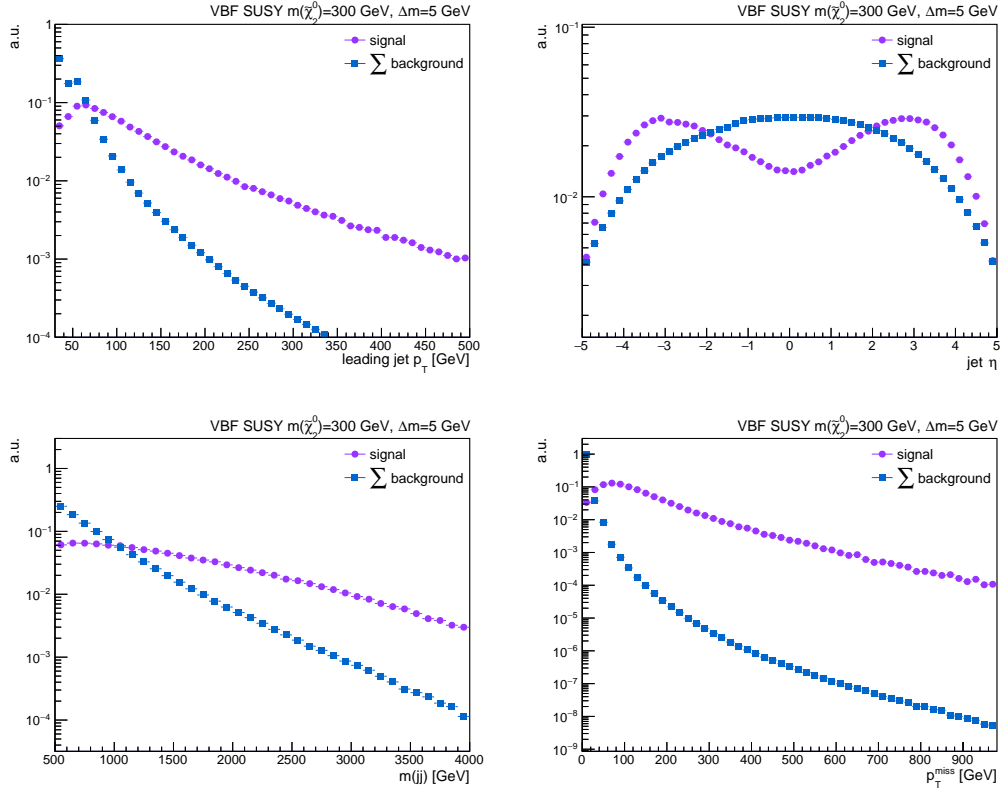


Figure 9.3: Initial kinematic comparison for the jet $p_{T,j}$, jet η , leading $m(jj)$, and p_T^{miss} distributions between signal and the sum of all expected backgrounds.

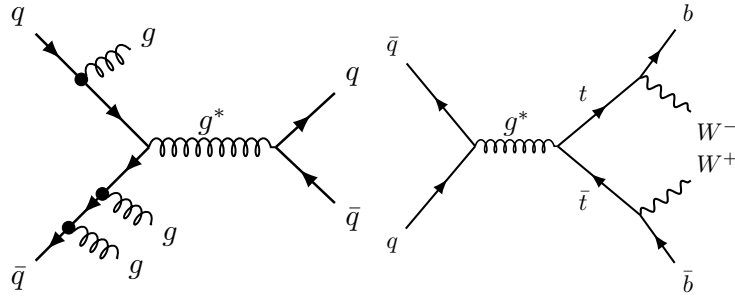


Figure 9.4: Representative Feynman diagrams for the $t\bar{t}$ and QCD multijet production. We assume $W \rightarrow \ell\nu_\ell$.

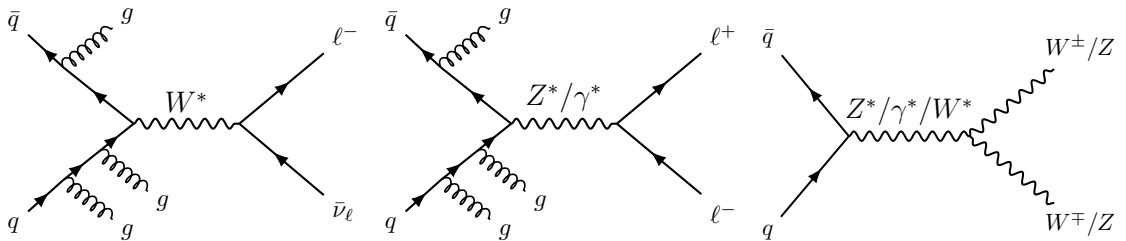


Figure 9.5: Representative Feynman diagrams for W +jets, Z +jets and diboson production. We assume $W \rightarrow \ell\nu_\ell$ and $Z \rightarrow \ell^+\ell^-$.

Decay channel	Dominant background	Final states
$0\ell+jj$	W+jets Z+jets	W($\rightarrow \ell\nu$), ℓ lost in reconstruction Z($\rightarrow \nu\nu$)
$\ell+jj$	$t\bar{t}$ W+jets QCD multijets	$t\bar{t} \rightarrow \ell\nu + \text{hadrons}$ W($\rightarrow \ell\nu$) or fully hadronic decays (τ_h+jj) jet $\mapsto \tau_h$
$2\ell+jj$	$t\bar{t}$ W+jets Z+jets Diboson QCD multijets	all decay channels all decay channels (LS) Z($\rightarrow \ell^+\ell^-$) leptonic decays $\ell\tau_h+jj$ channels with jet $\mapsto \tau_h$

Table 9.1: Selection criteria for the loose and tight muon ID definitions.

9.2 Signal region event selections

Continuing the discussion started in Sec. 9.1, the definitions of the physics objects in the signal region are listed in Tabs. 9.2-9.3, and the event selections in Tabs. 9.5-9.4.

Object	Selection cuts
e	Medium WP of the cut-based ID, $10 < p_T(e) < 40$ GeV, $ \eta(\mu) < 2.1$
μ	Tight WP of the muon ID, $I_\mu < 0.15$, $8 < p_T(\mu) < 40$ GeV, $ \eta(\mu) < 2.1$
τ_h	Tight WPs of anti-jet, anti- e and anti- μ discriminators of the DEEPTAU algorithm $20 < p_T(\tau_h) < 40$ GeV, $ \eta(\tau_h) < 2.1$, 1 or 3 prongs,
Jet	for $30 < p_T \leq 50$ GeV, tight WP of the PU jet ID, for $p_T > 50$ GeV loose (tight) PF jet ID in 2016 (2017-2018) $p_T(j) > 30$ GeV, $ \eta(j) < 4.7$, $\Delta R(e/\mu/\tau_h, j) > 0.4$
b-jet	Medium WP of the DeepCSV b-jet discriminator, $p_T(b) > 30$ GeV, $ \eta(b) < 2.4$

Table 9.2: Definition of physics objects in the signal regions.

Object	Selection cuts
e veto	$p_T(e) > 10$ GeV
additional e veto	$p_T(e) > 40$ GeV
μ veto	$p_T(\mu) > 8$ GeV
additional μ veto	$p_T(\mu) > 40$ GeV
τ_h veto	$p_T(\tau_h) > 20$ GeV
additional τ_h veto	$p_T(\tau_h) > 40$ GeV

Table 9.3: p_T requirements for the lepton vetoes applied in the signal regions.

	Object	Selection cuts
	Trigger	HLT_PFMETNoMu120_PFMHTNoMu120_IDTight
Central	Lepton requirements	Listed on Tab.9.5
	b-jet veto	$N(b) = 0$
	p_T^{miss}	$p_T^{\text{miss}} > 250$ GeV
	$m_T(\ell, p_T^{\text{miss}})$	$m_T(\ell, p_T^{\text{miss}}) > 110$ GeV (only 1-lepton channels)
VBF1	Jets	$N(j) \geq 2$ with $p_T(j) > 60$ GeV
	Dijet combinations	$N(j_1, j_2) \geq 1$, $\Delta\eta(j_1, j_2) > 3.8$, $\eta(j_1) \times \eta(j_2) < 0$, $m(j_1, j_2) > 1000$ GeV
VBF2	Jets	$N(j) \geq 2$ with $p_T(j) > 30$ GeV
	Dijet combinations	$N(j_1, j_2) \geq 1$, $\Delta\eta(j_1, j_2) > 3.8$, $\eta(j_1) \times \eta(j_2) < 0$, $m(j_1, j_2) > 500$ GeV

Table 9.4: Event selections in the signal regions for the VBF SUSY analysis.

Final state	e	e veto	add. e veto	μ	μ veto	add. μ veto	τ_h	τ_h veto	add. τ_h veto
$0\ell+jj$	-	✓	-	-	✓	-	-	✓	-
$e+jj$	$N = 1$	-	✓	-	✓	-	-	✓	-
$\mu+jj$	-	✓	-	$N = 1$	✓	-	-	✓	-
τ_h+jj	-	✓	-	-	✓	-	$N = 1$	✓	-
$ee+jj$	$N = 2$	-	✓	-	✓	-	-	✓	-
$e\mu+jj$	$N = 1$	-	✓	$N = 1$	-	✓	-	✓	-
$\mu\mu+jj$	-	✓	-	$N = 2$	-	✓	-	✓	-
$e\tau_h+jj$	$N = 1$	-	✓	-	✓	-	$N = 1$	-	✓
$\mu\tau_h+jj$	-	✓	-	$N = 1$	-	✓	$N = 1$	-	✓
$\tau_h\tau_h+jj$	-	✓	-	-	✓	-	$N = 2$	-	✓

Table 9.5: Lepton multiplicity selections for the different signal regions considered in the VBF SUSY analysis.

9.3 Event selection optimization in the 2-lepton signal regions

The selections described in Tabs. 9.4 and 9.5 proved to be optimal for the invisible and 1-lepton channels, which will provide the best sensitivity to regions where $\Delta m\tilde{\chi}_2^0, \tilde{\chi}_1^0 < 50$ GeV. In contrast, the 2-lepton channels will be largely sensitive to the $\Delta m\tilde{\chi}_2^0, \tilde{\chi}_1^0 \geq 50$ GeV region.

These conclusions stem from the fact that the lepton momentum is highly determined by the $\Delta m\tilde{\chi}_2^0, \tilde{\chi}_1^0$ value, as stated in the previous section. For small and very small values of $\Delta m\tilde{\chi}_2^0, \tilde{\chi}_1^0$, the leptons will be softer, and therefore, it makes more challenging to reconstruct the full lepton multiplicity in the final state. However, as $\Delta m\tilde{\chi}_2^0, \tilde{\chi}_1^0$ increases, the average lepton p_T , as well as the probability of reconstructing more than one lepton, will be larger. Therefore, in the 2-lepton decay channels, the leptons will be usually be more energetic compared to those in the 0- and 1-leptons channels. This means that the upper bound on the lepton p_T ($p_T^{\text{max}} = 40$ GeV) could decrease the signal acceptance, and consequently, the signal sensitivity.

Also, by requiring the presence of two leptons in the final state, the amount of background events is reduced, because the number of processes which could have two leptons in the final state is smaller and with lower production cross sections and/or branching ratios. For example, diboson production has smaller production cross sections; in $t\bar{t}$ events where the top quark decays as $t \rightarrow bW$, the W boson decay branching ratios determine how likely will be to get two leptons in the final state. Leptonic W boson decays are smaller than the fully hadronic decay modes [162], thus, $\mathcal{BR}(t\bar{t} \rightarrow 2\ell 2\nu 2b) < \mathcal{BR}(t\bar{t} \rightarrow 1\ell 1\nu 2b) < \mathcal{BR}(t\bar{t} \rightarrow \text{hadrons})$. The lower background rates in the 2-lepton channels motivates the relaxation of the p_T^{miss} or VBF selection criteria in the 2-lepton SRs. This could help to increase the signal acceptance, maintaining similar background yields, and therefore resulting in a larger signal sensitivity.

A second optimization of the signal region selections in the 2-lepton channels was performed to study potential improvements to the signal sensitivity based on the previous discussion. In this section, only the results obtained for the $\mu\tau_h + \text{jj}$ channel are presented. The results and conclusions obtained in this channel are consistent with those in the rest of the 2-lepton channels.

Initial studies on event selections for the $\mu\tau_h + \text{jj}$ channels

The final states with at least one τ_h are expected to provide the greatest sensitivity to the SUSY wino-bino interpretation with $\tilde{\tau}$ -dominated decays. The goal of the optimization studies is to find the most optimal event and object selections based on their kinematic characteristics, which will be mainly dictated by $\Delta m(\tilde{\chi}_2^0, \tilde{\chi}_1^0)$. Thus, the SR optimization studies were performed using $\tilde{\tau}$ -dominated signal samples, considering a fixed $m(\tilde{\chi}_2^0)$ value of 300 GeV and various $\Delta m(\tilde{\chi}_2^0, \tilde{\chi}_1^0)$ values.

The SR optimization studies can be divided in two main steps: since this is a shape-based analysis, the first step consists of finding the best kinematic variable to search for the presence of signal. Since data will be fit to the predicted background distribution, this kinematic variable is also referred to as a *fit variable*. The fit variable should provide good discrimination between signal and background shapes. Quantitatively, the figure of merit used in this analysis is the 95% confidence level (CL) upper limit (UL) on the signal cross section [161], which is denoted as σ_{UL} in this chapter.

The goal is to minimize the value of σ_{UL} as the result of the optimization, because a small σ_{UL} means that the range of signal cross sections that is possible to probe with the results of the analysis is larger.

σ_{UL} is calculated with the Higgs Combine Tool (HCT), a software tool for statistical analysis, based on the ROOSTATS [163] framework, a C++ class library based on the ROOT [164] and ROOFIT [165] packages. The kinematic variable that yields the lowest σ_{UL} is selected. Besides finding the fit variable, the most optimal binning of the distribution is found with the HCT as well.

The second step is to find the set of kinematic selections that provide the best (lowest) σ_{UL} . Ideally, every selection in the analysis could be optimized. However, there are event selections that are more important in terms of background rejection. Therefore, the subset of selections to be optimized is established by comparing the relative selection efficiencies for signal and background and choosing those selections that show the largest differences in efficiencies.

After applying the $\mu\tau_h+\text{jj}$ SR selections (OS and LS separately, with VBF2 selections), the kinematic variables that visually presented good signal and background separation were the invariant mass of the $\mu\tau_h$ pair, $m(\mu, \tau_h)$, the missing transverse momentum, $p_{\text{T}}^{\text{miss}}$, the absolute value of the η separation between the jet pairs in the event, $|\Delta\eta(\text{jj})|$, and the *leading invariant dijet mass* $m_{\text{lead}}(\text{jj})$. The kinematic variable with the lowest σ_{UL} was $m_{\text{lead}}(\text{jj})$, which was selected as the fit variable.

Process	OS $\mu\tau_h$			LS $\mu\tau_h$		
	2016	2017	2018	2016	2017	2018
EWK W/Z	0.57 ± 0.19	0.00 ± 0.00	0.79 ± 0.57	0.30 ± 0.00	0.31 ± 0.00	0.00 ± 0.00
QCD	0.00 ± 0.00	0.00 ± 0.00	0.00 ± 0.00	0.00 ± 0.00	0.00 ± 0.00	0.00 ± 0.00
Rares	0.04 ± 0.01	0.12 ± 0.02	0.71 ± 0.40	0.26 ± 0.22	0.00 ± 0.00	0.00 ± 0.00
Single- t	0.57 ± 0.28	0.10 ± 0.06	0.72 ± 0.44	0.07 ± 0.00	0.07 ± 0.06	0.06 ± 0.06
Diboson (VV)	1.62 ± 0.47	1.69 ± 0.46	3.62 ± 0.89	0.12 ± 0.03	0.16 ± 0.04	0.49 ± 0.17
W+jets	1.09 ± 0.50	1.14 ± 0.40	0.84 ± 0.11	1.49 ± 0.48	1.66 ± 0.38	1.28 ± 0.78
Z+jets	1.58 ± 0.35	2.34 ± 0.54	2.88 ± 0.62	0.00 ± 0.00	0.25 ± 0.00	0.03 ± 0.02
$t\bar{t}$	3.37 ± 0.50	3.02 ± 0.43	5.25 ± 0.65	0.44 ± 0.20	0.55 ± 0.25	0.52 ± 0.18
Total bkg	8.83 ± 0.98	8.40 ± 0.92	14.81 ± 1.51	2.67 ± 0.56	3.00 ± 0.46	2.39 ± 0.82
Signal $m(\tilde{\chi}_2^0) = 300$ GeV, $\Delta m = 50$ GeV	1.59 ± 0.15	1.74 ± 0.17	3.08 ± 0.22	0.36 ± 0.07	0.42 ± 0.09	0.68 ± 0.10
Signal $m(\tilde{\chi}_2^0) = 300$ GeV, $\Delta m = 75$ GeV	1.58 ± 0.15	1.84 ± 0.17	2.90 ± 0.22	0.37 ± 0.07	0.32 ± 0.07	0.46 ± 0.09

Table 9.6: Final event yields for signal and background in the $\mu\tau_h$ signal regions (OS and LS) for 2016-2018. Only statistical uncertainties have been included. **Note:** the QCD μ -enriched MC samples were used in these studies.

Next, the optimization of the binning was performed. As shown in Table 9.6, the event yields in both $\mu\tau_h+\text{jj}$ channels are small both for signal and background. This will be an important factor when selecting the optimal binning, since it will be important to have enough events in each bin to perform the statistic tests. In the OS $\mu\tau_h+\text{jj}$ channel, the binning that provided the largest sensitivity corresponds to the bin edges [0, 500, 750, 1000, 1500, 2000, 2500, 5000] GeV. In the LS $\mu\tau_h+\text{jj}$ channel, a similar binning is used, except that the last two bins are merged, resulting in the bin edges: [0, 500, 750, 1000, 1500, 2000, 5000] GeV. The distributions for $m_{\text{lead}}(\text{jj})$ with the optimal binning and using the three data subsets (2016-2018) are shown in Fig. 9.8 (Fig. 9.9) for the OS (LS) $\mu\tau_h+\text{jj}$ channel.

The dominant backgrounds in the OS $\mu\tau_h+\text{jj}$ channel are $t\bar{t}$, W+jets, Z+jets and diboson. In the LS $\mu\tau_h+\text{jj}$ channel, W+jets, $t\bar{t}$ and diboson are the largest backgrounds. Although the prediction

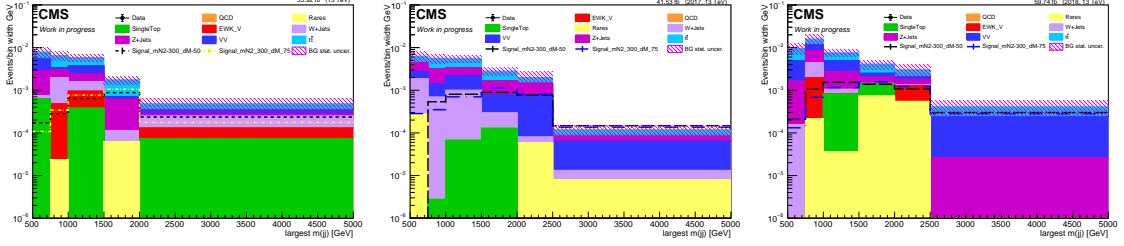


Figure 9.6: Leading $m(jj)$ distributions for the OS $\mu\tau_h$ signal region in the 2016-2018 data sets.

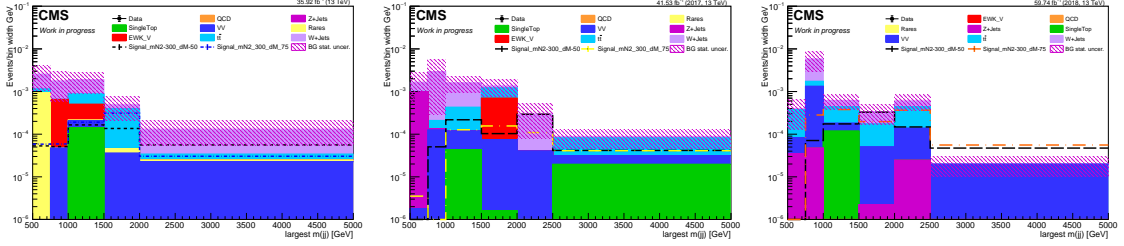


Figure 9.7: Leading $m(jj)$ distributions for the LS $\mu\tau_h$ signal region in the 2016-2018 data sets.

form QCD multijet simulated events is null, we expect to have a non-zero contribution in the $\ell\tau_h+jj$ SRs. The expected σ_{UL} values for two benchmark signal samples are listed in Tables 9.7 and 9.8. In the OS channel, the best ULs are obtained in 2018 for both Δm 's, and the ULs are better for $\Delta m = 50$ GeV comparing year-by-year, as well as the combination of all years. In the LS results, we observe that the central values of these limits are larger than those obtained in the OS channel. The best σ_{UL} 's are obtained in 2018 for both Δm 's, and the combination of the limits yield expected limits that are close to the values measured per year in the OS case. The full combination of Run II OS+LS expected limits is shown in Tab. 9.9.

Signal sample	Asymptotic limits (CLs)	σ_{UL}^{2016} [fb]	σ_{UL}^{2017} [fb]	σ_{UL}^{2018} [fb]	$\sigma_{UL}^{combined}$ [fb]
$\Delta m = 50$ GeV	-2σ (2.5%)	163.33	151.25	115.80	74.80
	-1σ (16.0%)	229.85	216.19	161.06	103.20
	Central (50.0%)	348.44	328.12	239.06	150.78
	$+1\sigma$ (84.0%)	541.49	509.93	361.99	224.71
	$+2\sigma$ (97.5%)	812.66	759.57	528.79	321.51
$\Delta m = 75$ GeV	-2σ (2.5%)	273.25	148.68	117.69	81.90
	-1σ (16.0%)	382.82	209.24	163.69	113.59
	Central (50.0%)	578.12	317.19	242.97	166.41
	$+1\sigma$ (84.0%)	893.83	494.19	368.87	247.33
	$+2\sigma$ (97.5%)	1232.66	740.38	540.85	355.45

Table 9.7: Expected ULs on the signal cross section for the signal point $m(\tilde{\chi}_2^0) = 300$ GeV and two Δm benchmark values in the OS $\mu\tau_h$ final state.

Signal sample	Asymptotic limits (CLs)	$\sigma_{\text{UL}}^{2016}$	$\sigma_{\text{UL}}^{2017}$	$\sigma_{\text{UL}}^{2018}$	$\sigma_{\text{UL}}^{\text{combined}}$
		[fb]	[fb]	[fb]	[fb]
$\Delta m = 50$ GeV	-2σ (2.5%)	469.97	367.82	293.73	179.13
	-1σ (16.0%)	689.27	545.03	438.23	256.82
	Central (50.0%)	1093.75	871.88	709.38	395.31
	$+1\sigma$ (84.0%)	1782.59	1434.88	1190.07	626.95
	$+2\sigma$ (97.5%)	2807.47	2261.63	1907.79	954.96
$\Delta m = 75$ GeV	-2σ (2.5%)	443.12	624.90	217.53	167.76
	-1σ (16.0%)	649.88	925.96	320.00	240.07
	Central (50.0%)	1031.25	1481.25	515.62	373.44
	$+1\sigma$ (84.0%)	1697.17	2437.75	856.81	593.74
	$+2\sigma$ (97.5%)	2652.56	3826.19	1356.19	906.99

Table 9.8: Expected ULs on the signal cross section for the signal point $m(\tilde{\chi}_2^0) = 300$ GeV and two Δm benchmark values in the LS $\mu\tau_h$ final state.

Asymptotic limits (CLs)	Full combination UL	
	$\Delta m = 50$ GeV [fb]	$\Delta m = 75$ GeV [fb]
-2σ (2.5%)	67.38	71.12
$= 1\sigma$ (16.0%)	92.65	98.21
Central (50.0%)	134.77	143.38
$+1\sigma$ (84.0%)	199.76	213.56
$+2\sigma$ (97.5%)	285.09	304.82

Table 9.9: Expected ULs on the signal cross section for the signal points $m(\tilde{\chi}_2^0) = 300$ GeV and $\Delta m = 50$ and 75 GeV, combining OS+LS and the full Run II luminosity in the $\mu\tau_h + \text{jj}$ SRs.

Moving to the beginning of the second step in the SR optimization, I calculated the relative selection efficiencies of each set of selections as displayed on Tab. 9.6. In Figures 9.8 (OS) and 9.9 (LS), the comparison of the relative cut efficiencies for signal and background is shown for each year data set. From these results, we can see that the selections for μ , τ_h , p_T^{miss} and VBF dijet combinations provide the greater discrimination power between signal and background.

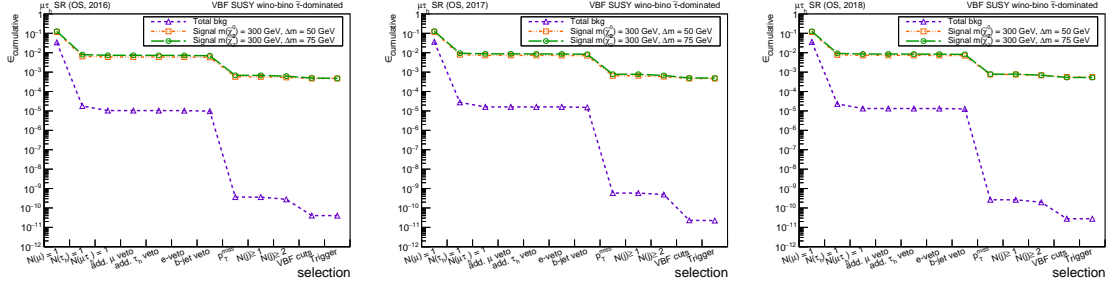


Figure 9.8: Cumulative efficiency in the baseline OS $\mu\tau_h$ signal region for signal $m(\tilde{\chi}_2^0) = 300$ GeV and $\Delta m = 50$ GeV, $\Delta m = 75$ GeV, and total background in the 2016-2018 data sets.

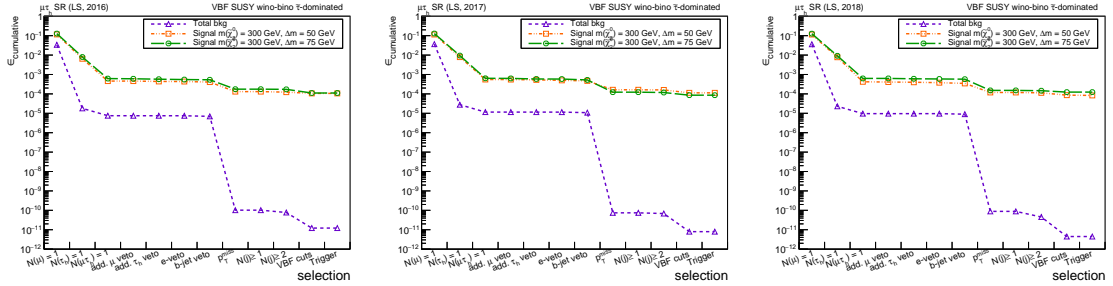


Figure 9.9: Cumulative efficiency in the baseline LS $\mu\tau_h$ signal region for signal $m(\tilde{\chi}_2^0) = 300$ GeV and $\Delta m = 50$ GeV, $\Delta m = 75$ GeV, and total background in the 2016-2018 data sets.

Before continuing with the optimization of these selections, I present a study on the shapes for signal and background in the SR and outline a strategy to improve the expected σ_{UL} 's before going into the actual optimization.

Smooth background shapes to improve limit calculation

The $m_{\text{lead}}(jj)$ shapes for signal and the sum of all backgrounds are compared across years in Figs. 9.10 and 9.11. The shapes are consistent in the OS channel for both signal points across years within statistical uncertainty. The total background shapes differ slightly across years. The largest differences are observed in the last three bins, but the data points are still within 2σ of statistical uncertainty. In the LS channel, the shapes for both signal points vary across years, observing larger dissimilarities for $\Delta m = 75$ GeV. The variations in the total background shapes are comparable to those observed in the OS channel. It is important to note that the statistics for both signal and backgrounds are comparably lower in the LS final state than in the OS case.

One of the challenges in this SR is the reduced amount of background event yields predicted from simulation. In Figures 9.6-9.7, one can observe that some backgrounds are present only in a subset

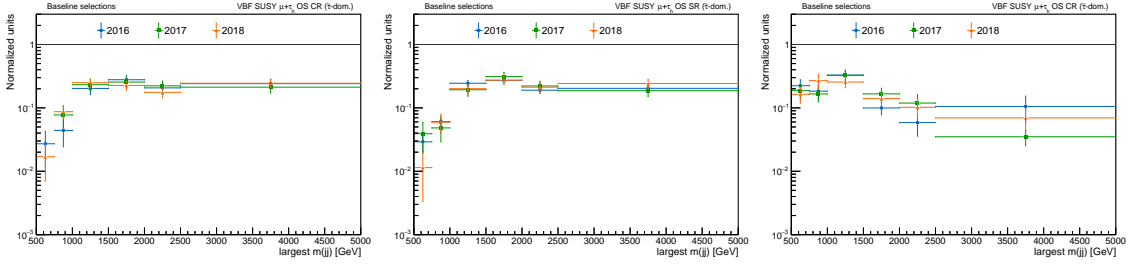


Figure 9.10: Shape comparison of the leading $m(\text{jj})$ distributions for signal $m(\tilde{\chi}_2^0) = 300$ GeV and $\Delta m = 50$ GeV (left), $\Delta m = 75$ GeV (middle) and total background (right) in the OS $\mu\tau_h$ signal region in the 2016-2018 data sets.

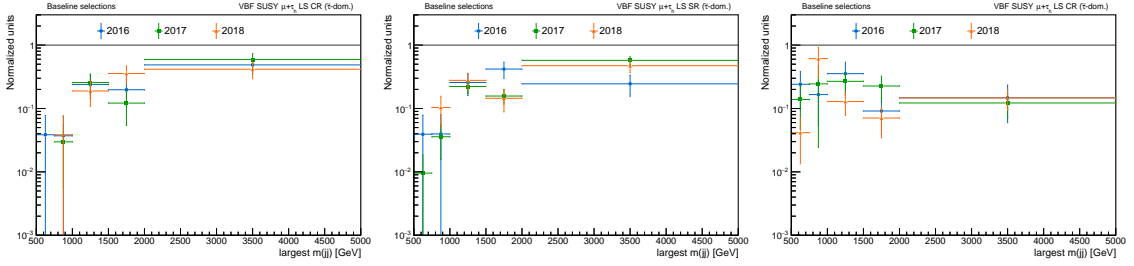


Figure 9.11: Shape comparison of the leading $m(\text{jj})$ distributions for signal $m(\tilde{\chi}_2^0) = 300$ GeV and $\Delta m = 50$ GeV (left), $\Delta m = 75$ GeV (middle) and total background (right) in the LS $\mu\tau_h$ signal region in the 2016-2018 data sets.

of the bins. Therefore, the prediction of the background shapes is impacted, and consequently, the value of the σ_{UL} .

In order to obtain a more accurate prediction of the shapes for each one of the backgrounds present in the SR, we need to increase the statistics of the predicted backgrounds per bin. A *loosened* SR was created, relaxing specific selections in the baseline SR, which are uncorrelated to the $m(\text{jj})$ distribution.

These relaxed selections in the loosened SR are:

- τ_h isolation (ID): from the Tight working point to the *VVVLoose* working point in DEEPTAU,
- μ relative isolation: from $I_{\text{rel.}}(\mu) < 0.15$ to $I_{\text{rel.}}(\mu) < 0.25$ (loose),
- μ ID: from Tight to *Loose*,
- b-jet veto removed,
- charge combination requirement was dropped (include OS and LS events).

This will result in smoother background shapes, which can be normalized to the right number of event yields predicted from simulation. As an example, the background shapes obtained in the loosened $\mu\tau_h + \text{jj}$ SR are shown in Fig. 9.12 for the 2016 simulation data set. The number of events for all major backgrounds in the OS and LS channels is increased ($t\bar{t}$, W+jets, Z+jets, diboson and EWK W/Z), managing to have contributions from each one of them in every bin of the $m(\text{jj})$ distribution, as intended.

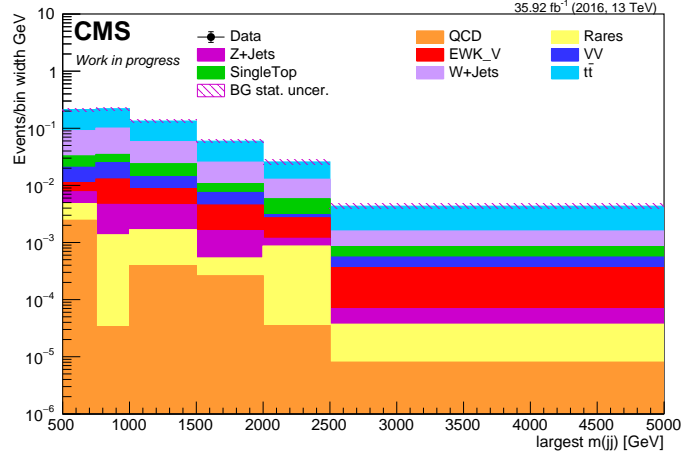


Figure 9.12: Smooth background shapes obtained after relaxing some of the central selections in the baseline $\mu\tau_h$ SR for 2016.

To verify that the modified cuts did not bias the *leading* $m(jj)$ shape for the sum of all backgrounds, compared to the original prediction obtained in the OS and LS channels, the ratio of such distributions was obtained and it is shown in Figs. 9.13-9.14.

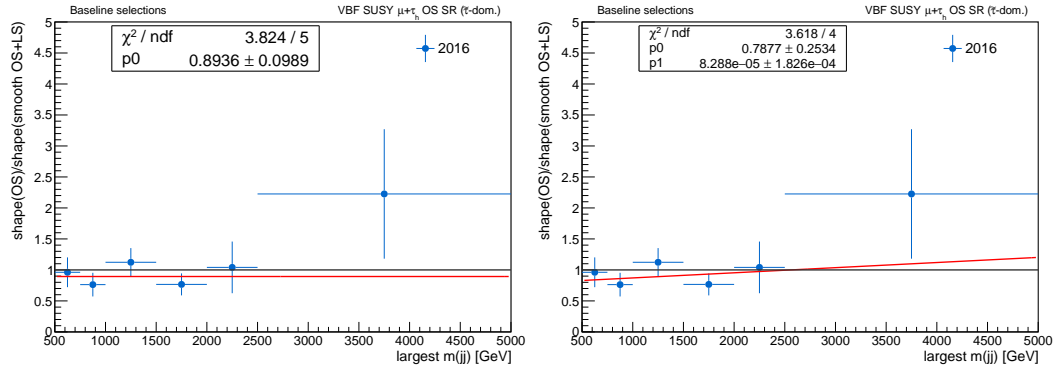


Figure 9.13: Comparison of the total background shapes in the OS $\mu\tau_h$ SR vs. the smooth background shapes obtained after relaxing some of the central selections in the baseline $\mu\tau_h$ SR for 2016.

A χ^2/N test is performed by fitting a 0-th and 1-degree polynomial to the obtained ratios. The ratio of these shapes is consistent with a constant function in both the OS and LS cases. For the LS channel, both sets of largest $m(jj)$ bins were tested, with the goal of understanding if the finer binning proposed in the OS channel could improve the expected σ_{UL} 's, once the smooth background shapes were used.

The methodology to calculate the expected σ_{UL} 's with the smooth background shapes consists of: (1) obtaining the predicted event yields for each background processes applying the *nominal (original)* selections in the SR; (2) re-normalize each background shape in the loosened SR with the

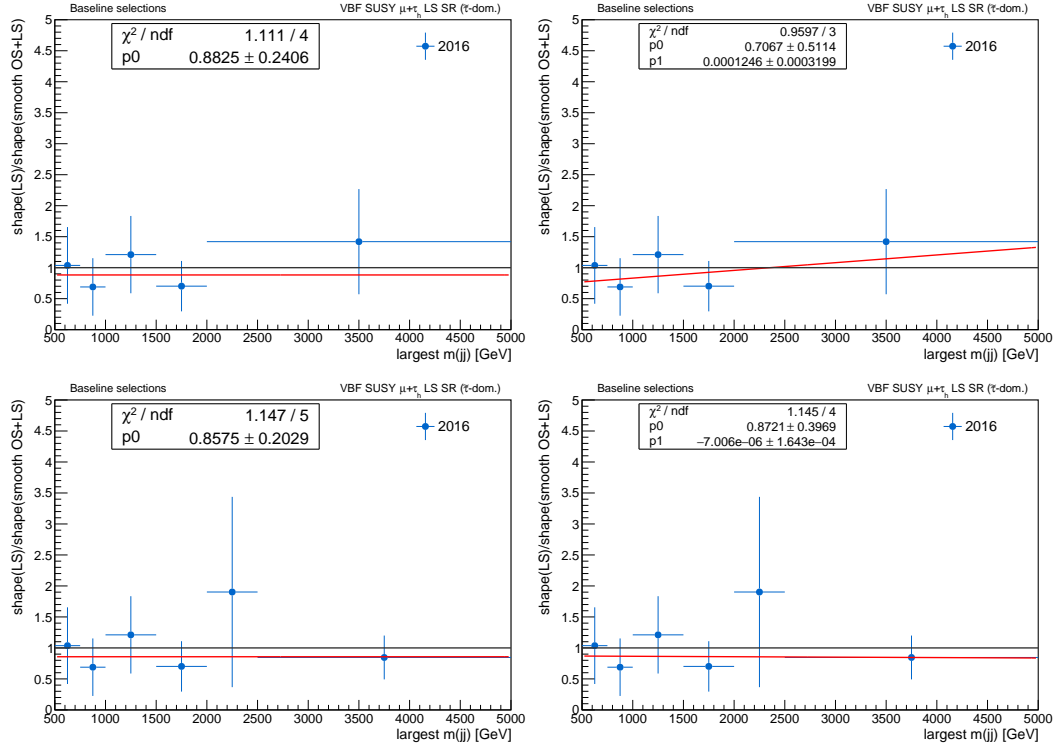


Figure 9.14: Comparison of the total background shapes in the LS $\mu\tau_h$ SR vs. the smooth background shapes obtained after relaxing some of the central selections in the baseline $\mu\tau_h$ SR for 2016. Both sets of bins derived for the leading $m(jj)$ in the in the LS (top) and OS (bottom) SR were tested.

Decay channel	OS		LS		
	Original	Smooth	Original	Smooth LS binning	Smooth OS binning
-2σ (2.5%)	163.33	151.97	469.97	444.41	410.16
-1σ (16.0%)	229.85	215.83	689.27	655.11	612.92
Central (50.0%)	348.44	329.69	1093.75	1043.75	1000.00
$+1\sigma$ (84.0%)	541.49	518.92	1190.07	1717.74	1677.63
$+2\sigma$ (97.5%)	812.66	787.18	1907.79	2707.47	2668.10

Table 9.10: Expected ULs on the signal cross section with the original and smooth background shapes for the signal point $m(\tilde{\chi}_2^0) = 300$ GeV and $\Delta m = 50$ GeV in the $\mu\tau_h$ SRs with the 2016 simulation data set.

Decay channel	OS		LS		
	Original	Smooth	Original	Smooth	Smooth
LS binning				OS binning	
-2σ (2.5%)	273.25	166.26	443.12	445.79	444.43
-1σ (16.0%)	382.82	235.45	649.88	650.52	648.54
Central (50.0%)	578.12	354.69	1031.25	1028.12	1025.00
$+1\sigma$ (84.0%)	893.83	552.62	1190.07	1675.63	1670.54
$+2\sigma$ (97.5%)	1232.66	827.91	1907.79	2616.35	2631.00

Table 9.11: Expected ULs on the signal cross section with the original and smooth background shapes for the signal point $m(\tilde{\chi}_2^0) = 300$ GeV and $\Delta m = 75$ GeV in the $\mu\tau_h$ SRs with the 2016 simulation data set.

corresponding transfer factor $\text{TF}_{\text{Loose-To-Nom SR}}$, defined as:

$$\text{TF}_{\text{Loose-To-Nom SR}}^{\text{bkg}} = \frac{N_{\text{nominal SR}}^{\text{bkg}}}{N_{\text{loose SR}}^{\text{bkg}}}; \quad (9.1)$$

(3) use the background shapes obtained after this re-normalization, together with the prediction for signal from simulation to calculate the expected σ_{UL} 's.

The comparison of the expected σ_{UL} 's obtained with the original and smoothed shapes is summarized in Tables 9.10 and 9.11. The results indicate that the expected σ_{UL} 's improve in both SRs, especially in the OS $\mu\tau_h+\text{jj}$ for the $\Delta m = 75$ GeV signal point ($\sim 40\%$). In the LS SRs, there is a smaller improvement in the central value of the expected limit ($\sim 1\text{-}5\%$). However, the expected limits $[-2\sigma, +2\sigma]$ ranges obtained with the original and smooth background shapes are consistent. The same conclusion applies when using either the LS or OS binning. Thus, the LS binning is kept for the LS SR, and from now on, all expected σ_{UL} 's are calculated using the smooth background shapes.

Optimization of the event selections in the $\mu\tau_h+\text{jj}$ SR

In the light of the previous results presented, the SR optimization was performed in the OS $\mu\tau_h$ channel using the 2016 data set. Based on the efficiencies obtained in the baseline SR, the optimization plan was established as follows:

- τ_h selections: DEEPTAU ID anti-jet discriminator working point, anti-electron discriminator working point, $p_{\text{T}}^{\text{max}}(\tau_h)$;
- $p_{\text{T}}^{\text{miss}}$: the cut value used is based on the trigger efficiency (Sec. 8.3); however, we were interested in studying any potential benefit of lowering the $p_{\text{T}}^{\text{miss}}$ threshold,
- μ selections: μ ID, and p_{T} range ($p_{\text{T}}^{\text{min}}(\mu)$ and $p_{\text{T}}^{\text{max}}(\mu)$).

Starting with the τ_h identification, seven working points (WPs) from the anti-jet DEEPTAU identification algorithm were tested: VVLoose, VLoose, Loose, Medium, Tight (baseline), VTight,

and VVTight. In Figure 9.15, the ratio of each expected UL obtained for each WP and the minimum expected UL obtained among all the ULs obtained with the WPs tested ($\sigma_{\text{UL}}/\sigma_{\text{UL}}^{\text{min}}$) is shown for the signal points with $\Delta m = 50$ and 75 GeV.

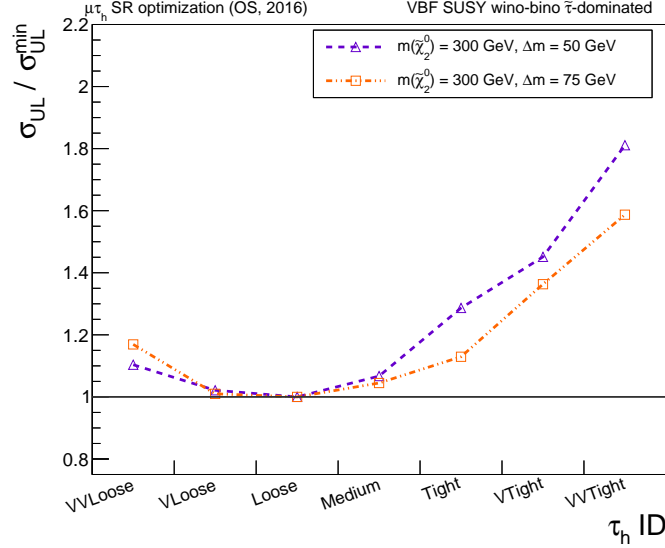


Figure 9.15: Ratio of the σ_{UL} 's for each τ_h isolation working point tested and the minimum UL obtained among all cuts tested.

According to these results, the most optimal τ_h isolation³ is *Loose ID*. However, choosing a looser τ_h isolation could increase the contribution from backgrounds with larger τ_h mis-identification rates. This would also increase the total systematic uncertainty in the analysis, which in the end, will be detrimental to the signal sensitivity of the analysis. Before selecting a definite τ_h isolation point, we continue with the optimization of subsequent event selections with the Loose and Tight anti-jet discriminator WPs, and assess any significant differences in the signal sensitivity once more selections are optimized.

The next selection to be optimized was the number of prongs in the τ_h 's. Three options were considered: 1-prong, 3-prongs, and 1- or 3-prongs (baseline), and the results are shown in Fig. 9.16. The best σ_{UL} 's are obtained when selecting τ_h 's with *1- or 3-prongs*, for both τ_h ID WPs.

Continuing with the $p_{\text{T}}^{\text{max}}(\tau_h)$ selection, five thresholds were tested: 30, 40 (baseline), 50, 60, and 70 GeV. For this optimization, the signal sample of $m(\tilde{\chi}_2^0) = 300$ GeV and $\Delta m = 60$ GeV was added. The idea is to consider the three largest Δm values in the signal mass scan. The most optimal selection found is $p_{\text{T}}^{\text{max}}(\tau_h) = 70$ GeV, as can be seen in Fig. 9.17 for both τ_h isolation WPs, and all signal points considered. *Therefore, the new $p_{\text{T}}(\tau_h)$ range to be used in the SR will be $20 \leq p_{\text{T}}(\tau_h) \leq 70$ GeV.*

The next selection to be optimized was $p_{\text{T}}^{\text{miss}}$. Six $p_{\text{T}}^{\text{miss}}$ cuts were tested: 200, 210, 220, 230, 240, and 250 GeV (baseline). For the optimization of this selection, two other signal points were added to the list: $m(\tilde{\chi}_2^0) = 300$ GeV with $\Delta m = 20$ and 30 GeV. The purpose was to compare the optimization results for a slightly different (more compressed) phase space. In Figure 9.18 left, the $\sigma_{\text{UL}}/\sigma_{\text{UL}}^{\text{min}}$ ratio is shown for the case in which the Loose τ_h isolation is used. For all signal points

³This is another way to refer to the anti-jet discriminator working point.

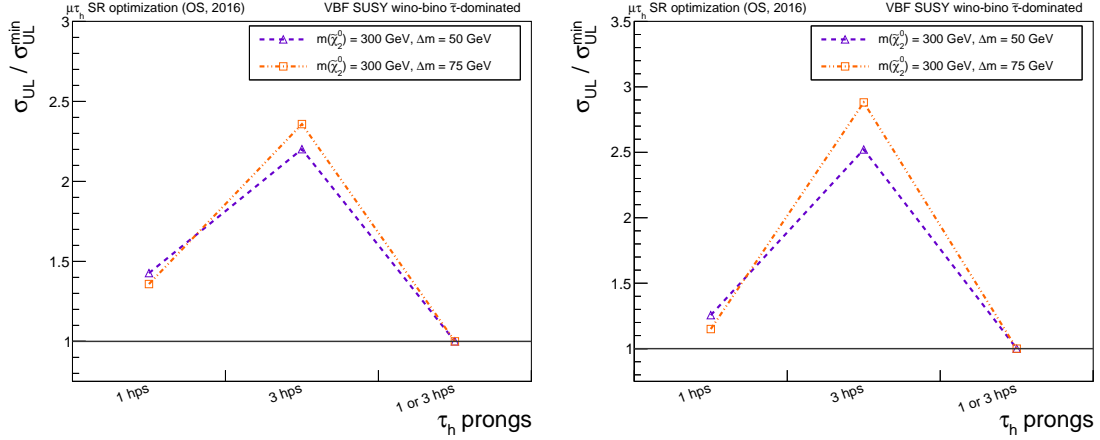


Figure 9.16: Ratio of the σ_{UL} 's for each selection of number of τ_h prongs tested and the minimum UL obtained among all cuts tested, considering the Loose (left) and Tight (right) τ_h ID WPs.

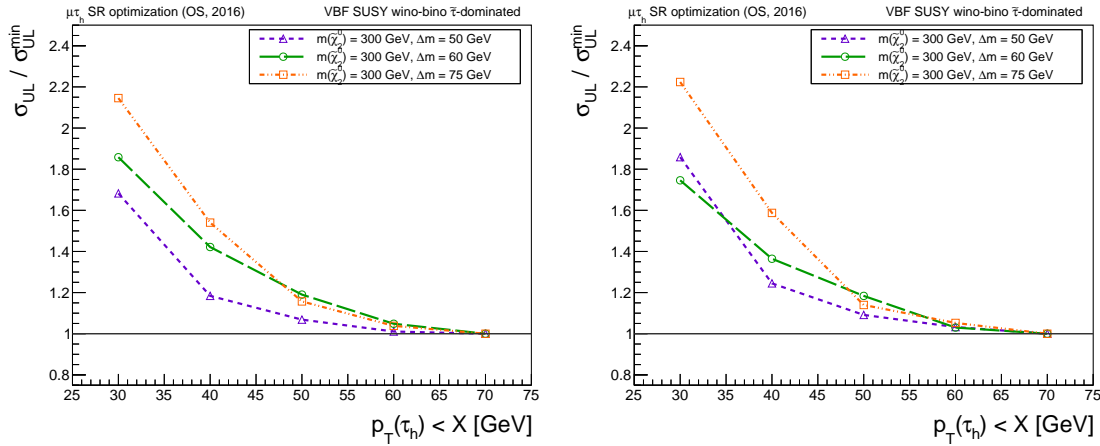


Figure 9.17: Ratio of the σ_{UL} 's for each selection of $p_T^{\max}(\tau_h)$ tested and the minimum UL obtained among all cuts tested, considering the Loose (left) and Tight (right) τ_h ID WPs.

considered, the most optimal p_T^{miss} lower threshold is 200 GeV. It is worth noting that the maximum relative difference between the best expected limit at 200 GeV the limits for the other p_T^{miss} cuts is 20%.

In Figure 9.18 right, the results obtained when using Tight τ_h isolation are shown. The most optimal p_T^{miss} cut is 200 GeV for all signal points with $\Delta m \geq 30$ GeV, except for the signal with $\Delta m = 20$ GeV, for which the most optimal cut is instead 220 GeV. Once again, the expected limits for the rest of the cuts differ no more than 30% with respect to the best limit obtained for each signal point. This is important because of the following reasons:

- the order of the sum of all systematic uncertainties obtained in previous iterations of this analysis have been found to be of about 25% of the background prediction. Therefore, the improvement on the expected central σ_{UL} obtained by lowering the p_T^{miss} cut will be small ($\sim 5\%$).

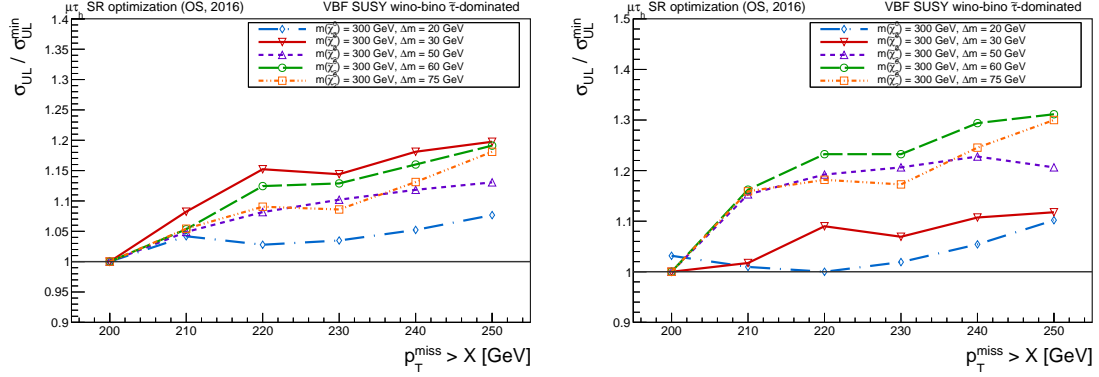


Figure 9.18: Ratio of the σ_{UL} 's for each selection of p_T^{miss} tested and the minimum UL obtained among all cuts tested, considering the Loose (left) and Tight (right) τ_h ID WPs.

- a looser p_T^{miss} threshold can increase the contribution from backgrounds containing fake τ_h 's, like QCD multijet production and W +jets. The systematic uncertainty associated with the τ_h mis-identification rate is larger than the corresponding uncertainty for genuine τ_h identification. Therefore, the total systematic uncertainty will increase, producing no gain in sensitivity at all,
- more importantly, the trigger used in this analysis is a MET trigger which reaches maximum efficiency above 250 GeV (Sec. 8.3).

Thus, we decided to keep the $p_T^{\text{miss}} > 250$ GeV selection in the signal region.

On the other hand, comparing the expected limits obtained with Loose vs. Tight τ_h isolation at this stage, the improvement from using the Loose τ_h ID WP ranges from 1% to 16% for each signal point considered. Using the same argument regarding the increase in the systematic uncertainties from mis-identified τ_h 's⁴, we decided to move forward using the Tight τ_h anti-jet discriminator WP.

The next set of selections considered for optimization were μ ID and $p_T^{\text{min}}(\mu)$. Four combinations were tested: tight PF μ ID + $p_T^{\text{min}}(\mu) = 3$ GeV, tight PF μ ID + $p_T^{\text{min}}(\mu) = 8$ GeV (baseline), soft SUSY μ ID + $p_T^{\text{min}}(\mu) = 3$ GeV, and soft SUSY μ ID + $p_T^{\text{min}}(\mu) = 8$ GeV. The customized soft SUSY μ ID was proposed and studied in [128, 166] (Sec. 7.2, Tab. 7.2), where the use of this ID provided an increase in signal significance for this search. The results for different Δm values of the wino- $\tilde{\chi}_2^0$, $\tilde{\chi}_1^\pm$, bino- $\tilde{\chi}_1^0$ with $\tilde{\tau}$ -dominated decays scenarios are shown in Fig. 9.19 (left). In this case, any light leptons (e, μ) will come from the decay of a τ lepton.

For all Δm 's considered, except $\Delta m = 10$ GeV, the best expected σ_{UL} 's are obtained with the *Tight PF μ ID + $p_T^{\text{min}}(\mu) = 3$ GeV*. A similar exercise was done considering signal samples where the decay of the heavier electroweakinos happens through virtual W and Z bosons, and the results are shown in Fig. 9.19 (right). In this scenario, the most optimal combination is *soft SUSY μ ID + $p_T^{\text{min}}(\mu) = 3$ GeV*, which is in consistency with results observed in [128, 166].

The difference in results to come from the fact that the customized soft SUSY μ ID imposes additional requirements on the impact parameter quantities (IP), IP_{3D} and $\sigma_{IP_{3D}}$. These selections are more stringent than those in the definition of the Tight PF μ ID, and were optimized to select

⁴Not only in this channel $\mu\tau_h$, but specially in the $\tau_h\tau_h$ channel.

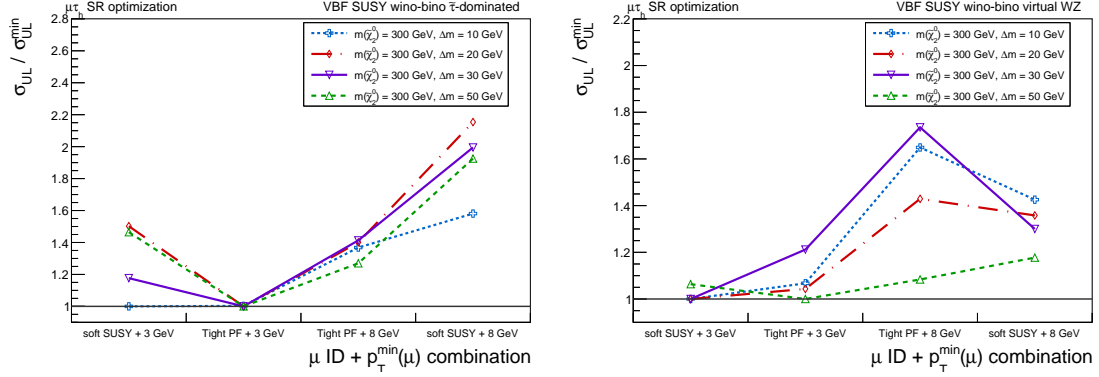


Figure 9.19: Ratio of the σ_{UL} 's for each selection of μ ID + $p_T^{\min}(\mu)$ combinations tested and the minimum UL obtained among all cuts tested, considering different signal points for the $\tilde{\tau}$ -dominated decay scenario (left) and the virtual W/Z decay scenario (right).

prompt electrons and muons. In such optimization, light leptons coming from b-hadron decays, mis-identified jets and τ lepton decays were regarded as “background” leptons [166].

Given that the difference in σ_{UL} comparing Tight PF μ ID vs. soft SUSY μ ID with $p_T^{\min}(\mu) = 8$ GeV in the virtual W/Z decay scenario is $< 25\%$ (similar to the order of our expected systematic uncertainties), and that it does make a greater difference in the $\tilde{\tau}$ -dominated decay scenario, we keep using the *Tight PF μ ID* with a lower $p_T^{\min}(\mu)$ selection of 3 GeV.

A similar study was performed for electron ID and $p_T^{\min}(e)$. The combinations considered for optimization were: $(e$ ID, $p_T^{\min}(e)) = \{(\text{medium CB}^5, 10 \text{ GeV}), (\text{medium CB}, 5 \text{ GeV}), (\text{soft SUSY}, 10 \text{ GeV}) \text{ and } (\text{soft SUSY}, 5 \text{ GeV})\}$. It was found that the best expected limits were obtained using the medium CB ID in combination with $p_T^{\min} = 5$ GeV, for the same reasons found in the optimization of the muon selections.

The next selection to be optimized was the upper bound on the muon transverse momentum $p_T^{\max}(\mu)$. The selections tested are similar to those in the $p_T^{\max}(\tau_h)$ optimization: 30, 40, 50, 60, and 70 GeV. The results are shown in Fig. 9.20. For each Δm tested, there is a different optimal $p_T^{\max}(\mu)$ cut: for $\Delta m = 30$ and 50 GeV, the optimal cut is 30 GeV; for $\Delta m = 60$ GeV, the optimal value is 40 GeV, and for $\Delta m = 70$ GeV, it is 50 GeV. However, the difference in expected σ_{UL} 's for any of the cuts tested is below 10%. Therefore, we decided to continue using the $p_T^{\max}(\mu) = 40$ GeV baseline selection.

Finally, the last selection considered for optimization was the τ_h anti-electron discriminator. Three working points were considered: loose, medium, and tight (baseline). The results from the optimization are shown in Fig. 9.21. The most optimal point for the various signal benchmark scenarios tested is the *loose working point*, therefore, it is chosen as the selection to be used in the SRs. Since the relative difference observed in the σ_{UL} 's for most of the signal points studied is below 10%, the *medium anti-electron WP* is used in the CRs, to reduce the contributions from mis-identified τ_h 's.

⁵CB stands for cut-based.

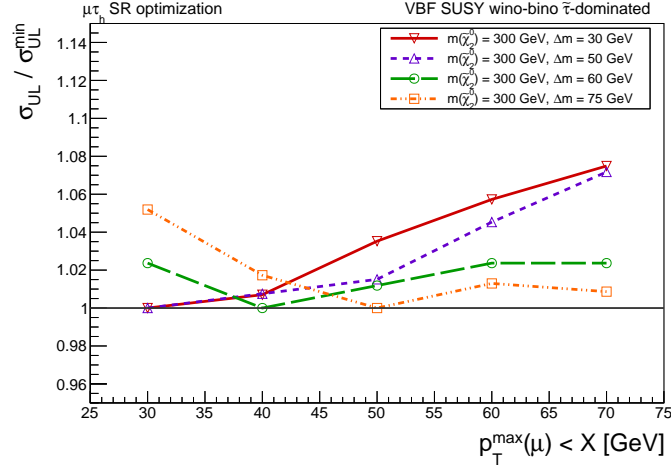


Figure 9.20: Ratio of the σ_{UL} 's for each selection of $p_T^{\max}(\mu)$ tested and the minimum UL obtained among all cuts tested.

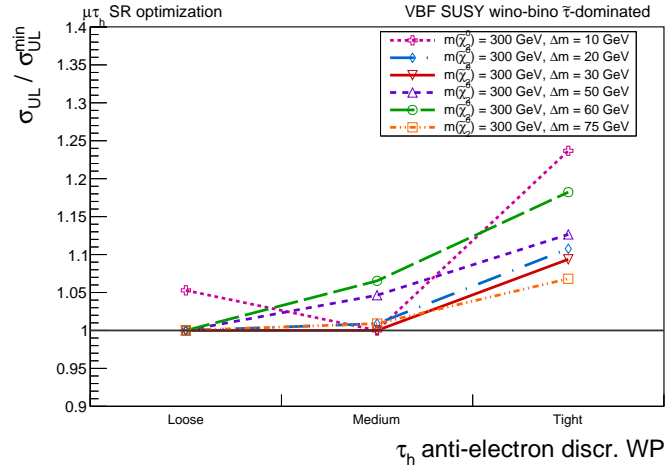


Figure 9.21: Ratio of the σ_{UL} 's for each selection of τ_h anti-electron discriminator tested and the minimum UL obtained among all cuts tested.

VBF1 vs. VBF2 selections

As explained earlier in this chapter, two sets of VBF selections were considered in the SR. A quick study was performed to understand the difference in signal sensitivity for the 2-lepton channels when using VBF1 vs. VBF2 selections, focusing in the $\mu\tau_h+jj$ channels with the 2016 data set. Two benchmark signal points of the SUSY wino-bino $\tilde{\tau}$ -dominated decays interpretation were used in the study, where $m(\tilde{\chi}_2^0) = 200$ GeV and $\Delta m = 30$ and 50 GeV.

The signal sensitivity was quantified by the σ_{UL} in each of the SRs considered. The distributions for the leading $m(jj)$ are shown in Figures 9.22 and 9.23 for the OS and LS $\mu\tau_h+jj$ decay channels, respectively. Tables 9.12 and 9.13 summarize the resulting σ_{UL} and the $\pm 1\sigma$ and $\pm 2\sigma$ variations, for the OS and LS final states, respectively.

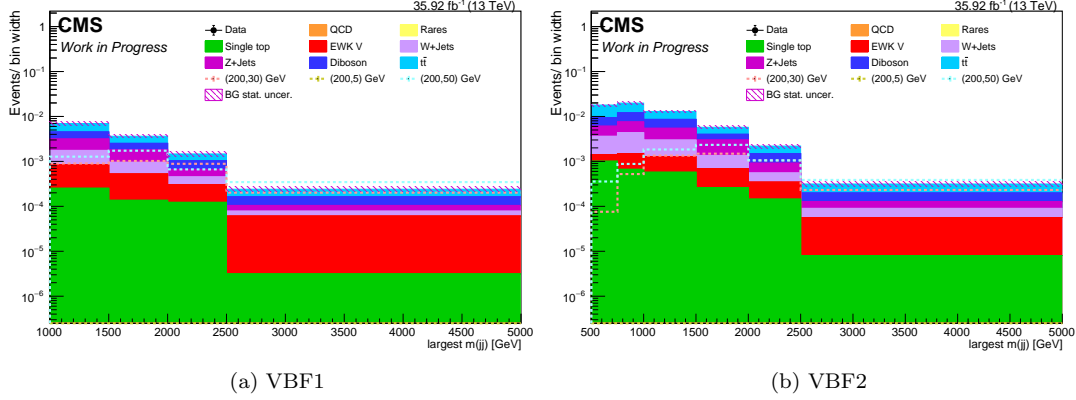


Figure 9.22: Leading $m(jj)$ distribution for predicted backgrounds and three benchmark signal points in the OS $\mu\tau_h+jj$ SR, after applying VBF1 (left) and VBF2 (right) selections.

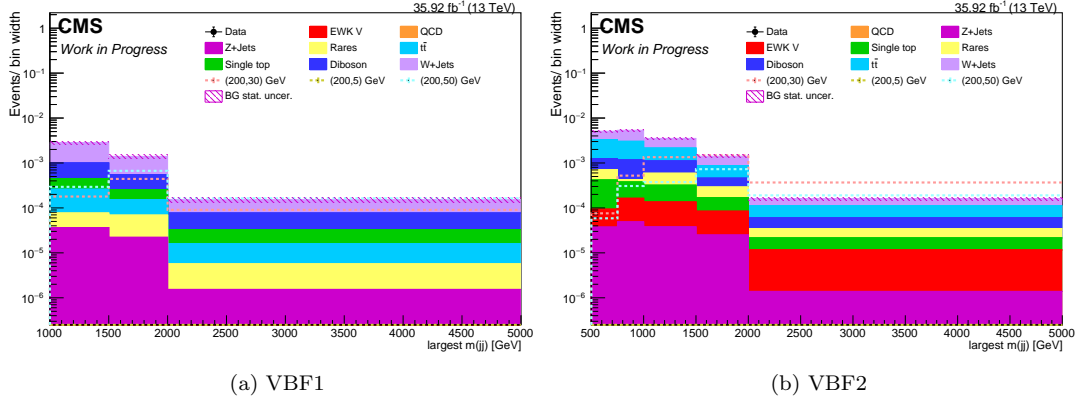


Figure 9.23: Leading $m(jj)$ distribution for predicted backgrounds and three benchmark signal points in the LS $\mu\tau_h+jj$ SR, after applying VBF1 (left) and VBF2 (right) selections.

Expected σ_{UL}	$\Delta m = 30$ GeV		$\Delta m = 50$ GeV	
	VBF1	VBF2	VBF1	VBF2
-2σ (2.5%)	139.16	129.88	96.60	89.71
-1σ (16.0%)	195.84	181.44	137.44	125.33
Central (50.0%)	296.88	270.31	207.81	186.22
$+1\sigma$ (84.0%)	458.99	411.46	322.95	285.71
$+2\sigma$ (97.5%)	684.34	602.29	482.27	419.03

Table 9.12: Expected σ_{UL} for the signal points with $m(\tilde{\chi}_2^0) = 200$ GeV and $\Delta m = 30$ and 50 GeV in the OS $\mu\tau_h+jj$ SR with the 2016 simulation data set, comparing VBF1 and VBF2 selections.

Expected σ_{UL}	$\Delta m = 30$ GeV		$\Delta m = 50$ GeV	
	VBF1	VBF2	VBF1	VBF2
-2σ (2.5%)	297.95.	75.49	177.73	155.86
-1σ (16.0%)	430.51	109.29	258.07	227.87
Central (50.0%)	675.00	169.53	406.25	356.25
$+1\sigma$ (84.0%)	1089.35	270.90	658.87	574.93
$+2\sigma$ (97.5%)	1698.89	414.23	1023.67	888.69

Table 9.13: Expected σ_{UL} for the signal points with $m(\tilde{\chi}_2^0) = 200$ GeV and $\Delta m = 30$ and 50 GeV in the LS $\mu\tau_h + \text{jj}$ SR with the 2016 simulation data set, comparing VBF1 and VBF2 selections.

In the OS channel, there is a 9-10% difference in the expected σ_{UL} between VBF1 and VBF2, for both signal points considered, favoring VBF2 selections. In the case of the LS channel, VBF2 selections yield better sensitivity, with a relative difference in the expected σ_{UL} is larger for the $\Delta m = 30$ GeV signal sample, which is of about 75%, and for the $\Delta m = 50$ GeV signal sample, the difference is of about 12%. The results obtained in the 2-light lepton channels also indicate that the signal sensitivity is higher when using VBF2 selections.

This data analysis is composed of various decay channels and final states, and the most optimal selections will be those that provide the best overall signal sensitivity when combining the results of all decay channels. Given the conclusions from this study, we have determined to use VBF2 selections in the 2-lepton decay channels.

Final event selections

The definition of physics objects was updated after the optimization of the selections in the signal region, specifically for leptons. The $p_{\text{T}}^{\text{miss}}$ cut was kept in order to remain in the range of highest trigger efficiency. The changes to the object definitions are shown in Table 9.14.

Object	Selection cuts
e	Medium WP of the cut-based ID, $5 < p_{\text{T}}(e) < 40$ GeV, $ \eta(\mu) < 2.1$
μ	Tight WP of the muon ID, $I_{\mu} < 0.15$, $3 < p_{\text{T}}(\mu) < 40$ GeV, $ \eta(\mu) < 2.1$
τ_h	Tight WPs of the anti-jet and anti- μ discriminators, loose WP of the anti-e discriminator of the DEEPTAU algorithm, $20 < p_{\text{T}}(\tau_h) < 70$ GeV, $ \eta(\tau_h) < 2.1$, 1 or 3 prongs,
Jet	for $30 < p_{\text{T}} \leq 50$ GeV, tight WP of the PU jet ID, for $p_{\text{T}} > 50$ GeV loose (tight) PF jet ID in 2016 (2017-2018) $p_{\text{T}}(j) > 30$ GeV, $ \eta(j) < 4.7$, $\Delta R(e/\mu/\tau_h, j) > 0.4$
b-jet	Medium WP of the DeepCSV b-jet discriminator, $p_{\text{T}}(b) > 30$ GeV, $ \eta(b) < 2.4$

Table 9.14: Updated definition of physics objects after optimization of selections in the signal regions.

The signal acceptance ϵ_{sig} , defined as

$$\epsilon_{\text{sig}} = \frac{N_{\text{sig}}^{\text{pass SR}}}{N_{\text{sig}}^{\text{initial}}}, \quad (9.2)$$

was measured in the different decay channels for two benchmark scenarios: (a) wino-bino model with $\tilde{\tau}$ -dominated decays and (b) wino-bino model with virtual W/Z decays. The signal samples used for this study consider a $m(\tilde{\chi}_2^0) = 300$ GeV and all the $\Delta m(\tilde{\chi}_2^0, \tilde{\chi}_1^0)$ available for each scenario. The comparison for the channels is shown in Figs. 9.24 and 9.25. In these plots, the signal acceptance of the OS and LS charge combinations was merged under one category for the 2-lepton channels.

In the $\tilde{\tau}$ -dominated scenario, we can see that the channels with largest signal acceptance are the $0\ell+jj$ channel, as well as any channel containing at least one τ_h in the final state. In the virtual W/Z decay scenario, the $0\ell+jj$ and light lepton final states present the highest acceptance. Both of these conclusions agree with the expected behavior, since in the $\tilde{\tau}$ -dominated case, only τ leptons are obtained in the decay of the electroweakinos, and combined with the dominant branching ratio of τ leptons being the hadronic decays, the signal acceptance should be largest in the τ_h channels.

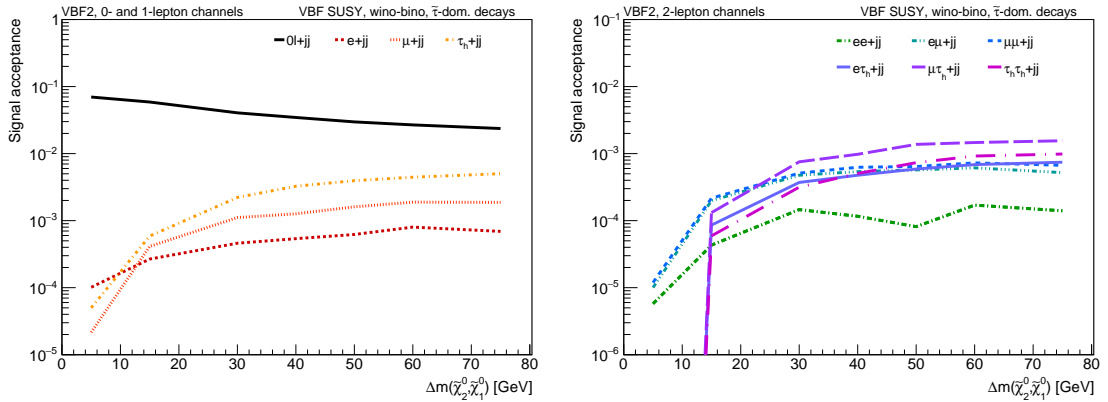


Figure 9.24: Signal acceptance in the wino-bino model with $\tilde{\tau}$ -dominated decays for the various decay channels considered in this analysis.

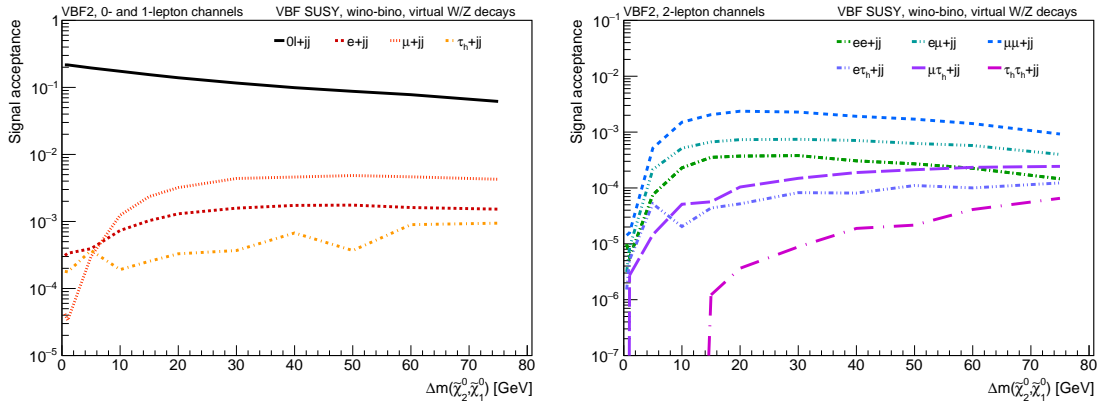


Figure 9.25: Signal acceptance in the wino-bino model with virtual W/Z decays for the various decay channels considered in this analysis.

In the virtual W/Z decays, leptons will result from the decay of these bosons, having approximately equal branching fractions to e , μ and τ leptons. Hence, there will be prompt electrons and muons produced, besides those coming from the leptonic decays of τ 's. This already gives an indication of the signal sensitivity to the different physics interpretations based on the final state considered in each decay channel.

CHAPTER 10

Background estimation

In this chapter, the description of the background estimation methodology, as well as the results are presented. The main focus of the results is placed on CRs with $\ell\tau_h+jj$ final states.

10.1 Description of the methodology

As introduced in Chapter 9, the event selections in the SRs are divided in two categories: *central* and *VBF* selections. The methodology used for the estimation of the background contributions in the SR is based on simulation and data. The dominant backgrounds are identified for each decay channel and with the exception of the QCD multijet background, a semi data-driven methodology is adopted. The main goal is to measure the total efficiency of the signal region selection cuts ($\epsilon_{\text{total SR}}$):

$$\epsilon_{\text{total SR}} = \epsilon_{\text{central}} \cdot \epsilon_{\text{VBF}}, \quad (10.1)$$

where

$$\epsilon = \frac{\text{number of events that pass X selections}}{\text{total number of events}} = \frac{N_{\text{pass}}}{N_{\text{total}}}. \quad (10.2)$$

For this purpose, central ($\epsilon_{\text{central}}$) and VBF selection cuts (ϵ_{VBF}) are measured separately in dedicated *control samples* (also referred to as *control regions*), designed to favor the detection of a particular background. Then, the observed data and the prediction from MC simulations are compared both for normalization (total event yields), as well as the agreement in the shapes of the leading $m(jj)$, which is the fit variable used in this analysis.

The number of background events expected in each signal region is given by

$$N_{\text{bkg}} = \sigma_{\text{bkg}} \cdot \mathcal{L}_{\text{int}} \cdot \epsilon_{\text{total}}, \quad (10.3)$$

where σ_{bkg} represents the production cross section for a given background, and \mathcal{L}_{int} is the total integrated luminosity.

After comparing the event yields in each control region, *correction (scale) factors* are derived in order to match the obtained $\epsilon_{\text{central(VBF)}}^{\text{sim}}$ to the observed $\epsilon_{\text{central(VBF)}}^{\text{data}}$:

$$\text{SF}_{x, \text{bkg}} = \frac{N_{x \text{ bkg}}^{\text{data}}}{N_{x \text{ bkg}}^{\text{sim}}} = \frac{\epsilon_{x \text{ bkg}}^{\text{data}}}{\epsilon_{x \text{ bkg}}^{\text{sim}}}, \quad (10.4)$$

such that,

$$\epsilon_{x \text{ bkg}}^{\text{data}} = \text{SF}_{x, \text{bkg}} \cdot \epsilon_{x \text{ bkg}}^{\text{sim}}, \quad (10.5)$$

where x represents "central" or "VBF".

In a perfect world, each control sample would be 100% pure for the targeted background process. However, this is not possible in reality, due to the overlap in final states for different backgrounds.

Therefore, the expression in Eq. 10.4 is modified to account for the *contamination* effect in each control sample. The equation for the efficiency scale factor for central selections will be given by:

$$\text{SF}_{\text{bkg}}^{\text{central}} = \frac{N_{\text{data}}^{\text{central}} - N_{\text{non-bkg, sim}}^{\text{central}}}{N_{\text{bkg, sim}}^{\text{central}}}, \quad (10.6)$$

where $N_{\text{data}}^{\text{central}}$ is the number of events in data that pass the central selections, $N_{\text{non-bkg, sim}}^{\text{central}}$ is the sum of the number of events that do not correspond to the target background, as predicted in simulation, and $N_{\text{bkg, sim}}^{\text{central}}$ is the event yield predicted in simulation for the target background process.

Likewise, the correction factor for central+VBF selections is given by,

$$\text{SF}_{\text{bkg}}^{\text{central+VBF}} = \frac{N_{\text{data}}^{\text{central+VBF}} - N_{\text{non-bkg, sim}}^{\text{central+VBF}}}{N_{\text{bkg, sim}}^{\text{central+VBF}}}. \quad (10.7)$$

The correction factor for VBF selections can be obtained by factoring out $\text{SF}_{\text{bkg}}^{\text{central}}$ from $\text{SF}_{\text{bkg}}^{\text{central+VBF}}$,

$$\text{SF}_{\text{bkg}}^{\text{VBF}} = \frac{\text{SF}_{\text{bkg}}^{\text{central+VBF}}}{\text{SF}_{\text{bkg}}^{\text{central}}}. \quad (10.8)$$

The background prediction in the SR obtained from simulation will be rescaled with $\text{SF}_{\text{bkg}}^{\text{central}}$ and $\text{SF}_{\text{bkg}}^{\text{VBF}}$, such that the contribution from each background is estimated as,

$$N_{\text{bkg, data}}(\text{SR}) = N_{\text{bkg, sim}}(\text{SR}) \cdot \text{SF}_{\text{bkg}}^{\text{central}} \cdot \text{SF}_{\text{bkg}}^{\text{VBF}}. \quad (10.9)$$

The contribution to the event yields in the SR from QCD multijet production is estimated with a different methodology, described in detail on Sec. 10.3.

10.2 Calibration of central and VBF efficiencies

In this document, only the results relevant to the dominant backgrounds in the $\ell\tau_{\text{h}}$ channels are presented. In particular, four main control samples were constructed: (1) a $Z(\rightarrow \tau_{\text{h}}\tau_{\text{h}})+\text{jets}$ CR with the goal of measuring the central SF to correct for the mis-modeling of the τ_{h} identification efficiency; (2) a $Z(\rightarrow \tau_{\mu}\tau_{\text{h}})+\text{jets}$ CR to validate the results in the $Z(\rightarrow \tau_{\text{h}}\tau_{\text{h}})+\text{jets}$, as well as performing studies useful for the data-driven QCD multijet background estimation; (3) a $t\bar{t}(\rightarrow \mu\tau_{\text{h}})+\text{jets}$ CR to measure the central and VBF efficiencies for this process, and (4) a $VV(\rightarrow 3\mu)+\text{jets}$ CR to measure the efficiencies for the diboson processes.

10.2.1 Z+jets

One of the processes that has an important contribution to the signal region in the $\tau\tau$ final states is the production of a Z boson in association with jets, where the Z decays into two τ leptons. Since the τ lepton can decay leptonically and hadronically, there are different combinations of leptons in the final state, in which one hadronic tau is produced: $\tau_e\tau_{\text{h}}$, $\tau_{\mu}\tau_{\text{h}}$ and $\tau_{\text{h}}\tau_{\text{h}}$. Therefore, two control

regions have been constructed in order to enrich the fraction of events from Z+jets production decaying into:

- (1) $\tau_h\tau_h$: in this region, the τ_h identification efficiency will be measured in data and simulation. All mis-modeling from simulation will be related to the τ_h reconstruction and identification.
- (2) $\tau_\mu\tau_h$: this region is constructed with several purposes, (i) study the τ_h selection efficiency and compare to that observed in the $Z(\rightarrow \tau_h\tau_h)$ CR, (ii) calculate the efficiency of VBF selections, in order to compare to that calculated in the $Z\rightarrow \mu\mu$ CR and ensure that the τ_h selections do not affect this efficiency, and (iii) measure the OS \rightarrow LS transfer factor used in the QCD data-driven background estimation for the $\ell\tau_h$ channels;

Z($\rightarrow \tau_h\tau_h$)+jets CR

The event selections for the $Z(\rightarrow \tau\tau \rightarrow \tau_h\tau_h)$ control region are shown in Tab. 10.1. Events are required to fire the DoubleMedium(Charged)IsoPFTau triggers, and contain exactly two reconstructed τ_h 's, identified with the tight WP of the DEEPTAU anti-jet discriminator. The τ_h 's are required to have a $p_T > 70$ GeV, in order to remain in the region where the di- τ_h triggers have reached the plateau efficiency, and to be in the central region of the detector ($|\eta| < 2.1$), in order to ensure good quality tracks from the charged hadrons used for the τ_h reconstruction.

	Object	Selection cuts
Central	Trigger	2016: HLT_DoubleMediumIsoPFTau*, HLT_DoubleMediumCombinedIsoPFTau* 2017, 2018: HLT_DoubleMediumChargedIsoPFTau(HPS)*
	τ_h	$N(\tau_h) = 2$, $p_T(\tau_h) > 70$ GeV, $ \eta(\tau_h) < 2.1$, 1 or 3 prongs, Deep Tau tight ID medium anti- e discriminator, tight anti- μ discriminator.
	$\tau_h\tau_h$ combinations	$N(\tau_h\tau_h) = 1$, $q_1(\tau_h) \times q_2(\tau_h) < 0$, $\Delta R(\tau_h, \tau_h) > 0.4$, $m(\tau_h\tau_h) < 100$ GeV
	e veto	$N(e) = 0$, $p_T(e) > 5$ GeV, $ \eta(e) < 2.1$, medium ID (cut-based)
	μ veto	$N(\mu) = 0$, $p_T(\mu) > 3$ GeV, $ \eta(\mu) < 2.1$, tight ID, $I_{rel} < 0.15$
	b-jet veto	$N(b) = 0$, $p_T(b) > 30$ GeV, $ \eta(b) < 2.4$, medium DeepCSV WP, $\Delta R(e/\mu/\tau_h, b) > 0.4$
	QCD rejection	$ \Delta\phi(j, p_T^{miss}) _{min} > 0.5$, jet defined as in VBF2 selections.

Table 10.1: $Z(\rightarrow \tau_h\tau_h)$ +jets CR selection cuts.

Hadronic tau candidates with 1- or 3-prongs are included, and they also need to satisfy the medium anti-electron and tight anti-muon discriminator WPs. Additional electron, muon and b-jet vetoes are applied. Corrections for the τ_h identification and discrimination against e 's and μ 's have been applied, as described in Sec. 7.6.

A summary of the final event yields, and measured scale factors for all three years is shown on Table 10.2, where only statistical uncertainties are included. The results for different kinematic distributions after applying central and inverted VBF selections are shown in Figures 10.1, (2016), 10.2 (2017) and 10.3 (2018). The prediction for Z+jets from simulation has been corrected with the correction factors measured for each set of selections. In general, the prediction of the background shapes in simulation and the observed data are consistent within statistical uncertainties.

Process	Central		
	2016	2017	2018
EWK V	10.4 ± 1.2	12.0 ± 1.5	17.4 ± 2.2
QCD	0.0 ± 0.0	0.0 ± 0.0	0.0 ± 0.0
Rares	11.3 ± 1.7	7.3 ± 0.7	13.6 ± 1.6
Single top	0.0 ± 0.0	0.0 ± 0.0	0.5 ± 0.2
Diboson	9.0 ± 0.9	8.7 ± 0.8	13.5 ± 0.9
W+jets	2.8 ± 1.0	5.9 ± 2.2	3.5 ± 1.9
Z+jets	2.8 ± 1.0	5.9 ± 2.2	3.5 ± 1.9
$t\bar{t}$	1.1 ± 0.3	1.4 ± 0.8	1.4 ± 0.3
Total bkg	435.9 ± 10.3	587.8 ± 16.5	824.3 ± 16.8
Data	428	530	750
Data/MC	0.982	0.902	0.910
Purity [%]	92.1	94.0	93.9
SF	0.980 ± 0.063	0.895 ± 0.058	0.904 ± 0.046

Table 10.2: Summary of SFs for the $Z(\rightarrow \tau_h \tau_h) + \text{jets}$ CR for all years, including central selections.

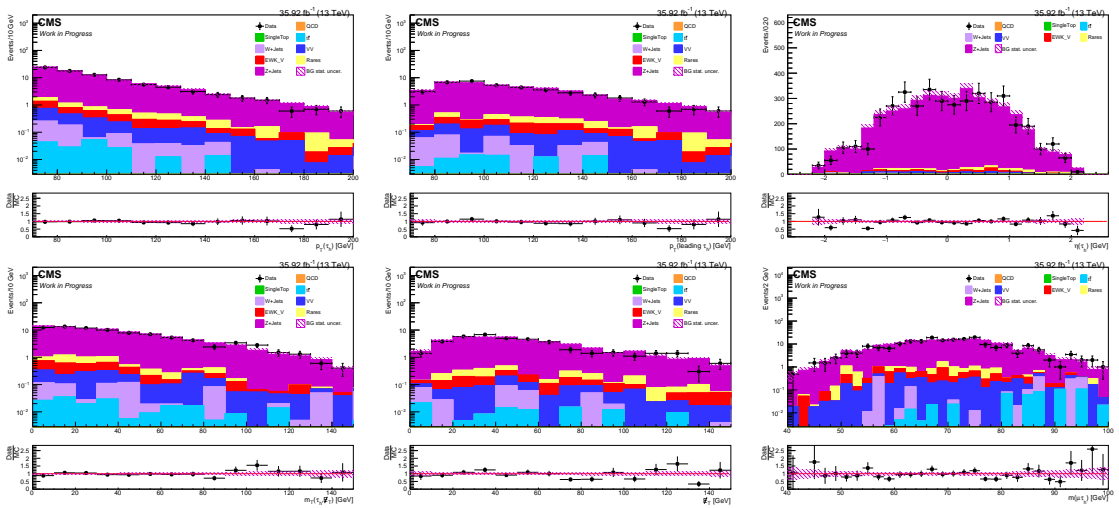


Figure 10.1: Kinematic distributions for the τ_h candidates, p_T^{miss} , $m_T(\tau_h, \cancel{E}_T)$ and $m(\tau_h \tau_h)$ after applying central selections for 2016 data.

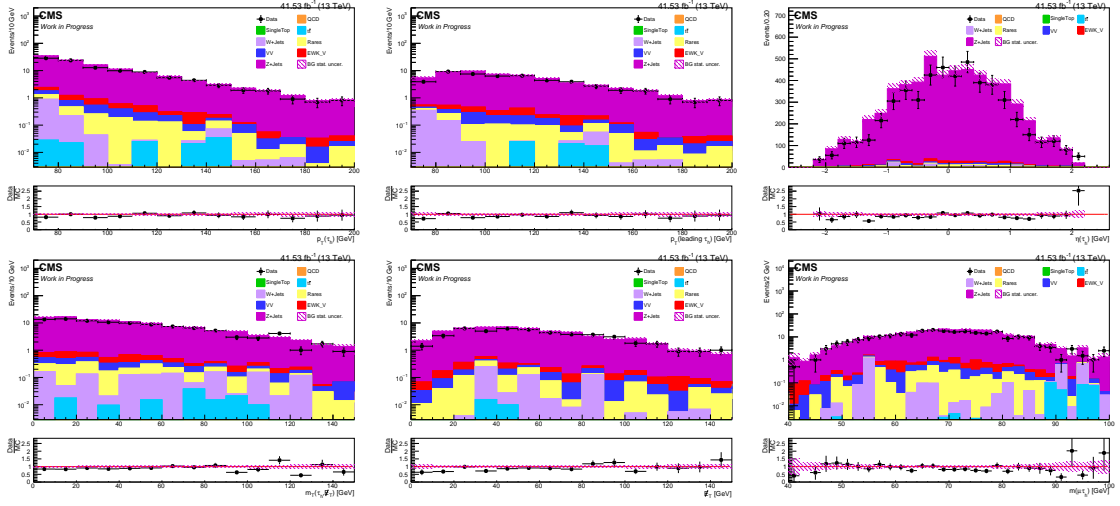


Figure 10.2: Kinematic distributions for the τ_h candidates, p_T^{miss} , $m_T(\tau_h, \cancel{E}_T)$ and $m(\tau_h\tau_h)$ after applying central selections for 2017 data.

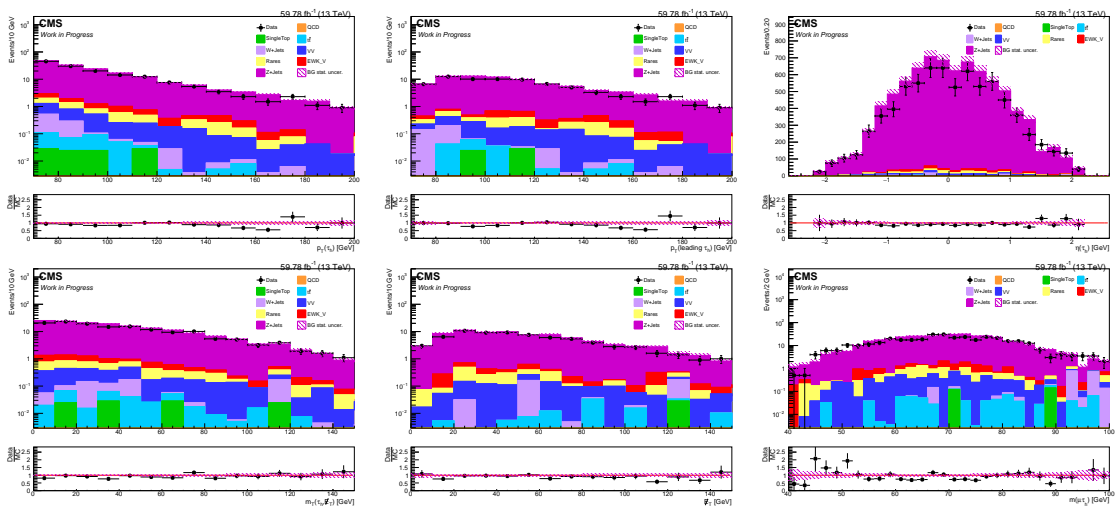


Figure 10.3: Kinematic distributions for the τ_h candidates, p_T^{miss} , $m_T(\tau_h, \cancel{E}_T)$ and $m(\tau_h\tau_h)$ after applying central selections for 2018 data.

Z($\rightarrow \tau_\mu \tau_h$)+jets CR

A Z($\rightarrow \tau^+ \tau^- \rightarrow \mu \tau_h$)+jets control sample is constructed with the following goals: (1) validate the results obtained in the Z($\rightarrow \tau_h \tau_h$)+jets control sample for the τ_h efficiency measurement; (2) measure the VBF selection efficiencies when a τ_h is present in the final state and compare to those measured in the Z $\rightarrow \mu^+ \mu^-$ control sample; (3) perform studies on QCD events which are relevant to the QCD background estimation in the signal regions.

Table 10.3 details the event selections used in this control region. The $p_T(\tau_h)$ requirement is lowered to 20 GeV. Events with additional μ 's are vetoed and a $m_T(\mu, p_T^{\text{miss}}) < 50$ GeV is applied, in order to increase Z+jets purity by rejecting $t\bar{t}$ events. The p_T -dependent corrections for τ_h identification (Sec. 7.6) have been applied to genuine τ_h in simulation, as well as η -dependent corrections to e 's and μ 's misidentified as τ_h in simulation. In addition, energy scale correction factors were applied to the τ_h 4-momentum.

	Object	Selection cuts
Central	Trigger	2016 and 2018: HLT_IsoMu24, 2017: HLT_IsoMu27
	μ	$N(\mu) = 1$, $p_T(\mu) > 30$ GeV, $ \eta(\mu) < 2.1$, $I_{rel.} < 0.15$ and tight ID, $m_T(\mu, p_T^{\text{miss}}) < 50$ GeV
	τ_h	$N(\tau_h) = 1$, $p_T(\tau_h) > 20$ GeV, $ \eta(\tau_h) < 2.1$, tight ID (Deep Tau), medium (tight) anti- $e(\mu)$ discr., 1 or 3 prongs
	$\mu\tau_h$ combinations	$N(\mu\tau_h) = 1$, $q(\mu) \times q(\tau_h) < 0$, $\Delta R(\mu, \tau_h) > 0.4$, $m(\mu, \tau_h) < 100$ GeV
	additional μ veto	$N(\mu) = 0$, $3 < p_T(\mu) < 30$ GeV, $ \eta(\mu) < 2.1$, $I_{rel.} < 0.15$ and tight ID.
	e veto	$N(e) = 0$ with $p_T > 5$ GeV, $ \eta < 2.1$, medium ID (cut-based)
	b-jet veto	$N(b) = 0$, $p_T(b) > 30$ GeV, $ \eta < 2.4$, medium DeepCSV WP
	QCD rejection	$ \Delta\phi(j, p_T^{\text{miss}}) _{min} > 0.5$, jet defined as in VBF2 selections.
VBF2	Jet	$N(j) \geq 2$, $p_T(j) > 30$ GeV, $ \eta(j) < 4.7$, $\Delta R(e/\mu/\tau_h, j) > 0.4$ ID: tight PU jet ID for $30 < p_T \leq 50$ GeV, and for $p_T > 50$ GeV 2016: Loose PF ID; 2017, 2018: Tight PF ID
	Dijet combinations	$N(j_1, j_2) \geq 1$, $\Delta\eta(j_1, j_2) > 3.8$, $\eta(j_1) \times \eta(j_2) < 0$, $m(j_1, j_2) > 500$ GeV

Table 10.3: Z($\rightarrow \tau^+ \tau^- \rightarrow \mu \tau_h$)+jets CR selection cuts.

Given that the $p_T(\tau_h)$ threshold is low, we expect a sizeable contribution from QCD multijet events. A data-driven estimation using the ABCD method¹, with the two variables of interest being the μ and τ_h isolation and the electric charge combination of these objects (Fig. 10.4):

- *CRA*: the control region of interest, Z($\rightarrow \tau^+ \tau^- \rightarrow \mu \tau_h$)+jets, where the QCD background will be estimated,
- *CRB*: in this region, the μ and τ_h isolation requirement is kept the same as in CRA, but the electric charge requirement is inverted (like-sign, or LS),
- *CRC*: here both the μ and τ_h isolation requirement is inverted and events with oppositely charged μ and τ_h combinations are selected,
- *CRD*: finally, in this region both requirements are inverted.

A transfer factor (TF) from OS to LS events is calculated with the events obtained in CRC and CRD, following the equation

$$\text{TF}_{\text{OS} \rightarrow \text{LS}} = \frac{N_{\text{data}}^{\text{CRC}} - N_{\text{non QCD MC}}^{\text{CRC}}}{N_{\text{data}}^{\text{CRD}} - N_{\text{non QCD MC}}^{\text{CRD}}}, \quad (10.10)$$

¹See introduction sections of Refs. [167]-[168] and references therein.

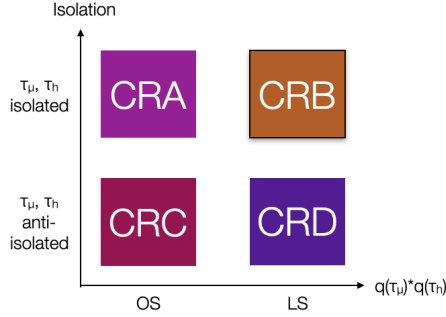


Figure 10.4: ABCD diagram for the QCD estimation in the $Z(\rightarrow \tau^+\tau^- \rightarrow \mu\tau_h)+\text{jets}$ CR, which corresponds to CRA. The OS/LS transfer factor is obtained from CRC and CRD, and the QCD shape is taken from CRB.

The event yield for QCD in CRA will be estimated as:

$$N_{\text{QCD}}^{\text{CRA}} = \text{TF}_{\text{OS} \rightarrow \text{LS}} (N_{\text{data}}^{\text{CRB}} - N_{\text{non QCD MC}}^{\text{CRB}}), \quad (10.11)$$

and the QCD shape is extracted from CRB, by subtracting the non-QCD background contributions as predicted in simulation from the observed data.

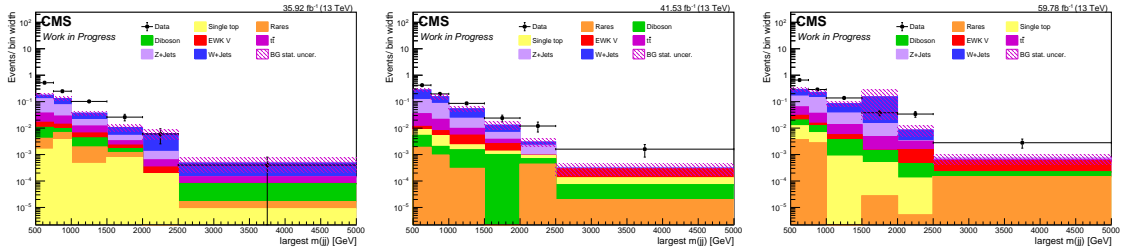


Figure 10.5: Kinematic distributions for the leading $m(\text{jj})$ in CRB for 2016 (left), 2017 (middle) and 2018 (right) after applying central and VBF2 selections.

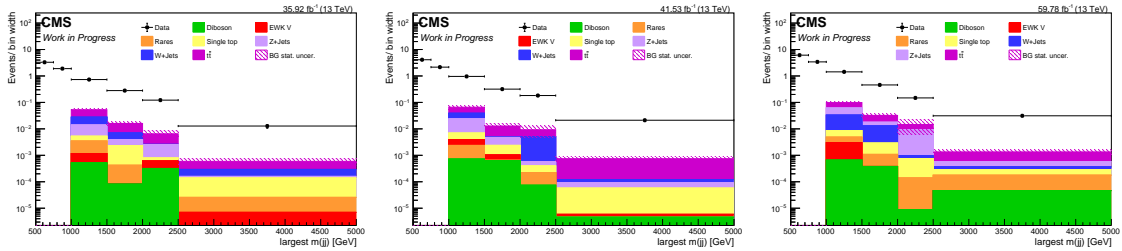


Figure 10.6: Kinematic distributions for the leading $m(\text{jj})$ in CRC for 2016 (left), 2017 (middle) and 2018 (right) after applying central and VBF2 selections.

The final event yields after applying central selections in each of the different regions for the QCD estimation with VBF2 selections are summarized in Tables 10.4, 10.5, and 10.6 for the 2016, 2017, and 2018 data sets, respectively. Leading $m(\text{jj})$ distributions in CRB, CRC, and CRD after applying central and VBF2 selections are shown for each year in Figures 10.5, 10.6, and 10.7.

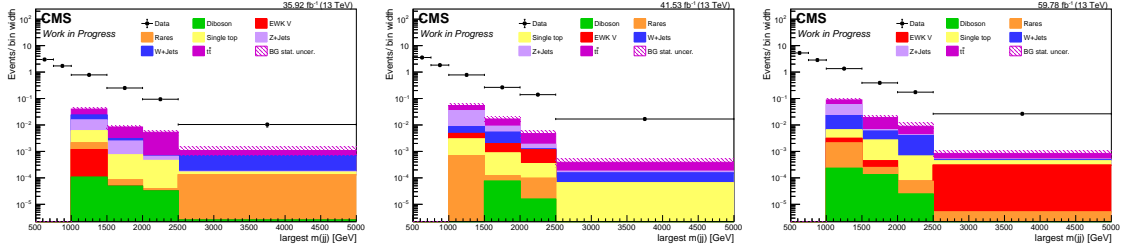


Figure 10.7: Kinematic distributions for the leading $m(jj)$ in CRD for 2016 (left), 2017 (middle) and 2018 (right) after applying central and VBF2 selections.

Process	CRA		CRB		CRC		CRD	
	Central	VBF2	Central	VBF2	Central	VBF2	Central	VBF2
EWK V	265.8 ± 6.4	30.5 ± 2.1	50.2 ± 2.9	4.1 ± 0.8	27.1 ± 2.1	0.5 ± 0.3	22.4 ± 1.9	0.5 ± 0.3
Rares	364.5 ± 9.7	14.4 ± 1.8	79.8 ± 4.5	2.1 ± 0.7	172.9 ± 6.7	1.4 ± 0.6	162.8 ± 6.5	0.8 ± 0.5
Single top	211.4 ± 6.1	6.1 ± 1.0	41.6 ± 2.3	2.0 ± 0.4	103.2 ± 3.8	2.2 ± 0.4	87.2 ± 3.5	2.6 ± 0.6
Diboson	563.6 ± 8.5	24.1 ± 1.6	110.8 ± 3.0	4.0 ± 0.5	44.7 ± 2.8	0.5 ± 0.1	42.4 ± 2.9	0.1 ± 0.0
W+Jets	6041.3 ± 284.8	63.0 ± 6.3	2865.5 ± 211.3	40.9 ± 4.9	804.6 ± 73.2	8.8 ± 2.3	653.3 ± 85.0	5.7 ± 1.8
Z+jets	23422.1 ± 172.8	348.6 ± 13.6	2932.5 ± 64.8	40.0 ± 6.6	2096.3 ± 50.3	6.1 ± 1.6	1978.2 ± 49.0	5.6 ± 1.4
$t\bar{t}$	1157.4 ± 8.9	75.1 ± 2.3	186.1 ± 4.5	12.0 ± 1.1	724.2 ± 9.3	19.8 ± 1.5	613.2 ± 8.5	14.2 ± 1.3
Total non QCD bkg	32026.2 ± 333.6	561.7 ± 15.5	6266.5 ± 221.1	105.1 ± 8.4	3973.1 ± 89.7	39.2 ± 3.2	3559.4 ± 98.8	29.6 ± 2.8
Data	38832	854	13951	260	59249	1897	53630	1763
$N_{\text{data}} - N_{\text{non QCD MC}}$	-	-	7684.5 ± 250.7	154.9 ± 18.2	55275.9 ± 259.4	1857.8 ± 43.7	50070.6 ± 251.8	1733.4 ± 42.1
QCD purity [%]	-	-	55.1	59.6	93.3	97.9	93.4	98.3

Table 10.4: Summary of event yields in the ABCD regions for the QCD estimation in the $Z(\rightarrow \tau_\mu \tau_h) + \text{jets}$ CR for 2016 after applying central and VBF2 selections. Uncertainties included in this table are only statistical.

Process	CRA		CRB		CRC		CRD	
	Central	VBF2	Central	VBF2	Central	VBF2	Central	VBF2
EWK V	376.3 ± 8.9	26.5 ± 2.3	82.5 ± 4.4	3.9 ± 1.0	45.5 ± 3.2	1.0 ± 0.4	36.6 ± 2.9	1.9 ± 0.7
Rares	220.2 ± 3.9	5.5 ± 0.6	60.8 ± 2.1	1.1 ± 0.4	84.2 ± 2.5	0.9 ± 0.2	73.8 ± 2.3	0.4 ± 0.2
Single top	270.4 ± 6.8	8.2 ± 1.1	66.7 ± 2.9	2.5 ± 0.5	172.1 ± 4.7	2.5 ± 0.4	125.2 ± 4.0	1.8 ± 0.4
Diboson	741.2 ± 10.9	28.0 ± 2.0	136.7 ± 4.3	2.5 ± 0.5	48.0 ± 2.5	0.7 ± 0.3	41.7 ± 3.0	0.0 ± 0.0
W+Jets	10706.8 ± 440.4	95.1 ± 11.8	4891.2 ± 314.2	76.0 ± 10.7	1636.3 ± 138.4	9.9 ± 3.4	1105.4 ± 123.1	3.8 ± 1.7
Z+jets	31270.6 ± 232.2	421.2 ± 16.8	4984.2 ± 104.9	46.6 ± 8.1	3146.7 ± 79.5	9.9 ± 3.5	3067.6 ± 78.7	15.5 ± 4.5
$t\bar{t}$	1366.9 ± 10.4	67.9 ± 2.3	254.2 ± 5.5	11.9 ± 1.2	878.3 ± 10.4	21.2 ± 1.6	732.0 ± 9.5	15.6 ± 1.4
Total non QCD bkg	44952.4 ± 498.2	652.5 ± 20.9	10476.3 ± 331.4	144.5 ± 13.5	6011.1 ± 160.1	46.1 ± 5.2	5182.2 ± 146.6	39.0 ± 5.0
Data	44814	772	14052	219	88515	2351	80137	1979
$N_{\text{data}} - N_{\text{non QCD MC}}$	-	-	3575.7 ± 351.9	74.5 ± 20.1	82503.9 ± 337.8	3401.0 ± 59.5	74954.8 ± 318.8	1940.0 ± 44.8
QCD purity [%]	-	-	25.4	34.0	93.2	98.0	93.5	98.0

Table 10.5: Summary of event yields in the ABCD regions for the QCD estimation in the $Z(\rightarrow \tau_\mu \tau_h) + \text{jets}$ CR for 2017 after applying central and VBF2 selections. Uncertainties included in this table are only statistical.

Process	CRA		CRB		CRC		CRD	
	Central	VBF2	Central	VBF2	Central	VBF2	Central	VBF2
EWK V	529.6 ± 12.8	57.8 ± 4.1	118.2 ± 6.4	5.7 ± 1.4	58.6 ± 4.4	1.2 ± 0.6	51.9 ± 4.1	1.4 ± 0.7
Rares	310.6 ± 7.9	9.9 ± 1.2	87.6 ± 4.3	1.9 ± 0.6	111.1 ± 4.8	1.7 ± 0.6	107.4 ± 4.7	1.0 ± 0.5
Single top	350.6 ± 9.0	12.4 ± 1.6	72.8 ± 3.4	3.9 ± 0.7	235.7 ± 6.4	3.4 ± 0.5	182.6 ± 5.6	3.4 ± 0.4
Diboson	1012.2 ± 10.9	41.5 ± 2.4	169.6 ± 4.1	5.5 ± 0.7	72.3 ± 3.1	0.6 ± 0.2	46.4 ± 2.3	0.2 ± 0.1
W+Jets	12651.5 ± 581.4	183.2 ± 55.8	5783.6 ± 426.4	150.1 ± 60.3	3021.8 ± 275.9	17.7 ± 4.1	1367.1 ± 156.2	11.4 ± 3.5
Z+jets	45299.4 ± 334.9	728.5 ± 27.5	6314.2 ± 144.2	67.4 ± 11.2	4910.7 ± 120.1	21.3 ± 6.0	4630.5 ± 116.5	18.6 ± 5.4
$t\bar{t}$	1809.3 ± 12.0	108.4 ± 2.9	285.4 ± 4.6	19.8 ± 1.2	1209.0 ± 9.4	30.1 ± 1.5	1010.8 ± 8.6	24.6 ± 1.3
Total non QCD bkg	61963.3 ± 671.4	1141.6 ± 62.5	12831.5 ± 450.3	254.2 ± 61.4	9619.1 ± 301.2	76.0 ± 7.5	7396.8 ± 195.3	60.6 ± 6.7
Data	63033	1251	18993	348	115742	3477	105273	3057
$N_{\text{data}} - N_{\text{non QCD MC}}$	-	-	6161.5 ± 470.9	93.8 ± 64.2	106122.9 ± 454.4	3401.0 ± 59.5	97876.2 ± 378.7	2996.4 ± 55.7
QCD purity [%]	-	-	32.4	27.0	91.7	97.8	93.0	98.0

Table 10.6: Summary of event yields in the ABCD regions for the QCD estimation in the $Z(\rightarrow \tau_\mu \tau_h) + \text{jets}$ CR for 2018 after applying central and VBF2 selections. Uncertainties included in this table are only statistical.

We studied the potential correlation in the leading $m(jj)$ shape with the OS/LS requirements by comparing the distributions in the corresponding regions. The OS/LS (CRC and CRD) leading $m(jj)$ shape+normalization comparison for QCD (data - non QCD MC) is shown in Fig. 10.8. The ratios were fit to a 0- and a 1-degree polynomial and the summary of the fit parameters is shown in Tab. 10.7.

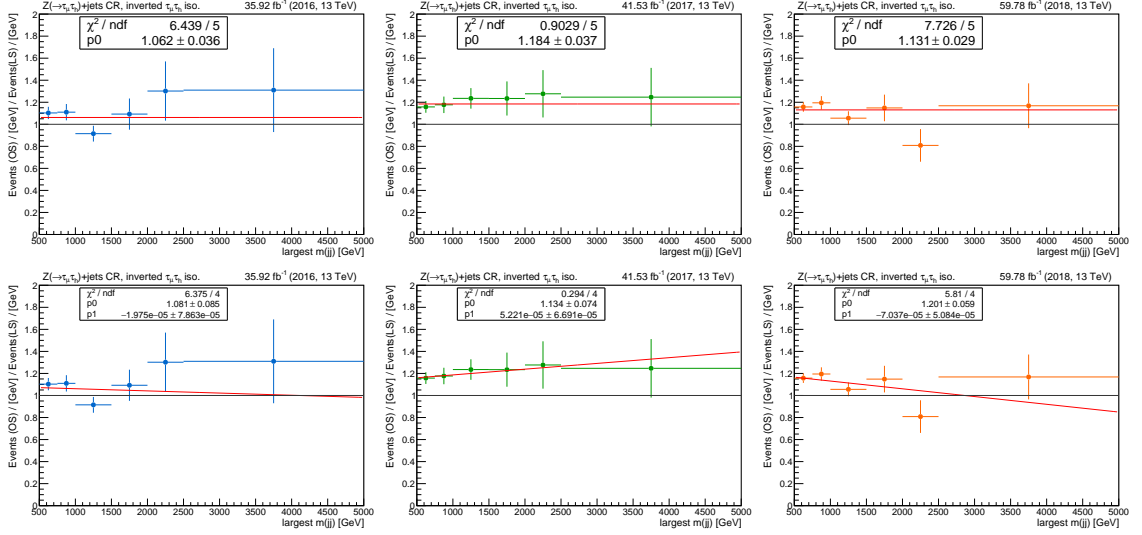


Figure 10.8: OS/LS transfer factor after VBF2 selections for 2016 (left), 2017 (middle), and 2018 (right) data and corresponding fits to a 0th degree (top) and 1st degree (bottom) polynomial.

Fit parameter	pol-0			pol-1		
	2016	2017	2018	2016	2017	2018
p_0	1.06 ± 0.04	1.18 ± 0.04	1.13 ± 0.03	1.08 ± 0.09	1.13 ± 0.07	1.20 ± 0.06
p_1	—	—	—	$(-1.98 \pm 7.86) \times 10^{-5}$	$(5.22 \pm 6.69) \times 10^{-5}$	$(-7.04 \pm 5.08) \times 10^{-5}$
χ^2/N	1.29	0.180	1.55	1.59	0.0735	1.45
$TF_{OS \rightarrow LS}$ (norm.)	1.07 ± 0.04	1.19 ± 0.04	1.14 ± 0.03	—		

Table 10.7: Summary of results from the fits to a pol-0 and pol-1 polynomials of the leading $m(jj)$ ratios in CRC and CRD ($TF_{OS \rightarrow LS}$) for VBF2 selections. The $TF_{OS \rightarrow LS}$ measured after applying central and VBF2 selections from the event yields in this region is also included.

The χ^2/N values obtained from the fits indicate $TF_{OS \rightarrow LS}$ is shape-independent within $1-2\sigma$ of statistical uncertainty. Therefore, $TF_{OS \rightarrow LS}$ is measured from the event yields obtained in CRC and CRD using Eq. 10.10. These values are included in Table 10.7 as well.

A similar study was performed for the nominal/inverted isolation transfer factor $TF_{nom. \rightarrow inv. iso}$ (CRB and CRD). The shape+normalization comparison for QCD is shown in Figure 10.9. After fitting these ratios to a 0- and 1-degree polynomials, we observe that these are consistent with a 0-degree polynomial within $1-2\sigma$ of statistical uncertainty (Tab. 10.8). In this case, however, we can see a stronger shape dependence from the results to a 1-degree polynomial. The results from the fit to the first degree polynomial will be used to assign systematic uncertainties to the QCD background estimation in the SRs, described later in this chapter.

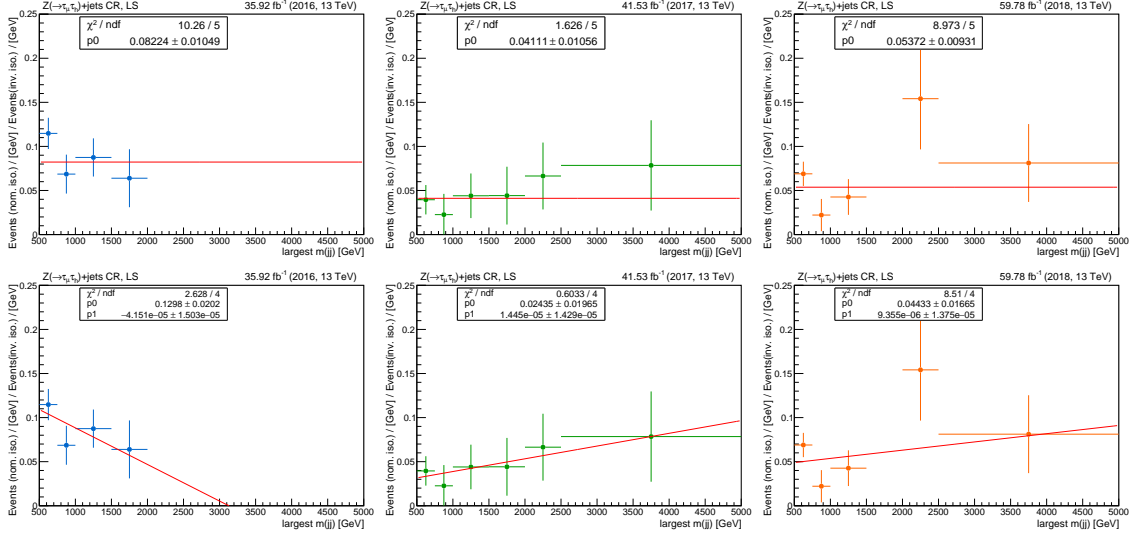


Figure 10.9: Nominal/inverted isolation transfer factor after VBF2 selections for 2016 (left), 2017 (middle), and 2018 (right) data and corresponding fits to a 0th degree (top) and 1st degree (bottom) polynomial.

Fit parameter	pol-0			pol-1		
	2016	2017	2018	2016	2017	2018
p_0	$(8.22 \pm 1.05) \times 10^{-2}$	$(4.11 \pm 1.06) \times 10^{-2}$	$(5.37 \pm 0.93) \times 10^{-2}$	$(13.0 \pm 2.0) \times 10^{-2}$	$(2.44 \pm 1.97) \times 10^{-2}$	$(4.43 \pm 1.67) \times 10^{-2}$
p_1	—	—	—	$(-4.15 \pm 1.50) \times 10^{-5}$	$(1.45 \pm 1.43) \times 10^{-5}$	$(0.94 \pm 1.38) \times 10^{-5}$
χ^2/N	2.05	0.325	1.79	0.657	0.151	2.13
$TF_{\text{nom.} \rightarrow \text{inv. iso.}} (\text{norm.})$	$(8.94 \pm 1.07) \times 10^{-2}$	$(3.84 \pm 1.04) \times 10^{-2}$	$(3.13 \pm 2.14) \times 10^{-2}$	—	—	—

Table 10.8: Summary of results from the fits to a pol-0 and pol-1 polynomials of the leading $m(jj)$ ratios in CRB and CRD ($TF_{\text{nom.} \rightarrow \text{inv. iso.}}$) for VBF2 selections. The $TF_{\text{nom.} \rightarrow \text{inv. iso.}}$ measured after applying central and VBF2 selections from the event yields in this region is also included.

The final event yields in the $Z(\rightarrow \tau_\mu \tau_h)$ +jets CR, with the data-driven estimation for QCD are shown in Table 10.9. The SFs for each set of selections (central and VBF2) are also included here. We can observe consistency between the central SFs in this control sample and those measured in the $Z(\rightarrow \tau_h \tau_h)$ +jets. Similarly, we get consistency within 1-2 σ of statistical uncertainty for the VBF2 efficiency SFs in this CR and the $Z(\rightarrow \mu^+ \mu^-)$ +jets CR. Therefore, for VBF1 selections we will take the VBF1 efficiency SFs measured in $Z(\rightarrow \mu^+ \mu^-)$ +jets. Figures 10.10-10.11, 10.12-10.13 and 10.14-10.15 include relevant kinematic distributions for this control sample after applying central and VBF2 selections and correcting the Z+jets prediction with the measured correction factors.

Process	Central			VBF2		
	2016	2017	2018	2016	2017	2018
EWK V	265.8 ± 6.4	376.3 ± 8.9	529.6 ± 12.8	30.5 ± 2.1	26.5 ± 2.3	57.8 ± 4.1
QCD	8237.7 ± 90.8	4248.0 ± 65.2	6993.4 ± 83.6	166.0 ± 12.9	88.5 ± 9.4	106.5 ± 10.3
Rares	364.5 ± 9.7	220.2 ± 3.9	310.6 ± 7.9	14.4 ± 1.8	5.5 ± 0.6	9.9 ± 1.2
Single top	211.4 ± 6.1	270.4 ± 6.8	350.6 ± 9.0	6.1 ± 1.0	8.2 ± 1.1	12.4 ± 1.6
Diboson	563.6 ± 8.5	741.2 ± 10.9	1012.2 ± 10.9	24.1 ± 1.6	28.0 ± 2.0	41.5 ± 2.4
W+Jets	6041.3 ± 284.8	10706.8 ± 440.4	12651.5 ± 581.4	63.0 ± 6.3	95.1 ± 11.8	183.2 ± 55.8
Z+jets	23422.1 ± 172.8	31270.6 ± 232.2	45299.4 ± 334.9	348.6 ± 13.6	421.2 ± 16.8	728.5 ± 27.5
$t\bar{t}$	1157.4 ± 8.9	1366.9 ± 10.4	1809.3 ± 12.0	75.1 ± 2.3	67.9 ± 2.3	108.4 ± 2.9
Total bkg	40263.9 ± 345.8	49200.3 ± 502.5	68956.7 ± 676.6	727.7 ± 20.2	741.0 ± 23.0	1248.0 ± 63.3
Data	38832	44814	63033	854	772	1251
Data/MC	0.964	0.911	0.914	1.17	1.04	1.00
Purity (%)	58.2	63.6	65.7	47.9	56.8	58.4
SF	0.939 ± 0.012	0.860 ± 0.012	0.869 ± 0.012	1.45 ± 0.13	1.25 ± 0.12	1.16 ± 0.13

Table 10.9: Summary of SFs for the $Z(\rightarrow \tau_\mu \tau_h)$ +jets CR for Run II including central and VBF2 selections, including the QCD data-driven estimation. Only statistical uncertainties are included.

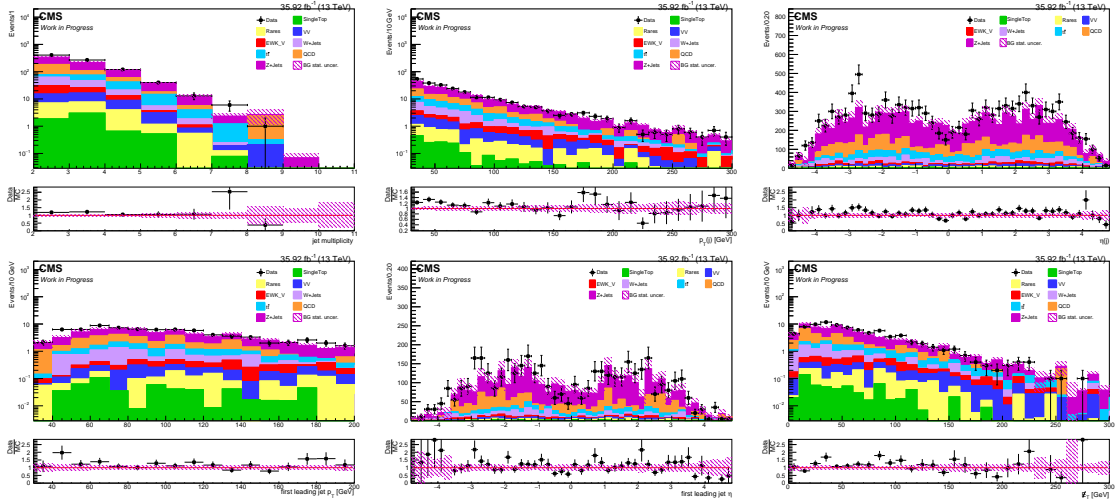


Figure 10.10: Distributions for jet multiplicity, $p_T(j)$, $\eta(j)$, leading jet p_T , η and p_T^{miss} after applying central and VBF2 selections for 2016 data in CRA. Distribution for QCD is obtained from the data-driven estimation.

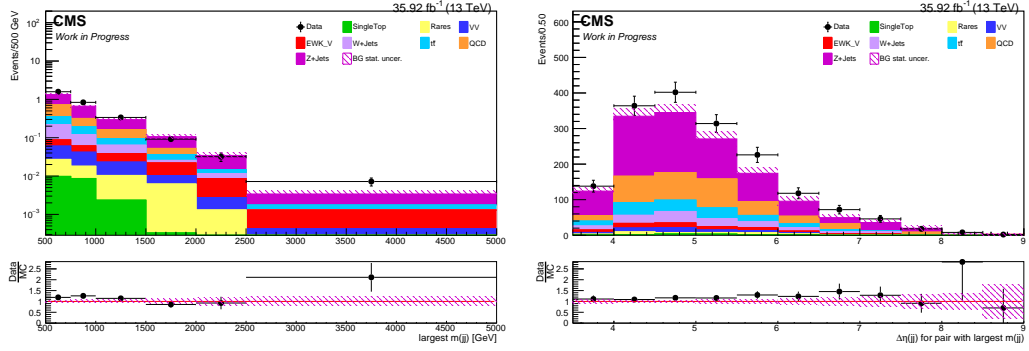


Figure 10.11: Distributions for leading $m(jj)$ and $\Delta\eta(jj)$ for this dijet pair after applying central and VBF2 selections for 2016 data in CRA. Distribution for QCD is obtained from the data-driven estimation.

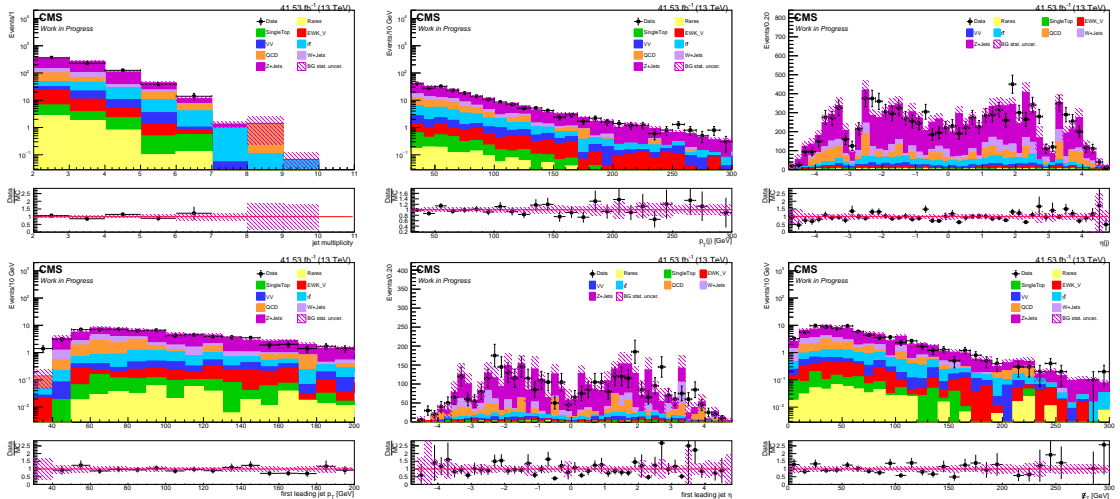


Figure 10.12: Distributions for jet multiplicity, $p_T(j)$, $\eta(j)$, leading jet p_T , η and p_T^{miss} after applying central and VBF2 selections for 2017 data in CRA. Distribution for QCD is obtained from the data-driven estimation.

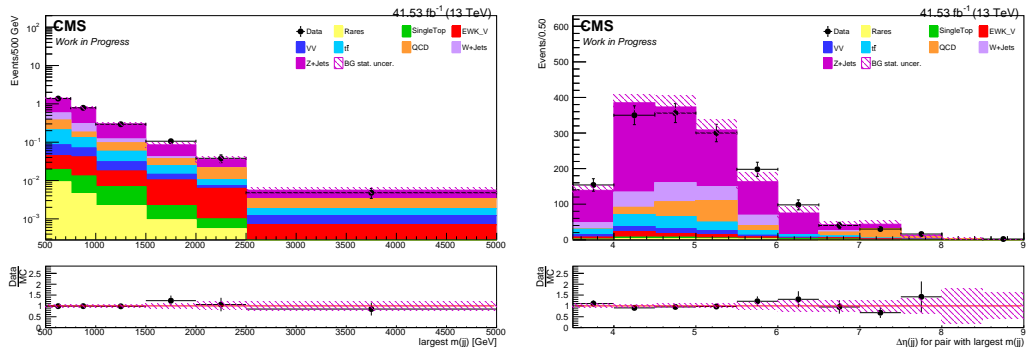


Figure 10.13: Distributions for leading $m(jj)$ and $\Delta\eta(jj)$ for this dijet pair after applying central and VBF2 selections for 2017 data in CRA. Distribution for QCD is obtained from the data-driven estimation.

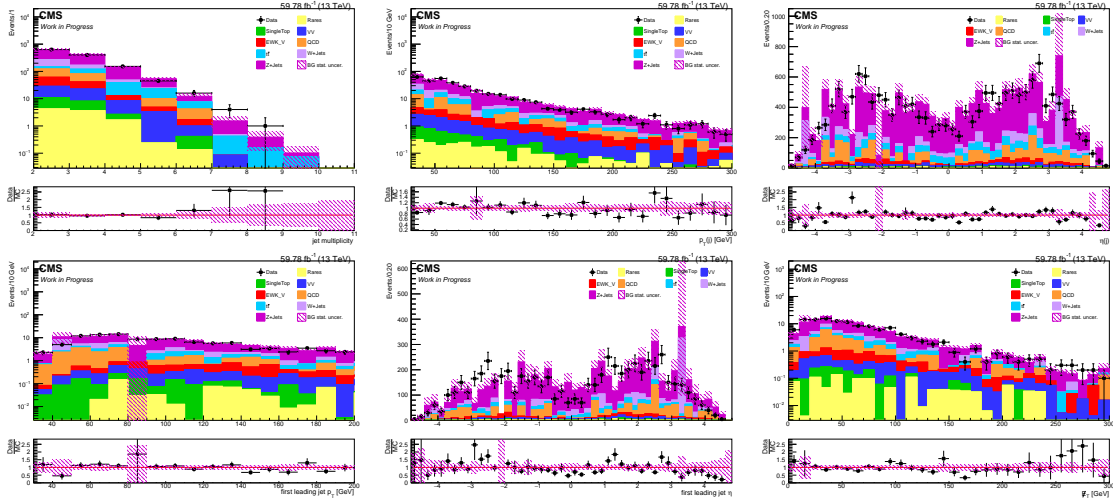


Figure 10.14: Distributions for jet multiplicity, $p_T(j)$, $\eta(j)$, leading jet p_T , η and p_T^{miss} after applying central and VBF2 selections for 2018 data in CRA. Distribution for QCD is obtained from the data-driven estimation.

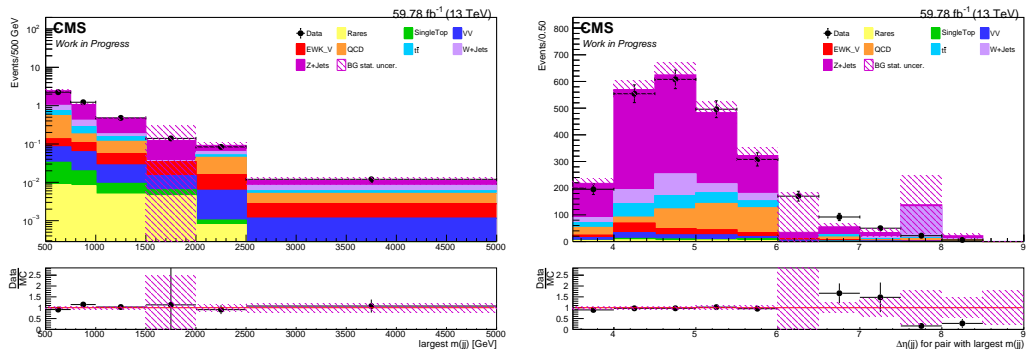


Figure 10.15: Distributions for leading $m(jj)$ and $\Delta\eta(jj)$ for this dijet pair after applying central and VBF2 selections for 2018 data in CRA. Distribution for QCD is obtained from the data-driven estimation.

10.2.2 $t\bar{t}$ +jets

Another background process which contributes to the signal region in the $\tau\tau$ final states, with similar final states to the Z +jets processes, is the production of top-antitop quark pairs ($t\bar{t}$), in which each top quark decays leptonically. This allows for different lepton combinations in the final state: $e\tau$, $\mu\tau$ and $\tau\tau$. In the cases where the τ lepton decays hadronically, the possible final states are $e\tau_h$, $\mu\tau_h$, and $\tau_h\tau_h$, where the e and μ can be prompt or product of the leptonic decay of the τ lepton.

In order to study the central and VBF efficiency of $t\bar{t}$ in simulation for the final states including at least one τ_h , a $t\bar{t}(\rightarrow \mu\tau_h)$ +jets control region was obtained. The event selections, described in Tab. 10.10, are similar to the selections for the $Z(\rightarrow \tau\tau \rightarrow \mu\tau_h)$ control region, except that the $m_T(\mu)$ requirement is inverted ($m_T(\mu) > 50$ GeV), instead of a b-jet veto, we select events with $N(\text{b-jet}) \geq 1$, and a $p_T^{\text{miss}} > 75$ GeV is included. Compared to the signal region, the p_T^{miss} requirement is looser, with the purpose of increasing the event yields in this control sample.

Scale factors are derived for central and VBF selections separately, to understand the modeling of each set of selections in simulation and compare with results obtained in a similar control region but in the other channels included (e.g. single μ and $\mu\mu$ channel). The central SF in this case will correct for the mis-modeling of τ_h identification, as well as b-jet tagging, whereas the VBF SF will only correct for the mis-modeling of these particular selections.

	Object	Selection cuts
Central	Trigger	2016 and 2018: HLT_IsoMu24; 2017: HLT_IsoMu27
	μ	$N(\mu) = 1$, $p_T(\mu) > 30$ GeV, $ \eta(\mu) < 2.1$ and tight ID, $I_{rel} < 0.15$; $m_T(\mu, p_T^{\text{miss}}) > 50$ GeV
	τ_h	$N(\tau_h) = 1$, $p_T(\tau_h) > 20$ GeV, $ \eta(\tau_h) < 2.1$, tight ID, 1 or 3 prongs, medium anti- e discriminator, tight anti- μ discriminator,
	b-jet	$N(b) \geq 1$, $p_T(b) > 30$ GeV, $ \eta < 2.4$, medium DeepCSV WP, $\Delta R(e/\mu/\tau_h, b) > 0.4$, official b-tagging SF applied.
	e veto	$N(e) = 0$, $p_T(e) > 5$ GeV, $ \eta(e) < 2.1$, medium ID (cut-based)
	p_T^{miss}	$p_T^{\text{miss}} > 75$ GeV
	QCD rejection	$ \Delta\phi(j, p_T^{\text{miss}}) _{min} > 0.5$, jet defined as in VBF2 selections.
VBF1	Jet	$N(j) \geq 2$, $p_T(j) > 60$ GeV, $ \eta(j) < 4.7$, $\Delta R(e/\mu/\tau_h, j) > 0.4$ 2016: Loose PF ID; 2017, 2018: Tight PF ID
	Dijet combinations	$N(j_1, j_2) \geq 1$, $\Delta\eta(j_1, j_2) > 3.8$, $\eta(j_1) \times \eta(j_2) < 0$, $m(j_1, j_2) > 1000$ GeV
VBF2	Jet	$N(j) \geq 2$, $p_T(j) > 30$ GeV, $ \eta(j) < 4.7$, $\Delta R(e/\mu/\tau_h, j) > 0.4$ ID: tight PU jet ID for $30 < p_T \leq 50$ GeV, and for $p_T > 50$ GeV 2016: Loose PF ID; 2017, 2018: Tight PF ID
	Dijet combinations	$N(j_1, j_2) \geq 1$, $\Delta\eta(j_1, j_2) > 3.8$, $\eta(j_1) \times \eta(j_2) < 0$, $m(j_1, j_2) > 500$ GeV

Table 10.10: $t\bar{t} \rightarrow \mu\tau_h$ CR selection cuts.

The event yields after central and VBF selections are shown in Table 10.11, together with the measured $\text{SF}_{\text{central}}^{t\bar{t}}$, $\text{SF}_{\text{VBF1}}^{t\bar{t}}$ and $\text{SF}_{\text{VBF2}}^{t\bar{t}}$. The results for $\text{SF}_{\text{central}}^{t\bar{t}}$ show that the normalization is well modeled in simulation after applying central selections for all three years. For $\text{SF}_{\text{VBF1}}^{t\bar{t}}$, the prediction of background yields is consistent with data within statistical uncertainty. The correction factor obtained for VBF1 selections with the 2017 data set shows a larger deviation from unity ($\text{SF}_{\text{VBF1}}^{t\bar{t}} = 1.21 \pm 0.11$), but it is still consistent within $2\sigma_{\text{stat}}$. For $\text{SF}_{\text{VBF2}}^{t\bar{t}}$, the scale factors are all consistent with unity within statistical uncertainty.

Process	Central			VBF1			VBF2		
	2016	2017	2018	2016	2017	2018	2016	2017	2018
EWK V	1.9 ± 0.6	12.2 ± 1.7	16.5 ± 2.5	0.0 ± 0.0	0.5 ± 0.3	0.4 ± 0.0	0.1 ± 0.0	0.9 ± 0.5	2.5 ± 1.0
QCD	0.0 ± 0.0	0.3 ± 0.2	13.7 ± 0.0	0.0 ± 0.0	0.1 ± 0.0	0.0 ± 0.0	0.0 ± 0.0	0.1 ± 0.0	0.0 ± 0.0
Rares	1.1 ± 0.4	1.6 ± 0.4	2.9 ± 0.6	0.0 ± 0.0	0.0 ± 0.0	0.1 ± 0.0	0.3 ± 0.3	0.5 ± 0.3	0.1 ± 0.1
Single top	880.0 ± 12.9	1239.6 ± 15.3	1713.2 ± 21.0	6.0 ± 1.1	8.7 ± 1.2	11.9 ± 1.7	72.3 ± 3.7	48.7 ± 2.9	124.2 ± 5.5
Diboson	23.3 ± 1.9	43.5 ± 2.8	71.4 ± 4.2	0.6 ± 0.3	1.0 ± 0.4	1.9 ± 0.7	4.0 ± 0.5	3.0 ± 0.6	10.1 ± 1.7
W+jets	57.8 ± 5.6	137.2 ± 42.2	101.8 ± 15.0	0.1 ± 0.1	0.1 ± 0.0	0.7 ± 0.1	4.5 ± 0.0	1.4 ± 1.2	6.6 ± 4.0
Z+jets	26.3 ± 3.7	71.5 ± 8.8	75.0 ± 10.0	0.0 ± 0.0	0.3 ± 0.1	0.3 ± 0.1	1.4 ± 0.5	0.7 ± 0.1	6.0 ± 2.1
$t\bar{t}$	9898.8 ± 23.7	12927.0 ± 29.2	18193.2 ± 38.3	105.6 ± 2.4	123.0 ± 2.9	186.8 ± 3.9	876.9 ± 7.1	720.4 ± 6.9	1623.2 ± 11.4
Total bkg	10889.3 ± 27.9	14433.0 ± 54.4	20187.8 ± 47.5	112.3 ± 2.7	133.7 ± 3.1	202.1 ± 4.3	959.4 ± 8.2	775.8 ± 7.6	1772.7 ± 13.6
Data	10196	14530	19520	100	160	191	860	808	1757
Data/MC	0.936	1.007	0.967	0.890	1.197	0.945	0.896	1.042	0.991
Purity (%)	90.9	89.6	90.1	94.0	92.0	92.4	91.4	92.9	91.6
SF	0.930 ± 0.011	1.01 ± 0.01	0.963 ± 0.008	0.950 ± 0.109	1.21 ± 0.11	0.976 ± 0.084	0.953 ± 0.042	1.04 ± 0.05	1.03 ± 0.03

Table 10.11: Summary of SFs for the $t\bar{t}(\rightarrow \mu\tau_h)$ +jets CR for all years, including central, VBF1 and VBF2 selections. Only statistical uncertainties are included.

Figures 10.16-10.24, 10.25-10.33, and 10.34-10.42 show some of the most important kinematic distributions for this control region for the 2016, 2017 and 2018 data sets, respectively. All distributions shown in these sections have been corrected with the SFs presented in Tab. 10.11.

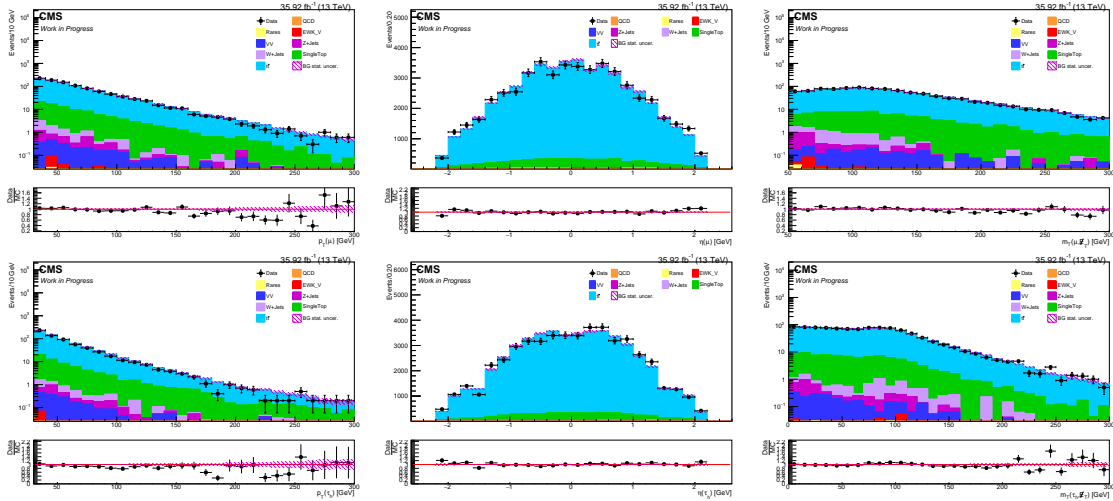


Figure 10.16: p_T (left), η (middle) and m_T (right) distributions for μ (top) and τ_h (bottom) after applying central selections for 2016 data.

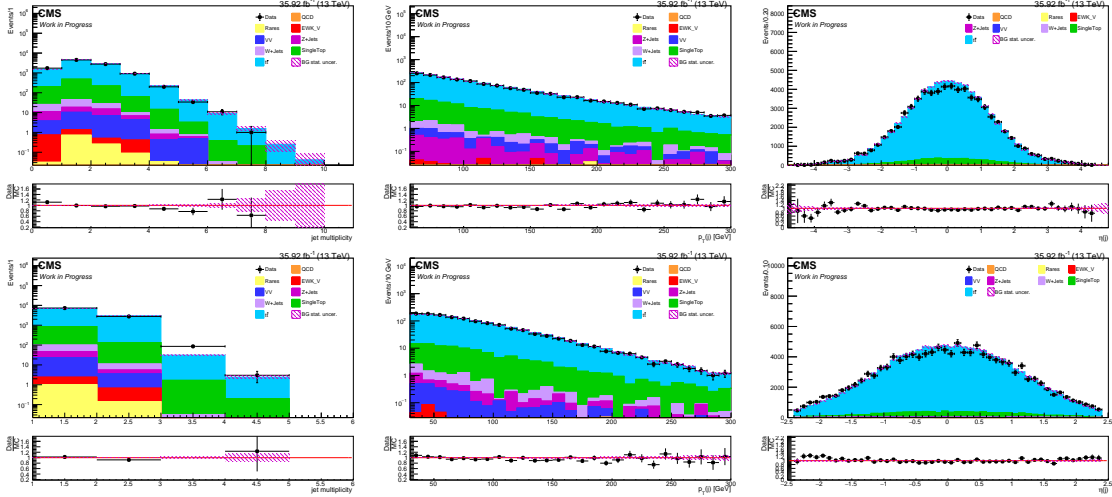


Figure 10.17: Multiplicity (left), p_T (middle) and η (right) distributions for jets (top) and b-jets (bottom) after applying central selections for 2016 data.

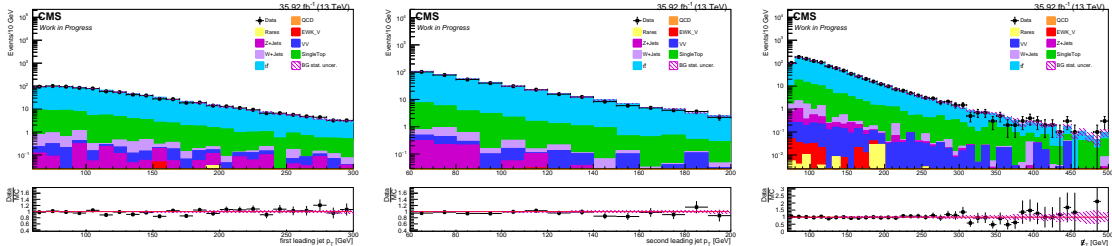


Figure 10.18: Distributions for the leading (left) and subleading jet p_T (middle), and p_T^{miss} (right) after applying central selections for 2016 data.

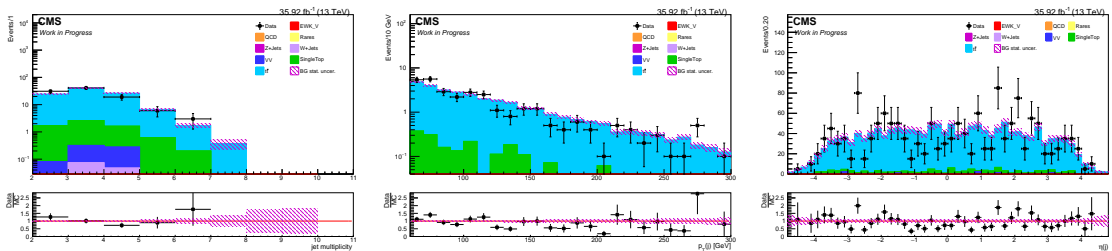


Figure 10.19: Jet multiplicity (left), p_T (middle) and η (right) distributions after applying central + VBF1 selections for 2016 data.

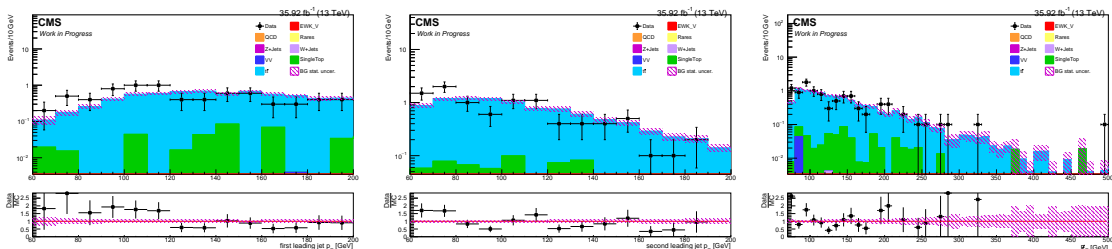


Figure 10.20: Distributions for the leading (left) and subleading jet p_T (middle), and p_T^{miss} (right) after applying central + VBF1 selections for 2016 data.

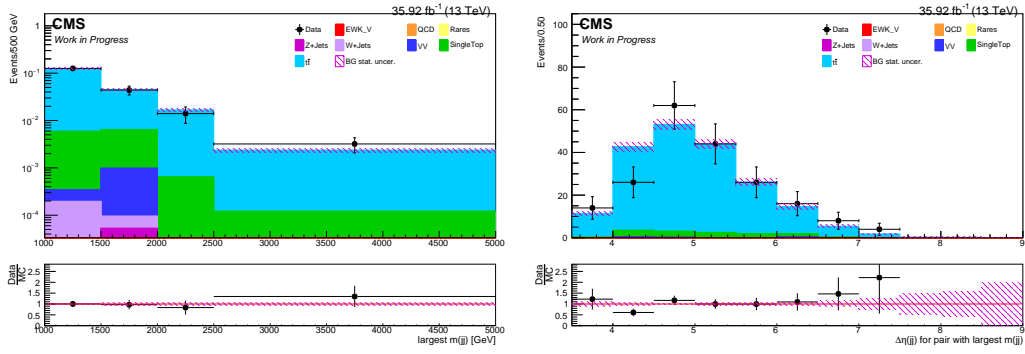


Figure 10.21: Distributions for the leading dijet mass $m(jj)$ and $\Delta\eta(jj)$ for this dijet pair after applying central + VBF1 selections for 2016 data.

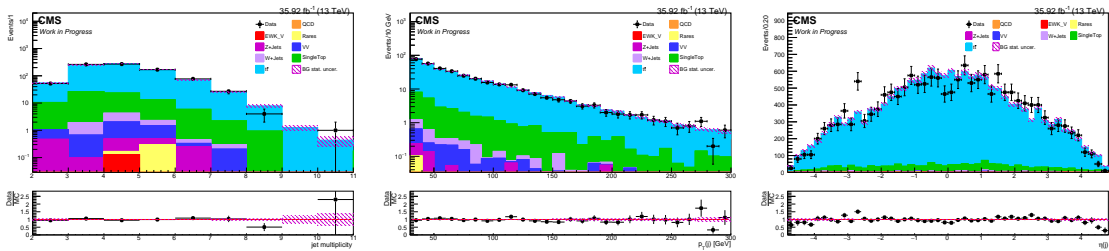


Figure 10.22: Jet multiplicity (left), p_T (middle) and η (right) distributions after applying central + VBF2 selections for 2016 data.

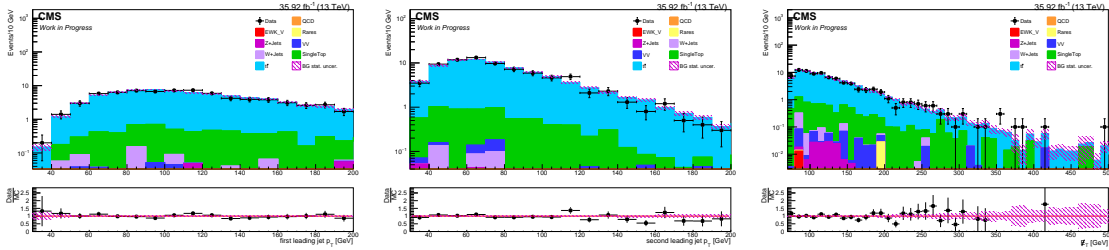


Figure 10.23: Distributions for the leading (left) and subleading jet p_T (middle), and p_T^{miss} (right) after applying central + VBF2 selections for 2016 data.

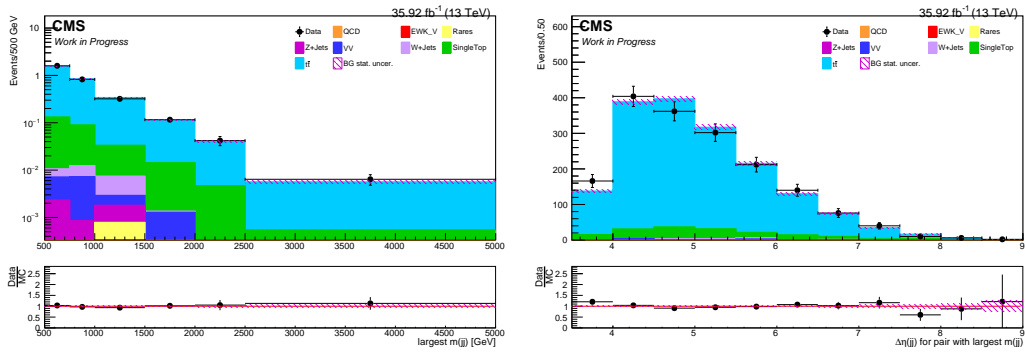


Figure 10.24: Distributions for the leading dijet mass $m(jj)$ and $\Delta\eta(jj)$ for this dijet pair after applying central + VBF2 selections for 2016 data.

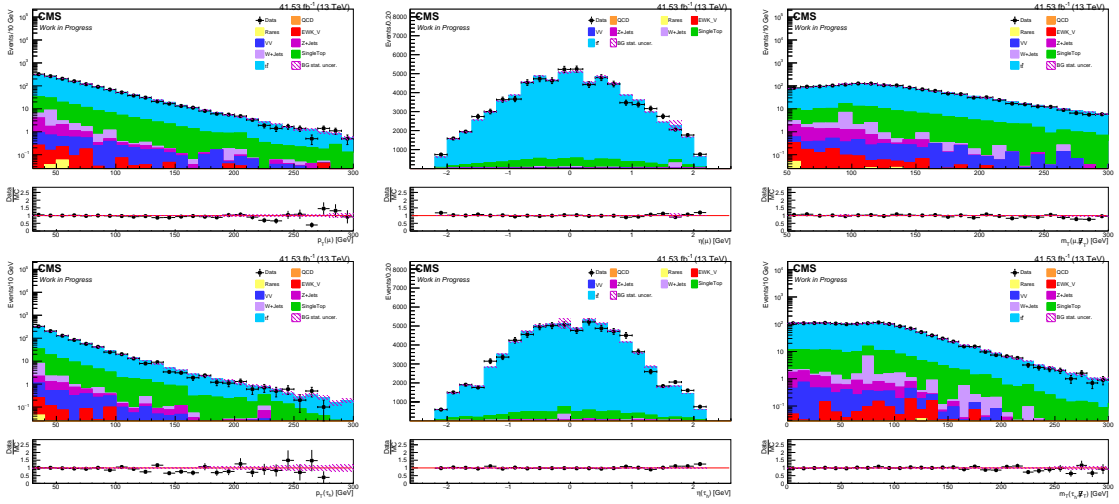


Figure 10.25: p_T (left), η (middle) and m_T (right) distributions for μ (top) and τ_h (bottom) after applying central selections for 2017 data.

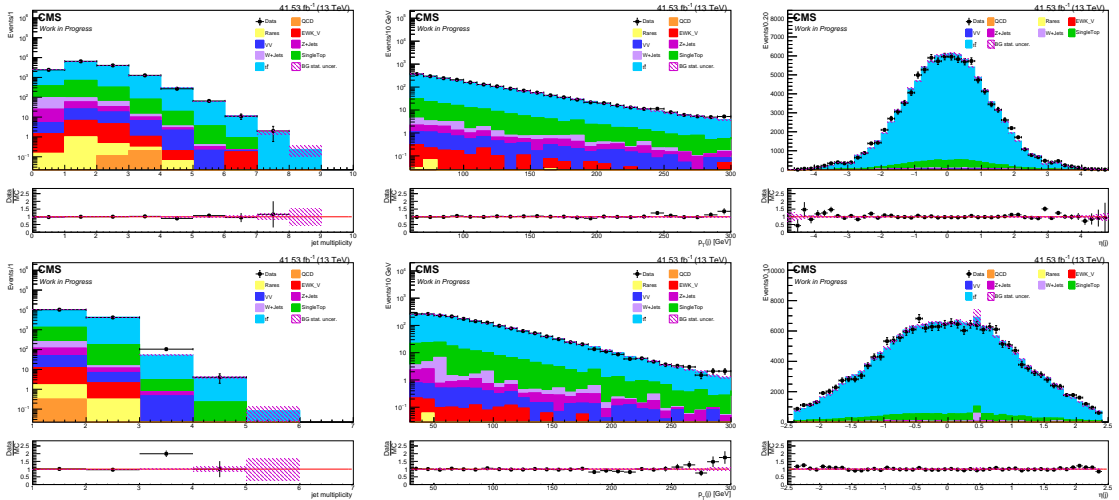


Figure 10.26: Multiplicity (left), p_T (middle) and η (right) distributions for jets (top) and b-jets (bottom) after applying central selections for 2017 data.

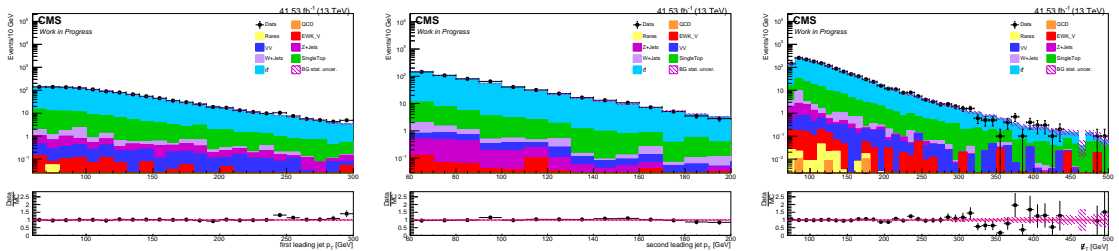


Figure 10.27: Distributions for the leading (left) and subleading jet p_T (middle), and p_T^{miss} (right) after applying central selections for 2017 data.

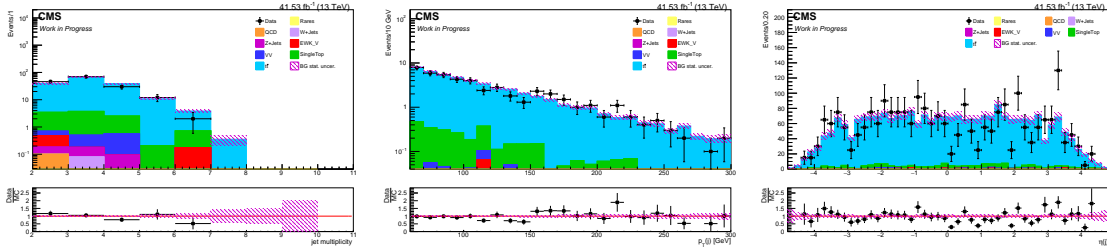


Figure 10.28: Multiplicity (left), p_T (middle) and η (right) distributions for jets after applying central + VBF1 selections for 2017 data.

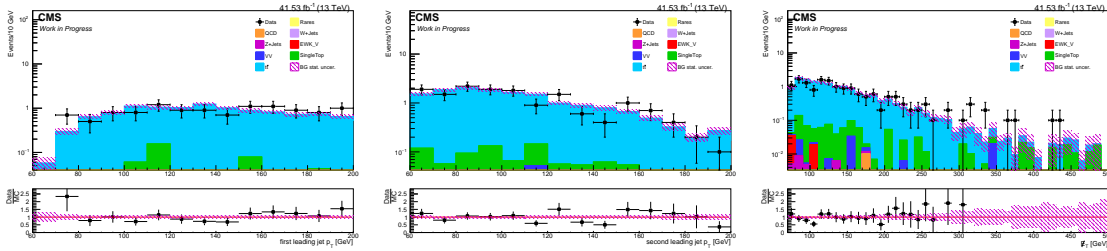


Figure 10.29: Distributions for the leading (left) and subleading jet p_T (middle), and p_T^{miss} (right) after applying central + VBF1 selections for 2017 data.

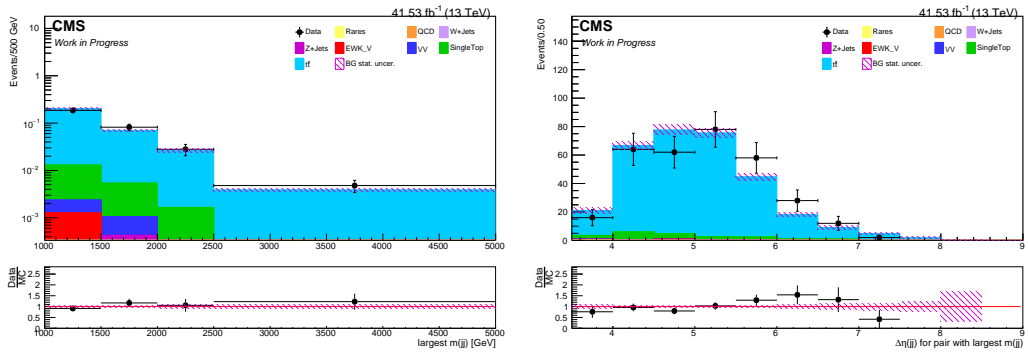


Figure 10.30: Distributions for the leading dijet mass $m(jj)$ and $\Delta\eta(jj)$ for this dijet pair after applying central + VBF1 selections for 2017 data.

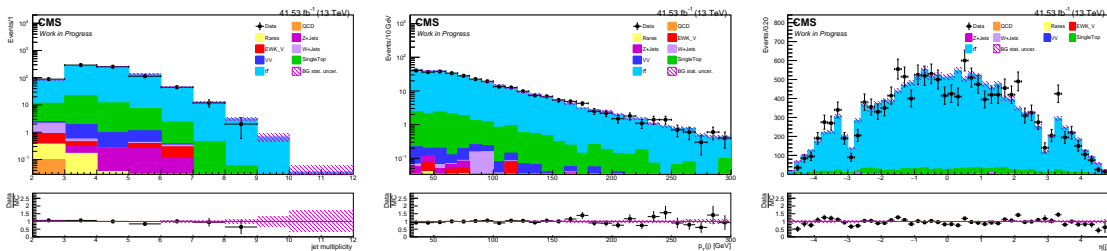


Figure 10.31: Multiplicity (left), p_T (middle) and η (right) distributions for jets after applying central + VBF2 selections for 2017 data.

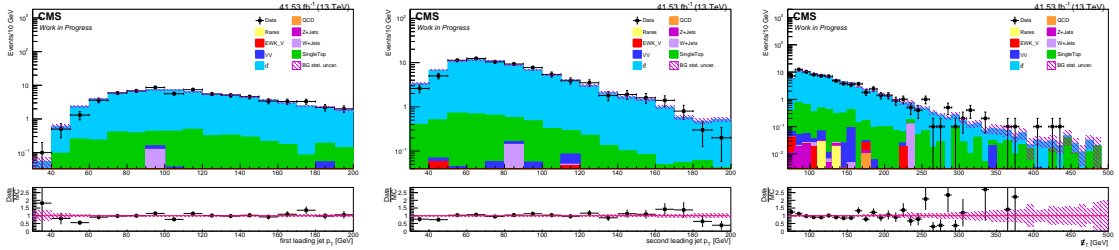


Figure 10.32: Distributions for the leading (left) and subleading jet p_T (middle), and p_T^{miss} (right) after applying central + VBF2 selections for 2017 data.

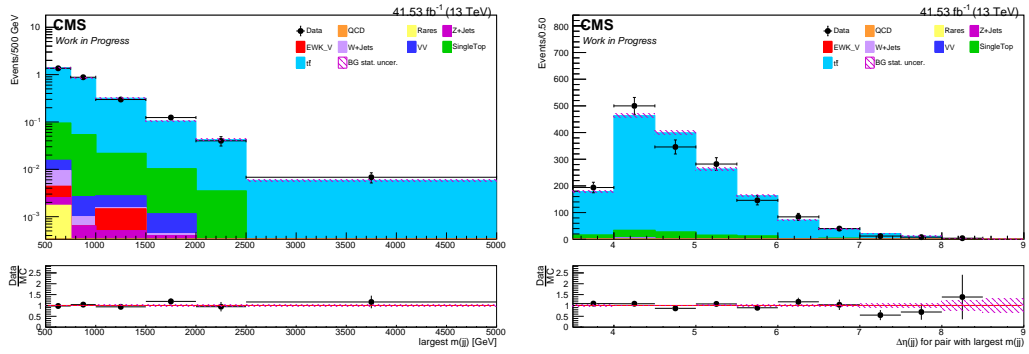


Figure 10.33: Distributions for the leading dijet mass $m(jj)$ and $\Delta\eta(jj)$ for this dijet pair after applying central + VBF2 selections for 2017 data.

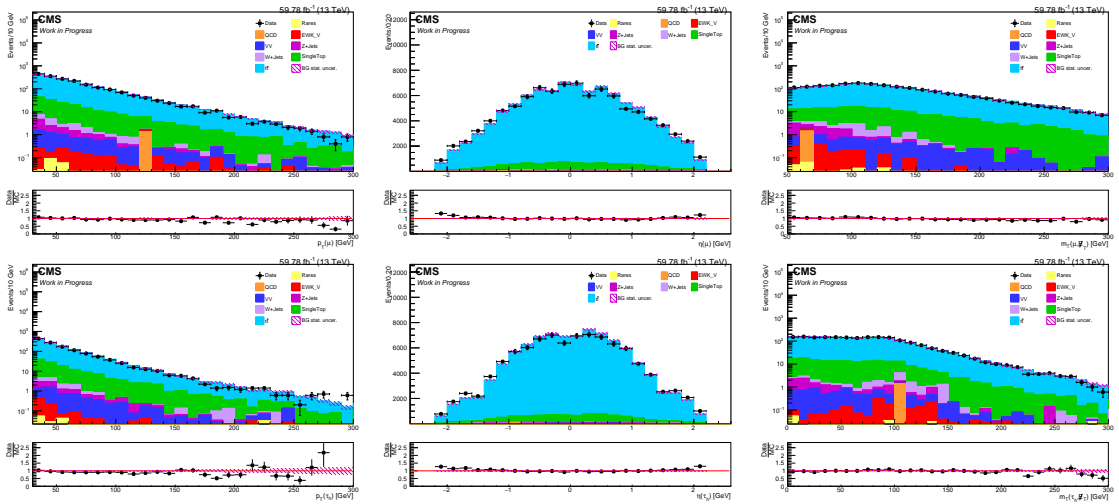


Figure 10.34: p_T (left), η (middle) and m_T (right) distributions for μ (top) and τ_h (bottom) after applying central selections for 2018 data.

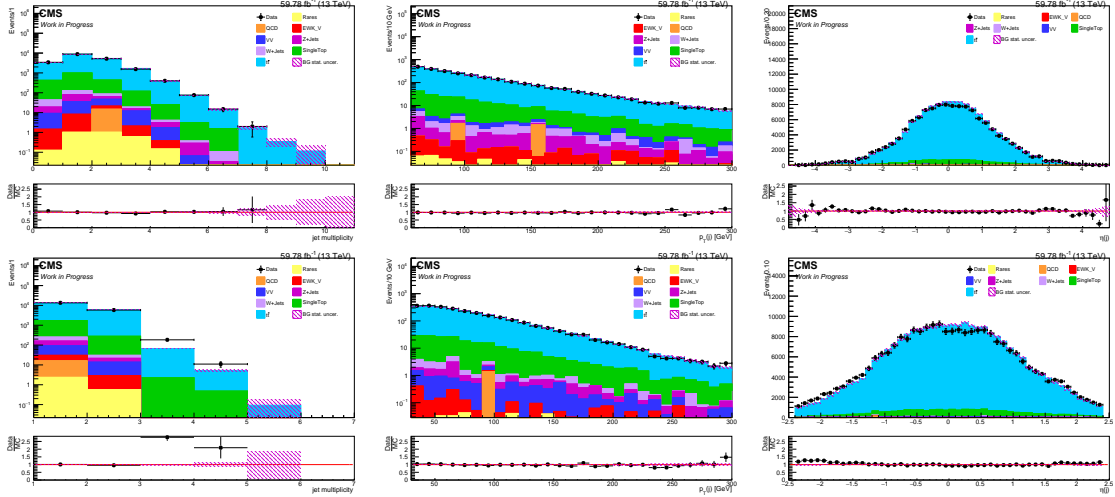


Figure 10.35: Multiplicity (left), p_T (middle) and η (right) distributions for jets (top) and b-jets (bottom) after applying central selections for 2018 data.

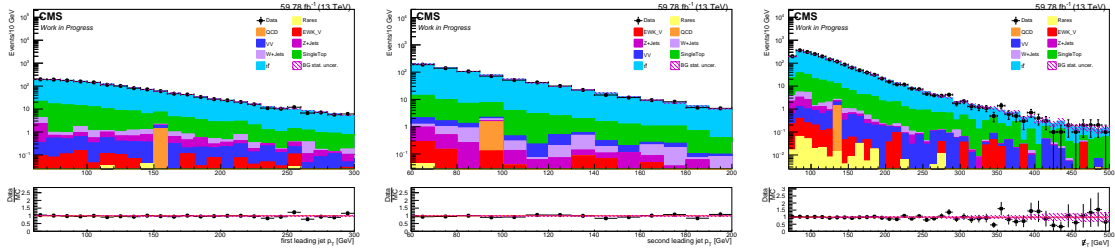


Figure 10.36: Distributions for the leading (left) and subleading jet p_T (middle), and p_T^{miss} (right) after applying central selections for 2018 data.

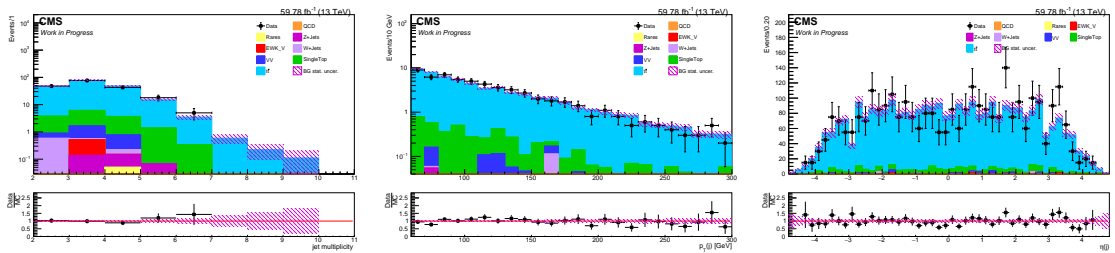


Figure 10.37: Multiplicity (left), p_T (middle) and η (right) distributions for jets after applying central + VBF1 selections for 2018 data.

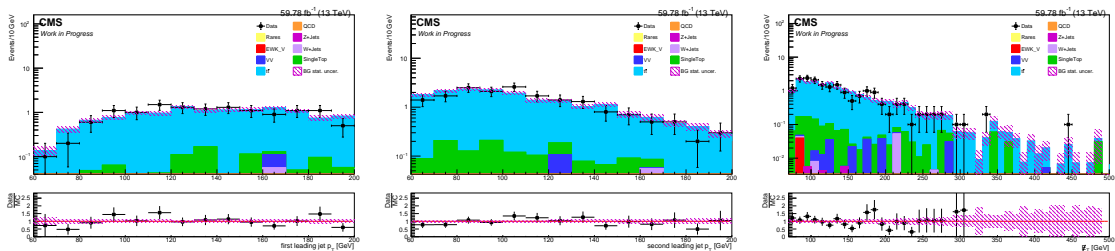


Figure 10.38: Distributions for the leading (left) and subleading jet p_T (middle), and p_T^{miss} (right) after applying central + VBF1 selections for 2018 data.

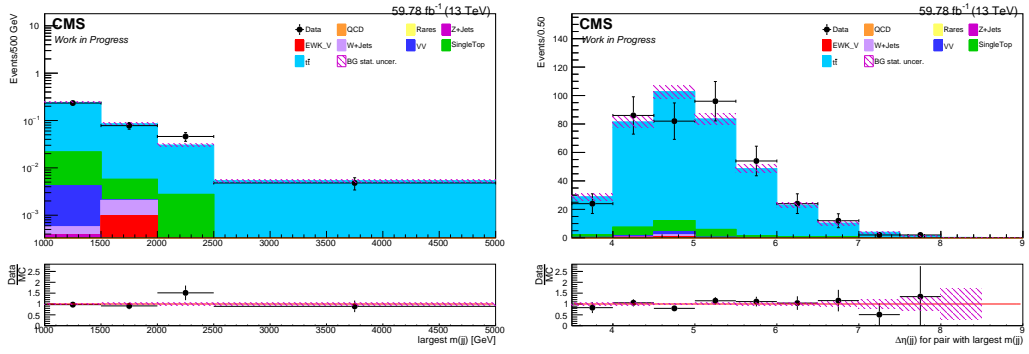


Figure 10.39: Distributions for the leading dijet mass $m(jj)$ and $\Delta\eta(jj)$ for this dijet pair after applying central + VBF1 selections for 2018 data.

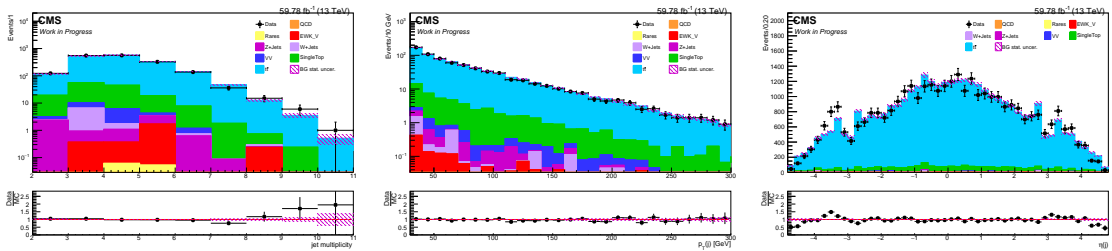


Figure 10.40: Multiplicity (left), p_T (middle) and η (right) distributions for jets after applying central + VBF2 selections for 2018 data.

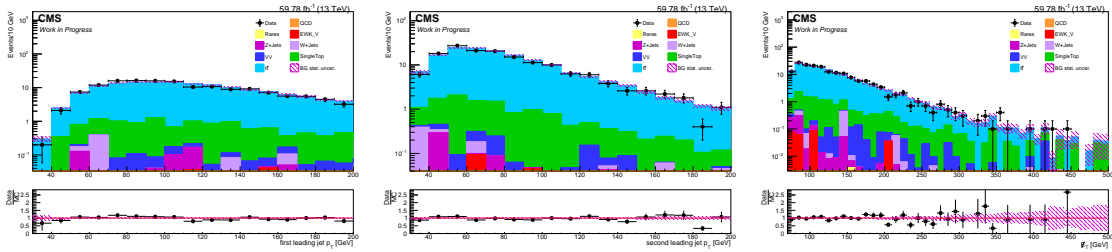


Figure 10.41: Distributions for the leading (left) and subleading jet p_T (middle), and p_T^{miss} (right) after applying central + VBF2 selections for 2018 data.

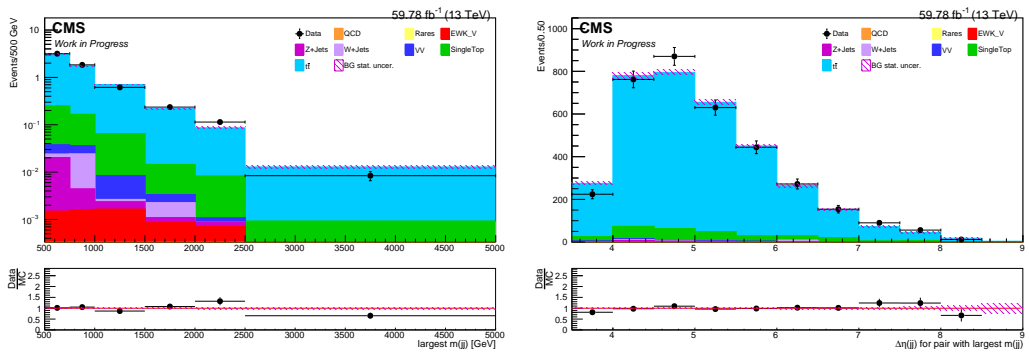


Figure 10.42: Distributions for the leading dijet mass $m(jj)$ and $\Delta\eta(jj)$ for this dijet pair after applying central + VBF2 selections for 2018 data.

Overall, for all kinematic distributions there is a good shape agreement between data and simulation. To evaluate quantitatively the shape agreement between simulation and data in the variable of interest (largest $m(\text{jj})$) a χ^2/N test was performed. The results from this test are summarized in Table 10.12.

		VBF1			VBF2		
		2016	2017	2018	2016	2017	2018
pol-0	χ^2/N	0.259	0.644	0.944	0.323	0.585	3.28
	p_0	0.992 ± 0.102	0.988 ± 0.081	0.976 ± 0.074	0.998 ± 0.035	0.996 ± 0.036	0.989 ± 0.025
pol-1	χ^2/N	0.331	0.388	1.42	0.403	0.633	3.19
	p_0	0.896 ± 0.301	0.757 ± 0.229	0.970 ± 0.191	1.00 ± 0.0	0.953 ± 0.077	1.06 ± 0.05
	p_1	$(0.61 \pm 1.80) \times 10^{-4}$	$(0.04 \pm 1.09) \times 10^{-4}$	$(4.39 \pm 6.99) \times 10^{-5}$	$(-0.22 \pm 6.92) \times 10^{-5}$	$(4.55 \pm 7.28) \times 10^{-5}$	$(-7.95 \pm 4.17) \times 10^{-5}$

Table 10.12: Summary of χ^2/N values in the largest $m(\text{jj})$ distributions in the $t\bar{t}(\rightarrow \mu\tau_h)$ +jets CR for 2016-2018, including VBF1 and VBF2 selections, after correcting with the central and VBF efficiency SFs.

10.2.3 Diboson

The contribution to the background in the signal region from the production of two weak bosons (WW, WZ, ZZ), also known as diboson (VV) is mainly relevant only in the final states that contain two leptons. Therefore, in order to measure the central and VBF efficiencies for this background, a control region with at least three muons in the final state has been created, in order to remain orthogonal to the signal region. These muons are required to have a $p_T > 20$ GeV and at least two of them must satisfy $p_T > 30$ GeV. In addition, at least one $\mu\mu$ combination with opposite sign electric charges is required and no $m(\mu\mu)$ cut is applied. Events with any electrons, hadronic taus or b-jets are vetoed. The VBF efficiency is measured for the VBF1 and VBF2 categories. A detailed description of the kinematic cuts applied to the events in this region are shown in Table 10.13.

	Object	Selection cuts
Central	Trigger	2016 and 2018: HLT_IsoMu24; 2017: HLT_IsoMu27
	μ	$N(\mu) \geq 3$, $p_T(\mu) > 20$ GeV, $ \eta(\mu) < 2.1$ and tight ID, $I_{rel} < 0.15$; $N(\mu) \geq 2$ with $p_T(\mu) > 30$ GeV
	$\mu\mu$ combinations	$N(\mu\mu) \geq 1$, $q_1(\mu) \times q_2(\mu) < 0$, $\Delta R(\mu, \mu) > 0.4$
	p_T^{miss}	$p_T^{\text{miss}} > 30$ GeV
	e veto	$N(e) = 0$ with $p_T > 5$ GeV, $ \eta < 2.1$, medium ID (cut-based)
	τ_h	$N(\tau_h) = 0$, $p_T(\tau_h) > 20$ GeV, $ \eta(\tau_h) < 2.1$, tight ID (Deep Tau), medium (tight) anti- $e(\mu)$ discr., 1- or 3-prongs
	b-jet veto	$N(b) = 0$, $p_T(b) > 30$ GeV, $ \eta < 2.4$, medium DeepCSV WP
	QCD rejection	$ \Delta\phi(j, p_T^{\text{miss}}) _{\text{min}} > 0.5$, jet defined as in VBF2 selections.
VBF1	Jet	$N(j) \geq 2$, $p_T(j) > 60$ GeV, $ \eta(j) < 4.7$, $\Delta R(e/\mu/\tau_h, j) > 0.4$ 2016: Loose PF ID; 2017, 2018: Tight PF ID
	Dijet combinations	$N(j_1, j_2) \geq 1$, $\Delta\eta(j_1, j_2) > 3.8$, $\eta(j_1) \times \eta(j_2) < 0$, $m(j_1, j_2) > 1000$ GeV
VBF2	Jet	$N(j) \geq 2$, $p_T(j) > 30$ GeV, $ \eta(j) < 4.7$, $\Delta R(e/\mu/\tau_h, j) > 0.4$ ID: tight PU jet ID for $30 < p_T \leq 50$ GeV, and for $p_T > 50$ GeV 2016: Loose PF ID; 2017, 2018: Tight PF ID
	Dijet combinations	$N(j_1, j_2) \geq 1$, $\Delta\eta(j_1, j_2) > 3.8$, $\eta(j_1) \times \eta(j_2) < 0$, $m(j_1, j_2) > 500$ GeV

Table 10.13: Diboson $\rightarrow 3\mu$ CR selection cuts.

The SFs for each of the selection sets are summarized in Table 10.14. The main contamination in this CR comes from Z +jets and $t\bar{t}$ +jets events, processes in which most likely one of the jets present in the event (from ISR activity) is mis-identified as a low p_T μ . Figures 10.43-10.75 show the relevant kinematic distributions for this CR across all years including central, VBF1 and VBF2 selections. The predicted diboson distributions have been corrected with the correction factors shown in Tab. 10.14.

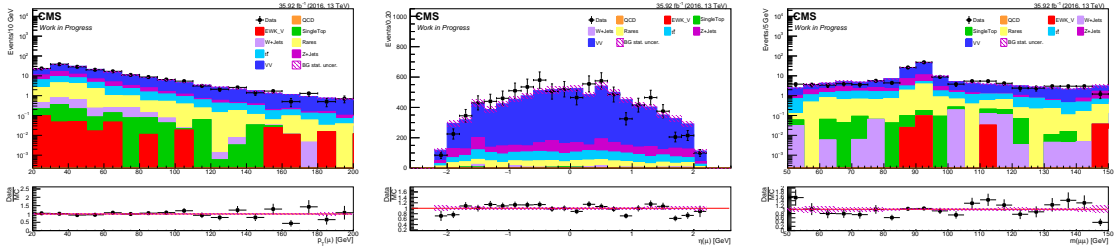


Figure 10.43: $p_T(\mu)$, $\eta(\mu)$, and $m(\mu\mu)$ distributions after applying central selections for 2016 data.

Process	Central			VBF1			VBF2		
	2016	2017	2018	2016	2017	2018	2016	2017	2018
EWK V	1.2 ± 0.4	3.2 ± 0.8	3.5 ± 1.0	0.2 ± 0.0	0.4 ± 0.3	1.0 ± 0.5	0.7 ± 0.3	1.2 ± 0.5	1.8 ± 0.7
QCD	0.0 ± 0.0	1.3 ± 0.0	0.0 ± 0.0	0.0 ± 0.0	0.0 ± 0.0	0.0 ± 0.0	0.0 ± 0.0	0.0 ± 0.0	0.0 ± 0.0
Rares	46.7 ± 2.2	70.4 ± 1.8	81.4 ± 2.7	6.5 ± 0.8	8.5 ± 0.6	9.0 ± 0.9	18.0 ± 1.4	21.3 ± 1.0	22.8 ± 1.4
Single top	3.5 ± 0.8	8.0 ± 1.2	14.4 ± 1.9	0.7 ± 0.4	1.7 ± 0.6	0.6 ± 0.3	1.2 ± 0.5	3.4 ± 0.8	4.4 ± 1.0
Diboson	459.2 ± 1.9	516.5 ± 9.1	675.9 ± 8.8	69.5 ± 0.7	77.2 ± 3.5	86.9 ± 3.1	164.8 ± 1.1	168.9 ± 5.2	204.0 ± 4.8
W+Jets	5.4 ± 1.8	10.9 ± 3.8	16.7 ± 5.6	0.8 ± 0.5	1.5 ± 0.4	3.3 ± 1.9	3.3 ± 1.3	6.5 ± 2.9	7.4 ± 3.0
Z+Jets	76.5 ± 8.2	131.0 ± 11.3	154.4 ± 15.9	4.5 ± 1.1	9.6 ± 1.6	8.2 ± 1.4	19.7 ± 3.6	27.0 ± 3.2	35.1 ± 4.1
$t\bar{t}$	71.6 ± 1.8	122.0 ± 2.6	146.6 ± 3.4	14.2 ± 0.8	22.2 ± 1.1	26.6 ± 1.4	33.2 ± 1.3	53.9 ± 1.8	67.3 ± 2.2
Total bkg	664.0 ± 9.1	863.3 ± 15.4	1092.9 ± 19.6	96.5 ± 1.8	121.1 ± 4.1	135.6 ± 4.3	241.0 ± 4.4	281.6 ± 7.1	342.9 ± 7.6
Data	582	848	1074	108	130	100	213	305	375
Data/MC	0.877	0.982	0.983	1.12	1.07	1.14	0.884	1.08	1.09
Purity [%]	69.2	59.8	61.8	72.1	63.7	64.1	68.4	60.0	59.5
SF	0.821 ± 0.056	0.970 ± 0.064	0.972 ± 0.056	1.42 ± 0.24	1.15 ± 0.20	1.26 ± 0.19	1.01 ± 0.16	1.17 ± 0.17	1.19 ± 0.15

Table 10.14: Summary of SFs for the diboson($\rightarrow 3\mu$) CR for all years, including central, VBF1 and VBF2 selections. Only statistical uncertainties are included.

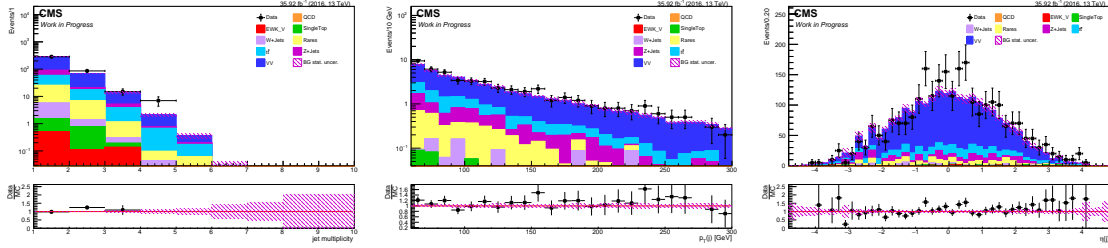


Figure 10.44: Jet multiplicity, $p_T(j)$, and $\eta(j)$ distributions after applying central selections for 2016 data.

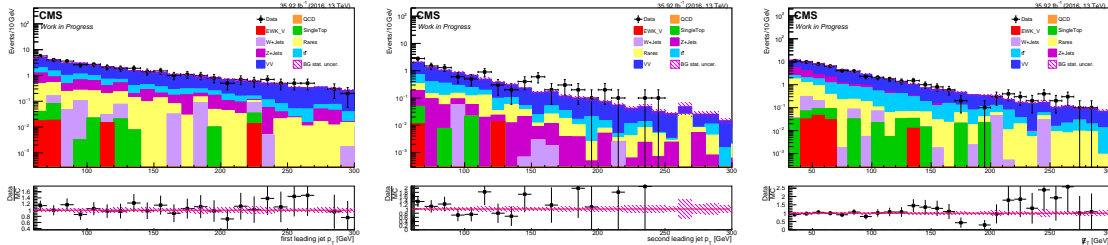


Figure 10.45: p_T distributions for leading jet, subleading jet, and p_T^{miss} after applying central selections for 2016 data.

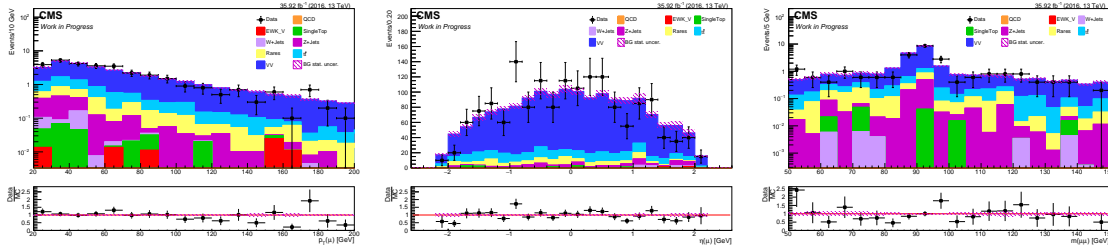


Figure 10.46: $p_T(\mu)$, $\eta(\mu)$, and $m(\mu\mu)$ distributions after applying VBF1 selections for 2016 data.

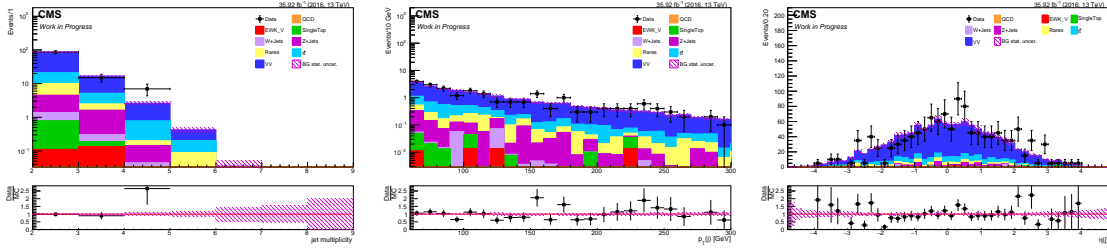


Figure 10.47: Jet multiplicity, $p_T(j)$, and $\eta(j)$ distributions after applying VBF1 selections for 2016 data.

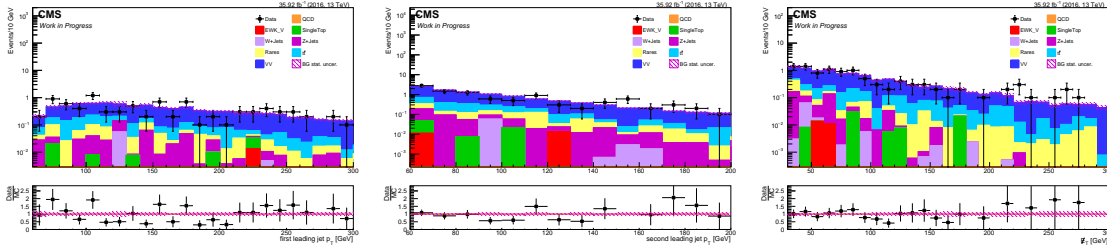


Figure 10.48: p_T distributions for leading jet, subleading jet, and p_T^{miss} after applying VBF1 selections for 2016 data.

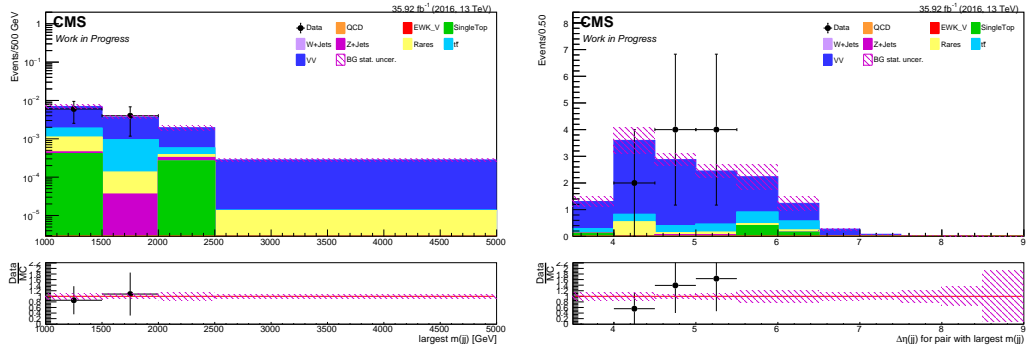


Figure 10.49: Kinematic distributions for the leading $m(jj)$ and $\Delta\eta(jj)$ for this dijet pair after applying VBF1 selections for 2016 data.

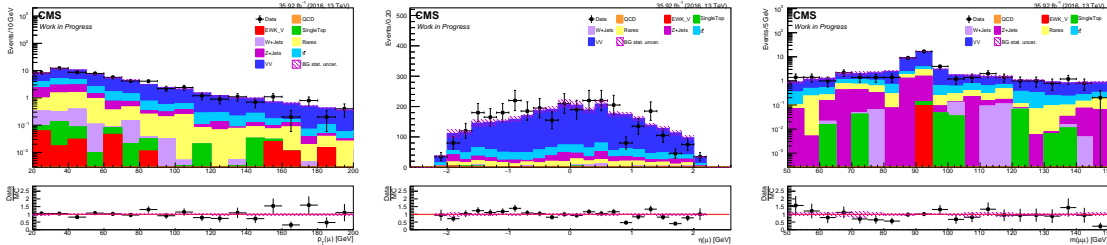


Figure 10.50: $p_T(\mu)$, $\eta(\mu)$, and $m(\mu\mu)$ distributions after applying VBF2 selections for 2016 data.

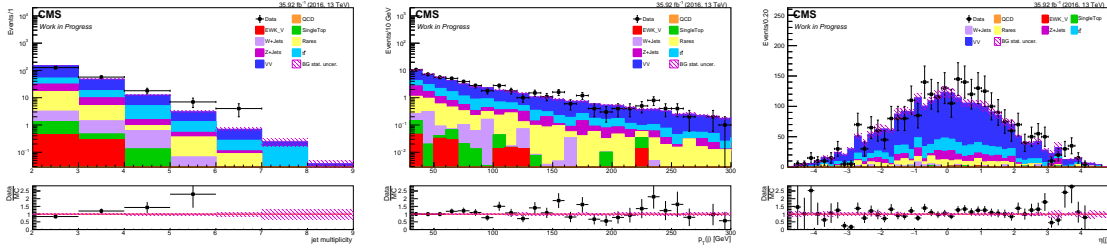


Figure 10.51: Jet multiplicity, $p_T(j)$, and $\eta(j)$ distributions after applying VBF2 selections for 2016 data.

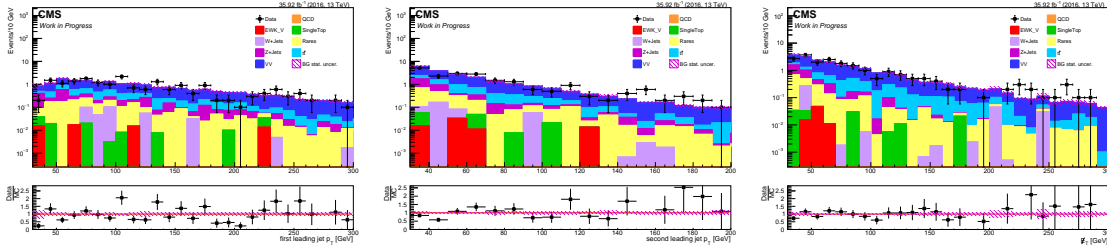


Figure 10.52: p_T distributions for leading jet, subleading jet, and p_T^{miss} after applying VBF2 selections for 2016 data.

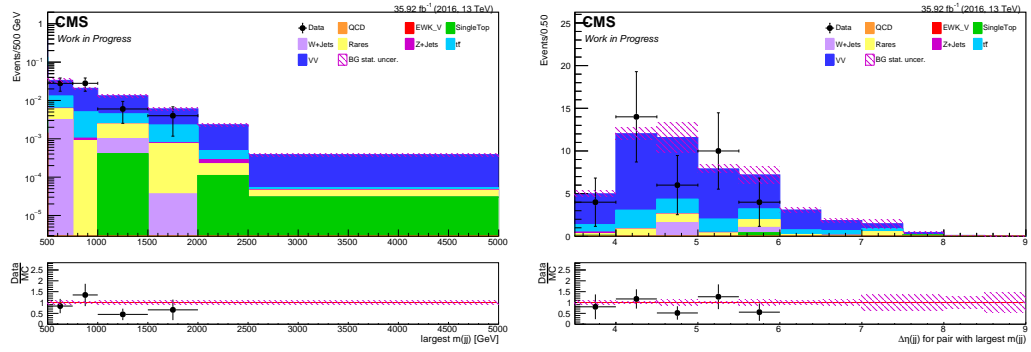


Figure 10.53: Kinematic distributions for the leading $m(jj)$ and $\Delta\eta(jj)$ for this dijet pair after applying VBF2 selections for 2016 data.

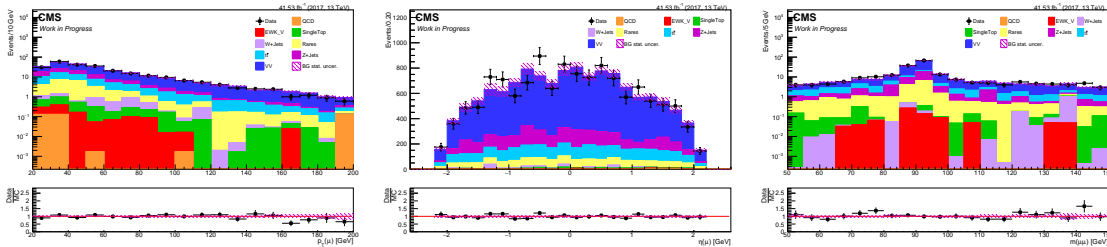


Figure 10.54: $p_T(\mu)$, $\eta(\mu)$, and $m(\mu\mu)$ distributions after applying central selections for 2017 data.

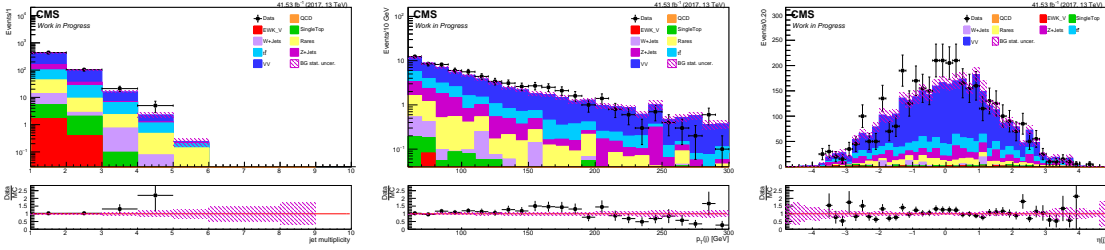


Figure 10.55: Jet multiplicity, $p_T(j)$, and $\eta(j)$ distributions after applying central selections for 2017 data.

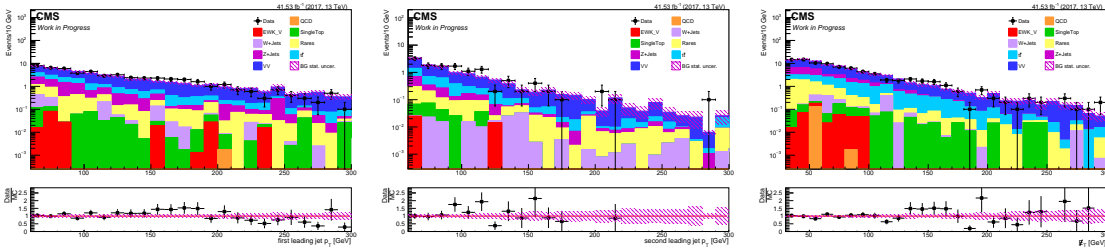


Figure 10.56: p_T distributions for leading jet, subleading jet, and p_T^{miss} after applying central selections for 2017 data.

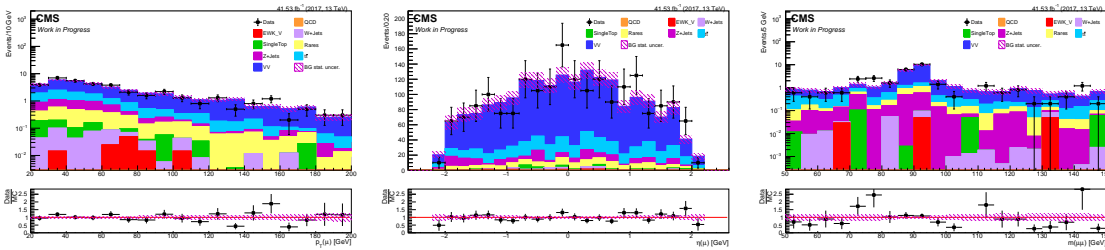


Figure 10.57: $p_T(\mu)$, $\eta(\mu)$, and $m(\mu\mu)$ distributions after applying VBF1 selections for 2017 data.

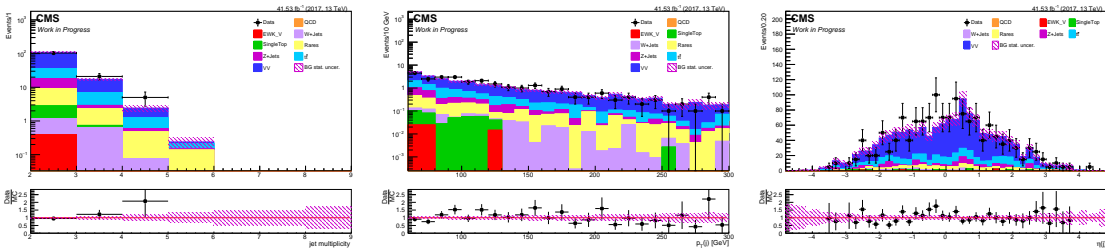


Figure 10.58: Jet multiplicity, $p_T(j)$, and $\eta(j)$ distributions after applying VBF1 selections for 2017 data.

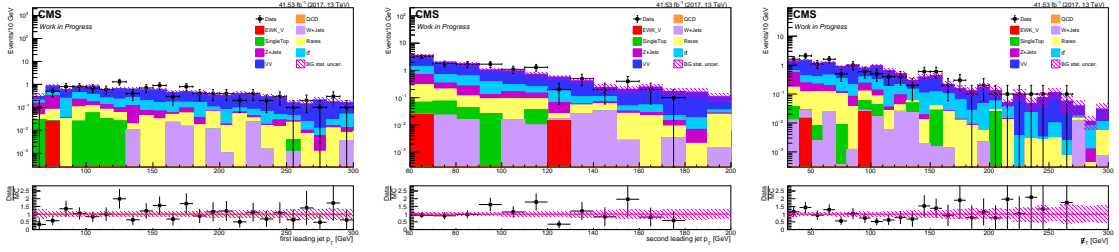


Figure 10.59: p_T distributions for leading jet, subleading jet, and p_T^{miss} after applying VBF1 selections for 2017 data.

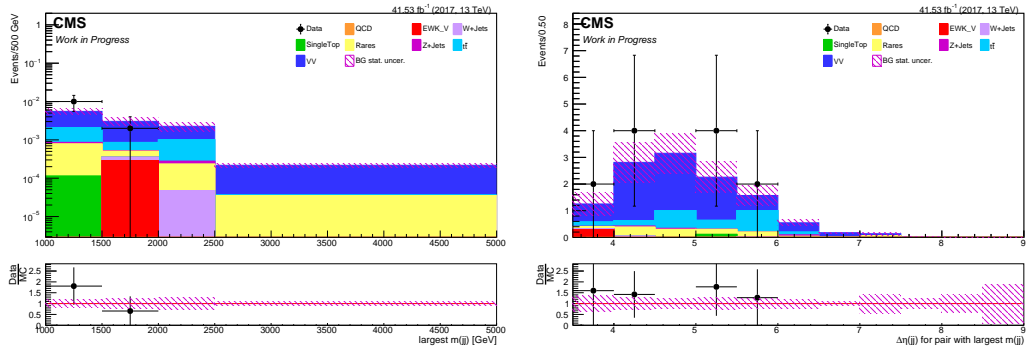


Figure 10.60: Kinematic distributions for the leading $m(jj)$ and $\Delta\eta(jj)$ for this dijet pair after applying VBF1 selections for 2017 data.

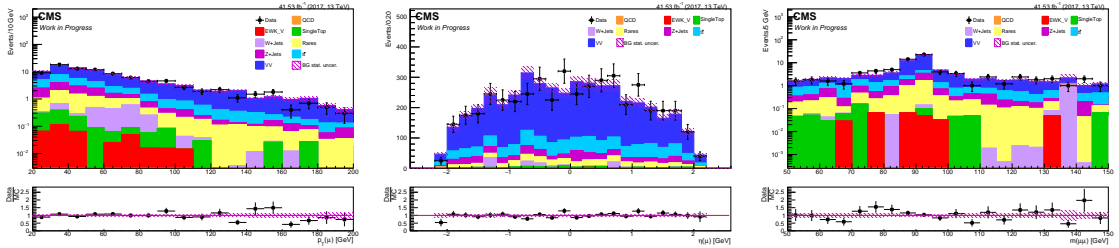


Figure 10.61: $p_T(\mu)$, $\eta(\mu)$, and $m(\mu\mu)$ distributions after applying VBF2 selections for 2017 data.

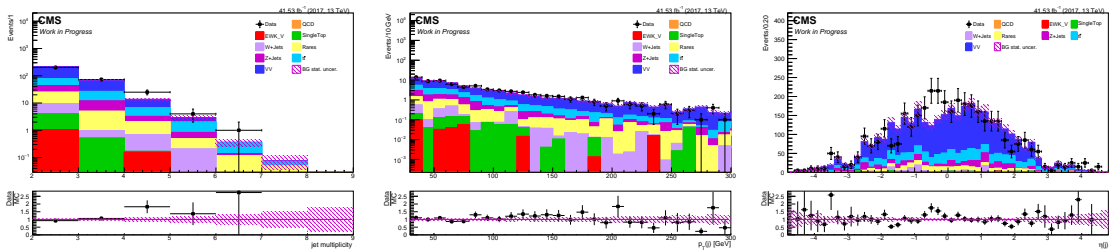


Figure 10.62: Jet multiplicity, $p_T(j)$, and $\eta(j)$ distributions after applying VBF2 selections for 2017 data.

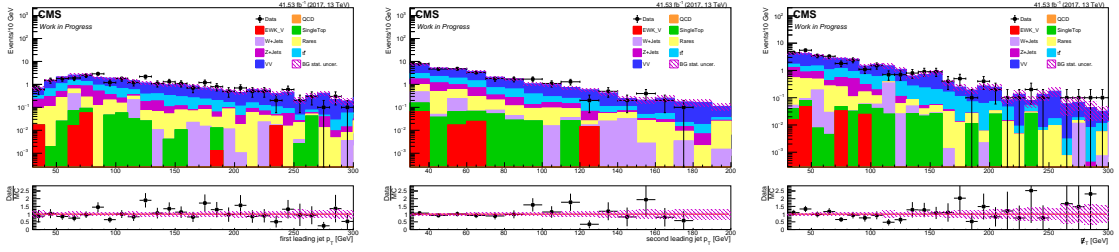


Figure 10.63: p_T distributions for leading jet, subleading jet, and p_T^{miss} after applying VBF2 selections for 2017 data.

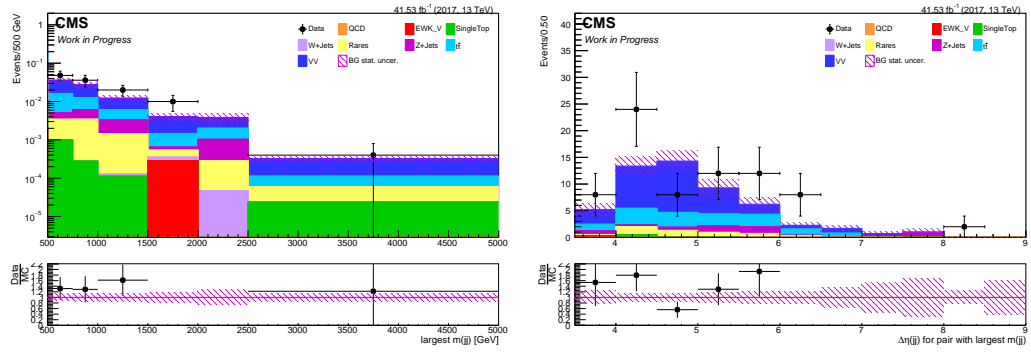


Figure 10.64: Kinematic distributions for the leading $m(jj)$ and $\Delta\eta(jj)$ for this dijet pair after applying VBF2 selections for 2017 data.

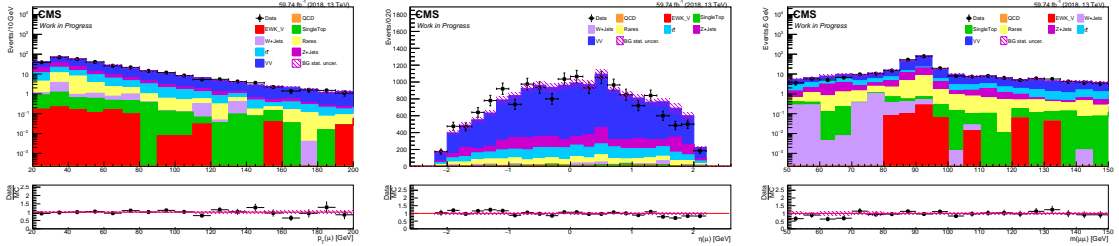


Figure 10.65: $p_T(\mu)$, $\eta(\mu)$, and $m(\mu\mu)$ distributions after applying central selections for 2018 data.

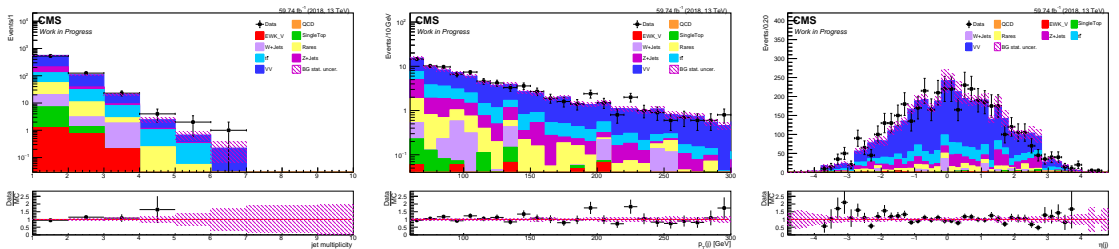


Figure 10.66: Jet multiplicity, $p_T(j)$, and $\eta(j)$ distributions after applying central selections for 2018 data.

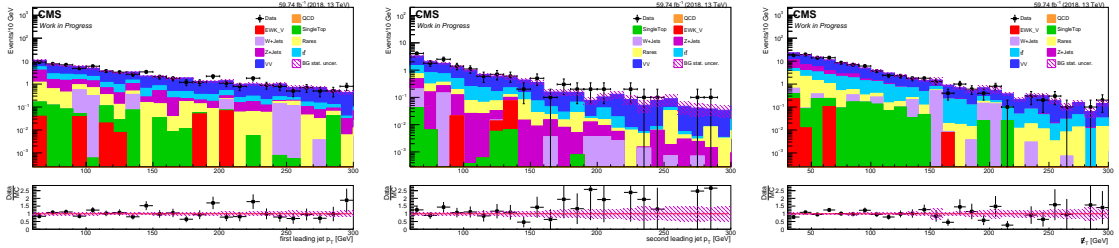


Figure 10.67: p_T distributions for leading jet, subleading jet, and p_T^{miss} after applying central selections for 2018 data.

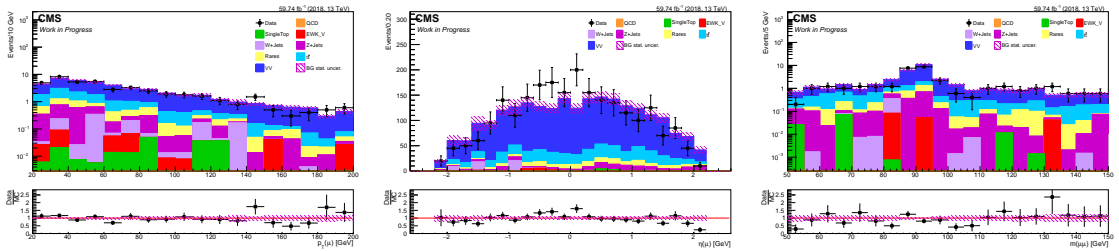


Figure 10.68: $p_T(\mu)$, $\eta(\mu)$, and $m(\mu\mu)$ distributions after applying VBF1 selections for 2018 data.

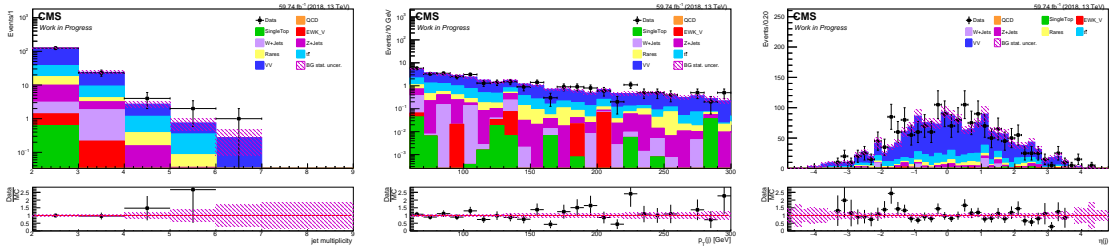


Figure 10.69: Jet multiplicity, $p_T(j)$, and $\eta(j)$ distributions after applying VBF1 selections for 2018 data.

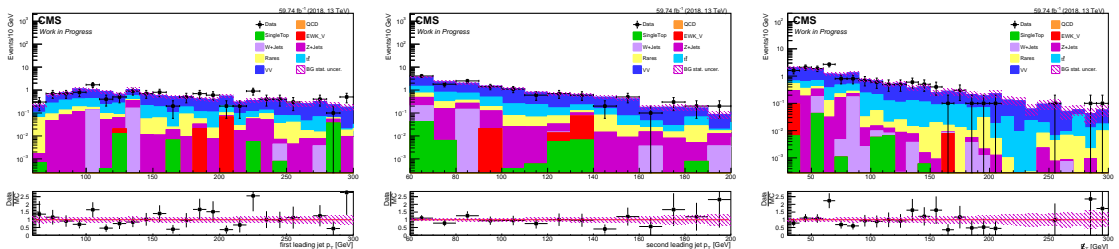


Figure 10.70: p_T distributions for leading jet, subleading jet, and p_T^{miss} after applying VBF1 selections for 2018 data.

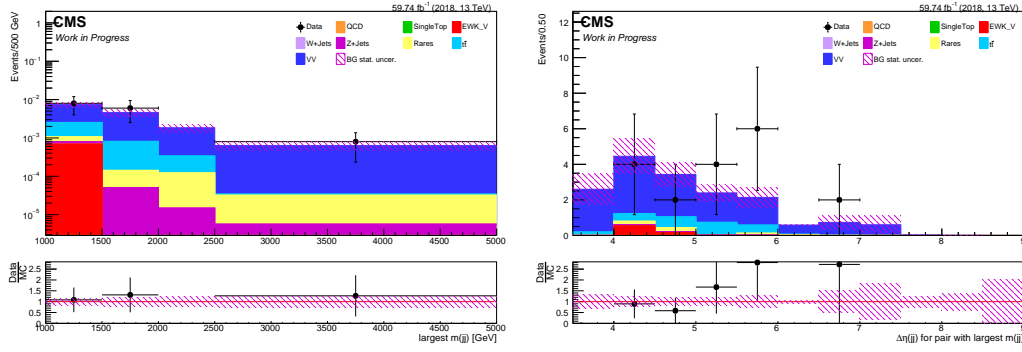


Figure 10.71: Kinematic distributions for the leading $m(jj)$ and $\Delta\eta(jj)$ for this dijet pair after applying VBF1 selections for 2018 data.

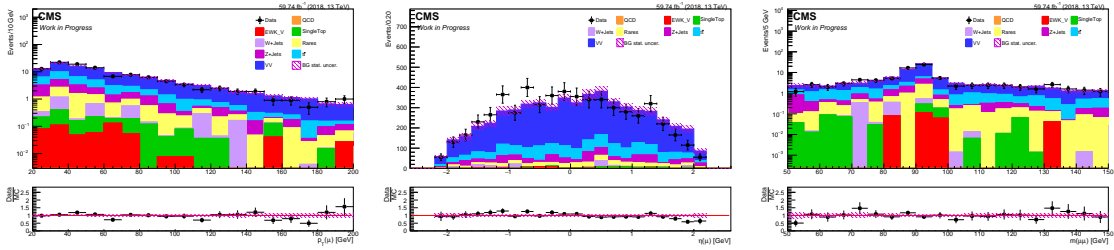


Figure 10.72: $p_T(\mu)$, $\eta(\mu)$, and $m(\mu\mu)$ distributions after applying VBF2 selections for 2018 data.

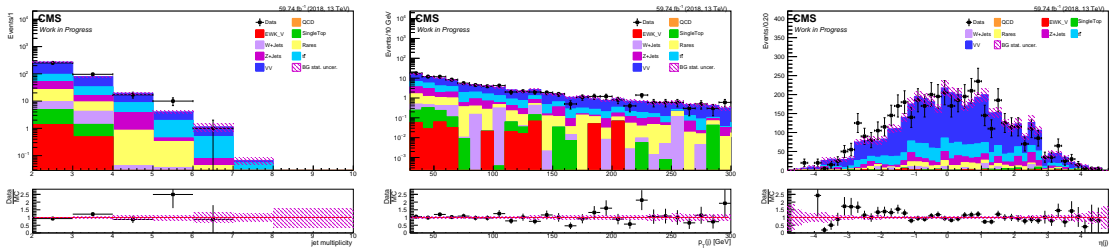


Figure 10.73: Jet multiplicity, $p_T(j)$, and $\eta(j)$ distributions after applying VBF2 selections for 2018 data.

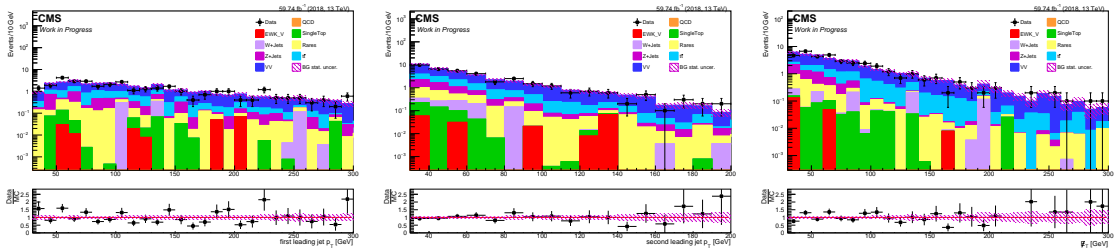


Figure 10.74: p_T distributions for leading jet, subleading jet, and p_T^{miss} after applying VBF2 selections for 2018 data.

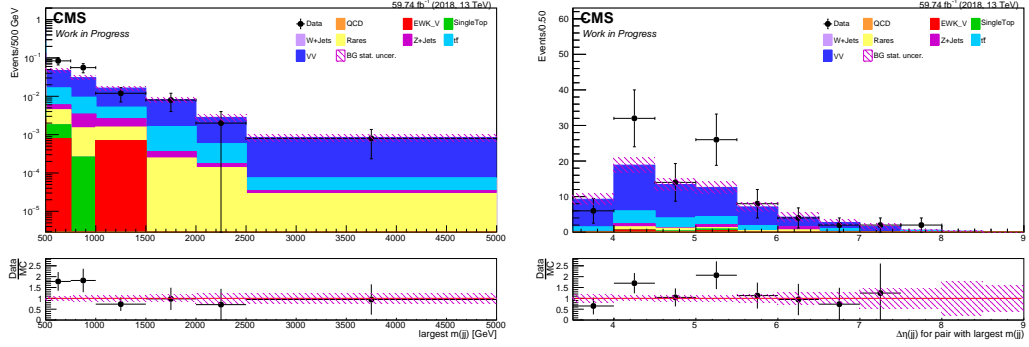


Figure 10.75: Kinematic distributions for the leading $m(jj)$ and $\Delta\eta(jj)$ for this dijet pair after applying VBF2 selections for 2018 data.

		VBF1			VBF2		
		2016	2017	2018	2016	2017	2018
pol-0	χ^2/N	0.0580	1.10	0.0326	0.882	0.261	1.20
	p_0	0.926 ± 0.421	1.09 ± 0.53	1.18 ± 0.42	0.700 ± 0.177	1.42 ± 0.26	1.13 ± 0.19
pol-1	χ^2/N			0.0418	0.965	0.327	1.13
	p_0	N/A	N/A	1.05 ± 0.92	1.14 ± 0.54	1.31 ± 0.48	1.54 ± 0.38
	p_1			$(0.68 \pm 4.42) \times 10^{-4}$	$(4.01 \pm 4.72) \times 10^{-4}$	$(1.00 \pm 3.93) \times 10^{-4}$	$(-2.92 \pm 2.39) \times 10^{-4}$

Table 10.15: Summary of χ^2/N values in the largest $m(jj)$ distributions in the diboson($\rightarrow 3\mu$)+jets CR for 2016-2018, including VBF1 and VBF2 selections, after correcting with the central and VBF efficiency SFs. N/A means that there were not enough data points to perform a fit.

10.3 QCD multijet background estimation

As described in previous subsections, the dominant backgrounds in the $\ell\tau_h$ channels include $t\bar{t}$, Z +jets, W +jets, diboson, and QCD multijet production. The estimation of the contribution from QCD multijet events to the event yields in the $\ell\tau_h$ SRs, a data-driven approach is taken, based on the ABCD method, which has been already introduced in this document for the $Z(\rightarrow \tau_\mu\tau_h)$ +jets CR studies.

In all the SRs of this analysis, the $|\Delta\phi(j, p_T^{\text{miss}})|_{\text{min}} > 0.5$ selection is included to suppress background events coming from QCD. Together with the results obtained in the $Z(\rightarrow \tau_\mu\tau_h)$ +jets control sample for QCD events, we established $|\Delta\phi(j, p_T^{\text{miss}})|_{\text{min}}$ and lepton isolation as the two independent variables to use with the ABCD method (Fig. 10.76).

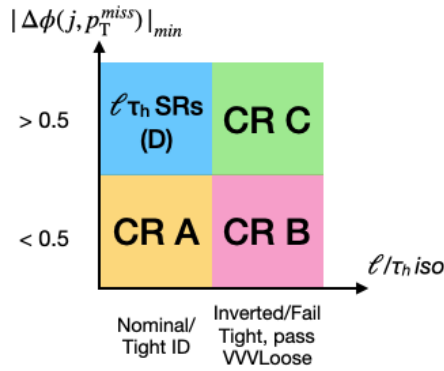


Figure 10.76: ABCD diagram for the QCD estimation in the $\ell\tau_h$ SRs ($\ell = e, \mu, \tau_h$).

There are three control samples, which are based on the corresponding SR selections with the following modifications:

- *CRA*: nominal isolation on the lepton leg ($\ell = e, \mu$), Tight isolation/ID on the τ_h leg(s), and inverted $|\Delta\phi(j, p_T^{\text{miss}})|_{\text{min}} (< 0.5)$,
- *CRB*: inverted isolation on the lepton leg ($\ell = e, \mu$), fail Tight and pass VVVLoose isolation/ID on the τ_h leg(s) and inverted $|\Delta\phi(j, p_T^{\text{miss}})|_{\text{min}} (< 0.5)$,
- *CRC*: inverted isolation on the lepton leg ($\ell = e, \mu$), fail Tight and pass VVVLoose isolation/ID on the τ_h leg(s) and nominal $|\Delta\phi(j, p_T^{\text{miss}})|_{\text{min}} (> 0.5)$.

Since the 2-lepton channels have small background event yields, the lepton pair charge requirement is dropped, in order to obtain larger number of events in the CRA-CRC samples. The QCD event yield in the corresponding SRs will be given by:

$$N_{\text{QCD}}^{\text{SR}} = N_{\text{CRA}} \cdot \text{TF}_{|\Delta\phi|_{\text{min}}} \cdot R_{\text{OS(LS)}}, \quad (10.12)$$

where $\text{TF}_{|\Delta\phi|_{\text{min}}}$ corresponds to the $|\Delta\phi(j, p_T^{\text{miss}})|_{\text{min}}$ transfer factor and it is defined as:

$$\text{TF}_{|\Delta\phi|_{\text{min}}} = \frac{N_{\text{data}}^{\text{CRC}} - N_{\text{non QCD MC}}^{\text{CRC}}}{N_{\text{data}}^{\text{CRB}} - N_{\text{non QCD MC}}^{\text{CRB}}}. \quad (10.13)$$

$N_{\text{non QCD MC}}^{\text{CRC}}$ ($N_{\text{non QCD MC}}^{\text{CRB}}$) is the sum of event yields for non-QCD backgrounds as predicted in simulation in CRC (CRB). These event yields are not corrected with the scale factors derived in the dedicated control regions. The factor $R_{\text{OS(LS)}}$ is the ratio for OS(LS)/(OS+LS) lepton combinations. This factor is derived from the $\text{TF}_{\text{OS} \rightarrow \text{LS}}$ measured for QCD events in the $Z(\rightarrow \tau_\mu \tau_h) + \text{jets}$ control sample (Sec. 10.2.1):

$$R_{\text{OS(LS)}} = \frac{N_{\text{OS(LS)}}}{N_{\text{total}}}. \quad (10.14)$$

Considering $N_{\text{OS+LS}} = N_{\text{OS}} + N_{\text{LS}}$ and combining with Equations 10.10 and 10.14, we find that:

$$R_{\text{OS}} = \frac{\text{TF}_{\text{OS} \rightarrow \text{LS}}}{\text{TF}_{\text{OS} \rightarrow \text{LS}} + 1}, \quad (10.15)$$

$$R_{\text{LS}} = \frac{1}{\text{TF}_{\text{OS} \rightarrow \text{LS}} + 1}. \quad (10.16)$$

Some of the items to consider before proceeding with this methodology include:

- in order to obtain an accurate measurement of the $\text{TF}_{|\Delta\phi|_{\min}}$, the QCD purity in CRB and CRC needs to be large enough,
- tests to verify there is no correlation between the relevant variables need to be performed (lepton ($e, \mu \tau_h$) isolation, $|\Delta\phi(j, p_T^{\text{miss}})|_{\min}$ and charge combination for the lepton pair). This will be tested by comparing the leading $m(\text{jj})$ shapes in the relevant control samples. If no shape bias is observed for the $\text{TF}_{|\Delta\phi|_{\min}}$, the QCD $m(\text{jj})$ shape in the SR will be taken from the combination CRB+CRC (Figure 10.76).

These considerations were tested in the $\tau_h \bar{\tau}_h$ final state, where the QCD contribution to the event yields in the SR is expected to be the largest, compared to the $e\tau_h$ and $\mu\tau_h$ final states. As an example, we include the results corresponding to the 2016 data set. Table 10.16 shows the final event yields for non QCD backgrounds in the $\tau_h \bar{\tau}_h$ CRB and CRC. *The purity in CRB (CRC) is $\sim 65.6\%$ (35.5%), which is sufficient to measure $\text{TF}_{|\Delta\phi|_{\min}}$.* Figure 10.77 provides a visual representation for the QCD purity as a function of $|\Delta\phi(j, p_T^{\text{miss}})|_{\min}$.

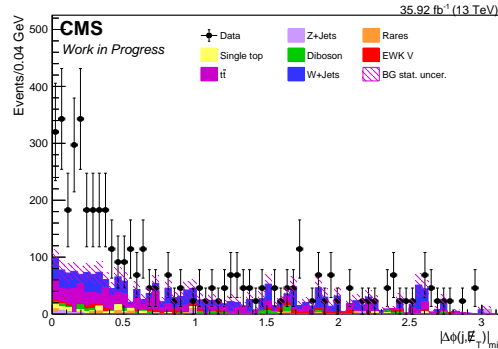


Figure 10.77: Kinematic distribution for the $|\Delta\phi(j, p_T^{\text{miss}})|_{\min}$ in CRB after applying central and VBF2 selections and before applying the $|\Delta\phi(j, p_T^{\text{miss}})|_{\min}$ cut for 2016.

For the correlation of $\text{TF}_{|\Delta\phi|_{\min}}$ with the leading $m(\text{jj})$, we compare the distributions for QCD in CRB and CRC (data - non QCD MC). These distributions are depicted in Figure 10.78 and the actual $\text{TF}_{|\Delta\phi|_{\min}}$ vs. leading $m(\text{jj})$ is shown in Figure 10.79 (top). The ratio was fit to a 0- and

Process	CRB+CRC	CRB	CRC	CRA	SR (OS)	SR (LS)
EWK V	7.6 ± 1.1	1.6 ± 0.5	4.1 ± 0.8	0.0 ± 0.0	0.0 ± 0.0	0.1 ± 0.0
Rares	2.6 ± 0.6	0.9 ± 0.4	1.0 ± 0.4	0.0 ± 0.0	0.0 ± 0.0	0.0 ± 0.0
Single top	3.9 ± 0.8	2.5 ± 0.6	1.2 ± 0.4	0.0 ± 0.0	0.3 ± 0.2	0.0 ± 0.0
Diboson	5.3 ± 0.8	1.2 ± 0.4	3.0 ± 0.6	0.1 ± 0.0	0.6 ± 0.0	0.1 ± 0.0
W+Jets	55.2 ± 4.1	14.2 ± 1.8	29.2 ± 3.2	0.0 ± 0.0	0.3 ± 0.0	0.3 ± 0.0
Z+jets	2.4 ± 0.6	0.7 ± 0.1	1.1 ± 0.3	0.2 ± 0.1	0.6 ± 0.1	0.0 ± 0.0
$t\bar{t}$	37.2 ± 2.0	13.4 ± 1.2	17.1 ± 1.4	0.3 ± 0.1	1.0 ± 0.3	0.1 ± 0.1
Total non-QCD bkg	114.2 ± 4.9	34.5 ± 2.4	56.8 ± 3.7	0.6 ± 0.1	2.8 ± 0.4	0.6 ± 0.1
Data	188	100	88	3	—	—
$N_{\text{data}} - N_{\text{non QCD MC}}$	73.8 ± 14.6	65.5 ± 10.3	31.2 ± 10.1	2.4 ± 1.7	—	—
QCD purity [%]	39.3	65.5	35.5	80.0	—	—

Table 10.16: Summary of event yields in CRB, CRC, their combination (before applying the $|\Delta\phi(j, p_{\text{T}}^{\text{miss}})|_{\text{min}}$ cut), and, CRA for the QCD estimation in the $\tau_{\text{h}}\tau_{\text{h}}$ SRs for 2016 after applying central and VBF2 selections. The prediction for non-QCD backgrounds in the OS and LS $\tau_{\text{h}}\tau_{\text{h}}$ SR are shown as well.

a 1-degree polynomial, and the resulting fit parameters are summarized in Table 10.17. *The χ^2/N values show that $\text{TF}_{|\Delta\phi|_{\text{min}}}$ is independent of $m(\text{jj})$ and therefore, $\text{TF}_{|\Delta\phi|_{\text{min}}}$ is uncorrelated with $m(\text{jj})$, and will be taken from the event yields in CRB and CRC.*

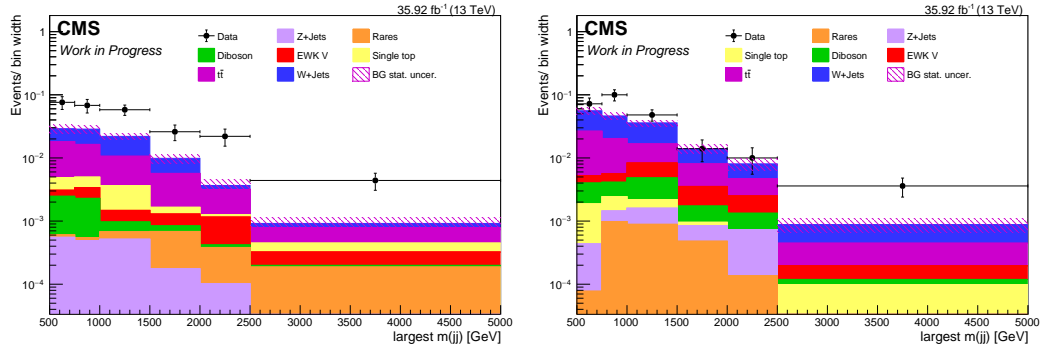


Figure 10.78: Kinematic distributions for the leading $m(\text{jj})$ in CRB (left) and CRC (right) after applying central, VBF2 and the corresponding $|\Delta\phi(j, p_{\text{T}}^{\text{miss}})|_{\text{min}}$ selections.

Fit parameter	pol-0	pol-1
p_0	0.286 ± 0.150	0.217 ± 0.350
p_1	—	$(0.38 \pm 1.73) \times 10^{-4}$
χ^2/N	0.829	1.02
$\text{TF}_{ \Delta\phi(j, p_{\text{T}}^{\text{miss}}) _{\text{min}}} \text{ (norm.)}$	0.476 ± 0.171	—

Table 10.17: Summary of results from the fits to a pol-0 and pol-1 polynomials of the $\text{TF}_{|\Delta\phi(j, p_{\text{T}}^{\text{miss}})|_{\text{min}}}$ vs. leading $m(\text{jj})$ for VBF2 selections. The $\text{TF}_{|\Delta\phi(j, p_{\text{T}}^{\text{miss}})|_{\text{min}}}$ measured from the event yields in this region is also included. The TF measured from the fit and event yields are consistent within statistical uncertainties.

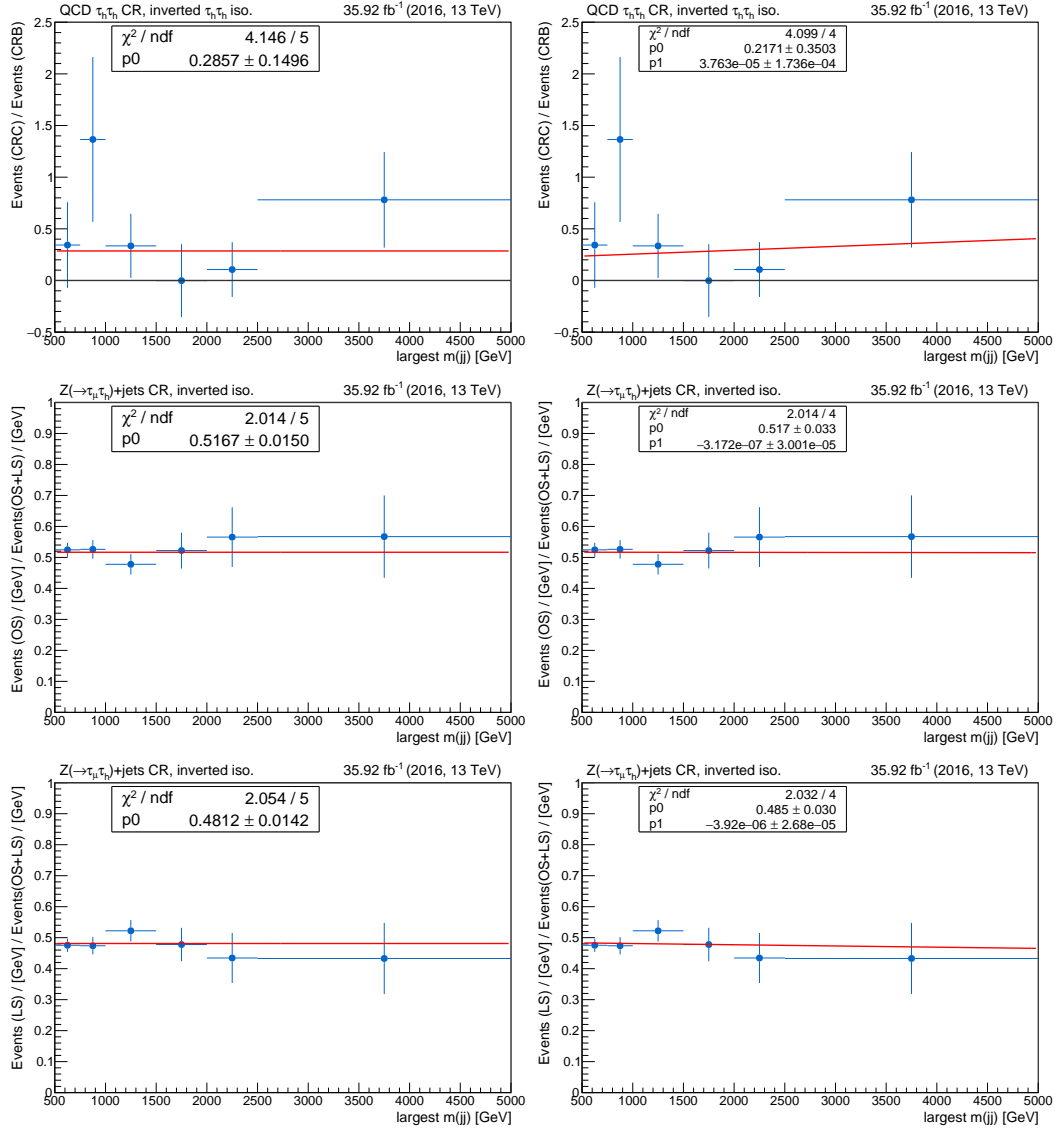


Figure 10.79: Top: $TF_{|\Delta\phi(j, p_{\text{T}}^{\text{miss}})|_{\text{min}}}$ vs. leading $m(jj)$ for QCD events in CRB and CRC (Figure 10.76). Middle and bottom: $R_{\text{OS(}LS)}$ vs. leading $m(jj)$ for QCD events in the Z($\rightarrow \tau_\mu \tau_\nu$)+jets CR measured from CRC, CRD and their combination (Figure 10.4).

The correlation of $m(\text{jj})$ with lepton isolation was studied for QCD events in the $Z(\rightarrow \tau_\mu \tau_h) + \text{jets}$ control sample (Sec. 10.2.1). The correlation of $\text{TF}_{\text{nom.} \rightarrow \text{inv. iso}}$ with $m(\text{jj})$ is contained within the statistical uncertainties. Thus, we take $\text{TF}_{\text{nom.} \rightarrow \text{inv. iso}}$ as independent of the $m(\text{jj})$ shape, and a systematic uncertainty will be assigned from the results to the 1-degree polynomial fit (Tab. 10.8).

Finally, the correlation with the charge combination requirement between OS (LS) and OS+LS events is studied for QCD events in the $Z(\rightarrow \tau_\mu \tau_h) + \text{jets}$ CR as well. In Figure 10.79 (middle and bottom), we plot $R_{\text{OS(LS)}}$ as a function of the leading $m(\text{jj})$. These ratios are fit to a 0- and a 1-degree polynomial and the results are summarized in Tab. 10.18. Since no correlation is observed for such ratios vs. leading $m(\text{jj})$, $R_{\text{OS(LS)}}$ is calculated using the $\text{TF}_{\text{OS} \rightarrow \text{LS}}$ measured in Sec. 10.2.1 (also included in Tab. 10.18).

Fit parameter	R_{OS}		R_{LS}	
	pol-0	pol-1	pol-0	pol-1
p_0	0.517 ± 0.015	0.517 ± 0.033	0.481 ± 0.014	0.485 ± 0.030
p_1	—	$(-0.03 \pm 3.00) \times 10^{-5}$	—	$(-0.39 \pm 2.68) \times 10^{-5}$
χ^2/N	0.403	0.504	0.411	0.508
$R_{\text{OS(LS)}} \text{ (norm.)}$	0.517 ± 0.019	—	0.483 ± 0.018	—

Table 10.18: Summary of results from the fits to a pol-0 and pol-1 polynomials of the $R_{\text{OS(LS)}}$ ratios vs. leading $m(\text{jj})$ in the $Z(\rightarrow \tau_\mu \tau_h) + \text{jets}$ CR. The $R_{\text{OS(LS)}}$ measured from the event yields in this region are also included. The ratios measured from the fit and event yields are consistent within statistical uncertainties.

The strategy proposed to estimate QCD in the $\ell \tau_h$ SRs is feasible and has been validated with the checks described above. We conclude that the shape for QCD in the SRs can be taken from the combination of CRB and CRD (Fig. 10.76), and we proceed with the actual estimation of the QCD event yields in the SR, using Equation 10.12:

$$N_{\text{QCD}}^{\text{OS } \tau_h \tau_h \text{ SR}} = 0.6 \pm 0.4, \quad \text{and} \quad N_{\text{QCD}}^{\text{LS } \tau_h \tau_h \text{ SR}} = 0.6 \pm 0.4. \quad (10.17)$$

Comparing with the total predicted background yield in the OS (LS) $\tau_h \tau_h$ SR, QCD represents 17.6% (50.0%) of the background composition and the statistical uncertainty is driving the estimation in these cases.

Following the same methodology, the QCD background was estimated in the rest of the $\ell \tau_h$ SRs and below is the summary of results:

Results in the QCD $\tau_h \tau_h + \text{jj}$ control samples

The event yields for CRB, CRC, and CRA in the $\tau_h \tau_h + \text{jj}$ channels for 2017 and 2018 are presented in Tables 10.19 and 10.20. The uncertainties shown are only statistical. In the 2018 CRA, $N_{\text{data}} - N_{\text{non QCD MC}}$ is negative, close to zero, and with a large uncertainty. Therefore, $N_{\text{data}} - N_{\text{non QCD MC}}$ is taken as zero. For completeness, the $\text{TF}_{|\Delta\phi|_{\text{min}}}$ as a function of the leading $m(\text{jj})$ is shown in Figures 10.80 and 10.81, for the 2017 and 2018 data sets, respectively. In these data sets, the $\text{TF}_{|\Delta\phi|_{\text{min}}}$ is consistent with a constant ratio within statistical uncertainties.

Process	CRB	CRC	CRA
EWK V	2.5 ± 0.8	4.2 ± 1.0	0.0 ± 0.0
Rares	0.8 ± 0.4	0.2 ± 0.1	0.0 ± 0.0
Single top	1.3 ± 0.4	2.9 ± 0.7	0.1 ± 0.1
Diboson	2.0 ± 0.6	1.9 ± 0.5	0.2 ± 0.0
W+Jets	14.5 ± 2.0	33.0 ± 4.6	0.2 ± 0.0
Z+jets	1.0 ± 0.3	1.1 ± 0.3	0.3 ± 0.1
$t\bar{t}$	13.7 ± 1.3	16.0 ± 1.4	0.4 ± 0.1
Total non-QCD bkg	35.9 ± 2.6	59.3 ± 4.9	1.3 ± 0.2
Data	178	162	2
$N_{\text{data}} - N_{\text{non-QCD MC}}$	142.1 ± 13.6	102.7 ± 13.6	0.7 ± 1.4
QCD purity [%]	79.9	63.4	37.1

Table 10.19: Summary of event yields in CRB, CRC, and CRA for the QCD estimation in the $\tau_h\tau_h+jj$ SRs for 2017 after applying central and VBF2 selections.

Process	CRB	CRC	CRA
EWK V	2.0 ± 0.8	7.5 ± 1.5	0.3 ± 0.3
Rares	1.0 ± 0.5	0.9 ± 0.3	0.0 ± 0.0
Single top	1.1 ± 0.5	3.0 ± 0.8	0.0 ± 0.0
Diboson	3.0 ± 0.7	3.8 ± 0.6	0.2 ± 0.1
W+Jets	21.9 ± 3.3	54.8 ± 6.5	0.3 ± 0.1
Z+jets	1.0 ± 0.1	0.9 ± 0.1	0.4 ± 0.1
$t\bar{t}$	15.7 ± 1.1	25.4 ± 1.4	0.9 ± 0.3
Total non-QCD bkg	45.7 ± 3.7	96.3 ± 6.9	2.1 ± 0.4
Data	281	189	2
$N_{\text{data}} - N_{\text{non-QCD MC}}$	235.3 ± 17.2	92.7 ± 15.3	-0.1 ± 1.5 (*)
QCD purity [%]	83.8	49.0	0%

Table 10.20: Summary of event yields in CRB, CRC, and CRA for the QCD estimation in the $\tau_h\tau_h+jj$ SRs for 2018 after applying central and VBF2 selections.

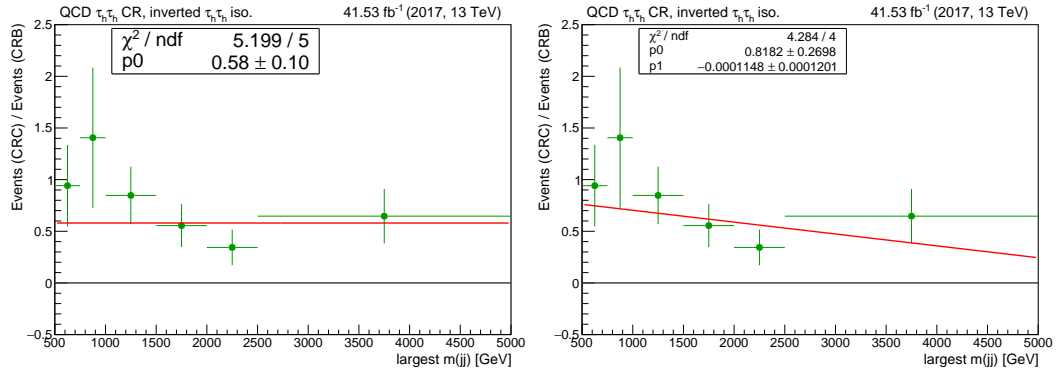


Figure 10.80: $\text{TF}_{|\Delta\phi(j, p_T^{\text{miss}})|_{\text{min}}}$ vs. leading $m(jj)$ for QCD events in CRB and CRC (Figure 10.76) for the $\tau_h\tau_h+jj$ SRs in 2017.

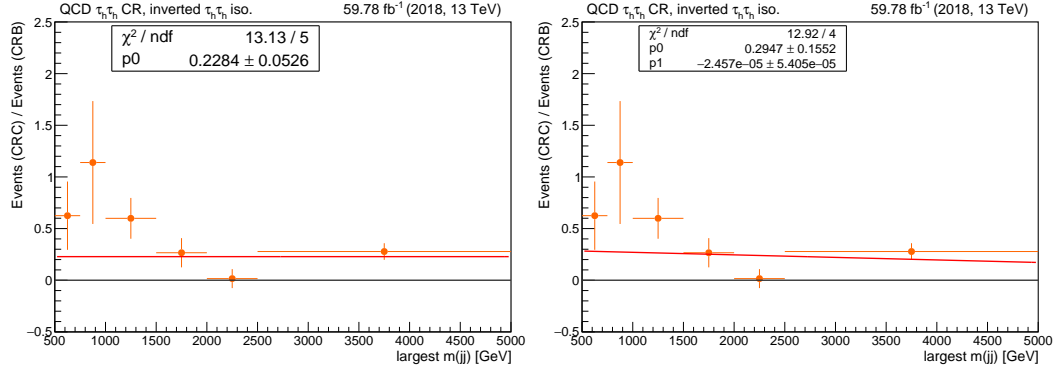


Figure 10.81: $\text{TF}_{|\Delta\phi(j, p_T^{\text{miss}})|_{\text{min}}}$ vs. leading $m(jj)$ for QCD events in CRB and CRC (Figure 10.76) for the $\tau_h\tau_h+jj$ SRs in 2018.

Results in the QCD $\mu\tau_h+jj$ control samples

The results obtained in the $\mu\tau_h+jj$ QCD CRB, CRC, and CRA are presented in Tables 10.21, 10.22, and 10.23, for the 2016, 2017, and 2018 data sets, respectively. The uncertainties included in the event yields are only statistical. In addition, the $\text{TF}_{|\Delta\phi(j, p_T^{\text{miss}})|_{\text{min}}}$ is plotted as a function of the leading $m(jj)$ for the three data sets of Run II, and the results from the corresponding fits to a 0- and a 1-degree polynomial. In the three data sets, the ratio is consistent with a constant function, further validating the results obtained in the $\tau_h\tau_h+jj$ control samples.

Process	CRB	CRC	CRA
EWK V	2.5 ± 0.6	5.3 ± 0.9	0.4 ± 0.0
Rares	1.4 ± 0.5	2.5 ± 0.7	0.3 ± 0.0
Single top	8.2 ± 1.2	13.0 ± 1.4	0.8 ± 0.4
Diboson	2.4 ± 0.6	4.7 ± 0.8	1.5 ± 0.4
W+Jets	20.7 ± 2.1	38.6 ± 1.4	3.1 ± 1.2
Z+jets	0.9 ± 0.1	1.9 ± 0.4	0.8 ± 0.1
$t\bar{t}$	60.7 ± 2.6	97.8 ± 3.2	3.1 ± 0.5
Total non QCD bkg	96.8 ± 3.6	163.8 ± 5.1	10.0 ± 1.4
Data	201	225	11
$N_{\text{data}} - N_{\text{non QCD MC}}$	104.2 ± 14.7	61.3 ± 15.9	1.0 ± 3.6
QCD purity [%]	51.8	27.2	9.1

Table 10.21: Summary of event yields in CRB, CRC, and CRA for the QCD estimation in the $\mu\tau_h+jj$ SRs for 2016 after applying central and VBF2 selections.

Process	CRB	CRC	CRA
EWK V	1.3 ± 0.5	3.2 ± 0.8	0.2 ± 0.0
Rares	1.1 ± 0.5	2.7 ± 0.7	0.4 ± 0.3
Single top	5.4 ± 0.9	9.7 ± 1.2	0.4 ± 0.2
Diboson	2.5 ± 0.6	3.6 ± 0.7	0.7 ± 0.1
W+Jets	17.3 ± 1.8	41.2 ± 4.5	1.4 ± 0.4
Z+jets	0.6 ± 0.1	1.3 ± 0.2	0.7 ± 0.1
$t\bar{t}$	57.1 ± 2.7	87.2 ± 3.3	4.6 ± 0.6
Total non QCD bkg	85.4 ± 3.5	148.8 ± 5.8	8.4 ± 0.8
Data	231	318	11
$N_{\text{data}} - N_{\text{non QCD MC}}$	145.6 ± 15.6	169.2 ± 18.7	2.6 ± 3.4
QCD purity [%]	63.0	53.2	23.8

Table 10.22: Summary of event yields in CRB, CRC, and CRA for the QCD estimation in the $\mu\tau_h+jj$ SRs for 2017 after applying central and VBF2 selections.

Process	CRB	CRC	CRA
EWK V	4.0 ± 1.2	11.5 ± 2.0	0.5 ± 0.4
Rares	2.0 ± 0.8	4.0 ± 1.0	0.2 ± 0.1
Single top	10.4 ± 1.5	12.8 ± 1.5	0.0 ± 0.0
Diboson	1.3 ± 0.3	5.3 ± 0.9	1.9 ± 0.6
W+Jets	29.8 ± 3.4	66.0 ± 7.2	2.1 ± 0.9
Z+jets	1.2 ± 0.1	2.4 ± 0.5	2.0 ± 0.5
$t\bar{t}$	83.4 ± 2.5	119.2 ± 3.0	5.4 ± 0.7
Total non QCD bkg	132.2 ± 4.7	221.1 ± 8.3	12.1 ± 1.4
Data	395	462	13
$N_{\text{data}} - N_{\text{non QCD MC}}$	262.8 ± 20.4	240.9 ± 23.0	0.9 ± 3.9
QCD purity [%]	66.5	52.1	6.7

Table 10.23: Summary of event yields in CRB, CRC, and CRA for the QCD estimation in the $\mu\tau_h+jj$ SRs for 2018 after applying central and VBF2 selections.

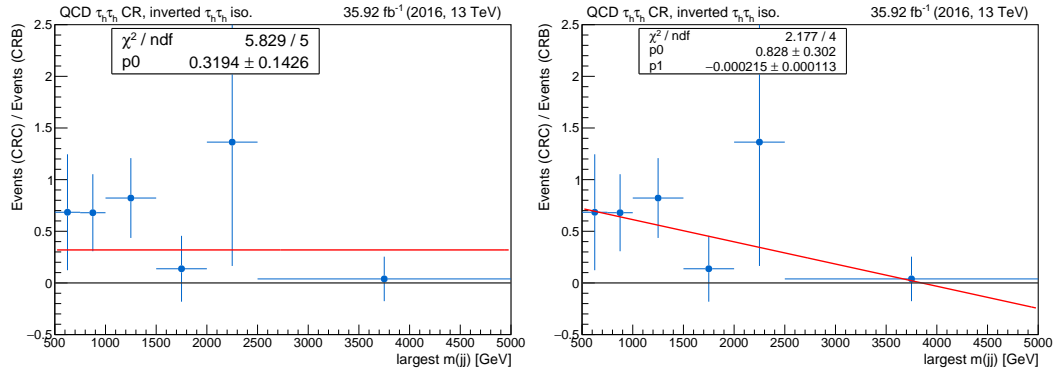


Figure 10.82: $\text{TF}_{|\Delta\phi(j, p_T^{\text{miss}})|_{\text{min}}}$ vs. leading $m(jj)$ for QCD events in CRB and CRC (Figure 10.76) for the $\mu\tau_h+jj$ SRs in 2016.

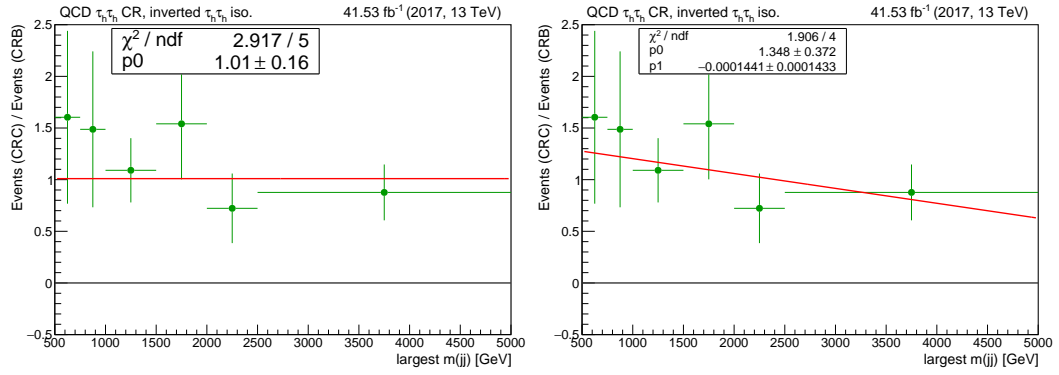


Figure 10.83: $TF_{|\Delta\phi(j, p_T^{\text{miss}})|_{\text{min}}}$ vs. leading $m(jj)$ for QCD events in CRB and CRC (Figure 10.76) for the $\mu\tau_h+jj$ SRs in 2017.

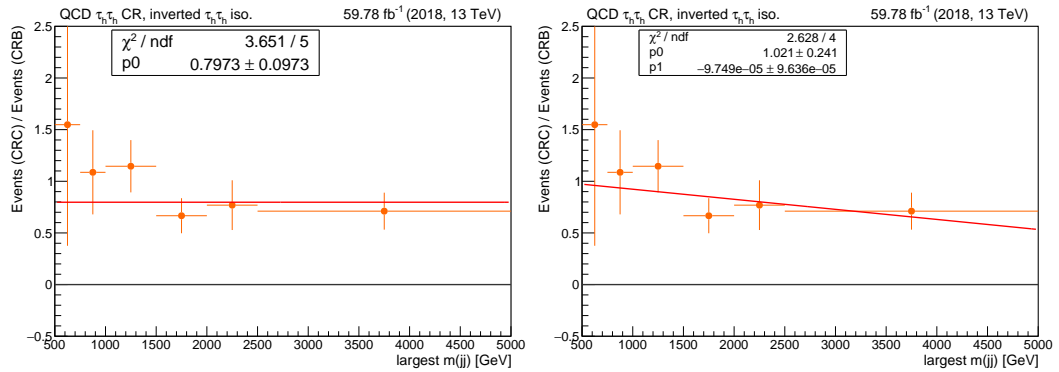


Figure 10.84: $TF_{|\Delta\phi(j, p_T^{\text{miss}})|_{\text{min}}}$ vs. leading $m(jj)$ for QCD events in CRB and CRC (Figure 10.76) for the $\mu\tau_h+jj$ SRs in 2018.

Results in the QCD $e\tau_h+jj$ control samples

Electrons and muons are expected to have similar kinematics in the $e\tau_h+jj$ and $\mu\tau_h+jj$ final states. Since we expect the $\text{TF}_{|\Delta\phi(j, p_T^{\text{miss}})|_{\text{min}}}$ to be uncorrelated with the lepton flavor combination, we make use of the $\text{TF}_{|\Delta\phi(j, p_T^{\text{miss}})|_{\text{min}}}$ measured in the $\mu\tau_h+jj$ QCD CRs for the estimation of the QCD background yields in the $e\tau_h+jj$ SRs. Therefore, only the event yields for CRA for the 2016, 2017, and 2018 data sets are shown in Table 10.24. In the 2016 data set, $N_{\text{data}} - N_{\text{non QCD MC}}$ is negative and it has a large uncertainty. This case is treated as the 2018 $\tau_h\tau_h+jj$ CRA results, where the predicted QCD event yield is taken to be null.

Process	2016	2017	2018
EWK V	0.6 ± 0.3	0.2 ± 0.2	0.3 ± 0.0
Rares	0.2 ± 0.0	0.0 ± 0.0	0.4 ± 0.1
Single top	0.2 ± 0.2	0.1 ± 0.1	0.2 ± 0.0
Diboson	1.0 ± 0.3	0.9 ± 0.3	1.3 ± 0.5
W+Jets	2.1 ± 0.7	2.6 ± 0.6	3.2 ± 1.0
Z+jets	0.5 ± 0.1	0.4 ± 0.1	1.0 ± 0.1
$t\bar{t}$	2.8 ± 0.5	2.4 ± 0.5	2.1 ± 0.4
Total non QCD bkg	7.4 ± 1.0	6.6 ± 0.9	8.5 ± 1.2
Data	4	7	17
$N_{\text{data}} - N_{\text{non QCD MC}}$	-3.4 ± 2.2 (*)	0.4 ± 2.7	8.5 ± 4.3
QCD purity [%]	0%	5.4	49.8

Table 10.24: Summary of event yields in CRA for the QCD estimation in the $e\tau_h+jj$ SRs for 2016-2018 after applying central and VBF2 selections.

Summary of transfer factors and event yields for QCD multijet events in the $\ell\tau_h+jj$ SRs

Combining the results from all the QCD CRs, the $|\Delta\phi(j, p_T^{\text{miss}})|_{\text{min}}$ transfer factors and charge combination ratios were calculated, and are summarized in Tables 10.25, and 10.26. The final prediction of QCD multijet events in the different SRs is presented in Table 10.27. The uncertainties presented in the tables are all statistical. The total prediction from simulation for non-QCD backgrounds was subtracted from data in CRB and CRC, and combined together to obtain the shape of the leading $m(jj)$ QCD background in the SRs. The distribution was re-normalized to match the predicted event yields in Table 10.27. Such distributions are presented in Chapter 13, together with the predictions from the other backgrounds.

Data set	R_{OS}	R_{LS}
2016	0.517 ± 0.015	0.483 ± 0.018
2017	0.543 ± 0.018	0.457 ± 0.015
2018	0.533 ± 0.014	0.467 ± 0.012

Table 10.25: Summary of R_{OS} and R_{LS} ratios obtained in the QCD background estimation for the $\ell\tau_h$ SRs.

Data set	$\mu\tau_h+jj$	$\tau_h\tau_h+jj$
2016	0.588 ± 0.174	0.476 ± 0.171
2017	1.16 ± 0.18	0.723 ± 0.118
2018	0.917 ± 0.113	0.393 ± 0.071

Table 10.26: Summary of $TF_{|\Delta\phi(j,p_T^{\text{miss}})|_{min}}$ obtained in the QCD background estimation for the $\ell\tau_h$ SRs.

Data set	$e\tau_h+jj$		$\mu\tau_h+jj$		$\tau_h\tau_h+jj$	
	OS	LS	OS	LS	OS	LS
2016	0.0 ± 1.0	0.0 ± 1.0	0.3 ± 1.1	0.3 ± 1.0	0.6 ± 0.4	0.6 ± 0.4
2017	1.6 ± 2.1	1.4 ± 1.8	1.6 ± 2.1	1.4 ± 1.8	0.3 ± 0.6	0.2 ± 0.5
2018	4.2 ± 2.1	3.6 ± 1.8	0.4 ± 1.9	0.4 ± 1.7	0.0 ± 1.0	0.0 ± 1.0

Table 10.27: Predicted event yields for the QCD multijet background in the various $\ell\tau_h+jj$ SRs.

10.4 Final remarks on background estimation

In this final section, general details about the calibration of the efficiencies in the other decay channels are described.

0-lepton channels

As described in Chapter 9 (Tab. 9.1), the dominant backgrounds in the $0\ell+jj$ channel are Z+jets in the invisible decay channel ($Z\rightarrow\nu\nu$), W+jets in the leptonic decays, when the charged lepton is lost in reconstruction, and QCD multijet events. Three control samples were created for each one of these backgrounds. Given that the kinematics of the Z boson decay are independent of the lepton flavor (i. e. charged lepton vs. neutrino), and the fact that it is not possible to create a $Z(\rightarrow\nu\nu)+jets$ control sample that could remain orthogonal to the SR, a $Z(\rightarrow\mu^+\mu^-)+jets$ control sample was created. Events were required to contain exactly two muons in the final state with opposite charges and a $m(\mu\mu)$ cut consistent with the Z mass width ($80 < m(\mu\mu) < 100$ GeV). The 4-momentum of these muons was then added to the \vec{p}_T^{miss} vector, to emulate the \vec{p}_T that the neutrinos would take after the Z decay. This technique is referred to as the $\mu\rightarrow\nu$ emulation. After this, a p_T^{miss} selection consistent with the one in the signal region was applied. The central and VBF efficiencies were measured in this control sample and also validated by comparing to the prediction obtained from $Z(\rightarrow\nu\nu)+jets$ MC simulation in the signal region, showing consistency in the both in the leading $m(jj)$ shape and normalization.

The same $\mu\rightarrow\nu$ emulation technique was used in a $W(\rightarrow\mu\nu)+jets$ control sample, requiring events containing exactly one muon, large p_T^{miss} (same requirement as in the SR), and a m_T selection consistent with the W mass width ($60 < m_T < 100$ GeV). In this case, the $\mu\rightarrow\nu$ emulation will serve as a way to model the events for which a lepton is lost in reconstruction, and thus showing up in the \vec{p}_T^{miss} vector. The efficiencies for central and VBF selections are measured for this process.

Finally, for the QCD background estimation, the same methodology used for the $\ell\tau_h$ SRs is used. Instead of using lepton isolation as one of the variables for the ABCD method, a p_T^{miss} side-band is chosen).

1-lepton channels

The dominant backgrounds in these signal regions are $t\bar{t}$ and W+jets events, where $W(\rightarrow\ell\nu)$. For the measurement of the $t\bar{t}$ central and VBF efficiencies, a control sample was constructed using the same event selections as in the SR except that the presence of exactly one b-jet is required, in order to enrich the $t\bar{t}$ purity and remain orthogonal to the signal region. The scale factors obtained were validated in a control sample containing exactly two b-jets. For W+jets, a control region was designed by using the SR selections but inverting the m_T cut from >110 GeV to $m_T < 110$ GeV. Finally, the QCD background estimation in the τ_h+jj channel is done with the same methodology used for the $\ell\tau_h+jj$ channels. The only differences are that (1) no charge requirement is necessary, since only one lepton is present in the final state (therefore, there is no need to measure $R_{\text{OS(LS)}}$), and (2) only the isolation of the single τ_h is inverted.

CHAPTER 11

Uncertainties

There are two important aspects that characterize an experimental result: accuracy and precision. *Accuracy* is defined as the degree to which a result agrees with the true value. *Precision* is related to the repeatability of the result [169]. In searches for new physics at the LHC, usually the true value of a quantity is almost always unknown a priori. Therefore, precision needs to be quantified by *uncertainty*.

Uncertainty is defined as the interval around the measurement in which repeated measurements will fall [169], and it is a way to quantify the limitation of the analysis design or some of its aspects for which the understanding is incomplete. Uncertainties can be divided in two main categories: *statistical (random) uncertainties* and *systematic uncertainties*. In general, statistical and systematic uncertainties are assumed to be *uncorrelated*, which means, they are independent of each other. The total uncertainty is then the sum in quadrature: $\sigma_{\text{total}} = \sqrt{\sigma_{\text{stat.}}^2 + \sigma_{\text{syst.}}^2}$.

11.1 Statistical uncertainties

Statistical uncertainties come from the inability of having infinitely accurate measurements. Every measurement will have unpredictable fluctuations, which can be reduced by increasing the amount of data used to perform such measurement. This will help to have a more accurate result, that is, the range in which the central value of a measurement can *randomly* fluctuate is reduced. When the average or mean value of a set of x_i measurements in a counting experiment, the spread in the measured values is quantified by the standard deviation σ ,

$$\sigma = \sqrt{\frac{\sum_{i=1}^N (x_i - \bar{x})^2}{N}}, \quad (11.1)$$

where \bar{x} is the average of the x_i values and N is the number of total measurements.

When an observation consists in counting independent random events in a given interval, the spread of the values will be usually larger than the accuracy of counting (which may be well exact). However, it is known that in this case, for an expected number of observations N , the spread is \sqrt{N} , and also known as the *Poisson error* [170].

It is important to make a distinction about the statistical uncertainties listed in Chapter 10. Simulation samples will be produced by event generators, which correspond to the “raw” count of events produced, without taking into account the cross section of a given process, nor the integrated luminosity of interest. As explained in Sec. 10.1, the mapping between the number of events produced for a specific process in simulation and the number of events of that we would observe in data is given by Eq. 10.3:

$$N_{\text{process}}^{\text{predicted}} = \sigma_{\text{process}} \cdot \mathcal{L}_{\text{int}} \cdot \epsilon_{\text{total}}. \quad (11.2)$$

Here, ϵ_{total} is the efficiency of the event selections considered. In the case of simulation,

$$\epsilon_{\text{sim}} = \frac{N_{\text{pass}}^{\text{raw sim}}}{N_{\text{total}}^{\text{raw sim}}}, \quad (11.3)$$

and the statistical uncertainty on ϵ_{sim} is given by

$$\delta\epsilon_{\text{sim}} = \frac{\delta N_{\text{pass}}^{\text{raw sim}}}{N_{\text{total}}^{\text{raw sim}}} = \frac{\sqrt{N_{\text{pass}}^{\text{raw sim}}}}{N_{\text{total}}^{\text{raw sim}}}. \quad (11.4)$$

In this way, the statistical uncertainty on the predicted yield for a specific process will be

$$\delta N_{\text{process}}^{\text{predicted}} = \sigma_{\text{process}} \cdot \mathcal{L}_{\text{int}} \cdot \frac{\sqrt{N_{\text{pass}}^{\text{raw sim}}}}{N_{\text{total}}^{\text{raw sim}}}. \quad (11.5)$$

Notice that what this uncertainty quantifies is how well we can predict the event yield for a process based on the statistics of our simulation sample. In other words, this is the *statistical uncertainty on the event yield prediction based on simulation*, and corresponds to the values displayed in the event yield tables of Chapter 10. $\delta N_{\text{process}}^{\text{predicted}}$ is *not the same* as the Poisson uncertainty of the event yield $N_{\text{process}}^{\text{predicted}}$, $\sqrt{N_{\text{process}}^{\text{predicted}}}$. The latter represents instead the spread of the fluctuations that, in case that $N_{\text{process}}^{\text{predicted}}$ was the true value, we would measure in data.

11.2 Systematic uncertainties

Systematic uncertainties represents a bias on the measurement that cannot be improved with the addition of more data. In a sense, systematic uncertainties are related with how well certain aspects of the analysis can be measured based on the limitations of the experimental devices, the methodologies or techniques used for predictions or estimations of, for example, the efficiency of the signal region selections, etc. Although it is possible to control and minimize the effects and sources of systematic uncertainties, they will always be present in our measurements.

A list of the systematic uncertainties relevant to this analysis are:

- *Luminosity*: an uncertainty on the estimation of the luminosity comes into play for the experimental measurements of cross sections for the various processes (Eq. 11.2), as well as the prediction of the amount of events present in the signal region for signal and backgrounds.
- *Event reconstruction and identification*: examples of these types of uncertainties are the calibration of the energy scales for reconstructed analysis physics objects (jets, τ_h 's, electrons, muons, p_T^{miss} , etc.), the reconstruction and identification efficiencies, momentum and energy resolution, etc. Even though extensive strategies are developed to minimize these uncertainties (in the form of corrections, described in Chapter 7), there will always be some residual effects that will impact the estimations and measurements done in a data analysis.
- *Experimental conditions*: sources of these uncertainties are related to unexpected issues or changes to the detector machine, the characteristics of the beam, etc.

- *Triggers*: this is related to the uncertainty related to the measurement of the efficiency of triggers with respect to the specific selections on the variables considered for the trigger decision.
- *Simulation*: event generators rely on complex phenomenological models, and some of the simplifications or assumptions, as well as the experimental uncertainties on any of the experimental inputs they take can lead to systematic uncertainties. In this category one can list models on parton showers (Appendix A), parton distribution functions (PDFs), normalization factors used to correct cross sections to higher orders (k -factors), etc.
- *Background estimation techniques*: these uncertainties arise from the limitations of the methodology used to estimate the number of background events in the signal region. In this analysis, for the cases in which simulation is used, these uncertainties can come from the contamination from other backgrounds in a specific CR, or the dependence of the normalization agreement between simulation and the observed data with the value of the fit variable. In the data-driven background estimations, these can come from the correlation between the variables chosen for the ABCD method.

For this particular analysis, the most important sources of systematic uncertainties include those relevant to the calibration of jets and the efficiencies of the VBF event selections. The general idea for systematic uncertainties related to calibration, reconstruction and identification of physics objects and the experimental conditions is to assess (1) the effect of the systematic uncertainties in the event yields for signal and the dominant backgrounds, and (2) any dependence on the value of the fit variable, in our case the leading $m(jj)$. We refer to (1) as a systematic uncertainty on *normalization* and to (2) as a systematic uncertainty on *shape*. For the background estimation, the uncertainties calculated for the scale factors in each control region to the efficiencies are considered as normalization uncertainties and if there is any shape bias on the data-to-simulation agreement on the largest $m(jj)$ distribution, then this is entered as a shape systematic uncertainty.

As an example, we can consider the effect of the systematic uncertainties in the calibration of the jet energy scale (JES). In this case, I will consider the effect in two channels: the invisible channel, which has the most statistics of all channels and the OS $\tau_h\tau_h$ channel, one of the channels with the smallest number of predicted events in the signal region. Tables 11.2 and 11.1 show the effect in normalization from JES on the event yields for both cases and the different experimental conditions for 2016, 2017 and 2018. For the 0-lepton channel, the up and down variations fluctuate around 7-10% of the nominal value. In the OS $\tau_h\tau_h$ channel, these fluctuations are more inconsistent across years and variations, and the main reason behind it is the limited statistics.

Now, we can look at any potential bias to the fit variable shape in the signal region. Figures 11.1 and 11.2 show the nominal leading $m(jj)$ distributions and the shapes obtained after including the $+1\sigma$ (up) and -1σ (down) JES variations. In the bottom pads, we can observe the systematic shift vs. nominal ratios in order to evaluate any shape bias. It is clear that in the 0-lepton case we observe shape biases both for signal and background. These biases go beyond the relative nominal statistical uncertainty, which is depicted with the magenta shaded area around the ratio at one. Since these biases show a linear trend with the $m(jj)$ value, then a first degree polynomial is fit to the ratios. The goal is to obtain a function that would help us determine the systematic uncertainty due to JES assigned to each bin in the distribution, in addition to the uncertainty in normalization.

Sample	Variation	Event yields			Absolute % diff w.r.t. nominal yield		
		2016	2017	2018	2016	2017	2018
Signal $m(\tilde{\chi}_2^0) = 300$ GeV, $\Delta m = 50$ GeV, $\tilde{\tau}$ -dom. decays	JES -1σ	2.14 ± 0.17	2.28 ± 0.20	3.94 ± 0.25	1.13	0.66	1.82
	JES nominal	2.12 ± 0.17	2.26 ± 0.20	4.02 ± 0.26	–	–	–
	JES $+1\sigma$	2.15 ± 0.17	2.27 ± 0.20	4.07 ± 0.26	1.37	0.40	1.32
Z+jets	JES -1σ	0.57 ± 0.11	1.28 ± 0.30	2.23 ± 0.47	1.05	1.69	5.19
	JES nominal	0.57 ± 0.11	1.30 ± 0.30	2.35 ± 0.47	–	–	–
	JES $+1\sigma$	0.65 ± 0.12	1.63 ± 0.37	2.53 ± 0.47	14.2	25.4	7.45

Table 11.1: Summary of event yield variations and absolute % differences $\left(\left|\frac{N_{\text{nom}} - N_{\text{shift}}}{N_{\text{nom}}}\right| \times 100\right)$ in the OS $\tau_h \tau_h$ channel for JES uncertainties, including a benchmark signal point and a dominant background in this SR.

Sample	Variation	Event yields			Absolute % diff w.r.t. nominal yield		
		2016	2017	2018	2016	2017	2018
Signal $m(\tilde{\chi}_2^0) = 300$ GeV, $\Delta m = 5$ GeV, W^*/Z^* decays	JES -1σ	121.6	117.3	196.1	0.49	1.01	0.76
	JES nominal	122.2	118.5	197.6	–	–	–
	JES $+1\sigma$	123.1	119.9	199.4	0.73	1.18	0.91
Z+jets	JES -1σ	13755.0	15352.5	23517.8	5.13	7.09	7.64
	JES nominal	14498.8	16524.7	25464.4	–	–	–
	JES $+1\sigma$	15613.7	18242.1	27952.2	7.69	10.4	9.77

Table 11.2: Summary of event yield variations and absolute % differences $\left(\left|\frac{N_{\text{nom}} - N_{\text{shift}}}{N_{\text{nom}}}\right| \times 100\right)$ in the 0-lepton channel for JES uncertainties, including a benchmark signal point and a dominant background in this SR.

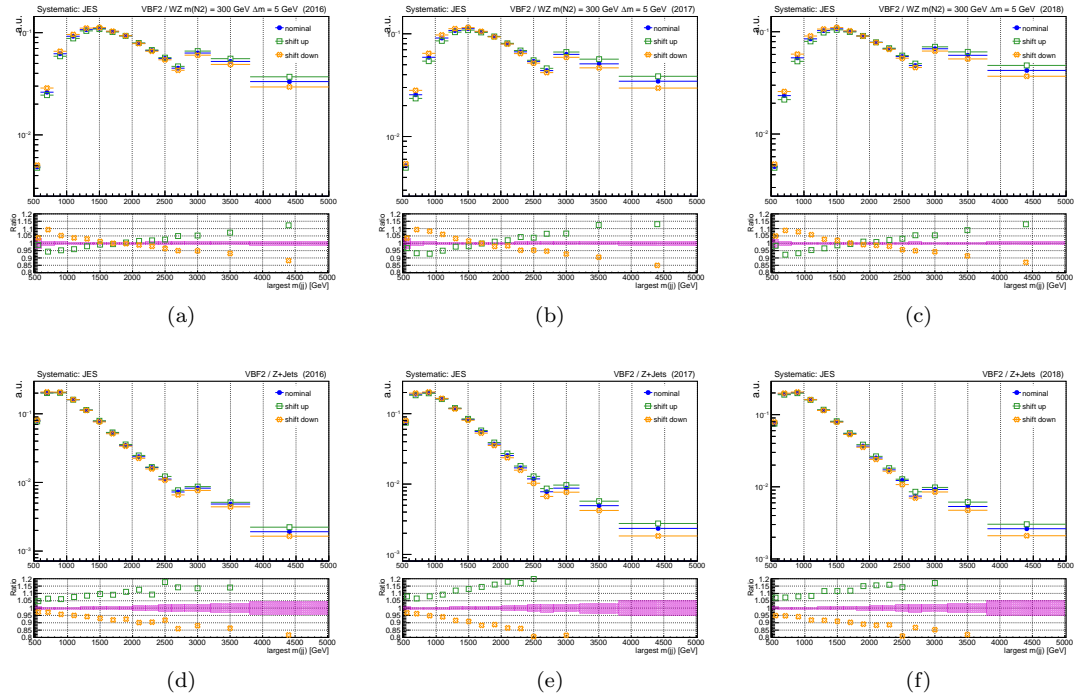


Figure 11.1: Leading $m(jj)$ distributions for the nominal and $\pm 1\sigma$ systematic variations on jet energy scale (top pad) and the corresponding ratios (bottom pad) for a signal benchmark scenario (a-c) and Z+jets (d-f) in the 0-lepton channel.

On the other hand, for the OS $\tau_h\tau_h$, although the ratios do not show a specific trend that could indicate a shape bias, the variations lie within the relative nominal statistical uncertainty. This indicates that in the OS $\tau_h\tau_h$, and in general for the 2-lepton channels, the total uncertainty (stat. + syst.) will be mainly driven by the statistical uncertainties. Therefore, we can assign only a normalization based systematic uncertainty due to JES in the OS $\tau_h\tau_h$ channel.

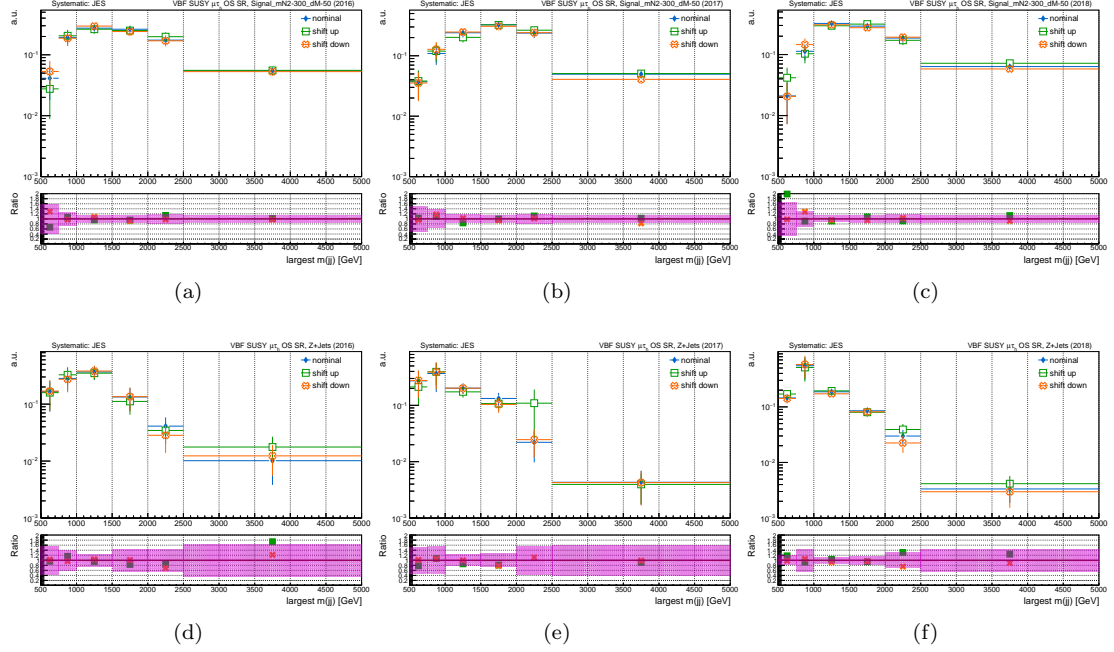


Figure 11.2: Leading $m(jj)$ distributions for the nominal and $\pm 1\sigma$ systematic variations on jet energy scale (top pad) and the corresponding ratios (bottom pad) for a signal benchmark scenario (a-c) and Z+jets (d-f) in the OS $\tau_h\tau_h$ channel.

CHAPTER 12

Results with $\mathcal{L}_{int} = 35.9 \text{ fb}^{-1}$ and interpretation

12.1 Results

Results for this analysis have been published with a fraction of the total integrated luminosity collected by the CMS experiment in Run II, corresponding to the $\mathcal{L}_{int} = 35.9 \text{ fb}^{-1}$ recorded during the 2016 data-taking period. In this analysis, only the $0\ell+jj$ and $\ell+jj$ channels were included and only VBF1 selections were considered (Sec. 9, Tab. 9.4). For this first iteration of the analysis, two kinematic variables were utilized to fit the observed data to the prediction in simulation and therefore search for any deviations from the SM predictions: the leading $m(jj)$ in the $0\ell+jj$ channel and $m_T(\ell, p_T^{\text{miss}})$ ($\ell = e, \mu, \tau_h$), which provided the best sensitivity with the set of event selections considered.

The number of predicted background contributions and observed data in the signal region for each decay channel, obtained integrating over the bins in the $m_{\text{lead}}(jj)$ and $m_T(\ell, p_T^{\text{miss}})$, are presented in Tab. 12.1. The kinematic distributions for the predicted SM background, expected signal and observed data in the $m_{\text{lead}}(jj)$ in the $0\ell+jj$ channel and the m_T in the $1\ell+jj$ channels are shown in Fig. 12.1. The bin sizes in these distributions were chosen to maximize the signal significance of the analysis. *We observe no significant excess above the SM prediction in any of the search regions. Therefore, this search does not reveal any evidence for new physics.*

Process	$0\ell + jj$	$e + jj$	$\mu + jj$	$\tau_h + jj$
Diboson	77 ± 18	1.5 ± 0.6	1.7 ± 0.7	0.9 ± 0.9
QCD	546 ± 69	$0_{-0}^{+1.2}$	$0_{-0}^{+0.2}$	23 ± 5
Single top quark	104 ± 10	0.2 ± 0.1	2.2 ± 0.9	0.6 ± 0.3
$t\bar{t}$	577 ± 128	11 ± 4	13 ± 4	5 ± 3
W+jets	2999 ± 620	6 ± 1	13 ± 3	7 ± 2
Z+jets	3714 ± 760	0.10 ± 0.04	0.20 ± 0.07	0.10 ± 0.04
Total background	8017 ± 992	19 ± 5	31 ± 5	37 ± 6
Data	8408	29	36	38

Table 12.1: Number of observed events and corresponding pre-fit background predictions, where “pre-fit” refers to the predictions determined as described in the text, before constraints from the fitting procedure have been applied. The uncertainties include the statistical and systematic components [171].

12.2 Interpretation

The results were interpreted in R-parity conserving MSSM, described in the Chapter 4, focusing specifically in the **bino-like $\tilde{\chi}_1^0$ and wino-like $\tilde{\chi}_2^0$ and $\tilde{\chi}_1^\pm$ model with (a) democratic light slepton**

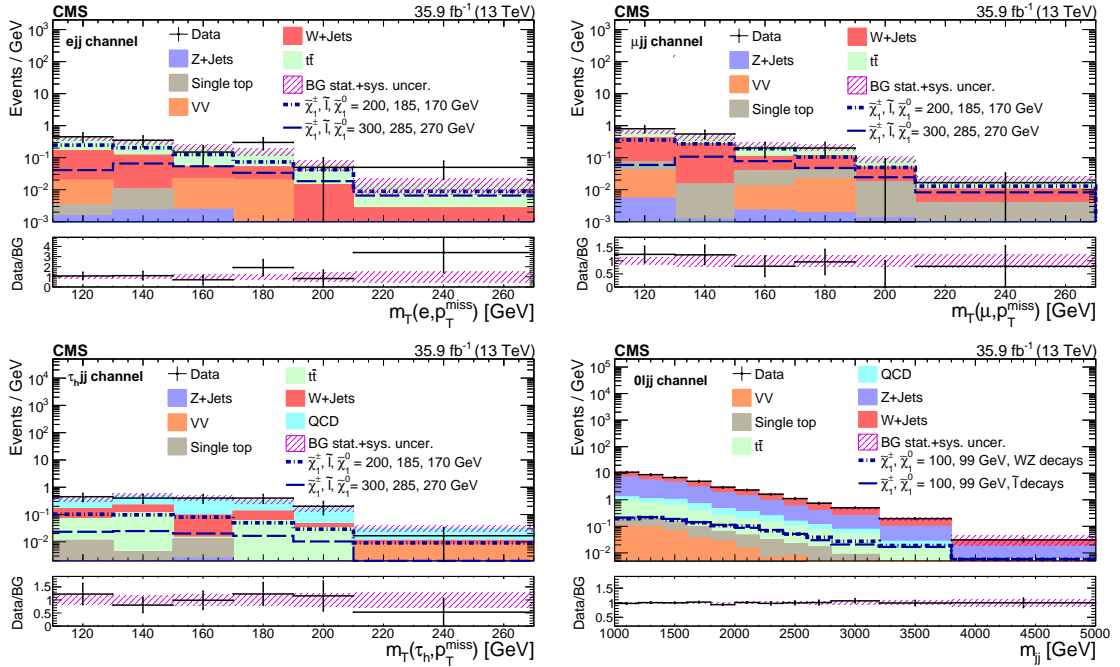


Figure 12.1: The observed m_T and $m(jj)$ distributions in the $e+jj$ (upper left), $\mu+jj$ (upper right), τ_h+jj (lower left), and $0\ell+jj$ (lower right) signal regions compared with the post-fit SM background yields from the fit described in the text. The pre-fit background yields and shapes are determined using data-driven methods for the major backgrounds, and based on simulation for the smaller backgrounds. Expected signal distributions are overlaid. The last bin in the m_T distributions of the $\ell+jj$ channels all events with $m_T > 210$ GeV. The last bin of the $m(jj)$ distributions of the $0\ell+jj$ channel include all events with $m(jj) > 3800$ GeV [171].

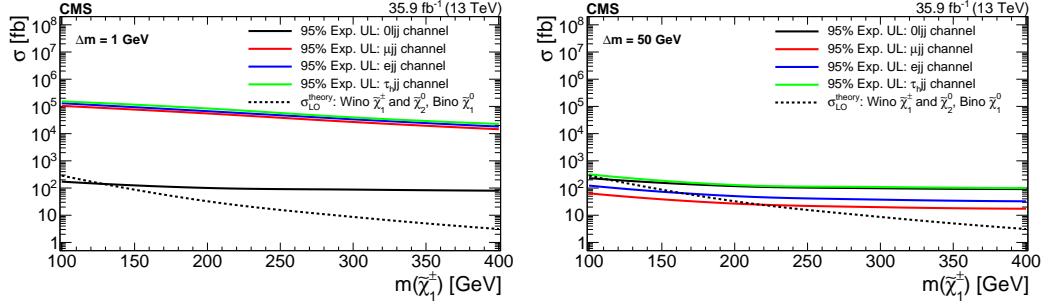


Figure 12.2: Expected 95% CL UL on the cross section as a function of $m(\tilde{\chi}_1^\pm)$. The results correspond to $\Delta m = 1$ GeV (left) and $\Delta m = 50$ GeV (right) for the wino-bino model with democratic light slepton decays.

decays¹, and (b) the virtual W/Z decays. The signal selection efficiency for the $\mu+jj$ ($e+jj$) channel in the democratic light slepton model, assuming $\Delta m = 30$ GeV is 0.9 (0.7)% for $m(\tilde{\chi}_1^\pm) = 100$ GeV and 2.5 (1.8)% for $m(\tilde{\chi}_1^\pm) = 300$ GeV. Similarly, the signal selection efficiency for the $0\ell+jj$ channel, assuming $\Delta m = 1$ GeV, is 2.8% for $m(\tilde{\chi}_1^\pm) = 100$ GeV and 5.3% for $m(\tilde{\chi}_1^\pm) = 300$ GeV.

The calculation of the exclusion limit is obtained using both the $m(jj)$ and m_T distributions in the corresponding decay channels, to construct a combined profile likelihood ratio test statistic in bins of $m(jj)$ and m_T , and computing a 95% confidence level (CL) upper limit (UL) on the signal region cross section using the asymptotic CL_s criterion.

Systematic uncertainties are taken into account as nuisance parameters, which are removed by profiling, assuming gamma function or log-normal priors for normalization parameters, and Gaussian priors for mass spectrum shape uncertainties. The combination of the four search channels requires simultaneous analysis of the data from the individual channels, accounting for all statistical and systematic uncertainties and their correlations. Correlations among backgrounds, both within a channel and across channels, are taken into consideration in the limit calculation. For example, the uncertainty in the integrated luminosity is treated as fully correlated across channels. The uncertainties in the predicted signal yields resulting from the event acceptance variation with different sets of PDFs in a given m_T or $m(jj)$ bin are treated as uncorrelated within a channel and correlated across channels. The uncertainties from the closure tests are treated as uncorrelated within and across the different final states.

The expected (observed) limits obtained for the democratic light slepton decay scenario as a function of $m(\tilde{\chi}_1^\pm)$ are shown in Fig. 12.2 (Fig. 12.3). The benchmark scenarios included consider Δm 's of 1 and 50 GeV. The breakdown per decay channel is presented and compared to the theoretical cross section. The $0\ell+jj$ channel provides the best sensitivity for the very compressed mass spectrum scenario ($\Delta m = 1$ GeV), whereas the $e+jj$ and $\mu+jj$ channels provide the best sensitivity for the largest compressed mass spectrum scenario considered in this iteration of the analysis ($\Delta m = 50$ GeV).

The expected and observed 95% CL UL on the cross section after the combination of all channels were interpreted in the wino-bino model with democratic light slepton and virtual W/Z decays. In the democratic light slepton model, for the $\Delta m = \{1, 10, 30, 50\}$ GeV scenarios, the combination

¹The mass of the slepton is defined as the average of the $\tilde{\chi}_1^0$ and $\tilde{\chi}_2^0$ masses: $m(\ell) = \frac{1}{2} [m(\tilde{\chi}_1^0) + m(\tilde{\chi}_2^0)]$.

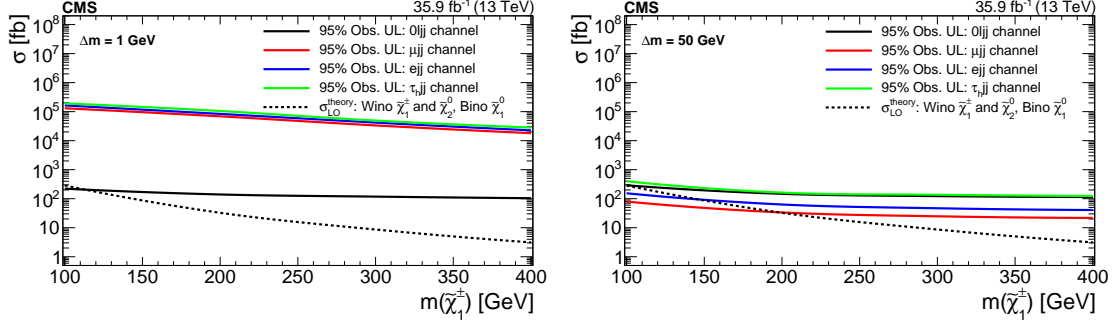


Figure 12.3: Observed 95% CL UL on the cross section as a function of $m(\tilde{\chi}_1^\pm)$. The results correspond to $\Delta m = 1$ GeV (left) and $\Delta m = 50$ GeV (right) for the wino-bino model with democratic light slepton decays [171].

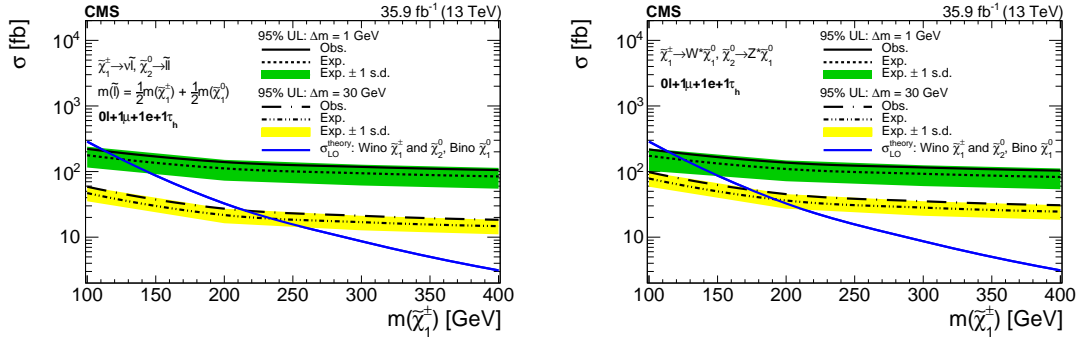


Figure 12.4: Expected and observed 95% CL UL on the cross section as a function of $m(\tilde{\chi}_1^\pm) = m(\tilde{\chi}_2^0)$, for the $\Delta m = 1$ GeV and 30 GeV hypotheses. The wino-bino model with democratic light slepton decays (left) and for the virtual W/Z decays (right) were considered [171].

of the four channels results in an observed (expected) exclusion of the $\tilde{\chi}_2^0$ and $\tilde{\chi}_1^\pm$ gaugino masses below $\{112, 159, 215, 207\}$ ($\{125, 171, 235, 228\}$) GeV. In the virtual W/Z model, for the same set of Δm assumptions, the observed (expected) exclusion limits rule out $\tilde{\chi}_2^0$ and $\tilde{\chi}_1^\pm$ gaugino masses below $\{112, 146, 175, 162\}$ ($\{125, 160, 194, 178\}$) GeV. As an example, Fig. 12.4 shows the expected and observed 95% CL UL on the cross section for the democratic light slepton decays (left) and for the virtual W/Z decays (right), as a function of $m(\tilde{\chi}_1^\pm)$, for two benchmark Δm assumptions, $\Delta m = 1$ and 30 GeV.

Figure 12.5 shows a two dimensional map for the expected and observed 95% CL ULs as functions of $m(\tilde{\chi}_1^\pm)$ and Δm for both physics interpretations. In the $1 < \Delta m < 10$ GeV region, the exclusion limits are quantitatively similar regardless of the physics interpretation (i.e., assuming the existence of a light slepton or not). The decay channel that drives the signal sensitivity in this case is the invisible channel, and the shape and normalization of the leading $m(jj)$ for both signal scenarios result in comparable shapes and normalization. However, as the Δm increases, the channels that provide the most sensitivity are the $\ell+jj$ channels, and in this case, the difference in branching ratios for leptonic final states in each interpretation (Chapter 4) will result in a larger sensitivity to the democratic light slepton decays model compared to the virtual W/Z decays hypothesis.

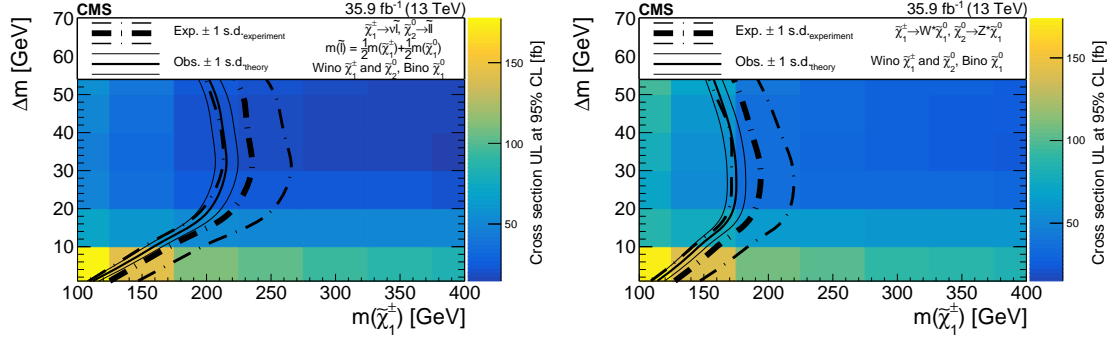


Figure 12.5: Expected and observed 95% CL UL on the cross section as a function of $m(\tilde{\chi}_1^\pm) = m(\tilde{\chi}_2^0)$ and Δm . The wino-bino model with democratic light slepton decays (left) and virtual W/Z decays (right) were considered [171].

In summary, this analysis provides the most stringent bounds on the $\tilde{\chi}_2^0$ and $\tilde{\chi}_1^\pm$ to date for the democratic light slepton model in the $1 < \Delta m < 30$ GeV region, and for the virtual W/Z model in the regions of $1 < \Delta m < 3$ GeV and $25 < \Delta m < 50$ GeV, surpassing the limits imposed by the LEP experiment results [172, 173, 174, 175]. Figure 12.6 shows a comparison of the expected and observed limits for various SUSY searches including LHC and LEP results, which provide a visual to the previous statement.

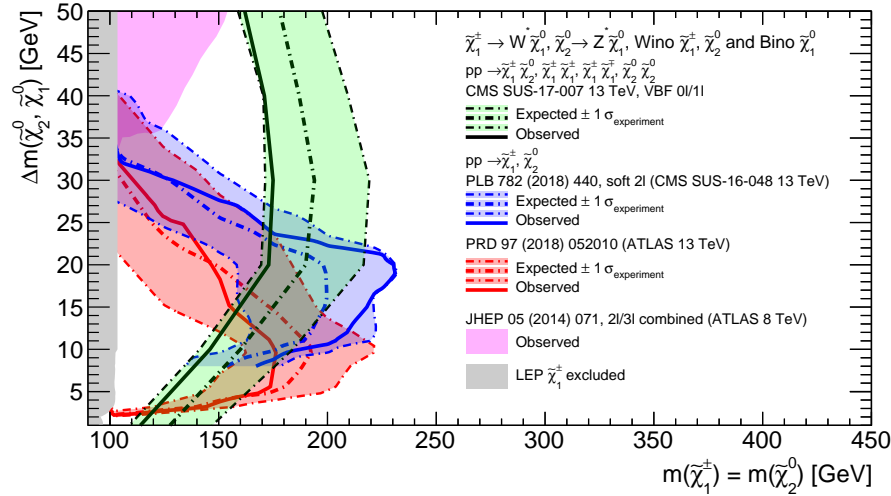


Figure 12.6: Exclusion limits for $\tilde{\chi}_i \tilde{\chi}_j$ searches at the LHC as a function of $m(\tilde{\chi}_2^0)$ and Δm . Results obtained with $(L)_{int} = 35.9 \text{ fb}^{-1}$ in the VBF SUSY analysis by CMS correspond to the green contour.

CHAPTER 13

Projection of interpretations with $\mathcal{L}_{int} = 137 \text{ fb}^{-1}$

13.1 Prediction in the signal region

In this chapter, the results for the current analysis including the full Run II data set are presented. The scope of this data analysis is broad in terms of the number of final states considered, as well as the number of physics interpretations included. In this document, I will primarily focus on the results for the final states with two leptons, where at least one of them is a hadronically decaying τ . The scenarios used for interpretation are the SUSY wino-bino model with (a) $\tilde{\tau}$ dominated decays and (b) W^*/Z^* decays.

Figures 13.1, 13.2 and 13.3 include the distributions for the leading $m(\text{jj})$ in the $e\tau_h+\text{jj}$, $\mu\tau_h+\text{jj}$ and $\tau_h\tau_h+\text{jj}$ signal regions. The prediction for the backgrounds are displayed by the filled histograms, and the distributions for four benchmark signal points in the wino-bino interpretation with $\tilde{\tau}$ -dominated decays are shown. The signal distributions are normalized to a dummy cross section of $0.1 \text{ pb} = 100 \text{ fb}$, and superimposed in the stacked histogram.

The expected 95% confidence level (CL) upper limits on the cross section as a function of the $m(\tilde{\chi}_2^0)$ mass are shown in Fig. 13.4 for each one of these channels considering the integrated luminosity of the full Run II data set, as well as the combination of the $\ell\tau_h$ channels together. As expected, the channel that drives the sensitivity in this case corresponds to the $\tau_h\tau_h$ final states. When looking at the rest of the decay channels, only the single τ_h channel shows slightly higher sensitivity than the $\tau_h\tau_h$ channel.

The combination of results from all decay channels can be found in Fig. 13.5. Compared to the results from one of the recent searches for electroweakino production in the compressed spectra, using boosted jet topologies from initial state radiation (ISR+ $\tilde{\tau}$) [176], the reach of the VBF SUSY analysis expected limits is expanded from 285 GeV to 300 GeV.

For the interpretation in the W^*/Z^* decay scenarios, the combination of the expected results in the all the signal regions is presented on Fig. 13.6 for two benchmark Δm values. Comparing to the most recent searches performed by the ATLAS collaboration on compressed SUSY via VBF processes and the total integrated luminosity from the LHC Run II [177], as well as a search for compressed SUSY with soft light lepton final states in boosted jet topologies by the CMS collaboration [128], the sensitivity obtained in the present analysis is better for these particular Δm signal points. In the case of the ATLAS search, the expected limits are able to exclude $\tilde{\chi}_2^0$ masses of 225 GeV and 160 GeV for $\Delta m = 5$ and 30 GeV, respectively. In the case of the soft light lepton search at CMS, the expected limits are 205 GeV and 260 GeV. In our analysis, the exclusion values for $\tilde{\chi}_2^0$ masses are 295 GeV and 260 GeV for $\Delta m = 5$ and 30 GeV, respectively.

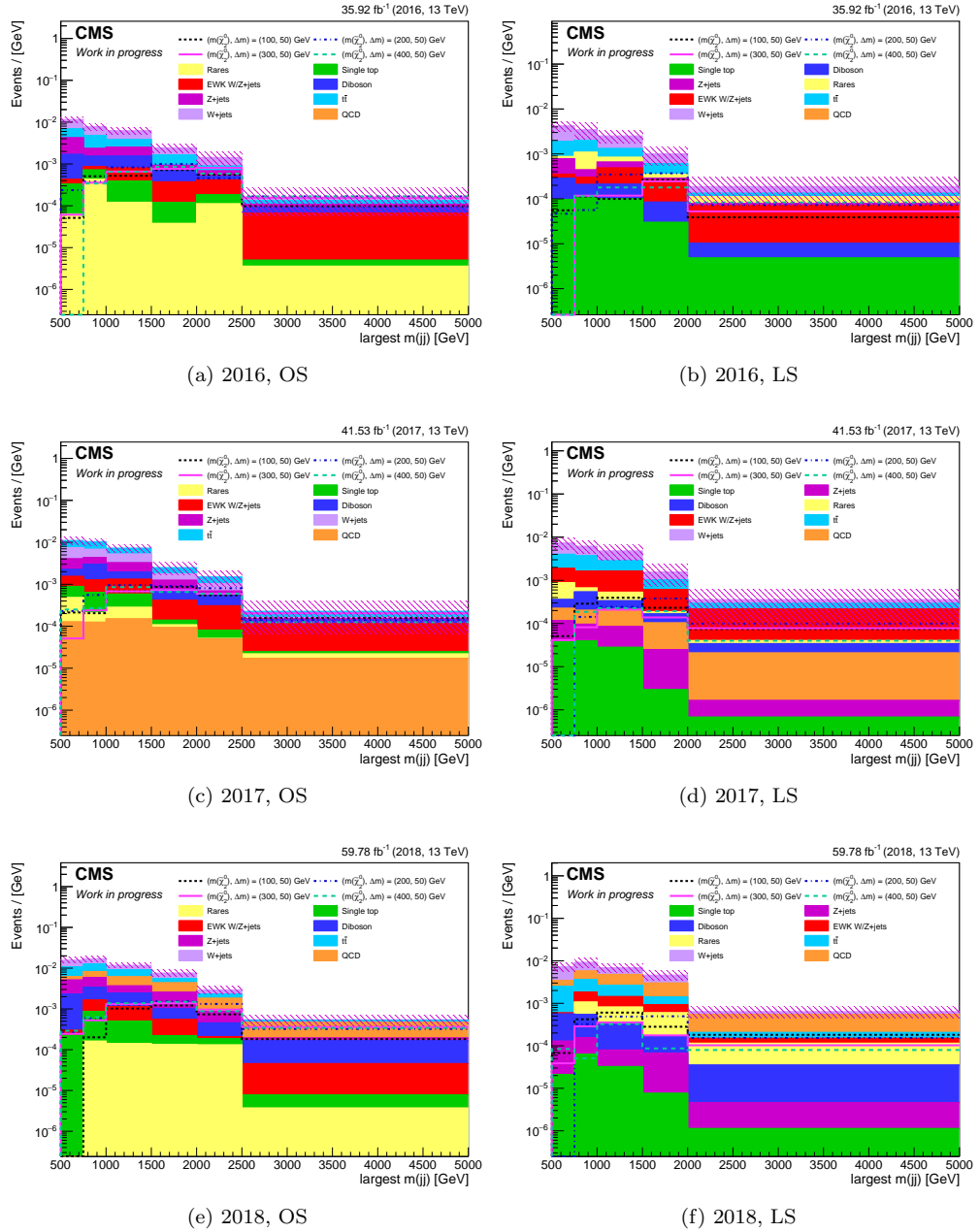


Figure 13.1: Leading $m(jj)$ distributions in the $e\tau_h+jj$ signal regions for the different subsets of the Run II data.

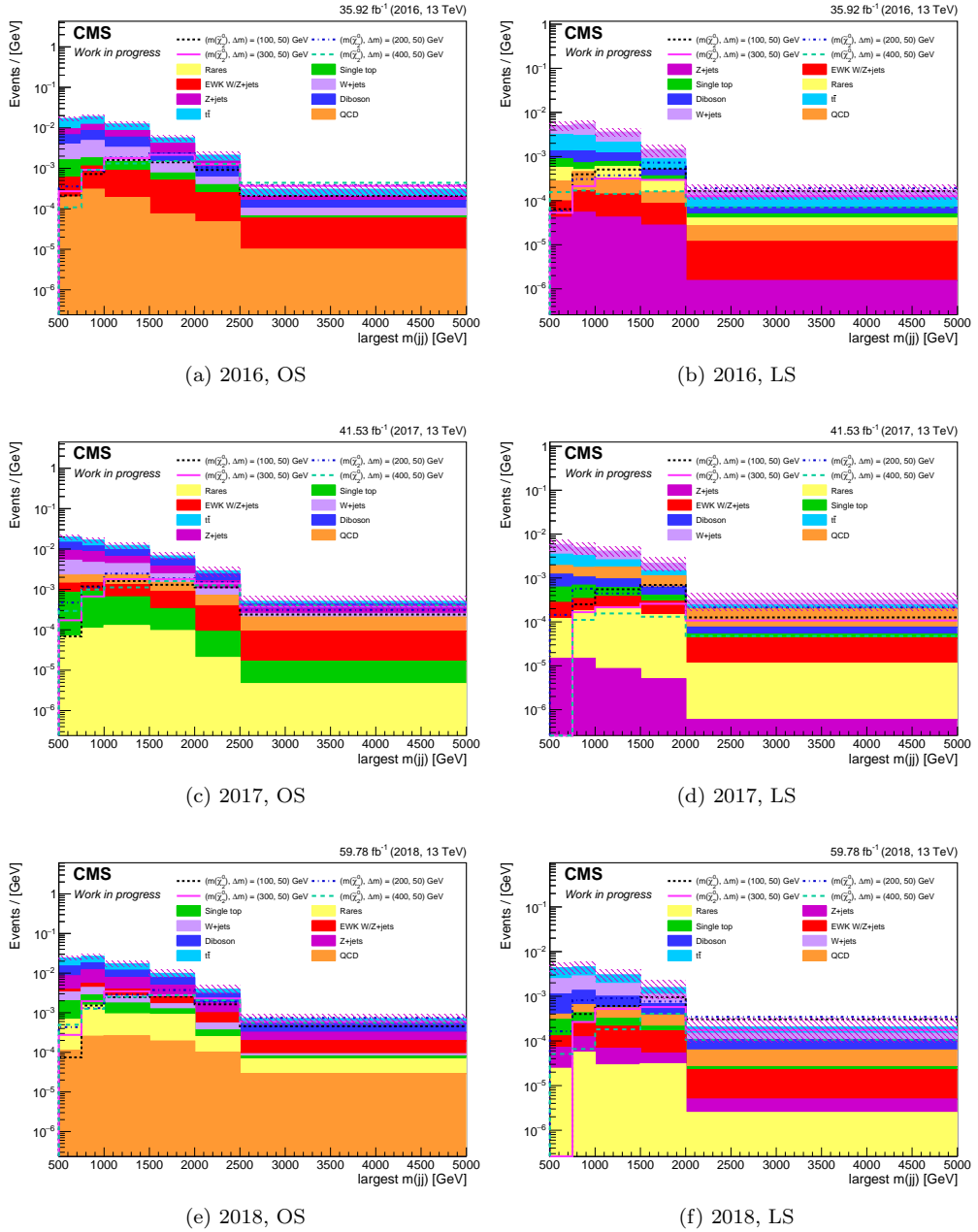


Figure 13.2: Leading $m(jj)$ distributions in the $\mu\tau_h+jj$ signal regions for the different subsets of the Run II.

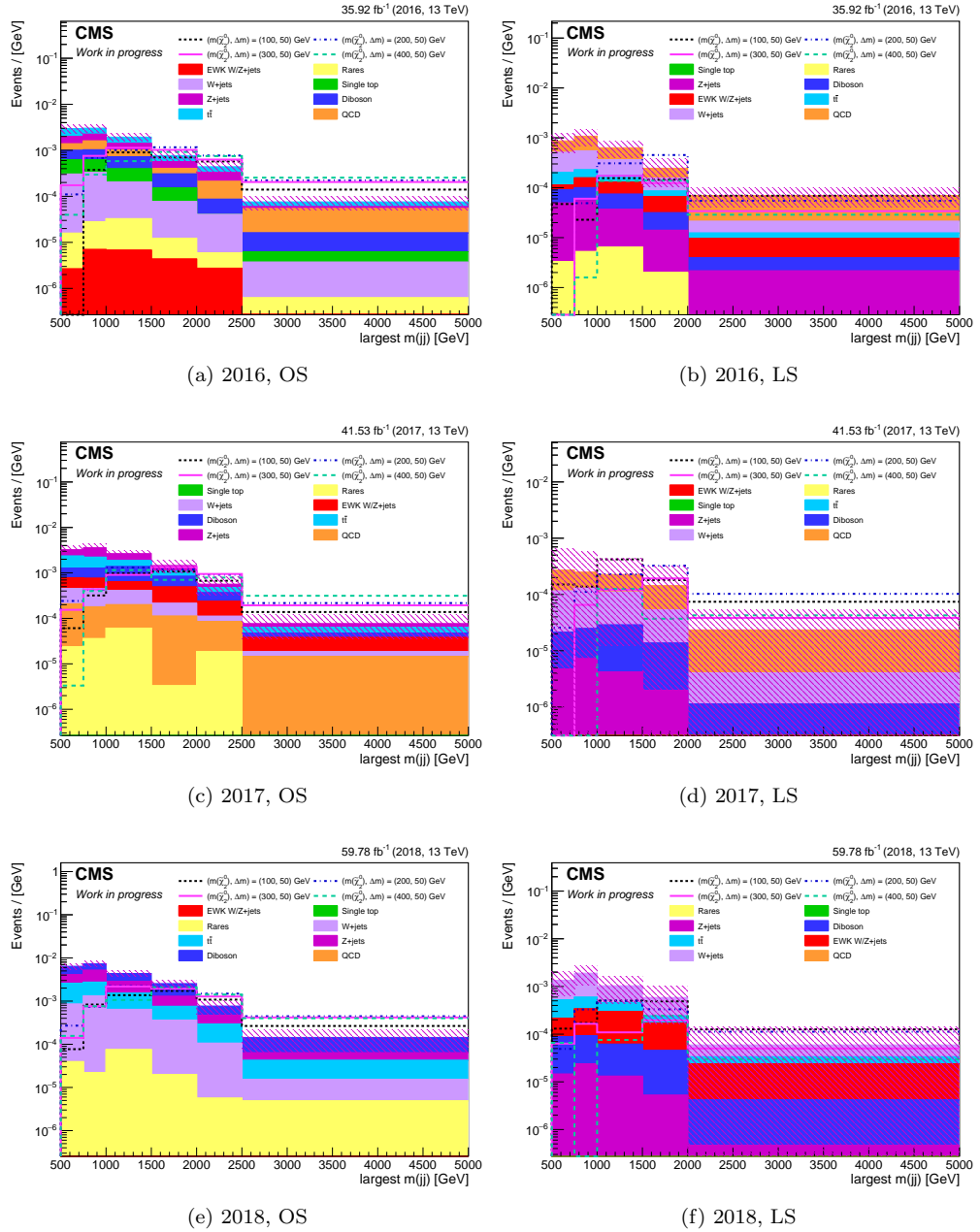


Figure 13.3: Leading $m(jj)$ distributions in the $\tau_h\tau_h+jj$ signal regions for the different subsets of the Run II data.

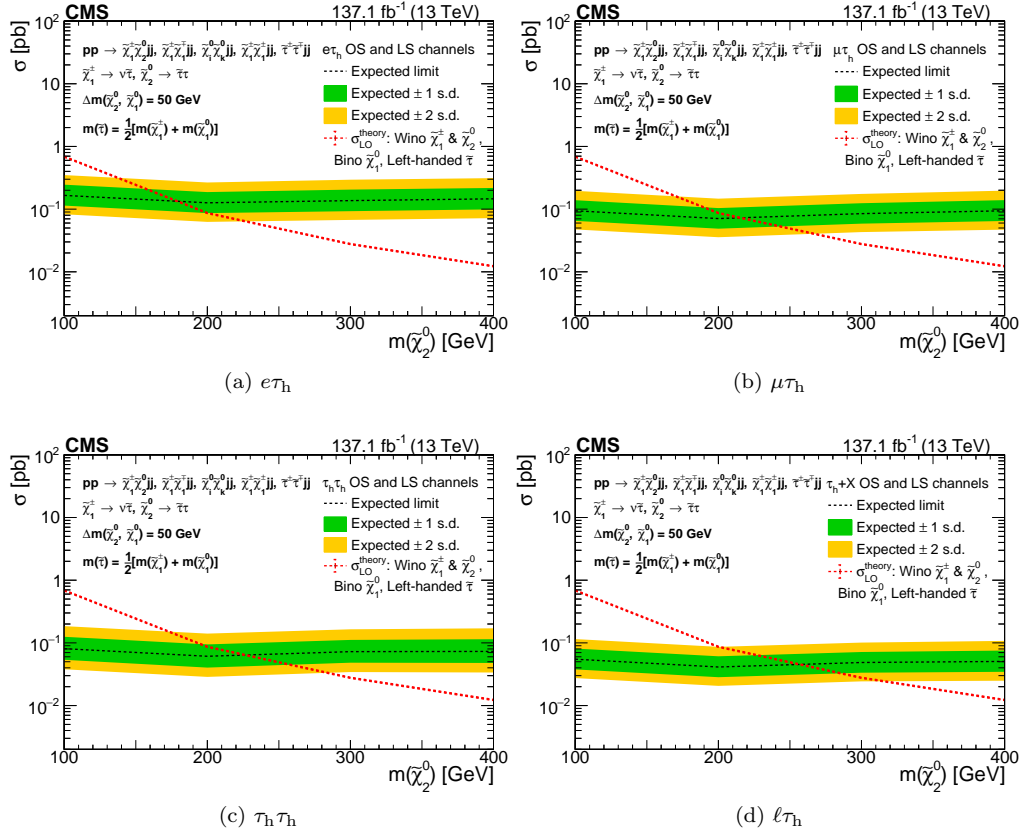


Figure 13.4: Expected 95% CL upper limits on the cross section as a function of $m(\tilde{\chi}_2^0) = m(\tilde{\chi}_1^\pm)$, for the $\tilde{\tau}$ -dominated decays hypothesis with $\Delta m = 50$ GeV. The expected ULs for the OS+LS combination of the $e\tau_h+jj$, $\mu\tau_h+jj$ and $\tau_h\tau_h+jj$ channels is shown separately, as well as the full combination of the $l\tau_h+jj$ channels.

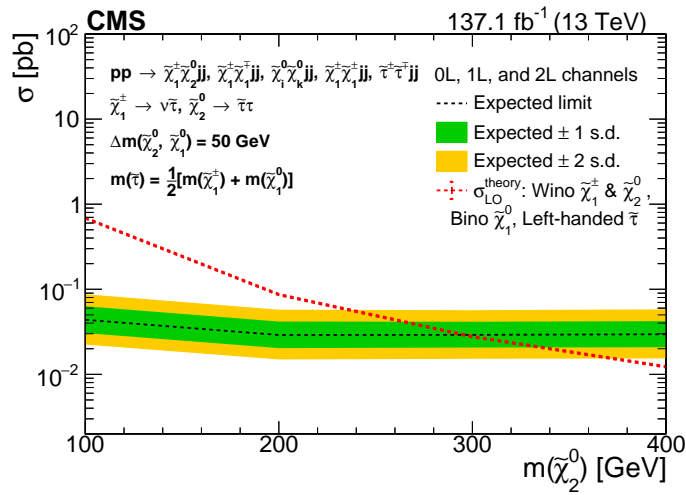


Figure 13.5: Expected 95% CL upper limits on the cross section for the combination of all decay channels considered in the analysis, displayed as a function of $m(\tilde{\chi}_2^0) = m(\tilde{\chi}_1^\pm)$, for the $\tilde{\tau}$ -dominated decays hypothesis with $\Delta m = 50$ GeV.

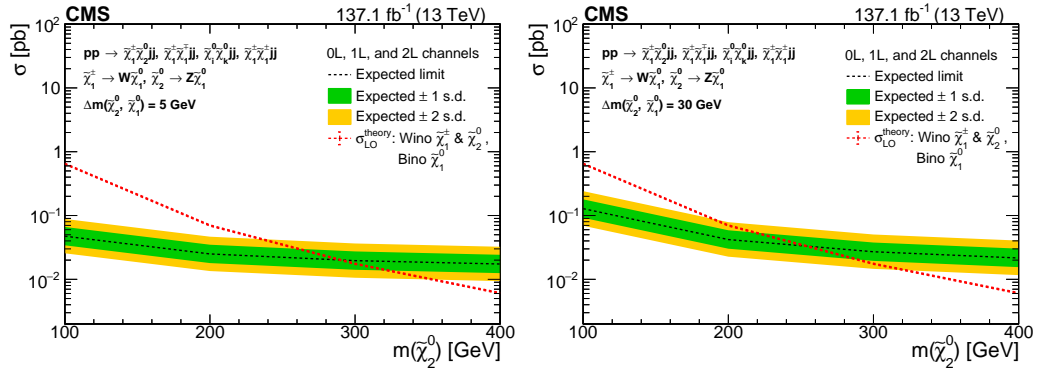


Figure 13.6: Expected 95% CL upper limits on the cross section for the combination of all decay channels considered in the analysis. They are displayed as a function of $m(\tilde{\chi}_2^0) = m(\tilde{\chi}_1^\pm)$, for the W^*/Z^* decays hypotheses with (left) $\Delta m = 5$ GeV, and (right) $\Delta m = 30$ GeV.

CHAPTER 14

Conclusions and future work

A search for dark matter motivated by supersymmetry (SUSY) in the compressed mass spectra region has been performed with $\mathcal{L}_{\text{int}} = 35.9 \text{ fb}^{-1}$ of proton-proton collision data at $\sqrt{s} = 13 \text{ TeV}$, recorded by the CMS detector at the LHC [171]. The final states considered in the analysis include two energetic jets with a large separation in rapidity and opposite hemispheres of the detector, large missing transverse momentum, and either one ($1\ell jj$) or zero ($0\ell jj$) low momentum leptons in the final state. The kinematics of the dijet pair are consistent with the topologies expected in electroweak vector boson fusion processes. This is the first search for compressed electroweak supersymmetry sector in these final states. The observed leading $m(jj)$ and $m_T(\ell, p_T^{\text{miss}})$ distributions are consistent with the SM predictions, therefore, not revealing evidence for new physics.

The results are interpreted with a simplified R-parity conserving MSSM model, where the second mass generation electroweakinos, namely $\tilde{\chi}_2^0$ and $\tilde{\chi}_1^\pm$ are 100% wino and the lightest neutralino, $\tilde{\chi}_1^0$ is 100% bino. Two scenarios with different branching fractions for the $\tilde{\chi}_2^0$ and $\tilde{\chi}_1^\pm$ are considered. In the first one, the electroweakinos always decay through light sleptons $\tilde{\ell}$. The $m(\tilde{\chi}_1^\pm) = m(\tilde{\chi}_2^0)$ values excluded is in this case for the $\Delta m = m(\tilde{\chi}_2^0) - m(\tilde{\chi}_1^0) = 1 (30) \text{ GeV}$ hypothesis corresponds to 112 (215) GeV at 95% CL.

In the second physics interpretation, the sleptons are considered to be too heavy and the electroweakinos decay via virtual W and Z bosons, and masses are excluded up to 112 (175) GeV for the same Δm hypothesis. At the time of publication, this work placed the most stringent limits on compressed supersymmetry in the very compressed regions of $1 \leq \Delta m \leq 30 \text{ GeV}$ in the light slepton interpretation and $1 \leq \Delta m \leq 3 \text{ GeV}$ and $25 \leq \Delta m \leq 50 \text{ GeV}$ ranges in the W^*/Z^* interpretation.

The present work presents some of the the most powerful results on supersymmetric dark matter searches up to date. It also confirms the novel and valuable potential of using electroweak vector boson fusion (VBF) as a technique for new physics searches, regardless of the several challenges faced when looking for these kind of processes at hadron colliders like the LHC. Therefore, it has been possible to probe SUSY parameter space regions that were historically thought to be inaccessible at the LHC. This is a testament to the great capabilities of the CMS detector, and the value of using creative ways to exploit the underlying potential of our experimental devices and our understanding of nature.

These results from this analysis were expanded to use the total integrated luminosity of the Run II, which corresponds to $\mathcal{L}_{\text{int}} = 137.1 \text{ fb}^{-1}$. One more set of decay channels was added, where two soft leptons are present in the final states ($2\ell+jj$), and all the lepton flavor combinations are included. In addition, more models for the interpretation of the results were considered. Among these physics interpretations are two simplified R-parity conserving MSSM models: in one of them, the composition of the electroweakinos is the same as for the results with 2016 data, except that they always decay via light tau sleptons $\tilde{\tau}$ ($\tilde{\tau}$ -dominated). The second one, considers all first and second mass generation electroweakinos to be fully higgsino. This interpretation has significant relevance for cosmological models in which the early Universe underwent a non-thermal evolution. Also, a

non-SUSY interpretation is considered, and corresponds to a effective field theory describing anapole dark matter.

In this document, a particular emphasis was placed to the $2\ell+jj$ final states that contained at least one hadronically decaying τ lepton, τ_h . The predicted results and expected 95% CL upper limits on the cross section are obtained for the $\tilde{\tau}$ -dominated physics interpretation. These channels are particularly sensitive to this scenario, given that theoretically, all events contain τ leptons in the final state and the hadronic decays of the τ lepton have the largest branching fraction compared to the leptonic τ decays. These results are also obtained for the W^*/Z^* scenario.

Several improvements were done to the analysis strategy for this analysis including the use of an upgraded tracking system in the 2017-2018 data taking periods, more efficient τ_h identification algorithms, more optimal VBF selections as well as a single fit variable in the signal region, which proved to yield increased signal sensitivity. The projections indicate that the results will complement and surpass other results that have been already published with the same integrated luminosities in searches performed by the ATLAS and CMS collaborations [177, 128]. This reaffirms the novelty and impact of the present research project, not only for particle physics, but also for cosmology. In case of a discovery, the experimental observables obtained in this analysis will make it possible to test if $\tilde{\chi}_1^0$ is the DM particle, through the calculation of its relic density $\Omega_{\tilde{\chi}_1^0} h^2$.

At the time of the completion of this document, the unblinding of data in the signal regions for the second iteration of the VBF SUSY analysis is in progress, as well as the interpretation of the results with all the contemplated physics models. Like any search for new physics, the tremendous effort and amount of work that was invested in this project was done with the hope of finally find evidence for new physics that could point to the existence of SUSY. The publication of the extended work will be done in the near future.

Appendix A

Jets

In this work an extensive review of the central physics contents behind the understanding of jet production in hadron-hadron high energy collisions is presented. Nowadays, a collision event is thought to be developed in several steps which are organized in such a way it is possible to simulate them using numerical approaches. These stages are: hard sub-process, parton shower, underlying event and multiple interactions, hadronization and the decay of unstable final state particles, excluding the latter in this presentation. A great emphasis is put on the basic theoretical aspects of QCD, which are important to understand part of the language used in the experimental analysis, related to the characteristics of Monte Carlo (MC) event generators and jet reconstruction algorithms. In addition, a brief discussion on jet fragmentation functions is included. The major motivation for this paper was to compile a solid basis of knowledge that could provide better insight and appreciation of the language and tools utilized in the study of jets, not only in hadron-hadron systems but also in nucleus-nucleus collision. As the results extracted from hadron-hadron events are the benchmark for the investigation of the phenomena observed in heavy-ion collisions, this knowledge becomes essential.

A.1 Introduction

In high energy collisions, jets are the experimental signatures of quarks and gluons. They abound in events containing high momentum transfer between the interacting particles. We can think of a jet to first approximation as a hard parton that has radiated soft gluons to its primary direction that later went to a low energy process that converted those partons in a spray of colorless particles (hadronization) that are experimentally detected as a large and localized deposition of energy in the detector. Since jets are not a fundamental object defined in the theory, we need a jet definition that will constitute the basis for jet reconstruction algorithms.

There are several reasons to study jet production in high energy collisions. Broadly speaking, the analysis of jet properties in high energy hadron-hadron collisions can provide an understanding of the complexity of strong interactions and theories beyond the Standard Model. Recently, new analysis techniques able to explore the inner structure of jets and areas surrounding hadron showers. Moreover, they can also study the off-jet directions in nucleon-nucleon and jet-matter interactions in nucleus-nucleus collisions, which are connected to the research of quark-gluon plasma (QGP), which requires a well-defined separation of the hard and soft components of the reactions [178].

Specifically, in proton-proton collisions, they are commonly used as an element of the final states of processes that involves new physics and as a tool to further test quantum chromodynamics (QCD) and the standard model of particle physics (SM). On the other hand, in heavy-ion collisions, jets are an excellent internal probe that is suitable to test the short-lived quark-gluon plasma (QGP), sensitive to QCD and that can help to determine some of the characteristics of QGP, specifically the

transport coefficients. In addition, they can help us to understand better the behavior of the strong interaction in the non-perturbative regime due to the energy range at which the QGP evolves.

The general picture of the structure of proton-proton, proton-nucleus and nucleus-nucleus collisions are very similar. The main difference is that the collisions in which we have a nucleus, the jet production is embedded in a medium of additional quarks and gluons. This difference leads to phenomena occurring at different energy regimes. We define an *event* in hadron-hadron collisions as a process that involves a hard interaction, which means it is a process in which heavy or energetic particles are created or it occurs a large momentum transfer. In Monte Carlo event generators, these kind of processes are simulated in several stages:

- primary hard sub-process,
- parton showers associated with the incoming and outgoing particles carrying color charge,
- process of hadronization,
- secondary interactions that give rise to the underlying event,
- decays of unstable particles that are detected.

The intention of this paper is to do a literature review that includes the principal physics arguments behind each of these steps in the picture of the hadron-hadron collision evolution, as the conclusions obtained in these systems are used as reference tool for the study of heavy-ion collisions. The physics concepts of the collision evolution are studied up to the stage of hadronization, leaving out of the review of the particle decays. A good portion of the material presented consists on information gathered from several sources using references [28, 179] as the guidelines of the structure of the paper.

A.2 Hard scattering processes

We define a hard sub-process as the one that involves a large momentum transfer and creates heavy and/or energetic objects. The total hadronic cross section for these reactions can be described using a perturbative approach, meaning that we can use Feynman diagrams. Even though the formation of final-state hadrons is non-perturbative, the fact that the total (*inclusive*) hadronic cross section can be described in a perturbative approach can be seen considering the process $e^+e^- \rightarrow q\bar{q}$; these results can be generalized to reactions where there are two hadrons in the initial state.

The electron and positron annihilate into a photon or Z boson of *virtuality* Q equal to the collision energy \sqrt{s} , which fluctuates into a quark and an anti-quark. By the uncertainty principle, the fluctuation occurs on a distance scale of order $1/Q$, and if Q is large, the production rate for this short-distance process should be predicted by perturbation theory. Hadronization occurs at a much later time characterized by $1/\Lambda$, where Λ is the scale at which the coupling becomes strong [180]. Although the interactions that change quarks and gluons into hadrons modify the outgoing state, they occur too late to modify the original probability for the event to happen; hence, the total hadronic cross section can be calculated applying perturbation theory [180, 28].

The total inclusive hadronic cross section in collinear factorization can be calculated as follows:

$$\sigma = \sum_{a,b} \int_0^1 dx_a dx_b \int f_a^{h_1}(x_a, \mu_F) f_b^{h_2}(x_b, \mu_F) \times \quad (\text{A.1})$$

$$\times d\hat{\sigma}_{ab \rightarrow n}(\mu_F, \mu_R)$$

where $f_i^{h_j}$, $i = a, b$, $j = 1, 2$ are the parton distribution functions (PDFs) which describe the probability density that a parton i carries a fraction x of the parent hadron's h_j longitudinal momentum and the factorization scale μ_F , and $\hat{\sigma}_{ab \rightarrow n}$ is the parton-level cross section for the production of the final state n through the initial partons a and b :

$$d\hat{\sigma}_{ab \rightarrow n} = d\Phi_n \frac{1}{2s} |\mathcal{M}_{ab \rightarrow n}(d\Phi_n, \mu_F, \mu_R)|^2. \quad (\text{A.2})$$

$\hat{\sigma}_{ab \rightarrow n}$, calculated at parton level, is given by the product of the unpolarized matrix element squared $|\mathcal{M}_{ab \rightarrow n}|^2$, averaged over the initial-state spin states and color degrees of freedom, the parton flux $\frac{1}{2s} = \frac{1}{2x_a x_b s}$, where s is the hadronic center of mass energy squared and $d\Phi_n$ that corresponds to the differential phase space element over the n final-state particles:

$$d\Phi_n = \prod_{i=1}^n \frac{d^3 p_i}{(2\pi)^3 2E_i} \cdot (2\pi)^4 \delta^{(4)} \left(p_a + p_b - \sum_{i=1}^n p_i \right). \quad (\text{A.3})$$

This parton level cross section will additionally depend on two arbitrary parameters, the *renormalization scale* μ_R and the *factorization scale* μ_F .

Renormalization and collinear factorization

In QCD, the value of the strong coupling α_s is not constant; it depends on the energy scale of the interaction considered. Predictions for observables are expressed in terms of $\alpha_s(\mu_R^2)$ as a function of a renormalization scale μ_R . When μ_R is taken close to the scale of the momentum transfer Q in a given process, then $\alpha_s(\mu_R^2 \simeq Q^2)$ indicates the effective strength of the strong interaction in that process [28].

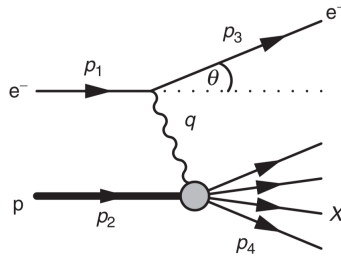


Figure A.1: Electron-proton inelastic scattering [181].

To describe the factorization scale μ_F , we will consider the electron-proton deep inelastic scattering (DIS) $ep \rightarrow eX$. The most general Lorentz invariant and parity conserving expression for the

$ep \rightarrow eX$ inelastic scattering cross section, mediated by the exchange of a single virtual photon, is [181]

$$\frac{d^2\sigma}{dx dQ^2} \approx \frac{4\pi\alpha_{em}^2}{Q^4} \left[(1-y) \frac{F_2(x, Q^2)}{x} + y^2 F_1(x, Q^2) \right] \quad (\text{A.4})$$

Here, x is a Lorentz-invariant dimensionless quantity defined as

$$x \equiv \frac{Q^2}{2p_2 \cdot q},$$

known as ‘‘Bjorken x ’’, p_2 is the initial 4-momentum of the proton, q is the transferred momentum of the electron to the proton and $Q^2 = -q^2$. This variable expresses the ‘‘elasticity’’ of the scattering process ($0 \leq x \leq 1$). The ‘‘inelasticity’’ y is defined as

$$y \equiv \frac{p_2 \cdot q}{p_2 \cdot p_1},$$

with p_1 the initial 4-momentum of the electron. Similar to x , we have $0 \leq y \leq 1$. The functions $F_1(x, Q^2)$ and $F_2(x, Q^2)$ are the *structure functions* of the proton; the origin of $F_1(x, Q^2)$ can be identified as purely magnetic [181].

In the quark-parton model, the basic interaction in electron-proton DIS is the *elastic* scattering from a spin-half quark within the proton $eq \rightarrow eq$. The kinematic variables for the underlying electron-*quark* process can be related to those for the electron-*proton* collision [181]. To zero order in α_s (no QCD vertices), the structure functions directly related to the parton distribution functions (PDFs) $f_i(x, Q^2)$ [28, 182],

$$F_2(x) \rightarrow \sum_i e_i^2 x f_i(x) \quad (\text{A.5})$$

$$F_1(x) \rightarrow \frac{1}{2x} F_2(x) \quad (\text{A.6})$$

In the quark-parton model, x is interpreted as the momentum fraction of the parton inside the proton. In the expressions above, the PDFs are independent of the scale Q , because we are assuming in this model that the photon interacts with point-like ‘‘free’’ quarks. Therefore, $F_{1,2}$ are also independent of Q and satisfy Bjorken scaling.

However, in perturbation theory there are higher order QCD corrections to the QED $eq \rightarrow eq$ process. As Q^2 increases, these corrections start to be important, in particular gluon emission. When calculating the gluon emission cross section (see e.g., [182, 183]), we can see the origin of the factorization scale and the *Altarelli-Parisi splitting functions*, which will be useful in our discussion of parton showering.

In general, including the corrections to all orders of perturbation theory, the structure function (Eq. A.9) becomes [28],

$$F_2(x, Q^2) = x \sum_{n=0}^{\infty} \frac{\alpha_s^n(\mu_R^2)}{(2\pi)^2} \times \sum_{i=q,g} \int_x^1 \frac{dx'}{x'} C_{2,i}^{(n)}(x', Q^2, \mu_F^2, \mu_R^2) f_i\left(\frac{x}{x'}, \mu_F^2\right) + \mathcal{O}\left(\frac{\Lambda^2}{Q^2}\right) \quad (\text{A.7})$$

where $C_{2,i}^{(n)}$ are coefficients that can be calculated using Feynman diagrams. Notice that the parton that comes from the proton can emit a gluon before it interacts with the photon. Then, $C_{2,i}^{(n)}$ depend on the ratio of the parton's momentum before and after the emission, denoted by x' , and we need to integrate over that ratio [28].

The majority of the gluon emissions that modify a parton's momentum are *collinear* (parallel) to that parton and do not depend on the fact that the parton will interact with a photon and these emissions are thought to modify the proton structure rather than being part of the coefficient function for the parton's interaction with the photon. The *collinear factorization* procedure gives a well-defined meaning to this distinction [28]. In the modified minimal subtraction ($\overline{\text{MS}}$) factorization scheme [184], this procedure involves the choice of an arbitrary scale μ_F , which can be interpreted as a resolution parameter: if the transverse momenta of the emissions is greater than μ_F , they are accounted in the coefficients $C_{2,i}^{(n)}$; otherwise, they are included within the PDFs, $f_i(x, \mu_F^2)$. Once we know what the PDFs are at certain factorization scale, its evolution with μ_F can be predicted by the Dokshitzer-Gribov-Lipatov-Altarelli-Parisi (DGLAP) equations [28]:

$$\mu_F^2 \frac{\partial f_i(x, \mu_F^2)}{\partial \mu_F^2} = \sum_j \frac{\alpha_s(\mu_F^2)}{2\pi} \int_x^1 \frac{dx'}{x'} P_{i \leftarrow j}(x') f_j\left(\frac{x}{x'}, \mu_F^2\right). \quad (\text{A.8})$$

where if, for instance, $i = q$ and $j = g$, then $P_{q \leftarrow g} = P_{g \rightarrow qq}$.

To illustrate what these means, let us consider the first order correction to the proton structure. Each parton distribution receives a correction of the form ($\mu_F^2 = Q^2$):

$$\frac{1}{x} F_2(x, Q^2) = \sum_i e_q^2 [f_i(x) + \Delta f_i(x, Q^2)]. \quad (\text{A.9})$$

For a quark, the correction due to a quark splitting into a quark and a gluon is given by,

$$\Delta f_i(x, Q^2) = \frac{\alpha_s}{2\pi} \ln\left(\frac{Q^2}{\mu_F^2}\right) \int_x^1 \frac{dx'}{x'} f_i(x') P_{q \rightarrow qg}\left(\frac{x}{x'}\right). \quad (\text{A.10})$$

The improved proton form factor no longer scales, since there is an explicit dependence on x and Q^2 . Physically, this means that valence quarks carrying large x are more likely to bremsstrahlung gluons; therefore, we have a depletion of quarks with large Q^2 and we are more likely to see gluons. On the other hand, sea quarks carrying small x are more easily resolved with larger Q^2 ; hence, there will be an enhancement of quarks with large Q^2 (Figure A.2). The evolution of $f(x, Q^2)$ with Q^2 is given by the DGLAP equations to first order as

$$\frac{d}{d \ln(Q^2)} [f_i(x, Q^2)] = \frac{\alpha_s}{2\pi} \int_x^1 \frac{dx'}{x'} [f_i(x, Q^2)] P_{q \rightarrow qg}\left(\frac{x}{x'}\right) \quad (\text{A.11})$$

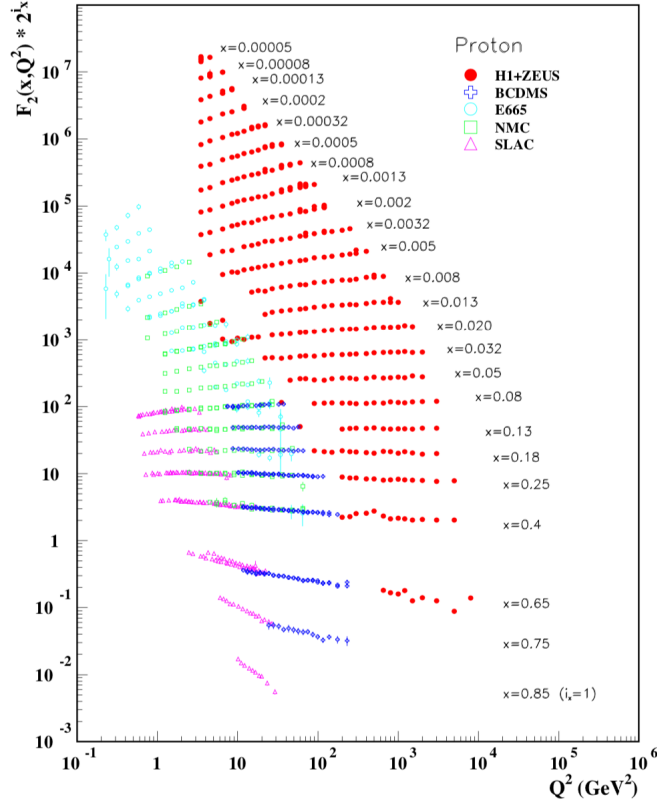


Figure A.2: The proton structure function F_2^p measured by different experiments [28].

The factorization and renormalization scales play similar roles at opposite ends of the energy range, the infrared (IR) and ultraviolet (UV), respectively. In addition, neither scale parameter is physical nor intrinsic to QCD. The physics does not depend on them, they tell us where did we choose to subtract the divergences coming from higher order corrections. These singularities are not physical either; what they indicate is the breakdown of the perturbative approach [180]. The range of values that these parameters can take are limited by the logarithmic structure of QCD. Typically, for $2 \rightarrow 1$ and $2 \rightarrow 2$ processes, $\mu_F = \mu_R = Q^2$. For instance, we can have the production of a resonance of mass M in the s -channel ($Q^2 = M^2$) or of a pair of massless particles with transverse momentum p_T ($Q^2 = p_T^2$). Another factor that needs to be taken into consideration is that Q^2 represents the starting scale for the subsequent initial- and final-state parton showers, so when the final-state consists of more than two particles μ_F and μ_R should be set such that we avoid introducing double counting between the matrix element calculation and the parton shower simulation [179].

We conclude this section by revisiting the form of the hard sub-process cross section (Eq. A.1). Since QCD can be *factorized*, *i.e.*, the confinement regime can be renormalized away from the perturbative regime, then we only need to consider the interacting partons participating in the hard scattering. The remaining “spectator” partons inside the proton are not resolved by the particle carrying the momentum transfer (the photon, in the case of DIS) between the interacting particles and, therefore, they do not contribute directly to the cross section. Although our discussion was based on electron-proton DIS, these conclusions apply to all processes where we have a hadron interacting in the initial state.

A.3 Parton showering

The perturbative cross section describes well the momenta of the jets originated in the hard sub-process but it does not provide further details on the jet internal structure which is necessary for jet reconstruction algorithms. Up to now, we ignored the low energy effects coming from the emission of gluons before and after the hard scattering applying the collinear factorization procedure. However, these higher order corrections play an important role in the characteristics of the observed final state. Therefore, we need an *exclusive* picture of the process, taking into account the effect of all higher order contributions, which can be simulated through a *parton shower algorithm* [179].

The parton shower represents an approximate perturbative treatment of multiple gluon bremsstrahlung that develop along the directions of the primary partons, resulting in an evolution in momentum transfer down from the high scales associated to the hard process to the low scales, greater than an infrared cutoff, typically taken to be of the order of ~ 1 GeV, associated with the confinement of the partons [179, 180].

Parton branching

In this section we will describe the physics behind the parton branching, based on the discussion in [180]. Let us consider a parton a that splits into two partons b and c , where parton a can be either an *incoming* or *outgoing* parton, as depicted in Figures A.3 and A.4, respectively. For the moment, we will consider all partons to be massless.

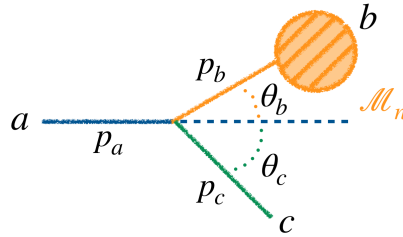


Figure A.3: Parton branching of an incoming parton, which corresponds to a space-like branching.

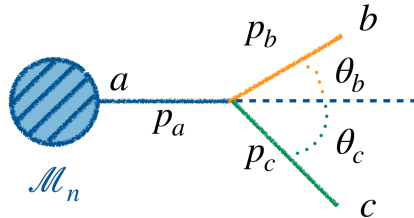


Figure A.4: Parton branching of an outgoing parton, which corresponds to a time-like branching.

Time-like parton branching.

This branching refers to the splitting of a parton which is coming out of the hard scattering, as shown in Figure A.4. Experimentally, it represents what is called *final state radiation* (FSR). Using the notations in the figure, we assume that

$$p_b^2, p_c^2 \ll p_a^2 \equiv t, \quad (\text{A.12})$$

where $t > 0$. We define the opening angle between partons b and c is $\theta = \theta_b + \theta_c$ and the energy fraction carried by the parton b as

$$z = \frac{E_b}{E_a} = 1 - \frac{E_c}{E_a}. \quad (\text{A.13})$$

We can calculate the energy scale of the parton splitting t applying 4-momentum conservation before and after the splitting, and we get that

$$t = 2E_a E_c (1 - \cos \theta), \quad (\text{A.14})$$

in terms of the energy fraction z and assuming that the *opening angle* θ is *small*,

$$t \approx z(1-z)E_a^2\theta^2. \quad (\text{A.15})$$

The probability amplitude or squared matrix element for the parton emission from the n -th parton produced in the hard scattering is proportional to the inverse of t times the probability amplitude of the hard scattering:

$$|\mathcal{M}_{n+1}|^2 \propto \frac{1}{t} |\mathcal{M}_n|^2 \approx \frac{1}{z(1-z)E_a^2\theta^2} |\mathcal{M}_n|^2 \quad (\text{A.16})$$

The expression above is enhanced in the two following scenarios:

1. when the energy fraction taken by parton b is very small ($z \rightarrow 0$), namely, it is emitted at almost zero momentum, or when b carries almost all the energy of the original parton ($z \rightarrow 1$) which is equivalent to say that the parton c is emitted with a small energy fraction,
2. when the opening angle between the b and c is close to zero, which is possible since we are working in the small angle approximation.

The first scenario corresponds to what is known as a *soft enhancement* or *infrared divergence* of the squared matrix element and the second one to the *collinear divergence*; physically, this implies that there is a large probability of emitting soft or collinear partons.

Space-like parton branching.

This situation consists on the branching of the incoming parton a into b and c , where b will later participate in the hard scattering (Figure A.3), and corresponds to the so-called *initial-state radiation*. Here, we can assume that

$$|p_a^2|, p_c^2 \ll |p_b^2| \equiv t \quad (\text{A.17})$$

Keeping the same definitions as before, the only change we need to make with respect to the time-like branching are the kinematics [180]. The value of t in the small angle approximation is given by

$$t \approx E_a E_c \theta_c^2 = (1-z) E_a^2 \theta_c^2. \quad (\text{A.18})$$

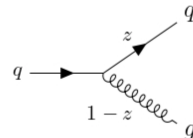
Splitting functions

The differential cross section of a time-like or space-like parton branching takes the following form [180]:

$$d\sigma_{n+1} = d\sigma_n \frac{dt}{t} \frac{\alpha_s}{2\pi} P_{ba}(z). \quad (\text{A.19})$$

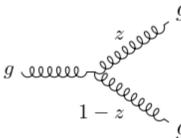
$d\sigma_{n+1}$ is proportional to the hard scattering differential cross section $d\sigma_n$, the inverse of the square of the original parton's 4-momentum (Eq. A.12), a factor of $\frac{\alpha_s}{2\pi}$ corresponding to the QCD vertex of the parton splitting and $P_{ba}(z)$ which is the probability of the parton a splitting into a second parton b carrying a momentum fraction z and a third parton of momentum fraction $1-z$; this factor is better known as the (Altarelli-Parisi) *splitting function*.

A fundamental property of the splitting functions is that they are *universal*, in other words, can be obtained considering a specific physical process, e.g., in electron-proton DIS, but once derived they are valid in any other physical process of our interest. The spin-averaged Altarelli-Parisi splitting functions [185] to leading order are shown in Figure A.5; it is worth to notice that the soft divergences only appear in the case of the emission of gluons.



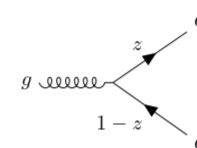
$$P_{q \rightarrow qg}(z) = \frac{4}{3} \left(\frac{1+z^2}{1-z} \right)$$

(a)



$$P_{g \rightarrow gg}(z) = 6 \frac{(1-z(1-z))^2}{z(1-z)}$$

(b)



$$P_{g \rightarrow q\bar{q}}(z) = \frac{1}{2} (z^2 + (1-z)^2)$$

(c)

Figure A.5: Spin-averaged Altarelli-Parisi splitting functions for (a) quark-gluon, (b) gluon-gluon and (c) quark-quark splittings. [182, 28].

Parton showering algorithm

In general, for any hard process that produces partons of any flavor i , the cross section for a hard configuration that has cross section σ_0 to be accompanied by the emission of a parton j with

momentum fraction z is given by

$$d\sigma \approx \sigma_0 \sum_{\text{partons}, i} \frac{\alpha_s}{2\pi} \frac{dt}{t} dz P_{ji}(z, \phi) d\phi \quad (\text{A.20})$$

where the splitting functions $P_{ji}(z, \phi)$ are flavor-dependent and through ϕ , the azimuth of j around the axis defined by i , spin-dependent as well. This expression constitutes the basic building block to write an iterative algorithm: we can use it on the hard process to generate one collinear splitting and then treating the final state of that splitting as a new hard process, generating an even more collinear splitting from it and so on [179].

However, we still need to know how to deal with the divergences. As we discussed in Section A.2, the analytic treatment of these divergences can be done by using an evolution equation for the PDFs. The DGLAP evolution equation (Eqs. A.8, A.11) has another physical interpretation: it can be thought as a master equation for the Markov process where any parton can emit another parton with a probability related to the splitting function. In this way, a QCD cascade develops and its dependence of the partonic densities on the energy scale t is easily understood [186]. In order to be able to know anything about the structure of the final states, a numerical approach based on the Monte Carlo technique is useful. For the moment, we assume there is only one type of branching. We introduce the function called the *Sudakov form factor* [180],

$$\Delta(t) \equiv \exp \left[- \int_{t_0}^t \frac{dt'}{t'} \int dz \frac{\alpha_s}{2\pi} \hat{P}(z) \right], \quad (\text{A.21})$$

with $\hat{P}(z)$ the unregularized (divergent) splitting functions. Then, the evolution equation for the parton density becomes

$$t \frac{\partial}{\partial t} f(x, t) = \int \frac{dz}{z} \frac{\alpha_s}{2\pi} \hat{P}(z) f\left(\frac{x}{z}, t\right) + \frac{f(x, t)}{\Delta(t)} t \frac{\partial}{\partial t} \Delta(t), \quad (\text{A.22})$$

hence,

$$t \frac{\partial}{\partial t} \left(\frac{f(x, t)}{\Delta} \right) = \frac{1}{\Delta} \int \frac{dz}{z} \frac{\alpha_s}{2\pi} \hat{P}(z) f\left(\frac{x}{z}, t\right). \quad (\text{A.23})$$

Integrating this equation to obtain an integral equation for $f(x, t)$ in terms of the initial parton distribution function $f(x, t_0)$:

$$f(x, t) = \Delta(t) f(x, t_0) + \int_{t_0}^t \frac{dt'}{t'} \frac{\Delta(t)}{\Delta(t')} \int \frac{dz}{z} \frac{\alpha_s}{2\pi} \hat{P}(z) f\left(\frac{x}{z}, t'\right) \quad (\text{A.24})$$

A simple interpretation for this equation can be derived using the (t, x) space paths in Figure A.6. The first term on the right-hand side is the contribution from paths that do not branch between scales t_0 and t . Therefore, the Sudakov form factor can be physically interpreted as the probability of evolution from t_0 to t without branching [180]. The second term is the contribution from all paths which have their last branching at scale t' . The factor $\frac{\Delta(t)}{\Delta(t')}$ represents the probability of evolving from t' to t without branching.

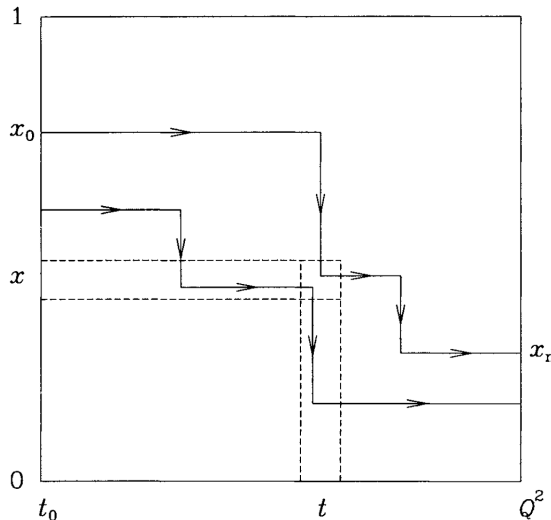


Figure A.6: Representation of a parton branching by paths in (t, x) -space. Each branching corresponds to a step downwards from a higher to a lower value of the momentum fraction x , at a value of t equal to the negative virtual mass-squared q^2 after the branching ($q^2 = -Q^2$) [180].

The generalization to several types of partons is as follows: each parton species i has its own form factor $\Delta_i(t)$. Since the probability branching has to be summed over all possible processes $i \rightarrow j$,

$$\Delta_i(t) \equiv \left[-\sum_j \int_{t_0}^t \frac{dt'}{t'} \int dz \frac{\alpha_s}{2\pi} \hat{P}_{ji}(z) \right], \quad (\text{A.25})$$

where $\hat{P}_{ji}(z)$ is the unregularized $i \rightarrow j$ splitting function. Then, the evolution equation is

$$t \frac{\partial}{\partial t} \left(\frac{f_i(x, t)}{\Delta_i} \right) = \frac{1}{\Delta_i} \sum_j \int \frac{dz}{z} \frac{\alpha_s}{2\pi} \hat{P}(z) f_j \left(\frac{x}{z}, t \right). \quad (\text{A.26})$$

To avoid the divergence of $\hat{P}(z)$ in the integral, we make use of the resolution criterion mentioned above. With this explicit infrared cutoff, $\epsilon(t) < z < 1 - \epsilon(t)$. Branchings with z above this range are classified as unresolvable, in other words, they involve the emission of an undetectable soft parton. Then, the Sudakov form factor gives the probability of evolving from t_0 to t without any *resolvable* branching [180].

The probability of resolvable branching gives the the sum of the virtual and unresolvable real gluon emissions, which we know are divergent. However, this probability can be obtained using the unitarity argument, which is the fact that the sum of the branching and non-branching probabilities must be unity, and thus, the sum of all contributions to the resolvable branching is finite. The definition the infrared cutoff $\epsilon(t)$ is arbitrary and depends on what we consider a resolvable emission [180]. For time-like branching a natural resolution limit is provided by the cutoff on the parton virtual mass squared $t > t_0$. In the frame in which all the parton energies are much larger than their

virtual masses, the transverse momentum is (Figure A.4),

$$p_T^2 = z(1-z)p_a^2 - (1-z)p_b^2 - zp_c^2 > 0. \quad (\text{A.27})$$

For $p_a^2 = t$ and $p_b^2, p_c^2 > t_0$ we require that

$$z(1-z) > \frac{t_0}{t} \quad \Rightarrow \quad z, 1-z > \epsilon(t) \approx \frac{t_0}{t}. \quad (\text{A.28})$$

For instance, with this cutoff, the Sudakov form factor of the quark becomes

$$\Delta_q(t) \simeq \exp \left[- \int_{2t_0}^t \frac{dt'}{t'} \int_{t_0/t'}^{1-t_0/t'} dz \frac{\alpha_s}{2\pi} \hat{P}_{qq}(z) \right] \quad (\text{A.29})$$

The choice of t_0 , although arbitrary, needs to be large enough to avoid introducing running coupling effects, in other words, to avoid the region where α_s becomes of the order of ~ 1 , in order to keep the perturbative treatment of the shower. This infrared cutoff is also valid for space-like branching.

It is important to mention that the DGLAP evolution equation was originally derived with the aid of the operator product expansion and the renormalization group methods in the *space-like region* [186, 187, 188]. In this region represents the distribution of parton momentum fraction inside the incoming hadron at a probed scale t . In time-like branching, $f_i(x, t)$ can be used to describe the momentum fraction distribution of the produced partons. The success obtained for the parton description of DIS, lead to the development of evolution equations for the *time-like region* and their generalization to other observables. These perturbative techniques include the Leading Logarithmic Approximation (LLA), the Double Logarithmic Approximation (DLA) and the Modified Leading Logarithmic Approximation (MLLA); a similar approach in terms of the Sudakov factor as discussed above is used in all of these techniques. More details about their differences, the evolution equations obtained in each technique and their applications can be found at [186, 189].

The formulation of parton branching in terms of the Sudakov form factor is well suited for its implementation as an iterative computer algorithm and this is the basis of the ‘*parton shower*’ in Monte Carlo programs for simulating QCD jets, following the logic shown in Figure A.7. In summary, the outgoing partons from the scattering process which are emitted at an energy scale $t = Q^2$ related to the momentum transferred in the hard sub-process radiate gluons; each emission occurs at an energy scale that evolves *downwards* towards a cutoff scale t_0 at which the partons are considered unresolvable and we enter the low energy regime in which non-perturbative effects cannot be neglected [180, 190].

Up to now, we have only considered collinear enhancements due to soft gluon emissions (small angle approximation). However, as we can see from Eq. A.12, even when θ is not small, infrared enhancements exist for the non-collinear amplitudes. Hence, it is valid to wonder if the emission gluons at a particular energy scale t_1 affects the emission of gluons at t_2 . The answer is provided by another important property of QCD related to the conservation of the color current, called *color coherence* and it is extensively discussed in [180, 186, 191, 192, 189, 193]. Color coherence leads to the property known as *angular ordering*. In electrodynamics, it accounts for the suppression of soft bremsstrahlung from electron-positron pairs (called the Chudakov effect [194]). Therefore, this radiation is confined to a cone bounded by the electron and positron momenta. Likewise, in

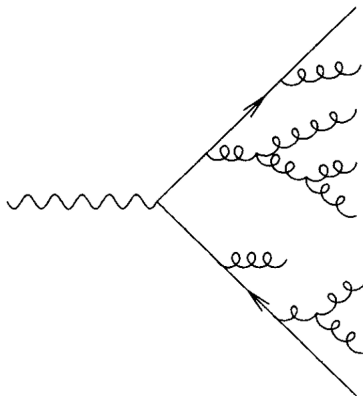


Figure A.7: Parton shower in e^+e^- annihilation [180].

leading order QCD, a soft gluon is emitted only inside a cone bounded by the momenta of its two immediate predecessors [186]. Thus, color coherence can be thought of as to suppress soft radiation at large angles, implying that the opening angles of subsequent emissions in the cascade will decrease [189].

A.4 Matching and merging

So far we have seen that in the parton shower model, the collinear and soft emissions that dominate in multi-parton cross section can be taken into account to all orders if one approximates the gluon emissions to be strongly ordered (angular ordering). Nevertheless, when we have several hard and widely separated jets, the strong ordering no longer holds and the parton shower models do not give a good description of these states, due to the fact that they do not include non-divergent contributions. In other words, not enough gluons are emitted with large energy and at a large angles from the shower initiator [195].

In order to improve the description of multi-jet final states, full matrix elements can be used, which describe the process correctly up to a given order in the strong coupling [196]. Fixed-order matrix elements are excellent when simulating well separated hard partons, but they have problems when trying to describe collinear and soft partons, including the case where the number of final-state partons increases. Then, a combination of both approaches could be done to get a good description of any partonic state and it will be necessary for hadronization models to work properly [179].

However, it is not possible to simply add a parton shower to an event generated with a matrix element. This is due to the fact that the tree-level matrix elements are *inclusive*, giving the probability of having *at least* n partons in a state calculated exactly to lowest order in α_s . On the other hand, the state generated by a parton shower is *exclusive*, given by the probability of having *exactly* n partons calculated approximately to all orders in α_s . There are different ways for combining matrix elements and parton showers, which are classified in two main groups [179]:

Fixed order and parton shower matching.

In this approach, the tree-level (LO) or next-to-leading order (NLO) matrix elements are modified to *match* the parton shower [196], based on the correction of the first emission, which is the hardest one and will determine the structure of the final state. This emission is calculated with tree-level accuracy, since this radiation constitutes a NLO correction to the basic process; in addition, NLO virtual corrections must be included [28]. Once this first emission is computed, it is subtracted from the higher order calculation to remove double counting and the subtracted result is processed by the parton shower [197].

In principle higher-order corrections will have two effects in a parton shower: they alter the shape of the distributions related to the first emission and the (norm) total cross section of the produced sample. To achieve $\mathcal{O}(\alpha_s)$ accuracy at the cross section level, two methods were developed under the names of **MC@NLO** [198] which removes the double counting by modifying the NLO subtraction, and **POWHEG** which distributes the hardest emission according to the exact NLO matrix element [153, 155]. Event generators using any of this general approach produce NLO accurate distributions for inclusive quantities and generate the hardest jet with tree-level accuracy.

Matrix element and parton shower merging.

A separate tree-level calculation is performed for each parton multiplicity of interest. Soft and collinear divergences of the hard matrix elements are regulated by resolution cuts. The parton shower is combined with these calculations and double-counting is removed by appropriate vetoes on shower branchings [197]. In simple terms, in this approach a scale is defined, usually based on the jet resolution scale. Any parton produced above that scale is generated with a corresponding higher-order matrix element and, any parton produced below this scale is generated by the shower [179].

In detail, this approach starts with the generation of LO matrix elements for the production of the basic process and an additional number of other partons, which is less than certain value n . A minimum separation is imposed on the produced partons (resolution criterion), which can be for example, that the minimum relative transverse momentum in any pair of parton is above a given cut Q_{cut} . Then, these amplitudes are reweighed such that the virtual effects are included in the shower algorithm in the strongly ordered region [28]. Before adding the parton showers, the configurations generated are LO accurate at large angles and they match the results of the shower algorithm at small angles, except that no emissions are present below Q_{cut} and there are no final states with more than n partons. The kinematic configurations are then passed through the shower algorithm, which generates all the branchings with relative transverse momentum below Q_{cut} for initial events with less than n partons, or below the scale of the smallest pair transverse momentum for events with n partons [28].

Multi-jet processes are used for many of the discovery channels in new physics searches and therefore, the main irreducible background is the production of multi-jets from Standard Model processes, experimentally referred as QCD, where these jets are well separated and have large transverse momenta. The main goal of the merging approach is to give an accurate predictions of the observables in these kind of events, being superior to those from the matching schemes [28]. The four main

algorithms that merge tree-level matrix elements and parton showers are CKKW [199], CKKW-L [200], Pseudo-Shower [195], and MLM [201, 202]. A nice description of the theory behind each merging algorithm and the experimental results can be found at [196].

We end this section by roughly outlining what a *infrared and collinear safe* algorithm is, which plays a crucial role for merging as well as for jet reconstruction algorithms: if a single parton is replaced with a set of collinear partons sharing its original energy, the jet configuration must remained unchanged. Similarly, if a soft parton is added to the original jet configuration, this configuration must not change according to the jet algorithm [197].

A.5 Underlying event

A realistic hadron-hadron collision not only consists on the a hard scattering and its subsequent shower evolution, but it also includes the so-called *underlying event* (UE) as shown in Figure A.8. This term was introduced by the CDF collaboration to separate and identify semi-hard contributions of a high-energy collision [203]. The UE is defined as any additional hadronic activity that cannot be attributed to the hadronization of partons involved in the hard scatter and it is not related to the initial- and final-state QCD radiation; therefore, it is attributed to the hadronization of partonic constituents that have undergone multiple parton interactions (MPI), as well as to the beam remnants that are concentrated along the beam direction [204].

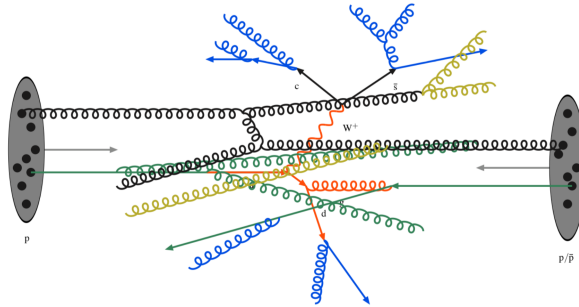


Figure A.8: Illustration of MC simulation of a proton-(anti)proton collision, where a hard scattering (orange) has occurred and the event contains particles from initial- (green) and final-state (blue) radiation. The remaining particles come from the beam remnants and their interaction, contributing to what is known as “underlying event”. Figure taken from [205].

In the following, a set of definitions and characteristics of the processes that contribute to the additional hadronic activity in a hadron-hadron collision will be briefly described, based on the discussion in [179].

Soft QCD processes

The total hadron-hadron cross section can be seen as the sum of all the *elastic* and *inelastic* reactions present in a single collision,

$$\sigma_{total}(s) = \sigma_{elastic}(s) + \sigma_{inelastic}(s), \quad (\text{A.30})$$

with s the beam-beam center-of-mass energy squared. Their definitions and further classifications as implemented in MC event generators are described below.

Elastic scattering (σ_{elastic}).

It consists on all the reactions that involve particles where the only quantity exchanged is momentum and all their quantum numbers remain the same, therefore they do not increase the particle multiplicity of the event:

$$A(p_A) + B(p_B) \rightarrow A(p'_A) + B(p'_B). \quad (\text{A.31})$$

Inelastic scattering ($\sigma_{\text{inelastic}}$).

It includes all reactions that are not elastic scattering,

$$A + B \rightarrow X, \quad X \neq A + B \quad (\text{A.32})$$

where there is a change of one or more quantum numbers, or additional particles are produced. The inelastic processes can be further classified qualitatively in terms of *diffraction*. The distinction between diffractive and non-diffractive topologies is usually based on whether the final state looks like the decay of an excitation of the beam particles (diffractive) or not (non-diffractive). Alternatively, it is defined in terms of a rapidity gap in the final state that are used to separate such excitations. More precisely, the differences between diffractive and non-diffractive events is given in two ways:

1. Theoretically, where each different physics sub-process within a model is defined as diffractive or non-diffractive. This approach presents two issues: (1) since it is model-dependent, individual components in one model are not directly comparable to those of another, and (2) if both the diffractive and non-diffractive events are allowed to be in certain regions of the phase space, their interference terms will not be assigned uniquely to a particular kind of diffraction, which makes its classification non meaningful from the quantum mechanics point of view;
2. Experimentally, based on physical observables, guaranteeing its validity at quantum level. The difficulty using this approach is that a choice of the meaning for “diffractive topology” at the level of final state observables, which has not a unique answer. Typically, the observable that defines the distinction between the diffractive and non-diffractive events is rapidity, where large gaps of rapidity (around 3 to 5 units) are consistent with the (multiple) decay of excited states.

Once a process is tagged as diffractive using either one of the approaches above, we can further categorize it under different classes of diffraction:

- *Central diffractive (CD)*. Both of the beam particles survive intact, leaving an excited system in the central region between them; this topology is also known as central exclusive production.
- *Single diffractive (SD)*. Only one of the beam particles gets excited and the other survives intact.
- *Double diffractive (DD)*. Both of the beam particles are excited and hence, neither of them survive the collision intact.

If a reaction is classified as *non-diffractive* (ND), we expect to observe no gaps in the event and it is understood to exclude elastic scattering. Thus, one can write the inelastic scattering cross section as:

$$\sigma_{\text{inelastic}}(s) = \sigma_{\text{CD}}(s) + \sigma_{\text{SD}}(s) + \sigma_{\text{DD}}(s) + \sigma_{\text{ND}}(s) \quad (\text{A.33})$$

A simple picture of the difference in rapidity gaps for each type of diffraction can be seen in Fig. A.9.

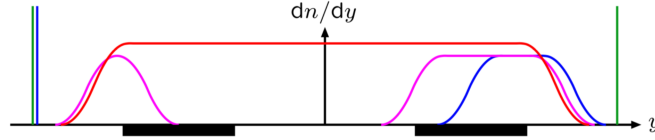


Figure A.9: Particle multiplicity per unit rapidity for elastic scattering (green) and some of the diffraction classes in inelastic scattering: single diffractive (blue), double diffractive (magenta) and non-diffractive (red). Figure taken from [206].

Minimum-bias and soft inclusive physics

The term *minimum-bias* has two different connotations depending on the context it is used:

- experimentally, “minimum-bias events” are those which have been selected with the minimum possible selection requirements, in order to be as inclusive as possible;
- theoretically, “minimum-bias” denotes specific classes of inclusive soft QCD sub-processes in a given model.

Jet pedestals

The underlying effect was first known as the *jet pedestal effect*, observed by the UA1 experiment at CERN Sp \bar{p} S collider, in a study dedicated to jet events [207]. This study observed a constant transverse energy E_T plateau was observed, independently of the jet E_T , which was higher than that observed in minimum-bias events. The characteristics of this additional activity have been studied in pp and $p\bar{p}$ collisions at RHIC, Tevatron and LHC energies (see [208] and references therein); nowadays, the study of this effect plays an important role in heavy-ion collisions.

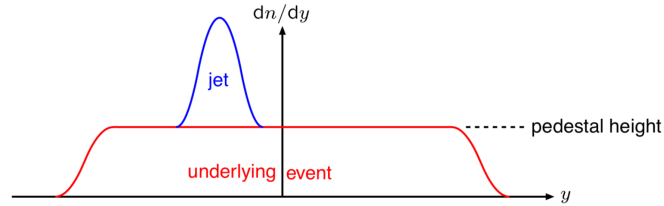


Figure A.10: Particle multiplicity per unit rapidity in the events with jet pedestals. Adapted from [206].

This effect can be interpreted as follows: when two hadrons collide at non-zero impact parameter, interactions with high transverse momentum can only take place in the overlapping region. When in an event high p_T selection cuts are applied, we have more probability to keep events with more central collisions (small impact parameter) and consequently, these events will present larger underlying activity.

Multi-parton interactions (MPI)

In hadron-hadron collisions, more than one pair of partons may interact, leading to the possibility of multiple interactions. As a consequence, we may observe more than one hard partonic scattering in a single collision. The main distinction between the hard scattering of interest and the one coming from additional interactions is that the latter tends to produce jets that are back-to-back with small total p_T . The implementation of MPIs in event generators is fundamental to describe the experimental data, as shown in Figure A.11

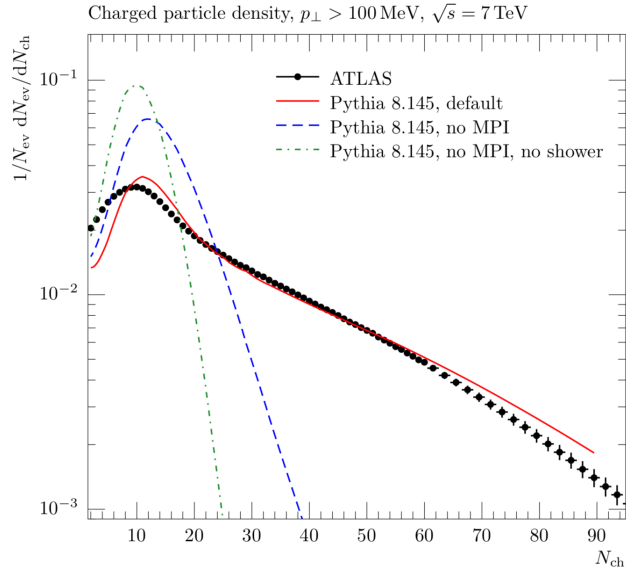


Figure A.11: Comparison of models that include (or not) MPI and parton showers and the charged particle multiplicity measured by the ATLAS experiment for particles with $p_T > 100$ MeV, $|\eta| < 2.5$ and $c\tau > 10$ mm, in events where at least to particles satisfy these conditions. Figure taken from [179].

The basis of MPI and UE models is the dominant contribution of t -channel gluon exchange to the total hadronic cross section (Eq. A.1), which corresponds to the Rutherford scattering. There is no physical law that prevents several distinct pairs of partons inside each hadron to have more than one scattering in the same event. On the other hand, due to the non-abelian structure of QCD (due the existence of more than one color charge, in contrast to electrodynamics), the exchange of colored particles can cause non-trivial changes to the color topology of the colliding system as a whole, increasing the probability of a larger particle multiplicity in the final state.

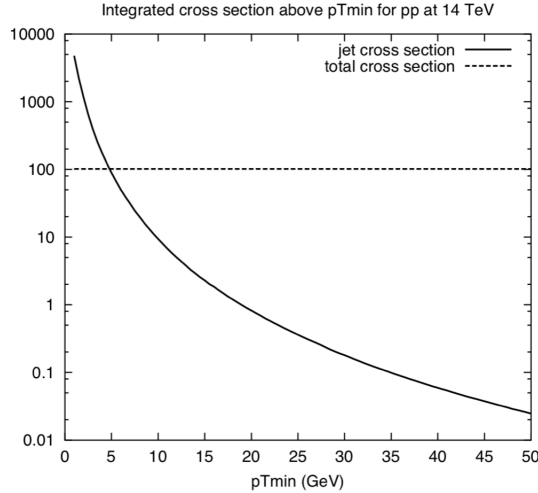


Figure A.12: Simple picture of the behavior of the jet production cross section and the total pp interaction cross section at $\sqrt{s} = 14$ TeV above a minimum value of p_T . Figure taken from [206].

In the soft QCD region ($p_T \rightarrow 0$), the t -channel gluon propagator almost goes on-shell, causing the sub-process differential cross section to become very large, behaving approximately as

$$\frac{d\hat{\sigma}_{2j}}{dp_T^2} \sim \frac{1}{p_T^4} \quad (\text{A.34})$$

depicted in Figure A.12. One can see that below certain value of p_T , the cross section for jet production exceeds the total proton-proton interaction cross section, which in principle is not physically possible. This behavior may be reinterpreted in terms of the number of interactions. Recall from previous sections that the computation of the interaction cross section is *inclusive*. This means that in an event with n parton-parton interactions, will count n times in the total jet production cross section σ_{2j} but only once in σ_{total} . σ_{2j} can be written as a function of the minimum transverse momentum $p_{T\text{min}}$ as

$$\sigma_{2j}(p_{T\text{min}}) = \langle n \rangle(p_{T\text{min}}) \sigma_{\text{total}} \quad (\text{A.35})$$

in the limit when all the individual parton-parton interactions are independent and equivalent. The term $\langle n \rangle(p_{T\text{min}})$ represents the average number of parton-parton interactions above $p_{T\text{min}}$ per collision. Hence, one may reinterpret the divergence of σ_{2j} as $p_T \rightarrow 0$ as the divergence of the *number of interactions per collision*. Additional effects from energy-momentum conservation and color screening/saturation need to be considered in order to fully regulate this divergence all the way down to the confinement scale, $\Lambda_{\text{QCD}} \sim 0.3$ GeV. Perturbative corrections need to be considered, as well as non-perturbative effects below $p_{T\text{min}} \sim 1$ GeV [179].

A.6 Hadronization models

The last step in the time evolution in a hadron-hadron collision corresponds to the transition of the quarks and gluons from hard scattering, parton showers and multiple interactions to color-neutral final states. In the context of MC simulations this process is known as *hadronization* and by nature it is non-perturbative and therefore, we need to formulate heuristic models based on our knowledge of the behavior of QCD at low-energy scale. In this section, the main ideas behind the first hadronization model proposed by R. Field and R. Feynman, known as the independent fragmentation model, are presented, constituting the basis of the most common hadronization models currently used: the *string* model, implemented in PYTHIA [209, 146] and the *cluster* model, the basis of the HERWIG [210, 211, 212] and SHERPA [213] event generators.

Local parton-hadron duality

One analytic approach to describe hadronization is the *local parton-hadron duality (LPHD)*, in which the non-perturbative difficulties are ignored. After running the parton shower down to the Λ_{QCD} scale, each outgoing parton is transformed into a hadron given a certain “weight” [205]. The energy and angular spectrum of the outgoing partons calculated in perturbative QCD with some low cutoff scale reproduces the corresponding hadron spectra surprisingly well [28, 205, 189]. This fact suggests that the hadronization is “*local*”, that is, it involves partons that are close in position and momentum. From its perturbative nature of LPHD, it can be used to calculate power correction to the NLO predictions for event shapes.

Although it is not possible to cannot generate realistic events by ignoring the non-perturbative effects, this method is instead formulated as an hypothesis, the *local parton-hadron duality hypothesis*, which proposes that the flow of momentum and quantum numbers at the hadron level tends to follow the flow established at the parton level, [180] and it is one of the foundations for the current phenomenological hadronization models. As a result, it implies that the flavor of the quark initiating a jet should be found in a hadron near the jet axis. The extent to which the hadron flow deviates from the parton flow reflects the irreducible smearing of order Λ due to hadron formation.

Independent fragmentation model

The simplest approach model proposed to generate hadron distributions was due to R. Field and R. Feynman [214, 215], in which we assume that each parton fragments independently. Their idea was to reproduce the (limited) transverse momenta and approximate the scaling of energy fraction distributions in jets observed in e^+e^- collisions at moderate energies [190]. At present, this model is interesting only for historic purposes.

The main idea is that the fragmenting quark is combined with an antiquark of a quark-antiquark ($q\bar{q}$) pair popped up from the vacuum to create a first generation meson with fraction energy z (Figures A.13). The leftover quark, with energy fraction $1 - z$, is fragmented the same way and so on, producing a hadronization chain, as shown in Figure A.14, until the leftover energy falls

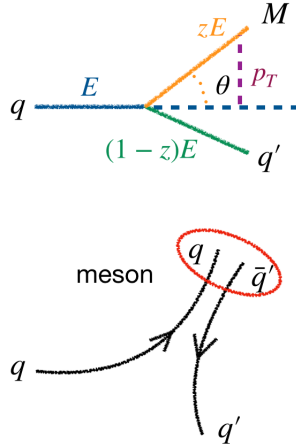


Figure A.13: Elementary hadronization vertex in the independent fragmentation model. Figure adapted from [216].

below some energy cutoff. For gluon fragmentation, the gluon is first split into a $q\bar{q}$ pair with two possibilities: (1) all of the gluon’s momentum is assigned to only the quark or antiquark, such that the gluon “behaves” as a quark of random flavor, or (2) the gluon’s momentum is distributed between the quarks using the $g \rightarrow q\bar{q}$ Altarelli-Parisi splitting function [190].

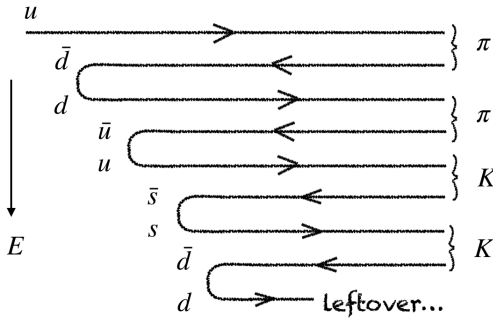


Figure A.14: Hadronization chain in the independent fragmentation model proposed by Field and Feynman. Figure adapted from [216].

The model is considered to be simple, since only four parameters were needed to describe the fragmentation function, the width of the transverse momentum distribution, the ratio of strange to non-strange pair creation, and the ratio of vector to pseudo-scalar meson production, and successful, due to the good characterization that provided for 2- and 3-jet final states in e^+e^- annihilations. Nevertheless, this scheme faces some complications: the fragmentation of a parton is supposed to depend on its energy rather than its virtuality. In other words, the fragmenting parton is assumed to be always on-mass shell, leading to violations of momentum conservation that required a rescaling of the momenta after the hadronization ends. In addition, the model does not explain how the hadronization of the low energy leftovers is achieved and it predicts that in events that have

multiple jets close to each other, these will remain distinguishable, which is not what is observed experimentally [190].

String model

The string hadronization model is based on the fundamental property of QCD known as *confinement*, which can be viewed as the consequence of an approximately linear term in the “*QCD potential*” of a colorless $q\bar{q}$ pair, which has the approximate form:

$$V_{\text{QCD}}(r) \approx \frac{4}{3} \frac{\alpha_s}{r} + \kappa r. \quad (\text{A.36})$$

The presence of a linear term was inferred from hadron spectroscopy (Regge trajectories), that predict $\kappa \approx 1 \text{ GeV/fm} = 0,2 \text{ GeV}^2$, and has been also confirmed by “quenched” lattice QCD calculations [217].

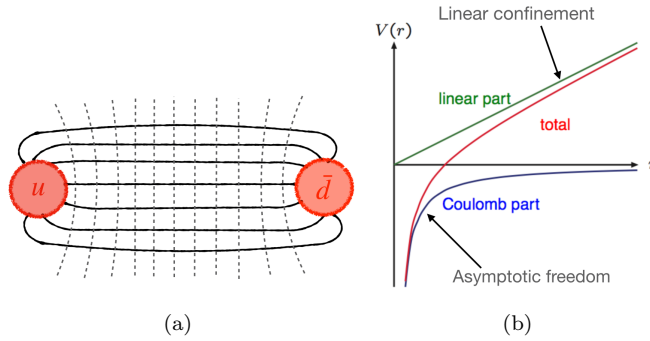


Figure A.15: (a) Color “flux tube” in a chromodynamic dipole. (b) Qualitative picture of the QCD potential between a colorless $q\bar{q}$ pair. Figures adapted from [216, 218].

In the Lund string model, the color field lines are approximated as a massless relativistic string of uniform linear energy density attached between the q and \bar{q} (Figure A.16), and only the linear term of the potential is considered as relevant in the hadronization scale.



Figure A.16: Simplified color-field topology in a $q\bar{q}$ system and its further simplified string representation. Figure taken from [217].

When the energy “stored” in the string is not big enough to produce a break, the motion of the simple $q\bar{q}$ system in its rest frame can be described as a “yo-yo” motion and it is associated to an excited meson. As the spatial separation between the $q\bar{q}$ system grows, the energy stored in the string increases, allowing the creation of a new $q\bar{q}$ pair, popped out of the vacuum, that can break the string (Figure A.17), which is similar to the independent fragmentation scheme. The difference

here is, that the string model has a more consistent and covariant picture [190]. For simplicity, when the breaks are simulated, the quarks are considered massless. If the invariant mass of any $q\bar{q}$ system is large enough, further breaks may occur, as depicted in Figure A.18.

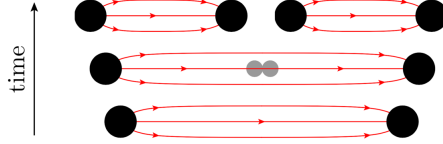


Figure A.17: Illustration of string breaking by $q\bar{q}$ creation in the string field. Figure taken from [28].

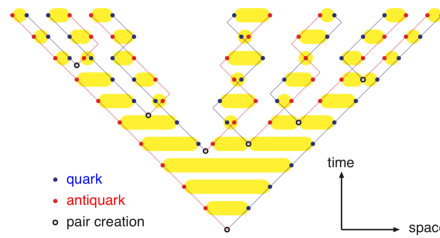


Figure A.18: Motion and breakup of a string system. The diagonal lines represent (anti)quarks and the horizontal ones are snapshots of the string field. Figure taken from [219].

More complicated configurations involving gluons are treated as transverse “kinks” connected to two string pieces corresponding to quarks, which represent the string motion in 3-jet $q\bar{q}g$ events (Figure A.19). Due to the two strings attached to the gluon, the relative energy loss per unit time is twice as big as the one for quarks, so the rate of hadron production is larger by a factor of 2 for gluons. The kinks grow in the transverse direction until all the kinetic energy is used up [28]. One of the key predictions of the string model is that in $q\bar{q}g$ events, there is an enhancement of particle production in the qg and $\bar{q}g$ angular regions, whereas there is a depletion in the $q\bar{q}$ region. This effect was experimentally confirmed [220] and inspired the study of perturbative coherence in such events, discussed at the end of Section A.3 [179].

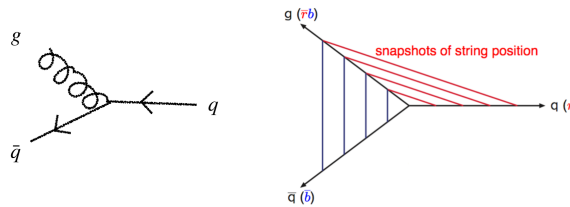


Figure A.19: Schematic illustration of the $q\bar{q}g$ configuration, showing the gluon as a kink in the string that connects the $q\bar{q}$ pair [179].

The time evolution of the string breaks is not causally connected, therefore the breakups do not have to occur in a particular time-ordered sequence. Thus, it is possible to describe the fragmentation

process starting from the hadron closest to the initial q and move towards the initial \bar{q} one and vice versa, implying a “*left-right symmetry*”. The hadron formation is done by randomly selecting between the left and right sides of the string. The first hadron generated will be the “outermost” one, formed by combining the original quark (antiquark) with an antiquark (quark) produced by a breakup [28]. Two adjacent breaks are conditioned by the fact that the string created by them has to be on the mass shell for the hadron to be produced [179] (Figure A.20):

$$m_{\perp}^2 = m_q^2 + p_{\perp}^2 \quad (\text{A.37})$$

with the \perp denoting the mass/momentum in the transverse direction, and m_q the quark mass.

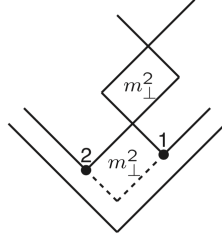


Figure A.20: Conditions on nearby string breaks. Figure taken from [179].

As a result of the left-right symmetry we obtain a unique probability distribution that determines how the individual vertices correlate in order to create a hadron of mass m_h by taking a fraction z of the energy-momentum left in the system [217], given by

$$f(z) \propto \frac{(1-z)^a}{z} \exp\left(-b \frac{m_{\perp}^2}{z}\right), \quad (\text{A.38})$$

where a and b are parameters to be obtained from experimental data. In this model, heavy quarks (c, b) are not produced at new string breaks but they may be at the endpoints of a string, as the product of hard interactions. Then, the fragmentation function for these quarks is modified,

$$f(z) \propto \frac{(1-z)^a}{z^{1+bm_Q^2}} \exp\left(-b \frac{m_{\perp}^2}{z}\right), \quad (\text{A.39})$$

where m_Q denotes the mass of the heavy-quark. The expressions for $f(z)$ are valid only when, for the breakup of a system into a hadron and a remainder-system, the mass of the latter is large [179].

In a color field a massless $q'\bar{q}'$ pair with zero transverse momentum can be created classically in one point and then be pulled apart by the field. If the pair is massive or carries transverse momentum, then they must classically be produced at a certain distance, so that the field energy between them can be transformed into the transverse mass m_{\perp} . Taking a quantum mechanical approach, the $q'\bar{q}'$ pair is produced at a specific space-time location as virtual particles and then, each particle has to “tunnel” out a distance m_{\perp}/κ to acquire enough energy from the string to correspond to its m_{\perp} [179, 28, 219, 217]. The production probability for this tunneling process,

$$\text{Prob}(m_q^2, p_{\perp}^2) \propto \exp\left(\frac{-\pi m_q^2}{\kappa}\right) \exp\left(\frac{-\pi p_{\perp q}^2}{\kappa}\right) \quad (\text{A.40})$$

A consequence of this mechanism is the suppression of heavy quark production in string breaks, with a ratio around $u\bar{u} : d\bar{d} : s\bar{s} : c\bar{c} \approx 1 : 1 : 0.3 : 10^{-11}$. The suppression of $s\bar{s}$ production is left as a free parameter in the simulation program but it agrees with the experimental value.

For baryon production, the simplest scheme consists on the occasional production of “anti diquark-diquark” pairs in a triplet-anti triplet representation. The popcorn model is a more general framework for baryon production, in which baryons appear from the successive production of several $q'\bar{q}'$ pairs. The flavor structure in the string model becomes complicated and requires the introduction of many free parameters, which is the main weakness of this approach [179].

Cluster model

The cluster hadronization model is based on a property of parton showering called *pre-confinement* [221]. This implies that the pairs of color-connected neighboring parton have an asymptotic mass distribution that falls rapidly at high masses and it is universal [190]. In this context, “universal” means that it depends only on the parton shower cutoff Q_0 and the QCD scale Λ and not on the scale Q of the hard process initiating the shower, whereas “asymptotic” refers to the fact that $t \gg t_0$ [179].

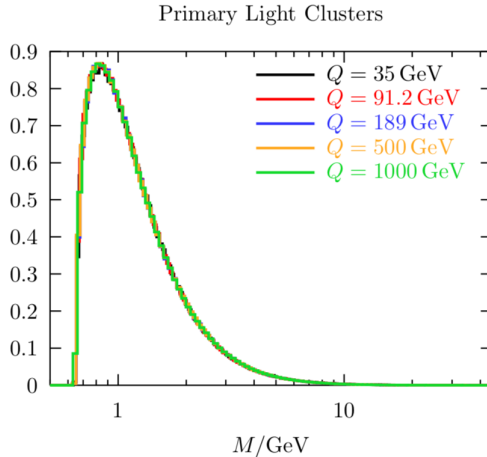


Figure A.21: Invariant mass distribution of color-singlet clusters in HERWIG. Figure taken from [179].

Pre-confinement can be better understood in the $N_c \rightarrow \infty$ limit (pictorially in Figure A.22). The gluons in the shower can be seen as pairs of color-anti color lines connected at the vertices. At the cutoff scale of the shower, each color line is connected to an anti-color line at the same scale; these partners are adjacent given that the color structure can be drawn on a plane in this limit.

Color singlets or “clusters” are formed by adjacent partners, while the probability of non-adjacent lines of doing so is small. This also indicates that the color singlets formed will have small masses, since their proximity usually implies they are close in phase space, leading to the suppression of large masses [179]. In summary, for any starting scale $Q \gg Q_0 \gg \Lambda_{\text{QCD}}$ only the number of clusters depends on t , while the shape of the cluster mass distribution only depends on t_0 and Λ_{QCD} [28].

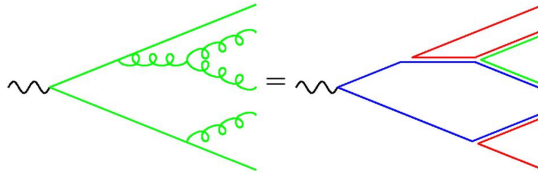


Figure A.22: Color structure of a parton shower to leading order in N_c . Figure taken from [179].

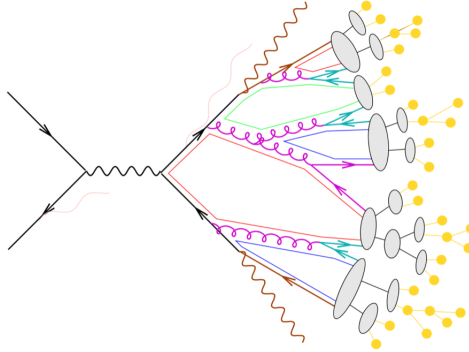


Figure A.23: General picture of the cluster hadronization algorithm. The pre-confinement is shown with local color flows. Figure taken from [205].

The second key idea of this model is to force all gluons at the end of the parton shower to split into $q\bar{q}$ pairs (Figure A.23), which in the string picture, is equivalent to see the gluons as the “seeds” of the string breaks [28]. The enforcement of gluon splitting corresponds to an enhancement of the $g \rightarrow q\bar{q}$ vertex. As a consequence, this would reduce the running of the QCD coupling at low-scales, notion suggested qualitatively by studies of hadronization corrections to event shapes and jet profiles as well as the large yield of soft photons in hadronic Z decays (for references, see [179]).

The momentum distributions and flavors of the quarks produced in gluon splittings are not an issue since the effective gluon (virtual) mass at the end of the showering is large enough to produce light quarks ($m_{u,d} \sim 300$ MeV, $m_s \sim 450$ MeV) with a small allowed kinematic range that has a negligible effect on the momenta and mass of the clusters. On the other hand, the scale of the process naturally forbids the production of heavy quarks and suppresses strange production. If the mass of a formed cluster is above 3-4 GeV, it is forced to undergo a sequence of cluster breakups until the sub-cluster masses fall below the cutoff value. Once all small mass clusters are formed, they isotropically decayed into two hadrons, according to a phase space weight which is a function of the spins of the hadrons to be formed, their momentum and mass, approximately as $\sim (2s_1 + 1)(2s_2 + 1)(2p/m)$ [205].

The cluster hadronization method is remarkably good predicting the hadron distributions observed in jet fragmentation, with practically one free parameter that is the shower cutoff. However, it has some problems dealing with the decay of very massive clusters and it presents an over-suppression of heavy states with multiple strange and charmed baryons [179]. Recently, some improvements

have been made to correct these issues, increasing significantly the agreement with experimental data (Figure A.24).

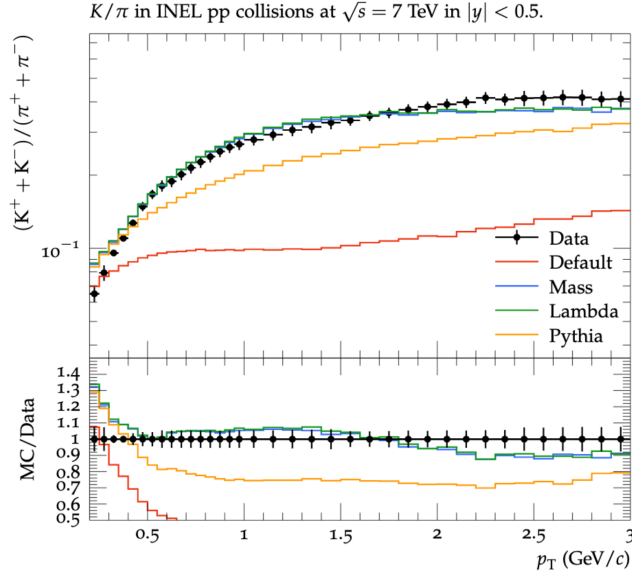


Figure A.24: K/π ratio as measured by ALICE at 7 TeV. Comparison between the default version of HERWIG, two new approaches including dynamical strangeness production and PYTHIA. One can appreciate that the default method used in HERWIG does not describe the experimental data properly, but after implementing improvements to the algorithm, in this case, related to strangeness production, it can have a similar prediction power as the string model. Figure taken from [222].

A.7 Jet fragmentation functions

The last section of this review will be dedicated to the introduction of the *jet fragmentation functions*. In pp collisions, the *inclusive* production of hadrons from partons can be studied with the formulation of fragmentation functions (FFs) D_i^h , in perturbative QCD. The main difference between the phenomenological models presented in the last section and this set of functions, is related to the energy scale dependence: FFs are defined at any arbitrary *perturbative* scale while hadronization models intrinsically need the choice of a hadronization scale Q_{had} . FFs are calculated in perturbative QCD given a non-perturbative initial condition obtained by fits to the hadron spectra.

If the final-state hadron is produced with an energy E_h , the fraction of the quark energy E_q that carries away is defined as

$$z = \frac{E_h}{E_q}. \quad (\text{A.41})$$

The differential cross section for inclusive hadron production in e^+e^- collisions is then [183]

$$\frac{d\sigma(e^+e^- \rightarrow hX)}{dz} = \sum_{q(\text{flavors})} \sigma(e^+e^- \rightarrow q\bar{q}) [D_q^h + D_{\bar{q}}^h] \quad (\text{A.42})$$

$D_i^h(z)$ represents the probability that the final-state hadron h carries an energy fraction z from the parent parton i . The FFs are subject to momentum and probability constraints:

- *energy conservation*: the energies of all final-state hadrons has to add up to the energy of the parent parton,

$$\sum_h \int_0^1 z D_q^h(z) dz = 1; \quad (\text{A.43})$$

- *hadron multiplicity*: the sum of the probabilities for producing a certain hadron h from all possible parent partons has to equal n_h the multiplicity of h observed in the final state,

$$\sum_i \int_{z_{min}}^1 D_i^h(z) dz = n_h. \quad (\text{A.44})$$

The lower limit in the integral is related to the threshold energy for producing a hadron of mass m_h , which for e^+e^- collisions is given by

$$z_{min} = \frac{m_h}{E_{beam}}. \quad (\text{A.45})$$

In the same way as the PDFs, FFs parametrize properties intrinsic to the partons and are thus universal, regardless of the parton production mechanism. Once the FFs are fixed in e^+e^- collisions or DIS, they can be applied to other systems, such as ep , pp and $p\bar{p}$. For example, the inclusive p_T distribution of a produced hadron h in pp collisions is [183]

$$\begin{aligned} \frac{d\sigma(pp \rightarrow hX)}{dz} &= 2p_T \int_{\theta_{min}}^{\theta_{max}} \frac{d\theta_{cm}}{\sin \theta_{cm}} \times \\ &\times \int dx_1 \int dx_2 f_i^p(x_1, Q^2) f_j^p(x_2, Q^2) \times \\ &\times \frac{D_q^h(z, Q^2)}{z} \frac{d\sigma_{ij}}{dt}, \end{aligned} \quad (\text{A.46})$$

this expression has a great similitude to the total hadronic cross section in the collinear factorization scale, as a result of their perturbative nature.

Two sets of commonly used FFs are by Kretzer [223], and Kniehl, Kramer and Potter (KKP) [224]; FFs for the lightest heavy flavor mesons D and B have also been extracted [183, 225, 226] A general way to parameterize for light hadrons is

$$D_i^h(z, \mu_0^2) = N z^\alpha (1-z)^\beta (1 + \gamma(1-z)^\delta), \quad (\text{A.47})$$

where the normalization N and the parameters α , β , γ , δ , depend on the energy scale μ_0^2 and the type of parton i and hadron h [28].

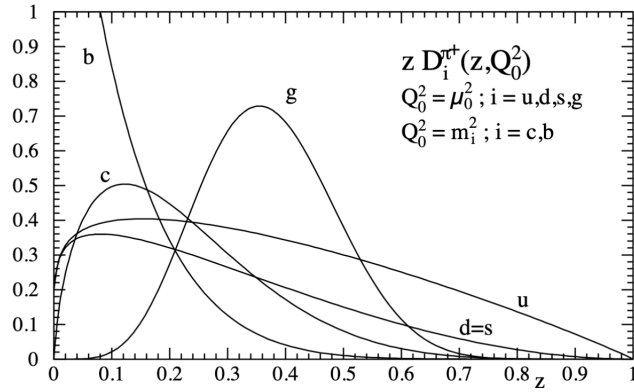


Figure A.25: Fragmentation functions $D_i^{\pi^+}$ at their respective input scales [223].

A.8 Summary and conclusions

The purpose of this work was to present a somewhat extensive literature review of the main physics ideas behind the steps simulated in hadron-hadron collision events as they are implemented in Monte Carlo event generators. These start with a hard scattering sub-process of a pair of partons, one of each incoming hadron that undergoes several gluon emissions that evolve down the energy scale known as parton shower. Most of the concepts necessary for the understanding of these stages can be more easily extracted from the study of e^+e^- collisions or ep deep inelastic scattering and, due to the perturbative treatment they receive, they can be applied in any other collision system. The approach of parton showering is fundamental in order to be able to predict, not only the kinematic spectra of the detected hadrons in each event, but also the characteristics of the jet structure.

However, the presence of more initial-state partons in hadron-hadron collisions forces us to include models for processes that are thought to be originated from the interaction of the beam remnants with the initial- and final-state radiation, provoking a rise in the particle multiplicity of each collision event due to effects classified collectively as underlying event: these include the soft QCD processes like elastic scattering and diffraction and multi-parton interactions. Their modeling is crucial to correctly predict the experimental observations.

Having included all these steps into account, then one can study the non-perturbative evolution of the system making use of hadronization models, which are inspired by the known properties of QCD at these scales as well as the local parton-hadron duality hypothesis, suggested by the fact that the parton (jet) fragmentation functions calculated for the final state describe surprisingly well the data. The two most common models currently used in MC event generators are the string and cluster model, based on the QCD confinement and pre-confinement, respectively. Both models have advantages and disadvantages and there is not such a thing as a correct model to use, but instead is a matter of convenience. The hadronization algorithms are being constantly improved, to account for some issues present in their definitions or the observed discrepancies with reference to experimental data .

In the study of heavy-ion collisions, the jet fragmentation functions were a fundamental tool for the observation of modifications due to nuclear effects when compared to those obtained for pp collisions; these effects are known as *jet quenching*. There is a big ongoing effort from the theoretical community to have a deeper understanding of these effects, as well as from the experimental community for the extraction of the physical observables of interest that can help to build extensions to the present phenomenological models of hadronization and include more complicated systems as in nucleus-nucleus collisions [219, 227]. It is evident that the collaboration between the high energy and heavy-ion communities will be indispensable to expand our knowledge of the QCD phenomena at all energy scales, which will impact positively their specific research goals, namely, the search for physics beyond the Standard Model and the understanding of early Universe evolution through the study of the quark-gluon plasma.

This review is beyond of being complete, since all the topics related to the experimental variables to study jet characteristics and the final stage of particle decays are not included. Also, the study of fragmentation functions is more extensive than to what was discussed in this work; more details can be found in the references cited throughout the text.

References

- [1] Peter Ware Higgs. Broken symmetries, massless particles and gauge fields. *Phys. Lett.*, 12: 132–133, 1964.
- [2] Peter W Higgs. Broken symmetries and the masses of gauge bosons. *Physical Review Letters*, 13(16):508, 1964.
- [3] François Englert and Robert Brout. Broken symmetry and the mass of gauge vector mesons. *Physical review letters*, 13(9):321, 1964.
- [4] Georges Aad et al. Observation of a new particle in the search for the Standard Model Higgs boson with the ATLAS detector at the LHC. *Phys. Lett.*, B716:1–29, 2012. doi: 10.1016/j.physletb.2012.08.020.
- [5] Serguei Chatrchyan et al. Observation of a New Boson at a Mass of 125 GeV with the CMS Experiment at the LHC. *Phys. Lett.*, B716:30–61, 2012. doi: 10.1016/j.physletb.2012.08.021.
- [6] CMS Collaboration. A measurement of the Higgs boson mass in the diphoton decay channel. Technical Report CMS-PAS-HIG-19-004, CERN, Geneva, 2019. URL <https://cds.cern.ch/record/2691211>.
- [7] Stephen P. Martin. A Supersymmetry primer. [*Adv. Ser. Direct. High Energy Phys.*18,1(1998)], pages 1–98, 1997. doi: 10.1142/9789812839657_0001,10.1142/9789814307505_0001.
- [8] Mikhail Shaposhnikov and Andrey Shkerin. Gravity, Scale Invariance and the Hierarchy Problem. *JHEP*, 10:024, 2018. doi: 10.1007/JHEP10(2018)024.
- [9] Ian J R Aitchison. Supersymmetry and the MSSM: An Elementary Introduction. *arXiv e-prints*, art. hep-ph/0505105, May 2005.
- [10] Y. Shadmi. Introduction to Supersymmetry. In *Proceedings, 2014 European School of High-Energy Physics (ESHEP 2014): Garderen, The Netherlands, June 18 - July 01 2014*, pages 95–123, 2016. doi: 10.5170/CERN-2016-003.95.
- [11] Howard E. Haber and Gordon L. Kane. The Search for Supersymmetry: Probing Physics Beyond the Standard Model. *Phys. Rept.*, 117:75–263, 1985. doi: 10.1016/0370-1573(85)90051-1.
- [12] John R. Ellis, J. S. Hagelin, Dimitri V. Nanopoulos, Keith A. Olive, and M. Srednicki. Supersymmetric Relics from the Big Bang. *Nucl. Phys.*, B238:453–476, 1984. doi: 10.1016/0550-3213(84)90461-9. [,223(1983)].
- [13] N. Aghanim et al. Planck 2018 results. VI. Cosmological parameters. *Astron. Astrophys.*, 641: A6, 2020. doi: 10.1051/0004-6361/201833910. [Erratum: *Astron. Astrophys.* 652, C4 (2021)].
- [14] Gerard Jungman, Marc Kamionkowski, and Kim Griest. Supersymmetric dark matter. *Phys. Rept.*, 267:195–373, 1996. doi: 10.1016/0370-1573(95)00058-5.
- [15] Carlos Avila, Andrés Flórez, Alfredo Gurrola, Dale Julson, and Savanna Starko. Connecting Particle Physics and Cosmology: Measuring the Dark Matter Relic Density in Compressed Supersymmetry at the LHC. 2018.
- [16] Keith A. Olive and Mark Srednicki. Cosmological limits on massive LSP ’s. *Nucl. Phys.*, B355:208–230, 1991. doi: 10.1016/0550-3213(91)90310-T.

- [17] D. N. Spergel et al. First year Wilkinson Microwave Anisotropy Probe (WMAP) observations: Determination of cosmological parameters. *Astrophys. J. Suppl.*, 148:175–194, 2003. doi: 10.1086/377226.
- [18] Kim Griest and David Seckel. Three exceptions in the calculation of relic abundances. *Phys. Rev.*, D43:3191–3203, 1991. doi: 10.1103/PhysRevD.43.3191.
- [19] Joakim Edsjo and Paolo Gondolo. Neutralino relic density including coannihilations. *Phys. Rev.*, D56:1879–1894, 1997. doi: 10.1103/PhysRevD.56.1879.
- [20] Michael J. Baker et al. The Coannihilation Codex. *JHEP*, 12:120, 2015. doi: 10.1007/JHEP12(2015)120.
- [21] Howard Baer, Csaba Balazs, and Alexander Belyaev. Neutralino relic density in minimal supergravity with coannihilations. *JHEP*, 03:042, 2002. doi: 10.1088/1126-6708/2002/03/042.
- [22] John R. Ellis, Toby Falk, and Keith A. Olive. Neutralino - Stau coannihilation and the cosmological upper limit on the mass of the lightest supersymmetric particle. *Phys. Lett.*, B444:367–372, 1998. doi: 10.1016/S0370-2693(98)01392-6.
- [23] Takeshi Nihei, Leszek Roszkowski, and Roberto Ruiz de Austri. Exact cross-sections for the neutralino slepton coannihilation. *JHEP*, 07:024, 2002. doi: 10.1088/1126-6708/2002/07/024.
- [24] Guang Hua Duan, Chengcheng Han, Bo Peng, Lei Wu, and Jin Min Yang. Vacuum stability in stau-neutralino coannihilation in MSSM. *Phys. Lett.*, B788:475–479, 2019. doi: 10.1016/j.physletb.2018.12.001.
- [25] Amin Aboubrahim, Pran Nath, and Andrew B. Spisak. Stau coannihilation, compressed spectrum, and SUSY discovery potential at the LHC. *Phys. Rev.*, D95(11):115030, 2017. doi: 10.1103/PhysRevD.95.115030.
- [26] Richard L. Arnowitt, Adam Aurisano, Bhaskar Dutta, Teruki Kamon, Nikolay Kolev, David A. Toback, Paul Simeon, and Peter Wagner. Measuring the $\tilde{\tau} - \tilde{\chi}_1^0$ mass difference and $M(\tilde{g})$ in coannihilation region at the LHC. 2006.
- [27] Albert M Sirunyan et al. Search for supersymmetry with a compressed mass spectrum in the vector boson fusion topology with 1-lepton and 0-lepton final states in proton-proton collisions at $\sqrt{s} = 13$ TeV. *JHEP*, 08:150, 2019. doi: 10.1007/JHEP08(2019)150.
- [28] M. Tanabashi et al. Review of Particle Physics. *Phys. Rev.*, D98(3):030001, 2018. doi: 10.1103/PhysRevD.98.030001.
- [29] Vardan Khachatryan et al. Search for supersymmetry in the vector-boson fusion topology in proton-proton collisions at $\sqrt{s} = 8$ TeV. *JHEP*, 11:189, 2015. doi: 10.1007/JHEP11(2015)189.
- [30] Bhaskar Dutta, Tathagata Ghosh, Alfredo Gurrola, Will Johns, Teruki Kamon, Paul Sheldon, Kuver Sinha, Kechen Wang, and Sean Wu. Probing Compressed Sleptons at the LHC using Vector Boson Fusion Processes. *Phys. Rev. D*, 91(5):055025, 2015. doi: 10.1103/PhysRevD.91.055025.
- [31] Bhaskar Dutta, Alfredo Gurrola, Will Johns, Teruki Kamon, Paul Sheldon, and Kuver Sinha. Vector Boson Fusion Processes as a Probe of Supersymmetric Electroweak Sectors at the LHC. *Phys. Rev. D*, 87(3):035029, 2013. doi: 10.1103/PhysRevD.87.035029.
- [32] Roel Aaij et al. Tests of lepton universality using $B^0 \rightarrow K_S^0 \ell^+ \ell^-$ and $B^+ \rightarrow K^{*+} \ell^+ \ell^-$ decays. 10 2021.
- [33] Dris Boubaa, Shaaban Khalil, and Stefano Moretti. Explaining B decays anomalies in SUSY models. *J. Phys. Conf. Ser.*, 1766(1):012018, 2021. doi: 10.1088/1742-6596/1766/1/012018.

- [34] T. Albahri et al. Measurement of the anomalous precession frequency of the muon in the Fermilab Muon g-2 Experiment. *Phys. Rev. D*, 103(7):072002, 2021. doi: 10.1103/PhysRevD.103.072002.
- [35] John R. Ellis, John S. Hagelin, and Dimitri V. Nanopoulos. Spin 0 Leptons and the Anomalous Magnetic Moment of the Muon. *Phys. Lett. B*, 116:283–286, 1982. doi: 10.1016/0370-2693(82)90343-4.
- [36] John R. Ellis, Dimitri V. Nanopoulos, and Keith A. Olive. Combining the muon anomalous magnetic moment with other constraints on the CMSSM. *Phys. Lett. B*, 508:65–73, 2001. doi: 10.1016/S0370-2693(01)00480-4.
- [37] E. Bagnaschi et al. Likelihood Analysis of the pMSSM11 in Light of LHC 13-TeV Data. *Eur. Phys. J. C*, 78(3):256, 2018. doi: 10.1140/epjc/s10052-018-5697-0.
- [38] David Griffiths. *Introduction to elementary particles*. 2008. ISBN 9783527406012.
- [39] Science by degrees. Particle physics – a primer on the standard model (part 1 of 2). URL <https://sciencebydegrees.com/2018/10/05/particle-primer1/>.
- [40] J. Schwichtenberg. *Physics from Symmetry*. Undergraduate Lecture Notes in Physics. Springer International Publishing, 2015. ISBN 9783319192017. URL https://books.google.com/books?id=_vLLCQAAQBAJ.
- [41] M. Thomson. *Modern Particle Physics*. Modern Particle Physics. Cambridge University Press, 2013. ISBN 9781107034266. URL <https://books.google.com/books?id=BV1sAAAAQBAJ>.
- [42] FT2, Wikimedia Commons. Spontaneous symmetry breaking. 2012. URL [https://commons.wikimedia.org/wiki/File:Spontaneous_symmetry_breaking_\(explanatory_diagram\).png](https://commons.wikimedia.org/wiki/File:Spontaneous_symmetry_breaking_(explanatory_diagram).png).
- [43] C. S. Wu, E. Ambler, R. W. Hayward, D. D. Hoppes, and R. P. Hudson. Experimental test of parity conservation in beta decay. *Phys. Rev.*, 105:1413–1415, Feb 1957. doi: 10.1103/PhysRev.105.1413. URL <https://link.aps.org/doi/10.1103/PhysRev.105.1413>.
- [44] Aleksandr Azatov. Status of Composite Higgs. *PoS*, EPS-HEP2017:255, 2017. doi: 10.22323/1.314.0255.
- [45] F. Zwicky. Republication of: The redshift of extragalactic nebulae. *General Relativity and Gravitation*, 41:207–224, Jan 2009. doi: <https://doi.org/10.1007/s10714-008-0707-4>. URL <https://link.springer.com/article/10.1007/s10714-008-0707-4>.
- [46] Sinclair Smith. The Mass of the Virgo Cluster. *The Astrophysical Journal*, 83:23, January 1936. doi: 10.1086/143697.
- [47] F. D. Kahn and L. Woltjer. Intergalactic Matter and the Galaxy. *The Astrophysical Journal*, 130:705, nov 1959. doi: 10.1086/146762.
- [48] Horace W. Babcock. The rotation of the Andromeda Nebula. *Lick Observatory Bulletin*, 498: 41–51, jan 1939. doi: 10.5479/ADS/bib/1939LicOB.19.41B.
- [49] Vera C. Rubin. One hundred years of rotating galaxies1. *Publications of the Astronomical Society of the Pacific*, 112(772):747–750, jun 2000. doi: 10.1086/316573. URL <https://doi.org/10.1086/316573>.
- [50] Matthew Newby. Galaxy rotation curve. URL <https://milkyway.cs.rpi.edu/milkyway/science.php>.
- [51] J. P. Ostriker and P. J. E. Peebles. A Numerical Study of the Stability of Flattened Galaxies: or, can Cold Galaxies Survive? *The Astrophysical Journal*, 186:467–480, dec 1973. doi: 10.1086/152513.

- [52] Donald Lynden-Bell. Statistical mechanics of violent relaxation in stellar systems. *Mon. Not. Roy. Astron. Soc.*, 136:101–121, 1967.
- [53] D. Fabricant, M. Lecar, and P. Gorenstein. X-ray measurements of the mass of M 87. *The Astrophysical Journal*, 241:552–560, October 1980. doi: 10.1086/158369.
- [54] Richard Massey, Thomas Kitching, and Johan Richard. The dark matter of gravitational lensing. *Rept. Prog. Phys.*, 73:086901, 2010. doi: 10.1088/0034-4885/73/8/086901.
- [55] Douglas Clowe, Marusa Bradac, Anthony H. Gonzalez, Maxim Markevitch, Scott W. Randall, Christine Jones, and Dennis Zaritsky. A direct empirical proof of the existence of dark matter. *Astrophys. J. Lett.*, 648:L109–L113, 2006. doi: 10.1086/508162.
- [56] Philip Tanedo. Notes on dark matter and particle physics. URL <https://www.physics.uci.edu/~tanedo/files/notes/DMNotes.pdf>.
- [57] Y. Shadmi. Introduction to Supersymmetry. pages 95–123, 2016. doi: 10.5170/CERN-2016-003.95.
- [58] Ethan Siegel. String Theory: A dream and a nightmare. URL <https://www.sott.net/article/431189-String-Theory-A-dream-and-a-nightmare>.
- [59] A. Arbey and F. Mahmoudi. Dark matter and the early Universe: a review. *Prog. Part. Nucl. Phys.*, 119:103865, 2021. doi: 10.1016/j.pnpnp.2021.103865.
- [60] Matts Roos. Expansion of the Universe - Standard Big Bang Model. 2 2008.
- [61] Ruth Durrer. *The Cosmic Microwave Background*. Cambridge University Press, 2008. ISBN 9780521847049. URL <http://proxy.library.vanderbilt.edu/login?url=https://search.ebscohost.com/login.aspx?direct=true&db=e000xna&AN=244502&site=ehost-live&scope=site>.
- [62] N. Aghanim et al. Planck 2018 results. VI. Cosmological parameters. *Astron. Astrophys.*, 641: A6, 2020. doi: 10.1051/0004-6361/201833910. [Erratum: *Astron. Astrophys.* 652, C4 (2021)].
- [63] Katherine Garrett and Gintaras Duda. Dark Matter: A Primer. *Adv. Astron.*, 2011:968283, 2011. doi: 10.1155/2011/968283.
- [64] Horst Schmidt-Böcking, Lothar Schmidt, Hans Jürgen Lüdde, Wolfgang Trageser, Alan Templeton, and Tilman Sauer. The stern-gerlach experiment revisited. *The European Physical Journal H*, 41(4):327–364, 2016.
- [65] Gordon Kane, Kuver Sinha, and Scott Watson. Cosmological Moduli and the Post-Inflationary Universe: A Critical Review. *Int. J. Mod. Phys. D*, 24(08):1530022, 2015. doi: 10.1142/S0218271815300220.
- [66] Patrick Brown. Non-standard thermal histories and temperature of the Universe. URL https://physics.unm.edu/pandaweb/undergraduate/programs/honorsThesis/2019_Brown.pdf.
- [67] Luis Aparicio, Michele Cicoli, Bhaskar Dutta, Francesco Muia, and Fernando Quevedo. Light Higgsino Dark Matter from Non-thermal Cosmology. *JHEP*, 11:038, 2016. doi: 10.1007/JHEP11(2016)038.
- [68] Rouzbeh Allahverdi, Bhaskar Dutta, and Kuver Sinha. Non-thermal Higgsino Dark Matter: Cosmological Motivations and Implications for a 125 GeV Higgs. *Phys. Rev. D*, 86:095016, 2012. doi: 10.1103/PhysRevD.86.095016.
- [69] H.E. Haber and G.L. Kane. The search for supersymmetry: Probing physics beyond the standard model. *Physics Reports*, 117(2):75–263, 1985. ISSN 0370-1573. doi: [https://doi.org/10.1016/0370-1573\(85\)90051-1](https://doi.org/10.1016/0370-1573(85)90051-1). URL <https://www.sciencedirect.com/science/article/pii/0370157385900511>.

- [70] Cardona Natalia, Flórez Andrés, Gurrola Alfredo, Johns Will, Sheldon Paul, and Tao cheng. Long-term LHC Discovery Reach for Compressed Higgsino-like Models using VBF Processes. 2 2021.
- [71] Dark matter. URL <https://particleastro.brown.edu/dark-matter/>.
- [72] Marta Felcini. Searches for Dark Matter Particles at the LHC. Technical report, CERN, Geneva, Aug 2018. URL <https://cds.cern.ch/record/2638603>. 10 pages, 7 figures, Proceedings of the 53rd Rencontres de Moriond on Cosmology, March 17-24 2018, on behalf of the ATLAS and CMS collaborations.
- [73] Michael Rauch. Vector-Boson Fusion and Vector-Boson Scattering. 10 2016.
- [74] Vardan Khachatryan et al. Search for supersymmetry in the vector-boson fusion topology in proton-proton collisions at $\sqrt{s} = 8$ TeV. *JHEP*, 11:189, 2015. doi: 10.1007/JHEP11(2015)189.
- [75] Vardan Khachatryan et al. Search for Dark Matter and Supersymmetry with a Compressed Mass Spectrum in the Vector Boson Fusion Topology in Proton-Proton Collisions at $\sqrt{s} = 8$ TeV. *Phys. Rev. Lett.*, 118(2):021802, 2017. doi: 10.1103/PhysRevLett.118.021802.
- [76] Stuart Raby and Geoffrey West. Experimental Consequences and Constraints for Magninos. *Phys. Lett. B*, 194:557–562, 1987. doi: 10.1016/0370-2693(87)90234-6.
- [77] Stuart Raby and Geoffrey West. Detection of Galactic Halo Magninos via Their Coherent Interaction With Heavy Nuclei. *Phys. Lett. B*, 200:547–552, 1988. doi: 10.1016/0370-2693(88)90169-4.
- [78] John Bagnasco, Michael Dine, and Scott D. Thomas. Detecting technibaryon dark matter. *Phys. Lett. B*, 320:99–104, 1994. doi: 10.1016/0370-2693(94)90830-3.
- [79] Kris Sigurdson, Michael Doran, Andriy Kurylov, Robert R. Caldwell, and Marc Kamionkowski. Dark-matter electric and magnetic dipole moments. *Phys. Rev. D*, 70:083501, 2004. doi: 10.1103/PhysRevD.70.083501. [Erratum: Phys.Rev.D 73, 089903 (2006)].
- [80] Maxim Pospelov and Tonnis ter Veldhuis. Direct and indirect limits on the electromagnetic form-factors of WIMPs. *Phys. Lett. B*, 480:181–186, 2000. doi: 10.1016/S0370-2693(00)00358-0.
- [81] Jean-Francois Fortin and Tim M. P. Tait. Collider Constraints on Dipole-Interacting Dark Matter. *Phys. Rev. D*, 85:063506, 2012. doi: 10.1103/PhysRevD.85.063506.
- [82] Tom Banks, Jean-Francois Fortin, and Scott Thomas. Direct Detection of Dark Matter Electromagnetic Dipole Moments. 7 2010.
- [83] Oleg Antipin, Michele Redi, Alessandro Strumia, and Elena Vigiani. Accidental Composite Dark Matter. *JHEP*, 07:039, 2015. doi: 10.1007/JHEP07(2015)039.
- [84] Moira I. Gresham and Kathryn M. Zurek. Light Dark Matter Anomalies After LUX. *Phys. Rev. D*, 89(1):016017, 2014. doi: 10.1103/PhysRevD.89.016017.
- [85] A. Liam Fitzpatrick and Kathryn M. Zurek. Dark Moments and the DAMA-CoGeNT Puzzle. *Phys. Rev. D*, 82:075004, 2010. doi: 10.1103/PhysRevD.82.075004.
- [86] Vernon Barger, Wai-Yee Keung, and Danny Marfatia. Electromagnetic properties of dark matter: Dipole moments and charge form factor. *Phys. Lett. B*, 696:74–78, 2011. doi: 10.1016/j.physletb.2010.12.008.
- [87] Chiu Man Ho and Robert J. Scherrer. Anapole Dark Matter. *Phys. Lett. B*, 722:341–346, 2013. doi: 10.1016/j.physletb.2013.04.039.

- [88] Andrés Flórez, Alfredo Gurrola, Will Johns, Jessica Maruri, Paul Sheldon, Kuver Sinha, and Savanna Rae Starko. Anapole Dark Matter via Vector Boson Fusion Processes at the LHC. *Phys. Rev. D*, 100(1):016017, 2019. doi: 10.1103/PhysRevD.100.016017.
- [89] Lyndon Evans and Philip Bryant. Lhc machine. *Journal of Instrumentation*, 3(08):S08001, 2008. URL <http://stacks.iop.org/1748-0221/3/i=08/a=S08001>.
- [90] *ALICE: Technical proposal for a Large Ion collider Experiment at the CERN LHC*. LHC Tech. Proposal. CERN, Geneva, 1995. URL <https://cds.cern.ch/record/293391>.
- [91] A. Airapetian et al. *ATLAS detector and physics performance: Technical Design Report, 1*. Technical Design Report ATLAS. CERN, Geneva, 1999. URL <https://cds.cern.ch/record/391176>.
- [92] *Technical proposal*. LHC Tech. Proposal. CERN, Geneva, 1994. URL <https://cds.cern.ch/record/290969>. Cover title : CMS, the Compact Muon Solenoid : technical proposal.
- [93] *LHCb : Technical Proposal*. Tech. Proposal. CERN, Geneva, 1998. URL <https://cds.cern.ch/record/622031>.
- [94] Jean-Luc Caron. Overall view of LHC experiments.. Vue d'ensemble des experiences du LHC. AC Collection. Legacy of AC. Pictures from 1992 to 2002., May 1998. URL <https://cds.cern.ch/record/841555>.
- [95] Maria Kuhn. Emittance Preservation at the LHC. Master's thesis, Hamburg U., 3 2013.
- [96] Jamie Boyd (CERN). The lhc machine in run-2, and physics highlights from the atlas experiment. URL <http://www.ccsem.infn.it/issp2018/docs/talkBoyd.pdf>.
- [97] Cinzia De Melis. The CERN accelerator complex. Complexe des accélérateurs du CERN. Jul 2016. URL <https://cds.cern.ch/record/2197559>. General Photo.
- [98] S. Chatrchyan et al. The CMS experiment at the CERN LHC. *JINST*, 3:S08004, 2008. doi: 10.1088/1748-0221/3/08/S08004.
- [99] How cms works? URL <https://cms.cern/detector>.
- [100] Siona Ruth Davis. Interactive Slice of the CMS detector. Aug 2016. URL <https://cds.cern.ch/record/2205172>.
- [101] CMS collaboration. Identifying tracks: Silicon pixels. URL <https://cms.cern/detector/identifying-tracks/silicon-pixels>.
- [102] Katja Klein. The phase-1 upgrade of the cms pixel detector. *Nuclear Instruments and Methods in Physics Research Section A: Accelerators, Spectrometers, Detectors and Associated Equipment*, 845:101–105, 2017. ISSN 0168-9002. doi: <https://doi.org/10.1016/j.nima.2016.06.039>. URL <https://www.sciencedirect.com/science/article/pii/S0168900216305824>. Proceedings of the Vienna Conference on Instrumentation 2016.
- [103] Oliver Pooth. The cms silicon tracker. *Nuclear Instruments and Methods in Physics Research. Section A, Accelerators, Spectrometers, Detectors and Associated Equipment*, 569(1):21–24, 2006. ISSN 0168-9002. doi: 10.1016/j.nima.2006.09.052. URL <https://browzine.com/articles/60426951>.
- [104] *The CMS electromagnetic calorimeter project: Technical Design Report*. Technical Design Report CMS. CERN, Geneva, 1997. URL <https://cds.cern.ch/record/349375>.
- [105] *The CMS hadron calorimeter project: Technical Design Report*. Technical Design Report CMS. CERN, Geneva, 1997. URL <https://cds.cern.ch/record/357153>.

- [106] Albert M Sirunyan et al. Calibration of the CMS hadron calorimeters using proton-proton collision data at $\sqrt{s} = 13$ TeV. *JINST*, 15(05):P05002, 2020. doi: 10.1088/1748-0221/15/05/P05002.
- [107] Serguei Chatrchyan et al. The performance of the CMS muon detector in proton-proton collisions at $\sqrt{s} = 7$ TeV at the LHC. *JINST*, 8:P11002, 2013. doi: 10.1088/1748-0221/8/11/P11002.
- [108] *The CMS muon project: Technical Design Report*. Technical Design Report CMS. CERN, Geneva, 1997. URL <https://cds.cern.ch/record/343814>.
- [109] The Phase-2 Upgrade of the CMS Muon Detectors. Technical report, CERN, Geneva, Sep 2017. URL <https://cds.cern.ch/record/2283189>. This is the final version, approved by the LHCC.
- [110] Vardan Khachatryan et al. The CMS trigger system. *JINST*, 12(01):P01020, 2017. doi: 10.1088/1748-0221/12/01/P01020.
- [111] A. M. Sirunyan et al. Particle-flow reconstruction and global event description with the CMS detector. *JINST*, 12(10):P10003, 2017. doi: 10.1088/1748-0221/12/10/P10003.
- [112] Wolfgang Adam, Boris Mangano, Thomas Speer, and Teddy Todorov. Track Reconstruction in the CMS tracker. Technical report, CERN, Geneva, Dec 2006. URL <https://cds.cern.ch/record/934067>.
- [113] Studies of Tracker Material. Technical report, 2010. URL <https://cds.cern.ch/record/1279138>.
- [114] Vardan Khachatryan et al. CMS Tracking Performance Results from Early LHC Operation. *Eur. Phys. J. C*, 70:1165–1192, 2010. doi: 10.1140/epjc/s10052-010-1491-3.
- [115] W Adam, R Frühwirth, A Strandlie, and T Todorov. Reconstruction of electrons with the gaussian-sum filter in the cms tracker at the lhc. *Journal of Physics G: Nuclear and Particle Physics*, 31(9):N9–N20, Jul 2005. ISSN 1361-6471. doi: 10.1088/0954-3899/31/9/n01. URL <http://dx.doi.org/10.1088/0954-3899/31/9/N01>.
- [116] Biao Huang Nima Sammaknejad, Yujia Zhao. A review of the Expectation Maximization algorithm in data-driven process identification. *Journal of Process Control*, 73:123–136, 2019. ISSN 0959-1524. doi: <https://doi.org/10.1016/j.jprocont.2018.12.010>.
- [117] Serguei Chatrchyan et al. Energy Calibration and Resolution of the CMS Electromagnetic Calorimeter in pp Collisions at $\sqrt{s} = 7$ TeV. *JINST*, 8:P09009, 2013. doi: 10.1088/1748-0221/8/09/P09009.
- [118] S. Agostinelli et al. Geant4—a simulation toolkit. *Nuclear Instruments and Methods in Physics Research Section A: Accelerators, Spectrometers, Detectors and Associated Equipment*, 506(3): 250–303, 2003. ISSN 0168-9002. doi: [https://doi.org/10.1016/S0168-9002\(03\)01368-8](https://doi.org/10.1016/S0168-9002(03)01368-8). URL <https://www.sciencedirect.com/science/article/pii/S0168900203013688>.
- [119] Vardan Khachatryan et al. Performance of Photon Reconstruction and Identification with the CMS Detector in Proton-Proton Collisions at $\sqrt{s} = 8$ TeV. *JINST*, 10(08):P08010, 2015. doi: 10.1088/1748-0221/10/08/P08010.
- [120] Serguei Chatrchyan et al. Performance of CMS Muon Reconstruction in pp Collision Events at $\sqrt{s} = 7$ TeV. *JINST*, 7:P10002, 2012. doi: 10.1088/1748-0221/7/10/P10002.
- [121] Vardan Khachatryan et al. Jet energy scale and resolution in the CMS experiment in pp collisions at 8 TeV. *JINST*, 12(02):P02014, 2017. doi: 10.1088/1748-0221/12/02/P02014.
- [122] Serguei Chatrchyan et al. Description and performance of track and primary-vertex reconstruction with the CMS tracker. *JINST*, 9(10):P10009, 2014. doi: 10.1088/1748-0221/9/10/P10009.

- [123] Matteo Cacciari and Gavin P. Salam. Pileup subtraction using jet areas. *Phys. Lett. B*, 659: 119–126, 2008. doi: 10.1016/j.physletb.2007.09.077.
- [124] Matteo Cacciari, Gavin P. Salam, and Gregory Soyez. The Catchment Area of Jets. *JHEP*, 04:005, 2008. doi: 10.1088/1126-6708/2008/04/005.
- [125] Serguei Chatrchyan et al. Measurement of the Inelastic Proton-Proton Cross Section at $\sqrt{s} = 7$ TeV. *Phys. Lett. B*, 722:5–27, 2013. doi: 10.1016/j.physletb.2013.03.024.
- [126] Albert M Sirunyan et al. Measurement of the inelastic proton-proton cross section at $\sqrt{s} = 13$ TeV. *JHEP*, 07:161, 2018. doi: 10.1007/JHEP07(2018)161.
- [127] A. M. Sirunyan et al. Performance of the CMS muon detector and muon reconstruction with proton-proton collisions at $\sqrt{s} = 13$ TeV. *JINST*, 13(06):P06015, 2018. doi: 10.1088/1748-0221/13/06/P06015.
- [128] Armen Tumasyan et al. Search for supersymmetry in final states with two or three soft leptons and missing transverse momentum in proton-proton collisions at $\sqrt{s} = 13$ TeV. 11 2021.
- [129] Albert M Sirunyan et al. Electron and photon reconstruction and identification with the CMS experiment at the CERN LHC. *JINST*, 16(05):P05014, 2021. doi: 10.1088/1748-0221/16/05/P05014.
- [130] Claire Shepherd-Themistocleous Sam Harper. Improving sigma eta eta. CMS EGamma guide to Shower Shape. Last accessed: 04/25/2022. URL <https://twiki.cern.ch/twiki/bin/view/CMSPublic/SWGuideEgammaShowerShape>.
- [131] Matteo Cacciari, Gavin P. Salam, and Gregory Soyez. FastJet User Manual. *Eur. Phys. J. C*, 72:1896, 2012. doi: 10.1140/epjc/s10052-012-1896-2.
- [132] Matteo Cacciari, Gavin P. Salam, and Gregory Soyez. The anti- k_t jet clustering algorithm. *JHEP*, 04:063, 2008. doi: 10.1088/1126-6708/2008/04/063.
- [133] Jet energy scale and resolution performance with 13 TeV data collected by CMS in 2016-2018. Apr 2020. URL <https://cds.cern.ch/record/2715872>.
- [134] The CMS collaboration. Determination of jet energy calibration and transverse momentum resolution in cms. *Journal of Instrumentation*, 6(11):P11002–P11002, Nov 2011. ISSN 1748-0221. doi: 10.1088/1748-0221/6/11/p11002. URL <http://dx.doi.org/10.1088/1748-0221/6/11/P11002>.
- [135] Jet algorithms performance in 13 TeV data. Technical report, CERN, Geneva, 2017. URL <https://cds.cern.ch/record/2256875>.
- [136] Albert M Sirunyan et al. Pileup mitigation at CMS in 13 TeV data. *JINST*, 15(09):P09018, 2020. doi: 10.1088/1748-0221/15/09/P09018.
- [137] Albert M Sirunyan et al. Performance of missing transverse momentum reconstruction in proton-proton collisions at $\sqrt{s} = 13$ TeV using the CMS detector. *JINST*, 14(07):P07004, 2019. doi: 10.1088/1748-0221/14/07/P07004.
- [138] Vardan Khachatryan et al. Reconstruction and identification of τ lepton decays to hadrons and τ_h at CMS. *JINST*, 11(01):P01019, 2016. doi: 10.1088/1748-0221/11/01/P01019.
- [139] Sebastien Brommer Janek Bechtel. Tau leptons. Talk presented at the 2019 CMS Physics Object School. Last accessed: 04/26/2022. URL <https://indico.cern.ch/event/797855/timetable/>.
- [140] A. M. Sirunyan et al. Performance of reconstruction and identification of τ leptons decaying to hadrons and ν_τ in pp collisions at $\sqrt{s} = 13$ TeV. *JINST*, 13(10):P10005, 2018. doi: 10.1088/1748-0221/13/10/P10005.

- [141] Armen Tumasyan et al. Identification of hadronic tau lepton decays using a deep neural network. 1 2022.
- [142] A. M. Sirunyan et al. Identification of heavy-flavour jets with the CMS detector in pp collisions at 13 TeV. *JINST*, 13(05):P05011, 2018. doi: 10.1088/1748-0221/13/05/P05011.
- [143] Serguei Chatrchyan et al. Identification of b-Quark Jets with the CMS Experiment. *JINST*, 8:P04013, 2013. doi: 10.1088/1748-0221/8/04/P04013.
- [144] Daniel Guest, Julian Collado, Pierre Baldi, Shih-Chieh Hsu, Gregor Urban, and Daniel Whiteson. Jet Flavor Classification in High-Energy Physics with Deep Neural Networks. *Phys. Rev. D*, 94(11):112002, 2016. doi: 10.1103/PhysRevD.94.112002.
- [145] Heavy flavor identification at CMS with deep neural networks. Mar 2017. URL <https://cds.cern.ch/record/2255736>.
- [146] Torbjörn Sjöstrand, Stefan Ask, Jesper R. Christiansen, Richard Corke, Nishita Desai, Philip Ilten, Stephen Mrenna, Stefan Prestel, Christine O. Rasmussen, and Peter Z. Skands. An Introduction to PYTHIA 8.2. *Comput. Phys. Commun.*, 191:159–177, 2015. doi: 10.1016/j.cpc.2015.01.024.
- [147] Vardan Khachatryan et al. Event generator tunes obtained from underlying event and multiparton scattering measurements. *Eur. Phys. J. C*, 76(3):155, 2016. doi: 10.1140/epjc/s10052-016-3988-x.
- [148] Albert M Sirunyan et al. Extraction and validation of a new set of CMS PYTHIA8 tunes from underlying-event measurements. *Eur. Phys. J. C*, 80(1):4, 2020. doi: 10.1140/epjc/s10052-019-7499-4.
- [149] Sea Agostinelli, John Allison, K al Amako, John Apostolakis, H Araujo, Pedro Arce, Makoto Asai, D Axen, Swagato Banerjee, GJNI Barrand, et al. Geant4—a simulation toolkit. *Nuclear instruments and methods in physics research section A: Accelerators, Spectrometers, Detectors and Associated Equipment*, 506(3):250–303, 2003.
- [150] J. Alwall, R. Frederix, S. Frixione, V. Hirschi, F. Maltoni, O. Mattelaer, H. S. Shao, T. Stelzer, P. Torrielli, and M. Zaro. The automated computation of tree-level and next-to-leading order differential cross sections, and their matching to parton shower simulations. *JHEP*, 07:079, 2014. doi: 10.1007/JHEP07(2014)079.
- [151] Richard D. Ball et al. Parton distributions from high-precision collider data. *Eur. Phys. J. C*, 77(10):663, 2017. doi: 10.1140/epjc/s10052-017-5199-5.
- [152] Rikkert Frederix, Emanuele Re, and Paolo Torrielli. Single-top t-channel hadroproduction in the four-flavour scheme with POWHEG and aMC@NLO. *JHEP*, 09:130, 2012. doi: 10.1007/JHEP09(2012)130.
- [153] Paolo Nason. A New method for combining NLO QCD with shower Monte Carlo algorithms. *JHEP*, 11:040, 2004. doi: 10.1088/1126-6708/2004/11/040.
- [154] Stefano Frixione, Paolo Nason, and Carlo Oleari. Matching NLO QCD computations with Parton Shower simulations: the POWHEG method. *JHEP*, 11:070, 2007. doi: 10.1088/1126-6708/2007/11/070.
- [155] Simone Alioli, Paolo Nason, Carlo Oleari, and Emanuele Re. A general framework for implementing NLO calculations in shower Monte Carlo programs: the POWHEG BOX. *JHEP*, 06:043, 2010. doi: 10.1007/JHEP06(2010)043.
- [156] Emanuele Re. Single-top Wt-channel production matched with parton showers using the POWHEG method. *Eur. Phys. J. C*, 71:1547, 2011. doi: 10.1140/epjc/s10052-011-1547-z.

- [157] Richard D. Ball et al. Parton distributions for the LHC Run II. *JHEP*, 04:040, 2015. doi: 10.1007/JHEP04(2015)040.
- [158] Johan Alwall et al. Comparative study of various algorithms for the merging of parton showers and matrix elements in hadronic collisions. *Eur. Phys. J. C*, 53:473–500, 2008. doi: 10.1140/epjc/s10052-007-0490-5.
- [159] Vardan Khachatryan et al. The CMS trigger system. *JINST*, 12(01):P01020, 2017. doi: 10.1088/1748-0221/12/01/P01020.
- [160] Sergio Cittolin, Attila Rácz, and Paris Sphicas. *CMS The TriDAS Project: Technical Design Report, Volume 2: Data Acquisition and High-Level Trigger. CMS trigger and data-acquisition project*. Technical design report. CMS. CERN, Geneva, 2002. URL <http://cds.cern.ch/record/578006>.
- [161] Glen Cowan, Kyle Cranmer, Eilam Gross, and Ofer Vitells. Asymptotic formulae for likelihood-based tests of new physics. *The European Physical Journal C*, 71(2):1–19, 2011.
- [162] P.A. Zyla et al. Review of Particle Physics. *PTEP*, 2020(8):083C01, 2020. doi: 10.1093/ptep/ptaa104. and 2021 update.
- [163] Lorenzo Moneta, Kevin Belasco, Kyle Cranmer, Sven Kreiss, Alfio Lazzaro, Danilo Piparo, Gregory Schott, Wouter Verkerke, and Matthias Wolf. The roostats project. *arXiv preprint arXiv:1009.1003*, 2010.
- [164] Ilka Antcheva, Maarten Ballintijn, Bertrand Bellenot, Marek Biskup, Rene Brun, Nenad Buncic, Ph Canal, Diego Casadei, Olivier Couet, Valery Fine, et al. Root—a c++ framework for petabyte data storage, statistical analysis and visualization. *Computer Physics Communications*, 180(12):2499–2512, 2009.
- [165] Wouter Verkerke and David Kirkby. The roofit toolkit for data modeling. In *Statistical Problems in Particle Physics, Astrophysics and Cosmology*, pages 186–189. World Scientific, 2006.
- [166] Albert M Sirunyan et al. Search for new physics in events with two soft oppositely charged leptons and missing transverse momentum in proton-proton collisions at $\sqrt{s} = 13$ TeV. *Phys. Lett. B*, 782:440–467, 2018. doi: 10.1016/j.physletb.2018.05.062.
- [167] Gregor Kasieczka, Benjamin Nachman, Matthew D. Schwartz, and David Shih. Automating the ABCD method with machine learning. *Phys. Rev. D*, 103(3):035021, 2021. doi: 10.1103/PhysRevD.103.035021.
- [168] Suyong Choi and Hayoung Oh. Improved extrapolation methods of data-driven background estimations in high energy physics. *Eur. Phys. J. C*, 81(7):643, 2021. doi: 10.1140/epjc/s10052-021-09404-1.
- [169] Deepak Kar. Uncertainties. In *Experimental Particle Physics*, 2053-2563, pages 6–1 to 6–11. IOP Publishing, 2019. ISBN 978-0-7503-2112-9. doi: 10.1088/2053-2563/ab1be6ch6. URL <https://dx.doi.org/10.1088/2053-2563/ab1be6ch6>.
- [170] Louis Lyons. *Statistics for Nuclear and Particle Physicists*. Cambridge University Press, 1986. doi: 10.1017/CBO9781139167710.
- [171] Albert M Sirunyan et al. Search for supersymmetry with a compressed mass spectrum in the vector boson fusion topology with 1-lepton and 0-lepton final states in proton-proton collisions at $\sqrt{s} = 13$ TeV. *JHEP*, 08:150, 2019. doi: 10.1007/JHEP08(2019)150.
- [172] A. Heister et al. Absolute mass lower limit for the lightest neutralino of the MSSM from e+e- data at $s^{**}(1/2)$ up to 209-GeV. *Phys. Lett. B*, 583:247–263, 2004. doi: 10.1016/j.physletb.2003.12.066.

- [173] A. Heister et al. Search for charginos nearly mass degenerate with the lightest neutralino in e^+e^- collisions at center-of-mass energies up to 209-GeV. *Phys. Lett. B*, 533:223–236, 2002. doi: 10.1016/S0370-2693(02)01584-8.
- [174] G. Abbiendi et al. Search for nearly mass degenerate charginos and neutralinos at LEP. *Eur. Phys. J. C*, 29:479–489, 2003. doi: 10.1140/epjc/s2003-01237-x.
- [175] M. Acciarri et al. Search for charginos with a small mass difference with the lightest supersymmetric particle at $\sqrt{S} = 189$ -GeV. *Phys. Lett. B*, 482:31–42, 2000. doi: 10.1016/S0370-2693(00)00488-3.
- [176] Albert M Sirunyan et al. Search for Supersymmetry with a Compressed Mass Spectrum in Events with a Soft τ Lepton, a Highly Energetic Jet, and Large Missing Transverse Momentum in Proton-Proton Collisions at $\sqrt{s} = \text{TeV}$. *Phys. Rev. Lett.*, 124(4):041803, 2020. doi: 10.1103/PhysRevLett.124.041803.
- [177] Georges Aad et al. Searches for electroweak production of supersymmetric particles with compressed mass spectra in $\sqrt{s} = 13$ TeV pp collisions with the ATLAS detector. *Phys. Rev. D*, 101(5):052005, 2020. doi: 10.1103/PhysRevD.101.052005.
- [178] A. G. Agocs, G. G. Barnafoldi, and P. Levai. Underlying Event in pp Collisions at LHC Energies. In *6th International Workshop on High-pT physics at LHC (HPT 2011) Utrecht, The Netherlands, April 4-7, 2011*, 2011.
- [179] Andy Buckley et al. General-purpose event generators for LHC physics. *Phys. Rept.*, 504:145–233, 2011. doi: 10.1016/j.physrep.2011.03.005.
- [180] R. Keith Ellis, W. James Stirling, and B. R. Webber. QCD and collider physics. *Camb. Monogr. Part. Phys. Nucl. Phys. Cosmol.*, 8:1–435, 1996.
- [181] Mark Thomson. *Modern particle physics*. Cambridge University Press, New York, 2013. ISBN 9781107034266. URL <http://www-spines.fnal.gov/spines/find/books/www?cl=QC793.2.T46::2013>.
- [182] F. Halzen and Alan D. Martin. *Quarks and Leptons: An Introductory Course In Modern Particle Physics*. 1984. ISBN 0471887412, 9780471887416.
- [183] Ramona Vogt. *Ultrarelativistic heavy-ion collisions*. Elsevier, Amsterdam, 2007. ISBN 97804444521965.
- [184] William A. Bardeen, A. J. Buras, D. W. Duke, and T. Muta. Deep Inelastic Scattering Beyond the Leading Order in Asymptotically Free Gauge Theories. *Phys. Rev.*, D18:3998, 1978. doi: 10.1103/PhysRevD.18.3998.
- [185] V. N. Gribov and L. N. Lipatov. Deep inelastic $e p$ scattering in perturbation theory. *Sov. J. Nucl. Phys.*, 15:438–450, 1972. [*Yad. Fiz.*15,781(1972)].
- [186] Valery A. Khoze, Wolfgang Ochs, and Jacek Wosiek. Analytical QCD and multiparticle production. 2000. doi: 10.1142/9789812810458_0028.
- [187] David J. Gross and Frank Wilczek. Ultraviolet Behavior of Nonabelian Gauge Theories. *Phys. Rev. Lett.*, 30:1343–1346, 1973. doi: 10.1103/PhysRevLett.30.1343. [,271(1973)].
- [188] H. David Politzer. Reliable Perturbative Results for Strong Interactions? *Phys. Rev. Lett.*, 30:1346–1349, 1973. doi: 10.1103/PhysRevLett.30.1346. [,274(1973)].
- [189] Yuri L. Dokshitzer, Valery A. Khoze, Alfred H. Mueller, and S. I. Troian. *Basics of perturbative QCD*. 1991.

- [190] B. R. Webber. Hadronization. In *Proceedings: Summer School on Hadronic Aspects of Collider Physics, Zuoz, Switzerland, Aug 23-31, 1994*, pages 49–77, 1994.
- [191] Yuri L. Dokshitzer, Valery A. Khoze, and S. I. Troian. Coherence and Physics of QCD Jets. *Adv. Ser. Direct. High Energy Phys.*, 5:241–410, 1988. doi: 10.1142/9789814503266.0003.
- [192] V A Khoze, Yu L Dokshitzer, and S I Troyan. Colour coherence in QCD jets. (LU-TP-90-12): 16 p, Oct 1990. URL <https://cds.cern.ch/record/216672>.
- [193] G Marchesini and Bryan R Webber. Simulation of QCD jets including soft gluon interference. *Nucl. Phys. B*, 238(CERN-TH-3525):1–29. 39 p, Feb 1983. URL <http://cds.cern.ch/record/143716>.
- [194] A.E. Chudakov. A study of nucleon interaction with light nuclei at the energy range of $10^9 + 10^{12}$ eV. *Izvest. Akad. Nauk S.S.S.R. Ser. Fiz.*, 19(650), 1955.
- [195] Stephen Mrenna and Peter Richardson. Matching matrix elements and parton showers with HERWIG and PYTHIA. *JHEP*, 05:040, 2004. doi: 10.1088/1126-6708/2004/05/040.
- [196] Nils Lavesson and Leif Lönnblad. Merging parton showers and matrix elements—back to basics. *Journal of High Energy Physics*, 2008(04):085–085, apr 2008. doi: 10.1088/1126-6708/2008/04/085. URL <https://doi.org/10.1088%2F1126-6708%2F2008%2F04%2F085>.
- [197] Stefan Höche. Introduction to parton-shower event generators. In *Proceedings, Theoretical Advanced Study Institute in Elementary Particle Physics: Journeys Through the Precision Frontier: Amplitudes for Colliders (TASI 2014): Boulder, Colorado, June 2-27, 2014*, pages 235–295, 2015. doi: 10.1142/9789814678766.0005.
- [198] Stefano Frixione and Bryan R. Webber. Matching NLO QCD computations and parton shower simulations. *JHEP*, 06:029, 2002. doi: 10.1088/1126-6708/2002/06/029.
- [199] S. Catani, F. Krauss, R. Kuhn, and B. R. Webber. QCD matrix elements + parton showers. *JHEP*, 11:063, 2001. doi: 10.1088/1126-6708/2001/11/063.
- [200] Leif Lonnblad. Correcting the color dipole cascade model with fixed order matrix elements. *JHEP*, 05:046, 2002. doi: 10.1088/1126-6708/2002/05/046.
- [201] M. Mangano. The so-called MLM prescription for ME/PS matching. 2002. URL <http://www-cpd.fnal.gov/personal/mrenna/tuning/nov2002/mlm.pdf.gz>.
- [202] Stefan Hoeche, Frank Krauss, Nils Lavesson, Leif Lonnblad, Michelangelo Mangano, Andreas Schaliche, and Steffen Schumann. Matching parton showers and matrix elements. In *HERA and the LHC: A Workshop on the implications of HERA for LHC physics: Proceedings Part A*, pages 288–289, 2005. doi: 10.5170/CERN-2005-014.288.
- [203] Rick D. Field. The Underlying event in hard scattering processes. *eConf*, C010630:P501, 2001.
- [204] Serguei Chatrchyan et al. Measurement of the Underlying Event Activity at the LHC with $\sqrt{s} = 7$ TeV and Comparison with $\sqrt{s} = 0.9$ TeV. *JHEP*, 09:109, 2011. doi: 10.1007/JHEP09(2011)109.
- [205] L. Lönnblad. Basics of Event Generators III. 2008. URL <https://indico.desy.de/indico/event/708/>.
- [206] T. Sjöstrand. Minimum-bias and underlying event physics in PYTHIA. 2008. URL <https://indico.desy.de/indico/event/708/>.
- [207] G. Arnison et al. Hadronic Jet Production at the CERN Proton - anti-Proton Collider. *Phys. Lett.*, 132B:214, 1983. doi: 10.1016/0370-2693(83)90254-X.

- [208] Tim Martin, Peter Skands, and Sinead Farrington. Probing Collective Effects in Hadronisation with the Extremes of the Underlying Event. *Eur. Phys. J.*, C76(5):299, 2016. doi: 10.1140/epjc/s10052-016-4135-4.
- [209] Torbjorn Sjostrand, Stephen Mrenna, and Peter Z. Skands. PYTHIA 6.4 Physics and Manual. *JHEP*, 05:026, 2006. doi: 10.1088/1126-6708/2006/05/026.
- [210] G. Corcella, I. G. Knowles, G. Marchesini, S. Moretti, K. Odagiri, P. Richardson, M. H. Seymour, and B. R. Webber. HERWIG 6: An Event generator for hadron emission reactions with interfering gluons (including supersymmetric processes). *JHEP*, 01:010, 2001. doi: 10.1088/1126-6708/2001/01/010.
- [211] M. Bahr et al. Herwig++ Physics and Manual. *Eur. Phys. J.*, C58:639–707, 2008. doi: 10.1140/epjc/s10052-008-0798-9.
- [212] Johannes Bellm et al. Herwig 7.0/Herwig++ 3.0 release note. *Eur. Phys. J.*, C76(4):196, 2016. doi: 10.1140/epjc/s10052-016-4018-8.
- [213] T. Gleisberg, Stefan. Hoeche, F. Krauss, M. Schonherr, S. Schumann, F. Siegert, and J. Winter. Event generation with SHERPA 1.1. *JHEP*, 02:007, 2009. doi: 10.1088/1126-6708/2009/02/007.
- [214] R.D. Field and R.P. Feynman. A parametrization of the properties of quark jets. *Nuclear Physics B*, 136(1):1 – 76, 1978. ISSN 0550-3213. doi: [https://doi.org/10.1016/0550-3213\(78\)90015-9](https://doi.org/10.1016/0550-3213(78)90015-9). URL <http://www.sciencedirect.com/science/article/pii/0550321378900159>.
- [215] R. D. Field and R. P. Feynman. Quark Elastic Scattering as a Source of High Transverse Momentum Mesons. *Phys. Rev.*, D15:2590–2616, 1977. doi: 10.1103/PhysRevD.15.2590.
- [216] R. Cavanaugh. Lecture 22. Quantum Chromodynamics. 2018. URL <https://indico.cern.ch/event/746657/timetable/>.
- [217] Silvia Ferreres-Solé and Torbjörn Sjöstrand. The space–time structure of hadronization in the Lund model. *Eur. Phys. J.*, C78(11):983, 2018. doi: 10.1140/epjc/s10052-018-6459-8.
- [218] T. Sjöstrand. Monte Carlo. Matching MPI’s and Hadronization. 2013. URL <http://home.thep.lu.se/~torbjorn/talks/van2ho.pdf>.
- [219] T. Sjöstrand. PYTHIA and other MC generators for pp physics. 2019. URL <https://indico.lucas.lu.se/event/1065/timetable/#20190225>.
- [220] W. Bartel et al. Particle Distribution in Three Jet Events Produced by $e^+ e^-$ Annihilation. *Z. Phys.*, C21:37, 1983. doi: 10.1007/BF01648774.
- [221] D. Amati and G. Veneziano. Preconfinement as a Property of Perturbative QCD. *Phys. Lett.*, 83B:87–92, 1979. doi: 10.1016/0370-2693(79)90896-7.
- [222] Cody B. Duncan and Patrick Kirchgaeßer. Kinematic strangeness production in cluster hadronization. *Eur. Phys. J.*, C79(1):61, 2019. doi: 10.1140/epjc/s10052-019-6573-2.
- [223] S. Kretzer. Fragmentation functions from flavor inclusive and flavor tagged $e^+ e^-$ annihilations. *Phys. Rev.*, D62:054001, 2000. doi: 10.1103/PhysRevD.62.054001.
- [224] Bernd A. Kniehl, G. Kramer, and B. Potter. Fragmentation functions for pions, kaons, and protons at next-to-leading order. *Nucl. Phys.*, B582:514–536, 2000. doi: 10.1016/S0550-3213(00)00303-5.
- [225] R. Seuster et al. Charm hadrons from fragmentation and B decays in $e^+ e^-$ annihilation at $s^{*(1/2)} = 10.6\text{-GeV}$. *Phys. Rev.*, D73:032002, 2006. doi: 10.1103/PhysRevD.73.032002.

- [226] G. Abbiendi et al. Inclusive analysis of the b quark fragmentation function in Z decays at LEP. *Eur. Phys. J.*, C29:463–478, 2003. doi: 10.1140/epjc/s2003-01229-x.
- [227] Various authors. Hard Probes 2018: International Conference on Hard and Electromagnetic Probes of High-Energy Nuclear Collisions. 2018. URL <https://indico.cern.ch/event/634426/>, <https://pos.sissa.it/345/>.